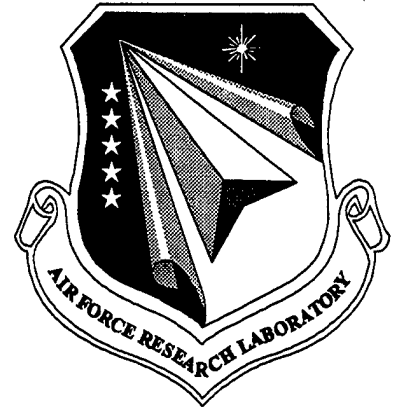


**AFRL-PR-WP-TR-1998-2101**

**COMBUSTION AND HEAT  
TRANSFER  
VOLUME 3: COMBUSTION STUDIES**



**D. R. Ballal                      F. Takahashi  
D. Pestian                      W. J. Schmoll  
M. D. Vangsness              R. Streibich**

**University of Dayton Research Institute  
300 College Park  
Dayton OH 45469-0110**

**DECEMBER 1997**

**FINAL REPORT FOR PERIOD 6/8/92 – 12/31/97**

**19990127 030**

**Approved for public release; distribution unlimited**

**PROPULSION DIRECTORATE  
AIR FORCE RESEARCH LABORATORY  
AIR FORCE MATERIEL COMMAND  
WRIGHT-PATTERSON AIR FORCE BASE, OH 45433-7251**

## NOTICE

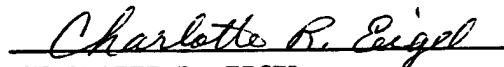
USING GOVERNMENT DRAWINGS, SPECIFICATIONS, OR OTHER DATA INCLUDED IN THIS DOCUMENT FOR ANY PURPOSE OTHER THAN GOVERNMENT PROCUREMENT DOES NOT IN ANY WAY OBLIGATE THE US GOVERNMENT. THE FACT THAT THE GOVERNMENT FORMULATED OR SUPPLIED THE DRAWINGS, SPECIFICATIONS, OR OTHER DATA DOES NOT LICENSE THE HOLDER OR ANY OTHER PERSON OR CORPORATION; OR CONVEY ANY RIGHTS OR PERMISSION TO MANUFACTURE, USE, OR SELL ANY PATENTED INVENTION THAT MAY RELATE TO THEM.

THIS REPORT IS RELEASABLE TO THE NATIONAL TECHNICAL INFORMATION SERVICE (NTIS). AT NTIS, IT WILL BE AVAILABLE TO THE GENERAL PUBLIC, INCLUDING FOREIGN NATIONS.

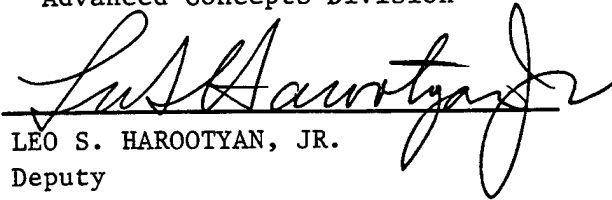
THIS TECHNICAL REPORT HAS BEEN REVIEWED AND IS APPROVED FOR PUBLICATION.



CHARLES W. FRAYNE  
Combustion Branch  
Propulsion Sciences and  
Advanced Concepts Division



CHARLOTTE R. EIGEL  
Chief, Combustion Branch  
Propulsion Sciences and  
Advanced Concepts Division



LEO S. HAROOTYAN, JR.  
Deputy  
Propulsion Sciences and  
Advanced Concepts Division

Do not return copies of this report unless contractual obligations or notice on a specific document requires its return.

# REPORT DOCUMENTATION PAGE

Form Approved OMB  
No. 0704-0188

Public reporting burden for this collection of information is estimated to average 1 hour per response, including the time for reviewing instructions, searching existing data sources, gathering and maintaining the data needed, and completing and reviewing the collection of information. Send comments regarding this burden estimate or any other aspect of this collection of information, including suggestions for reducing this burden, to Washington Headquarters Services, Directorate for Information Operations and Reports, 1215 Jefferson Davis Highway, Suite 1204, Arlington, VA 22202-4302, and to the Office of Management and Budget, Paperwork Reduction Project (0704-0188), Washington DC 20503.

1. AGENCY USE ONLY (Leave blank)		2. REPORT DATE December 1997	3. REPORT TYPE AND DATES COVERED Final 6/8/92 -- 12/31/97	
4. TITLE AND SUBTITLE COMBUSTION AND HEAT TRANSFER: Volume 3: COMBUSTION STUDIES			5. FUNDING NUMBERS C-F33615-92-C-2207 PE: 62203 PR: 3048 TA: 05 WU: AH	
6. AUTHOR(S) D. R. Ballal, F. Takahashi, D. Pestian, W. J. Schmoll, M. Vangsness, and R. Striebich				
7. PERFORMING ORGANIZATION NAME(S) AND ADDRESS(ES)  University of Dayton Research Institute 300 College Park Dayton, OH 45469-0110 50280			8. PERFORMING ORGANIZATION REPORT NUMBER  UDR-TR-1998-00095	
9. SPONSORING/MONITORING AGENCY NAME(S) AND ADDRESS(ES) Propulsion Directorate Air Force Research Laboratory Air Force Materiel Command Wright-Patterson Air Force Base OH 45433-7251 POC: Charles W. Frayne, AFRL/PRSC, 937-255-6250			10. SPONSORING/MONITORING AGENCY REPORT NUMBER  AFRL-PR-WP-TR-1998-2101	
11. SUPPLEMENTARY NOTES				
12. DISTRIBUTION / AVAILABILITY STATEMENT Approved for public release; distribution is unlimited			12b. DISTRIBUTION CODE	
13. ABSTRACT (Maximum 200 words)  The objective of the proposed research was to develop a fundamental understanding of the combustion process in a gas turbine combustor. Specifically, we performed WSR experiments, vortex-flame interaction studies, flame stabilization research, and studies of turbine blade film cooling. A toroidal WSR was used to study lean blowout, combustion efficiency, and emissions. We found that fuel hydrocarbons of different structure and (C/H) ratio produced a noticeable influence on the combustion and emissions performance of a gas turbine combustor. In the vortex-flame interaction, the extinction caused by internal vortex is primarily due to the unsteady transport effects on chemical kinetics and extinction due to external vortex is caused due to excess convective influx into the strained flame. We studied the structure and stability (especially LBO) of a turbulent swirling flame in a variety of model combustors and found that swirl promotes turbulence and creates a positive radial velocity component that increases flame spread and turbulent mixing. Our computations predicted the attached flame locations, the development of a strong inner recirculation zone, the flame lift-off height, the location of reattachment point of the recirculation bubble. In our research on turbine blade cooling, PIV measurements showed an almost doubling of the jet spread for an increase in free stream turbulence from 1% to 17%. and forcing of the film cooling flow resulted in a decrease in film cooling effectiveness by as much as 70%. Data obtained in these experiments are presented in a companion volume 4 entitled, "Combustion & Heat Transfer: Combustion Data Sets."				
14. SUBJECT TERMS Combustor Design, Flame Stabilization, Lean Blowout, Swirling Flames, Turbulent Combustion, Turbine Blade Cooling			15. NUMBER OF PAGES 260	
			16. PRICE CODE NSP	
17. SECURITY CLASSIFICATION OF REPORT UNCLASSIFIED	18. SECURITY CLASSIFICATION OF THIS PAGE UNCLASSIFIED	19. SECURITY CLASSIFICATION OF ABSTRACT UNCLASSIFIED	20. LIMITATION OF ABSTRACT SAR	

## TABLE OF CONTENTS

LIST OF TABLES .....	v
PREFACE.....	vi
1.0 INTRODUCTION.....	1
2.0 HIGHLIGHTS OF COMBUSTION STUDIES .....	2
2.1 Well Stirred Reactor (WSR) Studies .....	2
Objective	
Test Facility and Instrumentation	
Results and Discussions	
Highlights and Conclusions	
2.2 Vortex-Flame Interaction Studies.....	7
Objective	
Test Facility and Instrumentation	
Results and Discussions	
Highlights and Conclusions	
2.3 Turbulent Swirling Flame Structure and Stability .....	10
Objective	
Test Facility and Instrumentation	
Results and Discussions	
Highlights and Conclusions	
2.4 Film Cooling With High Free Stream Turbulence .....	17
Objective	
Test Facility and Instrumentation	
Results and Discussions	
Highlights and Conclusions	
3.0 SUMMARY AND CONCLUSIONS .....	19
4.0 REFERENCES.....	21
APPENDIX A.....	41
APPENDIX B.....	61
APPENDIX C.....	68
APPENDIX D.....	77
APPENDIX E.....	98
APPENDIX F.....	109
APPENDIX G.....	119
APPENDIX H.....	128
APPENDIX I.....	137
APPENDIX J.....	144
APPENDIX K.....	154
APPENDIX L.....	168



APPENDIX M.....	179
APPENDIX N .....	207
APPENDIX O .....	220
APPENDIX P .....	233

## FIGURES

Figure 1. Schematic Of The Toroidal WSR (all dimensions in mm) .....	24
Figure 2. WSR Test Facility and Associated Instrumentation .....	25
Figure 3. LBO Equivalence Ratio Versus Loading Parameter for Several Hydrocarbon Fuels.....	26
Figure 4. Combustion Efficiency Versus Fuel Carbon Number .....	26
Figure 5. Plots of Reaction Temperature for Minimum CO Emissions Versus Fuel Carbon Number .....	27
Figure 6. Emissions Index of CO Versus Fuel Carbon Number .....	27
Figure 7. Emissions Index of UHC Versus Fuel Carbon Number.....	28
Figure 8. Emissions Index of NO <sub>x</sub> Versus Fuel Carbon Number .....	28
Figure 9. Schematic of Coaxial Jet Diffusion Flame Burner .....	29
Figure 10. Velocity Vector Fields of Locally Extinguished Methane Jet Diffusion Flames .....	29
Figure 11. Sketch Illustrating Vortex-Flame Interactions in Jet Diffusion Flames.....	30
Figure 12. Schematic of (a) Double Concentric Jet Diffusion Flame Combustor, (b) Step Swirl Combustor (SSC) .....	31
Figure 13. Turbulent Intensity Distribution Across the Hydrogen Jet Flame at x = 25 mm.....	32
Figure 14. Radial Distribution of (a) Reynolds Shear Stress, and (b) axial Velocity Gradient Across the Hydrogen Jet Flame .....	32
Figure 15. LBO Data in SSC Comparing Inner Swirl Angle, Coswirl (CO), and counter swirl (ct) .....	33
Figure 16. Sketches Illustrating the Various Flame Configurations Observed in SSC.....	33
Figure 17. Schematic Diagram of a Model Research Combustor for LBO Studies.....	34
Figure 18. Sequence of Events Leading to LBO as Observed by Flame Visualization .....	35
Figure 19. LBO Versus LP Data for a Research Combustor.....	36
Figure 20. Effect of Back Pressure (Outlet Blockage) on LBO.....	36
Figure 21. Film Cooling and Heat Transfer Test Facility .....	37
Figure 22. Jet Spread for Various Blowing Ratios.....	38
Figure 23. Growth of the Shear Layer Thickness Near the Film Cooling Jet Exit.....	38
Figure 24. Film Cooling Effectiveness With Downstream Distance With and Without Forcing .....	39
Figure 25. Effect of Free Stream Turbulence and Forcing on Heat Transfer .....	40

## TABLES

Table 1. IHPTET-Phase III Goals and Payoffs .....	22
Table 2. WSR Test Matrix .....	22
Table 3. Vortex-Flame Interaction Test Conditions .....	23
Table 4. Experimental Test Conditions For Turbulent Swirling Jet Diffusion Flames .....	23
Table 5. Typical Flow Characteristics at the Film Cooling Station .....	23

## **PREFACE**

The University of Dayton Research Institute (UDRI), working under Air Force Contract No. F33615-92-C-2207 submitted this final report to the U.S. Air Force Wright Laboratory, Aero Propulsion and Power Directorate, Wright-Patterson AFB, OH. Mr. Charles Frayne of WL/POSC (now AFRL/PRSC) was the Contract Monitor and Dr. D. R. Ballal of the Aerospace Mechanics Division, UDRI was the Principal Investigator. This report covers work performed during the period June 8, 1992 through December 31, 1997.

The Principal Investigator wishes to express his gratitude and appreciation to Dr. W. M. Roquemore, for his encouragement and support and to Ms. Linda Nianouris for her assistance in report preparation.

## 1.0 INTRODUCTION

A long-term goal of the Air Force is to develop high-performance gas turbine engines with combustors that operate at near-stoichiometric conditions, burn broad-specification fuels, and have low maintenance and high durability. Conventional gas turbine combustor design methodology is based upon empirical correlation, experience, successful design scaling, and extensive development testing. The weakness of the traditional approach is twofold; (i) empirical correlation and phenomenological models provide limited insight into the fundamental physical and chemical processes of combustion and heat transfer, and (ii) extrapolations and radical departures are very risky--moreover the design methodology can seldom provide explanations or offer alternative solutions.

Although, the conventional approach has been amazingly successful to date, the IHPET-Phase III goals (Table 1) place tremendous demands on the engine hot-end components (combustor and turbine) by virtue of near-stoichiometric combustion. Therefore, the objective of the proposed research was to develop a fundamental understanding of the combustion process in the primary zone of a gas turbine combustor by designing a variety of laboratory experiments. These laboratory experiments also yielded benchmark quality data sets for refining existing and validating new computer-based models for predicting the performance of gas turbine combustors. Specifically, and as discussed in Phase II: Combustion Studies, Section 2.2.1 of UDRI Proposal R-8566, we proposed the following four investigations.

1. Plan and conduct combustion experiments to study combustion stability, lean blowout (LBO), and emissions using a well-stirred reactor (WSR) (section 2.2.1.2).
2. Examine vortex-flame interaction and gain insight into mixing, lean stability, ignition, and extinction (sections 2.2.1.3 and 2.2.1.4)
3. Perform studies of flame stabilization and lean blowout using a step swirl combustor (SSC) (section 2.2.1.5)
4. Study film cooling of hot-section components (e.g. turbine blade) under conditions of high free stream turbulence (section 2.2.1.7).

This report describes highlights of each of the four investigations and also presents our conclusions and directions for future research in combustion. This report is a companion to our report on Phase I: Advanced Fuels that describes our research on jet fuels (see Zabarnick et. al. 1998).

## 2.0 HIGHLIGHTS OF COMBUSTION STUDIES

To perform this research, we successfully designed and operated several laboratory combustors such as a WSR, a coflowing diffusion flame combustor, and a SSC. Each of these combustors simulated some important features of a practical gas turbine combustor. Thus, we ensured that our research results closely represent features of the combustion processes in practical combustors. In our first investigation, we performed a systematic and detailed study of the effects of fuel hydrocarbon structure on lean blowout and emissions of CO and NO<sub>x</sub>. Next, we studied the unsteady vortex-flame interactions and subsequent local extinction of a double-concentric turbulent methane jet diffusion flames stabilized on a thick-walled fuel tube. For our third investigation, we designed a SSC and studied flame length, shape, mixedness, lean blowout (LBO), and flow patterns in the combustor dome. Finally, in our fourth task, we conducted a study of flow unsteadiness and free stream turbulence on a flat-plate film cooling effectiveness.

### 2.1 Well Stirred Reactor (WSR) Studies

#### Objective

The function of an advanced combustor system in tomorrow's engine is to provide maximum heat release, high combustion efficiency, wide stability limits, minimum pressure loss, and multifuel capability. A WSR represents a laboratory simulation of the primary zone of an advanced combustor. Therefore, the objectives of this task were to study effects of fuel hydrocarbon structure, residence time, and flame temperature on WSR combustion performance such as combustion efficiency and lean blowout and emissions of unburned hydrocarbons, CO, and NO<sub>x</sub> from WSR.

Appendices A and B describe highlights of our research performed using WSR.

#### Test Facility and Instrumentation

A 250-ml toroidal WSR, as designed by Nenniger et al. [1] and modified by Zelina and Ballal [2], was used for these experiments. As shown in Fig. 1, the reactor was constructed of alumina cement, and featured a jet ring with 32 stainless steel jets, 1 mm I.D., to inject the fuel-air mixture at high subsonic velocity ( $Ma = 0.42$  to  $0.85$ ). Fig. 2 provides a schematic of the test facility and instrumentation. The WSR operated over the range of equivalence ratios  $\phi = 0.43$  to  $0.88$ , loading parameter (LP)  $\sim 1.3 \text{ g-mol/sec}\cdot\text{L}\cdot\text{atm}^{1.75}$ , residence times  $\tau \sim 5$  to  $8 \text{ msec}$  and reactor temperatures  $T_f = 1350$  to  $2000 \text{ K}$ . Hydrocarbons tested were: methane, ethane, cyclohexane, n-heptane, n-dodecane, toluene, ethylbenzene and a gaseous mix of 15 percent methane, 25 percent ethane, 60 percent ethylene by volume (a cracked fuel simulant).

The Horiba Emissions Analyzers comprised the following units: Model MPA-510 oxygen analyzer (0 to 50 volume percent), Model FIA-510 total hydrocarbon analyzer (0 to 10,000 ppm carbon), Model VIA-510 CO (0 to 20 volume percent) and CO<sub>2</sub> (0 to 100 volume percent) analyzer, and Model CLA-510 SS NO and NO<sub>x</sub> analyzer (0 to 2000 ppmV). These units were calibrated with gases of the following concentrations: hydrocarbon = 404 ppmV propane, NO =

92 ppmV, NO<sub>2</sub> = 1.6 ppmV, CO = 0.4 volume percent, O<sub>2</sub> = 4.03 or 5.02 volume percent and CO<sub>2</sub> = 11.06 volume percent. Water was scrubbed from the sample gas to a maximum dew point of 5C. All emissions are quoted on dry standard air basis.

A gas sample was drawn from the WSR by a water-cooled stainless steel probe designed by Blust et al. [3]. Hydrocarbon speciation at LBO conditions was performed by collecting sample gas in a Tedlar bag and directly injecting sample into a gas chromatograph-flame ionization detector (GC-FID, Hewlett-Packard HP 5890 A). Combustion temperature, T<sub>f</sub>, was measured by insertion of a Type B thermocouple (platinum-6% rhodium, platinum-30% rhodium) coated with alumina ceramic. Temperature measurements were corrected for heat loss by conduction and radiation to colder reactor walls, and heat gain by convection and catalysis. A vaporizer was built to prevaporize liquid fuels, mix the vaporized fuel with air, and then supply this combustible mixture to the WSR. Our test matrix is shown in Table 2.

### Results and Discussion

**Lean Blowout (LBO):** Fig. 3 shows a plot of LBO equivalence ratio,  $\phi$  vs. loading parameter LP for several hydrocarbons. Also shown are calculated stability loops for methane and ethane fuels which were calculated using the stability theory as described in detail elsewhere, e.g. Lefebvre [4]. Briefly, the rate of reaction between fuel and air is expressed by the material balance equation:

$$\eta_{\text{comb}}\phi m = CVT_f^{1/2}\exp(-E/RT_f)\rho^n x_f^r x_o^{n-r} \quad (1)$$

where  $m$  is molar flow rate of reactants,  $\rho$  is density of reactants,  $E$  is activation energy,  $x_i$  is the mole fraction of fuel,  $f$ , or oxygen,  $o$ , and superscripts  $n = 1.75$ ,  $r = 0.75$ . The global reaction order of methane and ethane was  $n = 1.75$ ; see Lefebvre [4], and  $r = n - 1$  and  $C$  is the molecular collision factor calculated as follows; see Kanury [5]:

$$C = \frac{RT_f^{1/2}}{hA} \exp\left(\frac{\Delta s^*}{R}\right) \quad (2)$$

where  $h$  is Planck's constant,  $A$  is Avagadro's number, and  $\Delta s^*$  is the entropy change between the states of activated complex and initial reactants. For lean mixtures, Eq. (1) is written as:

$$LP = \frac{m}{VP^n} = \exp\left(\frac{-E}{RT_f}\right) \frac{Cx_f^{0.75}x_o}{T_f^{1.25}\eta_{\text{comb}}\phi(R/M)^{1.75}} \quad (3)$$

Thus:

$$E = RT_f \ln\left(\frac{Cx_f^{0.75}x_o}{LP \cdot T_f^{1.25}\eta_{\text{comb}}\phi(R/M)^{1.75}}\right) \quad (4)$$

Entropy of the activated complex in Eq. (2) was found by applying a quantity of energy equal to  $E$  to the energy of reactants and evaluating entropy at this condition. Thus, to calculate  $C$  and  $E$  required iteration between Eqs. (2) and (4). In Eq. (4),  $\eta_{\text{comb}}$ ,  $LP$ ,  $T_f$ , and  $\phi$  were measured

or calculated at LBO. The stability curves in Fig. 3 were generated by varying  $\phi$  in Eq. (3), and substituting  $\eta_{\text{comb}}$  and  $T_f$  found at one LBO condition for all  $\phi$ . Also, it was possible to compute the activation energies and molecular collision factors at lean blowout by measuring  $\phi$ ,  $T_f$ , EI of CO and UHC, and flow rates of reactants, while making only an assumption of global reaction order,  $n$ . For methane, we calculated that  $E = 52 \text{ kcal/mol}$  and  $C = 9.4 \cdot 10^{14} \text{ K}^{-1/2} \text{ sec}^{-1} \text{ m}^{3n-3} \text{ mol}^{1-n}$ ; for ethane  $E = 49 \text{ kcal/mol}$  and  $C = 1.3 \cdot 10^{15} \text{ K}^{-1/2} \text{ sec}^{-1} \text{ m}^{3n-3} \text{ mol}^{1-n}$ .

**Combustion Efficiency:** Fig. 4 shows a plot of  $\eta_{\text{comb}}$  against CN. This figure illustrates that, in general, as CN increases the  $\eta_{\text{comb}}$  decreases. This relation appears to be independent of  $\phi$  or  $T_f$ . Combustion efficiency of the hydrocarbons studied herein at LBO is greater than 90 percent. Most fuels used in this experiment were single component hydrocarbons. These provide a rapid transition from combustion to extinction at LBO, and so demonstrate high  $\eta_{\text{comb}}$  up to the LBO limit. By contrast, wide-cut fuels used in practical gas turbine combustors display imprecise LBO limits due to the variability in flammability limits of the fuel components. For these fuels,  $\eta_{\text{comb}}$  is low near the LBO limit because combustion is incomplete but sustained by the most flammable components. This multicomponent characteristic is illustrated in Fig. 4 for a cracked fuel simulant (CN = 2.52), for which  $\eta_{\text{comb}}$  is slightly lower than ethane or cyclohexane.

**Emissions of CO:** CO and UHC emissions are important because they represent a direct measure of combustion inefficiency. If the combustion zone operates fuel-rich, has inadequate mixing, or is quenched by cold air, large quantities of CO (which is relatively resistant to oxidation) will be emitted due to the lack of oxygen needed to complete the reaction to  $\text{CO}_2$ , or insufficient time being provided for CO to be oxidized. UHC emissions include fuel which emerges from the combustor exit in the form of condensation or vapor, and the products of the thermal degradation of the parent fuel into species of lower molecular weight, such as methane, acetylene, ethylene and propylene. UHC emissions are associated with poor atomization, inadequate burning rates, insufficient residence time and premature quenching.

Measurements of CO emissions vs.  $T_f$  showed that, in general, all hydrocarbons exhibited a U-shaped trend in CO concentration, i.e., as temperature increased, CO concentration first decreased, a minimum was reached, and then CO increased. Fig. 5 shows the plots of temperature at which CO minima occurs versus carbon number of each hydrocarbon at residence times  $\tau = 7.3$  and 5.3 msec. This figure shows that as the carbon number of the fuel is increased,  $T_{\text{min}}$  decreases. The rule applied to alkanes and aromatics, with the cracked fuel simulant classified as an alkane. Also, the effect of decreasing residence time was to increase  $T_{\text{min}}$ . This was due to reduction of CO oxidation at short residence time, while  $\text{CO}_2$  dissociation rate proceeded quickly regardless of residence time. Results presented in Fig. 5 can be approximated by the equation ( $\tau = \text{msec}$ ):

$$T_{\text{min}} = -11.35\text{CN} - 11.27\tau + 1796 \quad (5)$$

Fig. 6 shows emissions index of CO from several hydrocarbons at several  $T_f$  plotted as a function of carbon number at residence time of 7.3 msec. Alkanes and aromatics are plotted separately, and the cracked fuel simulant is treated as an alkane. As shown, alkanes, sans methane, displayed a slight increase in CO as carbon number increased. Methane produced more CO than other hydrocarbons investigated. This was due in part to the stability of the methane molecule, which resulted in poor oxidation of methane compared to other fuels. The two



aromatics showed a reverse trend from alkanes, with a decrease in CO being observed as CN increased from 7 to 8. This observation is analogous to the difference between methane and ethane. The primary path of toluene consumption at high temperature is C-C rupture, resulting in  $C_7H_8 \rightarrow C_6H_5 + CH_3$ . C-H rupture of the methyl chain occurs quickly, but the  $C_7H_7 + H$  reaction is rapidly equilibrated, and toluene is recycled. Because of this recycling, toluene is resistant to oxidation, resulting in considerable UHC and CO in the products. Interestingly, the hydrocarbons methane and toluene that produced the most CO over the ranges of  $T_f$ , produced the least CO at LBO.

Emissions of UHC: Fig. 7 shows the emissions indices of UHC from several hydrocarbons at several  $T_f$ , plotted as a function of carbon number at residence time of 7.3 msec. As shown, alkanes showed a rapid decrease, then modest increase in UHC as carbon number increased. High UHC of methane reflected the hydrocarbon's narrow stability curve; 1500K was the LBO limit of methane. Ethane behaved more like other alkanes. Toluene produced more UHC at a given temperature than other hydrocarbons besides methane, while ethylbenzene produced a quantity of UHC more akin to alkanes of the same carbon number. As with CO, similarity between methane and ethane, toluene and ethylbenzene is observed. Of all the hydrocarbons tested at LBO, toluene and n-dodecane produced the most UHC.

Emissions of  $NO_x$ :  $NO_x$  formation in gas turbine combustors is typically associated with primary zone combustion at near-stoichiometric conditions and high-power settings. The formation of species such as NO and  $NO_2$  is a complex function of temperature, residence time, equivalence ratio, and detailed chemical kinetics. A better understanding of these effects would help designers of combustion devices to limit  $NO_x$  production without compromising combustion efficiency. A study of the chemical pathways responsible for  $NO_x$  production in a combustion environment with heavy hydrocarbons is becoming possible. The relative roles of the thermal NO (Zeldovich) mechanism, super-equilibrium effects, prompt NO mechanism,  $N_2O$  mechanism, and fuel nitrogen mechanisms are surveyed by Lefebvre [4].

Fig. 8 shows plots of EI  $NO_x$  from several hydrocarbons at  $T_f = 1800K$  and  $1950K$  vs. (C/H) ratio, with alkanes and aromatics plotted separately, and with cracked fuel simulant plotted with the alkanes. For the EI  $NO_x$  calculations, all  $NO_x$  is treated as  $NO_2$ . The hydrocarbons exhibited a gradual increase in  $NO_x$  as (C/H) ratio increased from 0.25 to 0.33 (methane to ethane). A decrease was detected between (C/H) ratio 0.33 and 0.4375 (ethane to n-heptane). Then, for (C/H) ratio > 0.4375 (n-dodecane, cyclohexane, cracked fuel simulant, respectively), an increase in  $NO_x$  was measured. Further, these trends became more apparent at higher temperature. At  $T_f = 1950 K$ , alkanes in general produced less  $NO_x$  than cracked fuel simulant ((C/H) = 0.5081). The two aromatics showed a similar increase in  $NO_x$  with (C/H) ratio, with toluene producing more  $NO_x$  than ethylbenzene. Our work suggested the following relationship:

$$NO_x = k\tau^{1/2} \exp\left(\frac{-E}{RT_f}\right) \quad (\text{ppmV}) \quad (6)$$

It was desirable to find a relation between activation energy or rate constant and a fuel property, and apply this relation to Eq. (6). An inverse third order polynomial was determined to be the best fit of the  $\ln(k)$  and  $E$  data versus  $(C/H)$  ratio. Thus:

$$E_{\text{calc}} = (A + B(C/H) + C(C/H)^2 + D(C/H)^3)^{-1} \quad (\text{kcal/g-mol}) \quad (7)$$

and

$$k = \exp(\ln(k)) = \exp((E + F(C/H) + G(C/H)^2 + H(C/H)^3)^{-1}) \quad (8)$$

where  $A = 2.432 \times 10^{-5}$ ,  $B = -3.938 \times 10^{-5}$ ,  $C = 9.237 \times 10^{-5}$ ,  $D = -6.813 \times 10^{-5}$ ,  $E = 0.08222$ ,  $F = -0.1486$ ,  $G = 0.3225$ ,  $H = -0.2249$ . Eqs. (7) and (8) have been tested over range  $0.25 \leq (C/H) \leq 0.875$ .

As shown in Fig. 8, the predictions made using Eqs. (6-8) compared favorably with measured  $\text{NO}_x$  data. This evidence suggests that designers should be concerned about the effects that decreasing hydrogen content in a fuel could have on  $\text{NO}_x$  emissions from combustors. The present work also offers some evidence that conversion to methane produces less  $\text{NO}_x$  during lean combustion with heavier fuels.

**Highlights and Conclusions:** A toroidal WSR, which represents a laboratory idealization of a primary zone of an LPP type of combustor, was used to study lean blow-out limits, combustion efficiency, and emissions from several pure hydrocarbons. Following were the highlights of this research.

1. All hydrocarbons except methane showed lean limits of  $\phi \sim 0.47$  with  $\text{LP} \sim 1.3 \text{ g-mol/sec} \cdot \text{L} \cdot \text{atm}^{1.75}$  (methane LBO was  $\phi \sim 0.55$  at similar LP). Global activation energies and collision factors were calculated via stability theory to be  $E = 52 \text{ kcal/mol}$  and  $C = 9.4 \times 10^{14} \text{ K}^{-1/2} \text{ sec}^{-1} \text{ m}^{3n-3} \text{ mol}^{1-n}$  for methane;  $E = 49 \text{ kcal/mol}$  and  $C = 1.3 \times 10^{15} \text{ K}^{-1/2} \text{ sec}^{-1} \text{ m}^{3n-3} \text{ mol}^{1-n}$  for ethane. Thus, WSR experiments yield fundamental chemical kinetic data.
2. For several different hydrocarbons, the combustion efficiency  $\eta_{\text{comb}}$  at LBO decreased as fuel carbon number increased. This relation was observed for alkanes, aromatics and cracked fuel simulant and suggests up to 2 percent drop in combustion efficiency when using heavy hydrocarbon fuels.
3. Hydrocarbons of different structure (alkanes, aromatics) and carbon number produced different amounts of CO at the same temperature and residence time. Increasing residence time decreased the concentration of CO. Eq. (5) provides a relationship between the temperature at which CO approaches a minimum concentration and the carbon number of the fuel. This relationship was consistent for alkanes and aromatics.
4. UHC concentration from alkanes at a given temperature decreased greatly from methane to ethane, but increased slightly for high carbon number hydrocarbons (i.e. n-dodecane). Toluene produced more UHC than alkanes at the same temperature (including n-heptane with the same carbon number) indicating that toluene oxidized poorly at low temperature. With respect to UHC emissions, Ethylbenzene behaved as an alkane.

5. Hydrocarbons of different structure and (C/H) ratio produced different amounts of  $\text{NO}_x$  at the same residence time. For alkanes, as (C/H) ratio increased,  $\text{NO}_x$  increased, then decreased, then increased again. For aromatics, as (C/H) ratio increased,  $\text{NO}_x$  increased. Toluene produced more  $\text{NO}_x$  than ethylbenzene. Eq. (6) provides a satisfactory prediction of  $\text{NO}_x$  emissions as a function of (C/H) ratio.

## 2.2 Vortex-Flame Interaction Studies

### Objective

Flame stability and extinction are of both fundamental and practical importance. In a gas turbine combustor, transient interaction between large-scale vortical structures and the flame zone may cause a local extinction of the combustion process. This can lead to either the premature extinction of the combustor and/or a rapid increase in CO and UHC emissions. Therefore, the objectives of this task were to reveal the physical and chemical aspects of unsteady vortex-flame interactions that cause local extinction and flame lift, and to contribute to a fundamental understanding of turbulent jet diffusion flames through numerical modeling.

Appendices C-F describe our contributions to this research.

### Test Facility and Instrumentation

Fig. 9 shows the schematic of the coaxial jet diffusion flame experiment. The burner consists of a thick-walled fuel tube (9.45-mm inner diameter, 2.4-mm lip thickness, and 806-mm length) and concentric air tube (26.92-mm inner diameter) through which coflowing air is supplied. This whole assembly is located at the center of a low-speed (0.5 m/s) external air stream in a vertical combustion chimney (150-mm x 150-mm square cross section, 483-mm length). The combustion chimney has quartz windows on all sides to permit visual observations and laser diagnostics. Methane was used as the fuel for the experiments. A variety of laser diagnostic techniques were employed for flame visualization, velocity measurements, and temperature measurements.

Planar Flow Visualization: In this instantaneous (10 ns) technique, zirconia particles ( $< 1 \mu\text{m}$ , 97%) seeded into the fuel jet are illuminated by a sheet of laser light from a pulsed Nd:YAG laser passing through the jet axis. The direct image of the flame and Mie scattering images from the particles are photographed at right angles to the laser sheet using the 35-mm camera. These images are digitized and the effective spatial resolution of the experiment is measured to be  $75 \mu\text{m}/\text{pixel}$ , where a pixel is defined as one digitized channel or  $1/512^{\text{th}}$  of a single sweep of a rotating mirror.

Velocity Measurements: Two techniques were employed; LDA and PIV. LDA measures instantaneous velocity of individual seed particles and this provides probability distribution of velocity components. However, due to nonuniform seeding, velocity bias problems exist. The experimental scheme for two-color PIV is similar to that reported by Goss [6]. A seeded flow field is illuminated by green and red pulsed laser sheets. Mie scattering from the seed particles is recorded on a color film with a 35-mm camera. The color film is digitized using a scanner into

individual red, green, and blue components at a resolution of 2702 pixels per inch. The digitized image is processed by customized PIV analysis software using a cross-correlation technique. The spatial resolution of this cross-correlation technique is 0.6 x 0.6 mm.

**Temperature Measurements:** Two techniques were used; a thin-film pyrometry (TFP) and a CARS system. In the TFP technique, a small 15- $\mu\text{m}$  dia. SiC filament is introduced into the flame. The black body radiation from the filament is collected by an optical system and focussed onto an InGaAs detector which provides the flame temperature profile as a function of space and time. The CARS system used consists of a Nd:YAG laser of 10-ns pulse width and 10-Hz repetition rate, dye laser optics, incident and collection optics, a  $\frac{3}{4}$ -m grating spectrometer, and a diode array rapid scanning spectrometer (DARSS) detector system. The effective probe volume of the CARS system is 25- $\mu\text{m}$  dia. x 250- $\mu\text{m}$  length. Typically 500 CARS signals are acquired at each location and processed a computer.

### Results and Discussion

**Vortex-Flame Interaction:** Fig. 10 shows the velocity vector fields of locally extinguished methane jet flames illustrating the internal and external vortex interference. In general, the velocity field depends locally on the ridges and troughs of internal and external large-scale vortices, whether or not the flame zone exists. Fig. 11 illustrates several features of the vortex-flame interactions in jet diffusion flames. As the jet spreads downstream, time scales for both convection and diffusive transport processes decrease because of lower velocities and smaller concentration gradients. Longer residence times allow fuel pyrolysis and soot formation, and the visible flame turns luminous. The flame zone can bulge out in response to the vortical motion in both internal and external structures. By contrast, in the near-jet region, the velocity of the annulus fluid passing through the flame zone is large. Therefore, the flame zone shifts inwards, i.e., closer to the jet-annulus fluid boundary, where the radial gradients of the mean axial velocity, fuel concentration, and, in turn, fuel diffusive flux are larger to match with an increased oxygen flux. As a result, the diffusive layer between the jet boundary and the flame zone becomes thin. This strains the flame surface and it loses its radial mobility. As explained below, both the internal shear generated large-scale vortices and the external shear-buoyancy-induced vortices are responsible for local flame extinction and lift.

In this manner, our experimental research using laser diagnostics measurements have shed new light on the transient vortex-flame interaction processes.

**Local Flame Extinction and Lifting Phenomenon:** Based upon our research on vortex-flame interaction, two distinct local flame extinction mechanisms have been identified:

1. Extinction caused by internal vortex-flame interaction is primarily due to unsteady transport effects on chemical kinetics. In our experiments, the characteristic diffusion time was estimated as 30 ms, the internal vortex transit time was 0.8 ms, and therefore, the Peclet number for mass transport (i.e., the ratio of two times) was relatively large around 40. Thus, an internal vortex can extend towards the flame zone without disturbing the surrounding fuel concentration field and subjecting the flame to an excessively high fuel flux. This extra fuel flux results in the scavenging of the radical pool, quenching of exothermic reactions, and local extinction of the flame.
2. Extinction due to external vortex-flame interaction is also an unsteady phenomenon that involves longer time scales because of lower vortex frequency. The external vortex frequency was

found to be 200Hz corresponding to a period of 5 ms. As the external vortex squeezes the annulus fluid, there is excess convective influx into the strained flame thereby reducing the residence time in the reaction zone. In addition, the flame is further pushed inward, where velocity and concentration gradients are steeper, further increasing the reactant leakage, decreasing the flame temperature and causing local flame extinction.

We have observed that the local extinction of a methane jet diffusion flame causes the flame to lift off few jet diameters downstream almost immediately. Sometimes, local extinction may also lead, (e.g. for hydrogen and propane fuels) to the formation of a stable split flame; i.e., a combination of a small laminar flame in the vicinity of the burner rim and a "lifted" turbulent flame downstream [7]. Such local extinction and the subsequent flame lift-off processes may represent an essential step in the lean blowout of gas turbine combustors.

Numerical Simulation: The above experimental observations on the dynamics of local extinction and lift-off prompted us to conduct a numerical simulation of vortex-flame interaction in a jet diffusion flame. We traced the dynamic behavior of a laminar jet diffusion flame in response to an artificial vortex that issues radially from the fuel-jet core towards the flame zone. A time-dependent, axisymmetric, implicit, third-order accurate numerical model was used assuming infinitely fast chemistry and unity Lewis number. Because of the axisymmetry and infinitely fast chemistry assumptions, our numerical analysis cannot simulate the three-dimensional nature of the vortex, nor the flame extinction condition. However, it provides global information on fluid dynamic and transport aspects of the vortex-flame interaction before local extinction.

The test cases we have studied are listed in Table 3. Referring to Table 3, cases 1 and 2 represent a laminar jet diffusion flame with low velocities of the primary jet  $U_j$  and annulus air  $U_a$ . At the grid points within the side jet, the radial component of the local velocity is replaced by  $V_s$  and the scalar variables are maintained at the local values for the time period  $t_s$ . Case 3 represents a flame with higher jet velocities as would be found in a turbulent flame and case 4 represents a condition in which a vortex is ejected inward from outside the flame. Finally, a Peclet number,  $Pe$  for mass transfer related to the side jet ejection, is defined as the ratio of characteristic diffusion time to characteristic convection time for vortex motion. These numerical studies led us to the following important observations.

The unsteady vortex-flame interactions leading to extinction can be divided into three regimes depending upon the dominant process: diffusion, convection, and chemical kinetics. The first two regimes are primarily physical vortex-flame interactions. During the physical interaction stage, if a Peclet number is sufficiently large (on the order of 100), the vortex system penetrates into the high-temperature highly viscous layer with a slight flame movement, thus rapidly thinning the thermo diffusive layer. The reactant leakage through the reaction zone increases, the flame temperature gradually decreases, and the heat release rate increases by enhanced diffusion in the early regime and then by convection. In the final chemical kinetic regime for the outward vortex ejection, an excess influx of methane and methyl radicals scavenge radicals ( $OH$ ,  $H$ , and  $O$ ) and terminate exothermic oxidation reactions of intermediate species ( $H_2$  and  $CO$ ). For the inward ejection, the convective contribution to the oxygen flux is responsible for the excessive reactant leakage, leading to extinction.

**Highlights and Conclusions:** We used a double-concentric coaxial methane-air jet diffusion flame configuration to study the vortex-flame interaction. A variety of laser diagnostic techniques were employed for flame visualization, velocity measurements, and temperature measurements. Also, we completed a numerical simulation of the vortex-flame interaction. Following were the important conclusions from our research.

1. We have sketched several features of the vortex-flame interactions in Fig. 11. As the jet spreads downstream the flame zone can bulge out in response to the vortical motion in both internal and external structures. By contrast, in the near-jet region, the flame zone shifts inwards and closer to the jet-annulus fluid boundary. As a result, the diffusive layer between the jet boundary and the flame zone becomes thin thereby straining the flame surface. Both the internal shear generated large-scale vortices and the external shear-buoyancy-induced vortices are responsible for local flame extinction and lift.
2. We identified two distinct local flame extinction mechanisms. First, the extinction caused by internal vortex-flame interaction is primarily due to unsteady transport effects on chemical kinetics. An internal vortex can extend towards the flame zone subjecting the flame to an excessively high fuel flux. This extra fuel flux results in the scavenging of the radical pool, quenching of exothermic reactions, and local extinction of the flame. Second, extinction due to external vortex-flame interaction is caused as the external vortex squeezes the annulus fluid and provides excess convective influx into the strained flame. This excess influx increases the reactant leakage, decreases the flame temperature, and causes local flame extinction. Finally, we have observed that local flame extinction causes the flame to lift off few jet diameters downstream almost immediately.
3. We performed numerical simulation, examining four cases relating to the dynamic response of a laminar jet diffusion flame to radial injection of an artificial vortex. We found that the unsteady vortex-flame interactions leading to extinction can be divided into three regimes: diffusion, convection, and chemical kinetics. The first two regimes are primarily physical vortex-flame interactions. During the physical interaction stage, if a Peclet number is sufficiently large (on the order of 100), the vortex system penetrates into the high-temperature highly viscous layer with a slight flame movement, thus rapidly thinning the thermo diffusive layer. For the inward ejection, the convective contribution to the oxygen flux is responsible for the excessive reactant leakage, leading to extinction. In the final kinetic regime for the outward vortex ejection, an excess influx of methane and methyl radicals scavenge radicals (OH, H, and O) and terminate exothermic oxidation reactions of intermediate species ( $H_2$  and CO) leading to local extinction.

## **2.3 Turbulent Swirling Flame Structure and Stability**

### **Objective**

In a modern gas turbine combustor, turbulence and swirling motion enhance fuel-air mixing, combustion intensity, and flame stabilization, especially near the lean blowout condition, to ensure an adequate stability margin. In a gas turbine combustor, swirl-induced recirculation

zone is generated by a combination of three mechanisms: an axial swirling air jet associated with each fuel introduction, sudden expansion of these jets as they enter the primary zone, and back pressure provided by an array of radial jets at the end of the primary zone. We designed a double-concentric jet diffusion flame type model combustor, Step Swirl Combustor (SSC), and a research step combustor to reproduce the complicated recirculation flow patterns. The objective of this research was to study the structure and stability (especially LBO) of a turbulent swirling flame in these model combustors.

Appendices G-M describe our research on turbulent flames in model combustors.

### Test Facility and Instrumentation

Fig. 12a shows the schematic of a double concentric jet diffusion flame model combustor. This combustor consists of a central fuel tube (9.45-mm inner diameter, 0.2-mm lip thickness, 806-mm length) and a concentric annular-air tube (26.92-mm inner diameter), centered in a vertical test section (150 x 150-mm square cross section with rounded corners, 486-mm length), through which external air is supplied. The test section has four quartz windows for laser diagnostic measurements. A helical vane swirler unit is placed in the annulus channel 96 mm upstream from the jet exit. Table 4 shows the test conditions employed using gaseous hydrogen as the fuel.

Fig. 12b shows a schematic diagram of SSC, which has a 150-x150-mm cross section, length of 754 mm, and a step height of 55 mm. Fuel is supplied to the combustor by the annular fuel tube (20 mm i.d. and 29 mm o.d.) coaxially sandwiched between swirling air streams; the inner air jet (20 mm dia.) and the outer annular air jet (29 mm i.d. and 40 mm o.d.). The combustor exit has a 45% blockage orifice plate on top which simulates the back pressure exerted by the dilution jets in a practical gas turbine combustor; see Sturgess et al.,[8]. The SSC has quartz windows on all four sides to permit visual observations and laser diagnostics measurements. Stationary helical vane swirlers were located 25 mm upstream from the burner tube exit in each of the air passages. The inner swirler had six vanes with a central 1.4 mm dia. hole to prevent the flame from anchoring to the swirler. The outer swirler had twelve vanes. Inner swirler lengths are 25, 19, and 19 mm, respectively, for 30°, 45°, and 60° swirlers; outer swirler lengths are 32, 25, and 19 mm, respectively, for 30°, 45°, and 60° swirlers.

We used flow visualization, CARS system for temperature measurements and LDA system for velocity measurements. The CARS and LDA are described below.

CARS System: The CARS optics layout described by Pan et al., [9] was used for temperature measurements. The laser source is provided by a Nd:Yag pulse laser with a 10-ns time resolution and a Boxcars configuration is used. The probe volume is approximately 25- $\mu$ m by 250- $\mu$ m. The CARS signal is collected by a Spex 1702 spectrometer, 2-D charge coupled diode (CCD) camera from Princeton instruments, and Tracor-Northern multichannel analyzer. A total of 250 samples were taken for each CARS temperature measurements. The raw data is processed by in-house software on a personal computer.

LDA System: A custom-made three-component LDA system used for velocity measurements. This is a three-beam two component (axial and radial) set using a 514.5 nm line of an 18 W argon-ion laser with a component separation based on polarization. A two-beam third component (tangential) set uses a 488.0 nm line with separation by color. Since the third component is normal

to the first and second components, the measurement volume had a quasi-spherical shape of 100  $\mu\text{m}$  diameter and the calculated fringe spacing was 3.6  $\mu\text{m}$ . The LDA system has Bragg cell frequency shifting (10 MHz for the first and second channels and 30 MHz for the third channel) for measurements in recirculatory flows, 4- $\sigma$  filtering software for spurious signals, for example, due to seed agglomeration, and a correction subroutine to account for the LDA signal biasing effects in combustor flows. A fluidized-bed seeder was used to inject submicron-sized (0.1  $\mu\text{m}$ )  $\text{ZrO}_2$  particles into each passage. Countertype (TSI 1990C) signal processors and a tailor-made coincidence circuit ensured valid data rate acquisition. All the LDA signals were processed using our custom-designed software which calculates intensity, shear stresses, higher moments (skewness and kurtosis), and pdfs. Typical LDA sampling rates exceeded 1 kHz for both isothermal and combustor flow measurements.

### Results and Discussion

**Turbulent Jet Diffusion Flame Structure:** Fig. 13 shows the turbulence intensity distribution across the hydrogen jet flame, 25 mm downstream of the nozzle exit. For case 2 (no swirl) and case 4 (with swirl) all components of turbulence intensities showed a peak in the shear layer of the jet where the radial gradient of mean axial velocity component was large, and the turbulence level of annulus fluid inside the flame zone increased rapidly in the turbulent stirring layer. As the swirl becomes stronger (case 4), turbulence intensities increased, particularly in the central region ( $y < 4$  mm).

Fig. 14 shows the radial profiles of the Reynolds shear stress and gradient of the mean axial velocity. These results indicate the radial diffusion of axial momentum by turbulent transport. The effect of swirl on the Reynolds shear stress is weak except for the central region ( $< 4$  mm) for case 4, where turbulent intensities increased.

In the developing region of the turbulent hydrogen jet diffusion flame, increasing the jet velocity shifts the apparent turbulent flame zone inward; this causes straining of the flame zone in the near field. On the other hand, swirl generally promotes turbulence and creates a positive radial velocity component even at the jet-exit plane, thereby shifting the flame zone outward and broadening the thermal layer. Also, swirl promotes early flame spread, this shifts the peak of turbulence intensity upstream and accelerates the decay of mean axial velocity.

**SSC Lean Blowout:** Fig. 15 shows LBO data comparing coswirl and counterswirl for two values of the inner vane angle, namely 30 and 45 deg, for both methane and propane gaseous fuels. Three important observations can be made:

1. LBO values were lower with propane than with methane. This is a result of enhanced methane-air mixing at the flame base followed by a lifted flame structure stabilized in the inner recirculation zone.
2. For a 30 deg. Inner vane angle, LBO values were lower for counterswirl as opposed to co swirl flow direction. This result arises because for counterswirl flow, shearing braids cause lower air velocities just above the fuel tube leading to an attached flame (which has a lower value of LBO). In contrast the coswirl produces higher axial mean velocity directly above the fuel tube, causing flame lift and compromising flame stability.



3. As the inner vane angle is increased from 30 to 45 deg, LBO values increase correspondingly and also LBO becomes less sensitive to swirl flow direction. Again, this happens because the higher inner swirl angle directs more inner airflow toward the fuel tube, causing flame lift.

It should be recognized that the observed differences in LBO between coswirl and counterswirling configurations has to do with how a flame stabilizes. Counterswirl conditions readily produce an attached flame for moderate inner swirl intensity (30 deg); however, both configurations produce lifted flames for higher swirl intensity (45 deg) and for this latter condition the LBO values are very similar. In a practical gas turbine combustor, Sturgess [10] and Ballal et al., [11] have observed three basic flame conditions: a thin sheath-like pilot anchored flame, a shear layer flame associated with the inner and outer recirculation zones, and a lifted main flame, which allows considerable premixing of reactants to take place prior to combustion. These observations further confirm the relevance and importance of the present research to practical gas turbine combustors.

SSC Flame Structure and Stability: Our research showed that flame stability in SSC depends upon the flame shape, structure, and location, e.g. attached vs. lifted. Fig. 16 sketches the flame shape, structure, and location in the SSC. As sketched in Fig. 16a, the following different flame configurations were observed:

1. *Multiattached flame:* This type of flame structure is produced for the combination of strong outer swirl (60 deg) and zero inner swirl. The flame is simultaneously attached at three locations: (i) inner air side of the fuel stream, (ii) outer air side of the fuel stream, and (iii) outside of the outer air stream. As the strength of the outer swirl is decreased (30 deg), the attached flame structure shifts to that sketched in Fig. 16b.
2. *Single-attached flame:* Fig. 16c illustrates this structure. It is observed for low inner (30 deg) and outer (30 deg) counterswirling air flows. Such flow conditions cause the collapse of the twin attached flame structure (Fig. 16b) to a single attachment just above the fuel tube.
3. *Lifted Flame:* Fig. 16d illustrates this type of flame. The flame lifts from the fuel tube lip because of the high mean axial velocity in the near-field region above the fuel tube. The lifted flame is stabilized by the inner recirculation zone. However, increasing the swirl intensity and/or combustor loading only slightly changes flame stability, i.e., LBO values remain fairly constant for lifted flames. This is because of the premixing of the fuel and air at the base of the flame.

Research Step Combustor Lean Blowout: Fig. 17 illustrates a schematic of a geometrically simple, optically accessible, and acoustically decoupled research combustor that was designed to reproduce the gross features of the flow field in a modern annular gas turbine combustor. We successfully documented a systematic and detailed sequence of events comprising an attached flame, a lifted shear flame, an intermittent shear flame, the large-scale instability of the flame front, and LBO. Also, we compared these results with those obtained using a generic gas turbine combustor.

Fig. 18 shows the sequence of events leading to LBO. As the overall equivalence ratio was reduced below unity, the attached flame moved further downstream into the combustor in a characteristic lifted-flame position and form. Continuing reduction in the equivalence ratio produces an onset of flow instability in the lifted flame, an increase in the amplitude of the

instability, the onset of intermittency, severe intermittency, and, finally, the onset of strong axial flame instability. This sequence clearly highlights the complexity of the LBO mechanism in a modern annular gas turbine combustor. In our research combustor, the piloting action of the flame in the jet shear layers by the attached flame at the step appears to be crucial to combustor stability. Thus, successful modeling of the combustor stability requires the prediction of the attached flame and its lift

We measured LBO as a function of air loading parameter (LP) over a range of propane fuel flows. To achieve a wide variation in LP with the simple atmospheric pressure research combustor, a subatmospheric pressure simulation was used as explained in Ref. [10]. This technique permitted (i) the simulation of subatmospheric pressure as low as 0.1 atm., (ii) the completion of the combustor stability loop (ranging from  $\phi = 0.5$  to 0.9), and (iii) increased LP by two orders of magnitude. Fig. 19 shows the LBO performance of our research combustor and stability loops for several well-stirred reactors from the literature, as well as two partial loops for practical gas turbine combustors. The trend of LBO vs. air loading shown in Fig. 19 is very similar to that found for a well-stirred reactor. Thus, it is reasonable to conclude that our research combustor correctly reproduced the LBO processes of a real gas turbine combustor.

To simulate the presence of dilution air jets, we investigated the effects of back pressure on the LBO in our research combustor. As seen in Fig. 20, LBO was improved by increasing the exit blockage. However, we found that (see Ref. 8) above a blockage of 45%, (i) significant interference occurs between the outlet and the combustor flame holding, and (ii) LBO does not improve much. Thus, we concluded that an exit blockage of 45 percent provides the best combustion stability and optimal configuration (i.e., for a combustor of exit blockage = 45 percent and  $L/D = 4.9$ , the LBOs were virtually independent of blockage and acoustic coupling).

Soot Emissions Studies: The emission of soot particulate from practical combustion systems (such as a gas turbine combustor) has a significant adverse impact on the environment and human health. Further, military aircraft engines leave a visible and an infrared signature if they produce exhaust smoke. Therefore, we performed a comprehensive study of sooting correlation for premixed combustion. This study is presented in Appendix Q. We found that in combustion systems employing backmixing and flow recirculation (e.g., a well stirred reactor and a gas turbine combustor), the equivalence ratio at sooting threshold is about 15 percent higher than for laminar premixed bunsen flames. Also, the (carbon/oxygen) ratio at sooting is nearly constant for alkanes, but for alkenes and alkynes, it strongly correlates with adiabatic flame temperature. Finally, we observed a strong correlation at sooting between (oxygen/fuel) molar ratio and fuel carbon number, C/H ratio, heat of formation, flame temperature, and averaged-distance-sum connectivity index.

Combustion Stability Modeling: We analyzed the SSC flame stability using a time-dependent axisymmetric model which solves for axial- and radial-momentum equations, continuity, swirl, turbulent energy ( $k$ ), turbulent-energy dissipation ( $\epsilon$ ), and enthalpy and species conservation equations. A simple global-chemical-kinetics model involving methane, oxygen, water, carbon dioxide and nitrogen was used.

The following observations were made from the calculated temperature fields: (i) For zero inner swirl the computations correctly predicted the locations of flames on either side of the fuel

jet, (ii) For 30° co-swirl, a recirculation bubble develops inside the inner air jet and it produces the dimple-shaped flame, and (iii) The lift-off height for case (ii) predicted by the model matches well with the experimental data. These computations support the qualitative observations on flame photographs described above. In summary, our simple turbulence model with a single-step global-chemical-kinetics provides a reasonable prediction of flame shape and location, flame temperatures, and axial and swirl velocities.

The analysis of LBO in a research step combustor was addressed at three levels: (i) characteristic time modeling, (ii) stirred reactor network modeling, and (iii) subgrid-level stirred reactor modeling.

In the characteristic time modeling, it is assumed that, at LBO, flame propagation will cease when the rate of mixing between small turbulent eddies of cold reactants and hot products is greater than the local chemical reaction rate. This quenching criteria finds its origin in the work of Lockwood and Megahed [12] and yields:

$$1.5\{D + C_{\mu}K^2/\sigma_t \varepsilon\}/\nu\{1 + S_L/(\varepsilon\nu)^{0.25}\} > 1.0 \quad (5)$$

where  $D$  is the laminar diffusion coefficient,  $K$  is the kinetic energy of turbulence,  $\varepsilon$  is the dissipation rate,  $C_{\mu}$  is a constant,  $\sigma_t$  is the turbulent Schmidt number, and  $S_L$  is the laminar flame speed. Eventually, this approach provided the reactor extinction criteria for the sub grid-level stirred reactor modeling.

In the local stirred reactor modeling, the combustor volume is represented by an equivalent global stirred reactor network. This enables the calculation of stability from thermo-chemistry considerations. For our research combustor, the resulting reactor was 44% of the combustor volume and corresponded reasonably well to the lifted flame observed in the real combustor. As shown in Ref. [11], good agreement was found between predictions and experiments for the research combustor.

In the subgrid scale reactor modeling the eddy dissipation concept (EDC) of Byggstoyl and Magnussen [13] represents a general model for chemical reaction in turbulent flow. In the EDC model, the reactants are homogeneously mixed within the fine structure (Kolmogoroff eddies) of turbulence; therefore, these fine structures can be treated as PSRs.

Axisymmetric CFD calculations were made using the Pratt and Whitney two-dimensional PREACH code. Three constraints were applied on the chemical reaction; (i) the EDC model with characteristic time-based extinction criterion was implemented, (ii) the local mixture should be within flammability limits (lean  $\phi = 0.2$  or  $0.5$  depending upon reactant temperature and upper  $\phi$  to  $2.0$ ), and (iii) turbulence effects on the flame burning velocity. These results show that the stoichiometric contour crosses the step recirculation zone from the confluence of the jets and reaches the combustor wall about halfway between the step and the recirculation reattachment plane. We can infer from these temperature contours that the main flame exists in the jet shear layers and originates about 10 cm from the step-plane (i.e., it is lifted and not attached). It is thick

and follows the stoichiometric contour across the recirculation zone. There is some agreement between the characteristics of the inferred flame and the actual flame observed in the time-mean photographs and in the near-instantaneous pictures of laser-induced OH fluorescence where concentrated islands of reaction in the jet shear layer thicken the flame region. However, it was found that this model calculated the lifted-flame condition but was unsuccessful in predicting the all-important attached-flame condition.

Highlights and Conclusions: We designed a variety of laboratory model combustors to reproduce the complicated swirl-induced recirculation flow patterns present in a modern gas turbine combustor. Next, we performed an experimental and numerical investigations of the structure and stability (especially LBO) of a turbulent swirling flame in these model combustors. We reached the following important conclusions.

1. In the developing region of the turbulent hydrogen jet diffusion flame, increasing the jet velocity shifts the apparent turbulent flame zone inward; makes the thermal layer thinner, and thus, strains the flame zone in the near field. On the other hand, swirl generally promotes turbulence and creates a positive radial velocity component even at the jet-exit plane, thereby shifting the flame zone outward and broadening the thermal layer. Swirl promotes early flame spread and turbulent mixing. These data may be used to validate advanced turbulent combustion models.

2. Our research work in SSC revealed that the observed differences in LBO between coswirling and counterswirling configurations has to do with how a flame stabilizes. Counterswirl conditions readily produce an attached flame for moderate inner swirl intensity (30 deg); however, both configurations produce lifted flames for higher swirl intensity (45 deg) and for this latter condition the LBO values are very similar. Also, LBO values were lower with propane than with methane. This is a result of enhanced methane-air mixing at the flame base followed by a lifted flame structure stabilized in the inner recirculation zone. These observations confirm the relevance and importance of the present research to practical gas turbine combustors.

3. Our research showed that flame stability in SSC depends upon the flame shape, structure, and location, e.g., attached vs. lifted. Following different flame configurations were observed: (i) *Multiattached flame* is produced for the combination of strong outer swirl (60 deg) and zero inner swirl, (ii) *Single-attached flame* is observed for low inner (30 deg) and outer (30 deg) counterswirling air flows and (iii) *Lifted flame* is produced because of the high mean axial velocity in the near-field region above the fuel tube. Our computations correctly predicted the attached flame locations, the development of a strong inner recirculation zone, the flame lift-off height, the location of reattachment point of the recirculation bubble, and confirm the transport of combustion products upstream.

4. We successfully documented a systematic and detailed sequence of events comprising an attached flame, a lifted shear flame, an intermittent shear flame, the large-scale instability of the flame front, and LBO. This sequence clearly highlights the complexity of the LBO mechanism in a modern annular gas turbine combustor. In our research combustor, the piloting action of the flame in the jet shear layers by the attached flame at the step appears to be crucial to combustor stability. Thus, successful modeling of the combustor stability requires the prediction of the attached flame and its lift. Finally, the trend of LBO vs. air loading was found to be very similar to that for a well-stirred reactor. Thus, it is reasonable to conclude that our research combustor correctly reproduced the LBO processes of a real gas turbine combustor.

5. We performed a comprehensive study of sooting correlation for premixed combustion. We found that in combustion systems employing backmixing and flow recirculation (e.g., a well stirred reactor and a gas turbine combustor), the equivalence ratio at sooting threshold is about 15 percent higher than for laminar premixed bunsen flames. Also, the (carbon/oxygen) ratio at sooting is nearly constant for alkanes, but for alkenes and alkynes, it strongly correlates with adiabatic flame temperature. Finally, we observed a strong correlation at sooting between (oxygen/fuel) molar ratio and fuel carbon number, C/H ratio, heat of formation, flame temperature, and averaged-distance-sum connectivity index.

6. We analyzed the SSC flame stability using a time-dependent axisymmetric model. These computations correctly predicted the locations of flames on either side of the fuel jet, the observed dimple-shaped flame, and flame lift-off height, flame temperatures, and axial and swirl velocities. The analysis of LBO in a research step combustor was addressed at three levels: (i) characteristic time modeling, (ii) stirred reactor network modeling, and (iii) subgrid-level stirred reactor modeling.

It was found that the dissipation gradient approach combined with an eddy dissipation model with a built-in characteristic extinction time criteria offered the best possibility of a priori LBO calculation.

## **2.4 Film Cooling With High Free Stream Turbulence**

### Objective

To permit near-stoichiometric combustor operating temperatures, a modern gas turbine stage employs film cooling. Air is injected through rows of small holes in the blade surface. It protects the blade surface until the coolant jet mixes with a hot surrounding flow with high free stream turbulence. The objective of our research was to investigate the influence on film cooling effectiveness and heat transfer coefficient of the coolant injection flow (steady and unsteady) and free stream turbulence.

Appendices N and O describe the results of our research.

### Test Facility and Instrumentation

Fig. 21 shows an overall view of the experimental facility and heat transfer surface. The tunnel is supplied with a nominal 1.5 kg/s airflow within a temperature range of 288K to 325K. The film cooling flow can be adjusted to provide temperature 10-20C in excess of free stream temperature.

Unsteady film cooling flow was generated by sinusoidal pulsing of the injected coolant. The flow pulsations were generated by a 25.4 cm dia. 150W audio speaker. Downstream of the transition nozzle, at the film cooling station, free stream turbulence levels of 0.7% to 17% were achieved. A single row of 1.905 cm film cooling holes ( $L/D = 2.4$ ) was located at an injection angle of 35 deg. to the primary flow. Table 5 lists typical flow characteristics at the film cooling station.

A TSI Model # IFA 100 hot wire anemometer was used for velocity measurements. Turbulence length scales were calculated by integrating to the first zero crossing of the autocorrelation coefficient function for the velocity obtained from the hot wire signal. An array of 0.33 mm bead diam. thermocouples measured surface temperatures. Finally, in a recent study,

a two-color PIV system was employed. This system resolves directional ambiguity using the color coding of the particle images and also provides higher data yields.

### Results and Discussion

Characterization of Film Cooling Jet: Fig. 22 shows jet spread for a blowing ratio of 0.7 at the free stream turbulence levels of 1% and 17%. This result shows a near doubling of jet spread, growth of the shear layer, and increase in turbulence scale with higher free stream turbulence level. Also seen is the roll up of the film cooling jet boundary layer in a direction opposite to what would be the anticipated free stream shear layer roll up.

Fig. 23 shows the thickness of the shear layer as a function of turbulence and blowing ratio. It is observed that at a blowing ratio of 1.5, the film momentum dominates that of the free stream with both angles decreasing with increasing turbulence. The shear layer over the film hole is clearly driven primarily by the blowing ratio and the free stream then dominating the eddy size after the film hole. The shedding frequency of the shear layer increases and the scale size decreases over the film hole with blowing ratio. The roll up frequency for the shear layer after the film hole decreases and the scale size increases with both blowing ratio and turbulence level.

Film Cooling Effectiveness: Fig. 24 shows plots of film cooling effectiveness vs. downstream distance. At low free stream turbulence level ( $Tu = 0.7\%$ ), the cooling effectiveness decreases by approximately 30 percent as the forcing frequency is increased from 5 Hz to 20 Hz. Our measurements of axial velocity profiles showed that forcing increases the velocity and velocity gradient near the wall significantly for the blowing ratio of 0.6. Also, the modulation results in enhanced mixing with the free stream thus reducing maximum coolant temperature even at the first measurement station.

Fig. 25 shows the effects of free stream turbulence and forcing on heat transfer coefficient. This shows a decrease in the heat transfer coefficient with high free stream turbulence ( $Tu = 17\%$ ) and forcing. Thus, it is seen that the forcing flow has a detrimental effect on film cooling as compared to that observed in nonperiodic high turbulence experiments at comparable amplitude.

Highlights and Conclusions: We performed a detailed characterization of the coolant injection flow (steady and unsteady) and its interaction with free stream turbulence. We examined the influence of these two parameters on film cooling effectiveness and heat transfer coefficient. Following conclusions were obtained.

1. PIV measurements showed an almost doubling of the jet spread for an increase in free stream turbulence from 1% to 17%. This observation suggests lower film cooling effectiveness and a proportionately higher mixed out temperature.
2. The forcing of the film cooling flow resulted in a decrease in film cooling effectiveness by as much as 70%. Moreover, the temperature profiles, their near-wall gradients, and heat transfer coefficients mimic this decrease in film cooling effectiveness.
3. The forced flows show detrimental effect on film cooling effectiveness comparable to the observed influence of nonperiodic, high free stream turbulence. Though the unsteadiness has an undesirable effect on film cooling, the results of increased mixing and penetration could make modulation a beneficial technology for dilution jets in gas turbine combustors.

### 3.0 SUMMARY AND CONCLUSIONS

A long-term goal of the Air Force is to develop high-performance gas turbine engines with combustors that operate at near-stoichiometric conditions, burn broad-specification fuels, and have low maintenance and high durability. Therefore, the objective of the proposed research was to develop a fundamental understanding of the combustion process in a gas turbine combustor by designing a variety of laboratory experiments. Specifically, we completed the following four key investigations.

1. WSR Experiments to study combustion stability, LBO, and emissions.
2. Vortex-flame interactions to study mixing, lean stability, ignition, and extinction.
3. Flame stabilization and lean blowout studies using a step swirl combustor.
4. Study film cooling of hot-section components.

A toroidal WSR was used to study lean blowout limits, combustion efficiency, and emissions from several pure hydrocarbons. We found that the LBO for several hydrocarbons was around  $\phi \sim 0.47$ . The combustion efficiency  $\eta_{\text{comb}}$  at LBO decreased by about 2 percent as fuel carbon number increased. Hydrocarbons of different structure (alkanes, aromatics) and carbon number produced different amounts of CO at the same temperature and residence time. Hydrocarbons of different structure and (C/H) ratio produced different amounts of NO<sub>x</sub> at the same residence time. The main conclusion is that hydrocarbon fuel structure will have a noticeable influence on the combustion and emissions performance of a gas turbine combustor. Moreover, WSR is an ideal laboratory combustor capable of yielding fundamental chemical kinetic data.

In a gas turbine combustor, transient interaction between large-scale vortical structures and the flame zone may cause a local extinction of the combustion process. Therefore, we studied the physical and chemical aspects of unsteady vortex-flame interactions that cause local extinction and flame lift in a double-concentric jet diffusion flame combustor. We found that both the internal shear generated large-scale vortices and the external shear-buoyancy-induced vortices are responsible for local flame extinction and lift. The extinction caused by internal vortex-flame interaction is primarily due to the unsteady transport effects on chemical kinetics. On the contrary, extinction due to external vortex-flame interaction is caused due to excess convective influx into the strained flame. Our numerical simulation showed that vortex-flame interactions leading to extinction can be divided into three regimes: diffusion, convection, and chemical kinetics. Finally, we observed that the local flame extinction causes the flame to lift off a few jet diameters downstream almost immediately.

In a modern gas turbine combustor, turbulence and swirling motion enhance fuel-air mixing, combustion intensity, and flame stabilization, especially near the lean blowout condition and ensure an adequate stability margin. Therefore, we studied the structure and stability (especially LBO) of a turbulent swirling flame in a variety of model combustors. We found that swirl promotes turbulence and creates a positive radial velocity component that increases flame spread and turbulent mixing. Our research in a SSC revealed that counter swirl produces an attached flame (hence better stability) for moderate inner swirl intensity. However, both counter-

and co-swirl configurations produce lifted flames for higher swirl intensity and similar LBO values. We observed different flame configurations such as multi-attached flame, single-attached flame, and lifted flame. Our computations correctly predicted the attached flame locations, the development of a strong inner recirculation zone, the flame lift-off height, the location of reattachment point of the recirculation bubble, and confirm the transport of combustion products upstream.

In our research step combustor, we successfully documented a systematic and detailed sequence of events comprising an attached flame, a lifted shear flame, an intermittent shear flame, the large-scale instability of the flame front, and LBO. Moreover, the piloting action of the flame in the jet shear layers by the attached flame at the step appeared to be crucial to combustor stability. Finally, we performed a comprehensive study of sooting correlation for premixed combustion. We found that in combustion systems employing backmixing and flow recirculation (e.g. a well stirred reactor and a gas turbine combustor), the equivalence ratio at sooting threshold is about 15 percent higher than for laminar premixed bunsen flames. Also, the (carbon/oxygen) ratio at sooting is nearly constant for alkanes, but for alkenes and alkynes, it strongly correlates with adiabatic flame temperature. Finally, we observed a strong correlation at sooting between (oxygen/fuel) molar ratio and fuel carbon number, C/H ratio, heat of formation, flame temperature, and averaged-distance-sum connectivity index.

Finally, we addressed the analysis of LBO in a research step combustor and found that the dissipation gradient approach combined with an eddy dissipation model with a built-in characteristic extinction time criteria offered the best possibility of an a priori LBO calculation.

In a modern gas turbine, a coolant film protects the turbine blade surface until the coolant jet mixes with a hot surrounding flow with high free stream turbulence. We investigated the influence on film cooling effectiveness and heat transfer coefficient of the coolant injection flow (steady and unsteady) and free stream turbulence. PIV measurements showed an almost doubling of the jet spread for an increase in free stream turbulence from 1% to 17%. The forcing of the film cooling flow resulted in a decrease in film cooling effectiveness by as much as 70%. Moreover, the temperature profiles, their near-wall gradients, and heat transfer coefficients mimic this decrease in film cooling effectiveness. The forced flows show detrimental effect on film cooling effectiveness comparable to the observed influence of non-periodic, high free stream turbulence. Though the unsteadiness has an undesirable effect on film cooling, the results of increased mixing and penetration could make modulation a beneficial technology for dilution jets in gas turbine combustors.

Appendices A-O are published copies of some of our journal papers. Appendix P is a list of honors and awards, publications, presentations, and reports produced on this successfully completed Air Force Contract No. F33615-92-C-2207.



#### 4.0 REFERENCES

1. Nenninger, J. E., Kridiotis, A. C., Chomiak, J., Longwell, J. P., and Sarofim, A. F., "Characterization of a Toroidal Well-Stirred reactor," Twentieth Symposium (International) on Combustion, The Combustion Institute, Pittsburgh, PA, pp. 473-479, 1984.
  2. Zelina, J., and Ballal, D. R., "Combustion Studies in a Well Stirred Reactor", *AIAA Paper No. 94-0114*, 1994.
  3. Blust, J. W., Getz, M. G., and Zabarnick, S., "Probe Design Optimization for the Well Stirred Reactor," *AIAA Paper No. 97-0907*, 1997.
  4. Lefebvre, A. H., *Gas Turbine Combustion*, Hemisphere Publishing Corp., NY, 1983.
  5. Kanury, A. M., *Introduction to Combustion Phenomena*, Vol. 2, Gordon and Breach Science Publishers, NY, pp. 30-42, 1984.
  6. Goss, L. P., Post, M. E., Trump, D. D., and Sarka, B., "Two-Color Particle Velocimetry," *Journal of Laser Applications*, Vol. 3, pp. 36-42, 1991.
  7. Takahashi, F. and Schmoll, W. J., "Lifting Criteria of Jet Diffusion Flames," Twenty-Third Symposium (International) on Combustion, The Combustion Institute, Pittsburgh, PA, pp. 677-683, 1991.
  8. G. J. Sturgess, S. P. Heneghan, M. D. Vangsness, D. R. Ballal, A. L. Lesmerises, and D. Shouse, "Effects of Back-Pressure in a Lean Blowout research Combustor," *Transactions of ASME, Journal of Engineering for Gas Turbines and Power*, Vol. 115, pp. 486-498, 1993.
  9. Pan, J. C., Vangsness, M. D., Heneghan, S. P., and Ballal, D. R., "Scalar Measurements of Bluff-Body Stabilized Flames Using CARS Diagnostics," *ASME Paper No. 91-GT-302*.
  10. Sturgess, G. J., Heneghan, S. P., Vangsness, M. D., Ballal, D. R., and Lesmerises, A. L., "Lean Blowout in a Research Combustor at Simulated Low Pressures," *Transactions of ASME, Journal of Engineering for Gas Turbines and Power*, Vol. 118, pp. 773-781, 1996.
  11. Ballal, D. R., Vangsness, M. D., Heneghan, S. P., and Sturgess, G. J., "Studies of Lean Blowout in a Research Combustor," *Proceedings of 81<sup>st</sup> AGARD Symposium, Conference Proceedings 536, Paper No. 23, Fiuggi, Italy*, 1993.
  12. Lockwood, F. and Megahead, I. E. A. "Extinction of Turbulent Reacting Flows," *Combustion Science and Technology*, Vol. 19, pp. 77-80, 1978.
- Byggstoyl, S. and Magnussen, B. F., "A Model for Flame Extinction in Turbulent Flows," *Turbulent Shear Flows*, Edt. L. J. S. Bradbury, F. Durst, B. E. Launder, F. W. Schmidt, and J. H. Whitelaw, Vol. 4, Springer Verlag, Berlin, 1985.

**Table 1: IHPTET-Phase III Goals and Payoffs**

Engine Type	Goals	Payoffs
Fighter	100% increase in thrust/weight 50% decrease in fuel consumption	Mach 3+ capability Supersonic aircraft 100% increase in payload over F-14
Rotorcraft	30% decrease in fuel consumption 100% increase in power/weight	100% increase in range/payload over CH-47
Commercial/ Transport	30% decrease in fuel consumption	Increased range/payload Longer life, reduced life cycle costs, Reduced parts count, improved maintenance

**Table 2: WSR Test Matrix**

Hydrocarbon	Carbon Number	(C/H)	$\tau$ (msec)	$\phi_{\min}$	$\phi_{\max}$	$T_{f\min}$ (K)	$T_{f\max}$ (K)
Methane	1	0.25	7.3	0.55	0.88	1507	1967
			6.32	0.59	0.83	1517	1918
Ethane	2	0.333	7.26	0.48	0.84	1407	1996
Cyclohexane	6	0.5	7.47	0.48	0.82	1429	1981
			5.22	0.51	0.78	1536	1922
n-Heptane	7	0.4375	7.19	0.53	0.84	1517	1975
			5.49	0.54	0.81	1595	1974
Toluene	7	0.875	7.32	0.46	0.79	1499	1946
			5.35	0.5	0.78	1552	1936
Ethylbenzene	8	0.8	7.43	0.48	0.76	1478	1958
			5.33	0.49	0.67	1546	1839
Cracked Fuel Simulant	2.52	0.5081	6.75	0.49	0.77	1530	2007
			5.17	0.46	0.76	1391	1969
n-Dodecane	12	0.4615	7.39	0.46	0.8	1357	1979
			5.2	0.55	0.79	1581	1983

**Table 3: Vortex-Flame Interaction Test Conditions**

Case	U <sub>j</sub> (m/s)	U <sub>a</sub> (m/s)	V <sub>s</sub> (m/s)	t <sub>s</sub> (msec)	Peclet No. Pe
1	1.5	1.5	7	0.5	100
2	1.5	1.5	14	0.5	220
3	15	3	20	0.06	260
4	15	3	-4	0.06	140

**Table 4: Experimental Test Conditions for Turbulent Swirling Jet Diffusion Flames**

Case	$\theta$ (deg.)	U <sub>j</sub> (m/s)	U <sub>a</sub> (m/s)	U <sub>c</sub> (m/s)
1	0	25	4	1
2	0	100	20	4
3	30	100	20	4
4	45	100	20	4

**Table 5: Typical Flow Characteristics at the Film Cooling Station**

Parameter	No Turbulence	Jet Flow Turbulence
<b>Data at <math>y/\delta = 2.6</math></b>		
Tu (%)	0.7 to 0.96	17.3
L <sub>gx</sub> (cm)		7.73
<b>Data at <math>y = \delta</math></b>		
U (m/s)	16.03	16.82
Re <sub>d</sub>	19,085	20,026
u (m/s)	0.59	3.16
Tu (%)	3.68	18.79
L <sub>gx</sub> (cm)		8.05
$\delta$	1.22	1.26
$\delta^*$	0.123	0.123
$\theta$	0.0927	0.0965
H	1.33	1.27
$\theta/\delta$	0.0487	0.051
Re <sub><math>\theta</math></sub>	929	1015

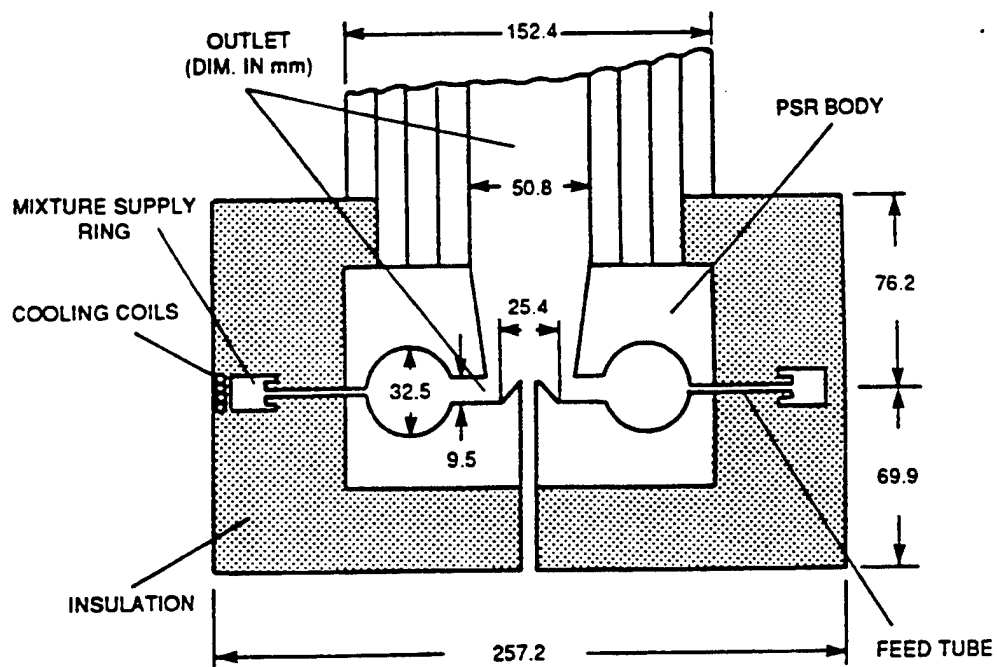


**Fig. 1: Schematic diagram of a toroidal WSR (dimensions in mms)**

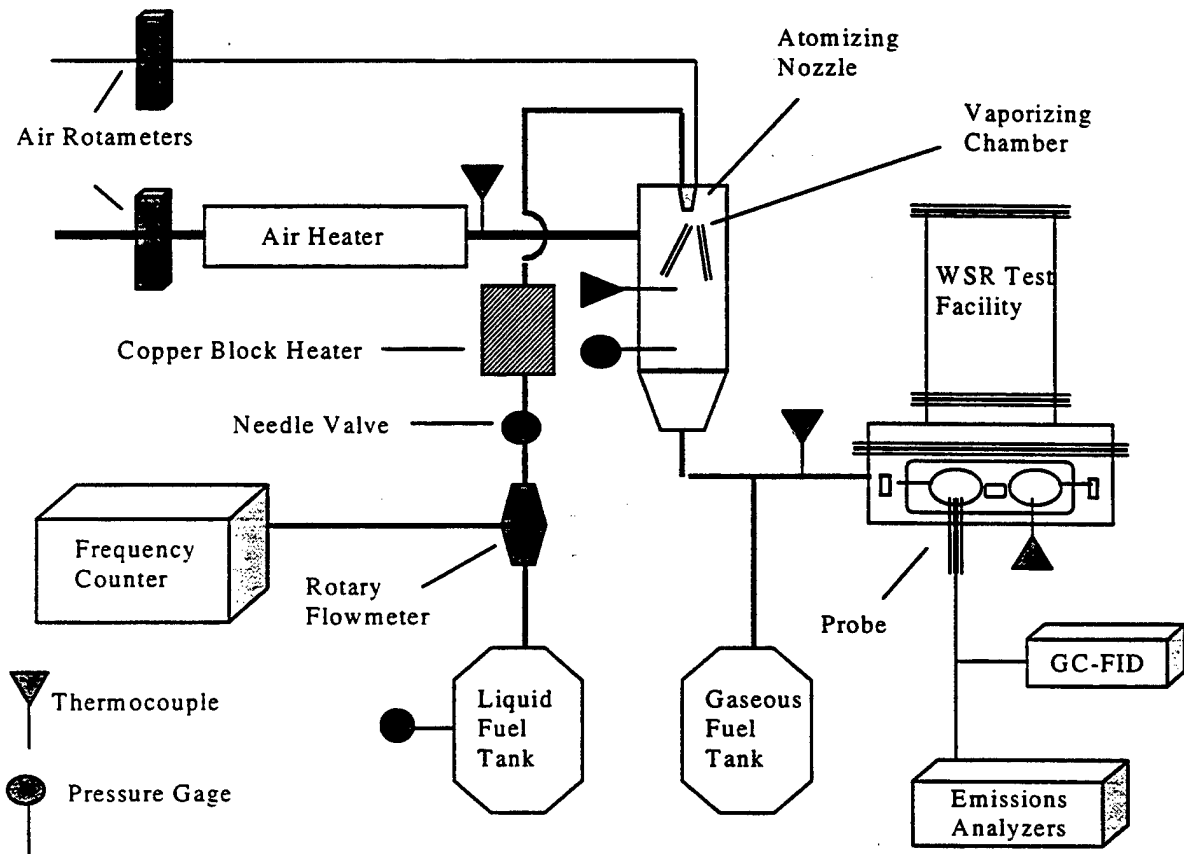


**Fig. 2: WSR test facility and associated instrumentation.**

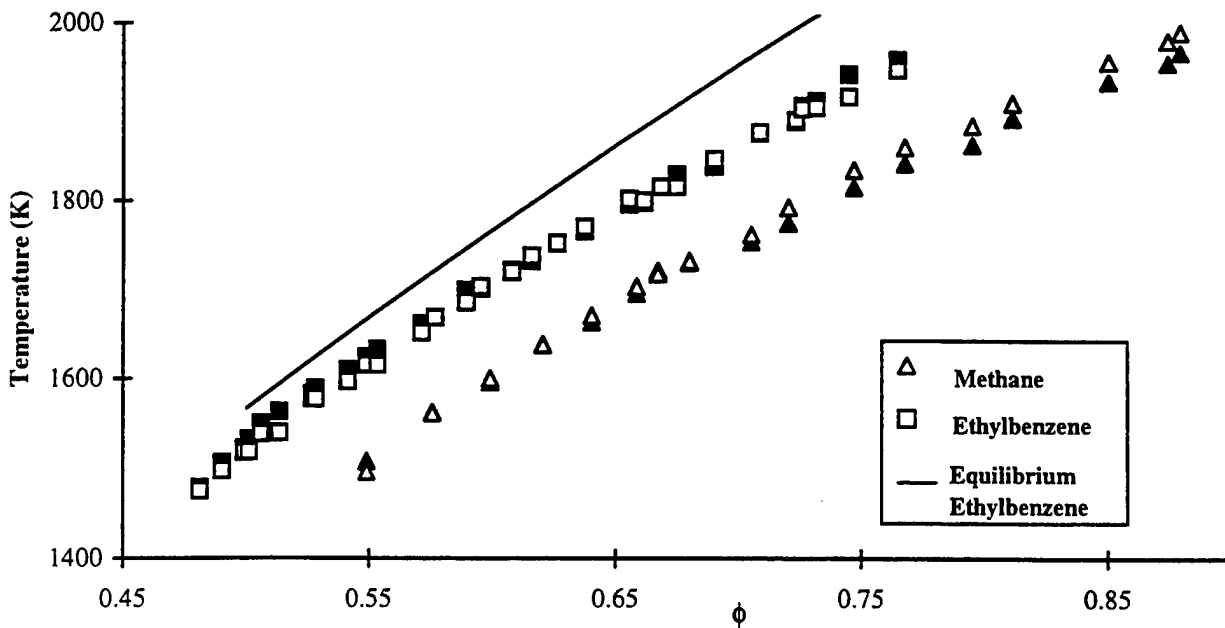


Fig. 3: LBO equivalence ratio versus loading parameter for several hydrocarbon fuels. (Note: methane (black diamond), ethane (circle), cyclohexane (triangle), n-dodecane (white diamond), toluene (X), and cracked fuel simulant (+). Also shown (solid lines) are calculated methane and ethane stability curves.)

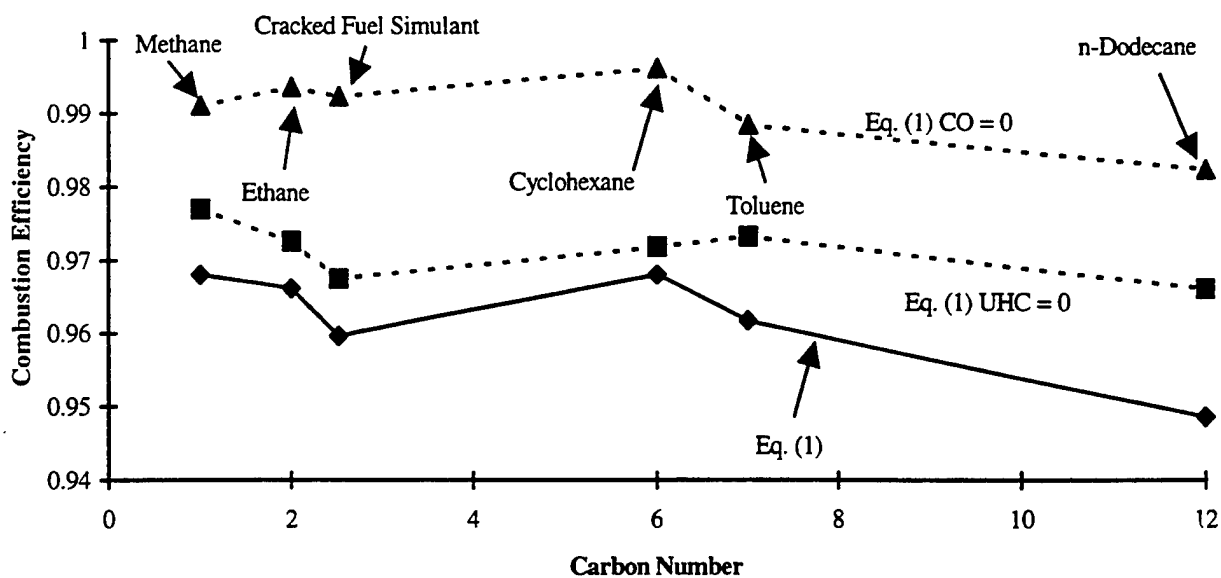


Fig. 4: Combustion efficiency versus fuel carbon number.  $LP \sim 1.3 \text{ g-mol/sec} \cdot \text{L} \cdot \text{atm}^{1.75}$ .

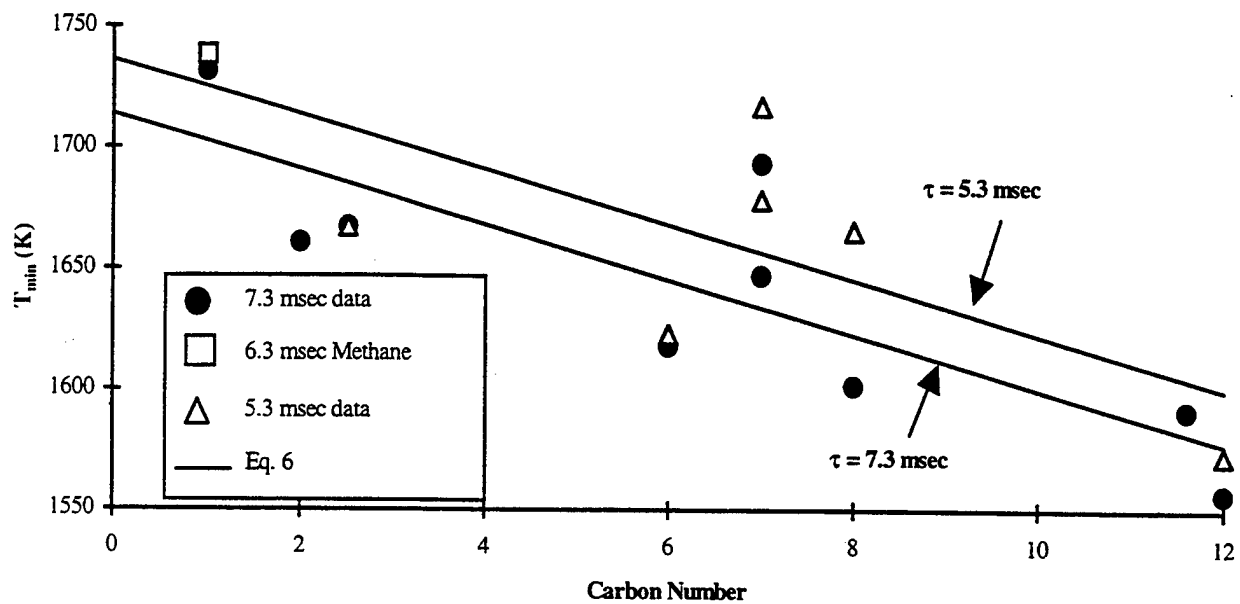


Fig. 5: Plots of reaction temperature for minimum CO emission versus fuel carbon number.

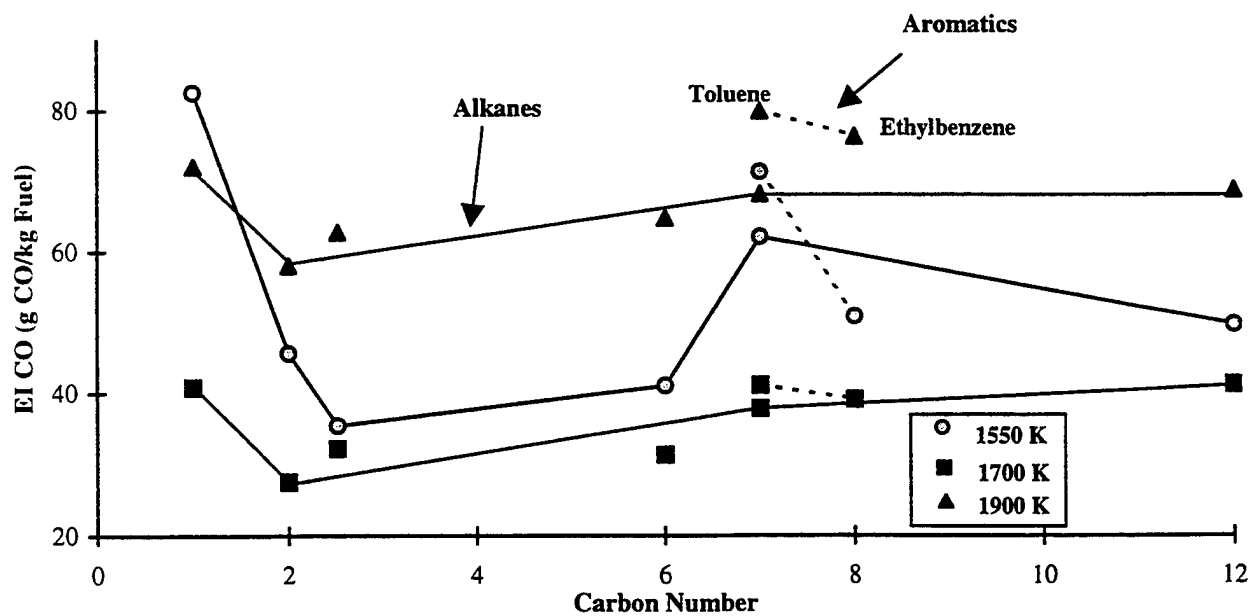


Fig. 6: Emissions indices of CO versus fuel carbon number.

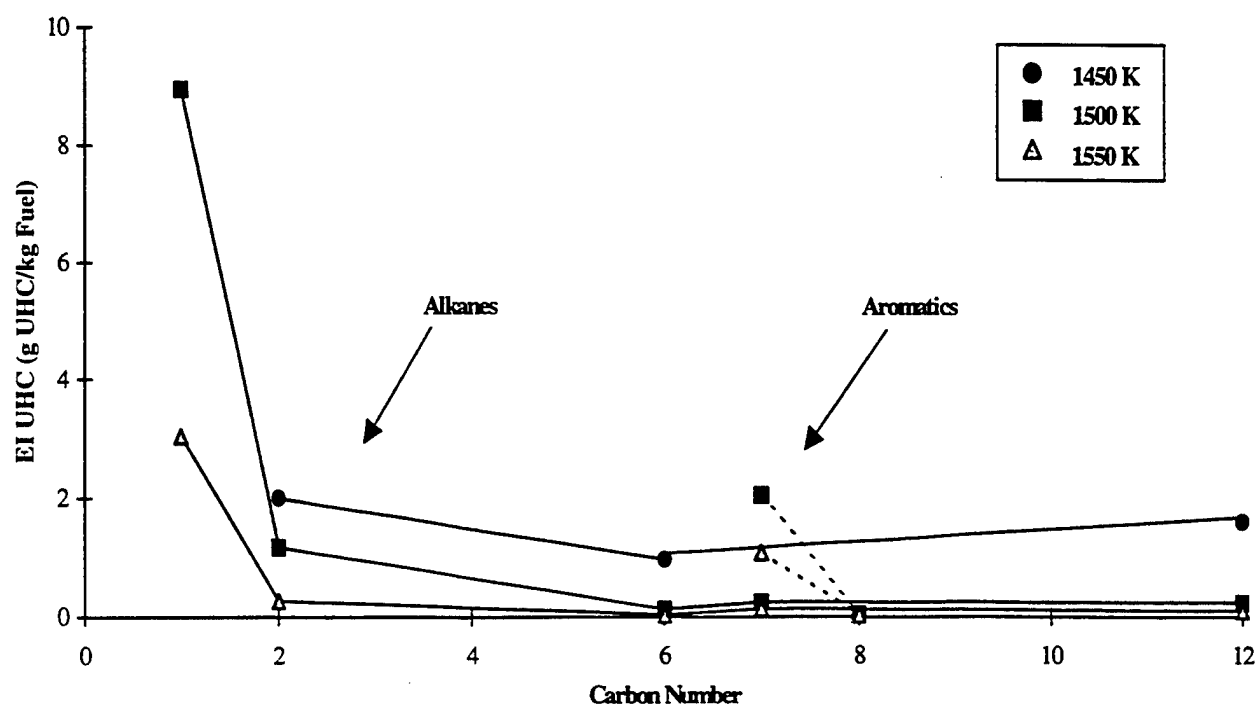


Fig. 7: Emissions index of UHC versus fuel carbon number.

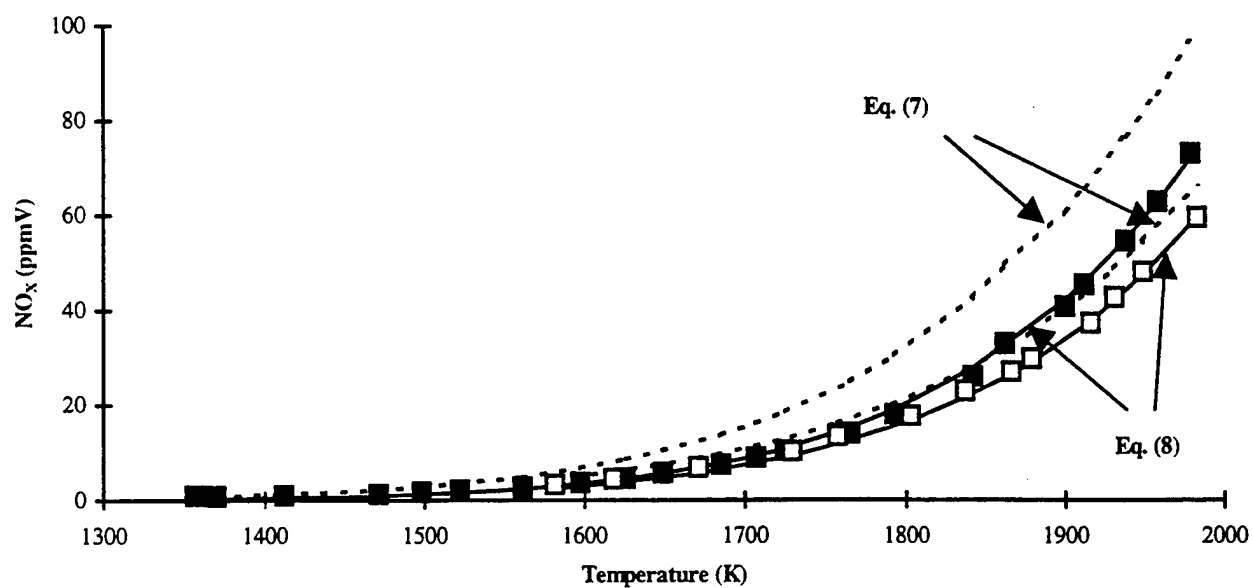


Fig. 8: Emissions index of  $\text{NO}_x$  versus fuel (C/H) ratio.



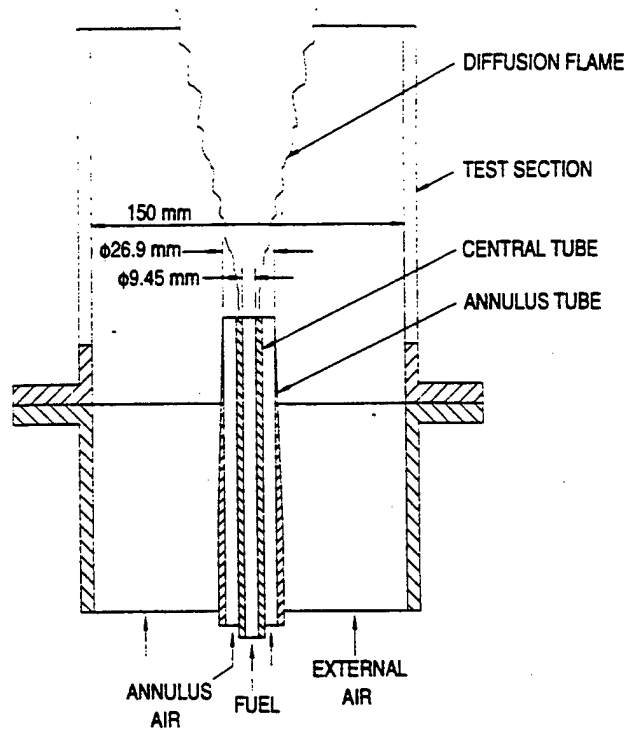


Fig. 9. Schematic of coaxial jet diffusion flame burner.

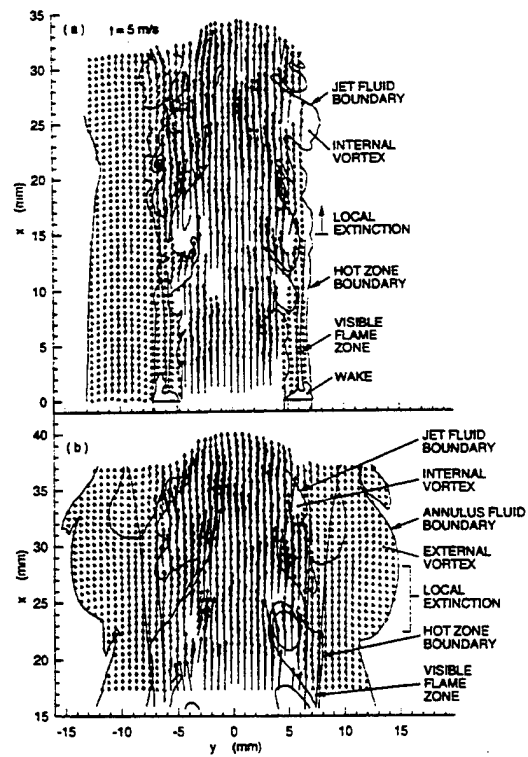


Fig. 10. Velocity vector fields of locally extinguished methane jet diffusion flames.



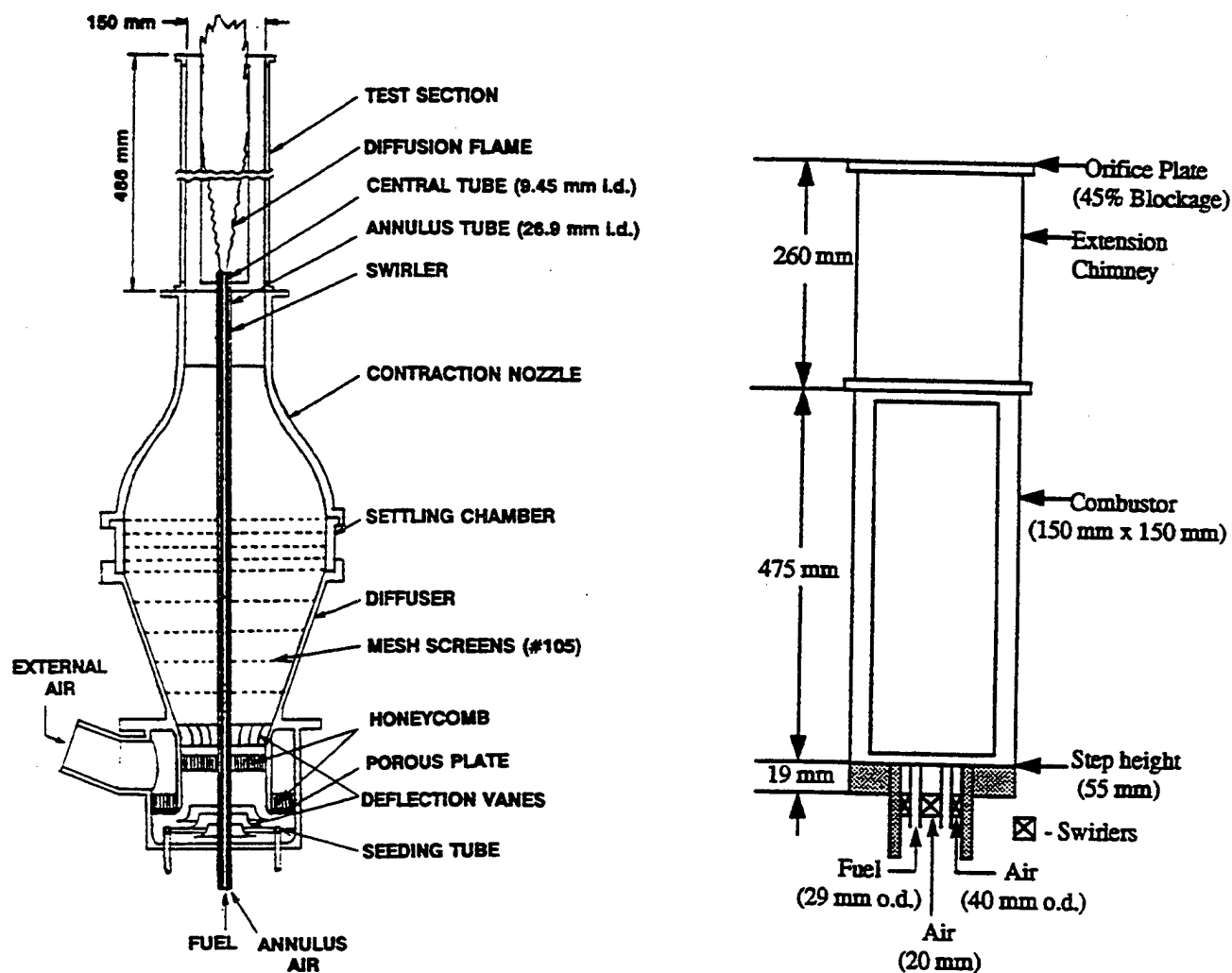


Fig. 12. Schematic of (a) Double concentric jet diffusion flame combustor, (b) Step Swirl Combustor (SSC).

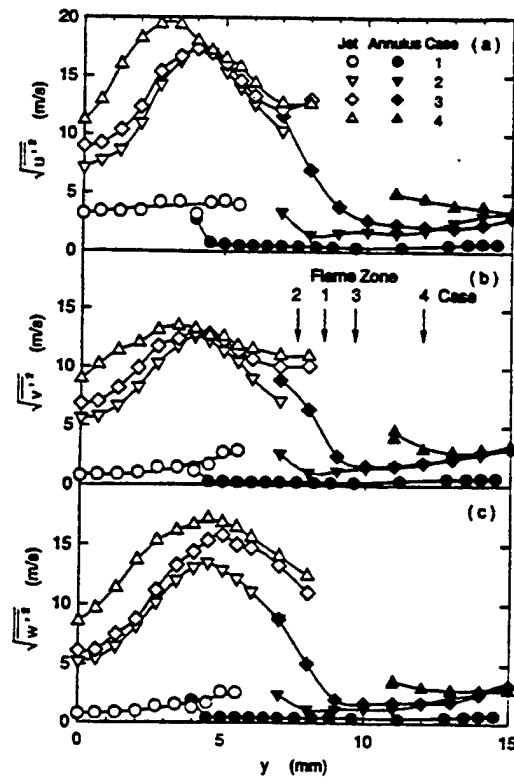


Fig. 13. Turbulent intensity distribution across the hydrogen jet flame at  $x = 25$  mm.

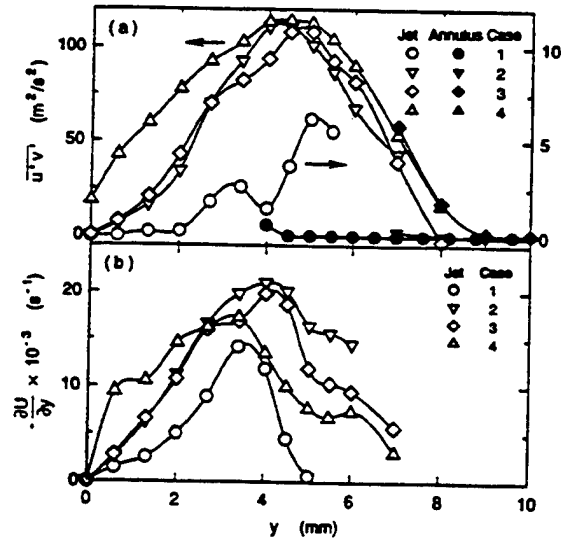


Fig. 14. Radial distribution of (a) Reynolds shear stress, and (b) axial velocity gradient across the hydrogen jet flame.

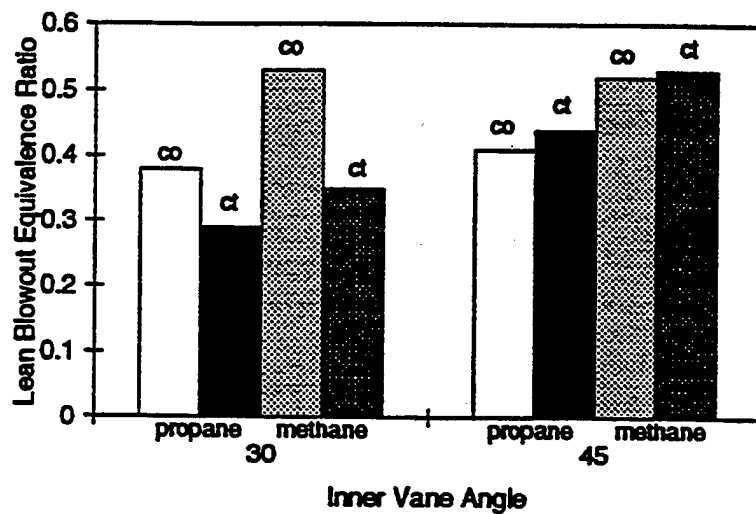


Fig. 15. LBO data in SSC comparing inner swirl angle, co-swirl (co), and counter-swirl (ct).

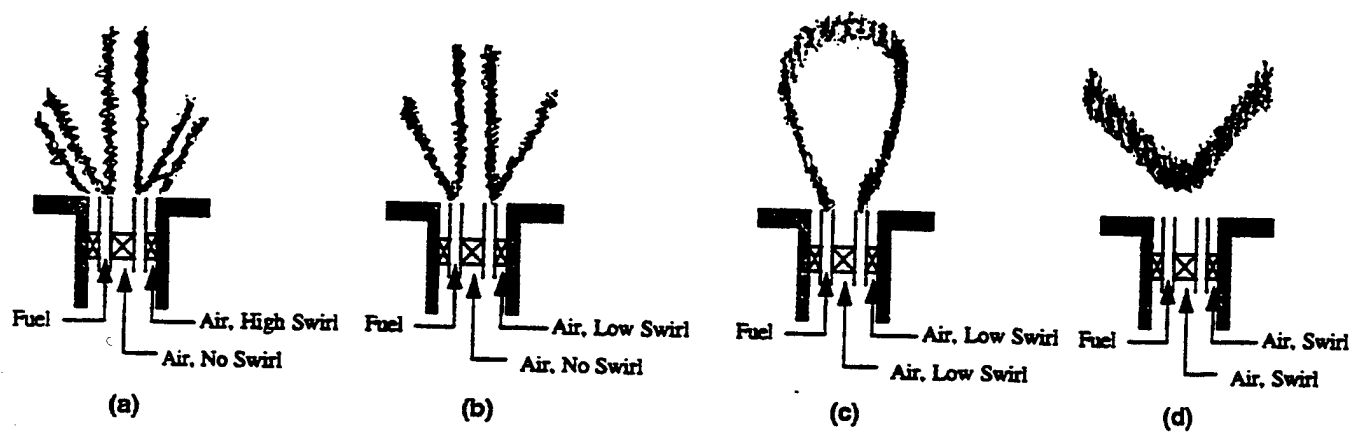


Fig. 16. Sketches illustrating the various flame configurations observed in SSC.

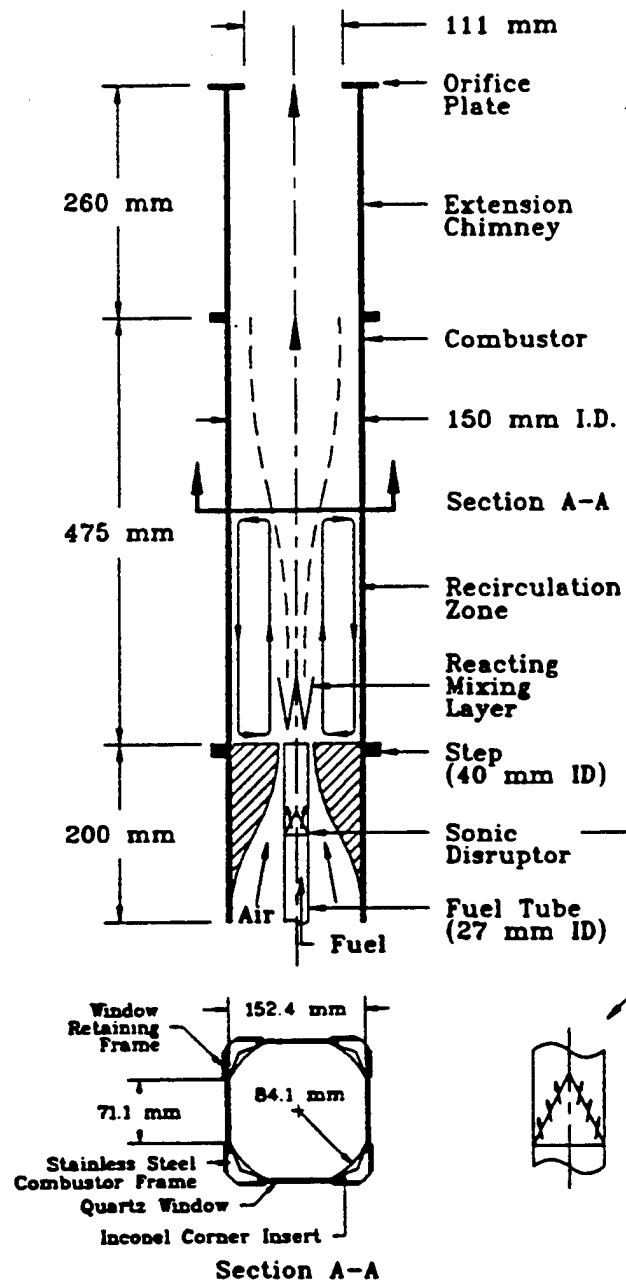


Fig. 17. Schematic diagram of a model research combustor for LBO studies.

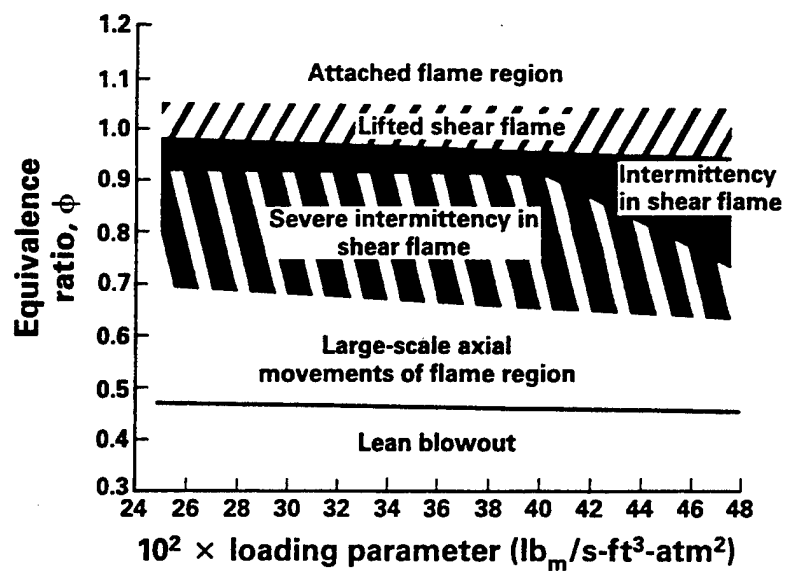


Fig. 18. Sequence of events leading to LBO as observed by flame visualization.

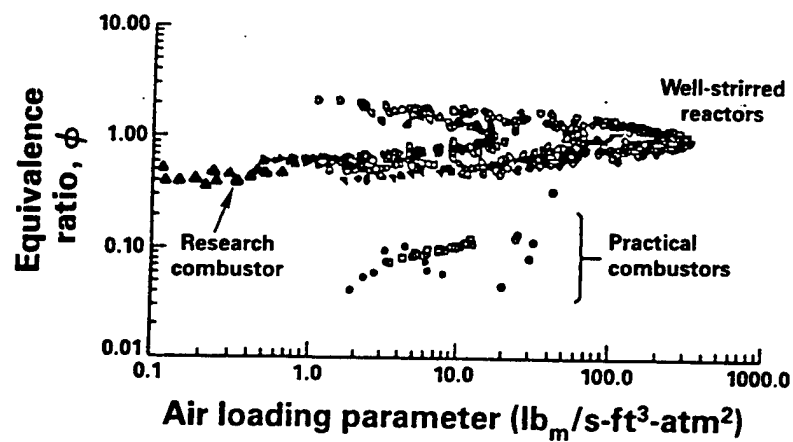


Fig. 19. LBO versus LP data for a research combustor.

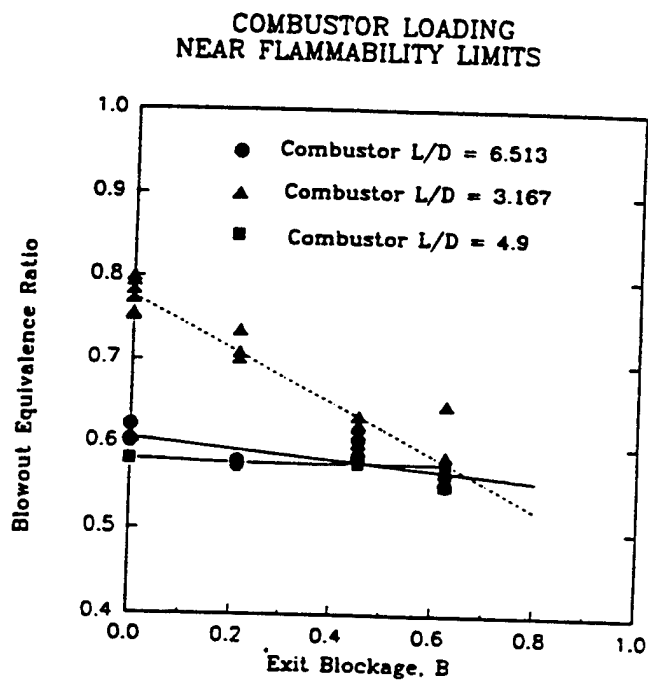


Fig. 20. Effect of back pressure (outlet blockage) on LBO.



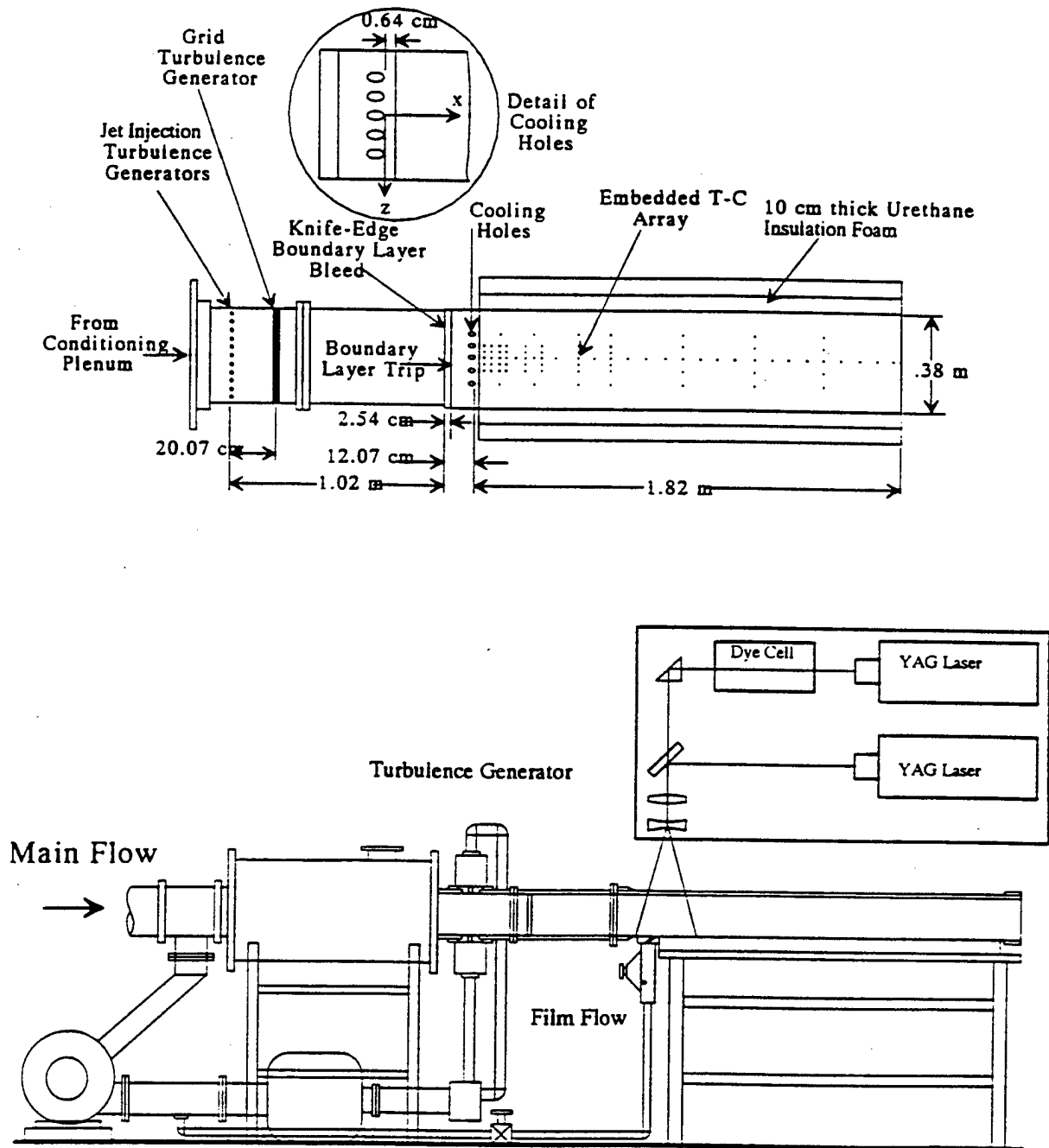


Fig. 21. Film cooling and heat transfer test facility.

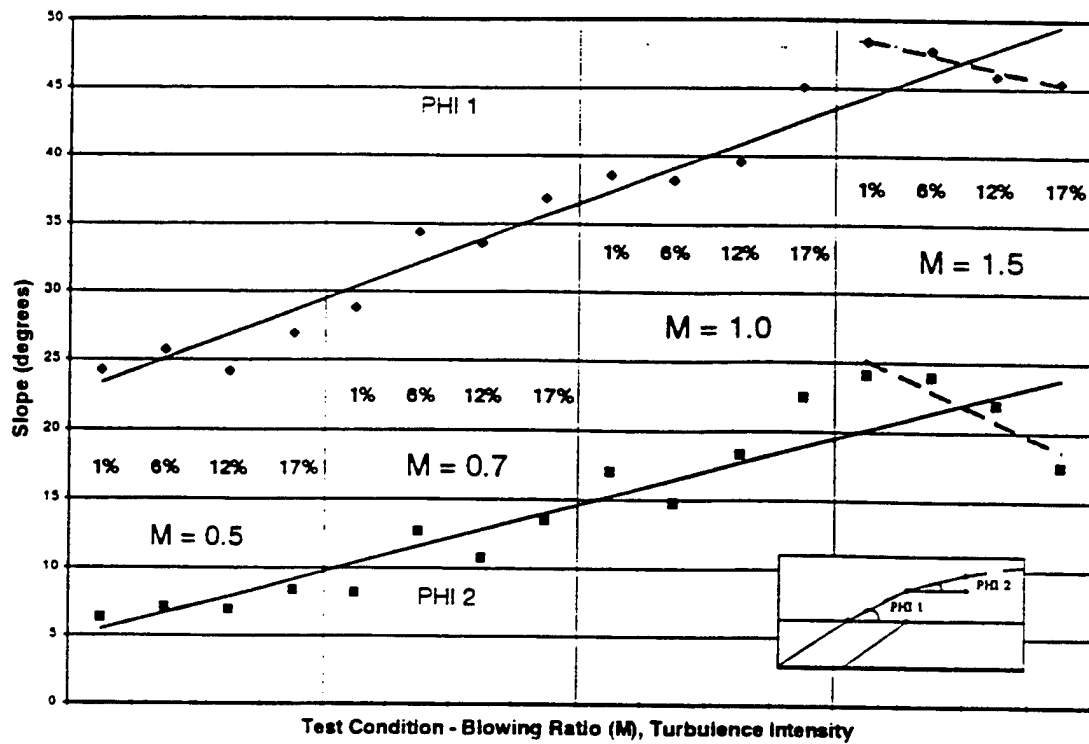


Fig. 22. Jet spread for various blowing ratios.

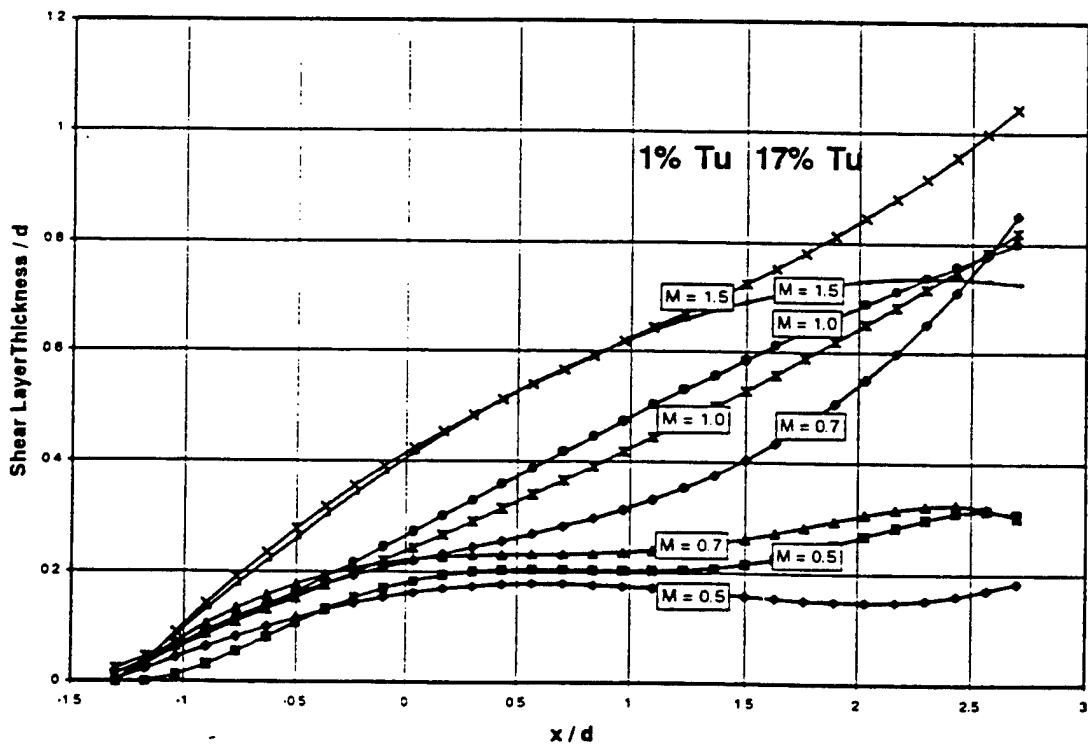


Fig. 23. Growth of the shear layer thickness near the film cooling jet exit.

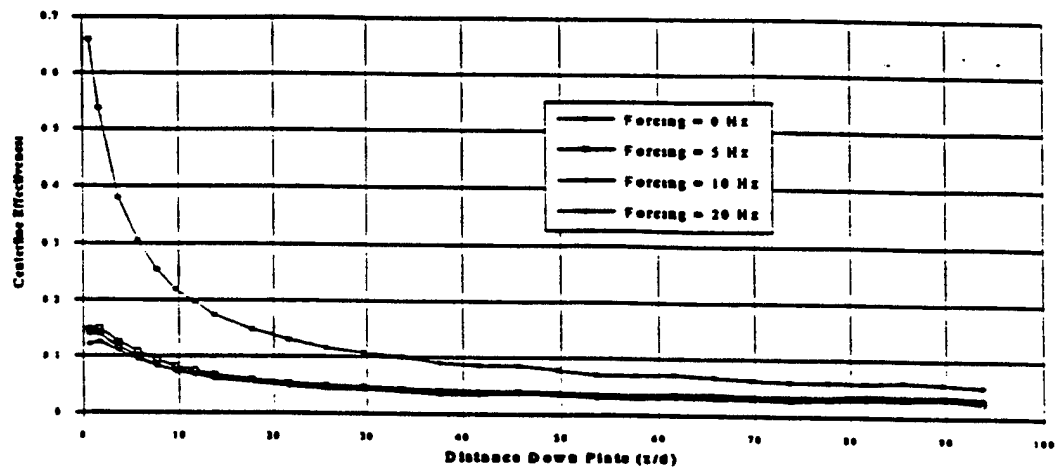


Figure 3a. Centerline Effectiveness at  $M = 0.6$

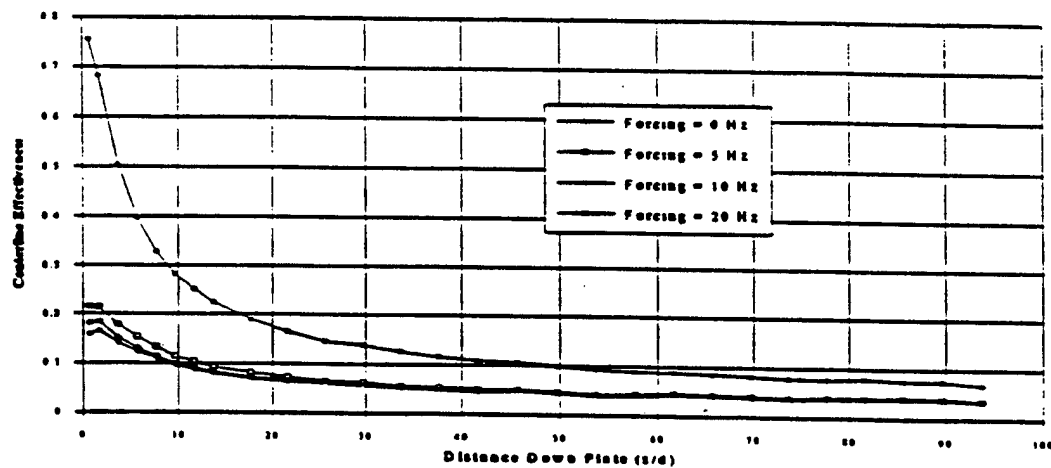


Figure 3b. Centerline Effectiveness at  $M = 0.8$

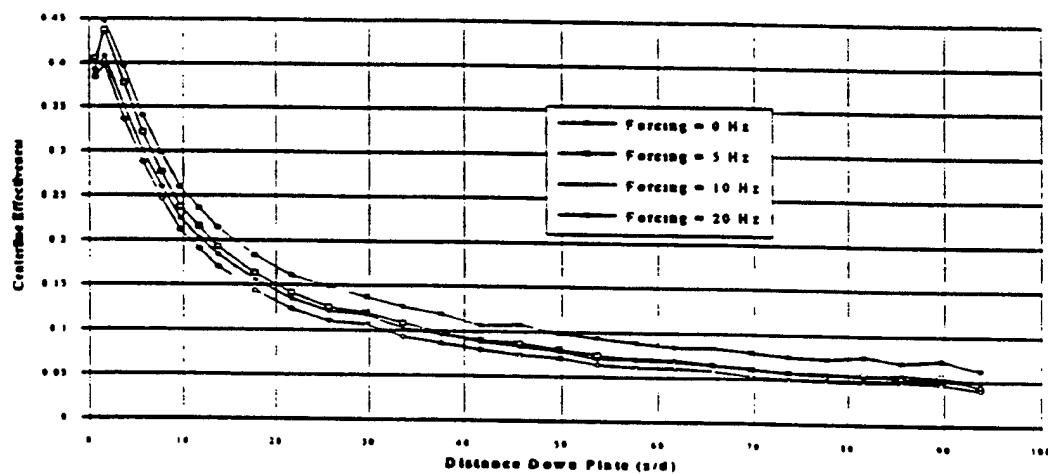


Fig. 24. Film cooling effectiveness with downstream distance with and without forcing.

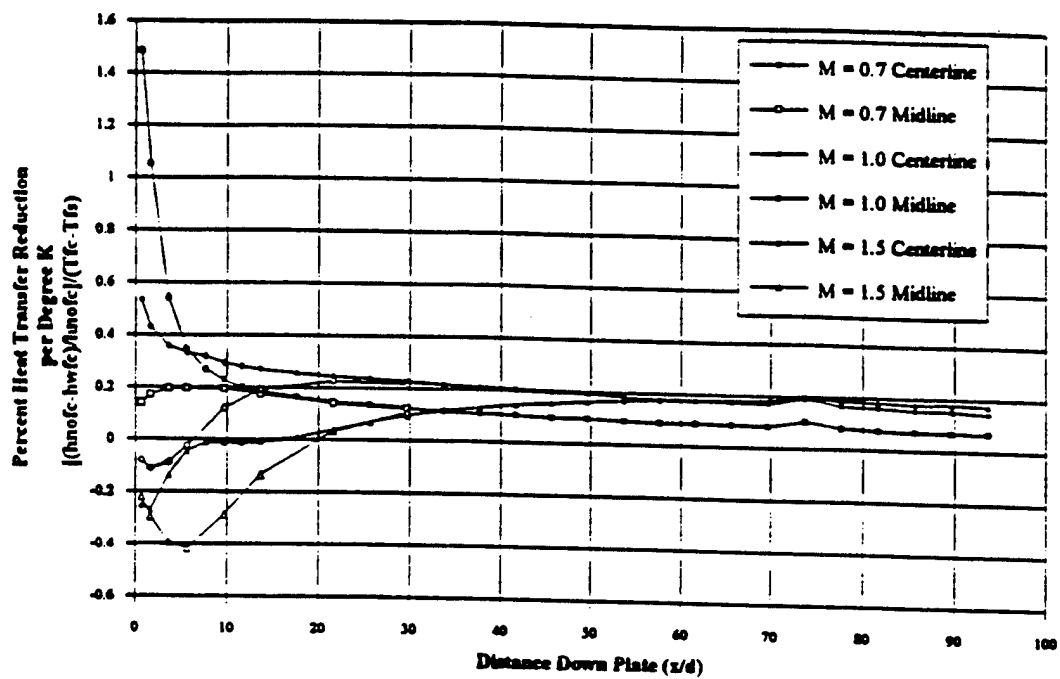


Fig. 25. Effect of free stream turbulence and forcing on heat transfer.

## **APPENDIX A**

### **Emissions Characteristics of Liquid Hydrocarbons In a Well Stirred Reactor**

**J. W. Blust, D. R. Ballal, G. J. Sturgess**



## **AIAA 97-2710**

### **Emissions Characteristics of Liquid Hydrocarbons in a Well Stirred Reactor**

J. W. Blust, D. R. Ballal

University of Dayton

Dayton, OH

G. J. Sturgess

Innovative Scientific Solutions, Inc.

Beavercreek, OH

## **33rd AIAA/ASME/SAE/ASEE Joint Propulsion Conference & Exhibit**

**July 6 - 9, 1997 / Seattle, WA**

# EMISSIONS CHARACTERISTICS OF LIQUID HYDROCARBONS IN A WELL STIRRED REACTOR

J. W. Blust\*, and D. R. Ballal†  
University of Dayton, Dayton OH

G. J. Sturgess‡  
Innovative Scientific Solutions, Inc., Beavercreek OH

## Abstract

The design and development of low-emissions, lean direct injection aero and lean premixed industrial gas turbine combustors is challenging because of a need to satisfy conflicting requirements of operability, combustion performance and low emissions. A toroidal well stirred reactor (WSR) provides a laboratory idealization of an efficient, highly compact primary zone of a gas turbine combustor, and facilitates the study of combustion and emissions. The WSR was used to study lean blow-out limits and emissions from a variety of pure hydrocarbons. In particular, effects of residence time and flame temperature on lean blow-out limits,  $\text{NO}_x$ , CO and unburned hydrocarbon emissions were measured from normal and cyclic alkanes, aromatics and a blend of hydrocarbons. Results showed that hydrocarbon structure plays a pivotal role in the production of emissions, and in determining lean blow-out limits.

## Nomenclature

A = Avagadro's number  
AFT = adiabatic flame temperature  
C = molecular collision factor  
(C/H)<sub>mole</sub> = carbon to hydrogen mole ratio  
CN = carbon number  
E = activation energy  
EI = emissions index (g emission/kg hydrocarbon)  
H = enthalpy  
h = Planck's constant  
LBO = lean blow-out  
LHV = lower heating value of hydrocarbon (J/kg)  
LP = loading parameter (g-mol/s<sup>1</sup>\*atm<sup>n</sup>)  
M = molecular weight of gas mixture  
Me = Mach number at exit of reactor jet

P = pressure  
PSR = perfectly stirred reactor  
ppmw = parts per million by weight  
ppmV = parts per million by volume  
Q = mass flow rate (g/sec)  
R = universal gas constant  
RTD = residence time distribution  
S = thermocouple surface area  
 $\Delta s^*$  = entropy change between states of activated complex and initial reactants  
T = temperature  
UHC = unburned hydrocarbons  
V = reactor volume  
WSR = well stirred reactor  
x = mole fraction of specie  
 $\phi$  = equivalence ratio  
 $\eta$  = efficiency  
 $\rho$  = density  
 $\tau$  = residence time

## Subscripts

cat = catalysis  
comb = combustion  
eb = eddy breakup  
f = flame, fuel  
in = inlet  
jr = jet ring  
o = oxygen  
tm = turbulent mixing

## Superscripts

n = apparent reaction order

## Introduction

As recommended by the 1990 Federal Clean Air Act, reduction of emissions of carbon monoxide (CO), unburned hydrocarbons (UHC), and oxides of nitrogen ( $\text{NO}_x$ ) is necessary for aero- and land based gas turbine engines. Reduction of emissions is challenging, as such reductions often conflict with concurrent performance requirements, such as efficiency, pattern factor, relight, part-load capability (for industrial combustors), and operability requirements such as combustion stability and altitude relight (for aero combustors). Thus, it becomes necessary to examine closely the fuels used by gas turbine engines to see what limitations these present to

\* Ph.D. Student, AIAA Student Member.

† AIAA Fellow.

‡ AIAA Senior Member.

Copyright ©1997 by Authors. Published by the American Institute of Aeronautics and Astronautics, Inc. with permission.

the designers of cleaner burning, high performance engines. In particular, it is desirable to investigate the effects of individual hydrocarbon components in a gas turbine fuel, as well as the fuel *in toto* (i.e. jet fuel for aero engines), on the emissions and performance characteristics of the engine under realistic combustion conditions. Additionally, it is important to study the effects of cracked heavy hydrocarbons on combustion performance and emissions. As a result, a need exists to determine the mechanisms responsible for the formation of pollutants in a gas turbine combustor as well as to determine the lean combustion limits of jet fuels and jet fuel components under these conditions. The well stirred reactor (WSR) provides a means to study these phenomena in a well-controlled laboratory combustor configuration.

A promising strategy to reduce  $\text{NO}_x$ , CO and UHC from gas turbine combustors is to fully vaporize the fuel, premix it with air and then burn this mixture fuel-lean. In support of this approach, experiments have been conducted in the past to establish the limits that might be achieved. These efforts have produced lean, premixed, prevaporized (LPP) combustors (e.g. Marek and Papathakos<sup>1</sup>; Mularz<sup>2</sup>), using geometrically simple hardware. In an LPP combustor, complete fuel vaporization and fuel-air mixing takes place prior to chemical reaction; reaction of this mixture at a very lean fuel-air ratio decreases combustion temperatures and hence reduces the formation of thermal NO.

The referenced experiments were geometrically axisymmetric, and were aerodynamically one-dimensional in a global sense while being three-dimensional locally at the perforated-plate flameholders used. While aerodynamic effects are minimized in such combustor configurations, nonetheless, they are present to a degree (Sturgess<sup>3</sup>). A perfectly stirred reactor (PSR), however, is a theoretical reactor that is zero-dimensional with respect to reactant concentration and temperature gradients. This homogeneity allows the combustion behavior to be uncoupled from any aerodynamic effects. Therefore, in the present investigation, we have supplied a toroidal WSR with premixed, prevaporized liquid hydrocarbons. The WSR is a laboratory reactor that emulates as much as possible the PSR condition. Thus, we have gained an understanding of the CO, UHC and  $\text{NO}_x$  emissions from just the combustion chemistry of these fuels.

It should be noted that similar research using liquid hydrocarbons has been performed previously in

various stirred reactor configurations (Brezinsky et al.<sup>4</sup>; Capehart et al.<sup>5</sup>; Dagaut et al.<sup>6</sup>; Vaughn, et al.<sup>7</sup>; Zelina et al.<sup>8</sup>). The present WSR benefits from previous work, and offers a refined test vehicle for this purpose.

### Experimental Setup

#### WSR Test Facility and Instrumentation

A 250-ml toroidal WSR of Nenniger et al.<sup>9</sup>, as modified by Zelina and Ballal<sup>10</sup>, was used for this experiment. The reactor was constructed of alumina cement, and featured a jet ring with 32 stainless steel jets, 1 mm I.D., to inject the fuel-air mixture at high subsonic velocity. A schematic of the test facility and instrumentation for gaseous fuels is shown in Fig. 1.

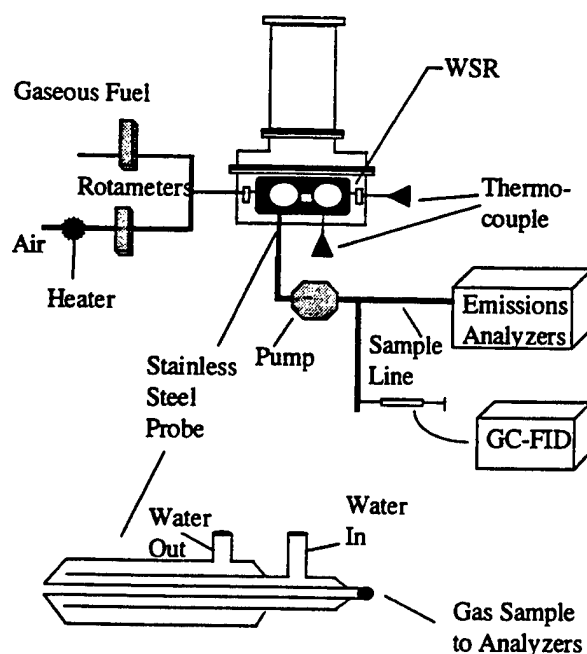


**Fig. 1: WSR test facility and associated instrumentation.**

The Horiba Emissions Analyzers comprised the following units: Model MPA-510 oxygen analyzer (0 to 50 percent), Model FIA-510 total hydrocarbon analyzer (0 to 10,000 ppm carbon), Model VIA-510 CO (0 to 20 percent) and CO<sub>2</sub> (0 to 100 percent) analyzer, and Model CLA-510 SS NO and NO<sub>x</sub> analyzer (0 to 2000 ppmV). These units were calibrated with gases of the following concentrations: hydrocarbon = 404 ppmV propane, NO = 92 ppmV, NO<sub>2</sub> = 1.6 ppmV, CO = 0.4 percent, O<sub>2</sub> = 4.03 or 5.02



percent and  $\text{CO}_2 = 11.06$  percent. Emissions readings were delivered on a dry basis, with water scrubbed from the sample gas to a maximum dew point of  $5^\circ\text{C}$ . The units required a total of 4 slpm gas sample, with a pressure within  $\pm 10$  cm of water of ambient.

A gas sample was drawn from the WSR by a water-cooled stainless steel probe (Blust et al.<sup>11</sup>) and pumped into each unit through a heated sampling line to be analyzed for the various product species. The stainless steel probe used in this experiment featured a small inside diameter, which resulted in a pressure drop when hot sample was drawn from the reactor. The subsequent vacuum necessitated connecting a single speed corrosion resistant pump rated 12 slpm to the sampling line.

Hydrocarbon speciation at LBO conditions was performed by collecting sample gas in a Tedlar bag and directly injecting sample into a gas chromatograph-flame ionization detector (GC-FID, Hewlett-Packard HP 5890 A). Qualitative identifications of products were performed by comparing retention times of unknown analytes to those of pure compounds. Relative quantitation was performed by analyzing selected standards. Overall quantitation was estimated by comparing total response from the GC-FID to the values measured from the FIA-510 total hydrocarbon analyzer.

Combustion temperature,  $T_f$ , was measured by insertion of a Type B thermocouple (platinum-6% rhodium, platinum-30% rhodium) into the toroidal volume. This thermocouple was coated with alumina ceramic to protect the thermocouple from its environment, because platinum-rhodium alloys are subject to high-temperature contamination that can embrittle the alloy.

Temperature measurements were corrected for heat loss by radiation and conduction, and heat gain by convection and catalysis. It has been suggested that reactions, particularly those involving a third body such as H, OH and O-recombination, occur at the hot ceramic surface. The exact form of the catalysis equation needed to make temperature corrections was unknown, so thermocouples were first calibrated by comparing measurements from thermocouples to  $T_f$  measured via the calorimetric method, which utilized combustion efficiency,  $\eta_{\text{comb}}$ , (ARP 1533<sup>12</sup>) and adiabatic flame temperature, AFT, to calculate the temperature of a combustion process. Combustion efficiency was calculated as follows:

$$\eta_{\text{comb}} = 1 - \frac{10109 \text{EI}_{\text{CO}} - \text{EI}_{\text{UHC}}}{\text{LHV} \cdot 1000} \quad (1)$$

Combustion temperature, then, was as follows:

$$T_f = \eta_{\text{comb}}(\text{AFT} - T_{\text{in}}) + T_{\text{in}} \quad (2)$$

This method was modified to account for measured reactor heat loss. In particular, the AFT term was corrected for heat loss using a curve-fit of heat loss as a function methane-air  $\phi$ . In turn, a relation of heat loss as a function of  $T_f$  of any fuel was created. Finding the proper flame temperature to substitute for AFT in Eq. 2 required iteration, but these formulae converged quickly to yield final  $T_f$ .

Once the temperature of the flame was calculated via the calorimetric method, a form of the catalysis equation evolved that forced the uncorrected measured temperature to match that calculated above. For thermocouples coated with alumina ceramic, this was:

$$H_{\text{cat}} = 928,000S \exp\left(\frac{-11,000}{RT_{\text{measured}}}\right) \quad (3)$$

where S is thermocouple surface area. Recombination reactions have low (~ zero) activation energies. That a non-zero E was calculated suggests that a barrier to surface catalysis is provided by the ceramic. Fig. 2 shows temperature measurements taken via the calorimetric method and by corrected thermocouple measurements for several fuels at  $\tau = 7.3$  msec.

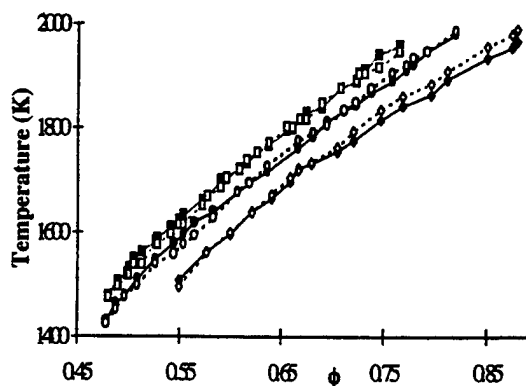


Fig. 2: Reactor temperature versus equivalence ratio for methane (diamond), ethylbenzene (square), and cyclohexane (circle). Solid symbol indicates measurement by corrected thermocouple, hollow symbol by calorimetric method.

The WSR was operated at atmospheric pressure. Air and gaseous flow rates to the WSR were measured via rotameters. In this facility, the air rotameter was rated at 0 to 600 slpm and fuel rotameter at 0 to 58 slpm range. Additionally, a rotameter was installed to meter nozzle air for delivery to an air-blast atomizer (see below), rated at 0 to 180 slpm.

A vaporizer was built to prevaporize liquid hydrocarbons, mix the vaporized hydrocarbon with air, and then supply this mixture to the WSR. A schematic of the vaporizer is shown in Fig. 3. The vaporizer design consisted of a 3 kW air heater (Hotwatt), pressurized fuel tank, vaporization chamber, various flowmeters, nozzle air line, safety devices, and a fuel atomization nozzle. Combustion air was metered through a rotameter and passed through a heater. This air was heated to a temperature sufficient to vaporize a hydrocarbon, but below autoignition temperature, measured by a Type K (chromel-alumel) thermocouple. This hot air was then injected into the vaporization chamber perpendicular to the hydrocarbon mist stream. This established a recirculation zone in the vaporizer to provide additional time for fuel vaporization.

Liquids were metered by a rotary flowmeter (Model E-15, Miniflow Systems, Inc.) and flowrate was varied by adjusting a needle valve. Liquid hydrocarbons were injected through an air-blast atomizing nozzle (Delavan Model 30609-2) into the high-temperature air stream in the vaporizer chamber. Vaporized hydrocarbons and air were transported through an insulated, heated line to the WSR. Also, a Type K thermocouple was inserted in the fuel/air mixture to monitor inlet temperature, and a second thermocouple was placed adjacent to the WSR jet ring to monitor fuel/air temperature just prior to injection into the reactor.

Residence time in the vaporizer was greater than 1.2 sec and was significantly greater than the vaporization time predicted for pure hydrocarbons (e.g. n-heptane 0.36 sec, Ballal and Lefebvre<sup>13</sup>). Additionally, this residence time provided insufficient time for cracking of hydrocarbons in the vaporizer (Stoffel and Reh<sup>14</sup>). When necessary, liquids were preheated prior to atomization via a copper block heater sandwiched on the fuel delivery tube.

Nominal reactor residence time,  $\tau$ , was obtained via the following formula:

$$\tau = \frac{PV}{(R/M)T_f Q} \quad (4)$$

The above flow conditions permitted the operation of the reactor over the range of equivalence ratios  $\phi = 0.43$  to 0.88, loading parameter  $LP \sim 1 \text{ g-mol/s} \cdot \text{l} \cdot \text{atm}^{1.75}$ , residence times  $\tau \sim 5$  to 8 ms and reactor temperatures  $T_f = 1350$  to 2000 K. Hydrocarbons available for study in the WSR included: methane, ethane, cyclohexane, n-heptane, n-dodecane, toluene, ethylbenzene and a gaseous mix of 15 percent methane, 25 percent ethane, 60 percent ethylene by volume. Gaseous fuels were commercially pure grade, pure hydrocarbon liquids were spectroscopic grade (99+ percent).

#### Error Analysis

Gaseous fuel flow was monitored to within  $\pm 2$  percent of reading using a Gilmont rotameter. Air flow was monitored to within  $\pm 2$  percent of full scale using a Brooks rotameter. The combined error produced an uncertainty of  $\pm 3.5$  percent in  $\phi$  during combustion of methane in air. Nozzle air was monitored to within  $\pm 2$  percent of full scale using a Gilmont rotameter. Liquid hydrocarbons were controlled to within  $\pm 0.3 \text{ g/min}$  by the liquid fuel

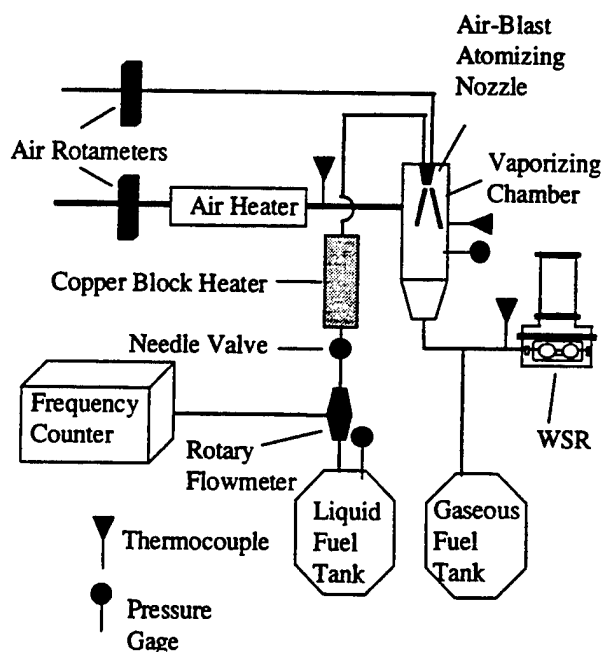


Fig. 3: Vaporizer system for study of liquid hydrocarbons.

Liquid hydrocarbons were contained in a five-gallon pressure tank charged to 60 psig with nitrogen.

delivery system. The combined error produced an uncertainty of  $\pm 3.5$  percent during combustion of a liquid fuel in air. The  $T_f$  measurements were accurate to within  $\pm 30$  K. The Horiba emissions analyzers quote an accuracy to within 1 percent of full scale. For these WSR experiments, this represented an error of: 2 ppmV  $\text{NO}_x$ , 50 ppmV CO, 10 ppmV carbon for UHC, 0.25 percent  $\text{O}_2$ , and 0.5 percent  $\text{CO}_2$ . Residence time,  $\tau$ , was typically controllable to within  $\pm 0.6$  ms. Additionally, CO measurements were repeatable from day to day within  $\pm 100$  ppmV, and  $\text{NO}_x$  within  $\pm 1.5$  ppmV. UHC measurements at very lean conditions suffered from poor repeatability due to variance in the LBO condition. This is discussed in detail in the CO and UHC measurements subsection.

Previous work (Blust et al.<sup>11</sup>) has shown that the sampling system was capable of retaining approximately 99 percent of the CO concentration simulated to be the WSR product concentration at  $\phi = 0.6$ ,  $\tau = 7.0$  ms.

#### Test Conditions

The test matrix shown in Table 1 was conducted with the WSR. Emissions measurements were performed for all test conditions shown. A mix of 13 vol%  $\text{CH}_4$ , 22 vol%  $\text{C}_2\text{H}_6$ , 52 vol%  $\text{C}_2\text{H}_4$ , 13 vol%  $\text{C}_7\text{H}_8$ ,  $\text{CN} = 2.52$ ,  $(\text{C}/\text{H})_{\text{mole}} = 0.5081$  was selected as simulant for heavy, aromatic-containing fuels that are

cracked using thermal or catalytic processes into light fractions with residual light aromatics. Additionally, several of the leanest conditions shown represented LBO, at which point bag sample emissions data were collected. This will be discussed in detail in later sections.

#### The Well Stirred Condition

In order for the WSR to be well mixed, the reactor must be both micromixed and macromixed. For micromixing to be successful, the turbulent mixing time of the combustion gas,  $t_m$ , must be less than the order of the fastest reactions occurring in the process. The turbulent mixing time in the reactor was calculated via turbulent theory (Nenniger<sup>15</sup>; Zelina and Ballal<sup>16</sup>) and compared to the reaction rate orders for methane at 1 atm estimated by Getz and Zabarnick<sup>17</sup>. Methane-air combustion at  $\tau = 6.0$  msec,  $T_f = 1747$  K,  $\phi = 0.7$ ,  $P = 1$  atm represents typical combustion conditions, during which  $\tau_m = 19$   $\mu\text{sec}$ . At similar conditions hydrocarbon reduction time is  $\sim 10$   $\mu\text{sec}$ , CO oxidation time is  $\sim 500$   $\mu\text{sec}$ , and  $\text{NO}_x$  formation time is  $\sim 20$  msec. Accordingly, the WSR was perhaps not well mixed with respect to the initial reduction reactions of hydrocarbons, but was sufficiently well mixed for the oxidation reactions that subsequently occurred in the reactor.

Table 1: WSR Test Matrix

Hydrocarbon	$\tau$ (msec)	$\phi_{\min}$	$\phi_{\max}$	$T_{f\min}$ (K)	$T_{f\max}$ (K)
Methane	7.3	0.55	0.88	1507	1967
	6.32	0.59	0.83	1517	1918
Ethane	7.26	0.48	0.84	1407	1996
	7.47	0.48	0.82	1429	1981
Cyclohexane	5.22	0.51	0.78	1536	1922
	7.19	0.53	0.84	1517	1975
n-Heptane	5.49	0.54	0.81	1595	1974
	7.32	0.46	0.79	1499	1946
Toluene	5.35	0.5	0.78	1552	1936
	7.43	0.48	0.76	1478	1958
Ethylbenzene	5.33	0.49	0.67	1546	1839
	6.75	0.49	0.77	1530	2007
13 vol% Methane, 22 vol% Ethane, 52 vol% Ethylene, 13 vol% Toluene	5.17	0.46	0.76	1391	1969
n-Dodecane	7.39	0.46	0.8	1357	1979
	5.2	0.55	0.79	1581	1983

Successful macromixing necessitates the WSR having the proper residence time distribution (RTD), and spatial homogeneity of species and temperature. To test RTD, Calo, et al.<sup>18</sup> injected various pulse times and concentrations of krypton tracer into the WSR jet ring during methane-air combustion ( $\tau = 11.6$  msec,  $T_f = 1754$  K,  $\phi = 0.7$ ,  $P = 1$  atm). Krypton concentration versus time for each pulse was monitored by a free-jet, molecular beam mass spectrometer (Ballenthin, et al.<sup>19</sup>) pulling sample from the WSR through an air-cooled quartz probe. A significant amount of pulse dispersion occurred in the jet ring, and this had to be accounted for prior to examining the reactor RTD. Ultimately, it was found that the measured RTD, adjusted for jet ring dispersion, exhibited the exponential growth and decay patterns typical of an inert pulse tracer in a stirred reactor. Spatial homogeneity was previously demonstrated by Zelina<sup>20</sup>. Maximum detected variabilities were:  $T_f = \pm 25$  K,  $\text{NO}_x = \pm 2.5$  ppmV,  $\text{CO} = \pm 90$  ppmV. These variabilities were approximately the same as the day to day repeatability in the WSR system, and may account for the repeatability limits. Thus, the WSR was successfully macromixed.

#### Calculations

To anchor the present results the methane experimental data were compared to calculations for a PSR using the GRI 2.1 reaction mechanism. The algorithm used for the solution of a system of non-linear, stiff, ordinary differential kinetics equations is CREK (Pratt and Wormeck<sup>21</sup>). This algorithm is incorporated in a reactor network code (Pratt and Pratt<sup>22</sup>). The calculations and measurements for  $\text{NO}_x$ ,  $\text{CO}$ ,  $\text{CO}_2$ ,  $\text{O}_2$ , and  $\text{H}_2\text{O}$  vapor were in close agreement. This agreement commented favorably on the high degree of mixing attained in the WSR, and successful operation of the sampling and temperature measurement systems.

#### Results and Discussion

Often, emissions concentrations are expressed by emissions index, EI. For EI calculation, all UHC is treated as methane, and  $\text{NO}_x$  as  $\text{NO}_2$ . All emissions are stated on dry basis.

#### Temperature Measurements

Measured  $T_f$  (via thermocouple) is plotted against  $\phi$  for several hydrocarbons at  $\tau \sim 7.3$  ms in Fig. 4. Also plotted are the equilibrium flame temperatures

versus  $\phi$  (Gordon and McBride<sup>23</sup>). Two observations were made with respect to this figure.

(i) Measured temperatures for a specific hydrocarbon never reach the corresponding equilibrium flame temperature because the reactor residence time was short enough that the products did not reach their equilibrium concentrations. Observed  $\eta_{\text{comb}}$  was less than equilibrium  $\eta_{\text{comb}}$  and measured  $T_f$  was lower than equilibrium flame temperature. Additionally, the WSR was not adiabatic. Heat loss of 3 to 5 percent was typical.

(ii) The measured temperature curves were concave down, with the measured temperature departing the equilibrium line more at low and high  $\phi$  than in the middle. This reflected changes in  $\eta_{\text{comb}}$  for each hydrocarbon with respect to  $\phi$ .

#### Lean Blow-Out

In aero and industrial combustors, flame stabilization is essential to combustor performance and safety. Combustion must be sustained over a wide range of operating conditions, and so it is essential to designers to know the stability limits of a fuel under realistic conditions. In practical combustors stability is provided by the primary zone. It has been proposed (Avery and Hart<sup>24</sup>; Bragg<sup>25</sup>; Childs<sup>26</sup>) that the primary zone of a gas turbine combustor could be modeled as a stirred reactor. To this end the WSR was used as a flameholder to maintain lean combustion and measure the LBO limits of fuels.

Defining unstable combustion and LBO limit in the WSR was difficult. No optical access was provided by the toroidal design, so temperature was used as the primary method of detecting LBO. In particular for this experiment, LBO was defined as the condition characterized by a rapid, large magnitude drop in temperature, and preceded by substantial increase in UHC and noise, as  $\phi$  was decreased while maintaining constant  $\tau$ .

At LBO, it was of interest to measure  $T_f$ ,  $\phi$ , EI of CO and UHC, and flow rates of reactants and thus to calculate  $\eta_{\text{comb}}$  and loading parameter (LP). Loading parameter is an expression of the maximum heat release capability of a fuel per volume of reactor and pressure to the  $n$ -th power. LBO  $\phi$  from several hydrocarbons are plotted against LP in Fig. 5.

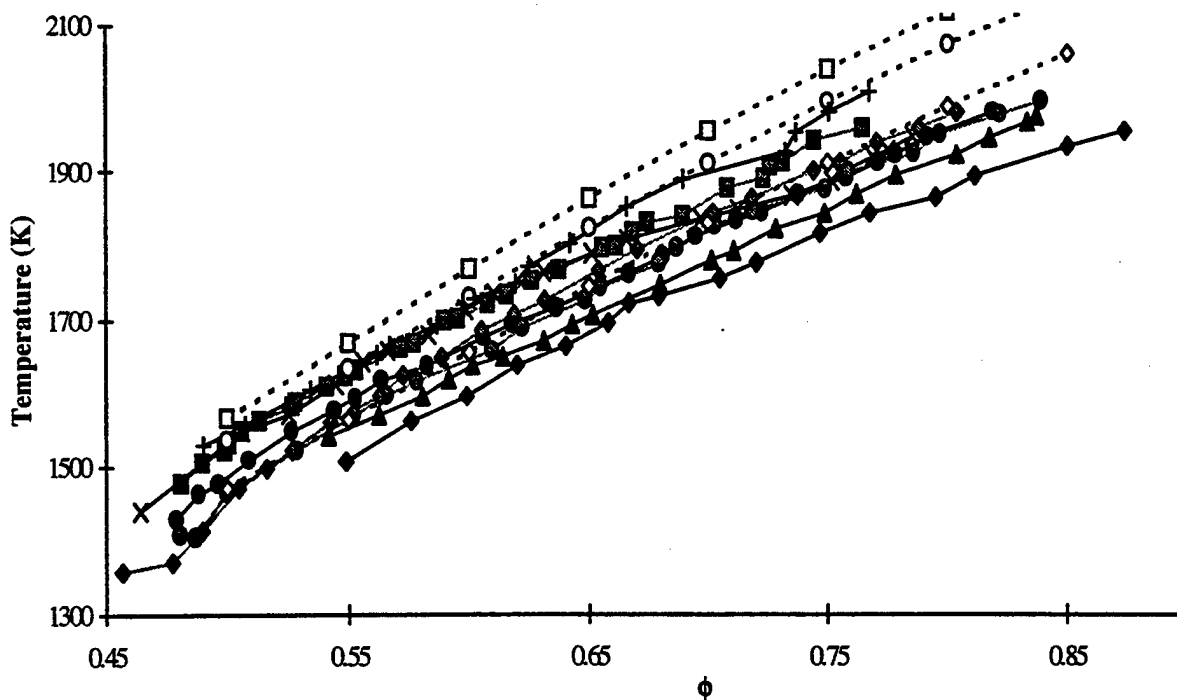


Fig. 4: Reactor temperature versus equivalence ratio for several hydrocarbons at nominal residence time 7.3 msec: methane (black diamond), ethane (gray circle), cyclohexane (black circle), n-heptane (black triangle), n-dodecane (gray diamond), toluene (X), ethylbenzene (gray square), cracked fuel simulant (+). Also shown (hollow symbols) are equilibrium methane, cyclohexane, and ethylbenzene (Gordon and McBride<sup>23</sup>).

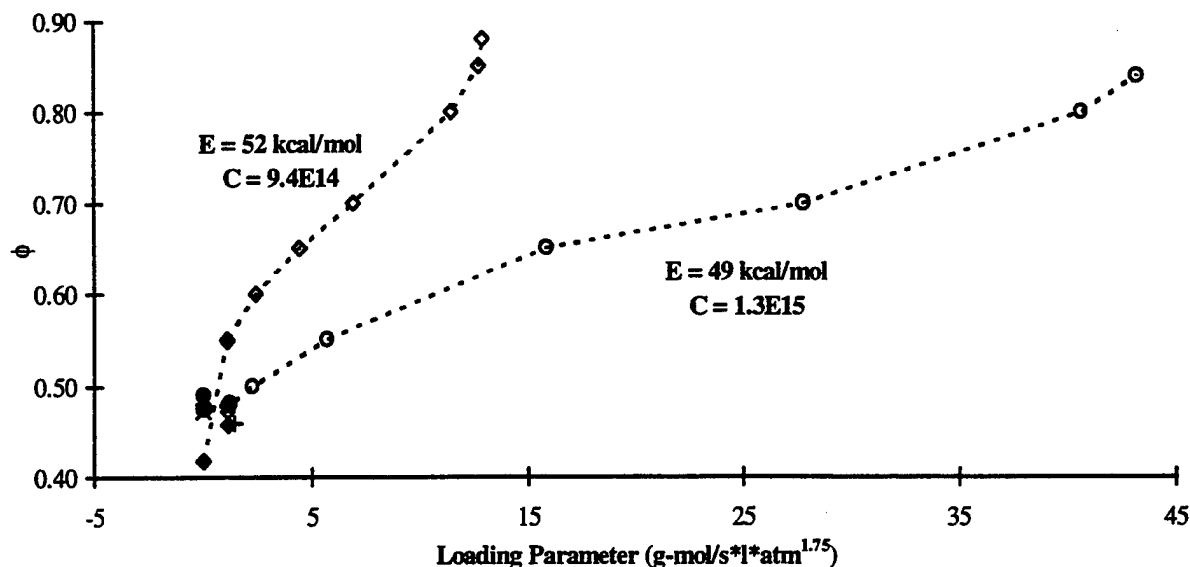


Fig. 5: Equivalence ratio versus loading parameter at LBO for several hydrocarbons: methane (black diamond), ethane (gray circle), cyclohexane (black circle), n-dodecane (gray diamond), toluene (X), cracked fuel simulant (+). Also shown (dotted lines) are calculated methane and ethane stability loops.

When available, LBO limits for each hydrocarbon as measured in a vertical glass tube experiment (Lefebvre<sup>27</sup>, except cyclohexane from Lewis and von Elbe<sup>28</sup>) are included in this figure, with these lean limits modified for  $T_{in}$  by the Burgess-Wheeler law (Lefebvre<sup>27</sup>). In this formula, measured jet ring temperature  $T_{jr}$  was substituted for  $T_{in}$  to give the following form:

$$\begin{aligned} \text{LBO (percent V in air)} \\ = \text{LBO}_{298K} \left[ 1 - \frac{0.75(T_{jr} - 298)}{\text{LBO}_{298K} \text{LHV(kcal/mol)}} \right] \end{aligned} \quad (5)$$

Flow of reactants in the glass tube was zero, so the LP of these LBO limits was zero.

LBO equivalence ratios from the vertical tube experiment were comparable to LBO equivalence ratios as measured in the WSR for most hydrocarbons, methane being an exception. This indicated that methane, for instance, possesses a significantly different stability loop from ethane, cyclohexane and toluene. To demonstrate this, the calculated stability loops of methane and ethane are also plotted on Fig. 5.

Stability theory has been described in detail elsewhere (Lefebvre<sup>27</sup>; Zelina<sup>20</sup>). In this theory, the rate of reaction between fuel and air is expressed by the material balance equation:

$$\eta_{\text{comb}} \phi Q = CVT_f^{1/2} \exp(-E/RT_f) \rho^n x_f^m x_o^{n-m} \quad (6a)$$

where  $n = 1.75$ ,  $m = 0.75$ ,  $x$  is the mole fraction of fuel or air and  $C$  is the molecular collision factor calculated as follows (Kanury<sup>29</sup>):

$$C = \frac{RT_f^{1/2}}{hA} \exp\left(\frac{\Delta s^*}{R}\right) \quad (6b)$$

where  $h$  is Planck's constant,  $A$  is Avagadro's number, and  $\Delta s^*$  is the entropy change between the states of activated complex and initial reactants. For lean mixtures, Eq. (6a) is written as:

$$LP = \frac{Q}{VP^n} = \exp\left(\frac{E}{RT_f}\right) \frac{Cx_f^{0.75} x_o}{T_f^{1.25} \eta_{\text{comb}} \phi R^{1.75}} \quad (6c)$$

Thus,

$$E = RT_f \ln\left(\frac{Cx_f^{0.75} x_o}{LPT_f^{1.25} \eta_{\text{comb}} \phi R^{1.75}}\right) \quad (6d)$$

Entropy of the activated complex in Eq. (6b) was found by applying a quantity of energy equal to  $E$  to the energy of reactants and evaluating entropy at this condition. Thus, to calculate  $C$  and  $E$  required iteration between Eqs. (6b) and (6d). The stability curves in Fig. 5, then, were generated by varying  $\phi$  in Eq. (6c), using the measured  $T_f$  for each  $\phi$ , including non blow-out conditions, but using  $\eta_{\text{comb}}$  corresponding to that measured at LBO.

Using the above analysis, for methane  $E = 52$  kcal/mole and  $C = 9.4 \times 10^{14} \text{ K}^{1/2} \text{ sec}^{-1}$ ; for ethane  $E = 49$  kcal/mole and  $C = 1.3 \times 10^{15} \text{ K}^{1/2} \text{ sec}^{-1}$ . Note that the activation energy calculated for methane is much greater than that calculated for surface catalysis, Eq. (3).

It is important to note, however, that LBO is a "soft" limit; that is, a great amount of hysteresis exists in the limit. If LBO is attempted after the reactor has been burned very hot, the mixture is capable of burning at leaner conditions than if the limit is approached from a cooler operating condition. A variance in  $T_{jr}$  of  $\pm 50$  K has been measured, depending on the temperature at which the reactor is run, and for how long that condition is sustained. Using Eq. (4), this corresponds to an uncertainty in the LBO  $\phi$  of  $\pm 0.02$ .

#### CO<sub>2</sub> and O<sub>2</sub> Measurements

In a WSR operating in the stable mode, CO<sub>2</sub> concentration should peak and oxygen concentration should drop to near zero at stoichiometric equivalence ratio. Fig. 6 shows measured CO<sub>2</sub> and O<sub>2</sub> concentrations (vol%) as a function of equivalence ratio from several hydrocarbons. Also plotted are calculated equilibrium values for cyclohexane-air combustion. As expected, CO<sub>2</sub> increased and O<sub>2</sub> decreased as  $\phi$  approached unity.

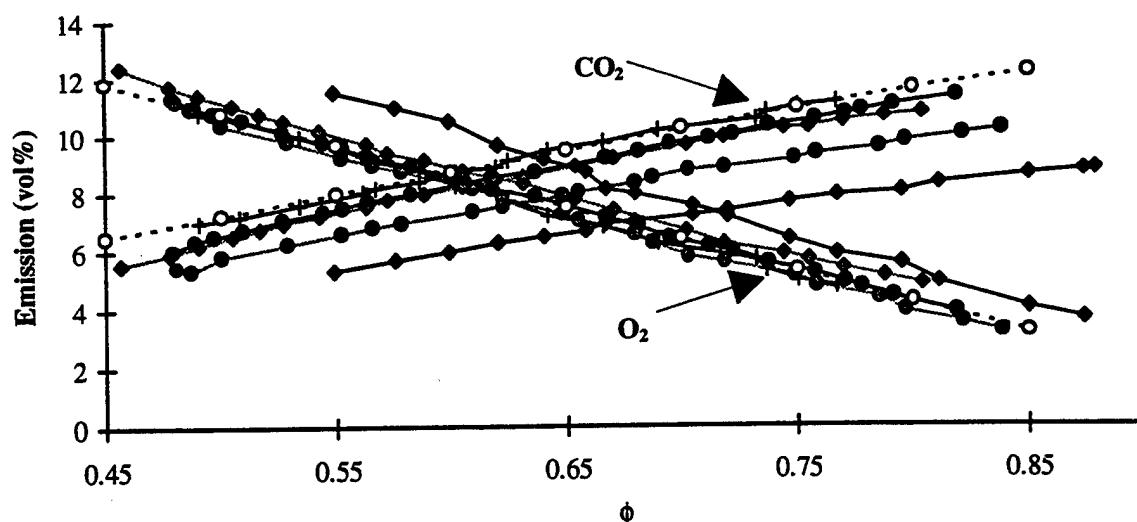


Fig. 6:  $\text{CO}_2$  and  $\text{O}_2$  concentration versus equivalence ratio for several hydrocarbons at nominal residence time 7.3 msec: methane (black diamond), ethane (gray circle), cyclohexane (black circle), n-dodecane (gray diamond), toluene (X), cracked fuel simulant (+). Also shown (hollow circle) is equilibrium cyclohexane (Gordon and McBride<sup>23</sup>).

#### CO and UHC Measurements

CO and UHC emissions are important because they also represent a direct measure of combustion inefficiency (see Eq. (1)). If the combustion zone operates fuel-rich, has inadequate mixing, or is quenched by cold air, large quantities of CO (which is relatively resistant to oxidation) will be emitted due to the lack of oxygen needed to complete the reaction to  $\text{CO}_2$ , or insufficient time being provided for CO to be oxidized. UHC emissions include fuel which emerges from the combustor exit in the form of condensate or vapor, and the products of the thermal degradation of the parent fuel into species of lower molecular weight, such as methane, acetylene, ethylene and propylene. UHC emissions are associated with poor atomization, inadequate burning rates, insufficient residence time and premature quenching. Thus, it is desirable to find combustor operating conditions that minimize the emission of CO and UHC, and therefore maximize combustion efficiency.

Clearly, operating the WSR fuel-rich will produce great amounts of CO and UHC. Although rich combustion is interesting for studying reaction chemistry, it is not interesting from an engine standpoint unless a lean afterburning approach is taken (as in a Rich, Quench, Lean combustor). This paper will focus, then, on lean combustion, and locating operating conditions that minimize CO and UHC production.

Fig. 7 shows emissions index of CO from several hydrocarbons at several  $T_f$  plotted as a function of carbon number at residence time of 7.3 ms. Alkanes and aromatics are plotted separately, and cracked fuel simulant is treated as an alkane. All hydrocarbons in general exhibited a U-shaped trend in CO production. As temperature increased, CO concentration first decreased as reaction rate of CO consumption increased. A minimum of CO was reached, then CO increased as temperature increased. This increase was due to an increased rate of  $\text{CO}_2$  dissociation.

As shown in Fig. 7, alkanes, *sans* methane, displayed a slight increase in CO as carbon number increased. This increase was modest, and discontinued for  $\text{CN} > 7$  (depending on the temperature this trend was occasionally reversed for  $\text{CN} > 7$ ). Increasing molecular weight from one heavy alkane to another (i.e. from n-heptane to n-dodecane) did not result in increase in CO. Aromatics showed a reverse trend from alkanes, with a decrease in CO being observed in general as CN increased from 7 to 8. Finally, methane produced more CO than all other hydrocarbons investigated. This distinction for methane is somewhat artificial due to the definition of emissions index. By ppmV, CO in the sample from methane is not so high. However, the low molecular weight of methane biases the EI high.

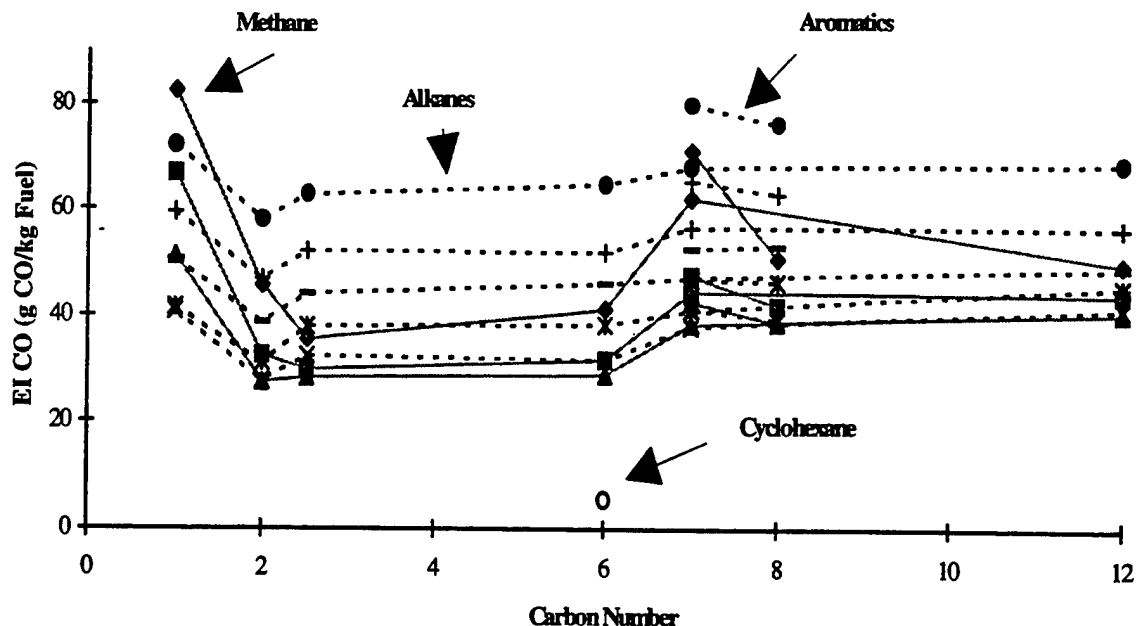


Fig. 7: Emissions indices of CO versus carbon number for several hydrocarbons at nominal residence time 7.3 msec at several temperatures: 1550 K (diamond), 1600 K (square), 1650 K (triangle), 1700 K (X), 1750 K (star), 1800 K (dash), 1850 K (+), 1900 K (black circle). Also shown (hollow circle) is equilibrium cyclohexane at 1900 K (Gordon and McBride<sup>23</sup>).

Also shown in Fig. 7 is the corresponding equilibrium concentration of CO from cyclohexane at 1900 K. As shown, measured CO values were much higher than equilibrium because reactor residence time was less than the time required for oxidation of CO. The CO concentration from equilibrium calculations increased at high temperatures due to CO<sub>2</sub> dissociation, and this was also observed in the measured CO concentrations.

The slow oxidation of CO suggests that changing residence time in the reactor will affect the measured CO. Fig. 8 shows profiles of CO (ppmV) versus  $T_f$  from several hydrocarbons at 7.3 and 5.3 msec residence times (methane  $\tau = 7.3$  or 6.3 msec). As shown, decreasing residence time increased CO. Also, at higher temperatures the longer and shorter residence time CO profiles tended to converge, indicating that the CO<sub>2</sub> dissociation rate proceeded faster than the CO oxidation under these conditions. A similar trend of decreasing CO with increased residence time was found by Steele<sup>30</sup>.

However, it must be noted that temperature produces the greatest effect on CO production from fuels. Thus, it is important to find at what temperature the minimum amount of CO is produced from each

hydrocarbon, and to find a predictive method to finding the temperature for minimal CO production from any fuel. Because liquid hydrocarbons are preheated more than gaseous fuels, Fig. 9 shows the temperature at which CO minima occur corrected for preheat versus carbon number of each hydrocarbon. This correction was made as follows:

$$T_{\text{correct}} = T_f - (T_{\text{in}} - 296) \quad (7)$$

This figure shows that as the carbon number of the fuel was increased the temperature at which CO minima occur decreased. Also, the figure shows that the rule applied to alkanes and aromatics, with cracked fuel simulant classified as an alkane. Within the uncertainty of  $T_f$ , all the data points in Fig. 9 can be approximated together as a line of the following form:

$$T_{\text{CO min correct}} = -11.35 \cdot \text{CN} + 1713 \quad (8)$$

Caution should be exercised in generalizing results of Eq. (8) to all combustors. The WSR represents a system with excellent mixing and minimal wall quenching and heat loss. A system with cold walls, for instance, would display a CO minimum at higher temperature than when the walls are hot. Also, Eq. (8) was derived from  $\tau \sim 7.3$  msec data. Reducing



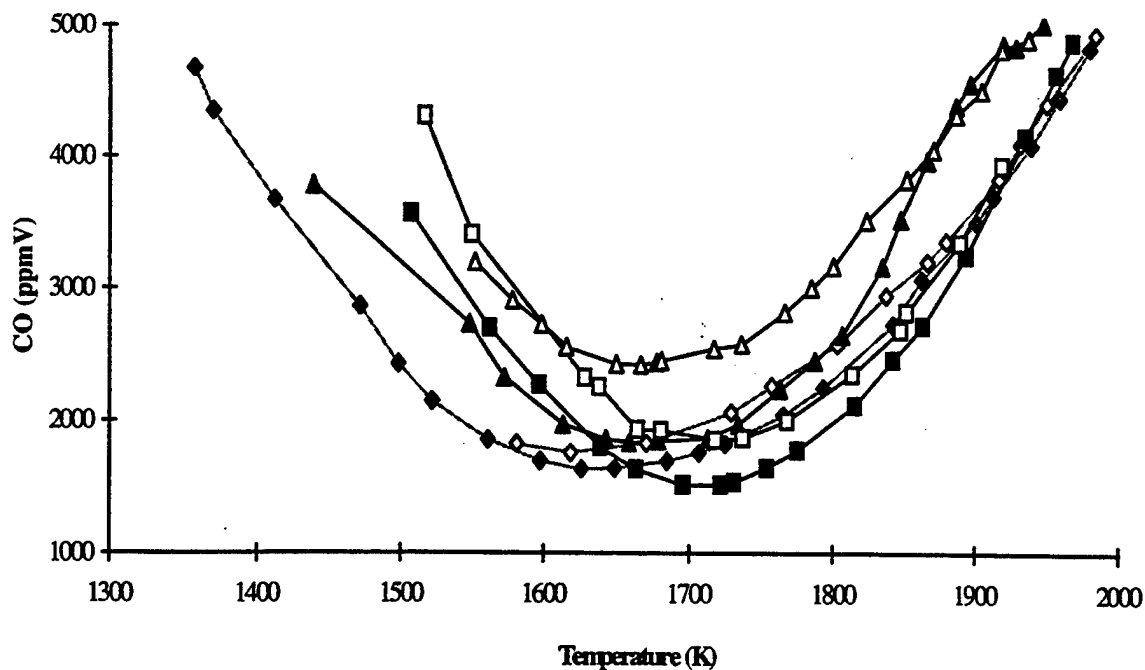


Fig. 8: CO versus reactor temperature. For methane (square), nominal residence time is 7.3 msec (solid symbol) or 6.3 msec (hollow symbol). For n-dodecane (diamond), and toluene (triangle), nominal residence time is 7.3 msec (solid symbol) or 5.3 msec (hollow symbol).

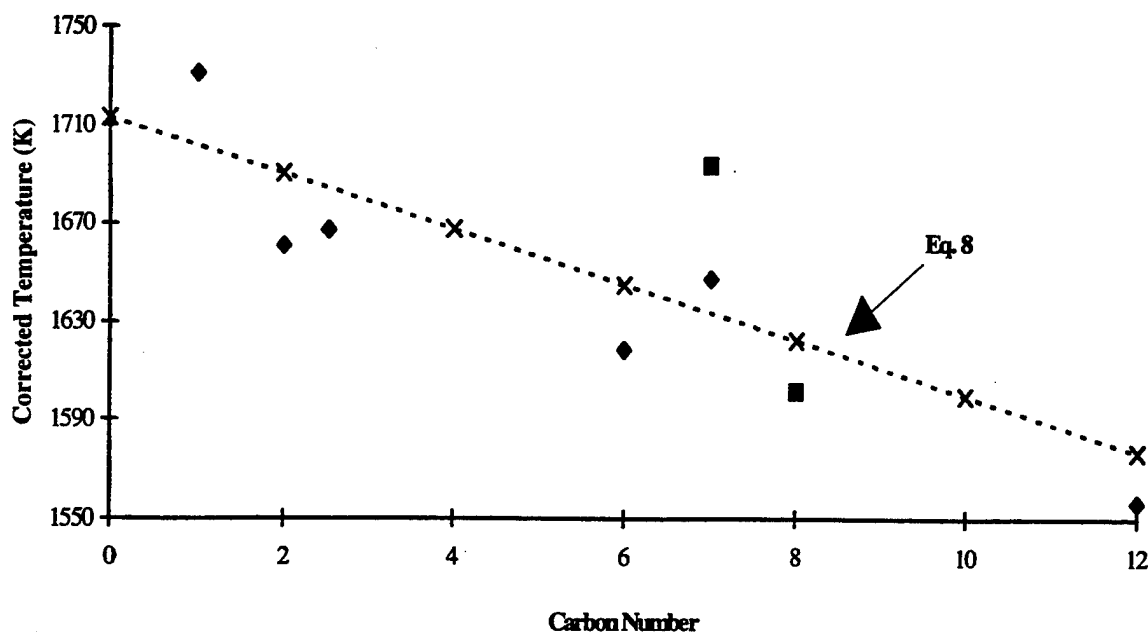


Fig. 9: Corrected temperatures of CO emissions index minima versus carbon number of hydrocarbon for alkanes (diamond) and aromatics (square). Also included (dotted line) is calculated relation of CO minima to carbon number, Eq. (8).

residence time tends to increase the temperature at which minima occur.

Fig. 10 shows emissions index of UHC from several hydrocarbons at several  $T_f$  plotted as a function of carbon number at residence time of 7.3 msec. All hydrocarbons in general produced only trace quantities of UHC at temperatures above 1600 K (for  $\phi < 1$ ). At  $T_f < 1600$  K, however, a rapid increase in UHC occurred, suggesting the reactants were approaching LBO, and insufficient residence time existed for complete oxidation at these lower temperatures.

As shown in Fig. 10, alkanes showed a rapid decrease, then modest increase in UHC as carbon number increased. High UHC of methane reflected the hydrocarbons' narrow stability loop (see Lean Blow-Out), with ethane behaving more like other alkanes. Toluene produced more UHC at a given temperature than other hydrocarbons besides methane, suggesting that this hydrocarbon did not oxidize rapidly at low temperature. Conversely, ethylbenzene produced UHC more equivalent to alkanes of the same carbon number.

Equilibrium calculations predicted no UHC in the sample, and for  $T_f > 1600$  K, this was also observed in the WSR. However, at lower temperatures complete oxidation proceeded slowly, and the residence time was

less than required to approach equilibrium. The slow oxidation of fuel at low temperatures suggests that change in residence time while  $T_f < 1600$  K will affect measured UHC. Fig. 11 shows profiles of UHC (ppmC) versus  $T_f$  from methane at 7.3 and 6.3 msec residence times, and cyclohexane at 7.5 and 5.2 msec residence times. As with CO, decreasing residence time increased UHC.

Composition of UHC at LBO from several hydrocarbons is compared in Table 2. That ethylene was the major component of UHC from lean alkane combustion is not surprising. Literature has suggested that ethylene is the most abundant intermediate hydrocarbon product from n-heptane (Maurice<sup>31</sup>), and the mechanisms for combustion of other alkanes are similar. Conversely, acetylene was the most abundant UHC component from toluene. Acetylene is a product of the decomposition of benzene, which itself is a common product of the decomposition of toluene. As a result, trace amounts of C6 were also identified in the UHC mixture from toluene. The cracked fuel simulant behaved more like an alkane than aromatic with regard to components in the UHC mixture. Also, the UHC species from all hydrocarbons in general were less saturated and of lower molecular weight than the parent fuel.

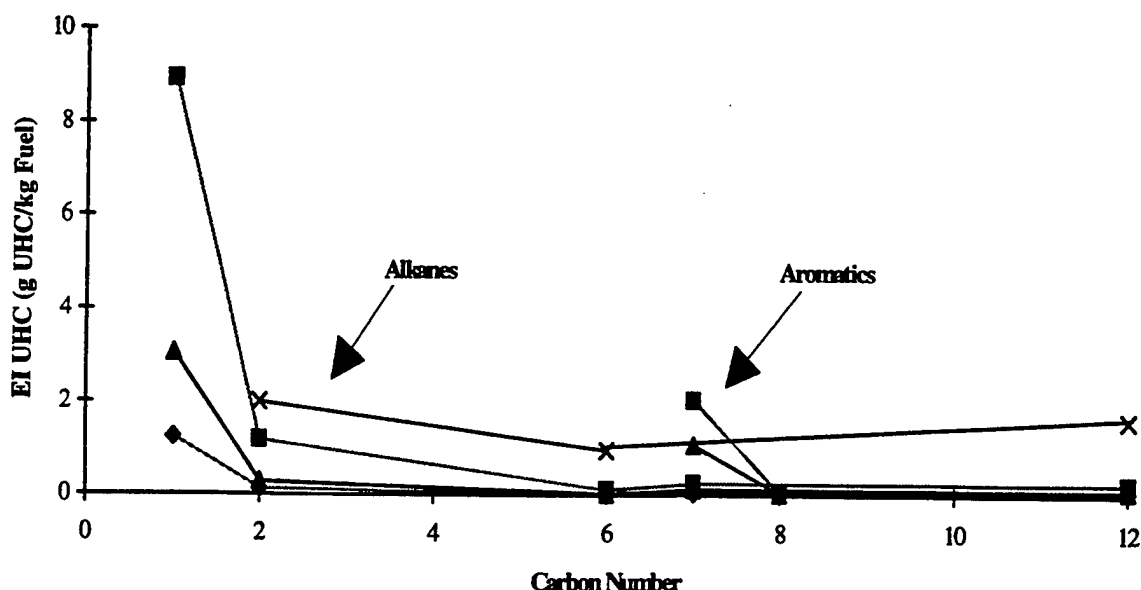


Fig. 10: Emissions indices of UHC versus carbon number for several hydrocarbons at nominal residence time of 7.3 msec at several temperatures: 1450 K (X), 1500 K (square), 1550 K (triangle), 1600 K (diamond).

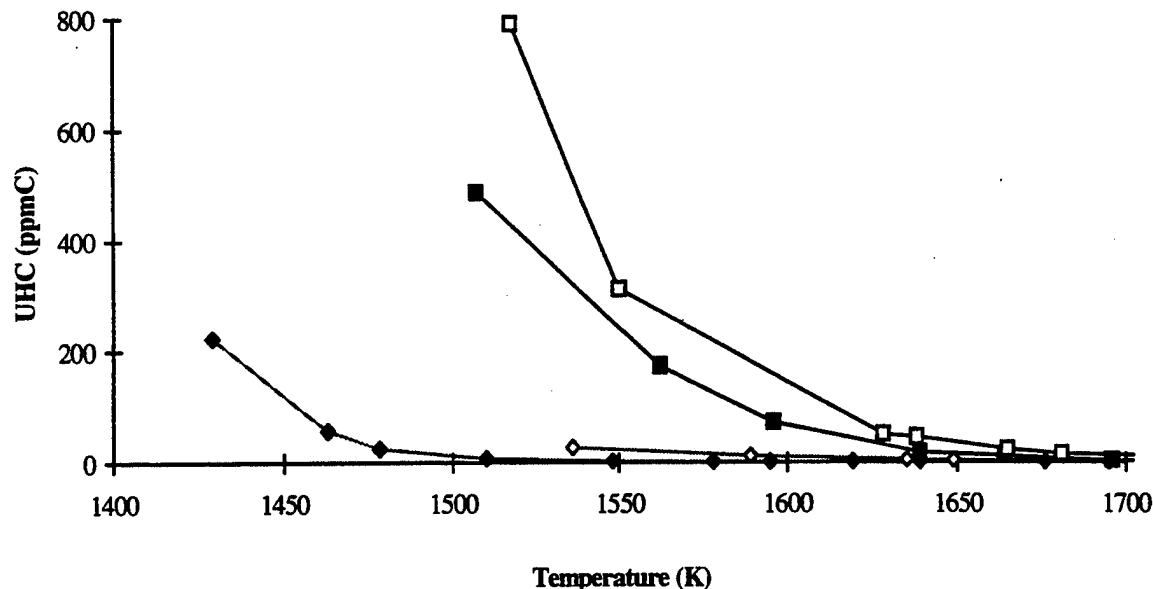


Fig. 11: UHC versus reactor temperature. For methane (square), nominal residence time is 7.3 msec (solid symbol) or 6.3 msec (hollow symbol). For cyclohexane (diamond), nominal residence time is 7.5 msec (solid symbol) or 5.2 msec (hollow symbol).

Table 2: Effluent Hydrocarbon Species by Percent Volume of UHC

Hydro-carbon	CH <sub>4</sub>	C <sub>2</sub> H <sub>4</sub>	C <sub>2</sub> H <sub>6</sub>	C <sub>2</sub> H <sub>2</sub>	C <sub>3</sub> H <sub>6</sub>	C <sub>4</sub>	C <sub>5</sub>	C <sub>6</sub>	$\tau$ (msec)	$\phi$	T <sub>r</sub> (K)
Toluene	27	15	0	56	0	0	0	3	7.56	0.46	1439
Cyclohexane	30	49	12	9	0	0	0	0	6.83	0.51	1513
Ethane	20	40	40	0	0	0	0	0	6.95	0.48	1407
13 vol% Methane, 22 vol% Ethane, 52 vol% Ethylene, 13 vol% Toluene	23	58	16	3	0	0	0	0	5.96	0.46	1391
n-Dodecane	19	60	6	2	6	3	2	2	7.71	0.46	1357

As previously mentioned, hysteresis occurred in LBO  $\phi$  in the reactor. As a consequence of this, UHC measurements suffer from a great amount of uncertainty at LBO. A difference in  $\phi$  of  $\pm 0.02$  near blow-out can result in an order of magnitude difference in UHC concentration.

#### NO<sub>x</sub> Measurements

In the study of NO<sub>x</sub> emissions, the formation of species such as NO and NO<sub>2</sub> is a complex function of temperature, residence time, equivalence ratio, and detailed chemical kinetics, a better understanding of which would help designers of combustion devices to

limit NO<sub>x</sub> production without compromising combustion efficiency. An understanding of the chemical pathways responsible for NO<sub>x</sub> production in a combustion environment with heavy hydrocarbons is becoming possible. The relative roles of the thermal NO (Zeldovich) mechanism, super-equilibrium effects, prompt NO mechanism, N<sub>2</sub>O mechanism, and fuel nitrogen mechanisms are suggested by other researchers for some fuels (Capehart et al.<sup>5</sup>; Nicol<sup>32</sup>; Steele<sup>30</sup>). The present work is an extension and verification of these earlier efforts.

Emissions indices of  $\text{NO}_x$  versus  $T_f$  from several hydrocarbons at nominal residence time of 7.3 msec are plotted in Fig. 12. Equilibrium  $\text{NO}_x$  concentrations were not shown because  $\text{NO}_x$  chemistry is slow and insufficient residence time is generally available in the WSR to allow  $\text{NO}_x$  concentration to approach equilibrium values.  $\text{NO}_x$  emissions from all hydrocarbons exhibited the same basic trend. As temperature increased, a slight decrease in  $\text{NO}_x$  emissions was detected. Elevated  $\text{NO}_x$  at near blow-out conditions was in general attributed to the  $\text{N}_2\text{O}$  mechanism. Then,  $\text{NO}_x$  increased as temperature increased, first gradually, then rapidly for  $T_f > 1800$  K. This response was generally attributed to the Extended Zeldovich NO mechanism.

Below 1800 K, the curves overlapped enough to be indistinguishable from one another. For  $T_f > 1800$  K, though, the  $\text{NO}_x$  emissions rapidly increase with increasing  $T_f$ . At the high  $T_f$  regime, normal paraffins in general produced less  $\text{NO}_x$  than aromatics and cyclohexane. Cracked fuel simulant produced more  $\text{NO}_x$  than other hydrocarbons.

The slow formation rate of  $\text{NO}_x$  suggests that changing residence time in the reactor will affect the

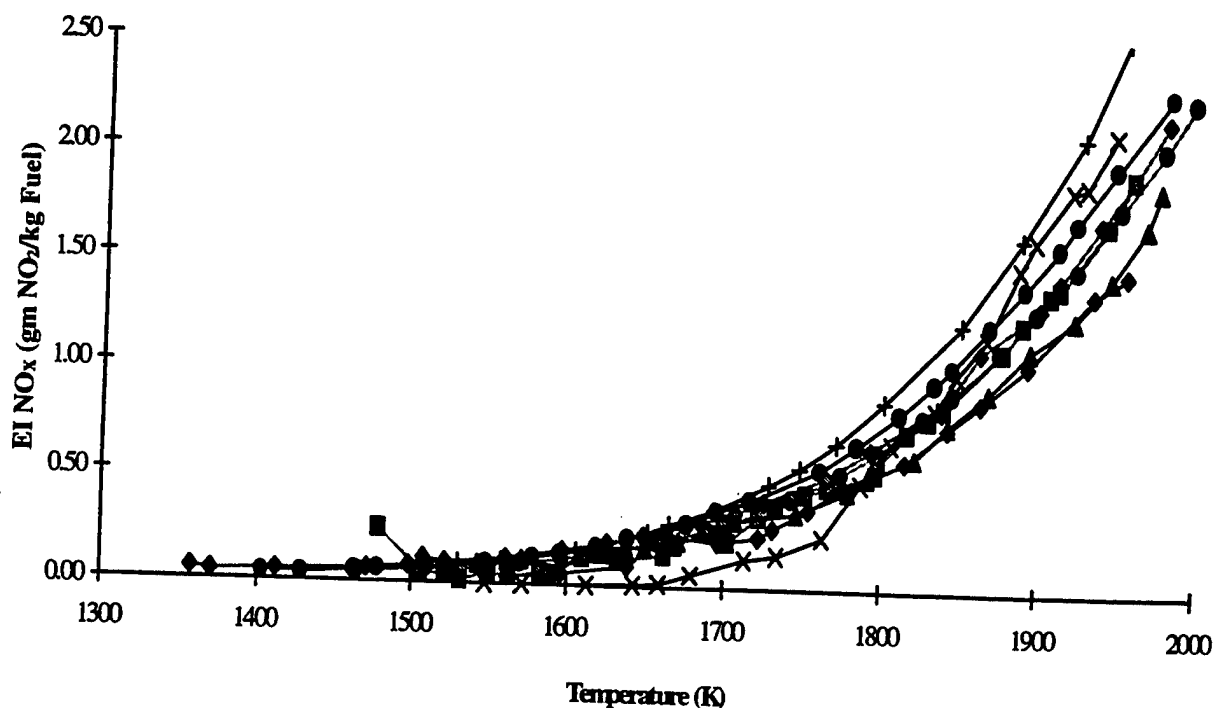


Fig. 12: Emissions indices of  $\text{NO}_x$  versus reactor temperature for several hydrocarbons at nominal residence time 7.3 msec: methane (black diamond), ethane (gray circle), cyclohexane (black circle), n-heptane (black triangle), n-dodecane (gray diamond), toluene (X), ethylbenzene (gray square), cracked fuel simulant (+).

measured  $\text{NO}_x$ . Fig. 13 shows profiles of  $\text{NO}_x$  (ppmV) versus  $T_f$  from several hydrocarbons at 7.3 and 5.3 msec residence times. As shown, increasing residence time increased  $\text{NO}_x$ . Capehart<sup>33</sup> has suggested a linear increase in  $\text{NO}_x$  with time. For n-dodecane, this formula is shown in Eq. (9)

$$\text{NO}_x = \left( \frac{20.95 - [\text{O}_2]}{20.95 - 15} \right)^{63,523\tau} \exp\left(\frac{-18,776}{T}\right) \quad (9)$$

Data to suggest E and k of Eq. (9) were acquired in a jet-stirred reactor of  $\tau \sim 3.3$  msec, and extrapolation of this work to 5.3 msec proved satisfactory, as shown in Fig. 13. However, Eq. (9) estimated high compared to measured  $\text{NO}_x$  at  $\tau = 7.3$  msec. The present work suggests the following equation for n-dodecane:

$$\text{NO}_x = \left( \frac{20.95 - [\text{O}_2]}{20.95 - 15} \right)^{690,000\tau^{1/2}} \exp\left(\frac{-22,100}{T}\right) \quad (10)$$

A  $\tau^{1/2}$  relation of residence time to  $\text{NO}_x$  emissions is suggested in Eq. (10) for n-dodecane, the results of which are shown in Fig. 13.

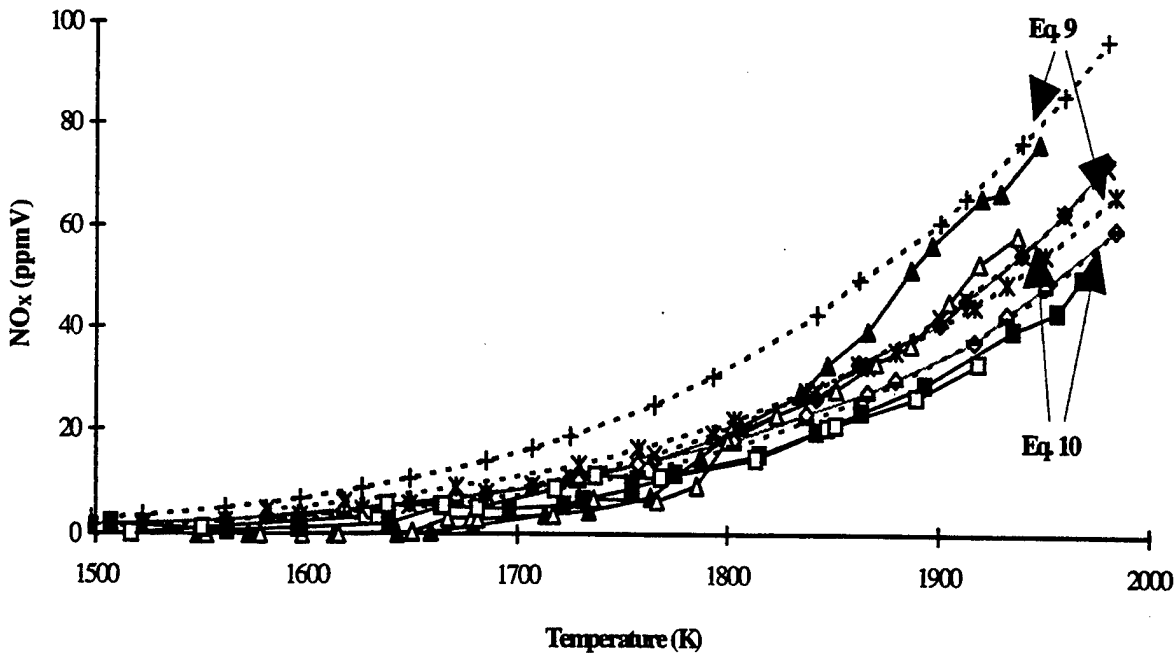


Fig. 13:  $\text{NO}_x$  versus reactor temperature. For methane (square), nominal residence time is 7.3 msec (solid symbol) or 6.3 msec (hollow symbol). For n-dodecane (diamond), and toluene (triangle), nominal residence time is 7.3 msec (solid symbol) or 5.3 msec (hollow symbol). Also included (dotted line) are estimates for n-dodecane by Capehart<sup>35</sup> for 7.3 msec (+), 5.3 msec (\*) and estimates (Eq. (10)) for 7.3 msec (X) and 5.3 msec (dash).

Researchers (Bahr<sup>34</sup>; Zelina et al.<sup>8</sup>) have previously suggested that  $\text{NO}_x$  increases with increase in (C/H) mole ratio. In the present work, EI  $\text{NO}_x$  from several hydrocarbons at  $T_f = 1800$  K and 1950 K were plotted vs. (C/H) mole ratio, with alkanes and aromatics plotted separately. Fig. 14 shows the result. Scatter existed in the trends, but the hydrocarbons exhibit a general increase in EI  $\text{NO}_x$  as (C/H) mole ratio increased. Further, the trend became more apparent at higher temperature. This evidence suggests that designers should be concerned about the effect decreasing hydrogen content in a fuel could have on  $\text{NO}_x$  emissions from combustors.

#### Conclusions

A toroidal WSR which represents a laboratory idealization of an efficient, highly compact primary zone of a gas turbine combustor was used to study lean blow-out limits and emissions from several pure hydrocarbons. A number of conclusions were drawn from the present work:

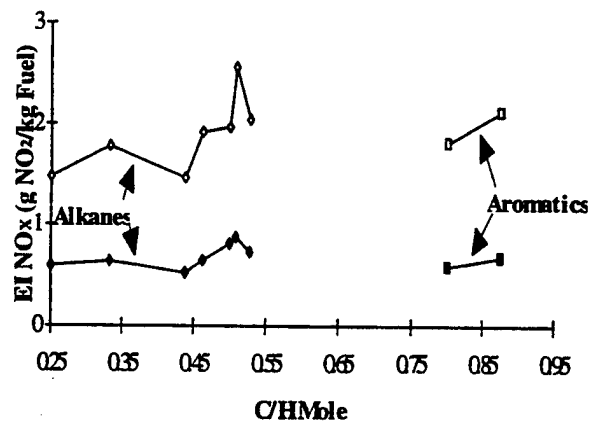


Fig. 14: Emissions indices of  $\text{NO}_x$  versus (C/H) mole ratio of hydrocarbon for alkanes (diamond) and aromatics (square) at 1800 K (solid symbol) and 1950 K (hollow symbol).

1. All hydrocarbons except methane showed lean limits of  $\phi \sim 0.47$  with  $\text{LP} \sim 1 \text{ g-mol/s} \cdot \text{l} \cdot \text{atm}^{1.75}$  (methane LBO was  $\phi \sim 0.55$  at similar LP). Global activation energies and collision factors were calculated via stability theory to be  $E = 52 \text{ kcal/mole}$

and  $C = 9.4 \cdot 10^{14} \text{ K}^{1/2} \text{sec}^{-1}$  for methane;  $E = 49 \text{ kcal/mole}$  and  $C = 1.3 \cdot 10^{15} \text{ K}^{1/2} \text{sec}^{-1}$  for ethane.

2. Hydrocarbons of different structure and carbon number produced different amounts of CO at the same temperature and residence time. To a limited degree, alkanes produced more CO as carbon number increased. This ceased to be true for  $CN > 7$ , nor was this true for methane, which produced high EI of CO due to the hydrocarbon's low molecular weight. Toluene produced more CO than ethylbenzene; the latter behaved more as an alkane than as toluene.

3. Reactor residence time affected CO production. In general, increasing residence time decreased the production of CO. Additional time enabled CO to be more completely oxidized. At  $T_f > 1850 \text{ K}$ , CO from longer and shorter residence time experiments tended to converge, indicating that  $\text{CO}_2$  dissociation reactions were competing with the oxidation of CO.

4. A linear relationship was found for the temperature at which CO approaches minimum production versus the carbon number of the fuel. This relationship was consistent for alkanes and aromatics.

5. UHC production from alkanes at a given temperature decreased greatly from methane to ethane, but increased slightly for high carbon number hydrocarbons (i.e. n-dodecane). Toluene produced more UHC than alkanes at the same temperature (including n-heptane with the same carbon number) indicating that toluene oxidized poorly at low temperature. Ethylbenzene behaved as an alkane with respect to UHC production.

6. For  $T_f < 1600 \text{ K}$ , residence time affected UHC production. In general, increasing residence time decreased the production of UHC. Additional time enabled UHC to be more completely oxidized.

7. Governing mechanisms of  $\text{NO}_x$  production changed as temperature increased. At  $T_f < 1500 \text{ K}$ , the  $\text{N}_2\text{O}$  mechanism was suggested to account for measured  $\text{NO}_x$ . At  $T_f > 1800 \text{ K}$ , the Extended Zeldovich mechanism accounted for most  $\text{NO}_x$  produced. For  $T_f > 1800 \text{ K}$ , hydrocarbons of different structure and carbon number produced different amounts of  $\text{NO}_x$  at the same residence time. Under these conditions, normal paraffins produced less  $\text{NO}_x$  than cyclohexane and aromatics.

8. Increasing residence time increased  $\text{NO}_x$  production. A square root relationship of  $\text{NO}_x$  production versus residence time was suggested for n-dodecane. Additionally, a modest increase in  $\text{NO}_x$  with an increase in the (C/H) mole ratio was detected for several hydrocarbons.

#### Acknowledgment

This work is supported by the Air Force Wright Laboratory, Aeropropulsion and Power Directorate, Wright Patterson Air Force Base, OH, under contract F33615-92-C-2207, with Mr. Charles W. Frayne serving as technical monitor. The authors are grateful to Mr. Rich Striebich for providing assistance with the GC-FID analysis, and Mr. Matthew Getz for providing technical assistance.

#### References

1. Marek, C. J., and Papathakos, L. C., "Exhaust Emissions from a Premixing, Prevaporizing Flame Tube Using Liquid Jet A Fuel," *NASA TM X-3383*, 1976.
2. Mularz, E. J., "Lean, Premixed, Prevaporized Combustion for Aircraft Gas Turbine Engines," *NASA TM-79148*, 1979.
3. Sturgess, G. J., "Assessment of an Abbreviated Jet A/JP-5/JP-8 Reaction Mechanism for Modeling Gas Turbine Engine Gaseous Emissions," *AIAA Paper No. 97-2709*, 1997.
4. Brezinsky, K., Litzinger, T. A., and Glassman, I., "The High Temperature Oxidation of the Methyl Side Chain of Toluene," *International Journal of Chemical Kinetics*, Vol. 16, pp. 1053-1074, 1984.
5. Capehart, S. A., Lee, J. C. Y., Williams, J. T. and Malte, P. C., "Effect of Fuel Composition on  $\text{NO}_x$  Formation in Lean Premixed Prevaporized Combustion," *ASME Paper No. 97-GT-336*, 1997.
6. Dagaut, P., Reuillon, M., and Cathonnet, M., "Experimental Study of the Oxidation of n-Heptane in a Jet Stirred Reactor from Low to High Temperature and Pressures up to 40 Atm," *Combustion and Flame*, Vol. 101, pp. 132-140, 1995.
7. Vaughn, C. B., Howard, J. B., and Longwell, J. P., "Benzene Destruction in Fuel Rich Jet-Stirred Combustion," *Combustion and Flame*, Vol. 87, pp. 278-288, 1991.

8. Zelina, J., Blust, J. W., and Ballal, D. R., "Combustion of Liquid Fuels in the Well Stirred Reactor," *ASME Paper No. 96-GT-047*, 1996.
9. Nenniger, J. E., Kridiotis, A. C., Chomiak, J., Longwell, J. P., Sarofim, A. F., "Characterization of a Toroidal Well-Stirred Reactor," *Twentieth Symposium (International) on Combustion, The Combustion Institute*, pp. 473-479, 1984.
10. Zelina, J., and Ballal, D. R., "Combustion Studies in a Well Stirred Reactor", *AIAA Paper No. 94-0114*, 1994,
11. Blust, J. W., Getz, M. G., and Zabarnick, S., "Probe Design Optimization for the Well Stirred Reactor," *AIAA Paper No. 97-0907*, 1997.
12. Aerospace Recommended Practice 1533, "Procedure for the Calculation of Gaseous Emissions from Aircraft Turbine Engines," *Society of Automotive Engineers, Inc.*, Warrendale, PA, pp. 1-36, 1994.
13. Ballal, D. R. and Lefebvre, A. H., "Ignition and Flame Quenching of Flowing Heterogeneous Fuel-Air Mixtures," *Combustion and Flame*, Vol. 35, pp. 155-168, 1979.
14. Stoffel, B., and Reh, L., "Conversion of Liquid to Gaseous Fuels for Lean Premixed Combustion," *ASME Paper No. 95-GT-412*, 1995.
15. Nenniger, J. E., "Polycyclic Aromatic Hydrocarbon Production in a Jet-Stirred Combustor," *Doctor of Science Thesis*, Massachusetts Institute of Technology, 1983.
16. Zelina, J., and Ballal, D. R., "Emissions Studies in a Well-Stirred Reactor and Applications to Combustion Modeling," *Proceeding of FACT, Vol. 21, ASME (Int.) Joint Power Generation Conference*, pp. 255-263, 1996.
17. Getz, M. G., and Zabarnick, S., internal communication, 1997.
18. Calo, J. M., Miller, T., Ballenthin, J. O., Striebich, R., Blust, J., and Getz, M., "The Residence Time Distribution (RTD) of the Well-Stirred Reactor (WSR)," to be published as USAF technical report, 1997.
19. Ballenthin, J. O., Miller, T., Calo, J. M., Striebich, R., Blust, J., and Getz, M., "Free-Jet, Molecular Beam Mass Spectrometer System for Monitoring the Gas-Phase Composition in a Well-Stirred Combustor," *Fifth International Congress on Toxic Combustion Byproducts.*, 1997.
20. Zelina, J., "Combustion Studies in a Well-Stirred Reactor," *Doctor of Science Thesis*, University of Dayton, 1995.
21. Pratt, D. T., and Wormeck, J. J., *CREK*, a computer program for calculation of combustion reaction equilibrium and kinetics in laminar or turbulent flow, 1976.
22. Pratt, B. S., and Pratt, D. T., *MARK2X* Computer Code, private communication, 1990.
23. Gordon S., and McBride, B. J., "Computer Program for Calculation of Complex Chemical Equilibrium Compositions, Rocket Performance, Incident and Reflected Shocks, and Chapman-Jouget Detonations" (NASA, Washington D. C.), *SP-273 Interim Revision*, 1976.
24. Avery, W. H., and Hart, R. W., "Combustor Performance with Instantaneous Mixing," *Ind. End. Chem.*, Vol. 45, No. 8, pp. 1634-1637, 1953.
25. Bragg, S. L., "Application of Reaction Rate Theory to Combustion Chamber Analysis" *ARC 16170*, Aeronautical Research Council, England, 1953.
26. Childs, J. H., "Preliminary Correlation to Efficiency of Aircraft Gas-Turbine Combustors for Different Operating Conditions," *NACA RM E50F15*, 1950.
27. Lefebvre, A. H., *Gas Turbine Combustion*, Hemisphere Publishing Corp., McGraw-Hill, NY, 1983.
28. Lewis, B., and von Elbe, G., *Combustion, Flames and Explosions of Gases*, 2nd Ed., Academic Press, 1961.
29. Kanury, A. M., *Introduction to Combustion Phenomena*, Vol. 2, Gordon and Breach Science Publishers, NY, pp. 30-42, 1984.
30. Steele, R. C., "NO<sub>x</sub> and N<sub>2</sub>O Formation in Lean-Premixed Jet-Stirred Reactors Operated From 1 to 7 atm," *Doctor of Science Thesis*, University of Washington, 1995.

31. Maurice, L. Q., "Detailed Chemical Kinetic Models for Aviation Fuels," *Doctor of Science Thesis*, Imperial College, 1996.
32. Nicol, D. G., Steele, R. C., Marinov, N. M., and Malte, P. C., "The Importance of the Nitrous Oxide Pathway to  $\text{NO}_x$  in Lean-Premixed Combustion," *Transactions of the ASME: Journal of Engineering for Gas Turbines and Power*, Vol. 117, pp. 100-111, 1995.
33. Capehart, S. A., " $\text{NO}_x$  Formation in Lean-Premixed Combustion of Liquid Hydrocarbons," *Master of Science Thesis*, University of Washington, 1995.
34. Bahr, D. W., "Control and Reduction of Aircraft Turbine Engine Exhaust Emissions," in W. Cornelius and W. G. Agnew (eds.), *Emissions from Continuous Combustion Systems*, pp. 345-372, Plenum, NY, 1972.



## **APPENDIX B**

### **Combustor Stability and Emissions Research Using a Well-Stirred Reactor**

**J. Zelina, D. R. Ballal**

# Combustor Stability and Emissions Research Using a Well-Stirred Reactor

J. Zelina

D. R. Ballal

Fellow ASME

Department of Mechanical and  
Aerospace Engineering,  
University of Dayton,  
Dayton, OH 45469

*The design and development of low-emissions, lean premixed aero or industrial gas turbine combustors is very challenging because it entails many compromises. To satisfy the projected CO and NO<sub>x</sub> emissions regulations without relaxing the conflicting requirements of combustion stability, efficiency, pattern factor, relight (for aero combustor), or off-peak loading (for industrial combustor) capability demands great design ingenuity. The well-stirred reactor (WSR) provides a laboratory idealization of an efficient and highly compact advanced combustion system of the future that is capable of yielding global kinetics of value to the combustor designers. In this paper, we have studied the combustion performance and emissions using a toroidal WSR. It was found that the toroidal WSR was capable of peak loading almost twice as high as that for a spherical WSR and also yielded a better fuel-lean performance. A simple analysis based upon WSR theory provided good predictions of the WSR lean blowout limits. The WSR combustion efficiency was 99 percent over a wide range of mixture ratios and reactor loading. CO emissions reached a minimum at a flame temperature of 1600 K and NO<sub>x</sub> increased rapidly with an increase in flame temperature, moderately with increasing residence time, and peaked at or slightly on the fuel-lean side of the stoichiometric equivalence ratio. Finally, emissions maps of different combustors were plotted and showed that the WSR has the characteristics of an idealized high-efficiency, low-emissions combustor of the future.*

## Introduction

The design and development of low-emissions, lean premixed aero or industrial gas turbine combustors is very challenging because it entails many compromises. Emissions of CO and NO<sub>x</sub> in the upper stratosphere and pollutant exhaust from coal-fired and/or the combined steam-gas turbine cycle power plants are a major contributor to atmospheric pollution, acid rain, and ozone depletion. The Clean-Air Act of 1991 is forcing the burning of natural gas fuel and the application of sophisticated aerospace-derived technology to improve ground-based industrial gas turbine combustion systems. To satisfy the projected CO and NO<sub>x</sub> emissions regulations without relaxing the conflicting requirements of combustion stability, efficiency, pattern factor, relight (for aero combustor) or off-peak loading (for industrial combustor) capability demands great design ingenuity. Also, in the design of future high-output combustors, minimizing combustor volume and maximizing combustor heat release are invariably the major goals. To meet these challenges, the designer has to search for basic concepts that provide a global, yet quantitative description of the combustion process in a gas turbine combustor. One such concept is to approximate the practical combustion zone as a WSR into which premixed fuel and air are fed and the overall kinetics of chemical reactions is controlling. The WSR provides a laboratory idealization of an efficient and highly compact advanced combustion system of the future that is capable of yielding global kinetics of value to the combustor designers.

In this paper, we describe the design of a WSR and measure combustion efficiency, combustion stability (lean blowout), and emissions of CO, unburned hydrocarbon (UHC), and NO<sub>x</sub>. These data were obtained for propane and an HC fuel blend (a

mixture of methane, ethane, and ethylene, which represents the products of thermal degradation of advanced endothermic jet fuels that are being developed for the high-speed flight). Finally, the combustion and emissions performance of the WSR are compared with a theoretical analysis and with measurements of pollutant emissions from gas turbine combustors, and implications to practical combustor design are discussed.

## WSR Design

**WSR Test Facility.** The first WSR was developed by Longwell and Weiss (1955) at Exxon Corporation, Linden, NJ. Subsequently, other researchers designed reactors of various geometries (see Table 1); this past work is summarized by Zelina and Ballal (1994). We capitalized on the findings of previous researchers, weighted the pros and cons of different designs, and constructed a 250-ml toroidal WSR designed by Nenniger et al. (1984). A schematic of this WSR design is shown in Fig. 1. The WSR volume is about 50 percent of the volume of a single swirl cup primary zone typically used in a modern aero-engine combustor. The design details of this toroidal WSR are given by Zelina and Ballal (1994).

The WSR is cast in two halves (each 125 ml) out of alumina ceramic cement. The lower half of the reactor has three holes on the centerline of the toroid for the thermocouple, gas sampling probe, and the ignitor. Notches are cast along the outside circumference of the reactor to accommodate the fuel jet ring, which is constructed of 304 stainless steel. Premixed fuel and air enter the ring through a 0.5 inch o.d. feed tube. Thirty-two tapped holes are placed on the ring and accommodate 1.2-mm-dia sonic jets, 20 deg off the radius. Finally, the top half of the reactor houses a flow straightener, which turns the flow 90 deg into a plug flow reactor (PFR).

Figure 2 illustrates the WSR test facility and its associated instrumentation: thermocouples, gas sampling probes, emissions analyzers, gas chromatography-mass spectrometry (GC-MS) system, and a Fourier transform infrared spectroscopy

Contributed by the International Gas Turbine Institute and presented at the 40th International Gas Turbine and Aeroengine Congress and Exhibition, Houston, Texas, June 5-8, 1995. Manuscript received by the International Gas Turbine Institute February 10, 1995. Paper No. 95-GT-109. Associate Technical Editor: C. J. Russo.

Table 1 Comparison of WSR designs

	Longwell and Weiss (1955)	Biazowski (1980a, b)	Thornton et al. (1987)	Nenniger et al. (1984)	Zelina and Ballal (1994)	GT Combustor
$\tau$	0.1-5 ms	0.6-4 ms	0.5-6 ms	1-6 ms	2-12 ms	2-12 ms
$T_o$	475K	290K	300-600 K	473K	300-500K	400-700K
P	0.13-1 atm	1.05 atm	1 atm	1 atm	1-5 atm	5-35 atm
V	240 mL	35 mL	15.8 mL	250 mL	250 mL	500 mL

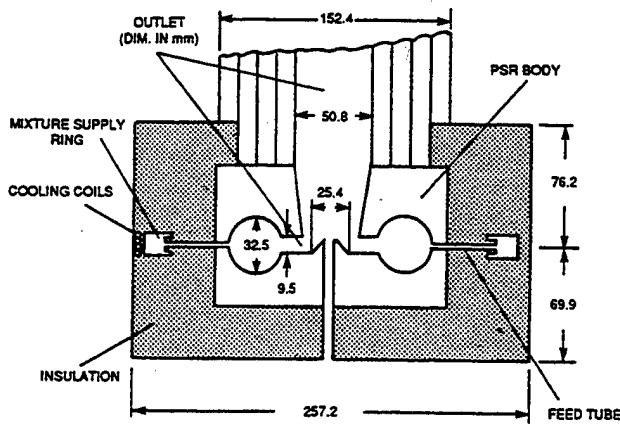


Fig. 1 Schematic of the toroidal WSR (all dimensions in mm)

(FTIR) equipment. Two Type B Pt-Rh thermocouples (0.01" dia bare wire) rated at 2100 K and two Type K, Cr-Al thermocouples rated at 1660 K were installed in the WSR and PFR, respectively. The Pt-Rh thermocouples were coated with an yttrium chloride/beryllium oxide substance as described by Kent (1970) to eliminate catalytic effects on the thermocouple surface. Air-cooled quartz gas-sampling probes were used to withdraw pollutant samples from the WSR. These gas samples pass through a water trap and a dehumidifier, then are fed into various emissions analyzers.

The Horiba emissions analyzers comprise the following units: model MPA-510 oxygen analyzer (0 to 50 percent), model FIA-510 total hydrocarbon analyzer (0 to 5000 ppm carbon), model VIA-510 CO (0 to 5000 ppmV), model VIA-510 CO (0 to 2 percent) and CO<sub>2</sub> (0 to 25 percent) analyzer, and model CLA-510 SS NO and NO<sub>x</sub> analyzer (0 to 200 ppmV). A gas sample of 500 ml/min is drawn in by each Horiba unit and analyzed for various pollutant species.

**Test Conditions.** The WSR test facility was operated slightly above atmospheric pressure and at room temperature (300 K). In this facility, the air rotameter was rated at 0 to 25 g/s and fuel supply was in the 0 to 5 g/s range. These flow conditions permitted the operation of the reactor over a broad range of loading parameter (LP) and equivalence ratios  $\phi = 0.4$  to 2.5, residence time  $\tau_o = 2.5$  to 12 ms, a cold mixture velocity in the toroid  $\approx 100$  m/s, mixing time  $\tau_m \approx 0.1$  ms, and reactor temperature  $T_f = 1200$  to 2050 K. In this study,

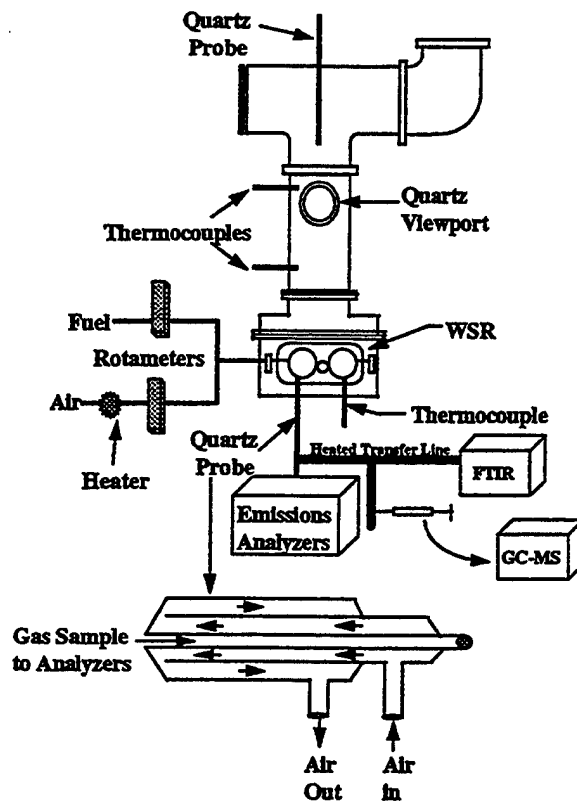


Fig. 2 Toroidal WSR test facility showing associated emissions and control instrumentation

focus was on fuel-lean combustion ( $\phi < 1$ ), at mean residence times of 2.5 ms and 12 ms.

The WSR was operated so that it does not suffer thermal shock and its wall temperature does not exceed 2300 K. Accordingly, the WSR was lightly loaded during the ignition sequence, allowed to reach over 1000 K and only then the lean blowout tests were performed. Propane and HC blend fuel (composition of 15 percent methane, 25 percent ethane, and 60 percent ethylene) were burned in the WSR. The HC blend fuel composition represents the products of thermal degradation of advanced endothermic jet fuels that are being developed for the high-speed civil transport (HSCT) and the Hypersonic System Technology Program (HySTP). A vaporizer chamber has been fabricated

## Nomenclature

$C_f$  = reaction rate constant  
 $E$  = activation energy, cal/g-mol  
 $EI$  = emissions index, g/kg fuel  
 $LP$  = loading parameter, g-mol/s-L-atm<sup>n</sup>  
 $m$  = fuel concentration exponent  
 $\dot{m}$  = air mass flow rate, kg/s  
 $n$  = global reaction rate  
 $P$  = pressure, kPa

$T_o$  = adiabatic flame temperature, K  
 $T_f$  = reactor temperature, K  
 $T_o$  = inlet temperature, K  
 $R$  = universal gas constant  
 $V$  = reaction volume, m<sup>3</sup>  
 $x_f, x_o$  = volume fraction in combustion gases of fuel and oxygen, respectively

$Z$  = exponent of equivalence ratio  
 $\beta$  = fraction of fuel burned  
 $\eta$  = combustion efficiency  
 $\rho$  = density, kg/m<sup>3</sup>  
 $\tau$  = residence time, ms  
 $\phi$  = equivalence ratio

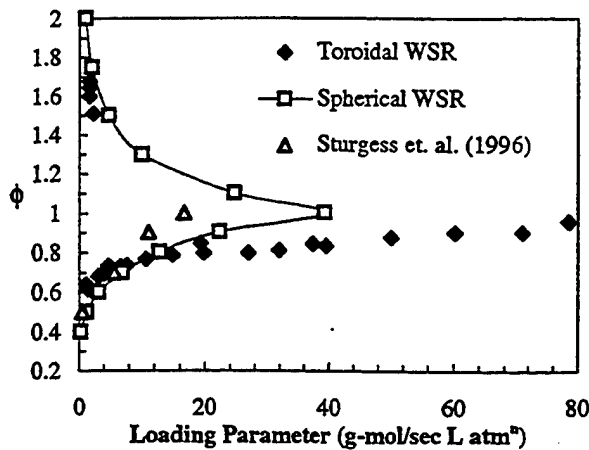


Fig. 3 Measured stability loops for propane/air mixtures at atmospheric pressure and 300 K inlet temperature

for future studies of the combustion of liquid fuels such as benzene, heptane, toluene, methyl cyclohexane, NORPAR, JP-4, JP-5, and JP-8.

**Error Analysis.** Both the fuel flow and airflow were monitored to within 2 percent. The combined error produced a maximum uncertainty of 5 percent in the value of equivalence ratio. The thermocouple temperature measurements, after correcting for radiation and conduction heat loss, were accurate to within 40 K. The Horiba emissions analyzers and the HP GC-MS system quote an accuracy to within 1 percent of full scale.

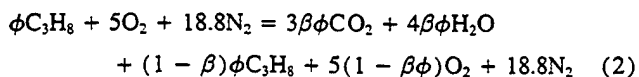
## Results and Discussion

**Combustion Stability and Lean Blowout.** Figure 3 shows a typical measured WSR stability loop for propane-air mixtures at 300 K inlet temperature. Also plotted on this figure is the stability loop for the spherical WSR (Kretschmer and Odgers, 1972) and stability curves for a mixing-controlled research step combustor (Sturgess et al., 1996). At light loading ( $LP < 20$ ), both the spherical WSR and the step combustor exhibit wide stability limits and better lean blowout performance. In contrast, the toroidal WSR is capable of better fuel-lean performance and peak loading (almost twice as high as that for the spherical design and step combustor) at medium to high loading ( $LP > 20$ ). The differences in stability limits for these combustor configurations can be attributed to the combined effects of imperfect mixing and heat losses in earlier reactors, and recirculation.

**Lean Blowout Theory.** In a WSR, the rate of reaction between fuel and air may be expressed by the material balance equation:

$$\beta\phi\dot{m} = C_f VT_f^{0.5} \exp\left(\frac{-E}{RT_f}\right) \rho^n x_f^m x_o^{(n-m)} \quad (1)$$

For fuel-lean propane-air mixtures ( $\phi < 1$ ):



From this equation, values of  $x_f$  and  $x_o$  can be calculated. Substituting these values into Eq. (1) gives

$$\frac{\dot{m}}{VP^n} = \frac{C_f}{R^n T_f^{n-0.5} \exp\left(\frac{E}{RT_f}\right)} \frac{1}{\phi^{1-m}} \frac{(1-\beta)^n (1-\beta\phi)^{n-m}}{\beta(23.8 + \phi + \beta\phi)} \quad (3)$$

The work of Kretschmer and Odgers (1972) suggests that the

value  $n$  depends upon the equivalence ratio at lean blowout. Ballal and Lefebvre (1979) used  $n = 1.25$ ,  $m = n/2 = 0.625$ , and  $E = 54$  kcal/mol. Using corresponding values of  $P$ ,  $T_f$ ,  $\beta$ , and  $\phi$  in the equation, it is possible to plot  $LP$  versus  $\beta$  for different equivalence ratios. Maximum loading occurs on the peaks of these curves, corresponding to the highest possible heat release rate at a stipulated values of  $T_o$  and  $\phi$ . By plotting  $\log(LP)$  versus  $\log(\phi)$  for different values of  $T_o$ , Ballal and Lefebvre (1979) found that

$$\left(\frac{\dot{m}}{VP^n}\right)_{\max} = 1.93 \exp\left(\frac{T_o}{150}\right) \phi^z \quad (4)$$

As shown in Fig. 4, Eq. (4) provides a satisfactory prediction of the WSR lean blowout limits when  $z = 7$  and  $n$  varies in a linear fashion from 1 to 1.25, depending upon the equivalence ratio.

**Combustion Efficiency.** As Lefebvre (1983) has stated, in a continuous-burn combustion system, the main factors affecting the level of combustion efficiency are evaporation or vaporization rate, mixing rate, and reaction rate. In practical combustors, the maximum heat release is rarely controlled by all three rates. Rather, one of the three key rates participates in determining overall combustion efficiency. In this investigation, the WSR combustion efficiency is reaction-rate controlled and may be calculated on an enthalpy basis by simply subtracting the inefficiencies due to incomplete burning in the form of CO and UHC. This method was developed to determine combustion efficiency based on emissions measurements from aircraft gas turbine engines (SAE ARP 1533, 1994). This method can be readily applied to a variety of practical and laboratory combustors and emissions measurements and the WSR results are shown in Figs. 5 and 6.

Figure 5 shows combustion efficiency as a function of the reactor temperature (equivalence ratio) and indicates that for a low value of the residence time ( $\tau = 2.5$  ms), the combustion efficiency of the propane-air mixture is above 99 percent over a wide range of mixture ratios ranging from near-lean blowout to stoichiometric ratio. The combustion efficiency decreases above 1800 K for longer residence times ( $\tau = 12$  ms) primarily due to the dissociation of  $CO_2$  in these high-temperature regions. As residence time is decreased, combustion gases do not remain in the high-temperature region long enough for dissociation reactions to take place and high values of combustion efficiency are obtained.

Figure 6 shows the variation in WSR combustion efficiency as a function of  $LP$  (for  $\phi = 0.8$ ), this latter parameter is

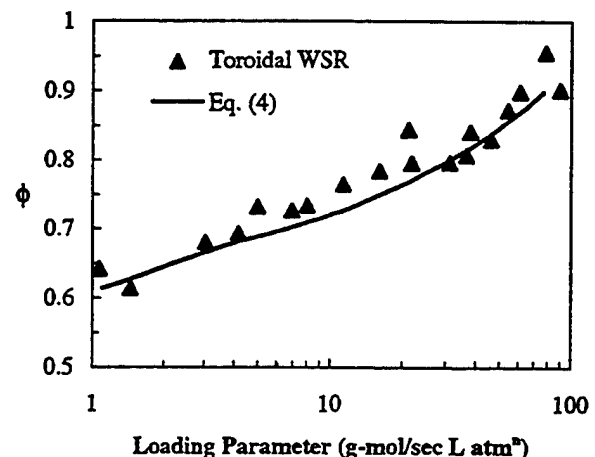


Fig. 4 Comparison between measured values of WSR lean blowout and predictions

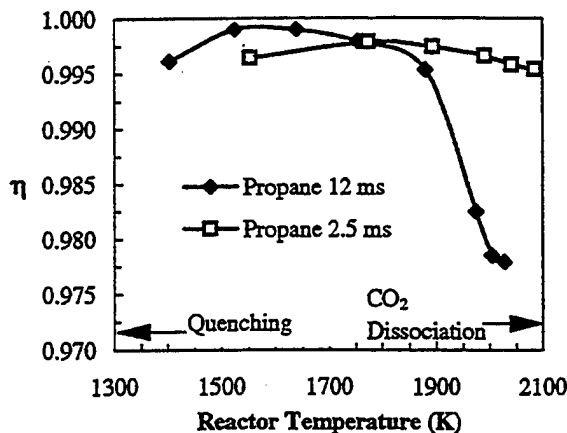


Fig. 5 Combustion efficiency as a function of reactor temperature for propane/air mixtures at two different residence times

inversely related to the residence time  $\tau$ . These data also confirm the generally high level of combustion efficiency of the WSR. Thus, it may be concluded that the WSR data represent the upper range of efficiency values that advanced gas turbine combustor designs should approach given adequate pressure drop (rapid mixing), reduced wall quenching, and good fuel atomization leading to rapid fuel evaporation.

**CO and UHC Emissions.** CO and UHC emissions represent a direct manifestation of combustion *inefficiency*. If the primary zone of a combustor operates fuel-rich, has inadequate mixing, or is prematurely quenched by cold air, large quantities of CO (which is relatively resistant to oxidation) will be formed due to the lack of oxygen needed to complete the reaction to  $\text{CO}_2$ . UHC emissions include fuel that emerges at the combustor exit in the form of droplets or vapor, and the products of the thermal degradation of the parent fuel into species of lower molecular weight such as methane and acetylene. UHC emissions are associated with poor atomization, inadequate burning rates, and premature quenching. In general, UHC emissions parallel those of CO. Any combustor design modification that decreases CO emissions will also decrease UHC emissions.

Figure 7 shows a measured combustion efficiency plotted versus emissions of CO and UHC. Also plotted is an efficiency versus emissions relationship developed by Bahr (1972) for gas turbine combustors:

$$\eta = 1 - \left( \frac{EI_{\text{UHC}} + 0.232EI_{\text{CO}}}{1000} \right) \quad (5)$$

A good agreement is obtained between WSR measurements and predictions of CO emissions using Eq. (5). This provides further evidence that the combustion performance of the primary zone of a gas turbine combustor is very similar to that of a WSR.

Figure 8 shows the emissions of CO from the toroidal WSR over a range of equivalence ratios. Also plotted are typical CO emissions from a practical gas turbine combustor burning jet fuel (Rizk and Mongia, 1993). Although trends are similar (i.e., CO emissions reach a minimum around  $\phi = 0.6$  corresponding to the combustion zone temperature of 1600 K), the CO emissions index for the practical gas turbine combustor are two to three times higher than those for the WSR. Two key factors influence CO emissions in practical systems: (i) for  $\phi < 0.6$  cold gas quenching and combustion temperatures are usually too low for CO to burn to  $\text{CO}_2$  and (ii) for  $\phi > 0.6$ , CO quickly reaches the equilibrium value, which is higher than the acceptable emission level. In such a situation, special care is required in practice to dilute hot combustion products to turbine entry temperatures. Other factors such as poor fuel atom-

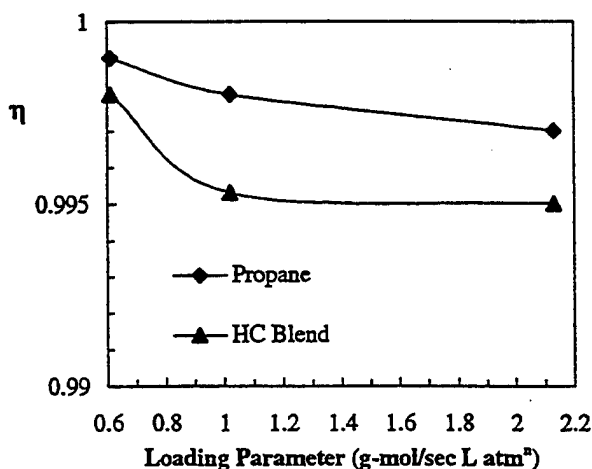


Fig. 6 WSR combustion efficiency versus loading parameter for two fuels

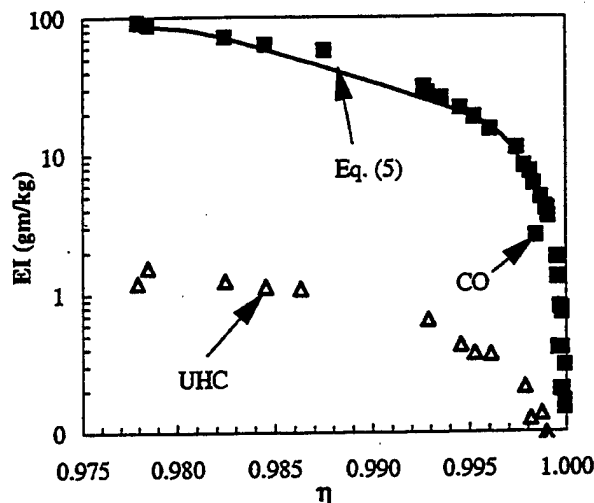


Fig. 7 Relationship between combustion efficiency and emissions of CO and UHC in a WSR

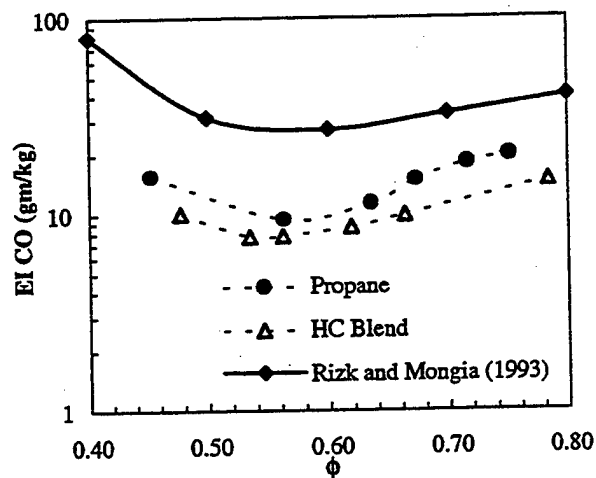


Fig. 8 Emissions of CO from the WSR compared to a practical gas turbine combustor

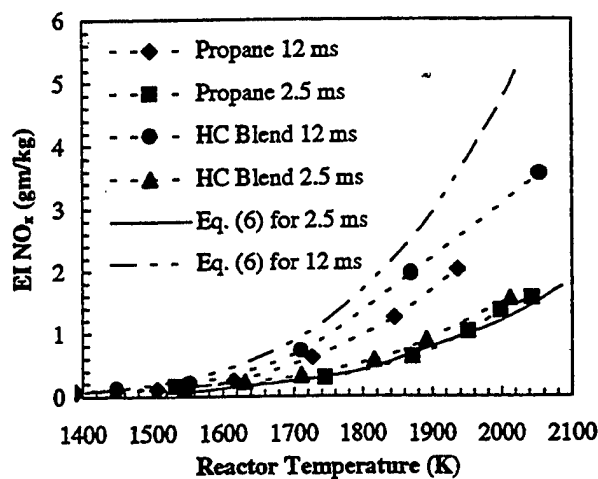


Fig. 9 Emissions of  $\text{NO}_x$  as a function of reactor temperature for two different residence times and different fuel/air mixtures

ization leading to inadequate fuel vaporization, improper fuel-air mixing, and premature quenching of combustion products due to film cooling air can also increase CO emissions levels in practical systems.

**$\text{NO}_x$  Emissions.** Variables affecting the production of  $\text{NO}_x$  have been extensively studied by Nicol et al. (1995) and Steele et al. (1997). Advanced combustor designs employing intense reactant mixing and high-temperature stoichiometric combustion produce a large quantity of  $\text{NO}_x$ . In fact,  $\text{NO}_x$  emissions rise moderately with high pressure and residence time, and exponentially with flame temperature. The WSR offers a unique opportunity to investigate the chemistry of  $\text{NO}_x$  emissions because of the absence of interaction between chemical reactions and the fluid dynamics processes of turbulent mixing and fuel evaporation.

$\text{NO}_x$  emissions comprise thermal  $\text{NO}$  produced by the oxidation of atmospheric nitrogen in the postflame gases, prompt  $\text{NO}$  produced by the high-speed reactions at the flame front, and fuel  $\text{NO}$  produced by the oxidation of fuel-bound nitrogen. For propane-air combustion systems, Roffe and Venkataramani (1978) have found that:

$$\ln \left( \frac{EI_{\text{NO}_x}}{\tau} \right) = -72.28 + 2.8\sqrt{T_a} - \frac{T_a}{38} \quad (6)$$

Figure 9 shows the measured effect of flame temperature on  $\text{NO}_x$  emissions for propane and HC blend fuels and for two different values of residence time. Although residence time certainly increases  $\text{NO}_x$  (for example, for propane-air combustion at 1900 K, 0.75 g/kg and 1.75 g/kg of  $\text{NO}_x$  are formed corresponding to residence times of 2.5 ms and 12 ms, respectively), it is the flame temperature that causes a major increase in  $\text{NO}_x$  emissions. As seen in Fig. 9, Eq. (6) provides a satisfactory prediction of  $\text{NO}_x$  when  $\tau = 2.5$  ms. Also, as seen in Fig. 10, our measured values of  $\text{NO}_x$  emissions were in close agreement with propane-air data of Steele et al. (1997) taken in a jet-stirred reactor. To decrease  $\text{NO}_x$  emissions from practical combustion systems, the primary goal must be to lower the reaction temperature (by using water or steam injection) and/or the elimination of hot spots inside the combustor.

Figure 11 shows emissions index of  $\text{NO}_x$  for four different combustors: (i) a research step swirl combustor of Durbin and Ballal (1994), (ii) an advanced axially staged combustor (ASC) of Segalman et al. (1993), (iii) a conventional gas turbine combustor design of Rizk and Mongia (1993), and (iv) the present WSR. As shown, data were obtained for the combustion of different fuels in the WSR. It is observed that

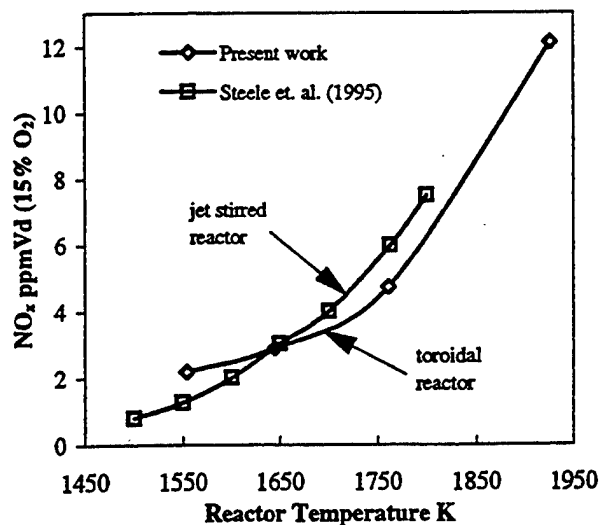


Fig. 10 Comparison of  $\text{NO}_x$  emissions from the toroidal WSR and the jet-stirred reactor at 3.5 ms residence time

the emissions indices of the various combustors burning different fuels were in fairly good qualitative agreement with the WSR data. These results again attest to the importance of WSR studies to practical combustor design. In Fig. 10, it should be noted that  $\text{NO}_x$  emissions index for the production gas turbine combustors are generally higher by a factor of two to three as compared to the WSR data. These higher values of  $\text{NO}_x$  emissions are presumably due to the unmixedness (see Fric, 1993) present in practical gas turbine combustor as compared to the near-perfectly mixed WSR.

**Emissions Map.** A basic feature of many methods of emissions abatement is that they represent trade-offs between CO/UHC and  $\text{NO}_x$  emissions. This led Verkamp et al. (1973) to advocate the idea of presenting the relation between CO and  $\text{NO}_x$  in the form of an emissions map, which distinguishes between true advances in emissions technology and mere emissions trade-offs. Figure 12 shows an emissions map. Included in this figure are published data from two practical combustors and the WSR data obtained in our experiments. It shows that the emissions characteristics of the WSR fall within the bandwidth that could be proposed for the low-emissions advanced combustor design of the future.

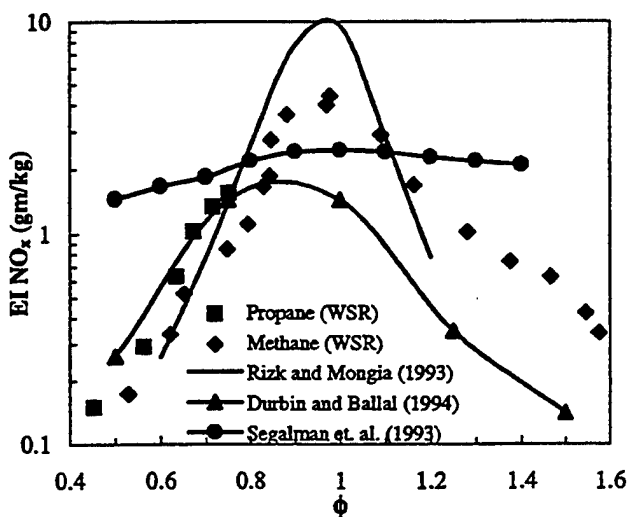


Fig. 11 Emissions of  $\text{NO}_x$  from the WSR compared to three different combustor configurations

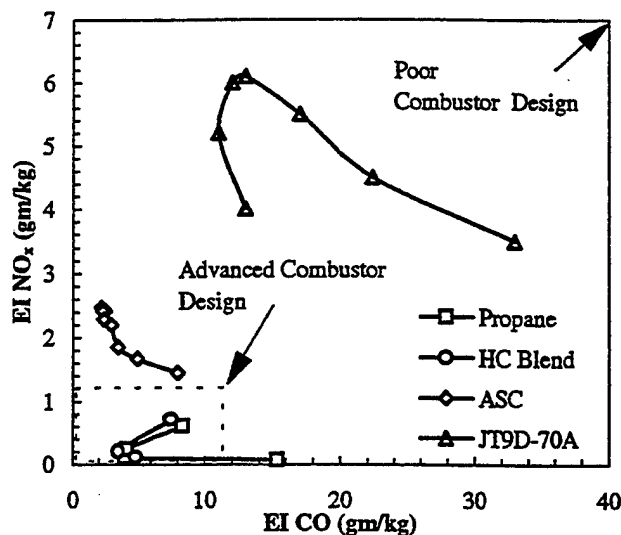


Fig. 12 Emissions map illustrating the status of emissions control technology for practical combustion systems

## Conclusions

A study of combustion stability and pollutant emissions was completed using a toroidal WSR burning propane and HC blend fuels. The WSR represents a laboratory idealization of an efficient, low-emissions advanced combustor of the future. The following conclusions emerged:

1 The toroidal WSR was capable of peak loading almost twice as high as that for a spherical WSR and also yielded a better fuel-lean performance at medium to high loading. A simple analysis based upon WSR theory (Eq. (4)) provided good predictions of the WSR lean blowout limits.

2 The WSR combustion efficiency was above 99 percent over a wide range of mixture ratios and reactor loading. Thus, the WSR provides an upper range of efficiency values that advanced gas turbine combustor designs should approach given good fuel atomization (and evaporation), adequate pressure drop, and reduced wall quenching.

3 CO emissions reached a minimum at  $\phi = 0.6$ , corresponding to flame temperatures of 1600 K. The predictions of CO emissions using a quantitative relationship developed for gas turbine combustors (Eq. (5)) showed a good agreement with WSR measurements. Of course, in a practical gas turbine combustor, absolute CO emissions were found to be higher presumably because of incomplete combustion arising due to insufficient residence time at high loading, inadequate mixing, or quenching of postflame combustion products.

4 Production of  $\text{NO}_x$  depends upon two main parameters: combustion temperature and residence time. As expected,  $\text{NO}_x$  increased rapidly with an increase in flame temperature, moderately with increasing residence time, and peaked at or slightly on the fuel-lean side of the stoichiometric equivalence ratio. Equation (6), developed for propane-air combustion systems, yields good agreement with WSR data. Also, the  $\text{NO}_x$  emissions index for the production gas turbine combustor was higher, presumably due to the unmixedness present in practical gas turbine combustors.

5 Finally, emissions maps of different combustors were plotted and show that the WSR has the characteristics of an idealized high-efficiency, low-emissions combustor of the future.

## Acknowledgments

This work was supported by the Air Force Wright Laboratory, Aero propulsion and Power Directorate, Wright-Patterson Air Force Base, OH, under contract F33615-92-C-2207 with Mr. Charles W. Frayne serving as the Technical Monitor. The authors are grateful to Professor J. P. Longwell of MIT and to Dr. R. C. Steele and Professor P. C. Malte of the University of Washington, Seattle, WA, for making available their WSR design, WSR data, and for useful discussions.

## References

- Bahr, D. W., 1972, "Control and Reduction of Aircraft Turbine Engine Exhaust Emissions," in: W. Cornelius and W. G. Agnew, eds., *Emissions From Continuous Combustion Systems*, Plenum, New York, pp. 345-372.
- Ballal, D. R., and Lefebvre, A. H., 1979, "Weak Extinction Limits of Turbulent Flowing Mixtures," *ASME JOURNAL OF ENGINEERING FOR POWER*, Vol. 101, pp. 343-348.
- Blazowski, W. S., 1980a, "Dependence of Soot Production on Fuel Structure in Backmixed Combustion," *Combustion Science and Technology*, Vol. 21, pp. 87-96.
- Blazowski, W. S., 1980b, "Dependence of Soot Production on Fuel Blend Characteristics and Combustion Conditions," *ASME JOURNAL OF ENGINEERING FOR POWER*, Vol. 102, pp. 403-408.
- Durbin, M. D., and Ballal, D. R., 1994, "Characteristics of Swirl Flames in a Step Combustor," *AIAA Paper No. 94-3272*.
- Fric, T., 1993, "The Effects of Fuel-Air Unmixedness on  $\text{NO}_x$  Emissions," *Journal of Propulsion and Power*, Vol. 9, pp. 708-713.
- Kent, J. H., 1970, "A Noncatalytic Coating for Platinum-Rhodium Thermocouples," *Combustion and Flame*, Vol. 14, pp. 279-282.
- Kretschmer, D., and Odgers, J., 1972, "Modeling of Gas Turbine Combustors—A Convenient Reaction Rate Equation," *ASME JOURNAL OF ENGINEERING FOR POWER*, pp. 173-180.
- Lefebvre, A. H., 1983, *Gas Turbine Combustion*, Hemisphere Publishing Corporation, New York.
- Longwell, J. P., and Weiss, M. A., 1955, "High Temperature Reaction Rates in Hydrocarbon Combustion," *Industrial and Engineering Chemistry*, Vol. 47, pp. 1634-1642.
- Nenniger, J. E., Kridiotis, A., Chomiak, J., Longwell, J. P., and Sarofim, A. F., 1984, "Characterization of a Toroidal Well Stirred Reactor," *Twentieth Symposium (International) on Combustion*, The Combustion Institute, pp. 473-479.
- Nicol, D. G., Steele, R. C., Marinov, N. M., and Malte, P. C., 1995, "The Importance of the Nitrous Oxide Pathway to  $\text{NO}_x$  in Lean-Premixed Combustion," *ASME JOURNAL OF ENGINEERING FOR GAS TURBINES AND POWER*, Vol. 117, pp. 100-111.
- Odgers, J., and Carrier, C., 1973, "Modeling of Gas Turbine Combustors: Consideration of Combustion Efficiency and Stability," *ASME JOURNAL OF ENGINEERING FOR POWER*, Vol. 95, pp. 105-113.
- Rizk, N. K., and Mongia, H. C., 1993, "Semianalytical Correlations for  $\text{NO}_x$ , CO and UHC Emissions," *ASME JOURNAL OF ENGINEERING FOR GAS TURBINES AND POWER*, Vol. 115, pp. 612-619.
- Roffe, G., and Venkataramani, K. S., 1978, "Emissions Measurements for Lean Premixed Propane/Air System at Pressures up to 30 Atmospheres," *NASA CR-159421*.
- Segalman, I., McKinney, R. G., Sturgess, G. J., and Huang, L. M., 1993, "Reduction of  $\text{NO}_x$  by Fuel-Staging in Gas Turbine Engines—A Commitment to the Future," *AGARD-CP-536*, Paris.
- Society of Automotive Engineers, 1994, "Procedure for the Calculation of Basic Emission Parameters for Aircraft Turbine Engines," *AIR 1533*.
- Steele, R. C., Jarrett, A. C., Malte, P. C., Tonouchi, J. H., and Nicol, D. G., 1997, "Variables Affecting  $\text{NO}_x$  Formation in Lean-Premixed Combustion," *ASME JOURNAL OF ENGINEERING FOR GAS TURBINES AND POWER*, Vol. 119, this issue, pp. 102-107.
- Sturgess, G. J., Heneghen, S. P., Vangsness, M. D., Ballal, D. R., and Lesmerises, A. L., 1996, "Lean Blowout in a Research Combustor at Simulated Low Pressures," *ASME JOURNAL OF ENGINEERING FOR GAS TURBINES AND POWER*, Vol. 118, pp. 773-781.
- Thornton, M. M., Malte, P. C., and Crittenden, A. L., 1987, "A Well-Stirred Reactor for the Study of Pyrolysis and Oxidation Kinetics—Carbon Monoxide and n-Pentane Oxidation," *Combustion Science and Technology*, Vol. 54, pp. 275-297.
- Verkamp, F. J., Verdouw, A. J., and Tomlinson, J. G., 1973, "Impact of Emission Regulations on Future Gas Turbine Engine Combustors," *AIAA Paper No. 73-1277*.
- Zelina, J., and Ballal, D. R., 1994, "Combustion Studies in a Well Stirred Reactor," *AIAA Paper No. 94-0114*.

## **APPENDIX C**

### **Vortex-Flame Interactions and Extinction in Turbulent Jet Diffusion Flames**

**Fumiaki Takahashi, W. John Schmoll,  
Darryl D. Trump, Larry P. Goss**



## VORTEX-FLAME INTERACTIONS AND EXTINCTION IN TURBULENT JET DIFFUSION FLAMES

FUMIAKI TAKAHASHI AND W. JOHN SCHMOLL

*University of Dayton  
Dayton, OH 45469, USA*

DARRYL D. TRUMP

*Systems Research Laboratories, Inc.  
Dayton, OH 45440, USA*

LARRY P. GOSS

*Innovative Scientific Solutions, Inc.  
Dayton, OH 45430, USA*

Unsteady vortex-flame interactions and subsequent local extinction have been investigated in double-concentric turbulent methane jet diffusion flames stabilized on a thick-walled fuel tube using joint Mie scattering/thin-filament pyrometry (MS/TFP) and two-color particle image velocimetry (PIV). Particle images visualized the evolution and development of large-scale vortices in the internal fuel jet shear layer and external annulus air jet boundary. The real-time MS/TFP technique captured the events when the internal vortices poked through the flame zone, and the PIV measurements revealed the instantaneous velocity fields in flames interfered by the internal or external vortices. The visible (blue) flame zone turns luminous due to soot formation downstream ( $>5$  jet diameter), where the flame bulges out in response to a radial movement of the internal or external vortices. By contrast, in the near-jet region where the flame zone was strained and relatively immobile, two modes of local extinction were observed: (1) interference by the internal jet-fluid vortices extending outward to the flame zone and (2) interference by the external annulus-fluid vortices perturbing air entrainment. In both cases, the entrainment velocity increased locally, and cold air passed through the quenched holes in the flame zone into the internal vortical structure in the intermittent mixing layer. Local flame extinction is attributed to two distinct unsteady mechanisms: (1) a sudden increase in the fuel diffusive influx as a result of a large Peclet number for mass transfer associated with the internal vortex and (2) an increase in the convective influx as a result of enhanced air entrainment due to the external vortex's squeezing motion.

### Introduction

Flame stability and extinction are of both fundamental and practical importance. In turbulent jet diffusion flames, transient interactions between the flame zone and large-scale vortices may lead to local extinction near the laminar-to-turbulent transition point, if the base of the flame is stabilized by a bluff body or pilot flame [1]. Local extinction may further lead to the formation of a stable split flame (i.e., a combination of a small laminar flame in the vicinity of the burner rim and a "lifted" turbulent flame downstream) for hydrogen [2-6] and propane [7], or it causes lifting of the flame almost immediately for methane [1,8-10]. The dynamic response and structure of jet diffusion flames interacting with vortices (shear-generated, buoyancy-induced, or artificially driven) have been studied experimentally [11-17]

and numerically [18-20]. In addition, the effects of curvature and unsteadiness in diffusion flames have been studied by direct numerical simulations [21]. The characteristics of turbulence (such as scales, intensities, and temporal properties) and, in turn, their effects on flame phenomena vary widely in various turbulent flames. If local extinction mechanisms are revealed in simple laboratory flames, their essential features must be applicable to certain regimes of various turbulent flames in complex practical combustion systems, such as gas-turbine combustors and industrial furnaces.

In a turbulent jet diffusion flame of a pure hydrocarbon in air, the flame zone is formed outside (air-side of) the jet-fluid boundary in which small-scale turbulence is confined because of a low stoichiometric mixture fraction and a high Damköhler number (a ratio of the characteristic flow or diffusion

time to the chemical reaction time, respectively). As a result, molecular diffusion of the fuel in the layer between the jet-fluid boundary and the flame zone is still an important factor in turbulent flames. Through a series of laser diagnostic and numerical studies [14,15,19] of methane jet diffusion flames, a Peclet number for mass transfer ( $Pe$ ; a ratio of the characteristic diffusion time to the convection time associated with the large-scale vortex) has been identified as an important parameter in determining the response of the flame zone to the shear-generated vortex motion, before finite-rate chemistry begins to play a role in local extinction. In addition to interference by internal shear-induced large-scale vortices, we have recently revealed that the external vortical structure also causes local extinction. Because of the time-dependent three-dimensional nature of vortex-flame interactions, single-shot point measurements are insufficient to resolve the phenomenon temporally and spatially. To improve this deficiency, joint line Mie scattering/thin-filament pyrometry (MS/TFP) and two-color particle image velocimetry (PIV) have been used, and this paper reports the new results obtained. The primary purposes of this study are (1) to gain a better understanding of the unsteady vortex-flame interactions that lead to local extinction and subsequent lifting of jet diffusion flames and (2) to advance our knowledge of turbulence-flame interactions applicable to more complex turbulent flames.

### Experimental Techniques

The burner system, described elsewhere in detail [1,14,15], consists of a thick-walled fuel tube (9.45-mm inner diameter, 806-mm long, 2.4-mm lip thickness, flat-end stainless steel tube) and a concentric air tube (26.92-mm inner diameter)—through which annulus coflow air is supplied—centered in a low-speed ( $\sim 0.5$  m/s) external airstream in a vertical combustion chimney (150- $\times$ -150-mm rounded-square cross section, 483-mm long, quartz windows on three sides). Methane ( $>98\%$ ) was used as the fuel.

The unique capabilities of the real-time measurement techniques, including line Mie scattering and thin-filament pyrometry [22,23], were combined to study the transient interactions of flames and their flow fields. As in the previous Mie-scattering experiments [14], a rotating mirror is employed to sweep the scattered or emitted light from a jet diffusion flame past a point detector. In the case of line Mie scattering, seed particles ( $ZrO_2$ ;  $<1\ \mu\text{m}$ , 97%) are introduced into the fuel jet and allowed to pass through a line formed from the focused output of an Argon ion laser (multiline, 1 to 3 W). The scattered light from the sample region is collimated and focused by a lens system toward the multifaceted

rotating mirror wheel that sweeps the converging light onto an optical fiber at 5000 sweeps per second. The optical fiber directs the collected light into a photomultiplier. The TFP technique is simultaneously implemented by placing a small SiC filament ( $\sim 15\ \mu\text{m}$  in diameter) near the laser beam location. As the flame heats the small filament, blackbody emission is collected by the same lens system and reflected to a second optical fiber, directing the light to an InGaAs detector (peak response:  $1.7\ \mu\text{m}$ ). This experimental arrangement allows both the line Mie scattering and the TFP signals to be simultaneously recorded as a function of space and time.

The experimental scheme for two-color PIV is similar to that reported by Goss et al. [24]. A seeded flow field is illuminated by green and red pulsed laser sheets. Because color is used to mark the particle positions as a function of time, the direction and displacement of the particles (velocity) can be uniquely determined. The green (532 nm) laser output from a frequency-doubled pulsed ( $\sim 8$  ns) Nd:YAG laser and the red (640 nm) laser output from a Nd:YAG-pumped dye laser are combined and routed through sheet-forming optics. The laser sheet energy is typically 20 mJ/pulse with a thickness of  $\sim 0.5$  mm at the test section. The temporal delay between the two lasers is controlled by a pulse generator and is varied depending on the gas velocity, optical magnification, and interrogation spot size. Mie scattering from the seed particles is recorded on color film with a 35-mm camera. The color film is digitized by a scanner into individual red, green, and blue components at a resolution of 2702 pixels per inch. The digitized image is then processed by customized PIV analysis software using a cross-correlation technique applied to two distinct (red and green) image fields. The size of the interrogation spot, that is, small subregions over which the cross-correlation is applied, is either  $64 \times 64$  or  $128 \times 128$  square pixels, which translates to the spatial resolution of  $0.6 \times 0.6$  mm with the 1.0 magnification employed.

### RESULTS AND DISCUSSION

#### Joint MS/TFP Measurements

Figure 1 shows real-time line intensities of Mie scattering and thin-filament radiation for different mean jet velocities ( $U_j$ ) and heights from the jet exit ( $x$ ). The Mie scattering is on the left, and the thin-filament radiation is on the right in each figure. At a low mean jet velocity (Fig. 1a), the high-temperature zone marked by the filament was thin and continuous, and the particle-laden jet fluid rarely reached the hot zone. By contrast, at a high mean jet velocity under the condition of local extinction (Fig. 1b), the jet fluid occasionally poked through the flame zone, and the high-temperature zone was sporadically

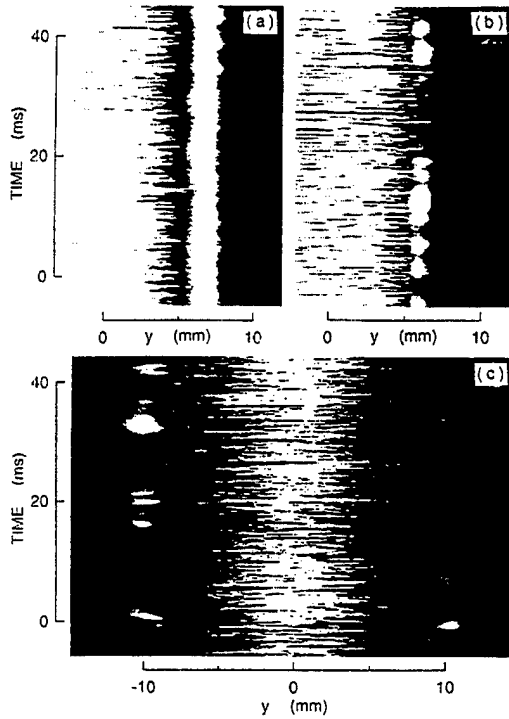


FIG. 1. Real-time Mie scattering and TFP intensities along a line across a methane jet flame.  $U_a = 3$  m/s. (a)  $U_j = 6$  m/s,  $x = 15$  mm; (b)  $U_j = 15$  m/s,  $x = 15$  mm; and (c)  $U_j = 15$  m/s,  $x = 50$  mm.

discontinuous. This result is consistent with the previous observation [25] of local extinction using joint planar Mie scattering and laser-induced fluorescence of OH radicals. However, in other instances, local extinction occurred even if the jet fluid stayed in the jet core region, because of the excess external fluid entrainment, as will be described later. At a downstream location under the high jet velocity (Fig. 1c), the discontinued high-temperature zone shifted outward, thickened, and lumped to form large packets. The radial movement of the interface of the jet fluid and external fluid increased downstream as a result of the growth of the large-scale structure.

Figure 2 shows the jet fluid intermittency ( $\bar{I}$ ), crossing frequency ( $f_c$ ), and mean TFP intensity normalized by its peak value ( $\bar{E}_T$ ). The mean temperature ( $T$ ) determined by coherent anti-Stokes Raman spectroscopy (CARS) previously [15] and the radial location of the visible flame zone are also included in the figure. The terms  $\bar{I}$  and  $f_c$ , determined from Mie scattering as defined in the previous paper [14], indicate the probability that the jet fluid is present at a specific point and the frequency of crossing from the jet to external fluid at the point, respectively.

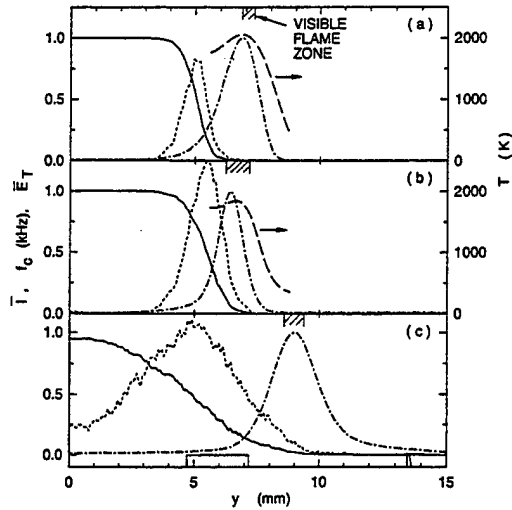


FIG. 2. Jet-fluid intermittency ( $\bar{I}$ ), crossing frequency ( $f_c$ ), mean TFP intensity ( $\bar{E}_T$ ), and mean CARS temperature ( $T$ ) across a methane jet flame.  $U_a = 3$  m/s. (a)  $U_j = 6$  m/s,  $x = 15$  mm; (b)  $U_j = 15$  m/s,  $x = 15$  mm; and (c)  $U_j = 15$  m/s,  $x = 50$  mm. —,  $\bar{I}$ ; - - -,  $f_c$ ; - · - · -,  $\bar{E}_T$ ; — — —,  $T$  [12].

Because the mean temperature data were available from previous CARS measurements [15], the TFP technique was used only for qualitative measurements in this paper. Under a low-velocity condition (Fig. 2a),  $\bar{I}$  decreased radially and vanished before reaching the high-temperature zone, whereas under a higher velocity (Fig. 2b),  $\bar{I}$  still maintained very low, but finite, values even where temperature was at its highest, reflecting the events of local extinction. As the jet velocity was increased, the peak value of  $f_c$  increased (from 810 to 1250 Hz) and its distribution widened, indicating a more frequent and high-amplitude radial motion of the jet fluid. These peak values are reasonably close to the results obtained in previous measurements using  $\text{TiO}_2$  particles (704 and 1330 Hz, respectively) [14]. Furthermore, the visible flame location shifted inward, and the mean flame temperature dropped from  $\sim 2050$  to  $\sim 1820$  K [15] as a result of reactant leakage through the flame zone and local extinction. At a downstream location (Fig. 2c), all distributions of  $\bar{I}$ ,  $f_c$ , and  $\bar{E}_T$  ( $T$  was not available) were wider as the jet spread and vortices grew.

#### Planar Flow Visualization

Planar particle scattering images taken for two-color PIV are useful to extract qualitative information on the vortical structures and local extinction, as well as quantitative velocity measurements. Figure 3 shows examples of the visualization

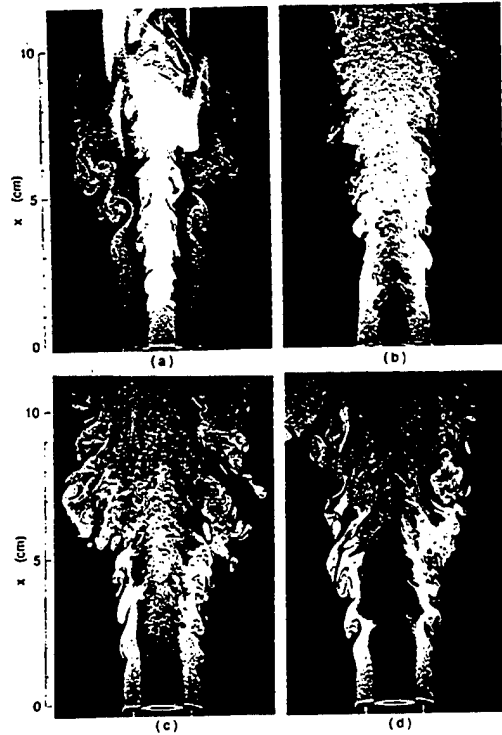


FIG. 3. Two-color planar flow visualization photographs of methane jet flames.  $U_a = 3$  m/s. (a) Attached flame,  $U_j = 6$  m/s,  $\Delta t = 40 \mu s$ ; (b) lifted flame,  $U_j = 16$  m/s,  $\Delta t = 20 \mu s$ ; (c) and (d) locally extinguished flames,  $U_j = 15$  m/s,  $\Delta t = 20 \mu s$ .

photographs, spanning a relatively wide field of view. The jet and annulus fluids can be identifiable in the images by their differences in color tone, mainly depending on the number density of the seed particles. The local laser intensity, temporal delay between two lasers ( $\Delta t$ ), and flow velocity also contribute to the properties of images. In addition, as a result of thermal expansion of the gases in a hot region and associated reduction in the particle number density, the hot regions near the flame zone can also be identified as darker regions, particularly in the near-jet field. This property is of great advantage in that it allows instantaneous recognition of local flame extinction, whereas the visible flame zone is a time-exposure record (typically 1/15 s). These features could not be obtained by one-color (green) laser-sheet visualization using either preformed particles [15] or reactive-Mie scattering [14].

At a low mean jet velocity (Fig. 3a), the evolution and growth of large-scale vortices in the shear layers in the central fuel jet and annulus air jet are clearly seen. The effects of the flame are evident when contrasting images of an attached flame (Fig. 3a) and a lifted flame (Fig. 3b). Since the liftoff height is large

( $x \approx 10$  cm), the region below the flame base is essentially identical to a cold jet. Although the instability in the fuel jet and annulus air shear layers first appeared at  $x \approx 0.3$  and 2 cm, respectively, in both attached and lifted flame conditions, the scales of vortices downstream were significantly larger for the attached flame because of the presence of the flame. An increase in viscosity ( $\propto T^{0.7}$ ), thermal expansion due to a decrease in density ( $\propto T^{-1}$ ), and, in turn, buoyancy certainly affected the differences. Also noticeable is the enhanced fuel-air mixing below the lifted flame as a result of the small-scale turbulence.

The visible (blue) flame zone was recorded in the photograph (Fig. 3a) in the near-jet field, and it turned luminous (yellow) because of soot formation downstream ( $x > 5$  cm). The internal vortex occasionally extended toward the visible flame zone (see  $x \approx 33$  mm on the left side), but the dark, hot zone adjacent to the flame was still thick, indicating the continuous flame zone. The external vortex downstream engulfed the external air close to the visible flame zone, thus squeezing the hot zone (see  $x \approx 45$  mm on both sides). The luminous flame zone bulged out due to both internal and external vortices (see  $x \approx 80$  mm on the left and  $x \approx 67$  mm on the right).

At a high mean jet velocity (Figs. 3c and 3d), the events of local extinction due to interference either by internal or external vortices were depicted. In Fig. 3c, the inner vortices extruded and extinguished the flame zone locally ( $x \approx 38$  mm on the left and  $x > 19$  mm on the right). In Fig. 3d, only annulus air was seeded; thus, the jet fluid appeared void black. The engulfment of the external air into the outer vortex ( $x \approx 28$  mm on the both sides) pushed the annulus air layer inward, and the dark hot zone discontinued. The event was in contrast to the aforementioned low jet velocity case in which the flame sustained combustion (Fig. 3a). In both cases of local extinction (Figs. 3c and 3d), cold annulus air passes through the quenched hole and contacts with the jet fluid (methane) directly. This result explains the large temperature fluctuations (from room temperature to flame temperature) near the flame zone, which were observed in TFP and CARS [15] measurements. Moreover, the annulus air reached deep into the mixing region, even near the jet axis (see Fig. 3d:  $x > 6$  cm).

#### PIV Measurements

Figure 4 shows PIV photographs in the near-jet field of a methane jet diffusion flame under internal and external vortex interference, respectively. A void in the particle image where almost no particle is present clearly shows a wake of the fuel tube (Fig. 4a). The base of the visible flame zone is stabilized at the upper part of the wake. The large-scale vortices evolved in the shear layer of the jet fluid (which looks greenish), grew downstream, and extended

# VORTEX-FLAME INTERACTIONS IN DIFFUSION FLAMES

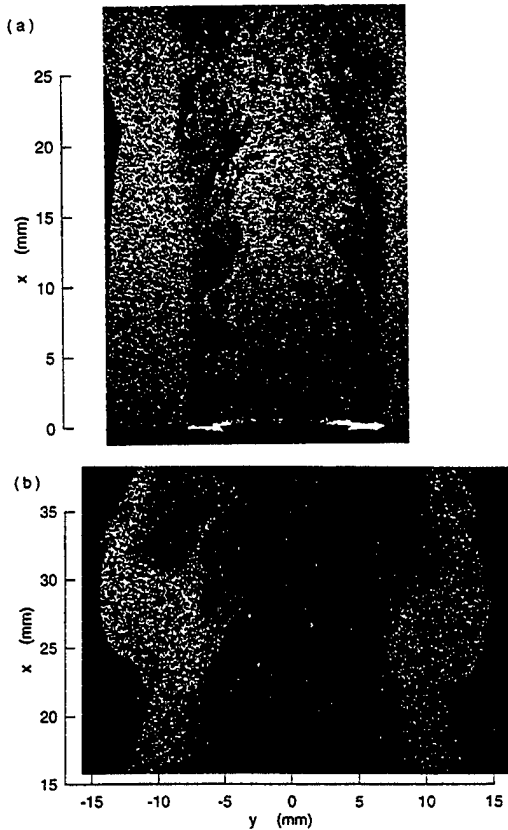


FIG. 4. Two-color PIV photographs of locally extinguished methane jet flames.  $U_j = 15$  m/s,  $U_a = 3$  m/s,  $\Delta t = 9 \mu\text{s}$ . (a) Internal vortex interference and (b) external vortex interference.

outward to the flame-zone location. Consequently, the dark hot zone became thin and discontinuous at  $x \approx 13$  mm on the left and  $x \approx 22$  mm on the right. On the other hand, external vortex interference was captured in Fig. 4b. Because the visible flame zone was a time exposure (1/15 s) image, it did not match the instantaneous particle image, but revealed the average flame-zone location. The outer vortex created necking of the annulus fluid boundary at  $x \approx 24$  mm, thereby squeezing the annulus fluid toward the flame zone. The flame zone was locally extinguished (discontinuous, dark, hot zone) downstream ( $23 \text{ mm} < x < 33 \text{ mm}$  on the left and  $24 \text{ mm} < x < 30 \text{ mm}$  on the right), where cold annulus fluid came in.

The instantaneous two-dimensional velocity vector field with characteristic boundaries (Fig. 5) shows features that could not be revealed by point-measurement techniques such as laser-Doppler velocimetry (LDV) [14]. In general, the velocity field depended locally on the ridges and troughs of

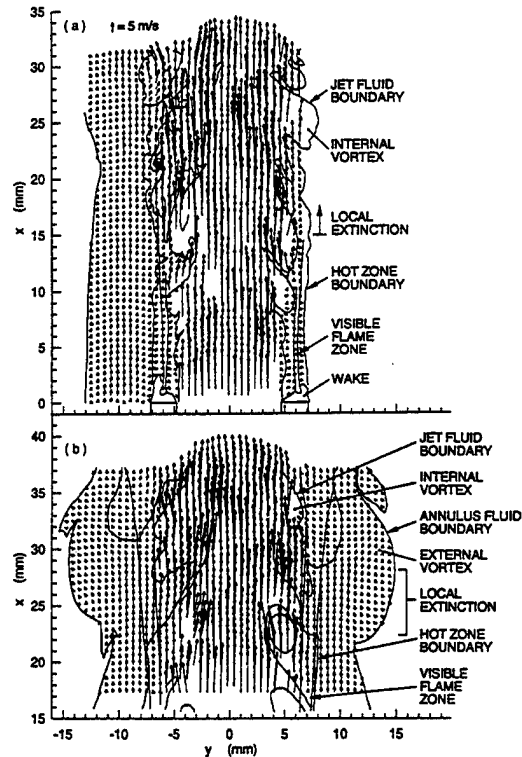


FIG. 5. Velocity vector fields of locally extinguished methane jet flames.  $U_j = 15$  m/s,  $U_a = 3$  m/s,  $\Delta t = 9 \mu\text{s}$ . (a) Internal vortex interference and (b) external vortex interference.

internal and external large-scale vortices, and whether or not the flame zone existed. Furthermore, the zigzag changes in the directions of the velocity vectors related to the ridges and troughs of both internal and external large vortices are apparent in the velocity vector field. If the average wave velocity of the vortex train were subtracted from the velocity vectors, rotation of the vortices would be visualized more clearly.

Figure 6 shows the mean axial ( $U$ ) and radial ( $V$ ) velocity components across and along the flame zone for the PIV image and vector field shown in Figs. 4a and 5a. At  $x = 4.8$  mm (Figs. 6a and 6b), the laminar flame zone was formed in a very low velocity ( $U, V < 0.5$  m/s) region (the distance from the jet axis:  $y \approx -6$  mm) in the extension of the fuel tube wake. The jet fluid elements had much higher axial velocities (up to 22 m/s) than those of annulus fluid. At downstream locations ( $x = 14.9$  and  $25$  mm and  $y = -6.6$  mm) where the flame was being locally extinguished, the axial velocity of external fluid increased substantially ( $U \approx 2-3$  m/s), while the radial component remained small. The instantaneous velocity distributions nearly along the flame-zone

# NON-PREMIXED TURBULENT COMBUSTION

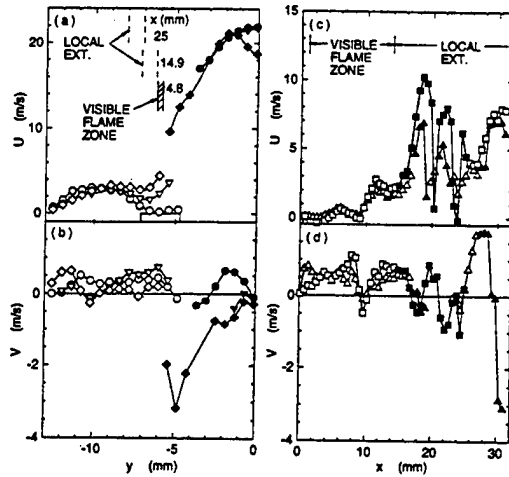


FIG. 6. Mean axial and radial velocity components across a methane jet flame and along the flame zone under internal vortex interference.  $U_j = 15$  m/s,  $U_a = 3$  m/s. (a) and (b)  $\circ$ ,  $x = 4.8$  mm;  $\nabla$ ,  $x = 14.9$  mm;  $\diamond$ ,  $x = 25$  mm. (c) and (d)  $\triangle$ ,  $y = -6.6$  mm;  $\square$ ,  $y = -6$  mm. Open symbols, annulus fluid; filled symbols, jet fluid.

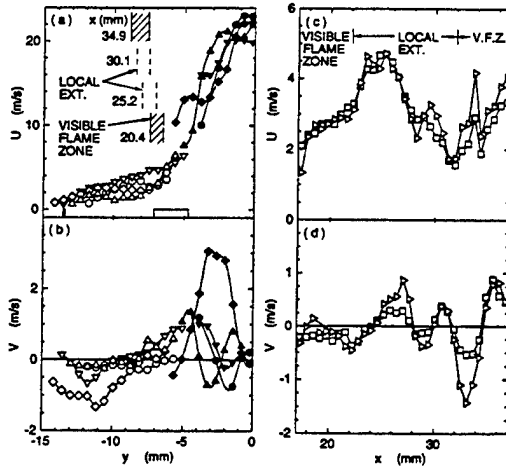


FIG. 7. Mean axial and radial velocity components across a methane jet flame and along the flame zone under external vortex interference.  $U_j = 15$  m/s,  $U_a = 3$  m/s. (a) and (b)  $\circ$ ,  $x = 20.4$  mm;  $\nabla$ ,  $x = 25.2$  mm;  $\diamond$ ,  $x = 30.1$  mm;  $\triangle$ ,  $x = 34.9$  mm. (c) and (d)  $\square$ ,  $y = -7.5$  mm;  $\triangleright$ ,  $y = -6.9$  mm. Open symbols, annulus fluid; filled symbols, jet fluid.

location (Figs. 6c and 6d) revealed typical features in the vortex-flame interactions and local extinction. In the region where the flame zone exists ( $x < 10$  mm), the annulus fluid elements pass through the flame zone at relatively low velocities ( $U < 1$  m/s,  $V < 1$  m/s). In the region where the visible flame zone

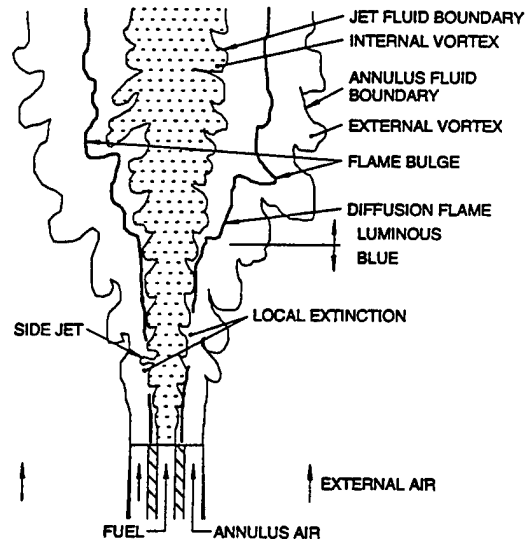


FIG. 8. Schematic of vortex-flame interactions in jet diffusion flames.

fades out and the external fluid flows at shallow angles with the jet axis ( $10 \text{ mm} < x < 16 \text{ mm}$ ), the axial velocities increased to  $\sim 3$  m/s. As the jet fluid extended out in the extinguished region ( $x < 16$  mm), the axial velocity fluctuated significantly (0–10 m/s).

Figure 7 shows the mean axial and radial velocity across and along the flame zone for the PIV image and vector field in Figs. 4b and 5b. At  $x = 20.4$  mm (Fig. 7a), the flame zone was formed at a radial location ( $y \approx -7$  mm), where the axial velocity profile showed a small dip around  $U \approx 3$  m/s. At  $x = 25.2$  mm, where the flame was quenched, the axial velocity was higher (4 to 5 m/s). Farther downstream ( $x = 34.9$  mm), the axial velocity was lower again ( $\sim 2.5$  m/s), and the flame zone existed. The radial velocity component (Fig. 7b) showed complicated distributions, largely depending on the local vortex structure. The axial distributions of  $U$  and  $V$  nearly along the flame-zone location (Figs. 7c and 7d) show interesting features related to the vortex structure and local extinction: The sudden increase in  $U$  was obvious as a result of local extinction, and the sign of  $V$  changed depending on the internal vortices.

## Local Extinction Mechanisms

Figure 8 shows a conceptual illustration depicting several features of vortex-flame interactions in a double-concentric jet diffusion flame. As the jet spread downstream, timescales for both convective and diffusive transport processes decrease because of lower velocities and smaller concentration gradients. Longer residence times allow fuel pyrolysis and soot

formation, and the visible flame turns luminous. The flame zone can bulge out in response to the vortical motion in both internal and external structures. By contrast, in the near-jet region, the velocity of the annulus fluid passing through the flame zone is large. The flame zone therefore shifts inward, that is, closer to the jet-annulus fluid boundary, where the radial gradients of the mean axial velocity, fuel concentration, and, in turn, fuel diffusive flux are larger, to match with an increased oxygen flux. As a result, the thickness of the diffusive layer between the jet boundary and the flame zone becomes thin; thus, the flame becomes more strained and loses its radial mobility. Based on the current and previous [14,15] experimental findings and the recent [26] results of direct numerical simulations of laminar diffusion flames in which an artificial vortex is ejected as a side jet toward the flame zone from either the fuel side or the air side, two distinct local flame extinction mechanisms are considered as follows.

1. The local extinction caused by internal vortices is largely due to unsteady transport effects on chemical kinetics. The characteristic diffusion time was estimated as  $\sim 30$  ms, and the internal vortex transit time was estimated as  $\sim 0.8$  ms (consistent with the crossing frequency of the jet fluid  $\sim 1250$  Hz) [15]; thus, the Peclet number for mass transport (i.e., a ratio of these two times) was relatively large ( $\sim 40$ ). Therefore, if an internal vortex extends toward the flame zone, there is not sufficient time to re-establish the fuel concentration field, and thus, the vortex with a steep fuel concentration gradient ahead of its leading edge can reach the flame-zone location without causing significant disturbances in the surrounding concentration field. Consequently, the thickness of the layer between the leading edge of the vortex and the flame zone (diffusive layer) rapidly becomes thin, and the flame is subjected to an excessively high fuel flux due to the high concentration gradient. In addition, as a result of the vortex motion, the convective contribution to the fuel flux increases. The excessive methane (and methyl radical) fluxes into the reaction zone may result in scavenging of a radical pool, quenching exothermic reactions, and reducing the flame temperature and thus the net reaction and heat release rates.

2. The local extinction by external vortices is also an unsteady phenomenon, but it occurs over a longer timescale because of lower vortex frequency. The frequency can be estimated by dividing the external fluid velocity ( $\sim 3$  m/s) by a typical scale of the outer structure ( $\sim 15$  mm). This gives  $\sim 200$  Hz, which is equivalent to a period of  $\sim 5$  ms. As the external vortex squeezes the annulus fluid, the entrainment flow passing through the flame zone accelerates, thereby reducing the residence time in the reaction zone. In addition, the flame is further pushed inward, where velocity and concentration gradients are steeper, and is more strained, further increasing the

reactant leakage and decreasing the flame temperature and the net reaction and heat release rates.

## Conclusions

The laser diagnostic measurements have shed light on the transient interaction processes between the diffusion flame zone and the internal and external vortical structures and on mechanisms of subsequent local extinction. Both the internal shear-generated large-scale vortices and external shear-buoyancy-induced vortices are responsible for local flame extinction. The flame zone is locally extinguished if the internal fuel jet vortices approach the flame zone in a short period of time, or if the entrainment velocity is forced to increase due to the outer vortical structure. The former can be attributed to a characteristic diffusion time of the fuel, which is an order of magnitude longer than a convection time associated with the rapid growth of the inner large structure (large  $Pe$  effect) and subsequent excess diffusive influx of methane into the flame. The latter is caused by an excess convective influx into the strained flame.

## Acknowledgments

This work was supported by the U.S. Air Force, Wright Laboratory, Aero Propulsion and Power Directorate, Fuels and Lubrication Division, Wright-Patterson Air Force Base, OH, under Contract No. F33615-92-C-2207 (technical monitor: C. W. Frayne).

## REFERENCES

1. Takahashi, F. and Schmoll, W. J., *Twenty-Third Symposium (International) on Combustion*, The Combustion Institute, Pittsburgh, 1991, pp. 677-683.
2. Hattori, H., *Trans. JSME* 30:320-332 (1964).
3. Vranos, A., Taback, E. D., and Shipman, C. W., *Combust. Flame* 12:253-260 (1968).
4. Takeno, T. and Kotani, Y., *Acta Astronaut.* 2:999-1008 (1975).
5. Hall, L., Horch, K., and Günther, R., *Brennst. Wärme Kraft* 32:26-31 (1980).
6. Takahashi, F., Mizomoto, M., Ikai, S., and Tsuruyama, K., AIAA Paper 90-0034, 1990.
7. Shekarchi, S., Savas, Ö., and Gollahalli, S. R., *Combust. Flame* 73:221-232 (1988).
8. Eickhoff, H., Lenze, B., and Leuckel, W., *Twentieth Symposium (International) on Combustion*, The Combustion Institute, Pittsburgh, 1985, pp. 311-318.
9. Chen, T. H. and Goss, L. P., AIAA Paper 89-0156, 1989.
10. Coats, C. M. and Zhao, H., *Twenty-Second Symposium (International) on Combustion*, The Combustion Institute, Pittsburgh, 1989, pp. 685-692.

# NON-PREMIXED TURBULENT COMBUSTION

11. Chen, L.-D., Vilimpoc, V., Goss, L. P., Davis, R. W., Moore, E. F., and Roquemore, W. M., *Twenty-Fourth Symposium (International) on Combustion*, The Combustion Institute, Pittsburgh, 1992, pp. 303-310.
12. Lasheras, J. C., Liñán, A., Lecuona, A., and Rodriguez, P., *Twenty-Fourth Symposium (International) on Combustion*, The Combustion Institute, Pittsburgh, 1992, pp. 325-332.
13. Ståmer, S. H., Bilger, R. W., Dibble, R. W., Barlow, R. S., Fourguette, D. C., and Long, M. B., *Twenty-Fourth Symposium (International) on Combustion*, The Combustion Institute, Pittsburgh, 1992, pp. 341-349.
14. Takahashi, F. and Goss, L. P., *Twenty-Fourth Symposium (International) on Combustion*, The Combustion Institute, Pittsburgh, 1992, pp. 351-359.
15. Takahashi, F. and Vangsness, M. D., in *Dynamics of Heterogeneous Combustion and Reacting System* (A. L. Kuhl, J.-C. Leyer, A. A. Borisov, and W. A. Sirignano, Eds.), American Institute of Astronautics and Aeronautics, Washington, D.C., 1993, Vol. 152, p. 37.
16. Hsu, K. Y., Chen, L. D., Katta, V. R., Goss, L. P., and Roquemore, W. M., AIAA Paper No. 93-0455, 1993.
17. Schefer, R. W., Namazian, M., Filtopoulus, E. E. J., and Kelly, J., *Twenty-Fifth Symposium (International) on Combustion*, The Combustion Institute, Pittsburgh, 1994, pp. 1223-1231.
18. Yamashita, H., Kushida, G., and Takeno, T., *Twenty-Fourth Symposium (International) on Combustion*, The Combustion Institute, Pittsburgh, 1992, pp. 311-316.
19. Takahashi, F. and Katta, V. R., *J. Propulsion Power* 11:170-177 (1995).
20. Chen, J. H., Card, Day, M., and Mahalingam, S., *Paper presented at the 8th International Symposium on Transport Phenomena in Combustion*, San Francisco, July 1995.
21. Cuenot, B. and Poinot, T., *Twenty-Fifth Symposium (International) on Combustion*, The Combustion Institute, Pittsburgh, 1994, pp. 1383-1390.
22. Vilimpoc, V. and Goss, L. P., *Twenty-Second Symposium (International) on Combustion*, The Combustion Institute, Pittsburgh, 1989, pp. 1907-1914.
23. Roquemore, W. M., Chen, L.-D., Goss, L. P., and Lynn, W. F., in *Turbulent Reacting Flows* (R. Borghi and S. N. B. Murthy, Eds.), Springer-Verlag, New York, 1989, p. 49.
24. Goss, L. P., Post, M. E., Trump, D. D., and Sarka, B., *J. Laser Applications* 3:36-42 (1991).
25. Chen, T. H. and Goss, L. P., *Combust. Sci. Technol.* 79:311 (1991).
26. Takahashi, F. and Katta, V. R., *Twenty-Sixth Symposium (International) on Combustion*, The Combustion Institute, Pittsburgh, 1996, pp. 1151-1160.



## **APPENDIX D**

### **Near-Field CARS Measurements and the Local Extinction of Turbulent Jet Diffusion Flames**

**Fumiaki Takahashi, Marlin D. Vangsness**

**Near-Field CARS Measurements and the Local Extinction of  
Turbulent Jet Diffusion Flames**

Fumiaki Takahashi and Marlin D. Vangsness, *University of Dayton,  
Dayton, Ohio*

**Reprinted from Dynamics of Heterogeneous Combustion and Reacting Systems,**  
edited by A. L. Kuhl, J.-C. Leyer, A. A. Borisov, and W. A. Sirignano, Vol. 152 of *Progress  
in Astronautics and Aeronautics*, AIAA, Washington, DC, ISBN 1-56347-058-6.

# Near-Field CARS Measurements and the Local Extinction of Turbulent Jet Diffusion Flames

Fumiaki Takahashi\* and Marlin D. Vangsness†  
*University of Dayton, Dayton, Ohio 45469*

## Abstract

Local extinction and subsequent lifting mechanisms have been investigated in turbulent jet diffusion flames of methane stabilized on a thick-walled fuel tube in coflowing air. The laser-sheet flow visualization technique revealed a large-scale turbulent structure in the intermittent mixing layer inside the flame zone. Coherent anti-Stokes Raman spectroscopy (CARS) was used to determine the intermittency of the jet fluid (methane) as well as the gas temperature in the near-jet field. Packets of unmixed fuel, which were conveyed by the large-scale vortices or more rapid radial ejection (side jet), quenched the flame zone locally. Cold air was then entrained in the intermittent mixing layer through the quenched holes in the flame zone. Local flame extinction can be attributed to an order-of-magnitude longer diffusion time of the fuel compared to convection times associated with the large structure and the side jet in the jet-fluid core. There is not sufficient time available to re-establish the mass-flux field because the unmixed fuel packets approach rapidly and replace the gases in the flame zone, thereby quenching the flame locally.

## Introduction

The local extinction of jet diffusion flames near the laminar-to-turbulent flame transition point (breakpoint) is a well-known phenomenon.<sup>1</sup> If the flame base is stabilized securely by a bluff body or pilot flame, the flame zone may be quenched locally a few jet diameters downstream before the flame lifts off.

---

Copyright © 1993 by the American Institute of Aeronautics and Astronautics, Inc. All rights reserved.

\* Research Engineer, Research Institute.

† Associate Research Physicist, Research Institute.

Local extinction leads to the formation of a stable split flame (i.e., a combination of a small laminar flame in the vicinity of the burner rim and a "lifted" turbulent flame downstream) in the case of hydrogen<sup>2-6</sup> or propane,<sup>7</sup> or causes lifting of the flame almost immediately in the case of methane.<sup>1,8-10</sup> It has long been postulated<sup>4,8</sup> that local extinction near the breakpoint occurs as a result of turbulence-chemistry interactions (i.e., the excess transport rate in small-scale turbulence compared to the finite reaction rate). However, the diffusion flame zone of (pure) hydrocarbons in air, in general, resides in the less-turbulent external-fluid flow outside the small-scale turbulence region in the fuel-jet core. Therefore, it is less likely that the flame zone will interact directly with the small-scale turbulence. Instead, the large-scale vortices generated in the shear layer near the interface between the jet fluid and the external fluid play an important role because they indirectly affect the flow conditions of the external fluid passing through the flame zone and, in turn, the flame structure.

Vortex-flame interactions in turbulent methane jet diffusion flames have been studied<sup>11</sup> by means of laser-sheet flow visualization, real-time Mie scattering, and laser-Doppler velocimetry (LDV) techniques. One physical aspect of the vortex-flame interactions has been identified as the dominant process in a series of events leading to local extinction, at which point finite-rate chemistry takes over the process. More specifically, the fuel diffusion process requires an-order-of-magnitude longer time compared to the convective motion associated with the large-scale vortex structure and the radial mass ejection (side jets) from the jet-fluid core. Therefore, fuel packets can reach the flame zone location without causing significant disturbances in the adjacent concentration field. Consequently, they replace the gases on the passage through the flame zone, thereby quenching the flame locally. This paper complements previous efforts<sup>11</sup> and reports new results obtained by using CARS thermometry and the planar flow visualization technique. The primary purpose of this study is to gain a better understanding of the local extinction and subsequent lifting phenomena. Further development of the proposed local extinction mechanism is presented the following sections.

### Experimental Techniques

Figure 1 shows the schematic of the burner used. The burner consists of a thick-walled fuel tube (9.45-mm inner diameter, 806-mm length, 2.4-mm lip thickness; stainless steel) and a concentric air tube (26.92-mm inner diameter) — through which annulus coflow air is supplied — centered in a low-speed ( $\sim 0.5$  m/s) external airstream in a vertical combustion chimney (150- $\times$  150-mm rounded-square cross section; 483-mm length). The fuel tube is flat-ended at the exit, and the air tube is sharp-edged with a tapered outer wall at a half-cone angle of  $2^\circ$ . The combustion chimney has quartz windows on all

## LOCAL EXTINCTION OF DIFFUSION FLAMES

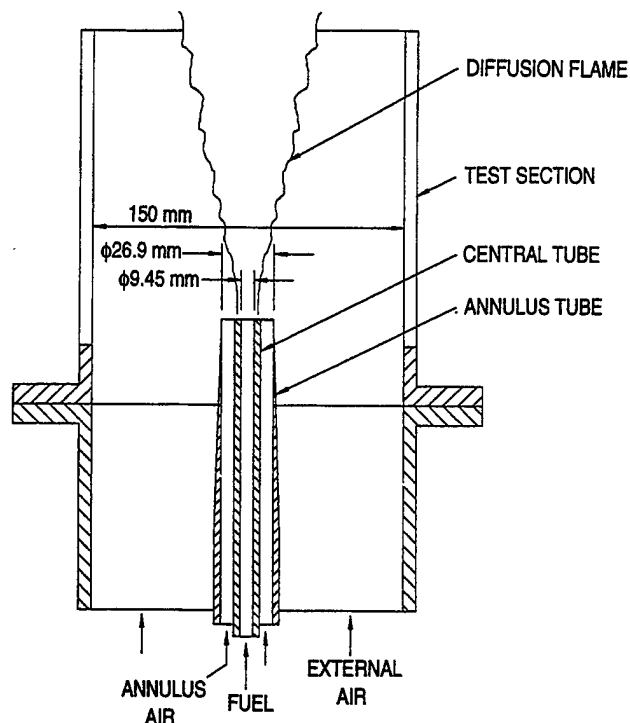


Fig. 1 Schematic of the burner used.

sides to permit visual observations and laser diagnostics. The burner assembly is placed on a custom-made, three-dimensional translational stage with a digital position readout (SONY GS-E/LA10; 5- $\mu$ m accuracy). Methane (>98%) was used as the fuel.

The instantaneous (10 ns) planar flow visualization technique was used to visualize the flow field. In this technique, zirconia particles (< 1  $\mu$ m, 97%) seeded into the fuel jet are illuminated by a sheet of laser light ( $\sim$ 0.25-mm thickness) from a pulsed Nd:YAG laser (Quanta-Ray DCR-3, frequency-doubled, 532 nm,  $\sim$ 250 mJ) passing through the jet axis. The direct image of the flame and Mie scattering images from the particles are photographed at right angles to the laser sheet using a 35-mm camera. The visible (blue) flame zone locations are measured by observing the edges of the flame zone with a stationary telescope while traversing the burner horizontally by the translational stage.

The CARS system (Fig. 2) used is essentially the same as that described by Goss et al.<sup>12</sup>. It consists of a pulsed Nd:YAG laser (Quanta Ray DCR-2A, 10-ns pulse width, 10-Hz repetition rate), dye laser optics, incident and collection optics, a 3/4-m grating spectrometer (Spex 1702), and a diode array rapid

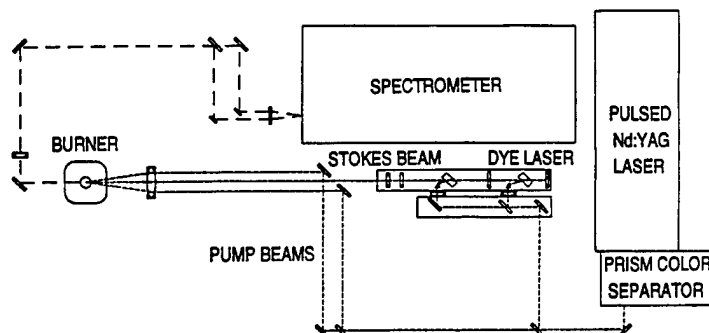


Fig. 2 Schematic of the CARS system.

scanning spectrometer (DARSS) detector system (Tracor-Northern, TN-6132) with a multichannel analyzer (TN-1710). The output from the laser is frequency-doubled (532 nm, ~150 mJ, spectral half-width at half-maximum (HWHM)  $< 0.5 \text{ cm}^{-1}$ ) and divided into four beams of nearly equal intensity. Two of these serve as the pump beams, while the other two pump a dye laser oscillator and amplifier. The dye laser is concentration-tuned (dye solution: Rhodamine 640 in methanol) to provide a broadband (HWHM  $\sim 60 \text{ cm}^{-1}$ ) Stokes beam centered at 607 nm. The red Stokes beam and the two green pump beams are then focused together by a 25-cm-focal-length lens in a folded BOXCARS configuration.<sup>13</sup> The effective probe volume size is estimated at approximately  $25 \mu\text{m}$  in diameter and  $250 \mu\text{m}$  in length. The CARS signal is collimated and focused onto the "apparent" slits of a spectrometer with a cylindrical lens and recorded by a DARSS detector and multichannel analyzer. The detector contains 1024 pixels, and the resolution of the system is  $1.24 \text{ cm}^{-1}$  per pixel. Typically, 500 CARS signals are acquired at each location and processed by a minicomputer (MODCOMP Classic 32/85).

## Results and Discussion

### Planar Flow Visualization

The laser-sheet flow visualization technique provides qualitative, but useful, information on the large vortex structure and its interactions with the flame zone. Figure 3 shows instantaneous planar flow visualization photographs of methane jet diffusion flames at three different mean jet velocities. These Mie scattering images from pre-seeded, manufactured (zirconia) particles are more grainy than those obtained previously<sup>11</sup> by the reactive Mie scattering technique<sup>14</sup> using  $\text{TiO}_2$  particles formed from the reaction of seeded  $\text{TiCl}_4$  vapor and water vapor in the combustion product mainly because of larger particle size. Although the reactive Mie scattering

## LOCAL EXTINCTION OF DIFFUSION FLAMES

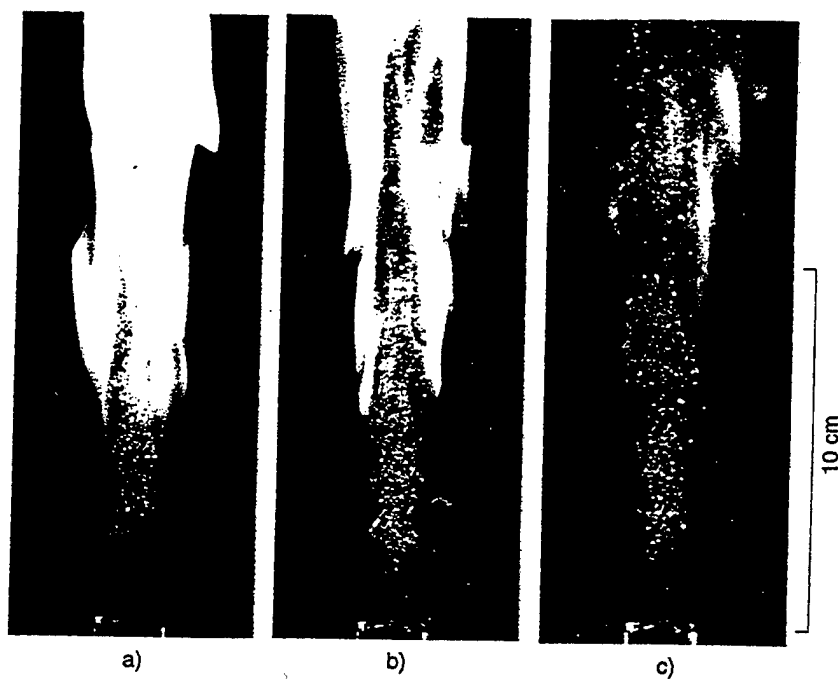


**Fig. 3** Instantaneous (10 ns) laser-sheet Mie scattering images superimposed with time-exposure (1/60 s) direct photographs of methane-air coflow jet diffusion flames. Seed:  $\text{ZrO}_2$ .  $U_a = 3$  m/s. a)  $U_j = 6$  m/s ( $Re_j = 3380$ ), b)  $U_j = 10$  m/s ( $Re_j = 5630$ ), c)  $U_j = 15.5$  m/s ( $Re_j = 8740$ ).

photographs allow the vortex structure to be examined in greater detail, the pre-seed method is superior for marking the boundary between the jet and external fluids as well as the jet fluid itself without the potential complications associated with the molecular diffusion, mixing, and reaction delay of  $\text{TiCl}_4$  and water vapor. Since submicron size particles seeded into the jet fluid do not diffuse into the laminar-like external-fluid flow (the hot combustion products) either by small-scale turbulent transport, gradient-type molecular diffusion, or thermal diffusion, they tend to remain within the jet-fluid convective boundary, at least, in the near field where the interface between the jet and external fluids is relatively clear.

At a low mean jet velocity ( $U_j = 6$  m/s; Fig. 3a), large-scale vortices were observed in the near-jet field at heights from the jet exit  $z > 30$  mm, forming an intermittent mixing layer. Notice that the jet-external fluid boundary is well inside (1-2 mm) the visible (blue) flame zone. As the mean jet velocity was increased ( $U_j = 10$  m/s; Fig. 3b), the large vortex structure extended outward and occasionally approached the visible flame zone. As  $U_j$  was increased further to  $\sim 15$  m/s, the local quenching became visible to the naked eye. The

frequency and area of local extinction increased, and the vibratory movement of the downstream portion of the flame started in the range of  $10 < z < 60$  mm. At a high mean jet velocity ( $U_j = 15.5$  m/s; Fig. 3c) near the critical mean jet velocity at lifting ( $U_{jc} = 16.5$ – $17$  m/s at  $U_a = 3$  m/s),<sup>1</sup> the flame zone was almost continuously extinguished in the range of  $10 < z < 60$  mm. As a result, a split flame was formed just before the entire flame lifted off. As cold ambient air was entrained into the intermittent mixing layer through the quenched region, the yellow luminosity due to the black-body radiation from soot particles was suppressed significantly.

### CARS Measurement

In CARS thermometry, temperatures are determined by comparing actual nitrogen spectra to theoretically calculated spectra using a least-square method. Signal interference by unmixed methane in the intermittent mixing layer in the near-jet region presented some difficulties. Figure 4 shows typical CARS spectra obtained from the same location but at different times. Figure 4a shows a nitrogen spectrum, without interference, which is composed of two peaks: a large primary peak (based on the lowest vibrational level,  $v = 0$ ) and a small side peak ( $v = 1$ ). Figure 4b shows a spectrum contaminated by nonresonant, background interference from methane. The nitrogen peaks were seated on a broad background shift. For such a spectrum, the temperature could not be determined accurately. Therefore, the temperature measurement was limited to the region outside the boundary between unmixed jet fluid (methane) and the external fluid.

Fortunately, since the jet-external fluid boundary was relatively clear in the near-jet region, the fraction of CARS realizations for which the methane interference was observed in the total number of data at each location could be utilized to determine the intermittency of the jet fluid ( $\bar{I}$ ). The intermittency represents the time fraction of jet fluid (unmixed methane) present at a particular location. To determine the presence of unmixed methane, each CARS spectrum was inspected at the base of the  $v = 1$  peak (at a wave number of the  $v = 0$  peak less  $74 \text{ cm}^{-1}$ ). A signal intensity normalized by the  $v = 0$  peak value that exceeds a threshold value indicates that unmixed methane is present. The threshold value (0.15) was set based on the measurement at a height close to the jet exit ( $z = 5$  mm) such that the radial location at which  $\bar{I} = 0.5$  coincided with the inner edge of the burner rim ( $r \sim 4.7$  mm).

Figure 5 shows the radial profiles of the mean gas temperature, the root-mean-square (rms) temperature fluctuation, and the intermittency of the jet fluid at  $z = 15$  mm for three different mean jet velocities. The radial locations of the visible flame zone and the burner rim are also included in the figure. The error bar on the mean temperature data point shows the minimum and maximum temperatures in a data set of valid (without interference) CARS measurements. The dotted curve shows the intermittency obtained previously<sup>11</sup> by using the real-time Mie scattering technique. Despite the two distinct



# LOCAL EXTINCTION OF DIFFUSION FLAMES

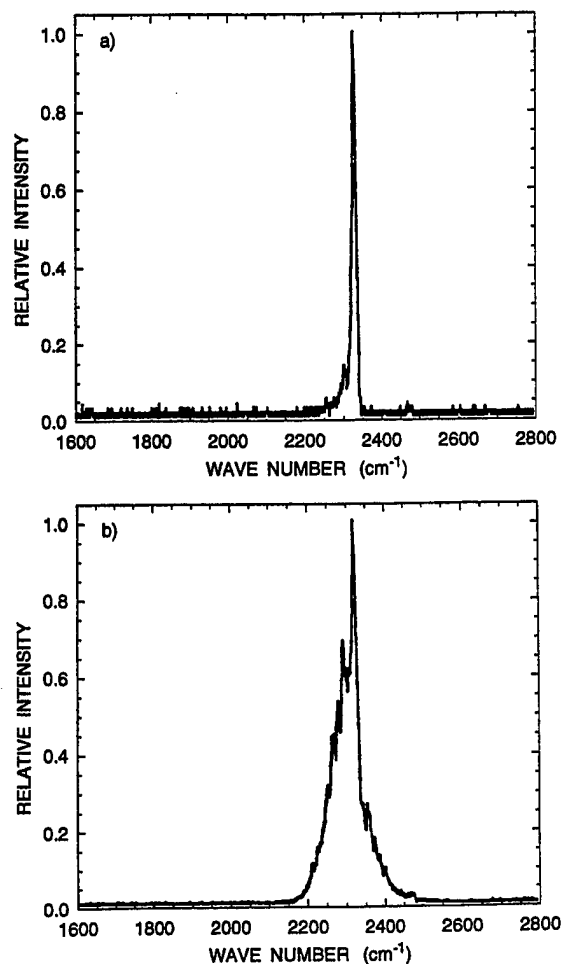


**Fig. 4**  $N_2$  CARS spectra.  $U_j = 15$  m/s,  $U_a = 3$  m/s,  $z = 15$  mm,  $r = 6$  mm.  
**a)** Spectrum without interference. **b)** Spectrum with interference by nonresonant background signal from  $CH_4$ .

marking media and detection criteria, the results are in fairly good agreement, although some difference exists in the sensitivity (slope).

At a low mean jet velocity ( $U_j = 6$  m/s, Fig. 5a), the intermittency was unity in the potential core region ( $r < 4.5$  mm) and decreased markedly in the intermittent mixing layer ( $4.5 < r < 5.5$  mm), vanishing to zero at a location ( $r \sim 6$  mm) well inside (the fuel side of) the visible flame region ( $6.9 < r < 7.3$  mm). The unmixed fuel packet rarely reached the flame zone location. This result is consistent with the photographic observations described in the preceding section (Fig. 3a). The fuel molecules were thus transported from the jet-external fluid boundary to the flame zone by molecular diffusion,

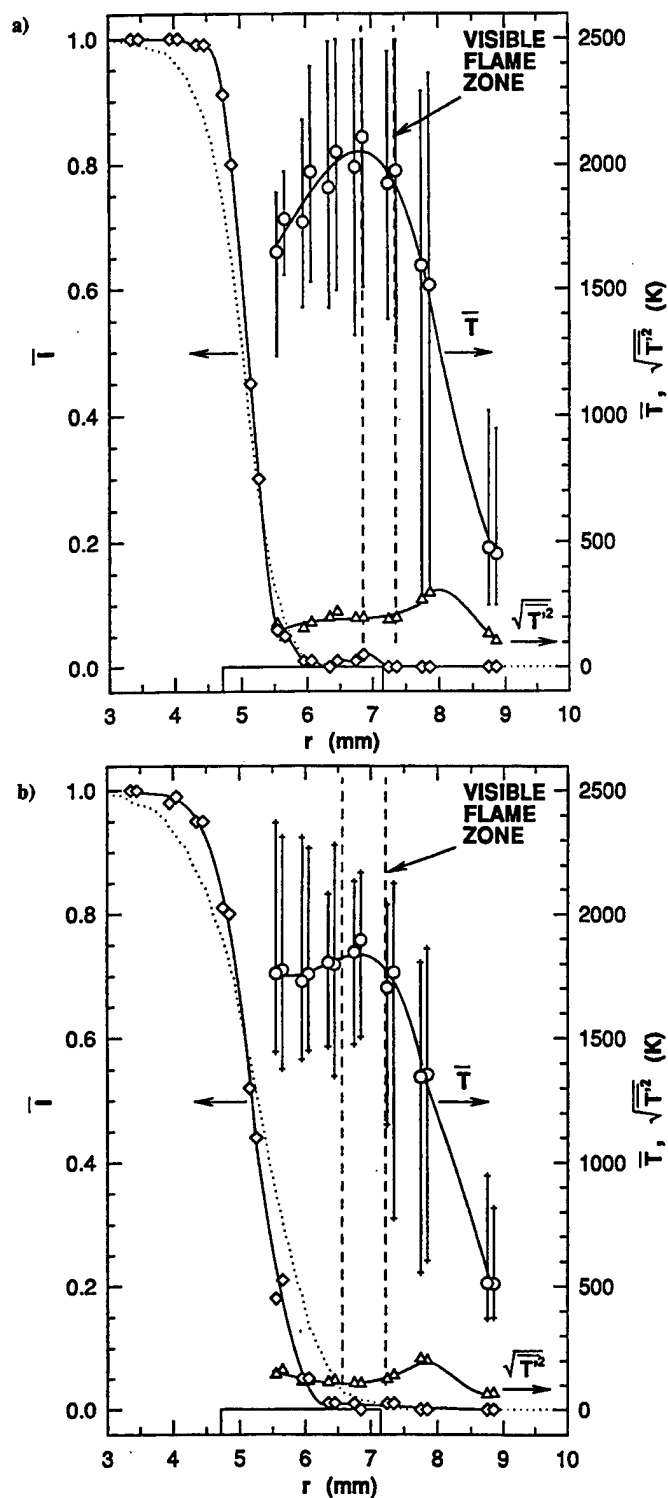


Fig. 5 Radial profiles of the mean temperature, rms fluctuation, and intermittency of the jet fluid at three different mean jet velocities.  $\bullet$ , mean temperature;  $\nabla$ , rms fluctuation;  $\diamond$ , Intermittency.  $U_a = 3$  m/s,  $z = 15$  mm. a)  $U_j = 6$  m/s, b)  $U_j = 10$  m/s, c)  $U_j = 15$  m/s.

# LOCAL EXTINCTION OF DIFFUSION FLAMES

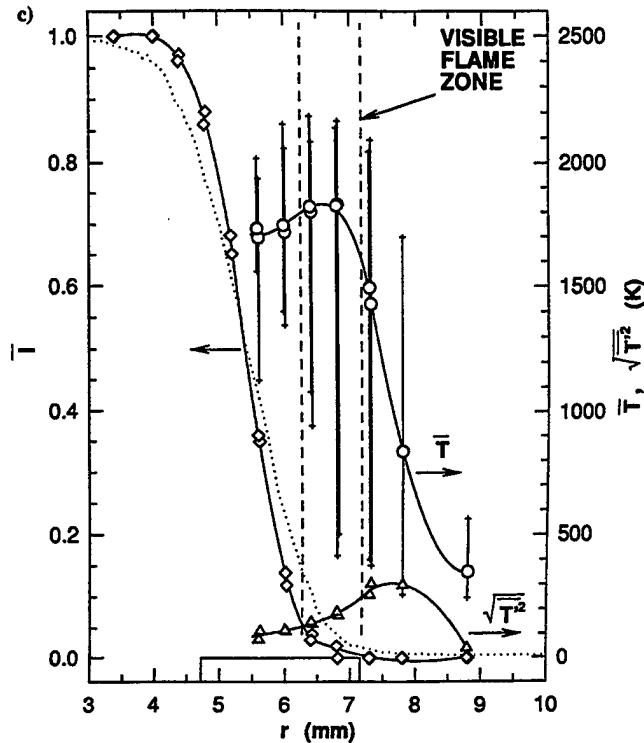


Fig. 5 (continued) Radial profiles of the mean temperature, rms fluctuation, and intermittency of the jet fluid at three different mean jet velocities.  $\bullet$ , mean temperature;  $\nabla$ , rms fluctuation;  $\diamond$ , intermittency.  $U_a = 3$  m/s,  $z = 15$  mm. a)  $U_j = 6$  m/s, b)  $U_j = 10$  m/s, c)  $U_j = 15$  m/s.

typical of laminar diffusion flames. The mean flame temperature peaked at the inner edge of the visible flame zone and was approximately 2100 K – about 110 K lower than the adiabatic flame temperature of the stoichiometric methane-air mixture. The rms fluctuation was maximum (~300 K) in the outer thermal layer on the air side of the flame zone.

At a moderate mean jet velocity ( $U_j = 10$  m/s; Fig. 5b), the peak (mean) temperature decreased significantly (~1900 K). The intermittency curve expanded outward, and the inner edge of the visible flame zone shifted slightly inward. As a result, the radial location at which intermittency vanished ( $r \sim 6.5$  mm) was nearly coincident with the inner edge of the visible flame zone ( $6.6 < r < 7.2$  mm). This finding is again consistent with the photographic observation (Fig. 3b). The interaction between the large-scale vortex and the flame zone became further evident at  $U_j = 15$  m/s (Fig. 5c). Intermittency at the inner edge of the visible flame zone was ~0.1. In other words, the unmixed

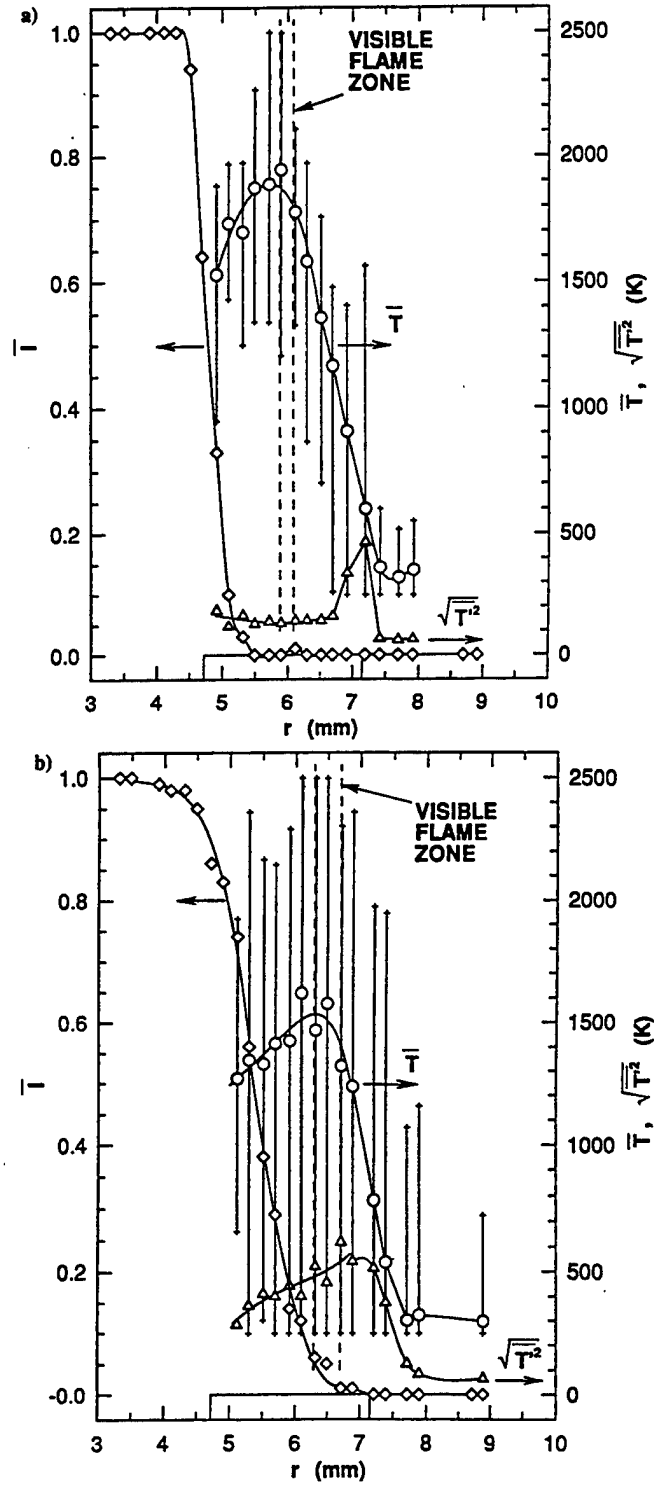
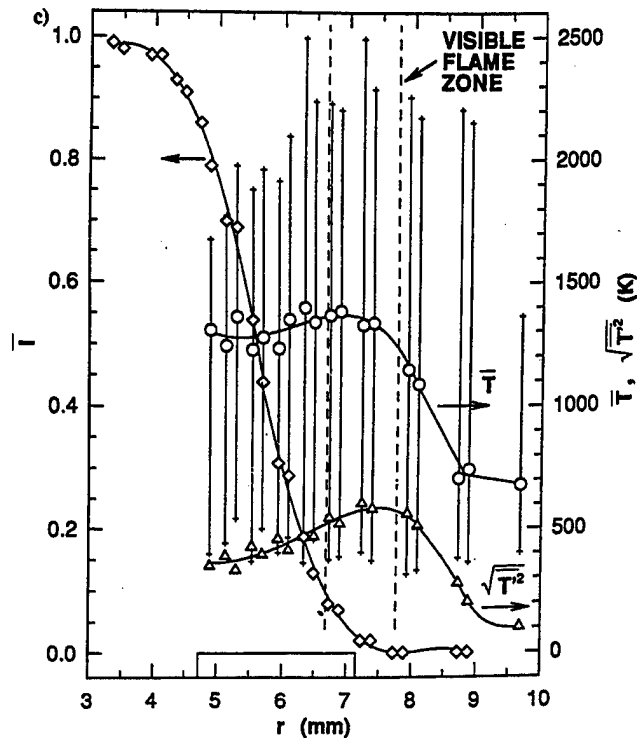


Fig. 6 Radial profiles of the mean temperature, rms fluctuation, and intermittency of the jet fluid at three different heights. •, mean temperature;  $\nabla$ , rms fluctuation;  $\diamond$ , Intermittency.  $U_j = 15$  m/s,  $U_a = 3$  m/s. a)  $z = 5$  mm, b)  $z = 15$  mm, c)  $z = 25$  mm.

# LOCAL EXTINCTION OF DIFFUSION FLAMES



**Fig. 6 (continued)** Radial profiles of the mean temperature, rms fluctuation, and intermittency of the jet fluid at three different heights. •, mean temperature; ▽, rms fluctuation; ◇, intermittency.  $U_j = 15$  m/s,  $U_a = 3$  m/s. a)  $z = 5$  mm, b)  $z = 15$  mm, c)  $z = 25$  mm.

fuel packet reached the flame zone location approximately 10% of the time. Further, although the peak (mean) temperature remained the same as that at  $U_j = 10$  m/s, the minimum temperature in the visible flame zone decreased substantially due to occasional entrainment of the ambient air.

Figure 6 shows the radial profiles of the mean gas temperature, the rms fluctuation, and the intermittency of the jet fluid at a near-limit mean jet velocity ( $U_j = 16.5$  m/s) at three different heights. The Mie scattering measurement could not be made under this flow condition because seeding induced flame-lifting prematurely. A comparison of Fig. 6b with Fig. 5c revealed dramatic changes. The minimum temperature dropped to room temperature at locations throughout the inner region (to  $r \sim 5.3$  mm) where intermittency increased to about 0.5. This result evidenced that cold air was entrained into the intermittent mixing layer on the fuel side of the flame zone through the quenched region. Consequently, the peak (mean) temperature decreased further ( $\sim 1500$  K), and the rms fluctuation increased ( $\sim 500$  K). At a

higher location ( $z = 25$  mm; Fig. 6c), the trends described above were even further enhanced; cold air was engulfed in the large vortex more deeply. Further, the maximum temperature in a data set on the air side of the flame zone increased due to fragmented hot-gas packets ejected sporadically. On the other hand, at a height close to the jet exit ( $z = 5$  mm; Fig. 6c), the temperature and intermittency profiles show a typical "laminar" flame structure similar to that of the low-velocity case shown in Fig. 5a. Because the height from the jet exit was less than the breakpoint, the flame zone resided ( $5.9 < r < 6.1$  mm) outside the intermittent mixing layer ( $4.5 < r < 5.5$  mm). Thus, the flame zone appeared to be laminar and the peak (mean) temperature was relatively high ( $\sim 1900$  K).

Figure 7 shows the probability-density functions (pdf), or probability-density histograms, of the measured temperatures at several radial locations for two different mean jet velocities ( $U_j = 15, 16.5$  m/s). The locations of the visible flame zone were approximately  $r = 6.2$  to  $7.2$  and  $6.3$  to  $6.7$  mm, respectively. At  $U_j = 15$  m/s and  $r = 8.8$  mm (Fig. 7a), the pdf showed a sharp peak near room temperature. In the outer hot-boundary region ( $r = 7.8, 7.3$  mm), the pdf spread over a wide range and the peak shifted gradually toward higher temperatures. In the flame zone and its fuel side ( $r = 6.8, 6.4, 6.0, 5.6$  mm), relatively narrow distributions were maintained. By contrast, the pdf at  $U_j = 16.5$  m/s (Fig. 7b) showed distinct behavior, resulting from more continuous flame extinction. The pdf peak near room temperature was observed on the air side of the flame zone ( $r = 8.9, 7.9$  mm). Bimodal distributions were observed in the close proximity to the flame zone ( $r = 7.4, 6.9$  mm). The pdf was distributed over a wide range (including room temperature) even on the fuel side of the flame zone ( $r = 6.5, 6.1, 5.7$  mm). Thus, cold air evidently passed through the quenched zone, being engulfed in the large-scale vortex in the intermittent mixing layer.

Figure 8 shows the effect of the mean jet velocity on the radial locations of three different intermittency values ( $\bar{I} = 0.1, 0.5, 0.9$ ) and the visible flame zone (Fig. 8a) and the mean and rms temperatures in the flame zone (Fig. 8b). The burner rim location is also included in Fig. 8a. As the mean jet velocity was increased, the intermittent mixing layer spread outward (see  $\bar{I} = 0.1$  in Fig. 8a), whereas the visible flame zone shifted inward. The apparent visible flame thickness increased slightly, probably because of flame wrinkling or transient radial movement which were the result of increased interaction with the large vortex rather than broadening of the reaction zone itself. The (time-averaged) thickness of the fuel transport layer, defined as the radial distance between a constant intermittency curve (e.g.,  $\bar{I} = 0.5$ ) and the center of the flame zone, decreased slightly. Thus, the characteristic diffusion time decreased. The  $\bar{I} = 0.1$  curve merged with the inner edge of the visible flame zone at  $U_j \sim 15$  m/s, at which point the local extinction was first noticed. As the mean jet velocity was increased further, the degree of local extinction in terms of area size and frequency increased, and the apparent visible flame zone eventually faded out at the lifting limit ( $U_j = 16.5$  to  $17$  m/s).

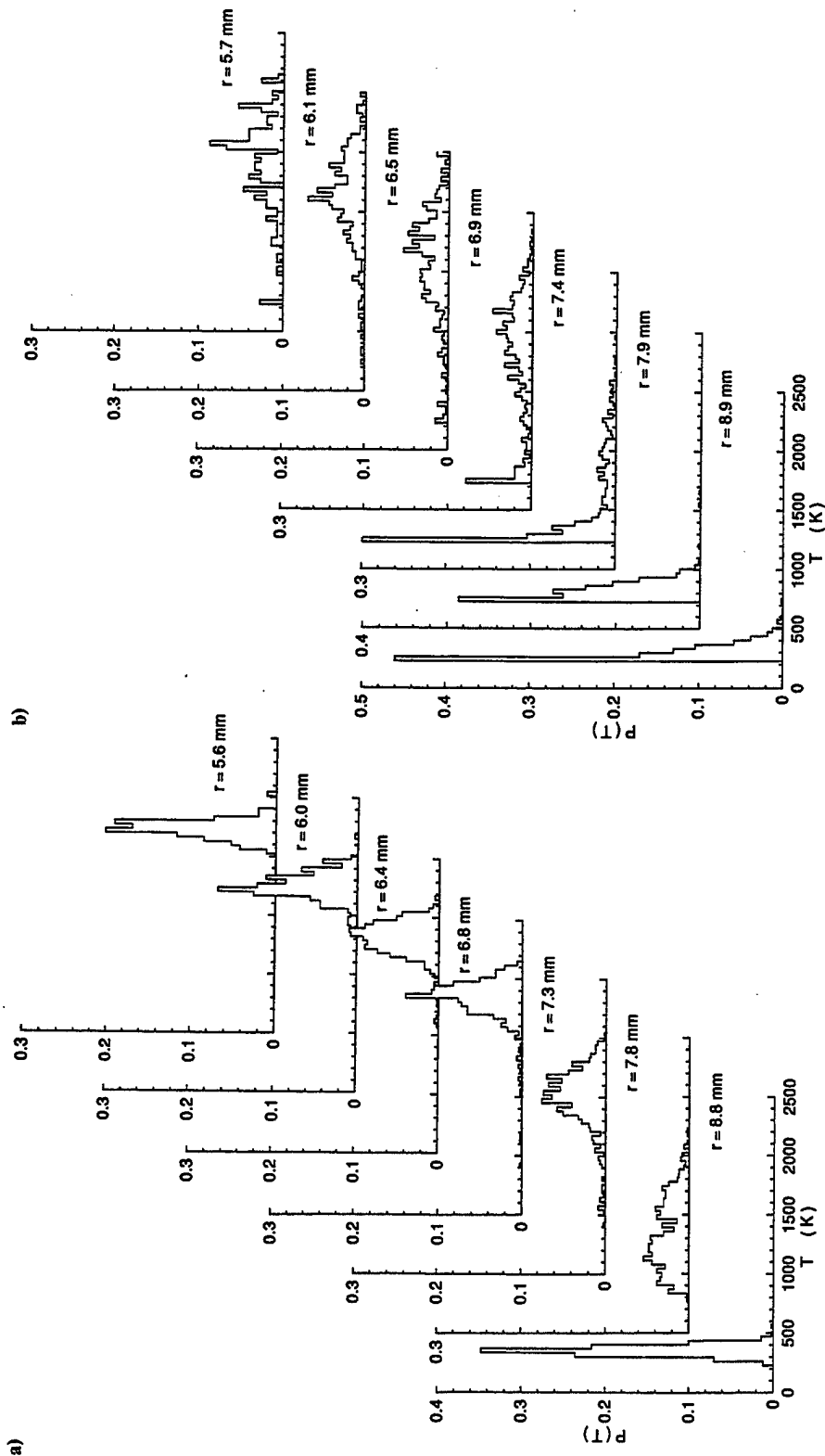


Fig. 7 Probability density functions (histograms) of the measured temperature.  $U_a = 3$  m/s,  $z = 15$  mm. a)  $U_j = 15$  m/s. b)  $U_j = 16.5$  m/s.

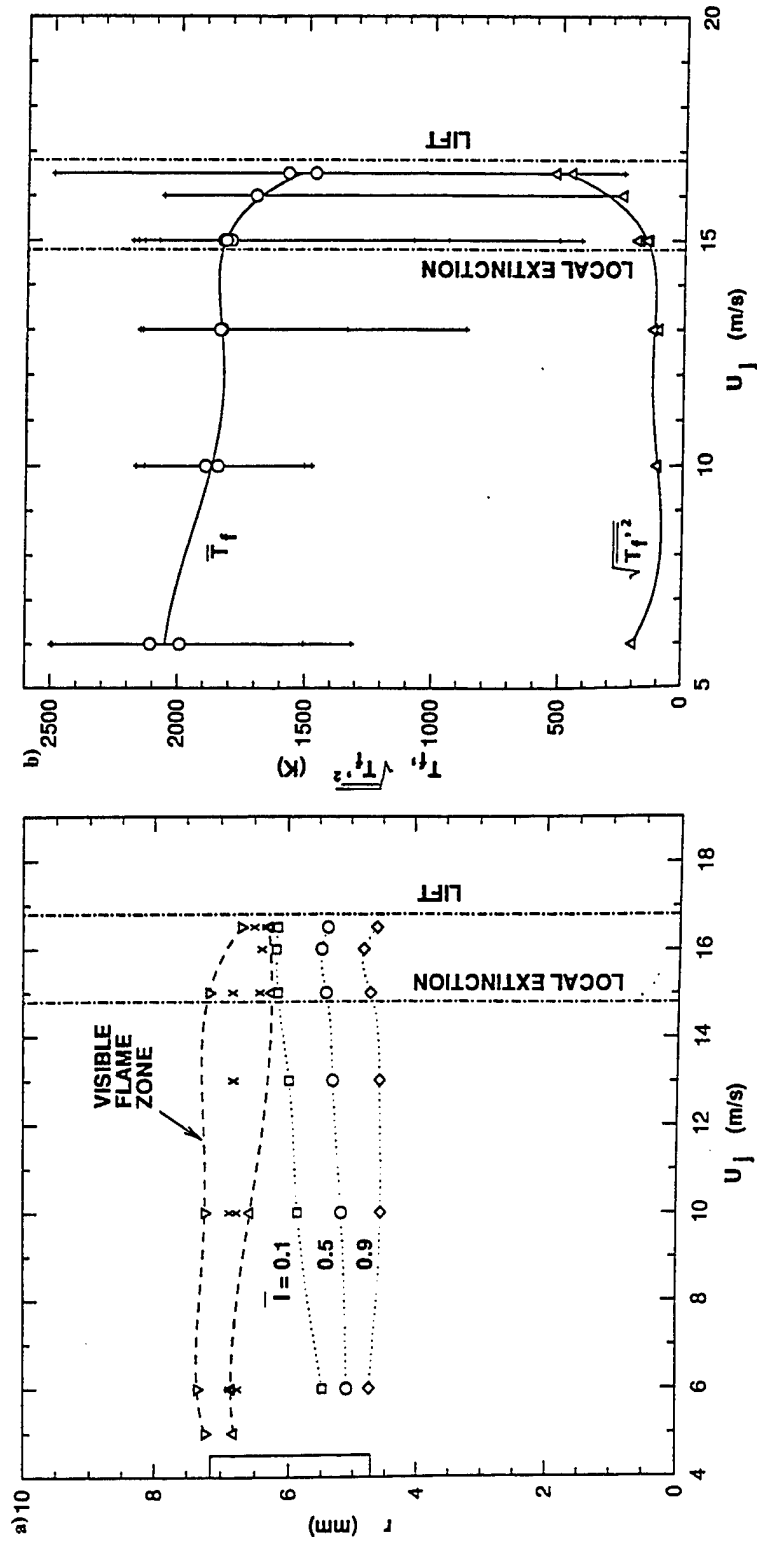


Fig. 8 The effect of the mean jet velocity on the flame structure.  $U_a = 3$  m/s,  $z = 15$  mm. a) Radial locations of the visible flame zone, peak temperature, and three intermittency values. b) Mean and rms temperatures in the flame zone.



## LOCAL EXTINCTION OF DIFFUSION FLAMES

Figure 8b shows the variations in the mean and rms temperatures in the flame zone (at radial locations shown by cross points in Fig. 8a). The error bar shows the minimum and maximum temperatures in a data set at a fixed  $U_j$ . As the mean jet velocity was increased, the peak (mean) temperature in the flame zone ( $\bar{T}_f$ ) decreased in the low velocity range ( $6 < U_j < 10$  m/s) – the range in which the flame zone was pushed into the outer boundary region of the intermittent mixing layer by increased entrainment flow velocity. The peak (mean) temperature remained constant in the range of  $10 < U_j < 15$  m/s. It decreased again when local extinction started at  $U_j \sim 15$  m/s, allowing cold air to be entrained into the intermittent mixing layer through the quenched region. As a result, the rms fluctuation increased from  $\sim 150$  K to  $\sim 500$  K.

### Local Extinction Mechanism

With the assistance of the results obtained previously by means of the laser-Doppler velocimetry and the real-time Mie scattering techniques<sup>11</sup> together with the results presented in this paper, the interactions between the large-scale vortex structure and the flame zone, leading to local extinction, are illustrated in Figure 9. The large-scale vortex train, consisting of nearly pure

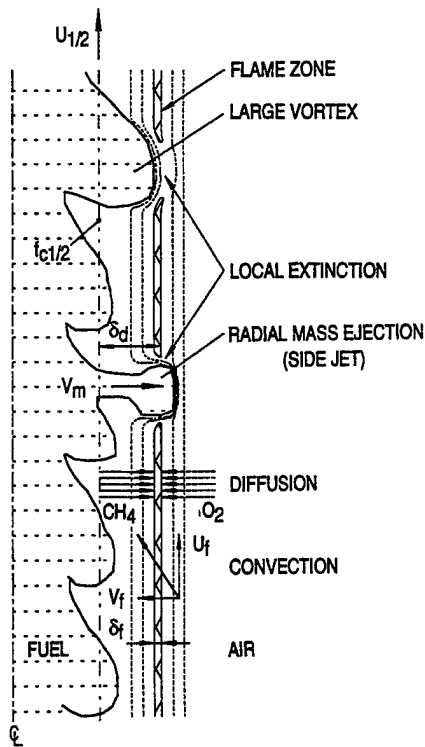


Fig. 9 Schematic illustration of the vortex-flame interactions in the near field of turbulent methane jet diffusion flames.

fuel, moves in the axial direction at a relatively high speed ( $U_{1/2} \sim 9.1$  m/s)<sup>11</sup> in the core region. The fuel molecules diffuse outward against the incoming external-fluid convection crossing the flame zone. The diffusion flame zone is formed where the mass fluxes of the fuel and oxygen are in stoichiometric proportion. As the local extinction limit is approached, the radial velocity component of the incoming external-fluid flow and, in turn, the convection contribution to the oxygen mass flux increase. As a result, the flame zone in the near-jet region ( $z < 60$  mm) shifts inward to a location where higher fuel mass flux can be obtained by diffusion to balance with the increased oxygen mass flux. Thus, the transport (diffusion and thermal) layer becomes thinner. The flame zone is thereby strained and loses its radial mobility. The LDV and real-time Mie scattering measurements<sup>11</sup> provided the velocity and time-scale information on the large-scale vortex structure, thus enabling order-of-magnitude comparisons to be made between some characteristic times under the near-limit condition.

The characteristic diffusion time of the fuel from the jet-fluid core to the flame zone ( $\tau_d$ ) is estimated as<sup>11</sup>

$$\tau_d = (\delta_d)^2 / D \sim 30 \text{ ms} \quad (1)$$

based on the diffusion coefficient of methane at 1500 K ( $0.7 \text{ cm}^2/\text{s}$ ) and the transport layer thickness ( $\delta_d = 1.5$  mm). The residence time ( $\tau_r$ ) of the incoming external fluid in the flame zone is estimated as

$$\tau_r = \delta_f / |V_f| \sim 2 \text{ ms} \quad (2)$$

based on the apparent visible flame zone thickness ( $\delta_f \sim 1$  mm; Fig. 5b)<sup>†</sup> and the radial velocity component of the flow crossing the flame zone ( $V_f \sim -0.5$  m/s at  $U_j = 15$  m/s).<sup>11</sup> Unfortunately, information on the species concentrations is not available, and the assessment of the chemical reaction time ( $\tau_c$ ) cannot be made directly. However, for a stable flame zone for which the influence of the large vortex is absent, the chemical reactions must be completed within the residence time in the flame zone. Thus,  $\tau_c < \tau_r$ . Therefore, the second Damköhler number<sup>18</sup> (i.e., the ratio of a characteristic diffusion time to a characteristic chemical reaction time) is more than unity,

<sup>†</sup> In laminar diffusion flames, in general, the reaction zone where the heat-release rate is positive is broadened over several times the visible flame zone thickness.<sup>15-17</sup> Further, the apparent visible flame zone determined here may be interpreted as an envelope of the thinner wrinkled laminar flame. Thus, the assessment for the residence time in the flame zone is ambiguous, but it must not make an order-of-magnitude difference.

## LOCAL EXTINCTION OF DIFFUSION FLAMES

perhaps the order of ten. The chemical reaction rate is fast compared to the rate-determining fuel transport rate by diffusion. Thus, without the vortex influence, the flame zone must be stable compared to the critical condition for stretch-induced extinction.

The fuel concentration fluctuation time (convection time) due to the large vortex structure in the jet-fluid core ( $\tau_l$ ) is estimated as<sup>11</sup>

$$\tau_l = 1/f_{l/2} \sim 0.8 \text{ ms} \quad (3)$$

based on the measured crossing frequency ( $f_{l/2} = 1330 \text{ Hz}$  at  $U_j = 15 \text{ m/s}$ ),<sup>11</sup> i.e., the number of crossings from jet to external fluid per unit time. The fuel concentration fluctuation time (convection time) due to sporadic radial mass ejection (side jet) from the jet-fluid core ( $\tau_m$ ) is estimated as<sup>11</sup>

$$\tau_m = \delta_d/V_m \sim 0.2 \text{ ms} \quad (4)$$

based on the maximum radial velocity ( $V_m \sim 6.6 \text{ m/s}$ )<sup>11</sup> and the same transport layer thickness. Therefore, the Pecret number for mass diffusion<sup>18</sup> (i.e., the ratio of a characteristic diffusion time to a characteristic convection time) is more than the order of ten or even a hundred. The diffusion process requires, at least, an order-of-magnitude longer time than the convective motion of either large vortices or more rapid radial mass ejection. Thus, time is not available to re-establish the mass-flux field in response to the fuel-concentration variations in the core region caused by rapid convective motion. Therefore, the mass-flux field in the vicinity of the flame zone is relatively insensitive to the movement of the inner vortices; consequently, the flame zone location eventually remains stationary. As a result, the unmixed fuel packets conveyed by the large-scale vortex or radial mass ejection can reach the flame zone location by replacing the gases on the way through the flame zone without causing significant disturbances in the adjacent mass-flux field. Consequently, the diffusion flame is locally quenched as the gas in a stoichiometric mass-flux balance is simply replaced with the unmixed fuel packet. This cause of extinction is apparently different from the stretch-induced extinction that occurs in a more gradual manner. The local extinction phenomenon reported in this paper must be categorized in a different regime.

## Conclusions

The CARS thermometry measurement, together with the real-time Mie scattering and LDV measurements made previously, in the near-jet region of turbulent methane jet diffusion flames provide physical insight into the dynamic vortex-flame interactions which lead to local extinction and

subsequent flame lifting. The diffusion process needs at least an order-of-magnitude longer time compared to convection times due to the large-scale vortices in the jet-fluid core and radial mass ejection (side jets) from the core. As a result, the flame is insensitive to the high-frequency fluctuation of the fuel concentration in the core, and the unmixed fuel packets can reach the flame zone location without causing significant disturbances in the species mass-flux field, thereby locally quenching the flame zone. Thus, local flame extinction near the breakpoint occurs primarily because of physical processes rather than the turbulence-chemistry interactions although the finite-rate chemistry must play a role in the final stage of the extinction process. A proper assessment of characteristic time scales is necessary — even in a more intense turbulent combustion field in which the turbulence-chemistry interactions become evident.

#### Acknowledgment

This work was supported by the U.S. Air Force, Wright Laboratory, Aero Propulsion and Power Directorate, Wright-Patterson Air Force Base, Ohio, under Contract No. F33615-92-C-2207 (Technical Monitor: C. W. Frayne). The authors would like to thank Drs. W. M. Roquemore and D. R. Ballal for their support and helpful comments, Dr. S. P. Heneghan for his suggestions on the CARS measurement, Dr. L. P. Goss for his assistance in the flow visualization experiment, and to Mr. F. W. Timko for his assistance in the design of the apparatus.

#### References

- <sup>1</sup>Takahashi, F. and Schmoll, W. J., "Lifting Criteria of Jet Diffusion Flames," *Twenty-Third Symposium (International) on Combustion*, The Combustion Institute, Pittsburgh, 1991, pp. 677-683.
- <sup>2</sup>Hattori, H., "Stability of Diffusion Flame," *Transactions of the JSME*, Vol. 30, 1964, pp. 320-332.
- <sup>3</sup>Vranos, A., Taback, E. D., and Shipman, C. W., "An Experimental Study of the Stability of Hydrogen-Air Diffusion Flames," *Combustion and Flame*, Vol. 12, 1968, pp. 253-260.
- <sup>4</sup>Takeno, T. and Kotani, Y., "An Experimental Study on the Stability of Jet Diffusion Flames," *Acta Astronautica*, Vol. 2, 1975, pp. 999-1008.
- <sup>5</sup>Hall, L., Horch, K., and Günther, R., "Die Stabilität von Freistrahldiffusionsflammen," *Brennst. Wärme Kraft*, Vol. 32, 1980, pp. 26-31.
- <sup>6</sup>Takahashi, F., Mizomoto, M., Ikai, S., and Tsuruyama, K., "Stability Limits of Hydrogen/Air Coflow Jet Diffusion Flames," AIAA Paper 90-0034, January 1990.
- <sup>7</sup>Shekarchi, S., Savas, Ö., and Gollahalli, S. R., "Structure of a Split Flame," *Combustion and Flame*, Vol. 73, 1988, pp. 221-232.
- <sup>8</sup>Eickhoff, H., Lenze, B., and Leuckel, W., "Experimental Investigation on the Stabilization Mechanism of Jet Diffusion Flames," *Twentieth Symposium (International) on Combustion*, The Combustion Institute, Pittsburgh, 1985, pp. 311-318.

## LOCAL EXTINCTION OF DIFFUSION FLAMES

<sup>9</sup>Chen, T. H., and Goss, L. P., "Flame Lifting and Flame/Flow Interactions of Jet Diffusion Flames," AIAA Paper 89-0156, January 1989.

<sup>10</sup>Coats, C. M. and Zhao, H., "Transition and Stability of Turbulent Jet Diffusion Flames," *Twenty-Second Symposium (International) on Combustion*, The Combustion Institute, Pittsburgh, 1989, pp. 685-692.

<sup>11</sup>Takahashi, F. and Goss, L. P., "Near-Field Turbulent Structures and the Local Extinction of Jet Diffusion Flames," *Twenty-Fourth Symposium (International) on Combustion*, The Combustion Institute, Pittsburgh, 1992, pp. 351-359.

<sup>12</sup>Goss, L. P., Trump, D. D., Lynn, W. F., Chen, T. H., Schmoll, W. J., and Roquemore, W. M., "Second-Generation Combined CARS-LDV Instrument for Simultaneous Temperature and Velocity Measurements in Combusting Flows," *Review of Scientific Instruments*, Vol. 60, 1989, pp. 638-645.

<sup>13</sup>Eckbreath, A. C., "Laser Diagnostics for Combustion Temperature and Species," Abacus Press, Cambridge, 1988, p.249.

<sup>14</sup>Roquemore, W. M., Chen, L. -D., Goss, L. P., and Lynn, W.F., "The Structure of Jet Diffusion Flames," *Turbulent Reactive Flows*, R. Borghi and S. N. B. Murthy (eds.), Springer-Verlag, New York, 1989, pp. 49-63.

<sup>15</sup>Pandya, T. P. and Weinberg, F. J., "The Structure of Flat, Counterflow Diffusion Flames," *Proceedings of the Royal Society*, Ser. A, Vol. 279, 1964, pp. 544-561.

<sup>16</sup>Tsuji, H. and Yamaoka, I., "Structure Analysis of Counterflow Diffusion Flames in Forward Stagnation Region of a Porous Cylinder," *Thirteenth Symposium (International) on Combustion*, The Combustion Institute, Pittsburgh, 1971, pp. 273-231.

<sup>17</sup>Kawamura, T., Asato, K., and Mazaki, T., "Structure Analysis of the Stabilizing Region of Plane, Laminar Fuel-Jet Flames," *Combustion Science and Technology*, Vol. 22, 1980, pp. 211-216.

<sup>18</sup>Strehlow, R. A., "Combustion Fundamentals," McGraw-Hill, New York, 1984, p. 120.

## **APPENDIX E**

### **Unsteady Extinction Mechanisms of Diffusion Flames**

**Fumiaki Takahashi, Viswanath R. Katta**

## UNSTEADY EXTINCTION MECHANISMS OF DIFFUSION FLAMES

FUMIAKI TAKAHASHI

*University of Dayton  
Research Institute  
300 College Park  
Dayton, Ohio 45469, USA*

VISWANATH R. KATTA

*Innovative Scientific Solutions, Inc.  
3845 Woodhurst Court  
Dayton, Ohio 45430, USA*

Unsteady chemical kinetic effects on the dynamics of local extinction of laminar methane jet diffusion flames have been studied by direct numerical simulations in which an artificial vortex issues radially from either fuel-jet core or ambient air toward the flame zone. The simulations were motivated by experimental observations of naturally forming internal and external shear-generated vortices that interfere with the flame zone. A time-dependent, axisymmetric, implicit, third-order accurate numerical model is used with variable transport properties and a semidetailed chemical kinetic model. A packet of fluid (with a local composition) is ejected outward or inward as a single-pulsed side jet at a given ejection velocity and period. A vortex system with a pair of counterrotating toroidal vortex rings is formed and penetrated into the high-temperature viscous layer. The unsteady vortex-flame interaction is divided into three sequential and overlapping regimes based on the controlling processes: diffusion, convection, and chemical kinetics. In the first two physical interaction regimes, the reaction and heat-release rates increase because of increased reactant fluxes by diffusion and convection. The detailed mechanisms of the final chemical-kinetic-controlled regime depend on whether the vortex is ejected from the fuel side or air side. The local extinction by the outward fuel-side vortex is largely attributable to excess fluxes of methane and methyl radicals, which scavenge a radical pool (OH, H, and O), thereby terminating chain reactions. The inward air-side vortex induces an excess oxygen flux primarily by convection, thereby accelerating the reactant leakage through the reaction zone and the temperature decrease.

### Introduction

Extinction of diffusion flames has long been studied predominantly in steady laminar counterflow diffusion flames [1,2] since a pioneering work by Tsuji and Yamaoka [3]. Stretch-induced flame extinction occurs as a result of reduced Damköhler number (i.e., the ratio of a characteristic flow [or diffusion] time to reaction time) and subsequent decrease in the flame temperature and reaction rates. Although the phenomenon is well understood in a global sense for its simple chemistry and flow configurations, various aspects of the subject need further investigation. The laminar flamelet model [4] assumes that turbulent diffusion flames are composed of ensembles of wrinkled, moving, laminar diffusion flame sheets and that sufficiently high strain rates (velocity gradients) cause local flamelet extinctions. Hence, questions arise as to how the structure of the laminar flamelets changes in response to local turbulent motions and whether the results obtained in steady (and

stationary) counterflow diffusion flames are applicable to such flamelet extinction. Complexities in practical turbulent flames stem from three-dimensional, transient, turbulence-flame interactions including the effects of strain rate, unsteadiness, flame curvature, and chemical kinetics. Although some of these effects on diffusion flame extinction have received increased attention in recent years [5-9], little is known about unsteady chemical kinetic effects on the interactions between vortices and flame zone that eventually lead to local extinction.

As the fuel jet velocity is increased in a jet diffusion flame, local extinction occurs near the laminar-to-turbulent flame transition point as a result of vortex-flame interactions [10-14]. A series of recent experiments [15-18] in methane jet diffusion flames using a variety of laser diagnostic techniques revealed that local extinction occurred in two stages: physical and chemical interactions. The physical interaction is caused mainly by convective motions; that is, the internal large-scale vortex rapidly reaches

# LAMINAR DIFFUSION FLAMES

TABLE 1  
Test conditions

Case No.	$U_j$ (m/s)	$U_a$ (m/s)	$V_s$ (m/s)	$t_s$ (ms)	$Pe$
1	1.5	1.5	7	0.5	100
2	1.5	1.5	14	0.5	220
3	15	3	20	0.06	260
4	15	3	-4	0.06	140

the flame zone location or the external vortex accelerates the entrainment flow passing through the flame zone [18]. The chemical interaction in the final stage is speculated [16] to be coupled with an excess fuel diffusion process but is largely unknown due to lack of knowledge of temporal variations in the concentrations of species, particularly radicals.

Recent development of numerical codes for studying various aspects of transient behaviors of flames [19-21] has enabled us to simulate more challenging numerical experiments with sufficiently high accuracy. The physical aspect of vortex-flame interactions were studied previously [22] by assuming infinitely fast one-step chemical kinetics and unity Lewis number. An attempt was made to simulate the transient response of a laminar flame zone to an artificial vortex that issues from a side jet. Although the fluid dynamic and transport phenomena of vortex-flame interactions have been simulated successfully, the fast chemistry model prohibited further investigation of the chemical aspect of local extinction phenomena. A semidetained chemical kinetic model for methane combustion has recently been incorporated into the code and validated [23] using the experimental results of counterflow diffusion flames [8]. In this work, the first numerical experiments were conducted on the local extinction of diffusion flames caused by an artificial vortex that issues from the fuel-jet core or ambient air. The primary objectives of this study are (1) to reveal physical and chemical aspects of local extinction caused by vortex-flame interactions (particularly the effects of unsteadiness and chemical kinetics in nonstationary flames) and (2) to contribute to a better understanding and further development of laminar flamelet models for turbulent diffusion flames.

## Numerical Models

Time-dependent governing equations, expressed in cylindrical coordinates, consist of mass continuity, axial and radial momentum conservation, energy conservation, and species conservation equations with the equation of state [20]. A body-force term

caused by the gravitational field is included in the axial momentum equation. A semidetained chemical kinetic model [24], including 52 elementary steps for 17 species ( $\text{CH}_4$ ,  $\text{O}_2$ ,  $\text{CH}_3$ ,  $\text{CH}_2$ ,  $\text{CH}$ ,  $\text{CH}_2\text{O}$ ,  $\text{CHO}$ ,  $\text{CO}_2$ ,  $\text{CO}$ ,  $\text{H}_2$ ,  $\text{H}$ ,  $\text{O}$ ,  $\text{OH}$ ,  $\text{H}_2\text{O}$ ,  $\text{HO}_2$ ,  $\text{H}_2\text{O}_2$ , and  $\text{N}_2$ ), is used to describe  $\text{CH}_4$ - $\text{O}_2$  combustion. Thermophysical and transport properties are considered to vary with temperature and species concentrations. Enthalpy of each species is calculated from polynomial curve fits, while the viscosity of the individual species is estimated from Chapman-Enskog collision theory [25]. The binary diffusion coefficient between any two species is estimated by the Chapman-Enskog theory and the Lennard-Jones potentials [25], and the effective diffusion coefficient of each species in the mixture is calculated.

The finite-difference form of the governing equations is constructed on a staggered grid system based on an implicit QUICKEST numerical scheme. It is third-order accurate in both space and time and has a very low numerical diffusion error. At every time step, the pressure field is accurately calculated by simultaneously solving the system of algebraic pressure Poisson equations. The computational domain of  $150 \times 60$  mm in axial ( $z$ ) and radial ( $r$ ) directions, respectively, is represented by a mesh system of  $241 \times 71$ . The inner diameter of the fuel tube ( $d = 9.6$  mm) is close to that used in the experiments [15]. Grid lines are clustered near the burner lip and side jet locations. The initial and boundary conditions for the axial and radial velocities and species and energy at different flow boundaries are similar to the previous work [22] except for the increased number of species in the present calculations.

The test cases reported in this paper are listed in Table 1. Cases 1 and 2 represent a laminar jet diffusion flame with low velocities of the primary jet ( $U_j$ ) and annulus air ( $U_a$ ). At the grid points within the side jet, the radial component of the local velocity is replaced by  $V_s$  and the scalar variables are maintained at the local values for a time period  $t_s$ . The primary jet has a parabolic velocity distribution, representing the fully developed laminar pipe flow. The radial location of the side jet ( $r_s = d/2$ ) is nearly coincident with a dividing streamline between the jet and external fluids, and the height of the side jet is  $z = 14.2 \sim 16.5$  mm. Case 3 represents a flame with higher jet velocities in consideration of a naturally forming radial mass ejection observed in turbulent flames [12,15,16]. Case 4 represents a condition in which a vortex is ejected inward from outside the flame ( $V_s < 0$ ). For cases 3 and 4, the velocity distribution of the primary jet is given by using the empirical equation of the  $1/n$ th power law [26] for the fully developed turbulent pipe flow with the exponent  $n = 6$  for a moderate Reynolds number (although the simulation considers laminar flows only).



# UNSTEADY EXTINCTION MECHANISMS OF DIFFUSION FLAMES

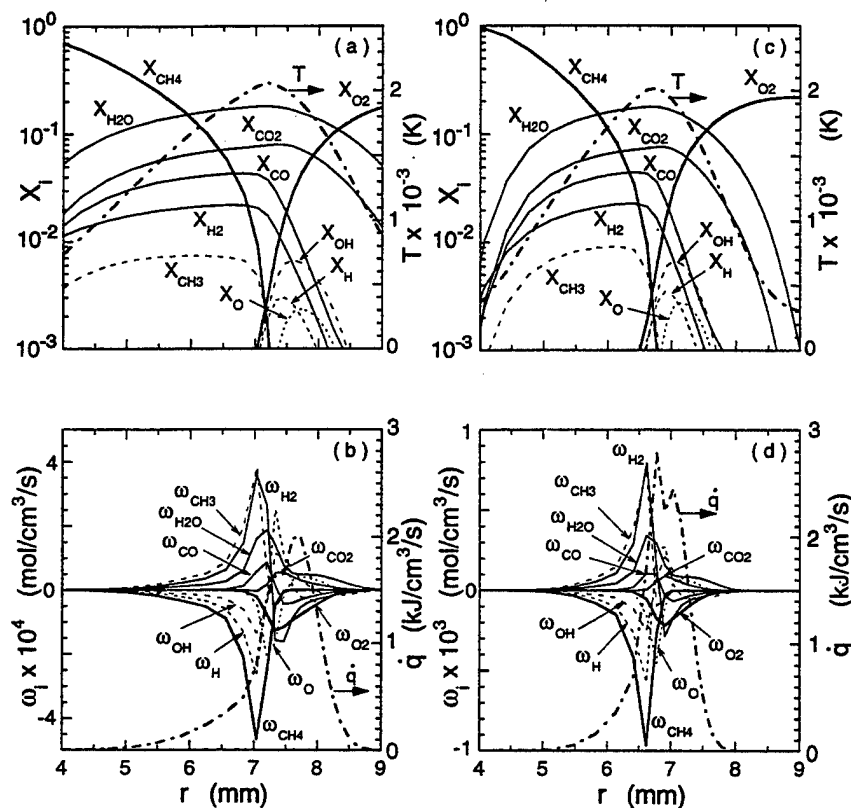


FIG. 1. Calculated temperature, mole fractions, molar production rates, and heat-release rate across a steady-state methane jet diffusion flame ( $t = 0$  s); (a)(b) case 2,  $z = 18.5$  mm; (c)(d) case 3,  $z = 16$  mm.

A Peclet number for mass transfer related to the side jet ejection defined previously [22] is

$$Pe = \tau_d / \tau_m = \delta_d V_m / D \quad (1)$$

where  $\tau_d$  is the characteristic diffusion time,  $\tau_m$  is the characteristic convection time for vortex motion,  $\delta_d$  is the diffusive transport layer thickness,  $V_m$  is the radial mass ejection velocity, and  $D$  is the diffusion coefficient. The values of  $Pe$  determined by substituting  $(r_f - r_s)$  at  $t = 0$  for  $\delta_d$  ( $r_f$  is the radial flame location) and  $V_s$  for  $V_m$  are listed in Table 1.

## Results and Discussion

A steady-state solution for the diffusion flame structure without a side jet was obtained first by numerous (typically several tens of thousands) iterative calculations using a long time step. By using the steady-state solution as the initial condition, the temporal changes in the flame structure in response to the side jet ejection were calculated using a short time step. Figure 1 shows the radial distributions of the gas temperature ( $T$ ), the mole fraction of species

$i$  ( $X_i$ ), the net rate of molar production of species  $i$  ( $\omega_i$ ), and the net rate of heat release ( $\dot{q}$ ) for steady-state solutions for the conditions of low velocities (case 2) and high velocities (case 3). In both cases, the flame structure is typical of laminar diffusion flames. The flame zone is formed on the air side of the dividing streamline ( $r \approx 4.8$  mm). The variations in the mole fractions of major and minor species (see Figs. 1a and 1c) show that the temperature peak coincides with the  $X_{H_2O}$  peak in the region where  $X_{CH_4}$  and  $X_{O_2}$  vanish. The  $X_{CH_3}$ ,  $X_{H_2}$ , and  $X_{CO}$  peaks are slightly on the fuel side, and the  $X_{CO_2}$ ,  $X_H$ ,  $X_{OH}$ , and  $X_O$  peaks are on the air side. On the fuel side, methane molecules diffuse radially based on its concentration gradient in the diffusion layer between the dividing streamline and the flame zone. In the high-temperature layer, methane decomposes to methyl radical by the fuel pyrolysis and dehydrogenation by radical species (OH and H) that produce  $H_2O$  and  $H_2$ , respectively (see Figs. 1b and 1d). On the air side, oxygen molecules diffuse inward based on its concentration gradient. Because the flame zone is inclined slightly outward downstream and the streamlines are almost parallel to the jet axis near

# LAMINAR DIFFUSION FLAMES

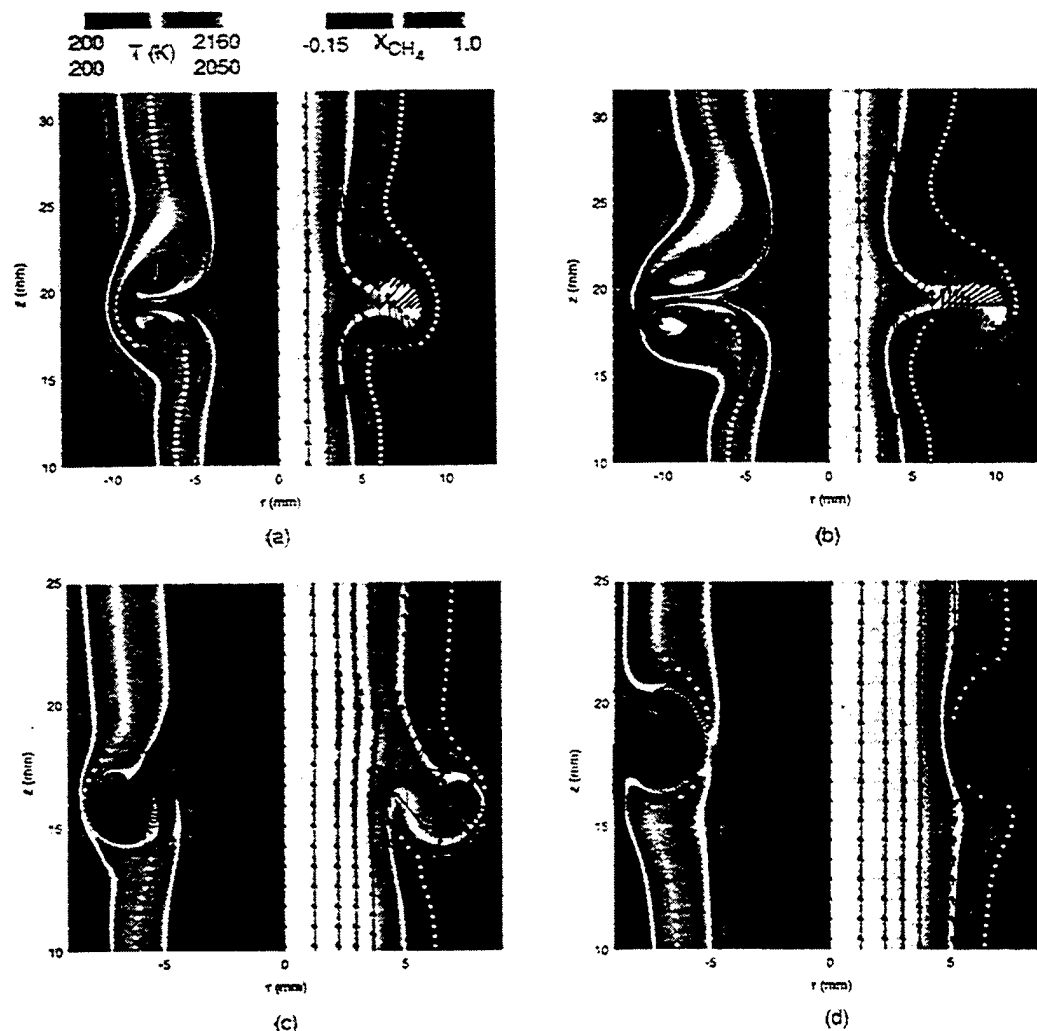


FIG. 2. Color-coded mapping of temperature field with injected particle image (left side), methane mole fraction field, and velocity vector field (right side) in a methane jet diffusion flame with a side jet; (a) case 1,  $t = 2.13$  ms; (b) case 2,  $t = 2.13$  ms; (c) case 3,  $t = 0.293$  ms; (d) case 4,  $t = 1.17$  ms. Temperature scale (maximum): (a)/(b) 2160 K, (c)/(d) 2050 K.

the flame zone, the external fluid passes through the flame zone with a narrow angle into the methane diffusion layer. Since the reaction rates are finite, oxygen can leak through the flame zone ( $X_{O_2} \neq 0$ ) and, thus, a convective transport contributes to the total oxygen influx. In the high-temperature layer on the air side, radical species (OH and O) are generated from  $O_2$  and  $H_2$  (Figs. 1b and 1d). Since a pool of radical species (OH, H, and O) is consumed by methane and methyl radicals on the fuel side, a major heat-release step of CO oxidation by OH radicals occurs mainly on the air side.

For the high-velocity condition (Figs. 1c and 1d), the peak temperature is lower (2010 K) than that

under the low-velocity condition (Figs. 1a and 1b; 2140 K), the high-temperature layer is thinner, and the leakage of reactants through the reaction zone is more evident as a result of finite-rate chemistry under a more strained condition.

Figure 2 shows color-coded mappings of the calculated gas temperature superimposed with locations of tracer particles (black dots) injected in front of the side jet (left-hand side) and the methane mole fraction superimposed with velocity vectors (right-hand side). The radial locations of the flame zone (yellow dots) determined by the temperature peak are also included in the figures. Notice that the elapsed time after ejection ( $t$ ) is an order of magni-

# UNSTEADY EXTINCTION MECHANISMS OF DIFFUSION FLAMES

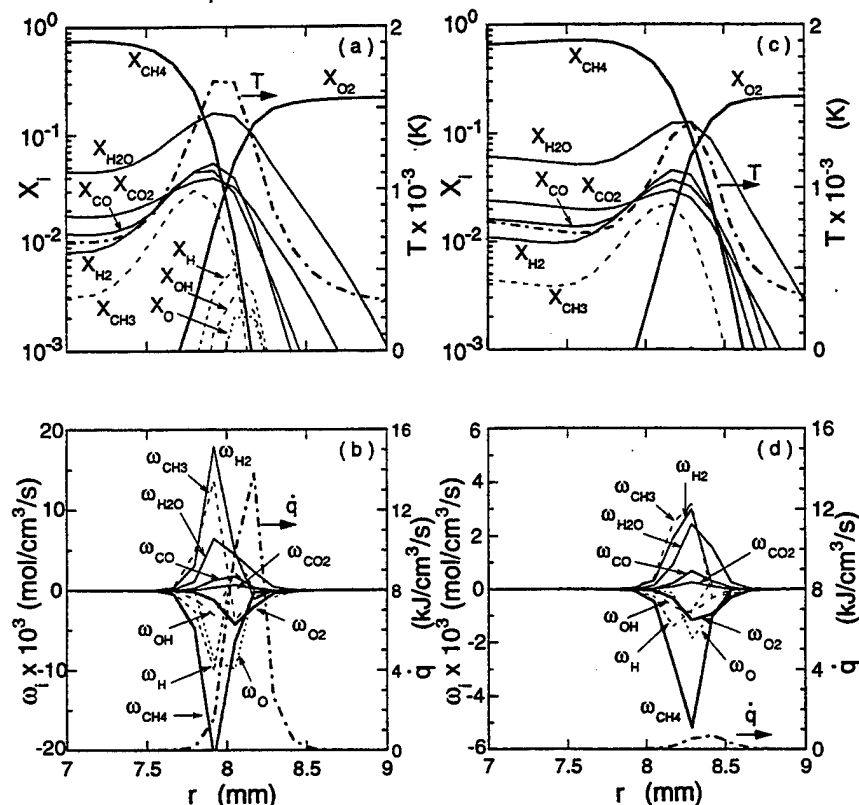


FIG. 3. Calculated temperature, mole fractions, molar production rates, and heat-release rate across a methane jet diffusion flame with a side jet; case 3,  $z = 16$  mm; (a)(b)  $t = 0.205$  ms; (c)(d)  $t = 0.264$  ms.

tude longer for cases 1 and 2 (Figs. 2a and 2b) than for case 3 (Fig. 2c). Despite the difference in the magnitude of side jet velocity and, in turn, the time scale of the process, the low- and high-velocity cases show the following common features in the flame structures, because the large-scale vortex formed dominates the global flow structure. As the side jet issues from the jet fluid core toward the flame surface, a sudden change in the radial-velocity distribution near the edges of the side jet induces the roll-up of the neighboring fluid and the subsequent formation of a vortex system, composed of a pair of counterrotating vortex rings. The vortex system grows as it engulfs surrounding gases and penetrates into a high-temperature (highly viscous) layer toward the flame zone. The vortex structure rotates as a whole naturally because of the uneven axial-velocity distribution in the shear layer, especially for case 3 because of its higher velocity gradient. The formation of the vortex structure with counterrotating vortex rings and the subsequent rigid-body rotation have also been observed experimentally [17].

For case 1 (Fig. 2a), the flame zone bulges out as the vortex system moves toward the flame. Conse-

quently, the thermal layer ahead of the vortex becomes significantly thin as the leading edge of the vortex (i.e., the outermost point of the injected particles) reaches the initial flame surface location. However, the vortex loses its radial momentum and drifts away downstream. By contrast, in case 2 (Fig. 2b), the vortex further pushes out the flame zone until local extinction occurs near the leading edge of the bulged flame zone. For case 3 (Fig. 2c), local extinction occurs as the vortex rapidly cuts through the thermal layer. Figure 2c shows large values of the methane mole fraction in the interior of the vortex system.

Figure 2d shows the results for the inwardly injected external vortex. Although the magnitude of the side jet velocity is small (4 m/s), local extinction occurs. Since the calculation is axisymmetric, the vortex may accelerate as its radial location decreases. Moreover, the jet fluid boundary does not deform as the vortex proceeds inward because methane flows at relatively high velocities inside the dividing streamline. Unlike the flame bulge observed in cases 1 and 2, the thermal layer cannot intrude into the

# LAMINAR DIFFUSION FLAMES

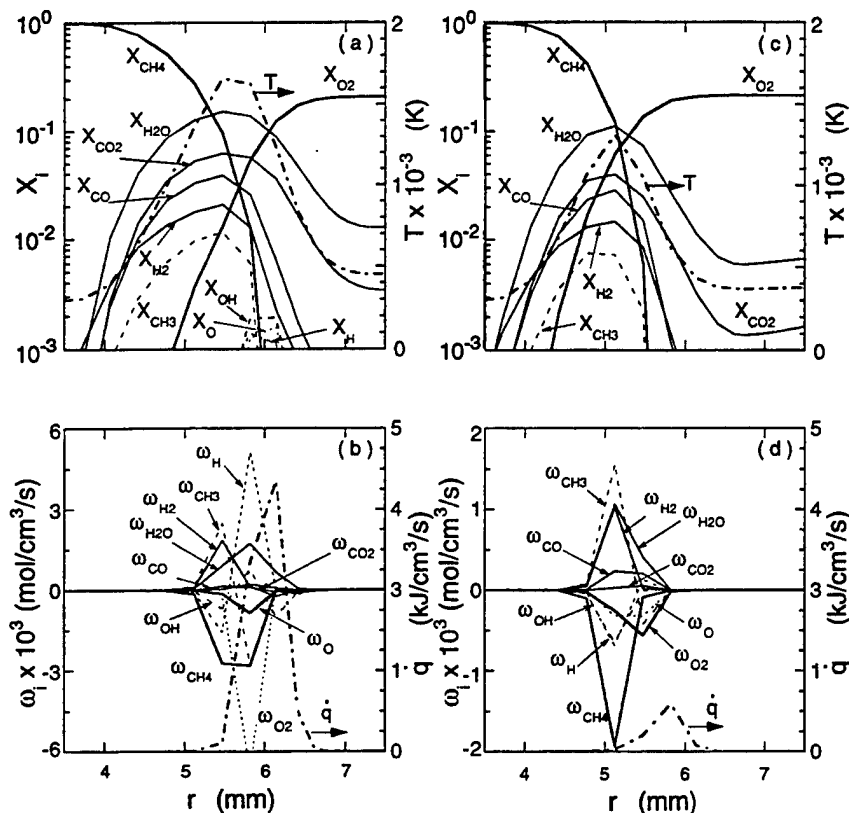


FIG. 4. Calculated temperature, mole fractions, molar production rates, and heat-release rate across a methane jet diffusion flame with a side jet; case 4,  $z = 18$  mm; (a)(b)  $t = 0.733$  ms; (c)(d)  $t = 1.026$  ms.

jet core; thus, the diffusive layer becomes very thin as the vortex approaches the jet fluid boundary.

Figure 3 shows the temporal changes in the structure of a methane flame with a side jet in case 3. The height chosen for the profile plots ( $z = 16$  mm) is nearly coincident with the height of the leading edge of the vortex near which local extinction occurs. At  $t = 0.205$  ms (Fig. 3a), the thermodiffusive layer near the flame zone becomes thin compared to the steady-state condition (Fig. 1c), the methyl radical concentration increases significantly, the peak temperature decreases to  $\sim 1700$  K, and the reactant leakage is more evident (overlapping at  $X_{CH_4} = X_{O_2} \approx 0.03$ ). As a result of a significant increase in the methane concentration gradient and, in turn, the methane flux in front of the leading edge of the vortex, the molar production rates and heat-release rate (Fig. 3b) increase by an order of magnitude compared to those before vortex ejection (Fig. 1d). As the wave of high methane concentration front proceeds outward (Figs. 3c and 3d), methane and methyl radicals scavenge and vanish the radical pool ( $X_{OH}$ ,  $X_H$ , and  $X_O$ ), which is critical for  $H_2$ - $O_2$  chain-branching reactions. The methane and oxygen leakage increases ( $X_{CH_4} = X_{O_2} \approx 0.07$ ), the peak tem-

perature decreases ( $\sim 1400$  K), and the heat release ceases. Thus, the combustion process can no longer be sustained under such conditions, thereby leading to extinction.

Figure 4 shows the results for the inward side jet ejection for case 4. Although the magnitude of the side jet ejection velocity is significantly smaller than that in case 3, the vortex-flame interaction and local extinction processes occur more gradually. There are similarities and distinct differences in the interaction phenomena between the inward and outward ejections. As the vortex pushes the flame zone inward (Fig. 4a), the reactant leakage increases and the peak temperature decreases as seen in the outward case. However, the methyl radical concentration does not increase much and the gradients of  $X_{CH_4}$  and  $X_{O_2}$  are significantly smaller (Figs. 4a and 4c), yet the oxygen penetrates deeper onto the fuel side compared to the outward ejection (Figs. 3a and 3c). Unlike the outward vortex motion toward ambient air, the inward motion is limited by the boundary of jet fluid that is flowing at high axial velocities, and thus, the vortex nearly cuts through the flame zone (Fig. 2d). At the final stage (Figs. 4c and 4d), the radical pool disappears and exothermic reactions stop.

# UNSTEADY EXTINCTION MECHANISMS OF DIFFUSION FLAMES

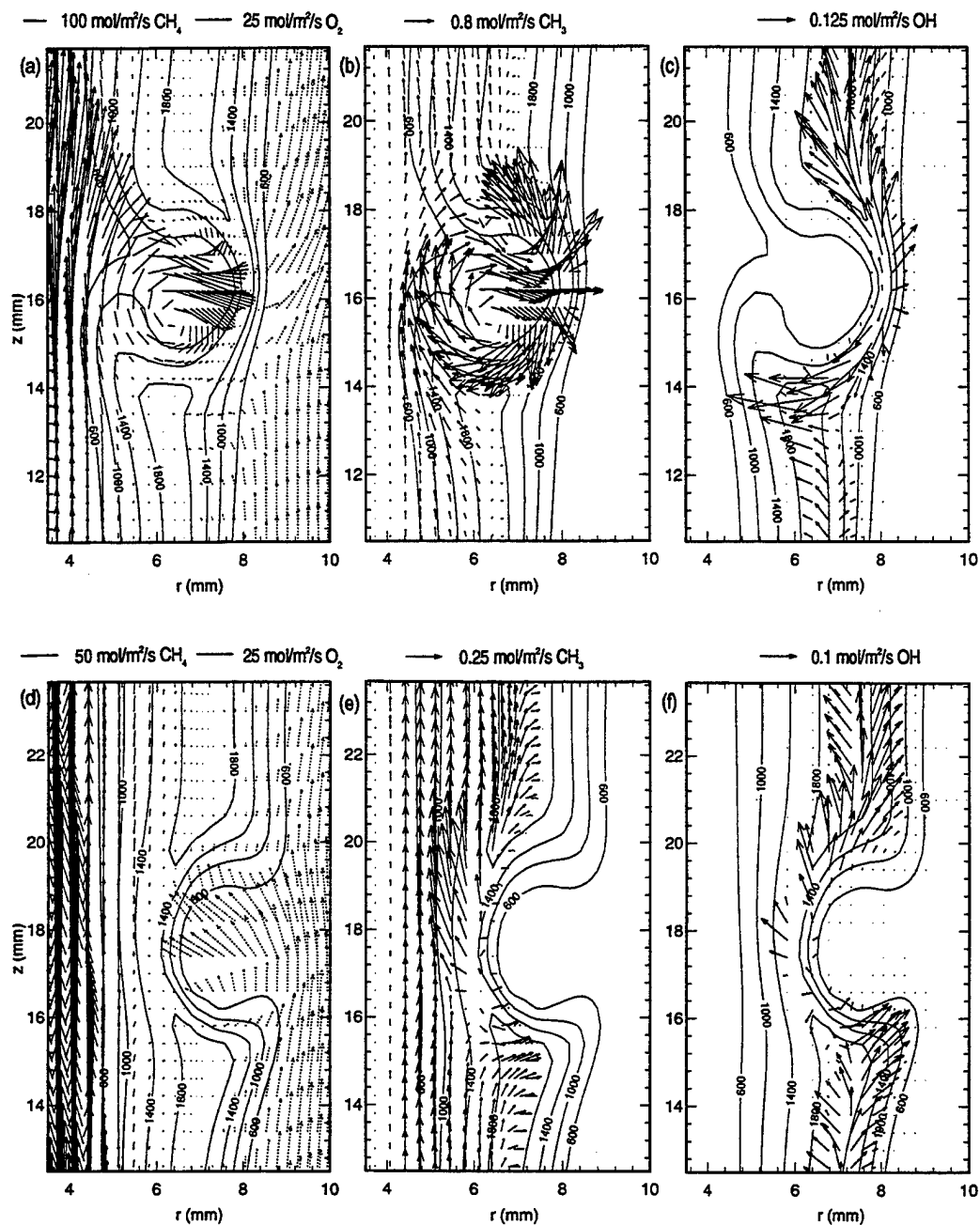


FIG. 5. Total molar flux fields of species in a methane jet diffusion flame with a side jet; (a)-(c) methane and oxygen, (b)(e) methyl radical, and (c)(f) hydroxyl radical; (a)-(c) case 3, (d)-(f) case 4.

Although the plots of the mole fractions and production rates show the flame structure in a static manner, the dynamic two-dimensional transport and kinetic phenomena need to be revealed by examining the species (and heat) flux vector fields. Figure

5 shows the total (diffusion plus convection) molar flux vector fields of selected species (methane, oxygen, methyl, and hydroxyl radicals), superimposed with the isotherms. In the case of outward ejection (Figs. 5a through 5c), significant fluxes of methane

# LAMINAR DIFFUSION FLAMES

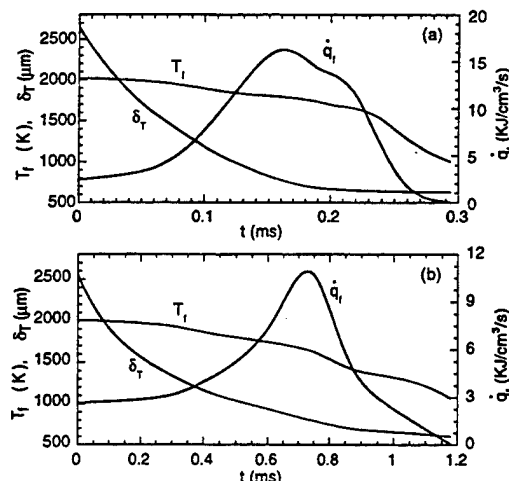


FIG. 6. Temporal variations in the peak temperature, full width at half peak temperature, and peak heat-release rate across a methane jet diffusion flame with a side jet at a height near extinction: (a) case 3, (b) case 4.

and methyl radical rush into the flame zone by both diffusion and convection. The flux of hydroxyl radicals, produced on the air side of the peak temperature and diffused both inward and outward in the steady-flame region, is small in the near-extinction flame zone as a result of scavenging by the methane and methyl radicals. In the case of inward ejection (Figs. 5d through 5f), the methane flux into the flame zone is an order of magnitude lower than that for the outward ejection, whereas the oxygen flux (mainly by convection) toward the flame zone is an order of magnitude larger. The methyl and hydroxyl radical fluxes even point inward from the near-extinction flame zone, showing distinctive differences compared to the outward ejection case. Thus, for the inward ejection, the oxygen leak through the reaction zone and the subsequent temperature decrease caused by reduced exothermic reactions play a significant role in local extinction.

Figure 6 shows the temporal variations in the peak temperature ( $T_f$ ), full width at half peak temperature ( $\delta_T$ ), and peak heat release rate ( $\dot{q}_f$ ) for the outward and inward ejection (cases 3 and 4). The heat-release-rate curves for both cases show two noticeable turning points ( $t \approx 0.06$  ms and  $t \approx 0.16$  ms for case 3;  $t \approx 0.3$  ms and  $t \approx 0.7$  ms for case 4). Thus, the unsteady vortex-flame interactions can be divided into three sequential and overlapping regimes based on the controlling processes: diffusion, convection, and chemical kinetics. In the early diffusion-controlled regime, the diffusion layer thickness (represented by  $\delta_T$ ) decreases rapidly as the vortex approaches the flame zone. The flame zone is more

strained, the reactant leakage through the reaction zone increases, and the flame temperature decreases. However, the reactant concentration gradients and, in turn, fluxes into the flame zone, increase, and the reaction and heat-release rates gradually increase. As the reactant leakage increases ( $X_{\text{CH}_4}$  and  $X_{\text{O}_2} \neq 0$  in the reaction zone), the convective contribution to the total reactant fluxes becomes significant. In the convection-controlled regime, the convective contribution to the reactant fluxes and, in turn, the reaction and heat-release rates increase more rapidly. However, because of the finite-rate chemistry, there is an upper limit to how much reactant can be consumed in the reaction zone. Thus, chemical kinetics begin to control the process. In the last chemical-kinetic-controlled regime, the rate of decrease in the diffusion layer thickness becomes small, while the peak temperature and the heat-release rate drop rapidly. The detailed chemical kinetic processes leading to extinction are different in the outward and inward ejection cases as described previously.

## Conclusions

A unique numerical experiment, in which a packet of fluid is ejected outward or inward toward a flame zone, illustrated essential physical and chemical aspects of unsteady vortex-flame interactions and local extinction of laminar methane jet diffusion flames. The unsteady vortex-flame interactions leading to extinction can be divided into three regimes depending on the dominant process: diffusion, convection, and chemical kinetics. The first two regimes are primarily physical vortex-flame interactions. During the physical interaction stage, if a Peclet number is sufficiently large (on the order of 100), the vortex system penetrates into the high-temperature (highly viscous) layer with a slight flame movement, thus rapidly thinning the thermodiffusive layer. The reactant leakage through the reaction zone increases, the flame temperature gradually decreases, and the heat-release rate increases by enhanced diffusion in the early regime and then by convection. In the final chemical kinetic regime for the outward vortex ejection, an excess influx of methane and methyl radicals scavenge radicals (OH, H, and O) and terminate exothermic oxidation reactions of intermediate species ( $\text{H}_2$  and CO). For the inward ejection, the convective contribution to the oxygen flux is responsible for the excessive reactant leakage, leading to extinction.

## Acknowledgments

This work was supported by the U.S. Air Force, Wright Laboratory, Aero Propulsion and Power Directorate, Fuels

## UNSTEADY EXTINCTION MECHANISMS OF DIFFUSION FLAMES

and Lubrication Division, Wright-Patterson Air Force Base, Ohio, under Contract No. F33615-92-C-2207 (Technical Monitor: C. W. Frayne).

### REFERENCES

1. Tsuji, H., *Prog. Energy Combust. Sci.* 8:93-119 (1982).
2. Law, C. K., *Prog. Energy Combust. Sci.* 10:295-318 (1984).
3. Tsuji, H. and Yamaoka, I., *Twelfth Symposium (International) on Combustion*, The Combustion Institute, Pittsburgh, 1966, pp. 979-984.
4. Williams, F. A., *Combustion Theory*, 2d ed., The Benjamin/Cummings, Menlo Park, CA, 1985, p. 408.
5. Tsuji, H., Yoshida, A., and Endo, N., *Twenty-Fifth Symposium (International) on Combustion*, The Combustion Institute, Pittsburgh, 1994, pp. 1191-1197.
6. Egolfopoulos, F. N., *Twenty-Fifth Symposium (International) on Combustion*, The Combustion Institute, Pittsburgh, 1994, pp. 1375-1381.
7. Im, H. G., Bechtold, J. K., and Law, C. K., *Combust. Sci. Technol.* 106:345 (1995).
8. Sung, C. J., Liu, J. B., and Law, C. K., *Combust. Flame* 102:481-492 (1995).
9. Cuenot, B. and Poinot, T., *Twenty-Fifth Symposium (International) on Combustion*, The Combustion Institute, Pittsburgh, 1994, pp. 1383-1390.
10. Takeno, T. and Kotani, Y., *Acta Astronaut.* 2:999 (1975).
11. Takahashi, F., Mizomoto, M., and Ikai, S., *Combust. Flame* 48:85 (1982).
12. Takahashi, F. and Schmoll, W. J., *Twenty-Third Symposium (International) on Combustion*, The Combustion Institute, Pittsburgh, 1991, p. 677.
13. Shekarchi, S., Savas, Ö., and Gollahalli, S. R., *Combust. Flame* 73:221 (1988).
14. Roquemore, W. M., Chen, L.-D., Goss, L. P., and Lynn, W. F., "The Structure of Jet Diffusion Flames," in *Turbulent Reactive Flows* (Borghi, R. and Murthy, S. N. B., Eds.), Springer Verlag, Berlin, 1993, p. 49.
15. Takahashi, F. and Goss, L. P., *Twenty-Fourth Symposium (International) on Combustion*, The Combustion Institute, Pittsburgh, 1992, pp. 351-359.
16. Takahashi, F. and Vangsness, M. D., "Near-Field CARS Measurements and the Local Extinction of Turbulent Jet Diffusion Flames," in *Dynamics of Heterogeneous Combustion and Reacting Systems*, (Kuhl, A. L., Leyer, J.-C., Borisov, A. A., and Sirignano, W. A., Eds.), American Institute of Aeronautics and Astronautics, Washington, D.C., 1993, p. 37.
17. Hsu, K. Y., Chen, L. D., Katta, V. R., Goss, L. P., and Roquemore, W. M., AIAA Paper No. 93-0455, 1993.
18. Takahashi, F., Schmoll, W. J., Trump, D. D., and Goss, L. P., AIAA Paper No. 95-0139, 1995.
19. Katta, V. R. and Roquemore, W. M., *Combust. Flame* 92:274 (1993).
20. Katta, V. R., Goss, L. P., and Roquemore, W. M., *AIAA J.* 32:84 (1994).
21. Katta, V. R., Goss, L. P., and Roquemore, W. M., *Combust. Flame* 96:60 (1994).
22. Takahashi, F. and Katta, V. R., *J. Propulsion Power* 11:170 (1995).
23. Katta, V. R. and Roquemore, W. M., "Extinction in Methane-Air Counterflow Diffusion Flames—A Direct Numerical Study," Central States Section/The Combustion Institute Meeting, St. Louis, May 1996.
24. Peters, N., "Flame Calculations with Reduced Mechanisms—An Outline," in *Reduced Kinetic Mechanisms for Applications in Combustion Systems* (Peters, N. and Rogg, Bernd, Eds.), Springer Verlag, Berlin, 1993, p. 3.
25. Hirschfelder, J. O., Curtis, C. F., and Bird, R. B., *The Molecular Theory of Gases and Liquids*, Wiley, New York, 1954.
26. Schlichting, H., *Boundary-Layer Theory* 7th ed., (Kestin, J., Trans.), McGraw Hill, New York, 1979, p. 599.

### COMMENTS

*Mitchell Smooke, Yale University, USA.* In your two-dimensional counterflow calculations, it was not clear what boundary conditions were employed in the radial direction. Could you comment on this?

Also, what conditions were imposed on the velocities (radial and axial) at the base of the two jets?

*Author's Reply.* The two-dimensional computer code used, including its chemistry model, has been validated [23] by simulating an axisymmetric counterflow diffusion flame prior to the present numerical experiment on the unsteady extinction of jet diffusion flames. In the two-dimensional counterflow flame calculations, weighted first- and second-order extrapolations were used for the outflow boundary conditions in the radial direction. In addition, to

reduce the influence of errors in the boundary conditions on the flame structure, the outflow boundary was located at 50 nozzle radii in the radial direction. An identical extrapolation scheme was used for the axial outflow boundary in the present jet diffusion flame calculations.

For the boundary conditions at the fuel and air jet nozzle exits in the counterflow diffusion flame calculations, flat axial and null radial velocity profiles (plug flow) were imposed.

*Habib N. Najm, Sandia National Laboratories, USA.* The plots of concentrations and production/consumption rates

## LAMINAR DIFFUSION FLAMES

in the reported flame-vortex interaction results show a very jagged representation of the flame structure. This suggests that the flame structure is not well resolved. Even though this implicit scheme is stable under these conditions, the results seem to suffer from excessive truncation error, and are therefore questionable. A grid refinement study should help resolve this issue.

*Author's Reply.* In the counterflow diffusion flame calculations [23] for the model validation, the flame structures under near-extinction conditions obtained with 0.2-mm and 0.04-mm spacing were found to be identical. The grid-independent results obtained with this code with reasonably coarse grids may be attributed to the implicit procedures used. Implicit schemes not only improve stability but also allow larger time and spatial steps without

loss of accuracy compared to those allowed by explicit schemes.

In the present jet flame calculations, a fixed mesh system with a varied grid spacing in the axial and radial directions was used. For the fuel-side vortex ejection, local extinction occurred when the flame zone was pushed radially outward into the grid zone where the grid spacing was 0.2 mm. Although the jagged profiles associated with the 0.2-mm grid spacing are shown in Fig. 3, we believe that the results have not suffered from any truncation error as demonstrated in the counterflow calculations. For the air-side vortex ejection, the flame zone moved into a zone where the grid spacing was 0.4 mm (Fig. 4). Although a finer grid spacing might be desirable for this case, the qualitative nature of the extinction mechanisms proposed should still be valid.



## **APPENDIX F**

### **Numerical Experiments on the Vortex-Flame Interactions in a Jet Diffusion Flame**

**Fumiaki Takahashi, Fiswanath R. Katta**

# **Numerical Experiments on the Vortex-Flame Interactions in a Jet Diffusion Flame**

**F. Takahashi and V. R. Katta**

Reprinted from

## **Journal of Propulsion and Power**

Volume 11, Number 1, Pages 170-177



*A publication of the*  
American Institute of Aeronautics and Astronautics, Inc.  
370 L'Enfant Promenade, SW  
Washington, DC 20024-2518

# Numerical Experiments on the Vortex-Flame Interactions in a Jet Diffusion Flame

Fumiaki Takahashi\*

University of Dayton, Dayton, Ohio 45469

and

Viswanath R. Katta†

Systems Research Laboratories, Inc., Dayton, Ohio 45440

Dynamic behavior of a laminar jet diffusion flame in response to an artificial vortex that issues radially from the fuel-jet core toward the flame zone has been studied numerically to illustrate essential physics of a naturally-forming shear layer vortex that has some radial velocity. A time-dependent, axisymmetric, implicit, third-order accurate numerical model is used with the infinitely-fast chemistry and unity Lewis number assumptions. A packet of fuel (methane) is ejected as a single-pulsed "side jet" at given initial and boundary conditions (the ejection velocity and period), which cover an order of magnitude in the time scale of the vortex-flame interaction. A vortex system with a pair of counter-rotating toroidal vortex rings is generated and penetrated into the high-temperature (highly viscous) layer with "solid-body" rotation. If the Peclet number  $Pe$  defined as the ratio of the characteristic diffusion to convection times, is small (the order of 10 or less), the vortex system pushes out the flame surface. If  $Pe$  is large (the order of 100), the vortex system nearly cuts through the high-temperature layer with a minimal flame movement, thus creating a significantly thin diffusive-thermal layer. In both cases, as the vortex approaches the flame surface, the net radial velocity of the incoming oxidizer stream crossing the flame and the reactants' diffusive fluxes into the flame increase. As a result, the flame structure similar to that of a strained counterflow diffusion flame is formed. A periodically-pulsed side jet has also been studied; the fuel packets ejected (at 500 Hz) induces the development of a large-scale vortex train in the shear layer of the primary jet, interacting with the flame zone.

## Introduction

IN most combustion systems of practical interest such as gas turbine combustors and industrial furnaces, turbulence plays an important role in determining various aspects of performance and efficiency, because it provides the most effective means of stirring fluids and enhancing molecular mixing and reactions. However, flow visualization in combustion systems shows inhomogeneous stirring of fluids, composed of packets and parcels of fuel, oxidizer, and products, because of large-scale turbulent structures generated in the shear layer. Therefore, the interactions between the large vortices and the flame zone are of essential importance as they relate to various aspects of combustion phenomena such as the transition to turbulent flames, flame stability, and local extinction.<sup>1–21</sup>

In a jet diffusion flame for which the flame base is securely stabilized, the local flame extinction occurs near the laminar-to-turbulent flame transition point (breakpoint) as the fuel jet velocity is increased.<sup>17</sup> Takeno and Kotani<sup>1</sup> postulated for hydrogen flames that the local extinction is a result of the excess transport rate as compared to the reaction rate at the breakpoint. The event when the vortex was ejected radially and interfered with the flame zone was captured in methane flames by using flow visualization techniques.<sup>5,8,9</sup> Eickoff et al.<sup>5</sup> speculated that the diffusion flame was quenched because too much heat was diffused by the small-scale turbulence superimposed in these vortices. However, in the near-

jet field of hydrocarbon-air flames, the flame zone is generally formed in the external fluid, not in the jet fluid, because of low stoichiometric fuel concentration and a high Damköhler number. It is, therefore, less likely that the flame zone interacts directly with the small-scale, high-intensity turbulence confined in the jet fluid.

A series of recent experiments<sup>15,17,19–21</sup> using a variety of diagnostic techniques revealed the essential features of the vortex-flame interactions that lead to the local extinction of methane jet diffusion flames. Figure 1 shows a schematic of

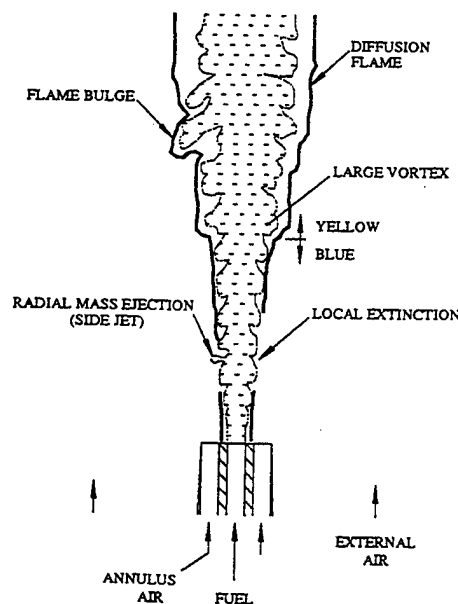


Fig. 1 Vortex-flame interactions observed in methane-air turbulent jet diffusion flames.

Presented as AIAA Paper 93-0456 at the AIAA 31st Aerospace Sciences Meeting and Exhibit, Reno, NV, Jan. 11–14, 1993; received Feb. 24, 1993; revision received March 21, 1994; accepted for publication April 14, 1994. Copyright © 1994 by the American Institute of Aeronautics and Astronautics, Inc. All rights reserved.

\*Research Engineer, Research Institute, 300 College Park, Senior Member AIAA.

†Senior Engineer, Research Applications Division, 2800 Indian Ripple Road, Member AIAA.

some features of a locally extinguished turbulent flame based on the flow visualization.<sup>17,19,20</sup> In the near-exit region (less than several jet diameters), the flame zone is close to the jet-fluid core and is blue in color. The flame zone shifts away from the core downstream and becomes yellow because of the soot formation. The local extinction occurs in the blue flame region near the jet exit when fuel packets, conveyed by the large-scale vortices or more rapid radial mass ejection (side jet), reach the flame zone location. The flame bulge is observed generally downstream (typically more than 10 jet diameters) in the yellow flame region. The time required for the fuel packet to reach the flame zone location in turbulent flames (typically less than 1 ms) is, at least, an order of magnitude shorter than the characteristic diffusion time required to re-establish the reactant concentration field (typically >10 ms).<sup>19,20</sup> In an axially-pulsed laminar flame,<sup>21</sup> the interaction between the flame zone and a large-scale vortex with a radial transit velocity of ~2 m/s occurred over a longer time (~10 ms), and the local quenching was observed near the leading edge of the vortex.

Recent developments of numerical models to simulate various aspects of the transient behavior of diffusion flames<sup>21-26</sup> enable more challenging numerical experiments on the dynamic vortex-flame interactions with sufficient accuracy. The computer code<sup>21,24-26</sup> used in this paper employs a time-dependent, axisymmetric, implicit, third-order accurate, upwind numerical scheme with assumptions of infinitely fast, one-step chemical kinetics and unity Lewis number. In laminar diffusion flames, the second Damköhler number, defined as the ratio of the mass source from chemistry to diffusive transport<sup>27</sup> (or the characteristic diffusion to chemical reaction times), is generally large, and therefore, the diffusion process is the rate-determining factor. As a vortex approaches the flame zone and the diffusion layer becomes thin (reducing the Damköhler number), finite-rate chemistry must become important in the process, eventually leading to local extinction. Because of the axisymmetry and infinitely fast chemistry assumptions, the current model cannot simulate the three-dimensional nature of a vortex, nor can the flame extinction condition. However, it must provide global information on the physical nature (fluid-dynamic and transport aspect) of the vortex-flame interaction before local extinction. This study attempts to simulate numerically the transient response of a laminar jet diffusion flame to an artificial vortex that issues from a side jet. The primary objective of this study is to gain a better understanding of essential physical features of the interactions between the flame zone and a naturally-forming shear-layer vortex that has some radial velocity.

## Numerical Experiment

### Numerical Scheme

The laminar diffusion flame considered in this article is formed between a central methane jet and a concentric annulus airflow. Time-dependent governing equations, expressed in cylindrical coordinates, consist of mass continuity, axial and radial momentum conservation, and two scalar conservation equations.<sup>24,25</sup> Shvab-Zel'dovich formulation,<sup>28</sup> in conjunction with the flame-sheet assumption, is utilized. Body-force term caused by the gravitational field is included in the axial momentum equation. The system of governing equations is completed by using the equation of state. Transport properties are considered to vary with temperature and species concentrations. Enthalpy of each species is calculated from polynomial curve-fits, whereas the viscosity of the individual species is estimated from Chapman-Enskog collision theory.<sup>29</sup> The binary diffusion coefficient between any two species on the fuel side of the flame is assumed to be identically equal to that of the fuel and nitrogen. Similarly, on the oxidizer side of the flame, it is made identical to that of the oxygen and nitrogen. The Chapman-Enskog theory and the Lennard-Jones potentials<sup>29</sup> have been used to estimate these two binary diffusion coefficients.

The finite difference form of the governing equations is constructed on a staggered grid system based on an implicit QUICKEST numerical scheme. It is third-order accurate in both space and time and has a very low numerical diffusion error. At every time-step, the pressure field is accurately calculated by solving the system of algebraic pressure Poisson equations simultaneously. An orthogonal grid system (Fig. 2) with rapidly expanding cell sizes in both  $z$  and  $r$  directions is utilized. The computational domain of  $150 \times 60$  mm in axial  $z$  and radial  $r$  directions, respectively, is represented by a mesh system of  $241 \times 71$ . The i.d. of the fuel tube ( $d = 9.6$  mm) is almost the same as that used in the experiments.<sup>15,17,19,20</sup> Grid lines are clustered near the burner lip and side jet locations. The outer boundaries of the computational domain are shifted sufficiently far enough to minimize the propagation of disturbances into the region of interest.

The initial and boundary conditions for the axial  $U$  and radial  $V$  velocities, and the scalar variables for species  $\beta_i$  and energy  $\beta_{25}$  at different flow boundaries are shown in Fig. 3. The fully developed pipe flow and flat-velocity profiles are used at the exits of the fuel tube and the annulus air channel, respectively. Along the burner-lip walls, no-slip boundary conditions are enforced. An extrapolation procedure with weighted zero- and first-order terms is used to estimate the flow variables on the outflow boundary. During the calculations, radial side jets are introduced from different locations in the flowfield.

### Test Conditions

The primary test cases reported in this article are listed in Table 1. Case 1 represents a laminar jet diffusion flame with low velocities of the primary jet  $U_p$ , annulus air  $U_a$ , and side jet  $V_s$ , and a long pulse width  $t_p$ . At the grid points within the side jet, the radial component of the local velocity and the scalar variables are replaced by  $V_s$ ,  $\beta_{1,s}$  ( $=\beta_{1,r}$ ), and  $\beta_{2,s}$  ( $=\beta_{2,r}$ ), respectively, for a time-period of  $t_p$ . The primary jet has a

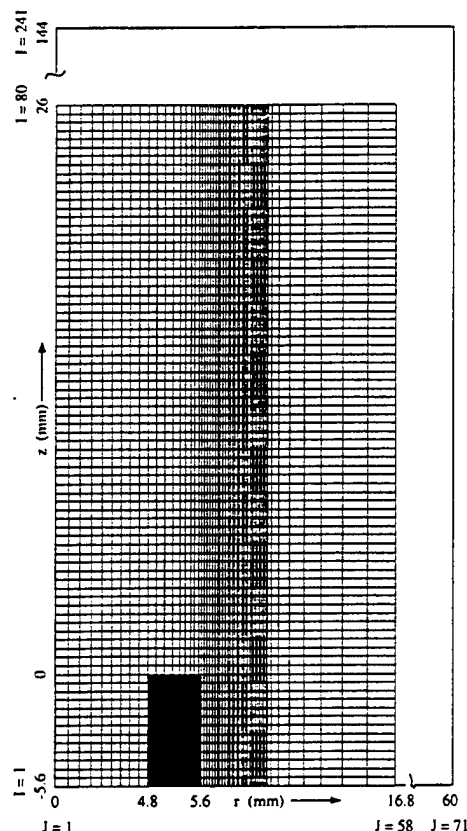


Fig. 2 Grid system.

Table 1 Test conditions

Case no.	Primary jet		Annulus air		Side jet			Pulse mode
	$U_j$ , m/s	Velocity profile	$U_a$ , m/s	$r_s$ , mm	$z_s$ , mm	$V_s$ , m/s	$t_s$ , $\mu$ s	
1	1.5	Parabolic	1.5	4.8	14.2–16.5	2.0	300	Single-shot
2a	15	$\frac{1}{4}$ th power	3	4.8	14.2–16.5	8.6	30	Single-shot
2b	15	$\frac{1}{4}$ th power	3	4.8	14.2–16.5	8.6	60	Single-shot
2c	15	$\frac{1}{4}$ th power	3	4.8	14.2–16.5	4.3	30	Single-shot
3	15	$\frac{1}{4}$ th power	3	4.8	4.2–9.5	2.0	30	Periodic, 500 Hz

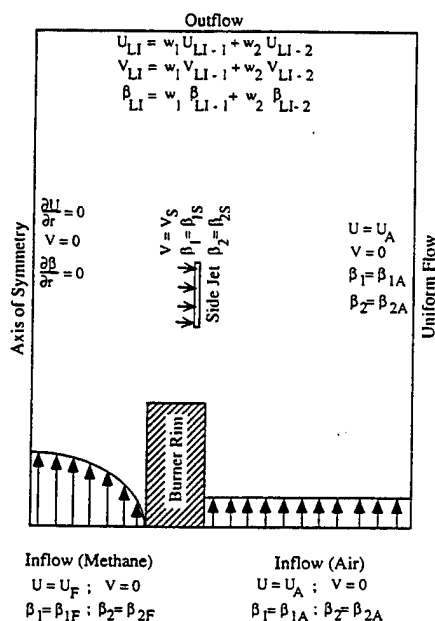


Fig. 3 Boundary conditions.

parabolic velocity distribution, representing the fully developed laminar pipe flow. The side-jet velocity in case 1 is the same magnitude as the radial velocity component of a large-scale vortex observed experimentally in the axially-pulsed laminar methane flame.<sup>21</sup> The radial location of the side jet ( $r_s = d/2$ ) is nearly coincident with a dividing streamline between the jet and external fluids. The height of the side jet is chosen near the jet exit such that the flame zone interacts with the vortex intensely because of the flame proximity to the jet-fluid core. Case 2a represents a flame with higher velocities of the primary jet, annulus air, and side jet, and a shorter pulse width in consideration of a naturally-forming radial mass ejection observed in turbulent flames.<sup>17,19,20</sup> In the turbulent methane jet diffusion flame stabilized on a thick burner lip, the local flame extinction occurred at the mean primary jet velocity of  $\sim 15$  m/s,<sup>15,17</sup> and the maximum radial velocity component (the mean plus three times the rms fluctuation) observed was  $\sim 7$  m/s.<sup>19</sup> The velocity distribution of the primary jet is given by using the empirical equation of the  $1/n$ th-power law<sup>20</sup> for the fully developed turbulent pipe flow with the exponent  $n = 6$  for a moderate Reynolds number (although the simulation considers laminar flows only). In case 2b, the pulse width of the side jet is doubled from case 2a to see the effect of the total mass ejected. In case 2c, the side jet velocity is halved from case 2a to test the effect of momentum at a same total mass ejection. Case 3 is an attempt to simulate a naturally-forming train of large-scale vortices in the shear layer, observed experimentally,<sup>3,8,9,12,25</sup> and their interaction with the flame zone. A moderate-speed periodically-pulsed (50% duty cycle) side jet is ejected into the flame under the condition of the same primary jet velocity as that in case 2a.

## Results and Discussion

### Single Vortex vs Flame Interactions

A steady-state solution for the diffusion flame structure without a side jet was obtained first for each case by numerous (typically several tens thousand times) iterative calculations using a long time step ( $\sim 183 \mu$ s in case 1;  $\sim 37 \mu$ s in case 2). By using the steady-state solution as the initial condition, the temporal changes in the flame structure in response to the side-jet ejection were calculated using a short time step ( $\sim 12.2 \mu$ s in case 1;  $\sim 2.4 \mu$ s in cases 2a–2c and 3). Figures 4 and 5 show the flame structure near the side jet for cases 1 and 2a, respectively: a color-coded mapping of the gas temperature  $T$  and a superimposed tracer particles image (Figs. 4a and 5a) and a color-coded mapping of the mole fractions of methane and oxygen  $X_{CH_4}$ ,  $X_{O_2}$  with superimposed velocity vectors (Figs. 4b and 5b). The tracer particles in Figs. 4a and 5a were injected in front of the side jet (at  $r = 4.9$  mm) over the axial distance of 4 mm at every time step. Notice that the elapse time after ejection  $t$  is an order of magnitude longer for case 1 ( $t = 3.91$  ms) than case 2a ( $t = 0.391$  ms). Despite the difference in the magnitude of side-jet velocity and, in turn, the time scale of the process, the two cases show the following common features in the flame structures, because the vortex system formed dominates the global flow structure.

As a fuel packet issues from the side jet in the jet-fluid core toward the flame surface, a sudden change in the radial-velocity distribution near the edges of the side jet induces the roll-up of fluid and the subsequent formation of a vortex system composed of a pair of counter-rotating vortex rings. The vortex system grows as it engulfs surrounding gases and penetrates into a high-temperature (highly viscous) layer toward the flame surface. The vortex structure rotates as a whole naturally because of the uneven axial-velocity distribution in the shear layer. This tendency is more evident in case 2a because of its higher velocity gradient, and consequently, the upper portion of the double-vortex structure shrinks (Fig. 5a). The formation of the vortex structure with counter-rotating vortex rings and the subsequent solid-body rotation have been observed experimentally.<sup>21</sup> The vortex evolution processes described are depicted well by the injected particle images (such as Figs. 4a and 5a), and the consecutive time-series animation of the particle images and the color-coded temperature mappings on a computer display. The velocity vectors (Figs. 4b and 5b) show a zigzag motion (with respect to the stationary coordinate) typical of large-scale vortices. The rotating motion is more clearly seen in case 2a. The velocity vectors also show that the bulk flow comes into the upstream portion of the vortex system from the oxidizer side, crossing the flame surface, and goes out from the downstream portion, crossing the flame again. However, because the contribution of convection to the reactant fluxes vanishes at the flame surface (as will be described later), the reactant species enter the flame surface solely by diffusion from opposite directions, typical of diffusion flames.

Major differences in the response of the flame to the vortex movement between the two cases stem from the an-order-of-magnitude difference in the time scale of the process. In case 1, the vortex system pushes out the flame zone along with

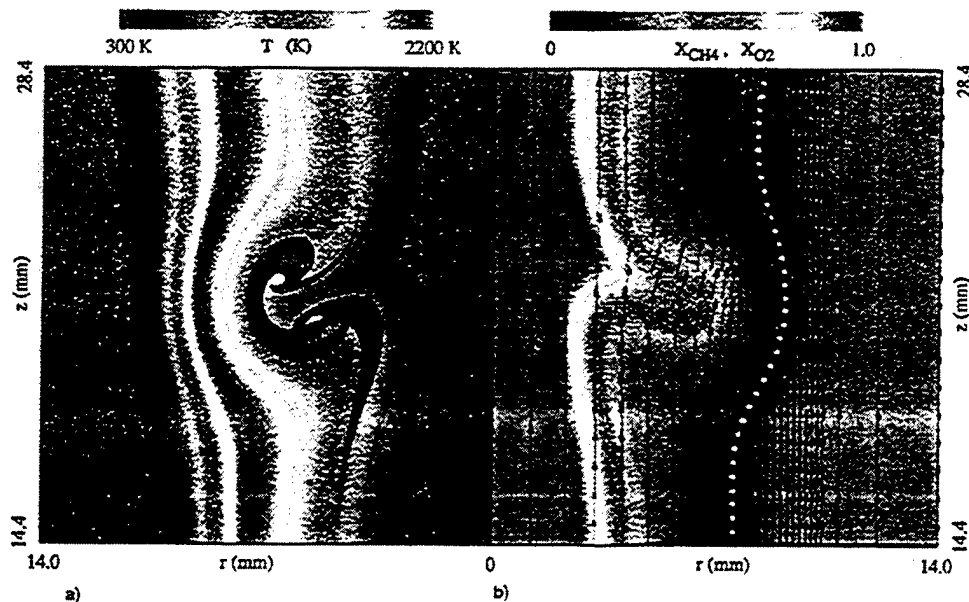


Fig. 4 Structure of a methane jet diffusion flame with a single side jet (case 1).  $t = 3.91$  ms: a) temperature field and injected particles and b) mole fraction field of  $\text{CH}_4$  and  $\text{O}_2$  and velocity vectors.

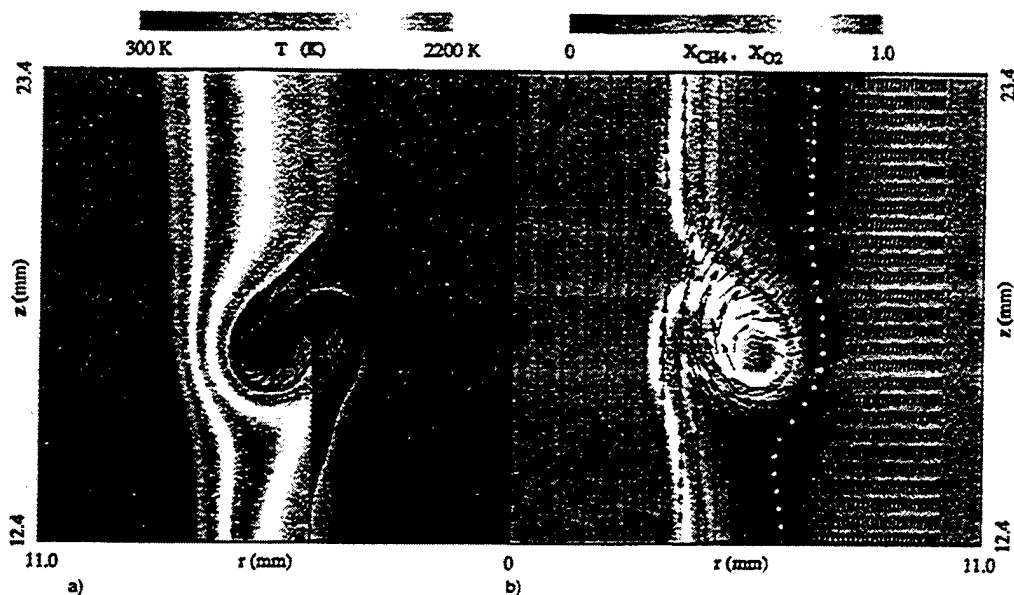


Fig. 5 Structure of a methane jet diffusion flame with a single side jet (case 2a).  $t = 0.391$  ms: a) temperature field and injected particles and b) mole fraction field of  $\text{CH}_4$  and  $\text{O}_2$  and velocity vectors.

the isothermal layers well before the vortex leading edge reaches the initial flame surface location (Fig. 4a). By contrast, in case 2a, the vortex almost cuts across the high-temperature zone while the flame zone shifts slightly at a very last stage of the process (Fig. 5a). Consequently, the thermal layer ahead of the vortex becomes significantly thin as the leading edge of the vortex reaches the initial flame surface location. Furthermore, although the total mass ejected is more than twice of that in case 1, the methane mole fraction in the vortex system becomes lower than case 2a because of the excess diffusion of the fuel molecules to the surroundings over a longer elapse time (Figs. 4b and 5b).

Figures 6 and 7 show the radial distributions of the mean axial and radial velocity components (Figs. 6a and 7a); the gas temperature, the mole fractions of methane and oxygen (Figs. 6b and 7b); and the instantaneous total (axial and radial) mole fluxes of methane and oxygen by convection ( $M_{\text{CH}_4, \text{conv}}$ ,  $M_{\text{O}_2, \text{conv}}$ ) and diffusion ( $M_{\text{CH}_4, \text{diff}}$ ,  $M_{\text{O}_2, \text{diff}}$ ) at a height near the center of the vortex system for cases 1 and 2a, respectively (Figs. 6c and 7c). The results at  $t = 0$  re-

present the steady-state solution. The radial location of the flame surface  $r_f$  at the height of the center of the side jet at  $t = 0$  is  $\sim 7.3$  mm in case 1, and  $\sim 6.5$  mm in case 2a. For the lower velocity condition (case 1) at  $t = 0$ , the axial velocity component shows a velocity overshoot near the flame because of the buoyancy effect. That is not seen in case 2a, in which the external air velocity is  $\sim 3$  m/s.

Because of the unity Lewis number assumption, heat transfer and mass diffusion processes must be similar. Therefore, the thickness of the layer in which the temperature varies is coincident with that for the (fuel and oxygen) mole fractions. The thickness of this layer (the diffusive-thermal layer) can be characterized using the full width at half-maximum (FWHM) of the temperature distribution  $w_T$ ;  $w_T = 3.6$  mm in case 1, and  $w_T = 2.4$  mm in case 2a at  $t = 0$ . The higher primary jet and air velocity in case 2a result in a higher bulk flow velocity coming into the flame zone from the air side, pushing the contour of a stoichiometric mole-flux balance (where the flame surface is located) inward to the region where gradients of variables (velocity, temperature, and methane mole frac-

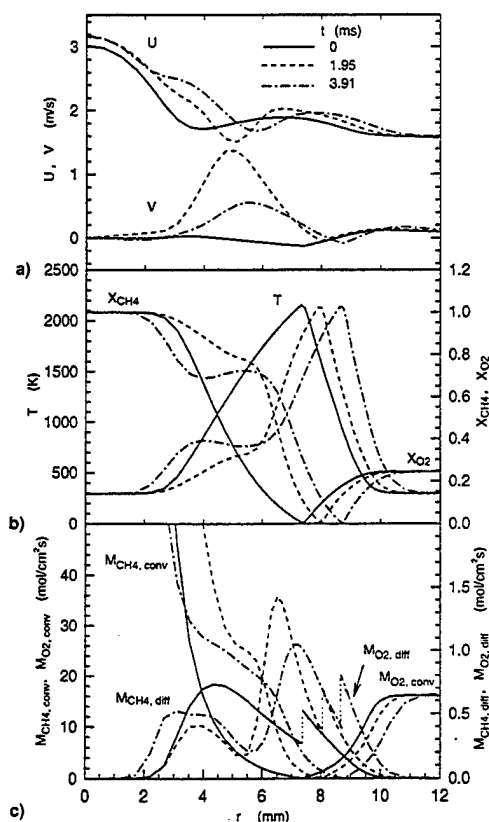


Fig. 6 Radial profiles of a) the axial and radial velocities; b) temperature, mole fractions of  $CH_4$  and  $O_2$ ; and c) mole fluxes of  $CH_4$  and  $O_2$  (case 1).

tion) are larger. Thus, the diffusive-thermal layer becomes thinner and the flame zone is more strained.

The magnitude of the instantaneous mole fluxes of the reactants by convection are large in the region away from the flame and decrease to zero at the flame surface, because the convection terms ( $\rho Y_i v / W_i$ , where  $\rho$  is density,  $Y$  is mass fraction,  $v$  is velocity vector,  $W$  is molecular weight, subscript  $i$ : species  $i$  for  $CH_4$  and  $O_2$ ) vanish as  $Y_i \rightarrow 0$  at  $r \rightarrow r_f$ . On the other hand, the diffusion terms ( $\rho_i D \nabla Y_i / W_i$ ) have finite values at  $r = r_f$ . The mole flux of methane by diffusion on the flame surface at  $t = 0$  is  $M_{CH_4, diff} = 0.27$  mole/m<sup>2</sup>s ( $M_{O_2, diff} = 0.54$  mole/m<sup>2</sup>s) in case 1 and  $M_{CH_4, diff} = 0.40$  mole/m<sup>2</sup>s ( $M_{O_2, diff} = 0.80$  mole/m<sup>2</sup>s) in case 2a. Because of the null contribution of convection to the methane and oxygen mole fluxes at the flame surface, the diffusion contribution is always at a stoichiometric ratio (1:2). Incidentally, the oxygen mole flux determined experimentally<sup>31</sup> in the luminous zone near the base of a laminar diffusion flame of methane is  $\sim 1$  mole/cm<sup>2</sup>s.

At  $t > 0$  in both cases, the peak temperature remains nearly constant (2100–2150 K), and a secondary temperature peak appears on the fuel side of the flame as a result of the roll-up of hot surrounding gases into the vortex structure. The diffusive-thermal layer becomes thinner ( $w_T = 2.4$  mm at  $t = 3.91$  ms in case 1, and  $w_T = 1.0$  mm at  $t = 0.391$  ms in case 2a), and the methane mole flux by diffusion increases with time ( $M_{CH_4, diff} = 0.40$  mole/m<sup>2</sup>s at  $t = 3.91$  ms in case 1, and  $M_{CH_4, diff} = 0.75$  mole/m<sup>2</sup>s at  $t = 0.391$  ms in case 2a). The reactant mole fluxes on the flame surface are thus almost proportional to  $w_T$ . In case 2a, in particular, the radial gradient of the methane mole fraction becomes significantly steep, thus resulting in the high methane flux diffusing into the flame zone (Fig. 7a).

Figure 8 shows the comparisons between the flame structures for cases 2a, 2b, and 2c at a fixed elapsed time ( $t = 0.293$

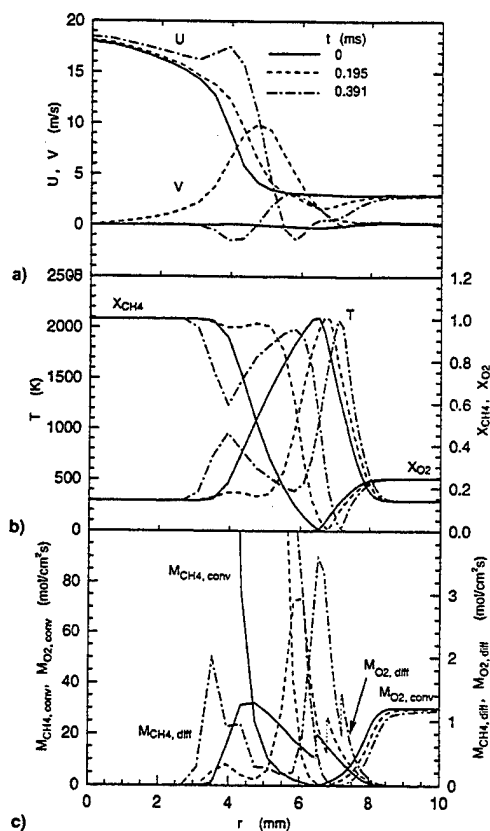


Fig. 7 Radial profiles of a) the axial and radial velocities; b) temperature, mole fractions of  $CH_4$  and  $O_2$ ; and c) mole fluxes of  $CH_4$  and  $O_2$  (case 2a).

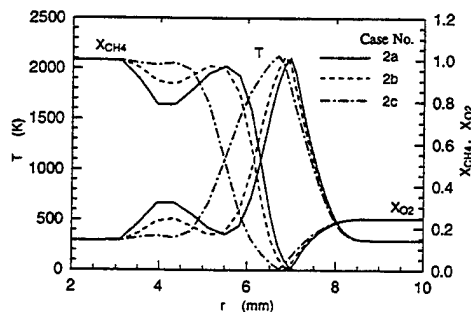


Fig. 8 Radial profiles of the temperature and mole fractions of  $CH_4$  and  $O_2$ .

ms). In case 2b, the ejection period and, in turn, the total mass of the side jet is doubled from case 2a. Although the size of the vortex system becomes larger in the temperature field mapping (not shown) in case 2b, the structure remained similar because the vortex system penetrated into the hot zone at almost the same degree. In case 2c, the velocity of the side jet is halved under a fixed total mass. Because of the lower momentum of the vortex system in case 2c, it could not penetrate into the hot zone to reach the flame zone location and, thus, drifted away downstream.

If the movement of the vortex system toward the flame surface was extremely slow, changes in the fuel concentration by the movement would propagate around the vortex by diffusion simultaneously. As a result, a quasi-steady-state concentration field would be re-established in time, and thus, the flame surface would be shifted to a renewed equilibrated position. On the other hand, if the vortex speed was extremely fast compared to the rate required for the diffusion process, the surrounding concentration field would not be able to re-

spond to the changes except for a narrow region in the immediate vicinity of the vortex. Therefore, the Peclet number  $Pe$  for mass transfer, defined as the ratio of the convective to conductive (diffusive) mass transfer<sup>27</sup> (or the characteristic diffusion to convection times), must be an important dimensionless parameter in determining the degree of the vortex-flame interaction. Because of the unity Lewis number assumption, the Peclet number for mass transfer is identical to its counterpart for heat transfer.<sup>27</sup> In the previous paper,<sup>19,20</sup> the characteristic diffusion time  $\tau_d$ , and the convection time caused by radial mass ejection  $\tau_m$  were determined as  $\tau_d = (\delta_d)^2/D$  ( $\delta_d$  is diffusive transport layer thickness,  $D$  is diffusion coefficient), and  $\tau_m = \delta_d/V_m$  ( $V_m$  is radial mass ejection velocity), respectively. Therefore, the Peclet number relevant to the side-jet ejection under current consideration becomes

$$Pe = (\tau_d/\tau_m) = (\delta_d V_m/D) \quad (1)$$

It was estimated<sup>19,20</sup> that  $\tau_d \sim 30$  ms and  $\tau_m \sim 0.2$  ms using  $\delta_d \sim 1.5$  mm,  $D \sim 0.7$  cm<sup>2</sup>/s (methane at 1500 K), and  $V_m = 6.6$  m/s, resulting in  $Pe \sim 150$ . By substituting  $(r_f - r_s)$  at  $t = 0$  for  $\delta_d$  and  $V_f$  for  $V_m$ , the flames under investigation in this article,  $Pe \sim 71$  ( $\tau_d \sim 89$  ms,  $\tau_m \sim 1.25$  ms) was obtained for case 1, and  $Pe \sim 209$  ( $\tau_d \sim 41$  ms,  $\tau_m \sim 0.2$  ms) for case 2a. Thus, the characteristic convection time is one to two orders of magnitude shorter than the characteristic diffusion (or heat transfer) time.

Figure 9 shows the temporal variations in the radial locations and transit velocities of the leading edge of the vortex system ( $r_v$ ,  $V_v$ ), the flame surface ( $r_f$ ,  $V_f$ ), and the width at half-maximum of the temperature distribution for cases 1 and 2a. As the vortex approaches the flame zone at  $t < 2$  ms in case 1 (Fig. 9a), the vortex loses its speed while the flame surface gains its moving velocity. As the vortex pushes the flame,  $(r_f - r_v)$  and  $w_T$  decrease and become nearly constant, and  $V_f \approx V_v$  at  $t > 2$  ms. Because of unity Lewis number,  $w_T$  is almost proportional to  $(r_f - r_v)$ . In case 2a (Fig. 9b),  $(r_f - r_v)$ ,  $w_T$ , and  $V_f$  continue to decrease and  $V_v$  increases until the leading edge of the vortex reaches the initial flame zone location at  $t \sim 0.4$  ms. The  $V_v$  curve changes its slope as the vortex starts the "solid-body" rotation described before.

Since the flame surface moves outward as the vortex system approaches, it is necessary to consider the net radial velocity

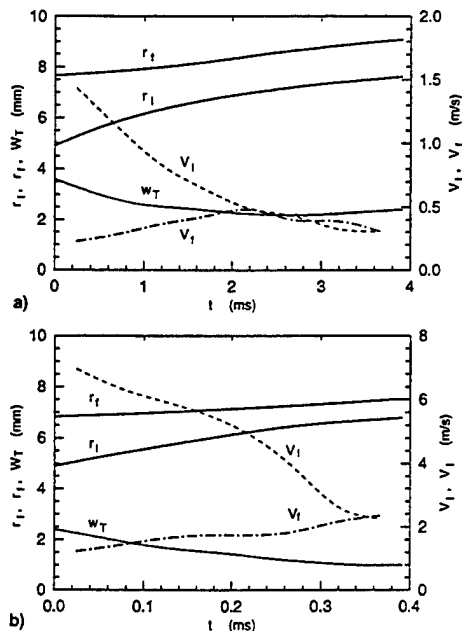


Fig. 9 Temporal variations in the radial locations and velocities of the vortex leading edge and flame surface and the FWHM of the temperature distribution: a) case 1 and b) case 2a.

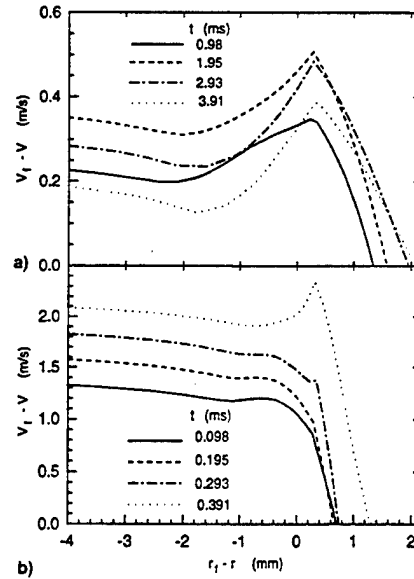


Fig. 10 Radial profiles of the net radial velocity relative to the flame surface.

component relative to the flame surface in order to examine the instantaneous structure near the flame. Figure 10 shows the relative radial velocity component ( $V_f - V$ ), which is positive for the incoming flow direction crossing the flame surface, as a function of the relative location ( $r_f - r$ ) in the near-flame region for cases 1 and 2a. In case 1 (Fig. 10a), as the vortex system approaches the flame surface, the profile of  $(V_f - V)$  becomes similar to the one observed in strained counterflow diffusion flames<sup>32,33</sup> (with a peak at slightly downstream of the flame surface) at a relatively early stage of the vortex-flame interaction process. In case 2a (Fig. 10b), the temperature peak does not appear until a later stage of the process when the vortex leading edge approaches the close proximity of the flame surface and  $(r_f - r_v)$  becomes constant. Because the velocity peak is caused by the longitudinal acceleration by gas expansion at high temperatures, the peak would not appear (or would be small, if any) if the gases (stream tubes) were able to expand laterally under a given flow configuration. Furthermore, unlike the counterflow diffusion flames, the velocity gradient (deceleration) of the approach flow just before entering the flame (which is normally used to assess the strain rate in the counterflow diffusion flames), is small because the net radial velocity component is nearly constant ( $\sim V_v$ ) away from the flame surface as the actual velocity with respect to the laboratory coordinate is nearly zero. In jet diffusion flames, in general, the streamlines are nearly parallel to the flame surface (and thus, the velocity component perpendicular to the flame is small), while in counterflow diffusion flames, the streamlines are perpendicular for the stagnation-point flow. The radial side jet ejection has altered the normal jet diffusion flame structure. Therefore, the differences in the geometric configuration and velocity of the incoming flow play an important role in determining the flame structure, and a proper consideration needs to be made when applying a property (such as the critical strain rate for extinction) of one type of flames to another type.

#### Periodic-Vortices vs Flame Interactions

In case 3, the periodically-pulsed side jet induced the development of a train of large-scale vortices in the shear layer, similar to the structure observed experimentally.<sup>8,9,12</sup> A preliminary test showed that the evolution frequency of the large structure was  $\sim 500$  Hz and nearly independent of the side jet frequency in the range of 500–1000 Hz. Figure 11 shows the structure of the flame with a periodic (500-Hz) side-jet ejection: a color-coded mapping of the temperature field (Fig.



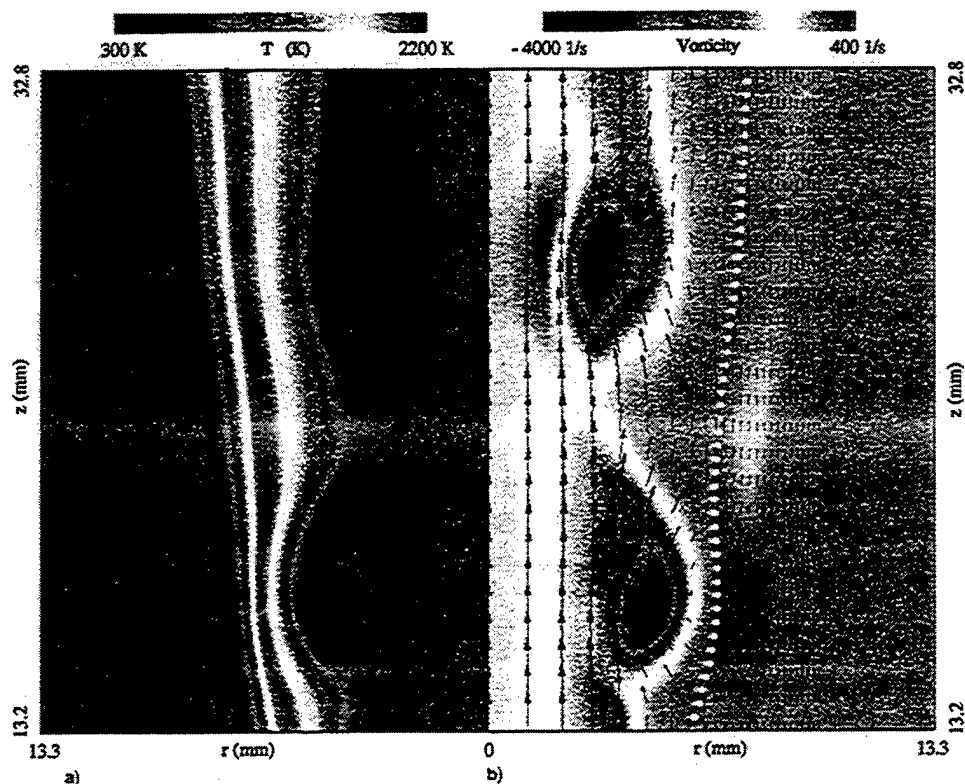


Fig. 11 Structure of a methane jet diffusion flame with a periodically-pulsed (500-Hz) side jet (case 3): a) temperature field and b) vorticity field and velocity vectors.

11a) and the vorticity field with superimposed velocity vectors (Fig. 11b). The temperature field image (Fig. 11a) shows the engulfment of the hot combustion products into the upstream side of the vortex and the thinned diffusive-thermal layer near the vortex upstream. Although the vortex interacts with the flame in a similar manner with the single-pulsed cases in the upstream region, the interaction becomes weaker downstream as the vortex loses its radial momentum and the distance between the vortex and the flame (or the diffusive-thermal layer thickness) increases. Unlike the single-shot side jet described before, the large vortex has the only one rotation direction as is normally seen in the shear layer. Thus, the vorticity (Fig. 11b) shows a negative peak. The velocity vectors again show a zigzag motion because of the large vortices.

### Conclusions

A unique numerical experiment, in which a packet of fuel issues from a side jet toward a flame zone, has illustrated essential physics of the interactions between a large-scale vortex and a laminar diffusion flame. The following are among major conclusions.

The formation of a large-scale vortex structure composed of a pair of counter-rotating vortex rings and subsequent solid-body rotation of the vortex structure caused by the uneven axial-velocity distribution in the shear layer, observed experimentally, are simulated numerically. If the side-jet velocity (or momentum) is large, the vortex system penetrates into the high-temperature (highly viscous) layer; otherwise, it drifts away downstream before reaching the initial flame surface location. The level of penetration is nearly independent of the total mass ejected. The solid-body rotation of the vortex system is more evident in the higher primary jet velocity case because of the higher velocity gradient.

A Peclet number, defined as a ratio of the characteristic diffusion (or thermal conduction) to convection times for the side jet, is an important parameter in determining the level of the vortex-flame interactions. If  $Pe$  is small (the order of 10 or less), the vortex system pushes out the flame surface

over the majority of the interaction period. If  $Pe$  is large (the order of 100), the vortex system nearly cuts through the high-temperature layer with a slight flame movement, thus resulting in an extremely thin diffusive-thermal layer with large gradients of the temperature and reactant concentrations. In both cases, as the vortex system approaches the flame surface, both the bulk flow velocity and the diffusive fluxes of reactants into the flame surface increase, and a flame structure becomes similar to that of a strained laminar counterflow diffusion flame. Therefore, the geometric flow configuration and incoming flow velocity, created by the large-scale vortex, are important factors in determining the flame structure.

The development of a train of large-scale vortices in the shear layer, observed experimentally, is simulated numerically by ejecting consecutive packets of fuel from the side jet periodically. Although the vortex-flame interactions similar to the single-pulsed cases take place in the upstream region, the level of the interactions decreases rapidly downstream, as the vortex loses its radial momentum.

### Acknowledgments

This work was supported by the U.S. Air Force, Wright Laboratory, Aero Propulsion and Power Directorate, Fuels and Lubrication Division, Wright-Patterson Air Force Base, Ohio, under Contract F33615-92-C-2207 (Technical Monitor, C. W. Frayne). The authors would like to thank W. M. Roquemore for helpful discussions.

### References

- <sup>1</sup>Takeno, T., and Kotani, Y., "An Experimental Study on the Stability of Jet Diffusion Flames," *Acta Astronautica*, Vol. 2, 1975, pp. 999-1008.
- <sup>2</sup>Yule, A. J., Chigier, N. A., Ralph, S., Boulderstone, R., and Ventura, J., "Combustion-Transition Interaction in a Jet Flame," *AIAA Journal*, Vol. 19, No. 6, 1981, pp. 752-760.
- <sup>3</sup>Eickhoff, H., "Instability and Coherent Structures in Jet Flames," *Recent Contributions to Fluid Mechanics*, edited by W. Haase, Springer-Verlag, 1982.

ger-Verlag, New York, 1982, pp. 50-57.

<sup>4</sup>Takahashi, F., Mizomoto, M., and Ikai, S., "Transition from Laminar to Turbulent Free Jet Diffusion Flames," *Combustion and Flame*, Vol. 48, No. 1, 1982, pp. 85-95.

<sup>5</sup>Eickoff, H., Lenze, B., and Leuckel, W., "Experimental Investigation on the Stabilization Mechanism of Jet Diffusion Flames," *Twentieth Symposium (International) on Combustion*, The Combustion Inst., Pittsburgh, PA, 1984, pp. 311-318.

<sup>6</sup>Gollahalli, S. R., Savas, Ö., Huang, R. F., and Rodriguez Azara, J. L., "Structure of Attached and Lifted Gas Jet Flames in Hysteresis Region," *Twenty-First Symposium (International) on Combustion*, The Combustion Inst., Pittsburgh, PA, 1988, pp. 1463-1471.

<sup>7</sup>Shekarchi, S., Savas, Ö., and Gollahalli, S. R., "Structure of a Split Gas Flame," *Combustion and Flame*, Vol. 73, 1988, pp. 221-232.

<sup>8</sup>Eickoff, H., Lehmann, B., Barsikow, B., and Winandy, A., "Instability of Ring Vortices and the Formation of Side Jets in Diffusion Flames and Hot Jets," 5th International Symposium on Flow Visualization, Prague, Czechoslovakia, Aug. 1989.

<sup>9</sup>Roquemore, W. M., Chen, L.-D., Goss, L. P., and Lynn, W. F., "The Structure of Jet Diffusion Flames," *Turbulent Reactive Flows*, edited by R. Borghi and S. N. B. Murthy, Springer-Verlag, Berlin, Vol. 40, 1989, pp. 49-63.

<sup>10</sup>Lewis, G. S., Cantwell, B. J., Vandsburger, U., and Bowman, C. T., "An Investigation of the Structure of a Laminar Non-Premixed Flame in an Unsteady Vortical Flow," *Twenty-Second Symposium (International) on Combustion*, The Combustion Inst., Pittsburgh, PA, 1989, p. 515.

<sup>11</sup>Gutmark, E., Parr, T. P., Parr, D. M., and Schadow, K. C., "Evolution of Vortical Structure in Flames," *Twenty-Second Symposium (International) on Combustion*, The Combustion Inst., Pittsburgh, PA, 1989, pp. 523-529.

<sup>12</sup>Chen, L.-D., Seaba, J. P., Roquemore, W. M., and Goss, L. P., "Buoyant Diffusion Flames," *Twenty-Second Symposium (International) on Combustion*, The Combustion Inst., Pittsburgh, PA, 1989, pp. 677-684.

<sup>13</sup>Coats, G. M., and Zhao, H., "Transition and Stability of Turbulent Jet Diffusion Flames," *Twenty-Second Symposium (International) on Combustion*, The Combustion Inst., Pittsburgh, PA, 1989, pp. 685-692.

<sup>14</sup>Takahashi, F., Mizomoto, M., Ikai, S., and Tsuruyama, K., "Stability Limits of Hydrogen/Air Coflow Jet Diffusion flames," AIAA Paper 90-0034, Jan. 1990.

<sup>15</sup>Takahashi, F., Schmoll, W. J., and Vangsness, M. D., "Effects of Swirl on the Stability and Turbulent Structure of Jet Diffusion Flames," AIAA Paper 90-0036, Jan. 1990.

<sup>16</sup>Pitts, W. M., "Large-Scale Turbulent Structures and the Stabilization of Lifted Turbulent Jet Diffusion Flames," *Twenty-Third Symposium (International) on Combustion*, The Combustion Inst., Pittsburgh, PA, 1991, pp. 661-668.

<sup>17</sup>Takahashi, F., and Schmoll, W. J., "Lifting Criteria of Jet Diffusion Flames," *Twenty-Third Symposium (International) on Combustion*, The Combustion Inst., Pittsburgh, PA, 1991, pp. 677-683.

<sup>18</sup>Chen, T. H., and Goss, L. P., "Statistical OH-Zone Structure of Turbulent Jet Flames from Liftoff to Near-Blowout," *Combustion*

*Science Technology*, Vol. 79, 1991, pp. 311-324.

<sup>19</sup>Takahashi, F., and Goss, L. P., "Near-Field Turbulent Structures and the Local Extinction of Jet Diffusion Flames," *Twenty-Fourth Symposium (International) on Combustion*, The Combustion Inst., Pittsburgh, PA, 1992, pp. 351-359.

<sup>20</sup>Takahashi, F., and Vangsness, M. D., "Near-Field CARS Measurements and the Local Extinction of Turbulent Jet Diffusion Flames," *Dynamics of Heterogeneous Combustion and Reacting Systems*, edited by A. L. Kuhl, J.-C. Leyer, A. A. Borisov, and W. A. Sirignano, Vol. 152, Progress in Astronautics and Aeronautics, AIAA, Washington, DC, 1993, pp. 37-55.

<sup>21</sup>Hsu, K. Y., Chen, L. D., Katta, V. R., Goss, L. P., and Roquemore, W. M., "Experimental and Numerical Investigations of the Vortex-Flame Interactions in a Driven Jet Diffusion Flames," AIAA Paper 93-0455, Jan. 1993.

<sup>22</sup>Davis, R. W., Moore, E. F., Roquemore, W. M., Chen, L.-D., Vilimovic, V., and Goss, L. P., "Preliminary Results of a Numerical-Experimental Study of the Dynamic Structure of a Buoyant Jet Diffusion Flames," *Combustion and Flame*, Vol. 83, Nos. 3/4, 1991, pp. 263-270.

<sup>23</sup>Eilzey, J. L., Laskey, K. J., and Oran, E. S., "Effects of Heat Release and Gravity on an Unsteady Diffusion Flame," *Twenty-Third Symposium (International) on Combustion*, The Combustion Inst., Pittsburgh, PA, 1991, pp. 1635-1640.

<sup>24</sup>Katta, V. R., Goss, L. P., and Roquemore, W. M., "Numerical Investigations of Transitional H<sub>2</sub>/N<sub>2</sub> Jet Diffusion Flames," *AIAA Journal*, Vol. 32, No. 1, 1994, pp. 84-94.

<sup>25</sup>Katta, V. R., and Roquemore, W. M., "Role of Inner and Outer Structures in Transitional Jet Diffusion Flame," *Combustion and Flame*, Vol. 92, No. 2, 1993, pp. 274-282.

<sup>26</sup>Katta, V. R., Goss, L. P., and Roquemore, W. M., "Effect of Nonunity Lewis Number and Finite-Rate Chemistry on the Dynamics of a Hydrogen-Air Jet Diffusion Flames," *Combustion and Flame*, Vol. 96, Nos. 1/2, 1994, pp. 60-74.

<sup>27</sup>Strehlow, R. A., *Combustion Fundamentals*, McGraw-Hill, New York, 1984, p. 120.

<sup>28</sup>Williams, F. A., *Combustion Theory*, 2nd ed., The Benjamin/Cummings, Menlo Park, CA, 1985, p. 10.

<sup>29</sup>Hirschfelder, J. O., Curtis, C. F., and Bird, R. B., *The Molecular Theory of Gases and Liquids*, Wiley, New York, 1954.

<sup>30</sup>Schlichting, H., *Boundary-Layer Theory*, 7th ed., translated by J. Kestin, McGraw-Hill, New York, 1979, p. 599.

<sup>31</sup>Robson, K., and Wilson, M. J. G., "The Stability of Laminar Diffusion Flames of Methane," *Combustion and Flame*, Vol. 13, 1969, pp. 626-634.

<sup>32</sup>Tsuji, H., and Yamaoka, I., "Structure Analysis of Counterflow Diffusion Flames in the Forward Stagnation Region of a Porous Cylinder," *Thirteenth Symposium (International) on Combustion*, The Combustion Inst., Pittsburgh, PA, 1971, pp. 723-731.

<sup>33</sup>Chelliar, H. K., Law, C. K., Ueda, T., Smooke, M. D., and Williams, F. A., "An Experimental and Theoretical Investigation of the Dilution, Pressure and Flow-Field Effects on the Extinction Condition of Methane-Air-Nitrogen Diffusion Flames," *Twenty-Third Symposium (International) on Combustion*, The Combustion Inst., Pittsburgh, PA, 1991, pp. 503-511.

## **APPENDIX G**

### **Structure of Turbulent Hydrogen Jet Diffusion Flames With or Without Swirl**

**F. Takahashi, M. D. Vangness,  
M. D. Durbin, W. J. Schmoll**

# Structure of Turbulent Hydrogen Jet Diffusion Flames With or Without Swirl

F. Takahashi

M. D. Vangsness

M. D. Durbin

W. J. Schmoll

University of Dayton,  
Research Institute,  
300 College Park,  
Dayton, OH 45469

*The near-field turbulent structure of double-concentric hydrogen-air jet diffusion flames, with or without swirl, has been investigated using conditionally sampled, three-component laser-Doppler velocimetry and coherent anti-Stokes Raman spectroscopy. The turbulent flame zone became thinner and shifted inward as the mean jet velocity was increased, whereas swirl created a radial velocity even at the jet-exit plane, thereby broadening and shifting the flame zone outward. The probability-density functions of velocity components, their 21 moments (up to fourth order), mean temperature, and root-mean-square temperature fluctuation were determined in the near field. The data can be used to validate advanced turbulent combustion models.*

## Introduction

In practical combustion systems such as gas turbines and industrial furnaces, turbulence and swirl play an essential role in enhancing fuel-air mixing, flame stabilization, and combustion intensity. Previous studies of turbulent jet diffusion flames (Bilger, 1976; Eickhoff, 1982; Faeth and Samuelsen, 1986; Dibble et al., 1987; Tangirala et al., 1987; Stårner, 1985; Stårner and Bilger, 1988; Drake, 1988; Pitz et al., 1991; Nandula et al., 1994; Barlow and Carter, 1994) have focused primarily on nonswirling flames and have not included detailed velocity and temperature data in the developing region of the flame. The majority of the existing velocity data in turbulent jet diffusion flames were obtained using single- or two-component laser-Doppler velocimetry (LDV). Thermocouples and, more recently, Raman scattering spectroscopy were used for temperature measurements. Reports on high-order moments, particularly triple correlations, of the probability-density functions (pdf) of velocity components are rare; they are available for nonreacting flows (Hinze, 1975; Wignanski and Fiedler, 1969). Accurate measurement of high-order moments is a challenge especially in reacting flows.

In addition, the conventional turbulence models such as a  $k-\epsilon$  model use gradient diffusion models for turbulent transport (Launder and Spalding, 1972; Eickhoff, 1982) and cannot predict high-order moments; thus, a demand for such data for model validation has been minimal. Unlike these models, recent turbulence models such as pdf methods do not need to model the turbulent transport terms because they appear in closed form (Pope, 1990). The joint velocity-scalar pdf method, capable of calculating high-order moments, has recently been applied to a number of reacting and nonreacting flows (Anand et al., 1993, 1996). Such advanced turbulent combustion models must be validated in detail in laboratory flames incorporating the essential features of practical flows. Therefore, the demand for the detailed experimental data, including high-order moments (in swirling or nonswirling flows), has been growing rapidly in recent years.

A major challenge in accurate LDV measurements is how to avoid inherent particle statistical bias problems (Edwards, 1987). Conditional sampling techniques (Libby et al., 1982)

have been applied to LDV measurements (Dibble et al., 1987; Tangirala et al., 1987; Stårner, 1985; Takahashi et al., 1992) to avoid velocity bias originated in different flow channels with different initial velocities. However, the conditionally sampled velocity data obtained specifically for model validation are unavailable. The developing region of the jet flame is particularly important because various physical and chemical processes occur rapidly in the near-nozzle region, and the flame structure downstream depends significantly on the early development. Moreover, substantial errors due to an elongated (ellipsoidal) measuring volume of a two-component LDV system (Durbin et al., 1993) were observed by comparisons with the results obtained by a three-component system with a small probe volume (Takahashi et al., 1995). Furthermore, the use of a thermocouple exerts serious limitations on the maximum measurable temperature, delayed time responses, radiation heat losses, flow and catalytic disturbances on the flame, and so forth.

This work is an attempt to provide a reliable data base in response to the above-mentioned demands and requirements for accurate velocity and temperature measurements. The contributions of the current results relative to previous work are as follows: (1) This study provides the first detailed velocity and temperature data in swirling and nonswirling turbulent hydrogen jet diffusion flames, specifically designed for the validation of advanced turbulent combustion models capable of predicting high-order moments. (2) A unique contribution of this study stems from the nonintrusive laser diagnostic techniques used. The conditionally sampled, three-component LDV measurements with a small probe volume were made, for the first time, to obtain the unbiased velocity data, including high-order cross-correlations. The coherent anti-Stokes Raman spectroscopy (CARS) thermometry generated the temperature data without causing disturbances on the flame. (3) All data obtained are tabulated (in ASCII file format) and plotted in five technical reports (Takahashi et al., 1993, 1994a, b). Therefore, selected results are presented in this paper to extract physical insights into the near-field turbulent structure of hydrogen jet diffusion flames.

## Experimental Techniques

The combustor (Fig. 1) consists of a central fuel tube (9.45-mm inner diameter [ $d$ ], 0.2-mm lip thickness, 806-mm length) and a concentric annulus-air tube (26.92-mm inner diameter), centered in a vertical test section (150 × 150-mm square cross section with rounded corners [quasi-octagonal], 486-mm length), through which external air is supplied. The test section

Contributed by the Heat Transfer Division and presented at the ASME International Mechanical Engineering Congress and Exposition, San Francisco, California, November 12–17, 1995. Manuscript received by the Heat Transfer Division November 27, 1995; revision received May 14, 1996. Keywords: Fire/Flames, Jets, Turbulence. Associate Technical Editor: S. H. Chan.

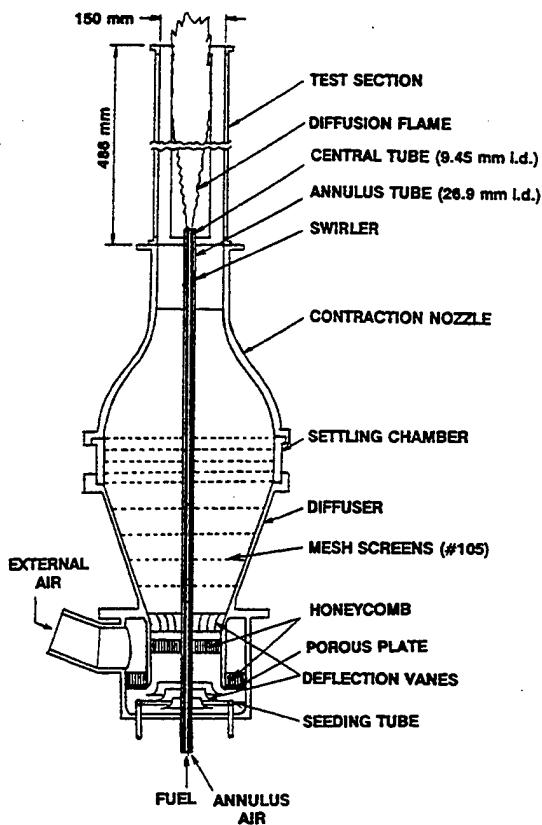


Fig. 1 Schematic of the combustor used

is sided with four quartz windows for optical observations and diagnostics. A helical vane swirler unit is placed in the annulus channel 96 mm upstream from the jet exit. Table 1 shows the experimental conditions ( $\theta$ : helical vane angle,  $U_j$ : mean jet velocity,  $U_a$ : mean annulus air velocity, and  $U_e$ : mean external air velocity). Hydrogen (purity: 99.3 percent) is the fuel. The jet Reynolds number ( $Re_j = U_j d / \nu$ , where  $\nu$  is the kinematic viscosity of hydrogen) is 2208 for Case 1 and 8830 for the others. Case 1 is in the pipe-flow transition region, in which breakpoint to the turbulent flame rapidly approaches the jet exit (Takahashi et al., 1982). Thus, Case 1 is a transitional (or weakly turbulent) flame, and Cases 2 through 4 are fully developed turbulent flames. Both LDV and CARS measurements were made at numerous radial locations at seven axial locations ( $x = 1.5, 10, 25, 50, 75, 150$ , and  $225$  mm).

The three-component LDV system, described in detail elsewhere (Takahashi et al., 1993, 1994a), consists of two segments: (1) three-beam two-channel optics and (2) two-beam one-channel optics. The former uses a 514.5-nm line of an argon-ion laser (15 W) and measures the velocity components in the directions of  $\pm 45$  deg off the jet axis. The latter uses a 488.0-nm line and measures the tangential velocity component. The coincident measuring volume is minimized to a 100- $\mu$ m-dia sphere by aligning the axes of the two segments perpendicularly. The calculated fringe spacing is approximately 3.6  $\mu$ m. Submicron-size zirconia particles ( $< 1$   $\mu$ m, 97 percent) are the tracer. LDV measurements are made by seeding one stream at a time. Thus, all LDV data reported are conditional upon the fluid originating from either the jet, annulus, or external flow channel. A portion of the data is filtered out by the so-called  $n\sigma$  method (i.e., velocities whose deviation from the mean exceeded  $n$  times the standard deviation  $[\sigma]$  are eliminated). Because the conventional  $3\sigma$  method occasionally cuts off some valid data and alters high-order moments significantly,  $n = 4$  is used in this study. The 21 independent flow variables determined are  $U, V, W, \sqrt{u'^2}, \sqrt{v'^2}, \sqrt{w'^2}, u'v', v'w', w'u', u'^3,$

$v'^3, w'^3, u'^2v', v'^2u', v'^2w', w'^2v', w'^2u', u'^2w', u'^4, v'^4,$  and  $w'^4$ . Hence,  $u, v$ , and  $w$  represent the axial, radial, and tangential velocity components, respectively; a capital letter indicates the mean value and a lowercase letter with a prime indicates the velocity fluctuation from the mean. The kinetic energy of turbulence, skewnesses, and kurtoses are derived from these quantities. The accuracy of the velocity measurements is estimated as  $\sim 2$  percent for the means and 5 to 10 percent for the higher moments.

The CARS system, described in detail elsewhere (Takahashi and Vangsness, 1993; Takahashi et al., 1994b), consists of a pulsed Nd:YAG laser, dye laser optics, incident and collection optics, and a spectrometer with an intensified charge-coupled device camera. A broadband Stokes beam ( $\sim 607$  nm) and the two pump beams (532 nm) are then focused together in a folded BOXCARS configuration using a lens (250-mm f.l.). The ellipsoidal probe volume size, estimated by assuming Gaussian beams with a 7-mm diameter and a 5-deg crossing angle, is approximately 25  $\mu$ m in diameter and 250  $\mu$ m in length. Typically, 500 CARS signals from nitrogen are acquired at each location. The accuracy of the temperature measurements is estimated to range between 10 percent near room temperature and 5 percent near the flame temperature, with the largest contribution to uncertainty from shot-to-shot variation in the Stokes-laser spectral distribution. The reproducibility of both LDV and CARS measurements is checked prior to final runs.

## Results and Discussion

**Thermal Structure.** Figures 2 and 3 show the radial profiles of the mean gas temperatures and root-mean-square (rms) values of temperature fluctuations at five selected heights in swirling and nonswirling turbulent hydrogen jet diffusion flames. The outermost data point is bounded by the location where the temperature is nearly room temperature (or the outer edge of the test section's window). The innermost data point is the location where the intermittency of the jet fluid (defined as the fraction of CARS realizations for which nonresonant background interference from the fuel occur in the total number of data [Takahashi and Vangsness, 1993]) is very high, and accurate temperature determination is prevented beyond this point.

In all cases (Cases 1–4), the flame base anchored near the fuel tube exit on the air side of the dividing streamline (whose radial distance from the axis:  $y \approx 4.7$  mm) as the sharp temperature peaks ( $\sim 1900$  K at  $x = 1.5$  mm,  $y = 5$  to  $5.5$  mm in Fig. 2(e)) indicate. The temperature peak shifted outward and broadened downstream, as expected. The rms temperature fluctuation reached a maximum (up to 900 K) in the outer thermal layer where the mean temperature gradient was large. As the jet velocity was increased in nonswirling flames (from Case 1 to Case 2), the flame zone (temperature peak) shifted inward and both mean and rms temperature peaks became narrower and slightly lower. Furthermore, the innermost data points shifted slightly outside from Case 1 to Case 2 as a result of faster

Table 1 Experimental conditions

Case No.	$\theta$ (°)	$U_j$ (m/s)	$U_a$ (m/s)	$U_e$ (m/s)
1	0	25	4	1
2	0	100	20	4
3	30	100	20	4
4	45	100	20	4

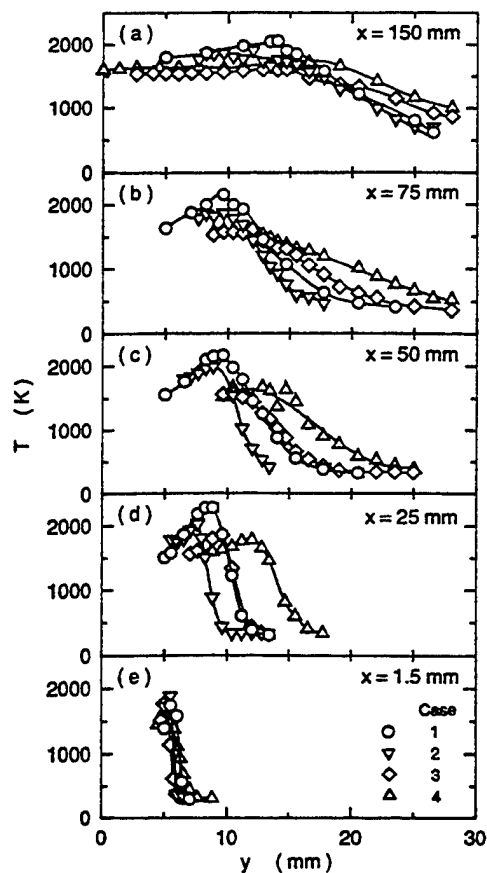


Fig. 2 Mean-temperature distribution across the hydrogen jet flame at five different heights

spread of the fuel jet. Consequently, the layer between the innermost data point and the temperature peak, where hydrogen was transported by both turbulent and molecular diffusion, became thinner. As swirl was added to the annulus airflow (see Cases 2–4), the innermost data points and the temperature peak locations shifted outward substantially, the mean temperature profiles became flatter, and both mean and rms temperature peak values decreased. Swirl-induced radial velocity, and thus, the hydrogen jet spread outward with a larger angle (as will be explained in detail in the next section).

Although the mean and rms temperature profiles show global features of the thermal structure of the flame, more precise information can be retrieved from temperature pdf's. Only few examples at selected locations for three conditions (Cases 1–3) are shown here, but the general trend peculiar to the radial location relative to the flame zone is illustrated well. In fact, qualitative trends are similar to that for methane jet diffusion flames (Takahashi and Vangsness, 1993) in which the jet velocities were much lower ( $<17$  m/s). Figure 4 shows the pdf's in nonswirling (Figs. 4(a)–4(e), Cases 1; Figs. 4(f)–4(j); Case 2) and swirling (Figs. 4(k)–4(o), Case 3) hydrogen flames at  $x = 25$  mm. At the edge of the outer thermal layer (Figs. 4(e), 4(j), and 4(o)), the pdf showed a sharp single peak with near room temperature. In the outer thermal layer outside the flame zone (Figs. 4(d), 4(i), and 4(n)), the pdf showed a bimodal distribution over a wide range from room temperature to flame temperature as a result of the radial movement of the flame zone. Thus, the rms value peaked in this layer. Occasional entrainment of cold air is seen still at the temperature peak location (Figs. 4(c), 4(h), and 4(m)). Inside the flame zone (Figs. 4(b), 4(g), and 4(l)), the pdf showed a single peak in a high-temperature range; thus, the rms value decreased. Further inside the innermost data point (Figs. 4(a),

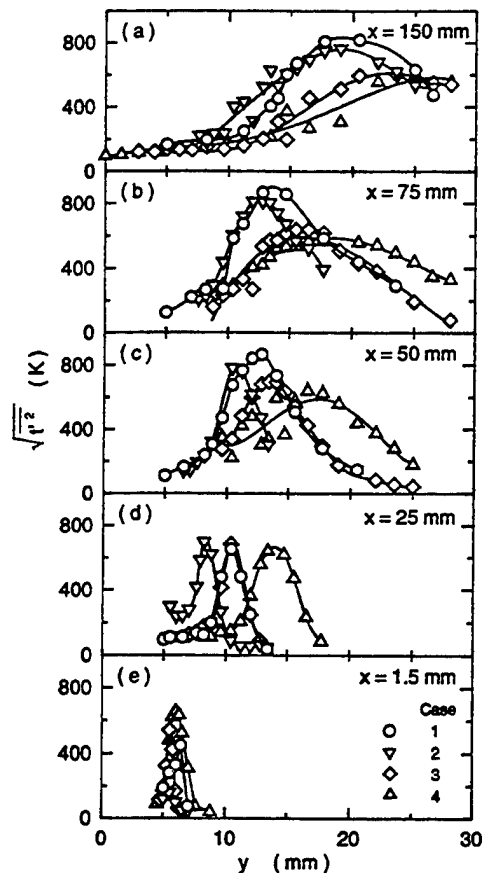


Fig. 3 Temperature fluctuation distribution across the hydrogen jet flame at five different heights

4(f), and 4(k)) where the intermittency began to increase, the mean temperature might be biased somewhat toward higher values than the time-average because the CARS measurement is based on nitrogen in hot combustion products.

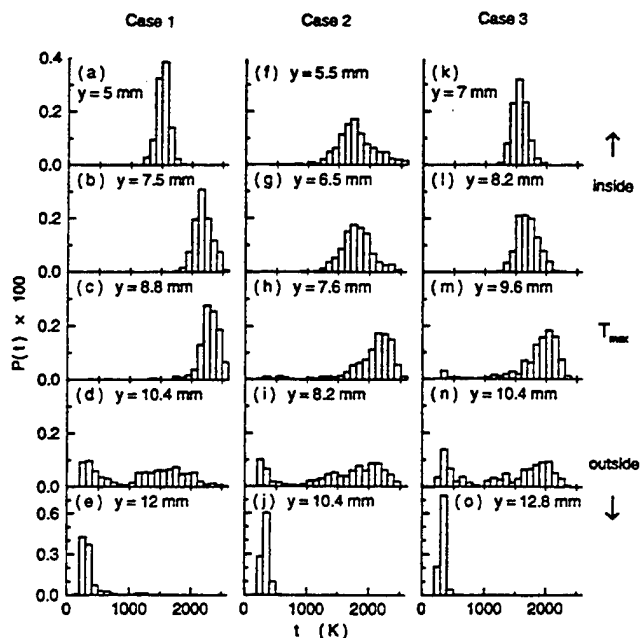


Fig. 4 Probability-density functions of temperature in the hydrogen flame (Cases 1–3) at five different radial locations at  $x = 25$  mm

**Mean and Turbulent Velocity Fields.** In addition to the quantitative LDV measurements, the conditional sampling based on the origin of seed particles provided qualitative characteristics of the turbulent structure of swirling and nonswirling hydrogen jet diffusion flames. Figure 5 shows the radial profiles of the mean axial velocity component at selected heights in the near field. Only the data points conditioned on the jet and annulus fluids are presented in the figure. The radial location of the apparent flame zone determined by the temperature peak is also included in the figure. Near the jet exit ( $x = 1.5$  mm; Fig. 5(c)), the data points for jet and annulus fluids do not overlap, and the shear layers originating from the boundary layers on both sides of the tube walls were observed in a wake region. The flame base is anchored in the low-velocity region of the annulus fluid stream. It is notable (in Figs. 5(a) and 5(b)) that the flame zone resides in the annulus fluid where the mean axial velocity profile is nearly constant; thus, not in the shear layer. As the jet velocity was increased for the nonswirling flow (from Case 1 to Case 2), the jet fluid spread with a larger angle because of enhanced turbulent stirring, whereas the flame zone shifted inward as mentioned earlier (Fig. 2). Swirl lowered the mean axial velocity of both jet fluid and annulus fluid (cf. Cases 2–4).

The impact of swirl appeared more evidently in the mean radial velocity profiles (Fig. 6); swirl induced the radial velocity component of the annulus fluid even at the near-exit plane. At  $x = 1.5$  mm (Fig. 6(c)), the mean radial velocity of the annulus fluid was small ( $<1$  m/s) for nonswirling flows (Cases 1 and 2), whereas for swirling flows (Cases 3 and 4), it increased up to  $\sim 2.5$  m/s and  $\sim 5$  m/s, respectively. Since the mean axial velocity of the annulus fluid was  $\sim 20$  m/s for Cases 3 and 4 (Fig. 5(c)), these values of radial velocity translate to the streamline off-axis angle of 7 and 14 deg, respectively. This peculiar behavior was not observed for cold air jets with swirl under the same jetting velocities (Takahashi et al., 1992). Since the effect of centrifugal forces on submicron-size tracer particles

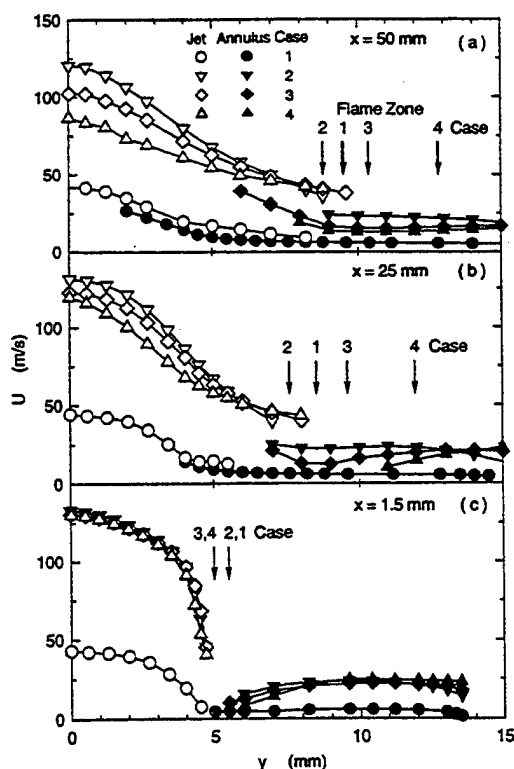


Fig. 5 Mean axial-velocity distribution across the hydrogen jet flame at three different heights

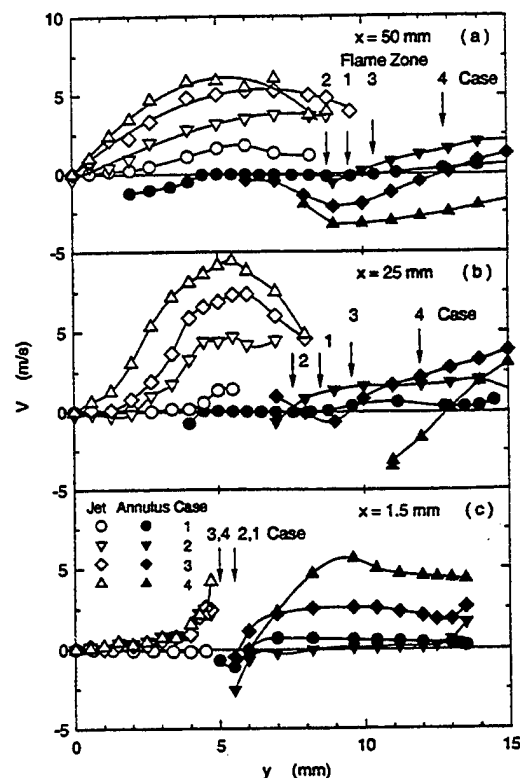


Fig. 6 Mean radial-velocity distribution across the hydrogen jet flame at three different heights

is small, the deflection of the streamlines was likely to be induced by the pressure field, which was distorted by swirl in a combusting flow with the density several times smaller than that of air. Although the geometric swirling number (based on the annulus flow) for  $\theta = 45$  deg was larger (0.78) than a critical value ( $\sim 0.6$  [Chigier and Beer, 1972]) for the formation of recirculation, no recirculation zone was formed because of a large jet velocity. However, the outward deflection of the annulus fluid apparently induced the radial velocity of the jet fluid downstream (Figs. 6(a) and 6(b)) to satisfy continuity of the fluid. Moreover, the differences in the mean velocities between jet fluid and annulus fluid at a same location were significant, particularly swirling flows. If conditional samplings were not made in the LDV measurement, the measured mean velocities would have been biased toward those of jet fluid, which had a higher axial velocity (and data rate), thus degrading the accuracy of measurements and covering the structure of the turbulent flow field.

Figure 7 shows the radial profiles of the mean tangential velocity component for swirling flows (Cases 3 and 4). The swirling motion, initially given only in the annulus fluid, spread into the jet fluid downstream. For  $\theta = 45$  deg, the tangential momentum penetrated into the jet fluid even near the axis at  $x = 25$  mm, whereas for  $\theta = 30$  deg, it did not reach the near-axis location even at  $x = 50$  mm.

Figure 8 shows the radial profiles of (absolute) turbulence intensities of axial, radial, and tangential velocity components at  $x = 25$  mm. The rms values of fluctuations (or the square root of second central moments) indicate the directional components of the absolute turbulence intensity (or twice turbulent kinetic energy [TKE]). For Case 1 ( $Re_j = 2208$ ), the turbulence intensities were relatively small ( $<5$  m/s) and nearly constant except for the region where the jet and annulus fluids overlap (the turbulent stirring layer). By contrast, for Cases 2–4 ( $Re_j = 8830$ ), all components of turbulence intensities showed a peak in the shear layer of the jet where the radial

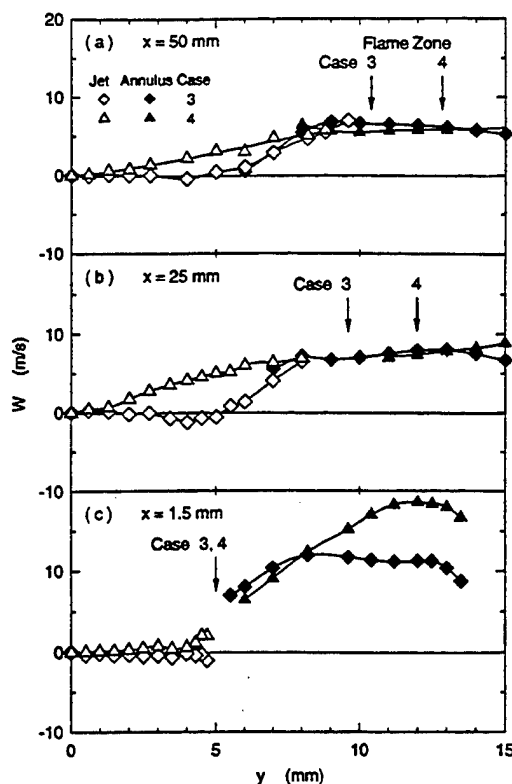


Fig. 7 Mean tangential-velocity distribution across the hydrogen jet flame at three different heights

gradient of mean axial velocity component was large, and the turbulence level of annulus fluid inside the flame zone increased rapidly in the turbulent stirring layer. The turbulence was aniso-

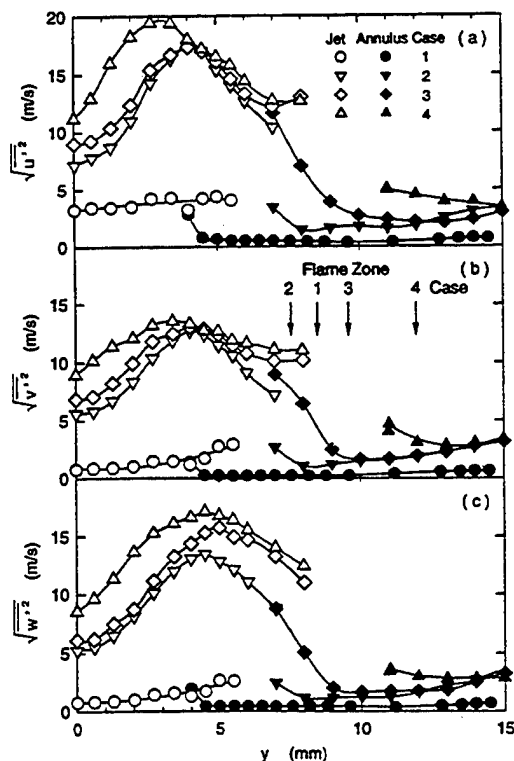


Fig. 8 Turbulence intensity distribution across the hydrogen jet flame at  $x = 25$  mm: (a) axial, (b) radial, and (c) tangential velocity components

tropic (i.e., the rms of the axial component was larger than those of radial and tangential components), typical of turbulent jets. As swirl became stronger (cf. Cases 2–4), the turbulence intensities increased, particularly in the central region ( $y < 4$  mm), where the mean axial velocity component decreased while the mean radial and tangential velocity components increased. It is noticed that for Case 4, the flame zone was subjected to high-intensity turbulence at  $x = 25$  mm; radial rms fluctuation reached  $\sim 4$  m/s in the near flame region where the mean radial velocity was  $\sim 3$  m/s.

Figure 9 shows the pdf's (histograms) of axial, radial, and tangential velocity components for both jet fluid (top three rows) and annulus fluid (bottom row) for Case 3 at selected radial locations at  $x = 25$  mm. Although these pdf's are selected samples, they represent typical characteristics of the mean and turbulent velocity fields in turbulent hydrogen jet diffusion flames shown as the mean velocity components (first central moments of the pdf's) in Figs. 5–7 and the turbulent intensities (second central moments) in Fig. 8. The characteristics related to shape of the pdf's (skewness and kurtosis) will be discussed in the next section.

Figure 10 shows the axial variations in the mean axial velocity component and turbulence intensities. As the jet velocity was increased for the nonswirling flames (from Cases 1 to 2), the mean axial velocity decayed more rapidly, and the turbulence intensities peaked at a location closer to the jet exit as a result of enhanced turbulent stirring, promoting transverse diffusion of turbulence. As swirl became stronger (cf. Cases 2–4), the velocity decay was accelerated further because of the faster spreading of the jet and enhanced turbulent mixing. The turbulence intensity peak shifted upstream further and became larger because of more intense turbulent stirring. Compared to nonreacting air jets studied previously (Takahashi et al., 1992), the axial velocity decayed more rapidly and turbulence intensity peak locations approached to the jet exit in current combusting flows (Cases 2–4).

**Turbulence Structure.** The detailed structure of the turbulence field in hydrogen jet diffusion flames is presented next for selected locations and conditions. Figure 11 shows the radial profiles of the Reynolds shear stress and gradient of the mean axial velocity. The most significant component of Reynolds shear stress tensor (or a cross central moment),  $u'v'$ , indicates

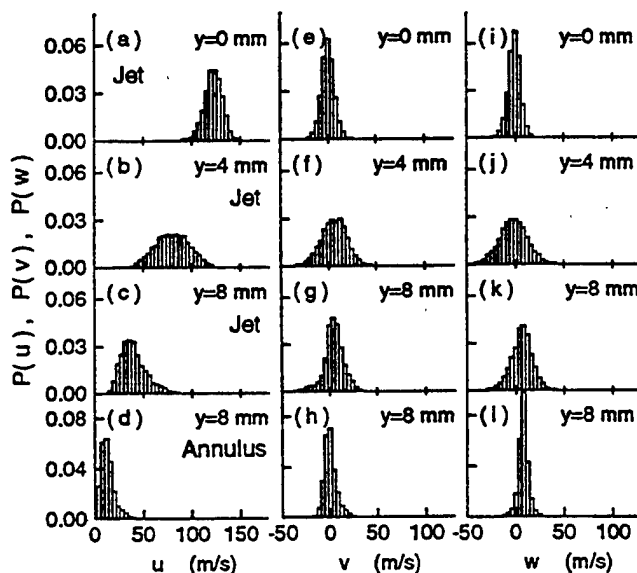


Fig. 9 Probability-density functions of velocity in the hydrogen jet flame (Case 3) at  $x = 25$  mm: (a–d) axial, (e–h) radial, and (i–l) tangential velocity components



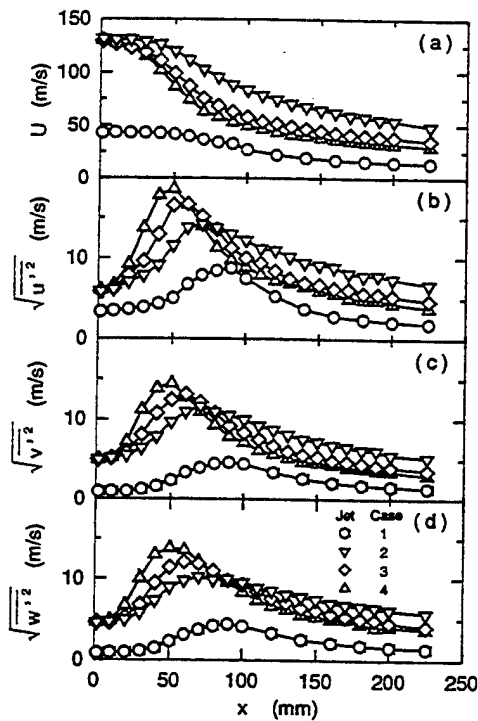


Fig. 10 (a) Mean axial velocity, (b) axial, (c) radial, and (d) tangential velocity fluctuations along the center-line of the hydrogen jet flame

the radial diffusion of axial momentum by turbulent transport. For all cases, the peak locations of the turbulence intensity of axial fluctuations (Fig. 8(a)) approximately coincide with those of the Reynolds shear stress (Fig. 11(a)) and the velocity gradient (Fig. 11(b)). The result is consistent with a most significant production term of the conservation equation for TKE: shear stress multiplied by strain. Thus, the production of TKE is primarily in the shear layer in the developing region in the near field, similar to self-preserving air jets (Hinze, 1975; Wygnanski and Fiedler, 1969). The production of TKE decays downstream as the shear stress and velocity gradient decrease (Takahashi et al., 1994a). For the low-velocity condition without swirl (Case 1), the peak values of the Reynolds shear stress are an order of magnitude smaller than that for the high-velocity

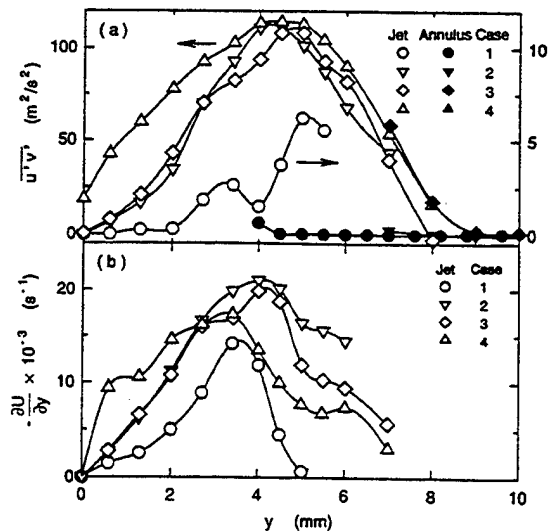


Fig. 11 Distribution of (a) Reynolds shear stress and (b) axial-velocity gradient across the hydrogen jet flame at  $x = 25$  mm

flame (Cases 2–4) and increased toward the outermost data point despite the vanished velocity gradient. This result might be caused by large-scale vortices that evolved near the boundary of the low-turbulence jet flame. The effect of swirl on the Reynolds shear stress is weak except for the central region ( $<4$  mm) for Case 4, where turbulence intensities increased. The other components of Reynolds shear stress tensor (not shown) are much smaller than  $u'v'$ .

Third-order central moments (triple correlations) provide characteristics of the diffusion term of the TKE equation. Figure 12 shows (a) the axial, (b) radial, and (c) tangential transport of the three components of TKE for Case 3 at  $x = 25$  mm. The axial diffusion of the axial and radial TKE components ( $u'^3$ ,  $v'^2u'$ ) and the radial diffusion of the axial and radial TKE components ( $u'^2v'$ , and  $v'^3$ ) show a common trend: They are negative in the inner region ( $y < 4$  mm) and positive in the outer region ( $y > 4$  mm) with a zero value at  $y = 0$  and 4 mm. The zero crossing point ( $y \approx 4$  mm) approximately coincides with the location where the second-order moments peaked (Figs. 8 and 11), as mentioned earlier. Therefore, the change in sign indicates that TKE was produced in the shear layer near  $y \approx 4$  mm and diffused both inward and outward. The radial gradients of these quantities appearing in the TKE balance equation indicate a gain or loss of each term. In the axial direction, TKE was transported upstream in  $y < 4$  mm and downstream in  $y > 4$  mm. The other moments are relatively small except for  $w'^3$ , which had a peak at  $y \approx 5$  mm.

Figure 13 shows the skewness and kurtosis (i.e., the third and fourth central moments, respectively, normalized by variance) of each velocity component for Case 3 at  $x = 25$  mm. Skewness is a measure of asymmetry of the pdf, with positive values implying a more gradual tailing off toward the higher-velocity side than the lower-velocity side. Kurtosis is a measure

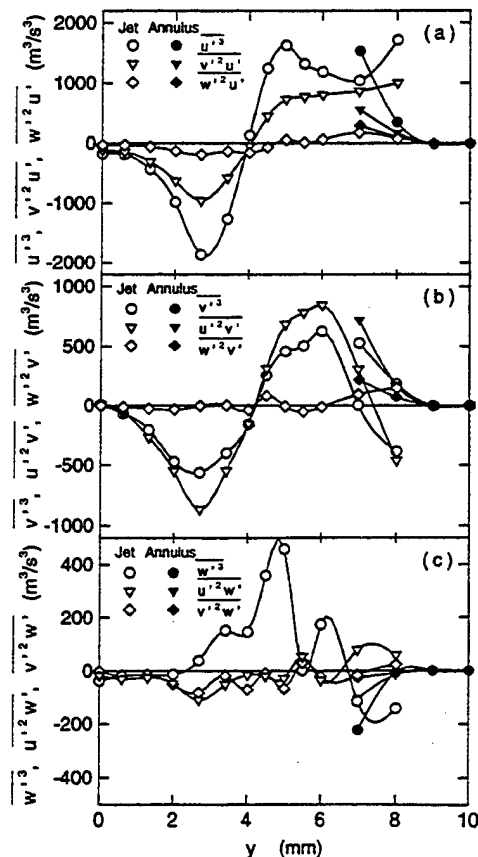


Fig. 12 Triple-correlation distribution across the hydrogen jet flame (Case 3) at  $x = 25$  mm

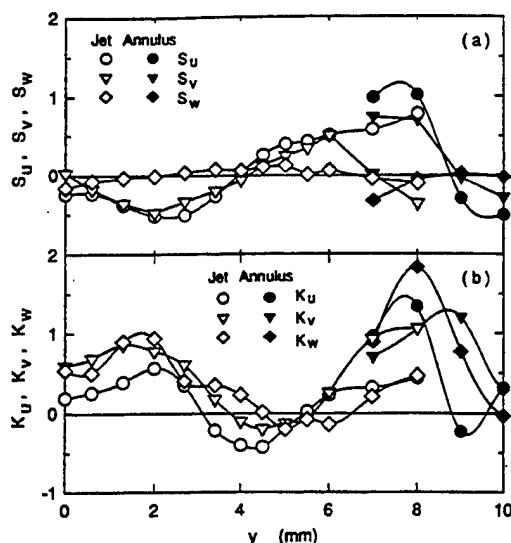


Fig. 13 Distribution of (a) skewness and (b) kurtosis across the hydrogen jet flame (Case 3) at  $x = 25$  mm

of the flatness of the pdf, with larger values corresponding to a top-hat shape rather than a gently curved hill. Both skewness and kurtosis for the Gaussian distribution are zero (kurtosis is defined here as the normalized fourth moment minus three). The skewness for the axial velocity component ( $S_u$ ) at  $x = 1.5$  mm and  $y = 0$  mm (not shown) was approximately  $-0.4$ , consistent with the value observed in fully developed turbulent pipe flows, implying upward TKE transport. Thus, the distributions of skewness and kurtosis in the developing region of jet flame are strongly affected by pipe-flow turbulence; they are different from self-preserving jets (Wyganski and Fiedler, 1969). The variations in skewness and kurtosis are consistent with the shape of the pdf's shown earlier (Fig. 9). The pdf's of the axial velocity component at  $y = 0$  and  $4$  mm (Figs. 9(a) and 9(b), respectively) show symmetric distributions ( $S_u \approx 0$ ), while at  $y = 8$  mm for both jet and annulus fluids (Figs. 9(c) and 9(d), respectively) the distribution was skewed toward the high-velocity side ( $S_u \approx 1$ ). Compared to the axial velocity component, the pdf's of radial and tangential components (Figs. 9(e)–9(l)) are fairly symmetric, except for the radial component for annulus fluid (Fig. 9(h)). Unlike self-preserving jets (Wyganski and Fiedler, 1969), in which both skewness and kurtosis increased monotonously toward the edge of the jet, their variations in the developing region of jet flames are more complicated due to the presence of the high-temperature region near the outermost data point for jet fluid.

## Conclusions

Detailed nonintrusive measurements of the velocity and temperature fields with the statistical treatment of the data revealed some characteristics of the developing region of turbulent hydrogen jet diffusion flames with or without swirl. Increasing the jet velocity shifts the apparent turbulent flame zone inward, makes the thermal layer thinner, and thus, strains the flame zone in the near field. On the other hand, swirl generally promotes turbulence and creates a positive radial velocity component even at the jet-exit plane (which, in turn, induces the radial velocity of the jet fluid), thereby shifting the flame zone outward and broadening the thermal layer. (The outward flow deflection was not observed in nonreacting air jets studied previously.) The peculiar result for the swirling flame is particularly important when applying the boundary conditions in computations; the upstream boundary may need to be taken well below the jet exit outside the pressure field variation due to swirl if the experimental results are not used as the boundary condition.

The distributions of second and third-order velocity moments provide a physical insight into the generation and diffusion of TKE. TKE is generated in the shear layer, where velocity gradient and Reynolds shear stress reach their peaks. TKE diffuses inward and outward from the shear layer and then downstream in the outer region and upstream in the inner region. Both skewnesses and kurtoses of velocity components in the near field were largely affected by the pipe-flow turbulence. The presence of swirl in the flame promoted early jet spread and turbulent stirring, thus accelerating the decay of the mean axial velocity and shifting the turbulence intensity peaks upstream. Bimodal temperature pdf's and, in turn, large rms values were observed on the air-side of the flame zone. The conditionally sampled velocity data and the nonintrusively measured temperature data presented in this paper can be used to validate advanced computational models capable of predicting the high-order moments (triple correlations) for each fluid.

## Acknowledgments

This work was supported by the U.S. Air Force, Wright Laboratory, Aero Propulsion and Power Directorate, Fuels and Lubrication Division, Wright-Patterson Air Force Base, Ohio, under Contract No. F33615-92-C-2207 (Technical Monitor: C. W. Frayne).

## References

- Anand, M. S., Pope, S. B., and Mongia, H. C., 1993, "PDF Calculations for Swirling Flows," AIAA Paper No. 93-0106.
- Anand, M. S., Takahashi, F., Vangsness, M. D., Durbin, M. D., and Schmoll, W. J., 1996, "An Experimental and Computational Study of Swirling Hydrogen Jet Diffusion Flames," *ASME Journal of Engineering for Gas Turbines and Power*, in press.
- Barlow, R. S., and Carter, C. D., 1994, *Combustion and Flame*, Vol. 97, p. 261.
- Bilger, R. W., 1976, "Turbulent Jet Diffusion Flames," *Progress in Energy and Combustion Science*, Vol. 1, pp. 87–109.
- Chigier, N. A., and Beer, J. M., 1972, *Combustion Aerodynamics*, Applied Science Publishing, London.
- Dibble, R. W., Hartmann, V., and Schefer, R. W., 1987, "Conditional Sampling of Velocity and Scalars in Turbulent Flames Using Simultaneous LDV-Raman Scattering," *Experiments in Fluids*, Vol. 5, pp. 103–113.
- Drake, M. C., 1988, "Stretched Laminar Flamelet Analysis of Turbulent  $H_2$  and  $CO/H_2/N_2$  Diffusion Flames," *Twenty-First Symposium (International) on Combustion*, The Combustion Institute, pp. 1579–1589.
- Durbin, M. D., Vangsness, M. D., and Takahashi, F., 1993, "Stability of Hydrogen/Air Double-Concentric Jet Diffusion Flames With and Without Swirl," Eastern States Section/The Combustion Institute Meeting, Princeton, NJ, Oct.
- Edwards, R. V., 1987, "Report of the Special Panel on Statistical Particle Bias Problems in Laser Anemometry," *ASME Journal of Fluids Engineering*, Vol. 109, pp. 89–93.
- Eickhoff, H., 1982, "Turbulent Hydrocarbon Jet Flames," *Progress in Energy and Combustion Science*, Vol. 8, pp. 159–168.
- Faeth, G. M., and Samuelsen, G. S., 1986, "Fast Reaction Nonpremixed Combustion," *Progress in Energy and Combustion Science*, Vol. 12, pp. 305–372.
- Gollahalli, S. R., Savas, O., Huang, R. F., and Roderiguez Azara, J. L., 1988, "Structure of Attached and Lifted Gas Jet Flames, in Hysteresis Region," *Twenty-First Symposium (International) on Combustion*, The Combustion Institute, pp. 1463–1471.
- Harsha, P. T., 1971, "Free Turbulent Mixing: A Critical Evaluation of Theory and Experiment," AEDC-TR-71-36, Arnold Engineering Development Center, Arnold Air Station, TN.
- Hinze, J. O., 1975, *Turbulence*, 2nd ed., McGraw-Hill, New York.
- Launder, B. E., and Spalding, D. B., 1972, *Lectures in Mathematical Models of Turbulence*, Academic Press, London.
- Libby, P. A., Chigier, N., and LaRue, J. C., 1982, "Conditional Sampling in Turbulent Combustion," *Progress in Energy and Combustion Science*, Vol. 8, pp. 203–231.
- Nandula, S. P., Brown, T. M., and Pitz, R. W., 1994, "Measurements of Scalar Dissipation in the Reaction Zones of  $H_2$ -Air Turbulent Diffusion Flames," *Combustion and Flame*, Vol. 99, p. 775.
- Pitz, R. W., Cheng, T. S., March, S. R., and Wehrmeyer, J. A., 1991, "Effects of Swirl on Finite-Rate Chemistry in Lifted Jet Diffusion Flames," AIAA Paper No. 91-2139.
- Pope, S. B., 1990, "Computations of Turbulent Combustion: Progress and Challenges," *Twenty-Third Symposium (International) on Combustion*, The Combustion Institute, pp. 591–612.
- Stärner, S. H., 1985, "Conditional Sampling in a Turbulent Diffusion Flame," *Combustion Science and Technology*, Vol. 42, pp. 283–299.

- Stärner, S. H., and Bilger, R. W., 1988, "Joint Measurements of Velocity and Scalars in a Turbulent Diffusion Flame With Moderate Swirl," *Twenty-First Symposium (International) on Combustion*, The Combustion Institute, pp. 1569-1577.
- Takahashi, F., Mizomoto, M., and Ikai, S., 1982, "Transition From Laminar to Turbulent Free Jet Diffusion Flames," *Combustion and Flame*, Vol. 48, pp. 85-95.
- Takahashi, F., and Goss, L. P., 1992, "Near-Field Turbulent Structures and the Local Extinction of Jet Diffusion Flames," *Twenty-Fourth Symposium (International) on Combustion*, The Combustion Institute, pp. 351-359.
- Takahashi, F., Vangsness, M. D., and Belovich, V. M., 1992, "Conditional LDV Measurements in Swirling and Nonswirling Coaxial Turbulent Air Jets for Model Validation," AIAA Paper No. 92-0580.
- Takahashi, F., and Vangsness, M. D., 1993, "Near-Field CARS Measurements and the Local Extinction of Turbulent Jet Diffusion Flames," *Dynamics of Heterogeneous Combustion and Reacting Systems*, A. L. Kuhl, J.-C. Leyer, A. A. Borisov, and W. A. Sirignano, eds., *Progress in Aeronautics and Astronautics*, Vol. 152, pp. 37-55.
- Takahashi, F., Durbin, M. D., Vangsness, M. D., and Schmoll, W. J., 1993, "LDV Measurements in Swirling and Nonswirling Coaxial Turbulent Hydrogen Jet Diffusion Flames—No. 1: No Swirl, 25 m/s," UDR-TR-93-88; "No. 2: No Swirl, 100 m/s," UDR-TR-94-116, University of Dayton, Dayton, OH.
- Takahashi, F., Durbin, M. D., Vangsness, M. D., and Schmoll, W. J., 1994a, "LDV Measurements in Swirling and Nonswirling Coaxial Turbulent Hydrogen Jet Diffusion Flames—No. 3: 30-degree Swirl, 100 m/s," UDR-TR-94-116; "No. 4: 45-degree Swirl, 100 m/s," UDR-TR-94-117, University of Dayton, Dayton, OH.
- Takahashi, F., Vangsness, M. D., Schmoll, W. J., and Durbin, M. D., 1994b, "CARS Temperature Measurements in Swirling and Nonswirling Coaxial Turbulent Hydrogen Jet Diffusion Flames," UDR-TR-94-89, University of Dayton, Dayton, OH.
- Takahashi, F., Durbin, M. D., and Vangsness, M. D., 1996, "Stabilization of Hydrogen Jet Diffusion Flames With or Without Swirl," *Transport Phenomena in Combustion*, S. H. Chan, ed., Taylor & Francis, Washington, DC, in press.
- Tangirala, V., Chen, R. H., and Driscoll, J. F., 1987, "Effect of Heat Release and Swirl on the Recirculation Within Swirl-Stabilized Flames," *Combustion Science and Technology*, Vol. 51, pp. 75-95.
- Wynanski, I., and Fiedler, H., 1969, "Some Measurements in the Self-Preserving Jet," *Journal of Fluid Mechanics*, Vol. 38, pp. 577-612.

## **APPENDIX H**

### **Study of Flame Stability in a Step Swirl Combustor**

**M. D. Durbin, M. D. Vangsness,  
D. R. Ballal, V. R. Katta**

# Study of Flame Stability in a Step Swirl Combustor

M. D. Durbin

M. D. Vangsness

D. R. Ballal

Fellow ASME

University of Dayton,  
Dayton, OH 45469

V. R. Katta

Innovative Scientific Solutions, Inc.,  
Dayton, OH 45430

*A prime requirement in the design of a modern gas turbine combustor is good combustion stability, especially near lean blowout (LBO), to ensure an adequate stability margin. For an aeroengine, combustor blow-off limits are encountered during low engine speeds at high altitudes over a range of flight Mach numbers. For an industrial combustor, requirements of ultralow  $\text{NO}_x$  emissions coupled with high combustion efficiency demand operation at or close to LBO. In this investigation, a step swirl combustor (SSC) was designed to reproduce the swirling flow pattern present in the vicinity of the fuel injector located in the primary zone of a gas turbine combustor. Different flame shapes, structure, and location were observed and detailed experimental measurements and numerical computations were performed. It was found that certain combinations of outer and inner swirling air flows produce multiple attached flames, a flame with a single attached structure just above the fuel injection tube, and finally for higher inner swirl velocity, the flame lifts from the fuel tube and is stabilized by the inner recirculation zone. The observed difference in LBO between co- and counterswirl configurations is primarily a function of how the flame stabilizes, i.e., attached versus lifted. A turbulent combustion model correctly predicts the attached flame location(s), development of inner recirculation zone, a dimple-shaped flame structure, the flame lift-off height, and radial profiles of mean temperature, axial velocity, and tangential velocity at different axial locations. Finally, the significance and applications of anchored and lifted flames to combustor stability and LBO in practical gas turbine combustors are discussed.*

## Introduction

A prime requirement in the design of a modern gas turbine combustor is good combustion stability, especially near lean blowout (LBO), to ensure an adequate stability margin. For an aircraft engine, combustor blow-off limits are encountered during low engine speeds at high altitudes over a range of flight Mach numbers and a good design ensures that the combustor steady-state burning remains within the operating envelope. This envelope should be extensive enough to encompass the under- and overshoots associated with the different response rates to the throttle movements of the fuel system and the rotating machinery. For an industrial combustor, requirements of ultralow  $\text{NO}_x$  emissions coupled with high combustion efficiency demand operation at or close to LBO, thereby eroding the safety margins. Therefore, a fundamental study of flame stability in a model step swirl combustor (SSC) has important practical applications, and this provided a strong motivation to undertake the present investigation.

The physical mechanisms responsible for the stabilization of a flame on the fuel injector lip (in the near-field region) are not fully understood. In the past, the stabilization mechanism of free jet diffusion flames has been investigated by Vanquickenborne and van Tiggelen (1966), Gollahalli et al. (1985), Pitts (1988, 1990), Bradley et al. (1990), Takahashi et al. (1984, 1990), and Takahashi and Goss (1992). A prime goal of these investigations was to predict flame blowout accurately. For example, Vanquickenborne and van Tiggelen (1966) developed the stabilization criterion that the total approach velocity should be balanced by the turbulent burning velocity of the mixture. Takahashi et al. (1984) found that the local velocities in the vicinity of an attached flame are laminar, and the flame stability mechanism is the balance of the total approach velocity

in the attached flame zone with the laminar burning velocity of the mixture. However, in a modern annular gas turbine combustor, the flame is stabilized by producing a swirl-induced recirculation zone in the flow field. This zone is generated by a combination of three mechanisms: an axial swirling air jet associated with each fuel introduction, sudden expansion of the axial swirling jets as they enter the primary zone, and back pressure provided by an array of radial air jets at the end of the primary zone. An SSC was designed to reproduce this type of complicated recirculation flow pattern. This paper discusses the different shapes, structure, and location of the stabilized flame in the SSC and how these various factors affect LBO.

## Test Facility

**The SSC.** Figure 1 shows a schematic diagram of the SSC, which has a  $150 \times 150$ -mm cross section with rounded corners, length of 754 mm, and a step height of 55 mm. The SSC provides a geometrically simple, optically accessible research combustor capable of reproducing the fuel-air mixing pattern downstream of the airblast atomizer located in the dome region of a modern annular gas turbine combustor. The SSC also offers independent control over inner and outer airstreams. The SSC was mounted on a vertical combustion tunnel with a three-axis traversing mechanism.

Fuel was supplied to the combustor by the annular fuel tube (20 mm i.d. and 29 mm o.d.), which is coaxially sandwiched between swirling airstreams: the inner air jet (20-mm-dia) and the outer annular air jet (29 mm i.d. and 40 mm o.d.). The combustor exit has a 45 percent blockage orifice plate on top, which simulates the back pressure exerted by the dilution jets in a practical gas turbine combustor (see Sturgess et al., 1990). The SSC has quartz windows on all four sides to permit visual observations and laser diagnostics measurements. The stationary helical vane swirlers were located 25 mm upstream from the burner tube exit in each of the air passages. The inner swirler has six vanes with a central 1.4-mm-dia hole to prevent the flame from anchoring to the swirler. The outer swirler has

Contributed by the International Gas Turbine Institute and presented at the 40th International Gas Turbine and Aeroengine Congress and Exhibition, Houston, Texas, June 5-8, 1995. Manuscript received by the International Gas Turbine Institute February 10, 1995. Paper No. 95-GT-111. Associate Technical Editor: C. J. Russo.

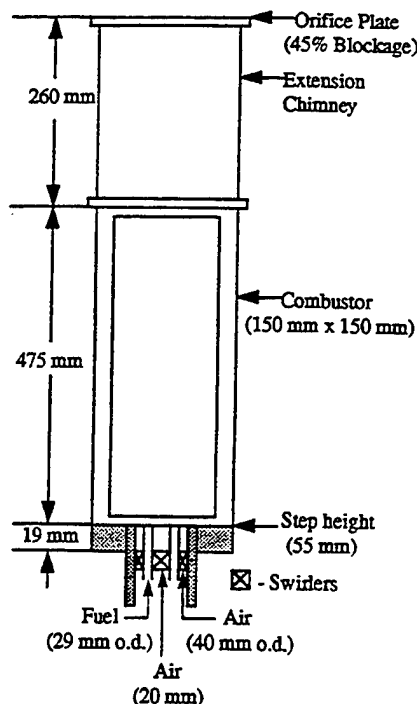


Fig. 1 Schematic diagram of a step swirl combustor

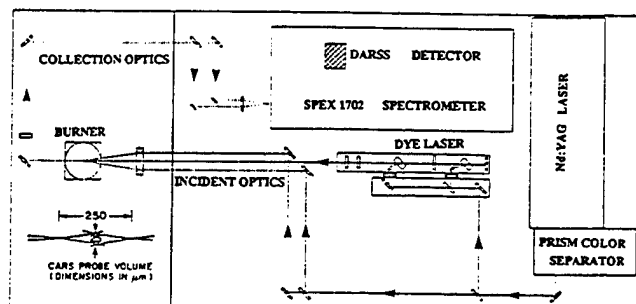


Fig. 2 Schematic of the CARS system optics

twelve vanes. Inner swirler lengths are 25 and 19 mm, respectively, for 30 and 45 deg swirlers; outer swirler length was 32 mm for the 30 deg swirler. Swirler lengths and number of vanes were adequate to ensure that the air closely follows the swirl vane angle. The swirlers were precision-fabricated in a rapid prototype manufacturing process known as stereolithography. These swirlers performed satisfactorily at the level of high temperatures present in the SSC.

#### Instrumentation

**CARS System.** Figure 2 shows a schematic of a Coherent Anti-Stokes Raman Spectroscopy (CARS) optics system, which was used for nonintrusive flame temperature measurements. Pan et al. (1991) have provided detailed information on

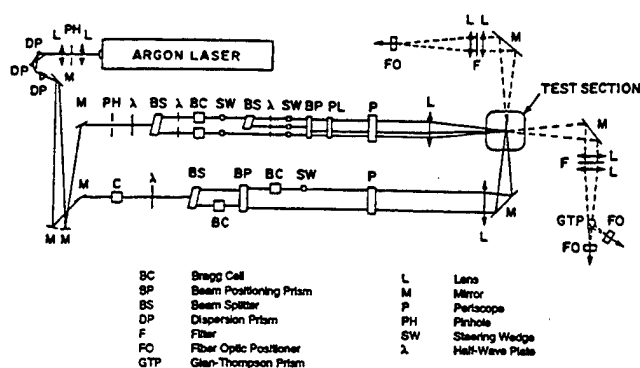


Fig. 3 Schematic of the LDA system optics

CARS measurements. Briefly, the CARS signal was generated by combining two 30 mJ doubled Nd:Yag beams at 532 nm and one 25 mJ broad band dye laser beam centered at 607 nm and pumped by the same Nd:Yag laser. The pulse laser and detector camera run at 10 Hz. A Boxcars configuration with an ellipsoidal probe volume approximately  $25 \mu\text{m}$  (dia)  $\times$   $250 \mu\text{m}$  (length) was used for collecting the signal. The detector is a Princeton Instruments intensified  $576 \times 384$  charge coupled device (CCD). The intensifier is triggered by a Princeton PG-10 pulser. A Princeton ST-130 controller operates the camera and the detector chiller. The collection process is controlled by Princeton's ST-130 CSMA software package running on a personal computer. Spectra are fit to a library of spectra by a nonlinear fitting routine running on a personal computer. A total of 250 samples were taken for each CARS temperature measurement.

**LDA System.** Figure 3 illustrated the optical setup of the LDA system. Nonintrusive velocity measurements were made using a Dantec Fiber-Flow LDA system. Essentially, this LDA system is an upgraded version of the system used by Durbin and Ballal (1996). The two-dimensional LDA system uses the 514 nm and 488 nm lines from an argon-ion laser. The laser output is directed into a Dantec Fiber flow transmitter where the colors are separated and directed to optical fiber couplers by a Bragg cell operating at 40 MHz. The four beams are guided to the probe via polarization preserving fibers. The recollimated and focused laser beams cross to produce an ellipsoidal probe volume approximately  $100 \mu\text{m}$  (dia)  $\times$   $1000 \mu\text{m}$  (length). A fluidized-bed seeder was used to inject submicron-sized (97 percent  $< 1 \mu\text{m}$ )  $\text{ZrO}_2$  particles into each burner tube passage. Velocity biasing was resolved by seeding one passage at a time in a manner similar to Takahashi et al. (1992). The forward scattered signal is collected and separated by dichroic mirrors before it is detected by photomultiplier tubes and processed by individual TSI burst counters. Typical coincident sampling rates exceeded 1 kHz in flames. A total of 2048 coincident samples were collected for each velocity measurement. Custom-designed software was used to reduce the data on a personal computer. Three-component noncoincident velocity measurements were made with the two-dimensional LDA system by scanning in the transverse and radial directions to get axial and

#### Nomenclature

$k$  = turbulent kinetic energy  
 $Re$  = Reynolds number  
 $T$  = mean temperature  
 $U, W$  = mean axial and tangential velocities, respectively

$X, Y, Z$  = transverse, radial, and axial directions, respectively  
 $\epsilon$  = turbulent-energy dissipation rate  
 $\theta$  = swirl vane angle  
 $\phi$  = overall equivalence ratio

#### Subscripts

$f$  = fuel  
 $i$  = inner  
 $o$  = outer

Table 1 Test matrix for the step swirl combustor experiments (all tests at room temperature and atmospheric pressure)

Variable	Range
Inner vane angle, $\theta_i$ , degrees	0, 30 and 45
Outer vane angle, $\theta_o$ , degrees	30
Vane configuration	co and counter-swirl
Inner air velocity, $U_i$ , m/s	14.4
Re	$18.0 \times 10^3$
Outer air velocity, $U_o$ , m/s	8.6
Re	$14.8 \times 10^3$
Fuel velocity, $U_f$ , m/s	2.5
Re	$3.2 \times 10^3$
Equivalence ratio, $\phi$	0.9
Fuel	methane

tangential velocities, and axial and radial velocities, respectively.

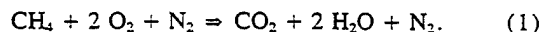
**Test Conditions.** Table 1 lists all the test conditions. Durbin and Ballal (1996) have shown that increasing the inner vane angle increases turbulent mixing and strengthens the inner recirculation zone; these changes dramatically affect the flame structure and the stability characteristics. Therefore, experiments were performed to reveal the differences in flame structure by changing the inner vane angle. Test conditions were also chosen to compare: (i) attached versus lifted flames and (ii) co-versus counterswirl configurations.

Experimental measurements included flame photography, three-component mean and rms velocities, mean and rms temperatures, and LBO. The LBO data were collected by maintaining a constant airflow rate, heating the combustor to a near steady-state temperature at stoichiometric fuel-air ratio, and then gradually decreasing the fuel flow rate until blowout occurred. This is a standard procedure that has been adopted in our laboratory since the work of Sturgess et al. (1991).

### Turbulent Combustion Model

A time-dependent axisymmetric model, which solves axial and radial-momentum equations, continuity, swirl, turbulent energy ( $k$ ), turbulent-energy dissipation ( $\epsilon$ ), and enthalpy and species conservation equations was used to simulate the flow-field in the SSC. The standard isotropic  $k$ - $\epsilon$  turbulence model was incorporated into this code. Details are described by Katta and Roquemore (1993) and Katta et al. (1994). Briefly, in this turbulence model, density ( $\rho$ ) was obtained by solving the state equation while pressure field at every time step is determined from pressure Poisson equations. Even though all the governing equations were solved in an uncoupled manner, the turbulence and species conservation equations are coupled through the source terms during the solution process to improve the stability of the algorithm.

In the present analysis of reacting flows, a simple global-chemical-kinetics model involving methane, oxygen, water, carbon dioxide, and nitrogen was used as follows:



The specific reaction rate for Eq. (1) was written in Arrhenius form with an activation energy of 20 kcal/mole and pre-exponential of  $2.0 \times 10^{19} \text{ m}^6/\text{mole}^2/\text{s}$ . These rate constants were determined by predicting the lift-off of a 8 m/s laminar methane jet flame (Katta, 1995).

An orthogonal, staggered grid system with varying cell sizes in both the  $z$  and  $y$  directions was utilized. The momentum and swirl equations were integrated using an implicit Quadratic Upstream Interpolation for Convective Kinematics with Estimated Streaming Terms (QUICKEST) numerical scheme

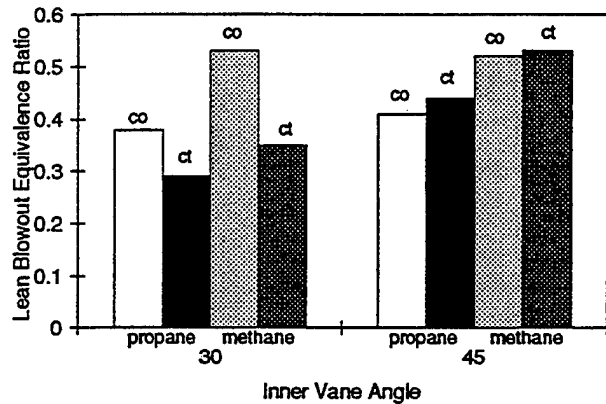


Fig. 4 Lean blowout data comparing inner vane angle, co-swirl (co) and counter-swirl (ct), and methane with propane. Test conditions were  $\theta_o = 30^\circ$ ,  $\phi = 0.9$ ,  $U_i = 14.4 \text{ m/s}$ ,  $U_o = 8.6 \text{ m/s}$ ,  $U_f = 2.5 \text{ m/s}$ .

(Katta et al., 1994; Leonard 1979), which is third-order accurate in both space and time and has a very low numerical diffusion error. On the other hand, the species, enthalpy, and turbulence-energy conservation equations, which have relatively large source terms, were integrated using the hybrid scheme of Spalding (1972). By rearranging the terms, the finite-difference form of each governing equation at all grid points was written as a system of algebraic equations, which was then solved by using Alternative Direction Implicit (ADI) technique. The time increment,  $\Delta t$ , was determined from the stability constraint and maintained as a constant during the entire calculation. The pressure field at every time step was accurately calculated by simultaneously solving the system of algebraic pressure Poisson equations at all grid points using the LU (Lower-Upper) decomposition technique.

Temperature- and species-dependent thermodynamic and transport properties were used in this formulation. The enthalpy of each species was calculated from polynomial curve-fits, while the viscosity, thermal conductivity, and diffusion coefficients of the species were estimated from the Leonard-Jones potentials. Measured velocity profiles were used at the fuel and air inflow boundaries. All other flow variables ( $k$ ,  $\epsilon$ , mass fractions, and  $T$ ) along these boundaries were assumed to be distributed uniformly. A simple extrapolation procedure (Katta et al., 1994) with weighted zero- and first-order terms was used to estimate the flow variables on the outflow boundary. The usual no-slip, adiabatic, and chemically inert boundary conditions were applied at the walls. Wall functions were used for determining the gradients of the flow variables near the walls.

### Results and Discussion

#### Experimental Observations

**Flame Stability.** LBO data were collected for all test conditions. In addition, some propane LBO data were collected to examine fuel effects on flame stability. Figure 4 shows LBO data comparing co- and counterswirl and propane with methane. These differences will be discussed after examining flame characteristics utilizing long exposure flame photographs taken with a 35-mm camera. Figure 5(a-e) reveal dramatic flame structure differences in the five test configurations. The only two variables in test conditions for the five cases were inner vane angle and co- or counterswirl configuration. Test conditions were  $\theta_o = 30^\circ$ ,  $\phi = 0.9$ ,  $U_i = 14.4 \text{ m/s}$ ,  $U_o = 8.6 \text{ m/s}$ ,  $U_f = 2.5 \text{ m/s}$ , using methane fuel.

Figure 5(a) shows that no swirl in the inner air stream produces a long tubelike central flame structure. The 30 deg outer-swirl produces an outer flame structure, which approximates the 30 deg pattern. The attached flame appears to be stabilized

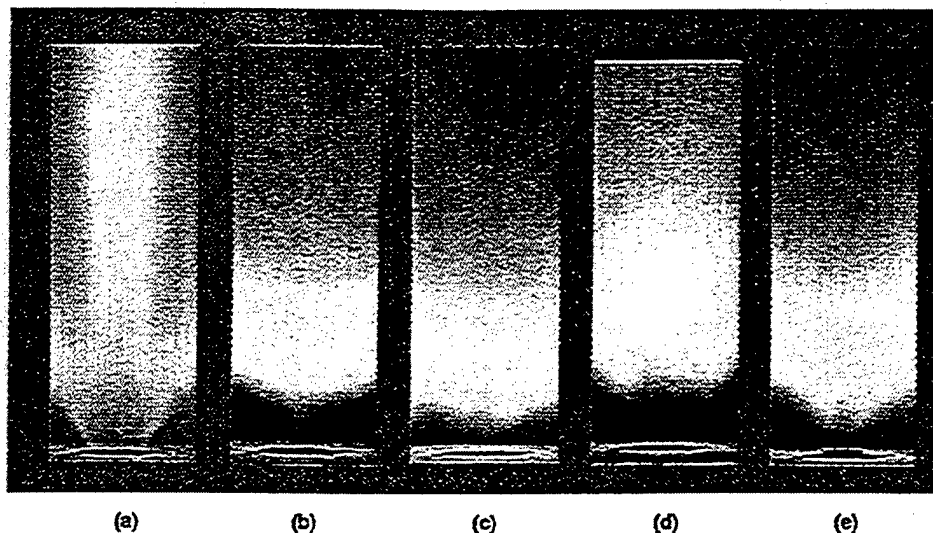


Fig. 5 Photographs illustrating the flame structure for (a)  $\theta_i = 0$  deg, (b)  $\theta_i = 30$  deg coswirl, (c)  $\theta_i = 45$  deg coswirl, (d)  $\theta_i = 30$  deg counterswirl, and (e)  $\theta_i = 45$  deg counterswirl. Test conditions were  $\theta_o = 30$  deg,  $\phi = 0.9$ ,  $U_i = 14.4$  m/s,  $U_o = 8.6$  m/s,  $U_r = 2.5$  m/s, methane.

at the inner air side of the fuel tube and also at the outer air side of the fuel tube. Small traces of flame structure outside the outer air stream are also visible and this can only occur if the fuel penetrates the fast-moving outer air stream or if the fuel recirculates in the outer recirculation zone before burning. It is suspected that the dynamic characteristics of the turbulent flow bring packets of fuel into the recirculation zone and these packets, in turn, burn in the mixing layer of the outer air and the recirculation zone. Sturgess et al. (1991) have observed similar results for a flame stabilized in the outer recirculation zone. This dynamic turbulent exchange phenomenon is more dramatic for an outer vane angle of 60 deg, which produces a stronger outer recirculation zone.

Figure 5(b) shows a flame photograph with coswirl configuration and 30 deg inner vane angle. The flame is lifted, there is premixing at its base, and it stabilizes with a dimple shape within the inner recirculation zone. The flame lifts because the

inner air stream penetrates the fuel stream with a velocity too high for an attached flame to stabilize and the flame is blown downstream. Also, the inner recirculation is caused by the inner air stream pushing out toward the wall, leaving a low-pressure region in the central portion of the combustor. Chen and Driscoll (1988) have made similar observations on the formation and structure of an inner recirculating vortex. Figure 5(c) shows that increasing the inner vane angle from 30 deg coswirl to 45 deg coswirl widens the flame shape and decreases the lift height. This occurs because an increase in vane angle increases the size and strength of the inner recirculation zone but it does not change the stability mechanism; i.e., flame is still stabilized within the inner recirculation zone.

Figure 5(d) shows the flame structure for 30 deg inner vane angle counterswirl. The flame has a bulbish shape above the fuel tube. Decreasing the fuel flow velocity causes the flame attachment just above the fuel tube. Figure 5(e) shows that

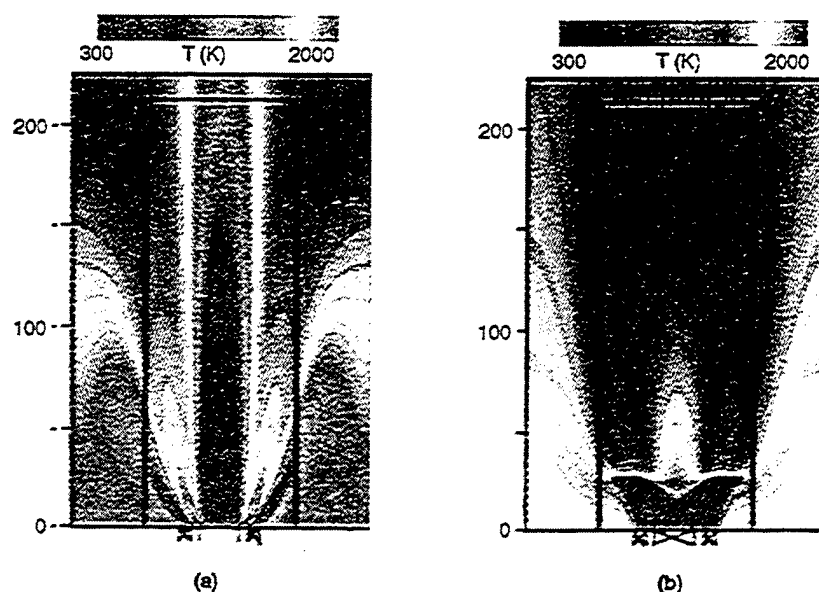
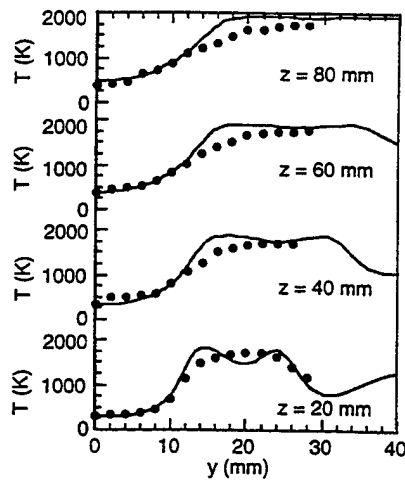
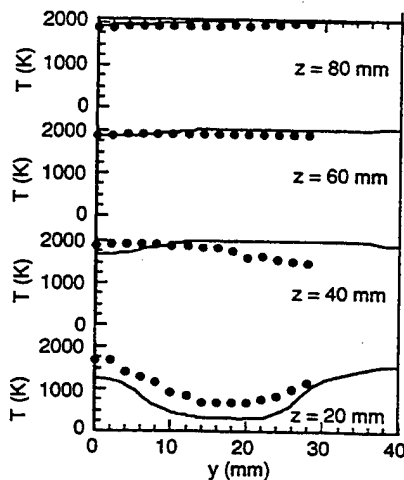


Fig. 6 Computed temperature distribution in SSC for (a)  $\theta_i = 0$  deg and (b)  $\theta_i = 30$  deg coswirl. Test conditions are identical to Figs. 5(a) and 5(b), respectively.





(a)



(b)

Fig. 7 Radial temperature profiles at different axial locations for (a)  $\theta = 0$  deg, and (b)  $\theta = 30$  deg. Test conditions correspond with Figs. 5(a) and 5(b), respectively.  $\bullet$  Experimental, —computational.

increasing the inner vane angle from 30 deg counterswirl to 45 deg counterswirl causes too much penetration of the inner air into the fuel zone and this causes the flame to lift and stabilize within the inner recirculation zone.

**Lean Blowout.** Figure 4 shows LBO data comparing co- and counterswirl for two values of the inner vane angle, namely 30 and 45 deg, for both methane and propane gaseous fuels. The propane data were taken at identical test conditions for comparison purposes. Three observations can be made:

1 LBO values were found to be lower with propane fuel than with methane fuel for all the conditions of the tests. A plausible explanation is that the air/methane mass velocity ratio  $(\rho U)_a/(\rho U)_m$  is higher than the corresponding air/propane ratio; this produces enhanced methane-air mixing (as compared to propane-air mixing) and hence a higher value of LBO. Figures 5(b), 5(c), and 5(e) for methane flames clearly show an evidence of premixing at the flame base followed by a lifted flame structure stabilized in the inner recirculation zone.

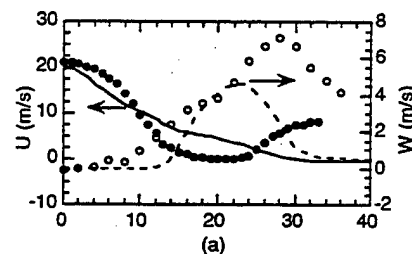
2 For a 30 deg inner vane angle, LBO values were lower for counterswirl as opposed to coswirl flow direction. This result

arises because for the counterswirl flow, shearing braids cause lower air velocities just above the fuel tube leading to an attached flame (which has a lower value of LBO); in contrast the coswirl flow gives higher axial mean velocity directly above the fuel tube, causing the flame to lift from the fuel tube thereby compromising flame stability; i.e., higher values of LBO are obtained.

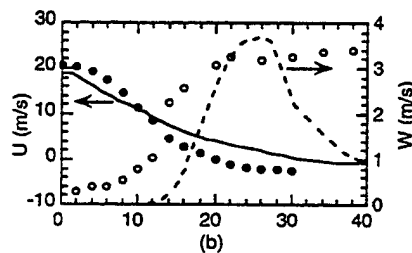
3 As the inner vane angle is increased from 30 to 45 deg, LBO values increase correspondingly and also LBO becomes less sensitive to swirl flow direction. This happens because the higher (45 deg) inner swirl angle directs more inner airflow toward the fuel tube, causing the flame to lift. This lifted flame produces higher values of LBO.

### Analysis

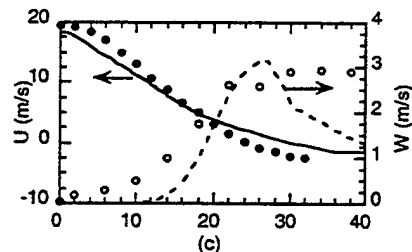
**Flame Stability—Computed Results.** Predictions were made for different flow conditions using the turbulent combustion model described earlier. Results in the form of temperature distributions for zero- and 30 deg inner coswirl cases (corresponding to Figs. 5(a) and 5(b) are shown in Figs. 6(a) and 6(b), respectively. Measured axial, radial, and tangential velocity profiles at the exits of the inner-air and fuel tubes and turbulent mass-averaged outer air velocity obtained from the volu-



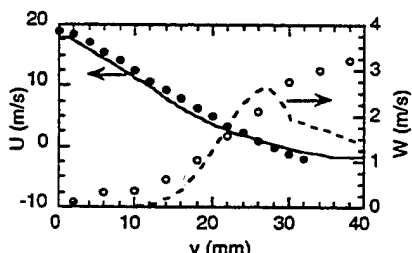
(a)



(b)



(c)



(d)

Fig. 8 Calculated and measured velocities for  $\theta = 0$  deg case at axial locations (a) 20 mm, (b) 40 mm, (c) 60 mm, and (d) 80 mm. Circles and lines represent measured and computed velocities, respectively.

metric flow rate provided the inlet boundary conditions for these predictions. Figures 6(a) and 6(b) show the predicted flame images, i.e., temperature distributions corresponding to flame photographs shown in Figs. 5(a) and 5(b). Note, the inner box marked on the computed-flame images corresponds with the dimensions of the flame photographs. The following observations were made from the calculated temperature fields: (i) In Fig. 6(a) (zero inner swirl), the computations correctly predicted the locations of flames on either side of the fuel jet. (ii) In Fig. 6(b) (30 deg coswirl), a recirculation bubble develops inside the inner air jet and it produces the dimple-shaped flame, and (iii) the lift-off height for case (ii) predicted by the model matches well with the experimental data. These computations support the qualitative observations on flame photographs described above.

The calculated radial temperature profiles at different axial locations are compared with the measured data in Figs. 7(a) and 7(b) for zero swirl and 30 deg swirl cases, respectively. In Fig. 7(a), in the absence of swirl, the inner air jet spreads gradually, leading to a long tubelike inner flame. Both the calculations and measurements show that the temperature at the center of the SSC over the measurement range ( $z = 0$  to 80 mm) is nearly the same as that of the room temperature air.

Figures 8 and 9 illustrate a comparison between predicted and measured velocities for the zero and 30 deg swirl cases, respectively. Axial ( $U$ ) and swirl ( $W$ ) velocity components were compared at different axial locations. For the no-swirl case, calculated velocity profiles agreed well with the experimental data. With 30 deg inner swirl, the measured swirl velocity was generally higher than the predictions, especially in the regions  $Y > 22$  mm. Since the outer air was not seeded and the outer velocity profile was approximated, there are discrepancies at locations radially away from the outer jet.

In summary, our simple turbulence model with a single-step global-chemical-kinetics provides a reasonable prediction of flame shape and location, flame temperatures, and axial and swirl velocities. Wherever differences exist between predictions and measurements, an explanation is offered and further investigations along those lines are proceeding.

**Flame Shape, Structure, and Location.** From the examination of numerous flame photographs and the detailed numerical computations, flame stability in the SSC at the tested flow conditions primarily depends upon the attached flame and the lifted flame processes as sketched in Fig. 10 and described below. Sturgess et al. (1991) and Sturgess and Shouse (1993) have found that studies of such fundamental flame stability processes have great relevance to flame stability in modern annular gas turbine combustors.

**1 Multi-attached flame.** This type of attached flame is sketched in Figs. 10(a, b). As shown in Fig. 10(a), for the combination of strong outer swirl (60 deg) and zero inner swirl, the flame is simultaneously attached at three locations: (i) inner air side of the fuel stream, (ii) outer air side of the fuel stream, and (iii) outside of the outer air stream. It may be postulated that the dynamic characteristics of the flow bring packets of fuel into the outer recirculation zone, then burn in the mixing layer of the outer air and the recirculation zone. As the strength of the outer air swirl is decreased (30 deg) the attached flame structure shifts to that sketched in Fig. 10(b) where the flame no longer has an attachment on the outer air side of the fuel stream.

**2 Single-attached flame.** Figure 10(c) illustrates this single attached flame structure. This type of attached flame is observed for low inner (30 deg) and outer (30 deg) countercircling air flows. Such flow conditions cause the collapse of the twin attached flame structure sketched in Fig. 10(b) to a

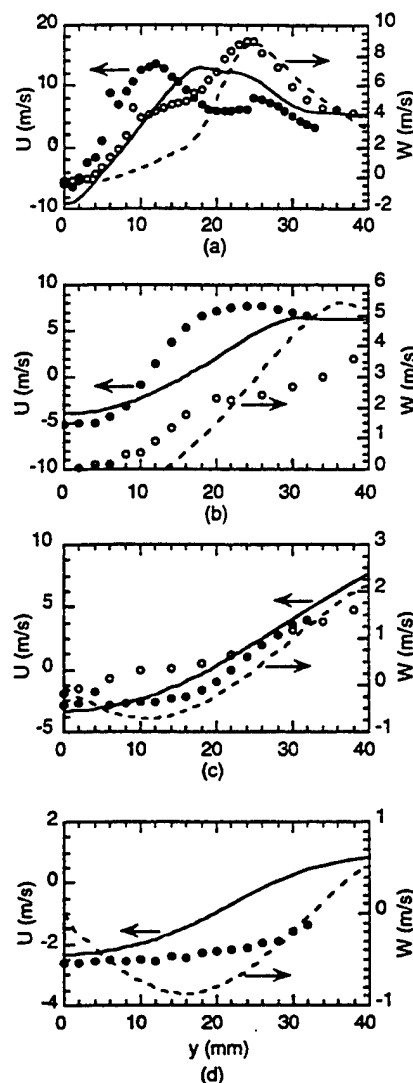


Fig. 9 Calculated and measured velocities for  $\theta = 30$  deg case at axial locations (a) 20 mm, (b) 40 mm, (c) 60 mm, and (d) 80 mm. Circles and lines represent measured and computed velocities, respectively.

single attachment just above the fuel tube. This type of attached flame was also observed for the coswirl configuration but at a lower combustor loading.

**3 Lifted flame.** Figure 10(d) illustrates this type of flame; also it is observed in the photographs of Figs. 5(b), 5(c), and 5(e). The flame lifts from the fuel tube lip because of the high mean axial velocity in the near-field region above the fuel tube. The lifted flame is stabilized by the inner recirculation zone. However, increasing the swirl intensity and/or combustor loading only slightly changes flame stability, i.e., LBO values remain fairly constant for lifted flames. This is because the lifting of a flame is usually accompanied by a premixing of fuel and air at the base of the flame. This premixing compromises the stability of the lifted flame over that of an attached flame, i.e., LBO values are higher for a lifted flame than for an attached flame.

Now, it is also clear that the observed difference in LBO between co- and countercircling configurations, as shown in Fig. 4, is primarily a function of how the flame stabilizes. Countercircling conditions readily produce an attached flame for moderate inner swirl intensity (30 deg); however, both configurations produce lifted flames for higher swirl intensity (45 deg) and for this

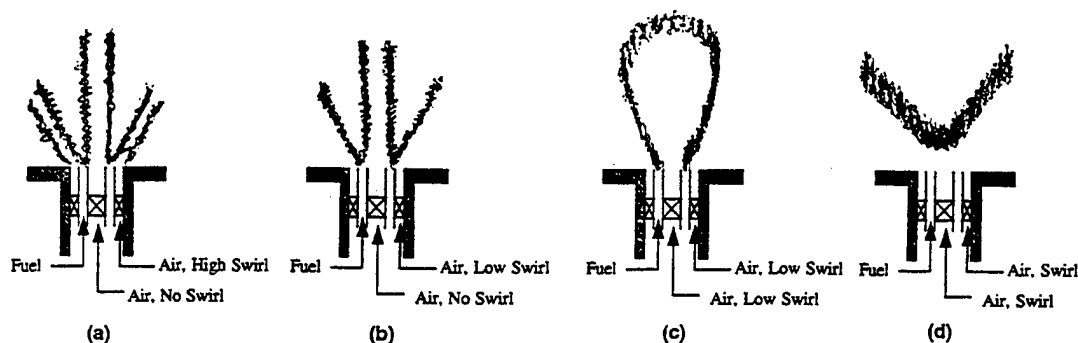


Fig. 10 Sketches illustrating the flame shape, structure, and location in the SSC

latter condition the LBO values are very similar. Finally, Sturgess et al. (1991) and Sturgess and Shouse (1993) have elucidated the significance and applications of anchored and lifted flames to practical gas turbine combustor stability and LBO. They observe three basic flame conditions: a thin sheathlike pilot anchored flame, a shear layer flame associated with the inner and outer recirculation zones, and a lifted main flame, which allows considerable premixing of reactants to take place prior to combustion. These observations further confirm the relevance and importance of the present work to practical gas turbine combustors.

## Conclusions

An SSC was designed to reproduce the swirling flow pattern present in the vicinity of the fuel injector located in the primary zone of a gas turbine combustor. Different flame shapes, structure, and location were observed and detailed experimental measurements and numerical computations were performed.

1 For the combination of strong outer swirl and zero inner swirl, a multiple attached flame exists simultaneously over the fuel and air injection tubes. As the strength of the outer air swirl is decreased and that of the inner swirl increased, the flame structure gradually shifts to a single attachment above the fuel injection tube.

2 For higher inner swirl velocity, the flame lifts from the fuel tube and is stabilized by the inner recirculation zone. Premixing of fuel and air at the base of the flame compromises the stability of the lifted flame over that of an attached flame, i.e., LBO values are higher for a lifted flame than for an attached flame.

3 The observed difference in LBO between co- and counterswirl configurations is primarily a function of how the flame stabilizes. Counterswirl conditions readily produce an attached flame for moderate inner swirl intensity; however, both configurations produce lifted flames for higher inner swirl intensity and for this latter condition the LBO values are very similar.

4 Computations based upon a turbulent combustion model correctly predict the attached flame locations, the development of an inner recirculation zone, which produces a dimple-shaped flame structure, and finally the flame lift-off height. The calculated radial mean temperature profiles at different axial locations agreed well with the measured CARS temperature. Also, the calculated velocity profiles agree reasonably well with the LDA measurements of mean axial and mean tangential velocities. These computations show the presence of a strong inner recirculation zone in the SSC, provide the location of the reattachment point of this recirculation bubble, and confirm the transport of combustion products upstream.

Finally, Sturgess et al. (1991) and Sturgess and Shouse (1993) have elucidated the significance and applications of an-

chored and lifted flames to practical gas turbine combustor stability and LBO. This confirms the importance and relevance of the present work to gas turbine combustors.

## Acknowledgments

This work was supported by the U.S. Air Force, Wright Laboratory, Fuels and Lubrications Division, Aero-Propulsion and Power Directorate, Wright Patterson Air Force Base, Dayton, OH, under contract No. F33615-92-C-2207, with Mr. Charles W. Frayne serving as the Air Force Technical Monitor. The authors wish to thank Mr. W. John Schmoll for the custom LDA processing software.

## References

- Bradley, D., Gaskell, P. H., and Lau, A. K. C., 1990, "A Mixedness-Reactedness Flamelet Model for Turbulent Diffusion Flames," *Twenty-Third Symposium (International) on Combustion*, The Combustion Institute, p. 685.
- Chen, R. H., and Driscoll, J. F., 1988, "The Role of the Recirculation Vortex in Improving Fuel-Air Mixing Within Swirling Flames," *Twenty-Second Symposium (International) on Combustion*, The Combustion Institute, p. 281.
- Durbin, M. D., and Ballal, D. R., 1996, "Studies of Lean Blowout in a Step Swirl Combustor," *ASME JOURNAL OF ENGINEERING FOR GAS TURBINES AND POWER*, Vol. 118, pp. 72-78.
- Gollahalli, S. R., Savas, O., Huang, R. F., and Rodriguez Azara, J. L., 1985, "Structure of Attached and Lifted Gas Jet Flames in Hysteresis Region," *Twenty-First Symposium (International) on Combustion*, The Combustion Institute, p. 295.
- Katta, V. R., and Roquemore, W. M., 1993, "Numerical Method for Simulating Fluid-Dynamic and Heat-Transfer Changes in Jet Engine Injector Feed-Arm Due to Fouling," *Journal of Thermophysics and Heat Transfer*, p. 651.
- Katta, V. R., Goss, L. P., and Roquemore, W. M., 1994, "Numerical Investigations of Transitional H<sub>2</sub>/N<sub>2</sub> Jet Diffusion Flames," *AIAA Journal*, Vol. 32, p. 84.
- Katta, V. R., 1995, internal report in preparation.
- Leonard, B. P., 1979, "A Stable and Accurate Convective Modeling Procedure Based on Quadratic Upstream Interpolation," *Computational Methods in Applied Mechanics and Engineering*, Vol. 19, p. 51.
- Pan, J. C., Vangsness, M. D., Heneghan, S., and Ballal, D. R., 1991, "Scalar Measurements of Bluff Body Stabilized Flames Using CARS Diagnostics," *ASME Paper No. 91-GT-302*.
- Pitts, W. P., 1988, "Assessment of Theories for the Behavior and Blowout of Lifted Turbulent Jet Diffusion Flames," *Twenty-Second Symposium (International) on Combustion*, The Combustion Institute, p. 809.
- Pitts, W. P., 1990, "Large-Scale Turbulent Structures and the Stabilization of Lifted Turbulent Jet Diffusion Flames," *Twenty-Third Symposium (International) on Combustion*, The Combustion Institute, p. 661.
- Spalding, D. B., 1972, "A Novel Finite Difference Formulation for Difference Expressions Involving Both First and Second Derivatives," *International Journal for Numerical Methods in Engineering*, Vol. 4, p. 551.
- Sturgess, G. J., Lesmerises, A. L., Heneghan, S. P., and Ballal, D. R., 1990, "Design and Development of a Research Combustor for Lean Blowout Research," *ASME JOURNAL OF ENGINEERING FOR GAS TURBINES AND POWER*, Vol. 114, p. 13.
- Sturgess, G. J., Sloan, D. G., Roquemore, W. M., Shouse, D., Lesmerises, A. L., Ballal, D. R., Heneghan, S. P., Vangsness, M. D., and Hedman, P. O., 1991, "Flame Stability and Lean Blowout—A Research Program Progress Report," Paper No. 91-7037, *Proceedings of Tenth ISABE*, Nottingham, United Kingdom.
- Sturgess, G. J., and Shouse, D., 1993, "Lean Blowout Research in a Generic Gas Turbine Combustor With High Optical Access," Paper No. 93-GT-332, to appear in the *Transactions of the ASME*.

Takahashi, F., Mizomoto, M., Ikai, S., and Fukati, N., 1984, "Lifting Mechanism of Free Jet Diffusion Flames," *Twentieth Symposium (International) on Combustion*, The Combustion Institute, p. 295.

Takahashi, F., Schmoll, W. J., and Vangsness, M. D., 1990, "Effects of Swirl on the Stability and Turbulent Structure of Jet Diffusion Flames," Paper No. AIAA-90-0036.

Takahashi, F., and Goss, L. P., 1992, "Near-Field Turbulent Structures and

the Local Extinction of Jet Diffusion Flames," *Twenty-Fourth Symposium (International) on Combustion*, The Combustion Institute, p. 351.

Takahashi, F., Vangsness, M. D., and Belovich, V. M., 1992, "Conditional LDV Measurements in Swirling and Non-swirling Coaxial Turbulent Air Jets for Model Validation," Paper No. AIAA-92-0580.

Vanquickenborne, L., and van Tiggelen, 1966, "The Stabilization Mechanism of Lifted Diffusion Flames," *Combustion and Flame*, Vol. 10, p. 59.

## **APPENDIX I**

### **Studies of Lean Blowout in a Step Swirl Combustor**

**M. D. Durbin, D. R. Ballal**

# Studies of Lean Blowout in a Step Swirl Combustor

M. D. Durbin

D. R. Ballal

Fellow ASME

Department of Mechanical  
and Aerospace Engineering,  
University of Dayton,  
Dayton, OH 45469

*The design requirements of a modern gas turbine combustor are increasingly dictated by wide stability limits, short flame length, and uniform mixing. To achieve the best trade-off between these three factors, flame characteristics (length, shape, mixedness), lean blowout (LBO), and optimum combustor configuration should be investigated over a wide range of inner and outer air velocities, inner and outer vane angles, and co- versus counterswirl arrangements. Such an investigation was performed in a step swirl combustor (SSC) designed to simulate the fuel-air mixing pattern in a gas turbine combustor dome fitted with an airblast atomizer. It was found that an increase in the outer vane angle and a decrease in inner air velocity decreased the flame length. LBO was improved when outer flow swirl intensity was increased. An optimum hardware and velocity configuration for the SSC was found for inner swirl = 45 deg, outer swirl = 60 deg, coswirl direction, and inner air velocity = outer air velocity = 16 m/s. This optimum SSC configuration yielded: (i) low values of LBO, (ii) short flame length, (iii) uniformly mixed stable flame, and (iv) little or no variation in these characteristics over the range of operation of SSC. Finally, the co- versus counterswirl arrangements and the operation of the optimized combustor configuration are discussed.*

## Introduction

An important design requirement of a modern gas turbine combustor is good combustion stability; that is, the combustor should sustain burning over a wide range of fuel-air ratios encompassing the entire range of engine operating conditions, including rapid acceleration and deceleration. Also, short flame length and uniform mixing are equally important. To achieve the best trade-off between wide stability limits, short flame length, and uniform mixing, the characteristics of the flame, lean blowout (LBO), optimum combustor geometry, and their influence on LBO should be investigated. This provides the necessary impetus for our research.

In this paper, experimental studies in a step swirl combustor (SSC) burning gaseous propane fuel were performed. The fuel was injected in the form of an annular jet coaxially sandwiched between two swirling airstreams. This configuration simulates the fuel-air mixing pattern just downstream of an airblast atomizer located in the dome region of a modern annular gas turbine combustor. The SSC was also intended to be a marriage between the two combustor configurations extensively studied earlier in our laboratory: a step combustor (Sturgess et al., 1990, 1991) and a swirl combustor (Takahashi et al., 1990). Specifically, we have investigated, over a wide range of inlet conditions of velocity, swirl vane angles, and swirl directions (coswirl versus counterswirl): (i) flame characteristics such as length, shape, and mixedness; (ii) LBO; and (iii) combustor flow field patterns. Special emphasis was given to assess the flame characteristics of coswirl versus counterswirl arrangements. For example, counterswirl may generate a strong shear layer but the opposed airstreams tend to nullify the swirling motion in the flow field. On the other hand, coswirl generates a high tangential momentum but produces a weaker shear layer. The combustion process in the SSC was also optimized in terms of a short flame length, high level of mixedness, and low LBO. Such results are presented and their implications to practical combustor design are discussed.

## Experimental Work

**The SSC.** Figure 1 shows a schematic diagram of the SSC, which has 150 × 150-mm cross section with rounded corners, length of 754 mm, and a step height of 55 mm. The SSC provides a geometrically simple, optically accessible research combustor capable of reproducing the fuel-air mixing pattern downstream of the airblast atomizer located in the dome region of a modern annular combustor. The SSC also offers independent control over inner and outer airstreams so that velocities can be easily optimized. In a practical airblast atomizer, effective areas would have to be changed to perform similar optimization; this is time consuming and expensive. The SSC was mounted on a vertical combustion tunnel with a three-axis traversing mechanism described by Sturgess et al. (1990). Measurements of various flame and flow parameters were performed using different instruments, the principal one being a three-component Laser-Doppler Anemometer (LDA).

Fuel was supplied to the combustor by the annular fuel tube (20 mm i.d. and 29 mm o.d.), which is coaxially sandwiched between two swirling airstreams; the inner air jet (20 mm dia) and the outer annular air jet (29 mm i.d. and 40 mm o.d.). The combustor exit has a 45 percent blockage orifice plate on top, which simulates the back pressure exerted by the dilution jets in a practical gas turbine combustor (see Sturgess et al., 1990). The SSC has quartz windows on all four sides to permit visual observations and laser diagnostics measurements. Optical access in the axial direction was about 250 mm from the burner tube exit; in the radial direction, it was about 30 mm (3-D LDA) and 70 mm (2-D LDA) from the centerline.

Stationary helical vane swirlers were located 25 mm upstream from the burner tube exit in each of the air passages. The inner swirler had six vanes with a central 1.4-mm-dia hole to prevent the flame from anchoring to the swirler. The outer swirler had 12 vanes. Inner swirler lengths are 25, 19, and 19 mm, respectively, for 30, 45, and 60 deg swirlers; outer swirler lengths are 32, 25, and 19 mm, respectively, for the 30, 45, and 60 deg swirlers. The lengths and number of vanes were designed to insure that there was no straight-through airflow into the combustor. Practical combustors usually employ axial-flow-type swirler vanes. The swirler vanes are usually flat for ease of manufacturing. However, the flow does not follow the angle of

Contributed by the International Gas Turbine Institute and presented at the 39th International Gas Turbine and Aeroengine Congress and Exposition, The Hague, The Netherlands, June 13-16, 1994. Manuscript received by the International Gas Turbine Institute February 19, 1994. Paper No. 94-GT-216. Associate Technical Editor: E. M. Greitzer.

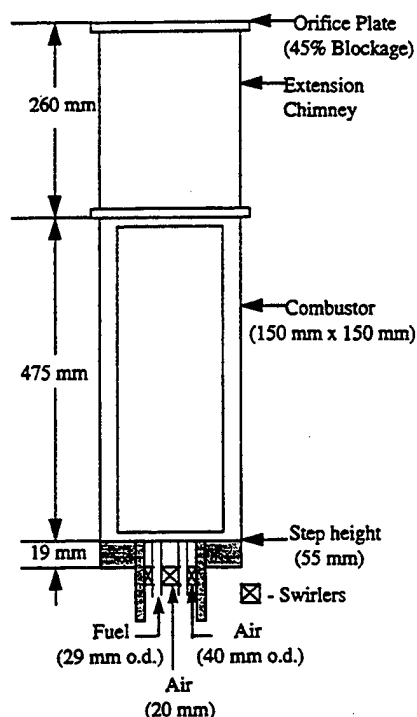


Fig. 1 Schematic diagram of a step swirl combustor

the flat vane as accurately as it does the angle of the helical vane. The swirlers were precision-fabricated in a rapid prototype manufacturing process known as stereolithography. These swirlers performed satisfactorily at high temperatures in our combustor.

**Instrumentation.** Figure 2 shows a custom-made three-component LDA system used for velocity measurements. This is a three-beam two-component (axial and radial) set using a 514.5 nm line of an 18 W argon-ion laser with a component separation based on polarization. A two-beam third component (tangential) set uses a 488.0 nm line with separation by color. Since the third component is normal to the first and second components, the measurement volume had a quasi-spherical shape of 100  $\mu\text{m}$  diameter and the calculated fringe spacing was 3.6  $\mu\text{m}$ . The LDA system has Bragg cell frequency shifting (10 MHz for the first and second channels, and 30 MHz for the third channel) for measurements in recirculatory flows, 4- $\sigma$  filtering software for spurious signals (e.g., due to seed agglomeration), and a correction subroutine to account for the LDA signal-biasing effects in combustor flows. A fluidized-bed seeder was used to inject submicron-sized ( $<1 \mu\text{m}$ )  $\text{ZrO}_2$  particles into each passage. Counter-type (TSI 1990C) signal processors and tailor-made coincidence circuit ensured valid data rate acquisition. All the LDA signals were processed using our custom-designed software, which calculates intensity, shear stresses, higher moments (skewness and kurtosis), and pdfs. Typical LDA sampling rates exceeded 1 kHz for both isothermal and combustor flow measurements.

**Error Analysis.** Both the fuel flow and airflow were monitored by separate electronic flow control units to within 1 and 3 percent, respectively. The combined error produced an uncertainty of 1.5 percent in equivalence ratio. The primary source of error in LDA measurement is the statistical bias of the final measured velocity toward higher mass flux (velocity  $\times$  density) when number-weighted averages are used to calculate stationary statistics. Chen and Lightman (1985) and Glass and Bilger (1978) have discussed bias correction schemes. After allowing for this bias, we estimated that for the single-stream seeding and relatively high-sampling rates of our experiments, the uncertainty in the measurement of mean velocity was 1 percent and for rms velocity 5 percent. Near the flame front, where intermittency would be much higher, the uncertainty in rms velocity could be as high as 7 percent. The long-term repeatability of measurements was found to be within 5 percent for turbulence quantities.

**Test Conditions.** Table 1 lists the test matrix for the SSC experiments. All tests were performed at room temperature and atmospheric pressure using gaseous propane fuel to establish a baseline. It should be noted that advanced, near-stoichiometric combustors of the future will admit fuel into the primary zone in a prevaporized state, and therefore, may not require high air velocities ( $>100 \text{ m/s}$ ) for liquid fuel atomization employed in conventional combustors. The SSC was operated to study flame characteristics, flow field, and LBO. Five variables were extensively tested: (i) inner air velocity, (ii) outer air velocity, (iii) inner vane angle, (iv) outer vane angle, and (v) coswirl versus counterswirl. The SSC was operated over a wide range of equivalence ratios. LBO data were collected by maintaining a constant airflow rate, heating the combustor to a near-steady-state temperature at stoichiometric fuel-air ratio, and then gradually decreasing the fuel flow rate until blowout occurred. This is a procedure similar to that adopted by Sturgess et al. (1991). The flame length was defined as the distance from the nozzle exit to the flame tip and measured by taking individual color snapshots of the combustion process, enlarging these photographs, and then carefully plotting the luminous boundary of the flame front. These photographs also provided data for visually assessing the quality of mixing (mixedness) within the combustion zone, e.g., for a constant fuel and airflow rate, a yellow or sooty flame indicates locally rich zones, which suggests poor mixing.

## Results

**Flame Characteristics.** Flame length measurements were performed because the length directly governs the length of the combustor dome. The measurements were taken at stoichiometric equivalence ratios to establish a baseline. Long-exposure photographs of the flame were taken with a 35-mm camera. Typical photographs are presented in Figs. 3(a)–(c) to illustrate how flame configuration (length, width, and shape) changes for no-swirl, inner swirl, and outer swirl conditions. As seen in Fig. 3(a), for the no-swirl case, the flame is lifted and the combustion zone is located closer to the combustor exit. Introducing a mild swirl in the inner airflow (Fig. 3(b)) not only shortens the flame, but also causes it to bulge out and fill the combustor cross section. Finally, as shown in Fig. 3(c),

## Nomenclature

$D$  = inner air nozzle diameter  
LBO = lean blowout  
 $P$  = pressure  
 $Re$  = Reynolds number  
 $U$  = axial mean velocity

$Y, Z$  = radial and axial distance, respectively  
 $\theta$  = swirl vane angle  
 $\phi$  = equivalence ratio

**Subscripts**  
 $i$  = inner  
 $o$  = outer

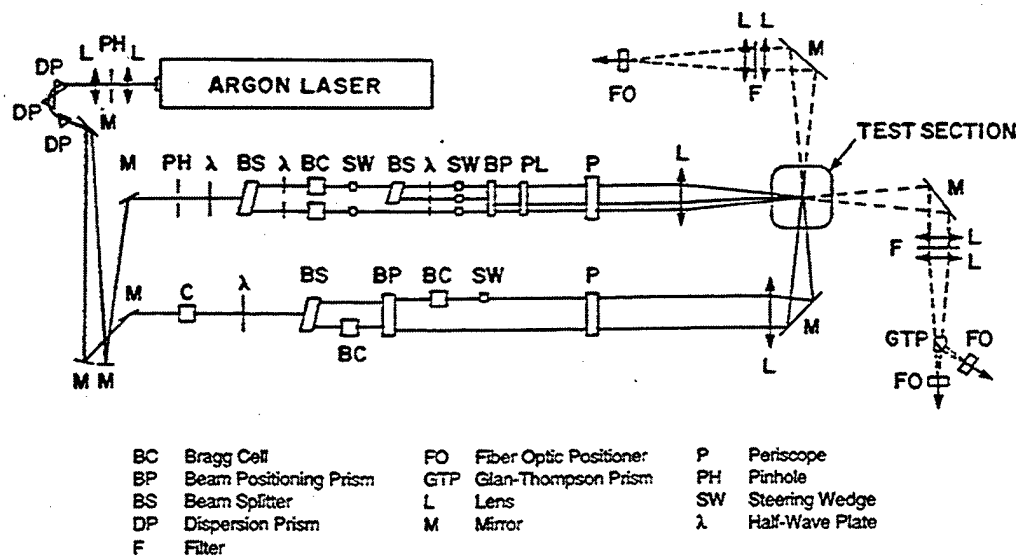


Fig. 2 Schematic of a custom-made three-component LDA system used for velocity measurements

swirling the outer *instead* of the inner airflow produces an attached flame with a *not-so-beneficial* elongated combustion zone downstream.

Flame lengths were measured for many different SSC operating conditions; these are shown plotted in Figs. 4–6. It should be noted that for all cases except the no-swirl conditions, the flame was nearly attached to the nozzle exit (at stoichiometric values). Figure 4 shows a substantial increase in flame length with a threefold increase in inner air velocity (for a constant value of outer air velocity and constant  $\phi = 1.0$ ) for all combinations of swirler angles. Clearly, this appears to be due to a direct decrease in the mixture residence time. Figure 5 compares flame length with changes in outer airflow for a constant value of inner airflow. It is found that the flame length decreases, but only when the outer vane angle is 60 deg or higher, i.e., only when the outer swirl intensity (both velocity and vane angle) is sufficiently high. Finally, Fig. 6 illustrates the variation of flame length with co- and counterswirl conditions for a velocity combination  $U_i = 48$  m/s and  $U_o = 16$  m/s. For all combinations of inner and outer vane angles, the coswirl direction produced shorter flames. It was also found that for equal velocities of inner and outer airstreams, the flame was very short and there was no noticeable difference in flame length between co- and counterswirl conditions.

To further assess the influence of swirl direction on the combustion process, Figs. 7(a) and 7(b) show the photographs of co- and counterswirl flame structures, respectively. Both flames rapidly spread outward. However, the coswirl flame (Fig. 7(a)) has a dimple shape at the center and shows some yellowish streaks downstream (evidence of nonuniform mixing and diffusion-controlled combustion), whereas the counterswirl flame

(Fig. 7(b)) has a bulb shape, which fully confines the bluish (evidence of uniform, premixed) combustion process.

Since the co- versus counterswirl effects are of great interest in practical combustor design, LDA velocity measurements were made to confirm the findings given above. Figures 8(a)–(c) show the radial variation of mean axial velocity at three different axial locations downstream of the fuel nozzle. These LDA measurements were made by seeding the fuel flow. A comparison between Figs. 8(a) and 8(b) demonstrates the changes in flowfield due to combustion, while Figs. 8(b) and 8(c) illustrate the co- versus counterswirl effects.

Figure 8(a) shows the inner recirculation zone, which grows from a width of  $0.25D$  (at  $Z/D = 0.35$ ) to  $0.45D$  (at  $Z/D = 2.25$ ) in the cold flow. In the annular fuel tube region, which is sandwiched between the inner and outer airflow, the axial velocity component is positive and decreases rapidly from its inner mean value of 16 m/s to the outer mean value of 8 m/s.

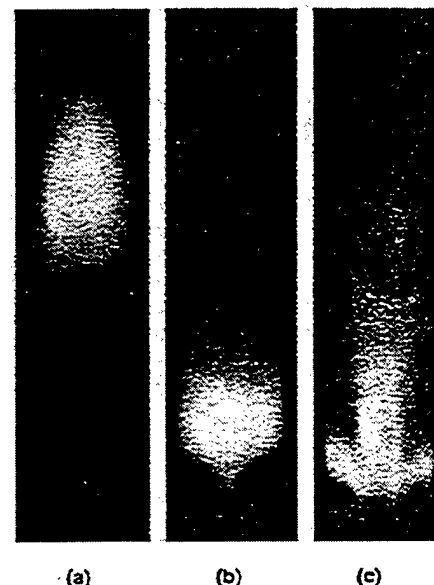


Fig. 3 Photographs illustrating the flame structure for different swirl configurations: (a) no-swirl,  $\theta_i = \theta_o = 0$ , (b) inner swirl,  $\theta_i = 45$  deg,  $\theta_o = 0$ , and (c) outer swirl,  $\theta_i = 30$  deg,  $\theta_o = 0$ . Test conditions were at  $\phi = 1.0$ ,  $U_i = 16$  m/s, and  $U_o = 8$  m/s.

Table 1 Test matrix for the step swirl combustor experiments (all tests at room temperature and atmospheric pressure with gaseous propane fuel)

Variable	Range
Inner vane angle, $\theta_i$ , degrees	30, 45, and 60
Outer vane angle, $\theta_o$ , degrees	30, 45, and 60
Vane configuration	co and counter-swirl
Inner air velocity, $U_i$ , m/s	16, 32, and 48
Re	20, 40, and $60 \times 10^3$
Outer air velocity, $U_o$ , m/s	8 and 16
Re	14 and $28 \times 10^3$



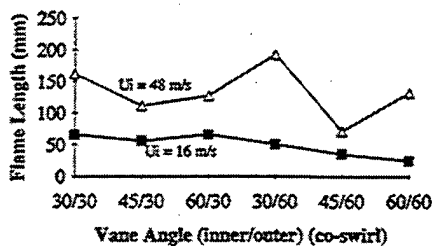


Fig. 4 Variation of flame length with vane angle at two different values of inner air velocity ( $U_o = 8 \text{ m/s}$ )

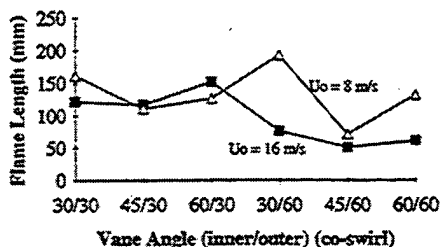


Fig. 5 Flame length as a function of vane angle and outer air velocity ( $U_o = 8 \text{ m/s}$ )

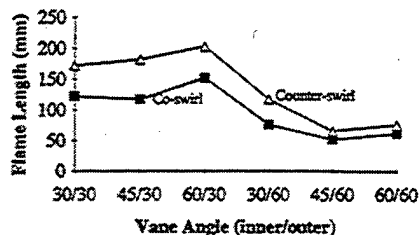


Fig. 6 A comparison of flame lengths with co- and counterswirl arrangements ( $U_i = 48 \text{ m/s}$ ,  $U_o = 16 \text{ m/s}$ )

Finally, the velocity decays to a low, but still positive value (i.e., no outer recirculation zone at least for  $Y/D$  up to 1.5) as one moves radially outward from the edge of the outer air tube to the combustor wall.

As seen in Fig. 8(b), the heat release of combustion produces the acceleration of the axial velocity component and elongation

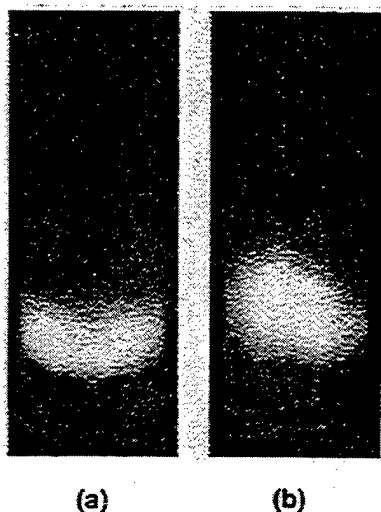
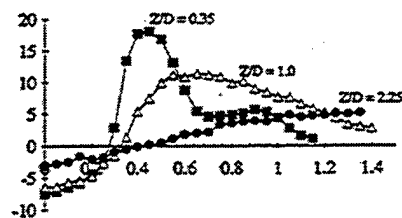
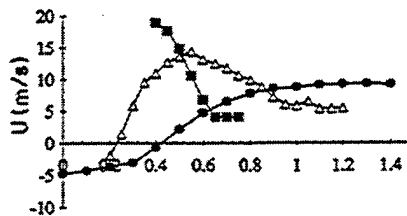


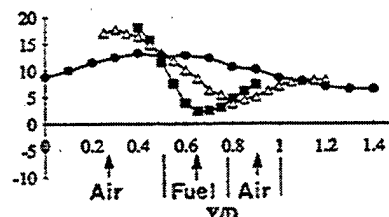
Fig. 7 Photographs illustrating the flame structure for (a) coswirl and (b) counterswirl arrangements. Test conditions were  $\phi = 1.0$ ,  $U_i = 16 \text{ m/s}$ ,  $U_o = 8 \text{ m/s}$ ,  $\theta_i = \theta_o = 30 \text{ deg}$ .



(a)



(b)



(c)

Fig. 8 Radial variation of mean axial velocity at three different locations downstream of the fuel nozzle: (a) cold flow coswirl, (b) hot flow coswirl, (c) hot flow counterswirl, test conditions were  $\phi = 1.0$ ,  $U_i = 16 \text{ m/s}$ ,  $U_o = 8 \text{ m/s}$ ,  $\theta_i = \theta_o = 30 \text{ deg}$

of inner recirculation zone in the axial (downstream) direction. For example, at  $Z/D = 1$ , combustion has elongated (and hence decreased) the recirculation zone width by 30 percent; and downstream of this location, it has increased the maximum mean axial velocity by 50 percent in this  $Y/D$  range. This means that throughout the inner recirculation zone, velocity gradients have increased significantly, contributing to intense mixing and uniformity. These results are consistent with the dimple-shaped central flame structure observed in the photograph in Fig. 7(a).

Figure 8(c) illustrates the axial mean velocity profiles for counterswirl direction. These results show no evidence of any inner recirculation zone. Moreover, in the annular gap corresponding to the fuel tube location, the velocity profile has a minimum. Presumably, this arises due to the flow velocity cancellation effect produced by the counterrotating swirl. Also, the annular fuel jet is subjected to strong shearing action of counterrotating braids along its inner and outer boundaries. As is evident in Fig. 7(b), this shearing action produces a very thin annular film near the nozzle exit ( $Z/D$  up to 1), which supports an attached flame structure in the combustor.

It should be noted that, in our experiments, the co- and counterswirl arrangement had identical overall pressure drop. Yet there is a difference in their mixing characteristics and, hence, in the flame structures. Thus, expressing the mixing quality only in terms of the overall pressure drop can be deceptive.

**LBO Observations.** LBO equivalence ratios were recorded for all the test conditions documented in Table 1. Rich blowout data were also collected to verify combustion stability of SSC for various parametric combinations. However, in Figs. 9 and 10, only LBO data are presented (repeatability to  $\pm 0.01$ ) because of their great practical importance. These data may be put into proper perspective by noting that, for a perfectly mixed

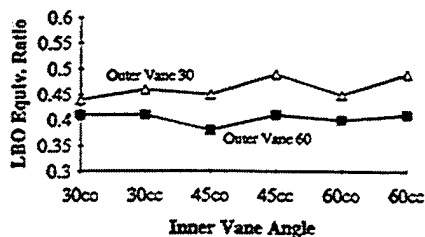


Fig. 9 Effect of outer vane angle on LBO at  $U_i = 32$  m/s,  $U_o = 16$  m/s (co represents coswirl, cc represents counterswirl)

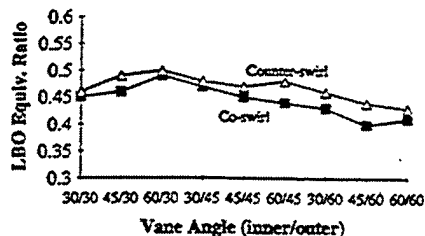


Fig. 10 A comparison of LBO data for co- and counterswirl arrangements ( $U_i = 32$  m/s,  $U_o = 16$  m/s)

propane-air flame, the value of equivalence ratio at the lean flammability limit is 0.55.

Figure 9 shows that an increase in outer swirl vane angle improves the stability of lean mixtures (i.e., LBO values decrease). An outer vane angle of 60 deg produces strong outer recirculation zones, which keep the flame attached to the exit nozzles and stabilize the combustion process. Strong outer swirl produces locally fuel-rich zones by directing the outer airflow away from the fuel jet, thereby further assisting flame stability.

Figure 10 shows LBO data for co- and counterswirl. When inner air velocity is significantly higher than the outer air velocity, coswirl provides more stable combustion and always yields slightly lower LBO values than the counterswirl condition. This presumably occurs because, as shown in Fig. 7(a), the coswirl flow direction produces less-uniform mixing in the combustor than the counterswirl flow direction. An imperfectly mixed diffusion flame blows out at a lower overall equivalence ratio because combustion is sustained in the locally rich mixture regions. This is good for stability but it should be recognized that the reactants are not uniformly mixed. Thus, there is an important *trade-off* to be considered when assessing burning characteristics of co- and counterswirl flows. No detectable differences in LBO values were found for co- and counterswirl flow conditions when inner and outer air velocities were equal.

**Optimum Configuration.** The preceding results on flame length and LBO suggest an optimum configuration of inner and outer velocities, inner and outer swirl vane angles, and co- versus counterswirl, which yields: (i) low LBO values, (ii) short flame length, (iii) uniformly mixed stable flame, and (iv) little or no variation in these characteristics over the SSC range of operation. Figure 11 shows that the optimum vane angle ( $\theta_i$

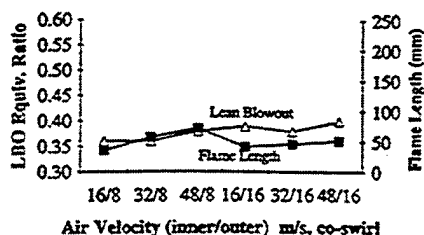


Fig. 11 Variation of LBO and flame length with airflow for an optimum vane angle configuration ( $\theta_i = 45$  deg,  $\theta_o = 60$  deg)

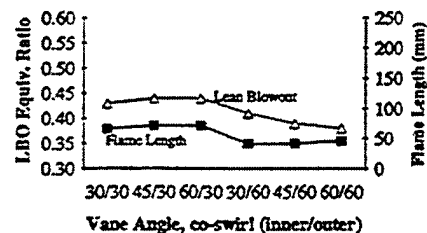


Fig. 12 Variation of LBO and flame length with vane angle for an optimum air velocity split ( $U_i = U_o = 16$  m/s)

= 45 deg,  $\theta_o = 60$  deg) provides low LBO values (average equivalence ratio =  $0.38 \pm 0.04$ ) and short flame lengths (average 55 mm  $\pm$  10 mm) over the range of air velocities tested. For all other inner and outer vane angle combinations, the average LBO values were greater, average flames were longer, or more data variability was present. Likewise, in Fig. 12, the optimum inner and outer velocity split ( $U_i = U_o = 16$  m/s) provides low values of LBO (average equivalence ratio =  $0.41 \pm 0.03$ ) and short flame length (average 52 mm  $\pm$  8 mm) over the range of vane angles tested.

Figures 13(a) and 13(b) show the flame structure at the optimum condition (inner swirl = 45 deg, outer swirl = 60 deg, coswirl direction, inner air velocity = outer air velocity = 16 m/s) for equivalence ratios  $\phi = 1$  and 0.5, respectively. It is observed that the flame structure remains confined to the combustor dome region over this range of equivalence ratio. At the overall stoichiometric mixture ratio (Fig. 13(a)), the flame is evenly dispersed throughout the combustor and the same observation holds true at the LBO operating condition (Fig. 13(b)). While this may be aerodynamically desirable, other factors such as combustor dome cooling, high-altitude ignition, and emissions requirements can dictate the optimum flame structure in a practical combustor. Finally, no noticeable change was observed in flame size and shape when the inner swirl angle was increased from 45 to 60 deg.

## Discussion

In these experiments it was observed that, compared to the counterswirling arrangement, the coswirling flow spread the fuel-air mixture to the combustor walls and produced a slightly shorter flame, a lower LBO value, and less variability of the

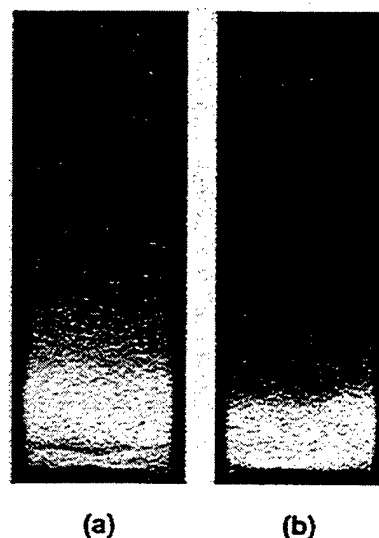


Fig. 13 Photographs illustrating the flame structure at the optimum conditions ( $\theta_i = 45$  deg,  $\theta_o = 60$  deg,  $U_i = U_o = 16$  m/s), (a)  $\phi = 1.0$ , (b)  $\phi = 0.5$

combustion characteristics with changes in hardware and flow conditions. For a coswirl arrangement, Brady and Samuelsen (1991), Brady et al. (1991), and Sowa et al. (1993) have observed an excessive transport of liquid fuel to the combustor walls, resulting in unstable operation. Since the momentum of their liquid fuel sheet was likely to be higher than that of our gaseous propane annular jet, their observations on combustor wall heating and combustion instability were absent in our tests. Also, as Sowa et al. (1993) have pointed out, the shorter combustor dome length required to confine this type of flame may suppress the formation and strength of large-scale turbulent eddies, which trigger combustion instabilities. As shown in Fig. 7(a), we did observe some yellow streaks downstream; these streaks indicate nonuniform mixing and diffusion-controlled combustion. However, combustion instability for the co-swirl arrangement at the LBO operating point was no worse than with the counterswirl flow arrangement.

Finally, detailed velocity and temperature mappings of the SSC using LDA and CARS diagnostics are currently being performed to ascertain the role of inner and outer recirculation zones on the combustion stability near lean blowout.

### Summary and Conclusions

A unique SSC was designed to simulate the fuel-air mixing pattern produced by an airblast atomizer located in the combustor dome of a modern annular gas turbine combustor. Experiments were performed to study flame characteristics (length, shape, and mixedness), LBO, and flow patterns in this combustor over a wide range of inner and outer velocities, inner and outer vane angles, and co- versus counterswirl arrangements. This research resulted in the following findings:

- 1 The two most significant parameters that contributed to decreasing the flame length are; an increase in the outer vane angle and a decrease in inner air velocity. Visual flame sooting decreased when the inner vane angle or air velocity was increased.

- 2 LBO improved when outer swirl intensity was increased. When inner air velocity was higher than outer air velocity, co-swirl yielded slightly lower values of LBO than the counterswirl arrangement. However, LBO values remained unchanged for equal inner and outer velocities.

- 3 An optimum hardware and flow configuration for the SSC was found for inner vane angle = 45°, outer vane angle = 60°, co-swirl direction, and inner air velocity = outer air velocity = 16 m/s. This configuration yielded: (i) low LBO values, (ii) short flame length, (iii) uniformly mixed stable flame, and (iv) little or no variation in these characteristics over the SSC range of operation.

- 4 Photographs indicated and LDA velocity measurements confirmed that the co-swirl flame has a dimple-shape, produces a slightly shorter flame stabilized by the inner recirculation zone, a lower value of LBO, and less variability of the combustion characteristics with changes in hardware and flow conditions. In contrast, the counter-swirl flame has a bulb-shape which fully confined the bluish, partially premixed combustion process to the center of the combustor dome, requires a slightly higher value of LBO, and needs a longer combustor dome length to confine it. These important differences between the two swirling arrangements can influence the off-design performance of the combustor.

- 5 Finally, no noticeable change was observed in the flame size and shape over a range of test conditions when the combustor was operated with the optimum configuration. This knowledge should be of value to the combustor designer.

### Acknowledgments

This work was supported by the U.S. Air Force, Wright Laboratory, Fuels and Lubrications Division, Aero-Propulsion and Power Directorate, Wright-Patterson Air Force Base, Dayton, OH, under contract No. F33615-92-C-2207, with Mr. Charles W. Frayne serving as the Air Force Technical Monitor. The authors wish to thank Drs. G. J. Sturgess and W. M. Roquemore for valuable discussions, and Mr. M. D. Vangsness for his help with the LDA measurements.

### References

- Brady, R. A., and Samuelsen, G. S., 1991, "Visualization of Dome Region Mixing in a Quartz Combustor," ASME Paper No. 91-GT-360.
- Brady, R. A., Sowa, W. A., and Samuelsen, G. S., 1991, "A Study of Dome Region Fuel-Air Mixing in a Model Rich Burn-Quick Mix Lean Burn Combustor," NASA TM189112.
- Chen, T. H., and Lightman, A. J., 1985, "Effects of Particle Arrival Statistics on Laser Anemometer Measurements," ASME FED-Vol. 33, pp. 172-176.
- Glass, M., and Bilger, R. W., 1978, "The Turbulent Jet Diffusion Flame in Coflowing Stream-Some Velocity Measurements," *Combustion Science and Technology*, Vol. 18, pp. 165-177.
- Sowa, W. A., Brady, R. A., and Samuelsen, G. S., 1993, "Mixing in the Dome Region of a Staged Gas Turbine Combustor," *AIAA Journal of Propulsion and Power*, Vol. 9, pp. 702-707.
- Sturgess, G. J., Lesmerises, A. L., Heneghan, S. P., and Ballal, D. R., 1990, "Design and Development of a Research Combustor for Lean Blowout Research," ASME JOURNAL OF ENGINEERING FOR GAS TURBINES AND POWER, Vol. 114, pp. 13-19.
- Sturgess, G. J., Sloan, D. G., Roquemore, W. M., Shouse, D., Lesmerises, A. L., Ballal, D. R., Heneghan, S. P., Vangsness, M. D., and Hedman, P. O., 1991, "Flame Stability and Lean Blowout—A Research Program Progress Report," Paper No. 91-7037, *Proceedings of Tenth ISABE*, Nottingham, England, pp. 372-384.
- Takahashi, F., Schmoll, W. J., and Vangsness, M. D., 1990, "Effects of Swirl on the Stability and Turbulent Structure of Jet Diffusion Flames," AIAA Paper No. 90-0036.

## **APPENDIX J**

### **Lean Blowout in a Research Combustor at Simulated Low Pressures**

**G. J. Sturgess, S. P. Heneghan, M. D. Vangsness,  
D. R. Ballal, A. L. Lesmerises**

G. J. Sturgess<sup>1</sup>  
Pratt & Whitney,  
East Hartford, CT 06108

S. P. Heneghan

M. D. Vangsness

D. R. Ballal

University of Dayton,  
Dayton, OH 45424

A. L. Lesmerises

WRDC,  
Wright-Patterson Air Force Base, OH 45433

# Lean Blowout in a Research Combustor at Simulated Low Pressures

*A propane-fueled research combustor has been designed to represent the essential features of primary zones of combustors for aircraft gas turbine engines in an investigation of lean blowouts. The atmospheric pressure test facility being used for the investigation made it difficult to approach the maximum heat release condition of the research combustor directly. High combustor loadings were achieved through simulating the effects on chemical reaction rates of subatmospheric pressures by means of a nitrogen diluent technique. A calibration procedure is described, and correlated experimental lean blowout results are compared with well-stirred reactor calculations for the research combustor to confirm the efficacy of the calibration.*

## Introduction

A propane-fueled research combustor, Fig. 1, has been designed (Sturgess et al., 1992) and developed (Heneghan et al., 1990) to investigate lean blowouts in simulated primary zones of the combustors for aircraft gas turbine engines. The fundamental flow features of a gas turbine combustor primary zone, within which the flame is held, are generated by the geometrically simple design of the research combustor.

The research combustor consists of co-axial jets with a 29.7 mm ID central fuel jet surrounded by a 40 mm diameter annular air jet. The fuel is gaseous propane. The jets are located centrally in a 150 mm nominal diameter duct. A backward-facing step at the jet discharge plane completes the sudden expansion, giving a step height of 55 mm. The step provides a recirculation region that can stabilize the flame. The combustor test section incorporates flat quartz windows to provide optical access. Curved metal fillets, located in the corners of the test section, reduce and distribute the vorticity generation due to wall secondary flows, and so eliminate their impact on the bulk flowfield in the combustor. An orifice plate with a 45 percent blockage ratio forms the exit from the combustor.

When operated in a fuel-rich mode, the flame in the combustor is very stable and is anchored in the jet shear layers by a pilot flame attached to the step near the outer edge of the air supply tube. Fuel for this flame is recirculated from downstream by the step recirculation zone; ignition is by hot gases also recirculated. As the bulk equivalence ratio is reduced, the flame becomes less stable, and eventually reaches a point where the pilot flame becomes detached from the base region (lifts), and the entire flame structure becomes stabilized downstream, Fig. 2. Thus, there are two distinct operating modes for the combustor: a fully anchored flame, and a lifted flame.

As a consequence of the flame-lift, a significant degree of partial premixing of the reactants takes place upstream of the lifted flame position. When the equivalence ratio is further reduced, the flame becomes progressively less stable (Heneghan et al., 1990) in its lifted condition, and eventually flows out. This lean blowout limit at atmospheric pressure has been found to correspond to a fuel equivalence ratio (around 0.5) that is

very close to the lean flammability limit of propane in air (Lewis and von Elbe, 1987). Due to the partial premixing, the combustor lean blowout performance characteristic has been observed to be consistent with that of well-stirred reactor data (Sturgess et al., 1992).

Lean blowout is strongly affected by chemical reaction rates. Application of chemical reaction rate theory to well-stirred reactors has resulted in the formulation of the gas loading parameter  $\dot{m}/(V P^n F)$ , where  $n$  is the effective order of the reaction,  $F$  is a temperature correction factor,  $V$  is the reactor volume,  $\dot{m}$  is the oxidant mass flow rate, and  $P$  the operating pressure, against which the equivalence ratio at blowout is frequently plotted. The concept of the well-stirred reactor can provide a simplified description of practical combustors. Bragg (1953) originated the view that any reasonably efficient practical combustor should consist of an initially well-stirred reactor section for ignition and flame holding, followed by a plug-flow reactor section for burnout. Since the research combustor was designed specifically to reproduce the major features of an aircraft gas turbine combustor primary zone (Sturgess et al., 1992), it might be expected to conform to well-stirred reactor behavior. The lean blowout behavior supports this expectation. Therefore, the loading parameter can be used to define lean blowout performance.

The research combustor is being tested in a facility that operates at atmospheric pressure and that was limited to maximum propane flow rates of about 20 kg/h. Under these circumstances, sufficient loading to approach the maximum heat release condition of the research combustor cannot be achieved. However, to investigate the lean blowout phenomenon thoroughly, it is desirable to probe the flow fields for flames that are anchored and lifted at both lightly strained and heavily strained flame conditions. Heavily strained flames occur at high loadings, and in practice, result from combustor operation at a given airflow with low air inlet temperatures and low (subatmospheric) pressures. Reducing air inlet temperatures alone to achieve high loadings without choking the combustor requires very low temperatures, and this demands drying of the air to avoid severe icing problems. Given these difficulties, alternative methods of achieving heavily strained flames were needed.

The quantities involved in the loading parameter are those that influence the speed at which chemical activity converts reactants to products. When the combustor inlet conditions cannot be manipulated to achieve a desired loading, the chemical reaction can be influenced by some other means to yield a

<sup>1</sup> Current address: Innovative Scientific Solutions, Inc., Beavercreek, OH 45432. Contributed by the International Gas Turbine Institute and presented at the 36th International Gas Turbine and Aeroengine Congress and Exposition, Orlando, Florida, June 3-6, 1991. Manuscript received at ASME Headquarters March 1991. Paper No. 91-GT-359. Associate Technical Editor: L. A. Riekert.

[ ALL DIMENSIONS ARE IN MM ]

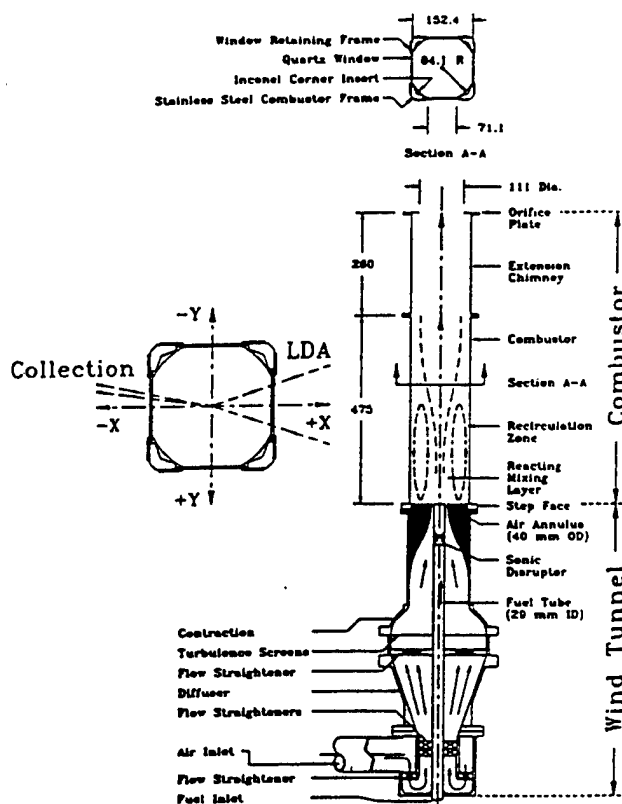


Fig. 1 Cross section of research combustor

similar rate of reactants conversion. If pressure is made the variable of influence, then a suitably altered chemical reaction would reflect the "simulated pressure."

Low pressures can be simulated by the introduction of an inert diluent that slows down the chemical reaction in approximately the same way that low pressures do. The addition of the diluent has two effects: first, it lowers the concentration of reactants, and second, it lowers the reaction temperature by virtue of its heat capacity. Thus, tests may be made at atmospheric pressure and high loadings still achieved.

Such a simulation technique for achieving high loadings while operating at room temperature and atmospheric pressure was developed for the research combustor.

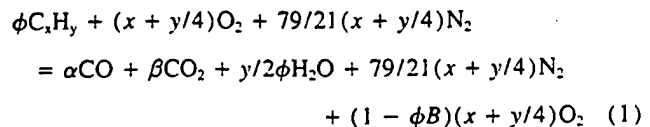
### Simulation Technique

A number of techniques for simulating low combustion pressures are available, e.g., Lefebvre and Halls (1959), Lefebvre

(1961), and Greenhough and Lefebvre (1956), using water as the diluent. However, water is inconvenient for the present purposes. It requires preheating of the inlet air to ensure complete vaporization of the droplets. Gaseous nitrogen has also been used with success (Norster, 1968), and does not require preheating. Although a direct calibration for nitrogen was not available, nitrogen as a diluent is extremely convenient for the present purposes, and was therefore selected.

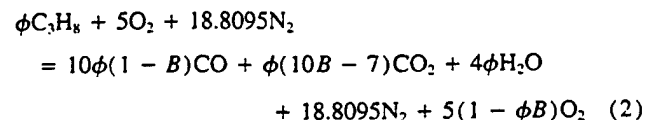
### Theoretical Background

Consider the combustion of the general hydrocarbon  $C_xH_y$  in air, and let the equivalence ratio  $\phi$  be such that there is an excess of air, i.e.,  $\phi < 1.0$ . Also, let the combustion efficiency be such that  $B$  is the fraction of fuel that is actually burned. The unburned fuel will not pass through the combustor unchanged, but will, in general, appear in the exhaust as carbon monoxide, hydrogen, and lower hydrocarbons. In modern combustors the lower hydrocarbons are always small in quantity under normal circumstances; further, the fast reaction rate of hydrogen suggests that it too, will not be a significant product. Therefore, a simple bimolecular global reaction can be proposed,



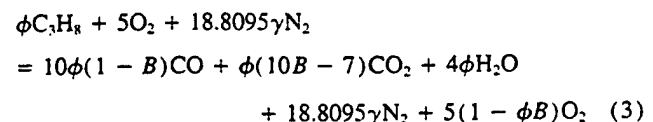
where all of the hydrogen in the fuel is burned to water vapor, and the inefficiency is reflected solely in the CO/CO<sub>2</sub> balance. This is reasonable because of the relatively slow conversion of CO to CO<sub>2</sub>. Nitrogen is assumed inert. The molar fractions  $\alpha$  and  $\beta$  are found from C/O balances.

For propane this reaction becomes,



Note that with this simple reaction mechanism CO<sub>2</sub> disappears from the products for a fractional conversion less than or equal to 0.7.

Let  $K$  be the mass ratio of diluent nitrogen to fuel. The reaction expression becomes



so that the additional mass of N<sub>2</sub> is 18.8095 × 28 (γ - 1).

### Nomenclature

$A$  = pre-exponential rate constant (may also include convenient unit conversion factors)  
 $B$  = combustion efficiency  
 $C = E/R$   
 $E$  = activation energy  
 $F$  = temperature correction factor  
 $K$  = mass ratio of excess nitrogen to fuel  
 $m$  = volumetric fractional concentration  
 $\dot{m}$  = mass flow rate  
 $\dot{m}'''$  = volumetric rate of oxidant mass consumption

$n$  = effective order of global chemical reaction  
 $P$  = pressure  
 $R$  = global reaction rate expression  
 $R$  = universal gas constant  
 $T$  = reaction temperature  
 $V$  = volume associated with combustion  
 $\alpha$  = molar fraction of CO in products of reaction  
 $\beta$  = molar fraction of CO<sub>2</sub> in products of reaction  
 $\gamma$  = defined by Eq. (4)

$\phi$  = fuel/air equivalence ratio

### Subscripts

air = air  
 $f$  = carbon monoxide in products of reaction, fuel  
LBO = lean blowout  
N<sub>2</sub> = excess nitrogen as diluent  
 $o$  = oxygen in products of reaction  
Tot = inlet sum of air, propane, and excess nitrogen

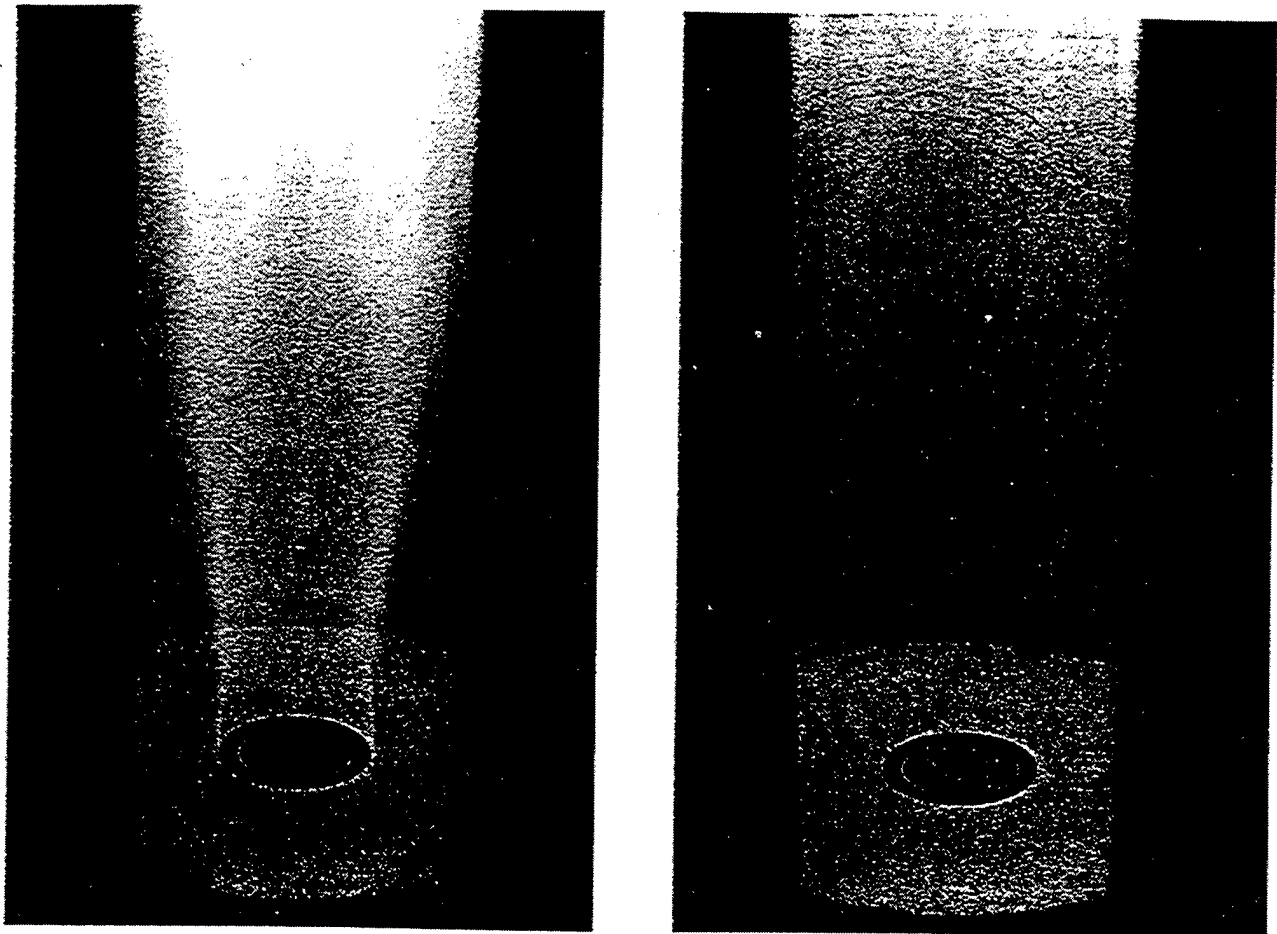


Fig. 2 Photographs of anchored and lifted flame operation

Hence,

$$\gamma = (\phi K / 11.9697 + 1) \quad (4)$$

Equations (3) and (4) together provide the volumetric fractional concentrations of oxidant and fuel present in the exhaust, i.e.,

$$m_f = \frac{10\phi(1-B)}{G} \quad (5)$$

where

$$G = 10\phi(1-B) + \phi(10B-7) + 4\phi + 18.8095\gamma + 5(1-\phi B)$$

and

$$m_o = \frac{5(1-\phi B)}{G} \quad (6)$$

From the kinetic theory of gases a reaction rate expression in Arrhenius form can be derived for bimolecular, single-step reactions. Longwell et al. (1953) have proposed that for lean mixtures this takes the form,

$$\phi B \dot{m}'' = A m_o m_f P^2 T^{-3/2} \exp(-E/RT) \quad (7)$$

where  $\dot{m}''$  is the volumetric rate of oxidant mass consumption.

Although Longwell and others have proposed fractional indices in Eq. (7) to accord with the results of various experiments, for the present purposes a pure second-order reaction in pressure and first order in concentrations is taken. In Eq. (7),  $E$  is a reaction rate constant (activation energy), and  $A$  can incorpo-

rate a pre-exponential rate constant as well as various unit conversion factors and other constant terms as may be convenient.  $T$  is the reaction temperature, and  $R$  the universal gas constant.

Rearranging Eq. (7) into a form incorporating the loading parameter yields,

$$\frac{\dot{m}_{air}}{VP^2} = \frac{Am_o m_f}{\phi B} \frac{1}{T^{3/2} \exp(E/RT)} \quad (8)$$

Combining Eqs. (5), (6), and (8) gives,

$$\frac{\dot{m}_{air}}{VP^2} = \frac{A(1-B)}{B} \times \frac{2(1-\phi B)}{(\phi(1.4-B) + 79/21\gamma + 1)^2} \frac{1}{T^{3/2} \exp(E/RT)} \quad (9)$$

Equation (9) represents the appropriate global kinetic expression for the reaction rate of propane in air with additional nitrogen. With  $K$  equal to zero, it also represents a similar expression for propane in pure air.

A reaction rate simulation can be obtained if

$$\left( \frac{\dot{m}_{air}}{VP^2 R} \right)_{\text{simulation}} = \left( \frac{\dot{m}_{air}}{VP^2 R} \right)_{\text{desired}} \quad (10)$$

where  $R$  is the appropriate reaction rate expression from the right-hand side of Eq. (9), i.e., with  $K > 0$  and  $P = 1$  atm for simulation and  $K = 0$  and  $P < 1.0$  atm for desired reaction rate. If it is taken that the presence of the diluent has no effect

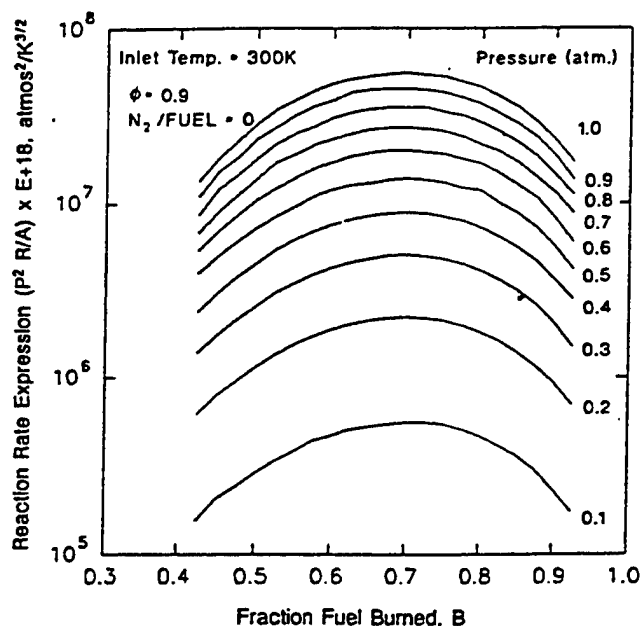


Fig. 3 Variation of reaction rate expression (Eq. (11)) with pressure

on the rate constants, the identity represented by Eq. (10) can be written,

$$\left( \frac{P^2 R}{A} \right)_{\text{simulation}} = \left( \frac{P^2 R}{A} \right)_{\text{desired}} \quad (11)$$

Thus,  $A$  does not have to be described explicitly. A typical value for  $E$  is 26,613 g·cal/g·mole, for near-stoichiometric mixtures (Clarke et al., 1960).

Figures 3 and 4 may be used to compare the left- and right-hand sides of the identity for an equivalence ratio of 0.9 and inlet temperature of 300 K. Figure 3 shows the effect of pressure on propane/air combustion, while Fig. 4 shows the effect of nitrogen addition on the combustion at one atmosphere pressure. The similarities of the two curves are obvious.

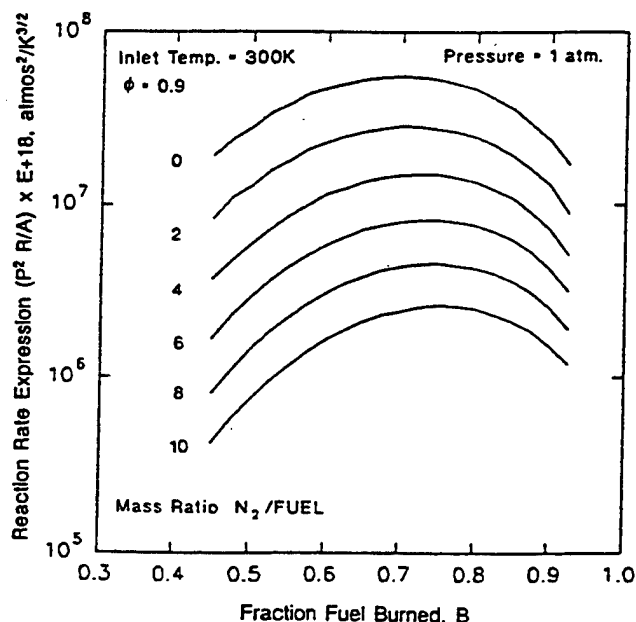


Fig. 4 Variation of reaction rate expression (Eq. (11)) with diluent addition

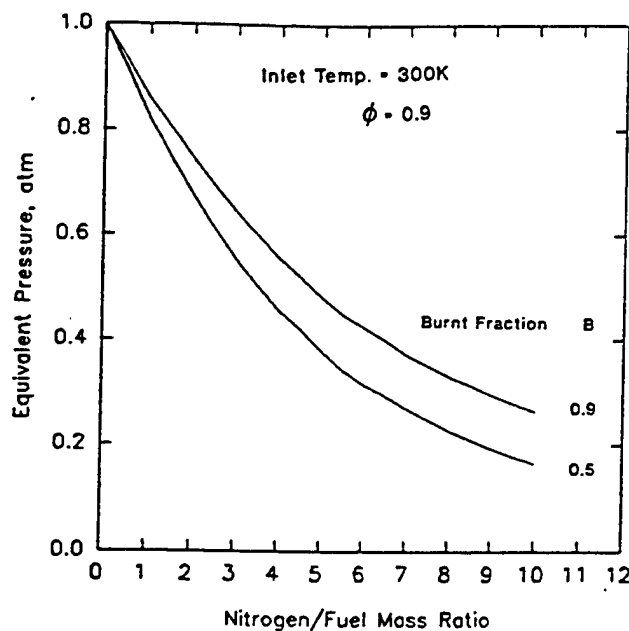


Fig. 5 Dependency of simulated pressure on diluent addition for a global reaction rate based on indices for  $\phi = 1.0$  (Eq. (7))

### Need for Calibration

The simplified reaction mechanism and rate expression used to derive the simulation are only a convenient representation of reality. A given rate expression cannot be expected to represent all the actual reactions taking place adequately so that the expression is appropriate over wide ranges of operating conditions. Therefore, if the simulation technique is to be used for other than merely comparative purposes, some form of calibration is required.

Various global Arrhenius rate expressions have been published in the literature to represent propane/air combustion at different conditions, e.g., Greenhough and Lefebvre (1956), Clarke et al. (1960), and Herbert (1960). One that is more appropriate for low equivalence ratios (around 0.5) is given by

$$\dot{m}'' = A m_o^{0.5} m_f^{0.5} P T^{-0.5} \exp(-56,600 / RT) \quad (12)$$

This has the form of Eq. (7), but different fractional indices and rate constants. When the simulation is based on Eq. (12) rather than Eq. (7), considerable differences result.

As is to be described, comparison of curves like Figs. 3 and 4 can be used to obtain the relationships between nitrogen to fuel mass ratio and the equivalent reaction pressure. This has been done in Figs. 5 and 6 for an equivalence ratio of 0.9 and a mixture initial temperature of 300 K, using simulations based on Eqs. (7) and (12), respectively. For given combustion efficiency and nitrogen/fuel mass ratio, the differences in equivalent pressure from the two curves are marked. This illustrates vividly the need for calibration of the technique.

### Calibration

An ideal calibration would be based on a comparison of the simulated pressure against true low-pressure tests in the same reactor. Unfortunately, such a direct approach was not immediately available for the research combustor. Therefore, an indirect approach is used. This maintains the bimolecular reaction mechanism Eq. (3), unchanged, but calibrates the Arrhenius reaction rate expression that goes with it.

Fortunately, a calibration of the Arrhenius rate expression for propane/air/excess nitrogen systems has already been carried out by Kretschmer and Odgers (1972), and their work has been utilized here.



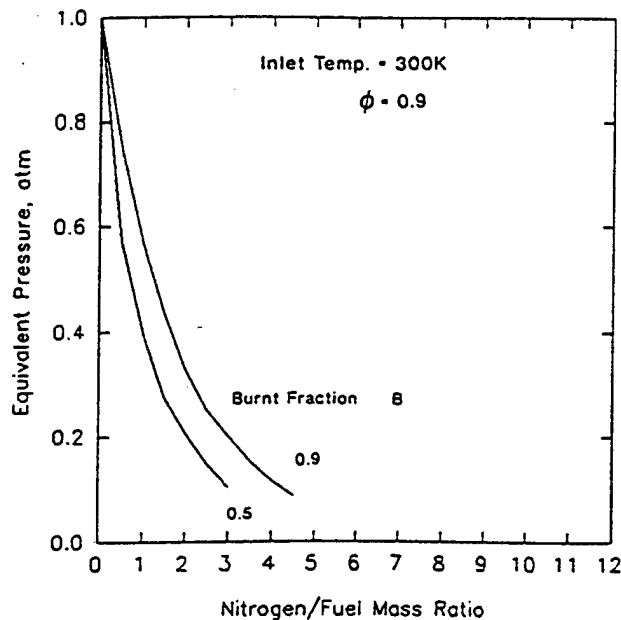


Fig. 6 Dependency of simulated pressure on diluent addition for a global reaction rate based on indices for  $\phi = 0.5$  (Eq. (12))

Kretschmer and Odgers used for their calibration experimental results from spherical stirred reactors and gas turbine combustors, burning fuels from propane to aviation kerosene over a wide range of operating conditions including pressures from 0.1 to 5.4 atm and inlet temperatures from 200 K to 900 K; equivalence ratios equal to and less than unity were included. Analysis of these data resulted in a rate expression giving the calibrated form for Eq. (8) as

$$\frac{\dot{m}_{\text{air}}}{VP^2\phi} = \frac{A(m_r m_f)^\phi}{\phi B} \frac{1}{T^{2\phi-0.5} \exp(C/T)} \quad (13)$$

where  $C$  is  $E/R$ . For an equivalence ratio of unity, Eq. (13) is identical to Eq. (8); while for an equivalence ratio of one-half, it is identical with the form of Eq. (12). Now, however, the exponential rate constant contained in  $C$  is a complex function of equivalence ratio and reactant inlet temperature. This variation arises because of the empirical character given to the rate equation.

Figure 7 gives the dependency on  $\phi$  of  $B$  at blowout for 300 K inlet temperature as produced by Kretschmer and Odgers. This dependency is compared with earlier recommendations also given by Kretschmer and Odgers (1972).

Unfortunately, Kretschmer and Odgers assumed a reaction mechanism that was different from that given in Eq. (2). Hence, their expression for  $m_f$  was different from that given in Eq. (5). Therefore, it was necessary to derive a variation of  $C$ , containing the exponential rate constant, with  $\phi$  that was appropriate to the present reaction mechanism.

The derivation of an appropriate  $C$  was done through Eq. (13) so that,

$$C = T [\ln (m_{f,\text{new}}/m_{f,\text{Kretschmer}}) \exp(C/T)_{\text{Kretschmer}}] \quad (14)$$

A comparison between the variations of two  $C$ 's with equivalence ratio for an inlet temperature of 300 K is shown in Fig. 8. Although the differences are small, it should be remembered that  $C$  is eventually to be used in an exponential relationship. The variation of  $C$  for the present reaction mechanism is conveniently represented by the polynomial

$$C = 14,926.5 + 73,774.7\phi - 109,826\phi^2 + 35,933.3\phi^3 \quad (15)$$

which has a correlation coefficient of 0.99998 and a maximum error of  $-54.3K$  in the range  $0.4 < \phi < 1.0$ .

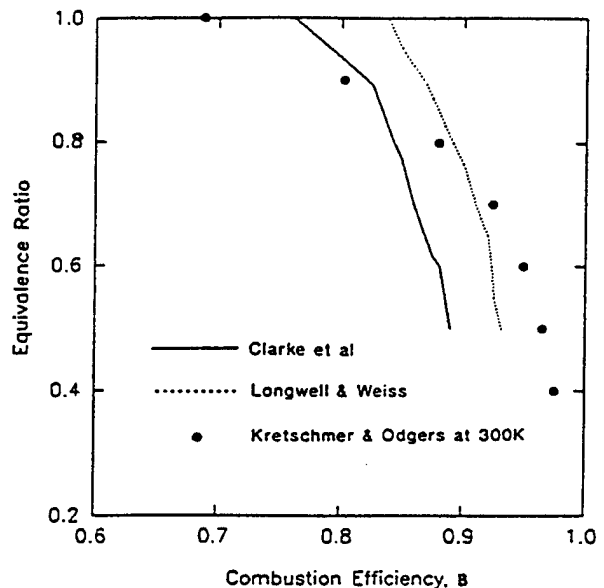


Fig. 7 Variation of combustion efficiency at blowout with equivalence ratio, from several sources

Equations (13) and (15) establish the form of the global reaction rate, and relate it to the selected reaction mechanism.

The calibration of simulated pressure may now be constructed for a range of equivalence ratios. The appropriate reaction rate expressions, one with variation in pressure and the other with variation in diluent mass flow rate, can be compared as functions of pressure and nitrogen/fuel mass ratio, respectively. The intersection of these expressions represents a common value of reaction rate expression indicating equivalency of pressure and nitrogen/fuel mass ratio. This enables the relationship between diluent mass flow rate and simulated pressure to be established. Figure 9 gives an example of this technique for a  $\phi$  of 0.8; Fig. 10 shows the resulting calibration curves for an inlet temperature of 300 K.

Figure 10 can be considered valid for well-stirred and partially stirred reactors. Although the empirical adjustment of the

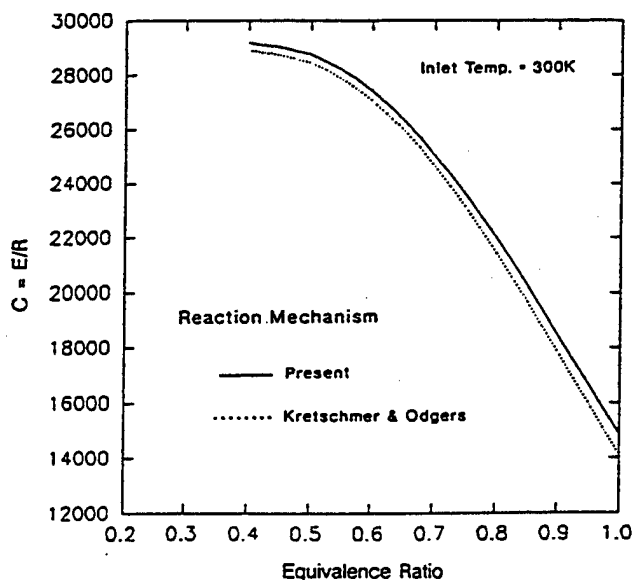


Fig. 8 Comparison of dependencies of activation energy on equivalence ratio for Kretschmer and Odgers reaction mechanism and present reaction mechanism

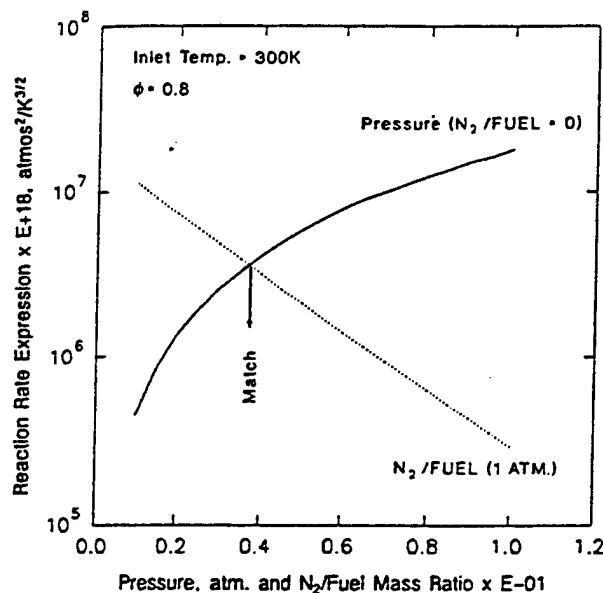


Fig. 9 Relationship between low pressure and simulated reaction rates for  $\phi = 0.8$

global Arrhenius reaction rate expression may be considered as being valid for a wide variety of hydrocarbons burning in air, the simulation calibration is for propane only. Further, it is limited to fuel-lean mixtures, as the figure indicates. The calibration shown is for 300 K inlet temperatures; Swithenbank (1974) contains sufficient information to construct curves for inlet temperatures from 200 K to 900 K.

### Experimental Results

After the ignition sequence was completed and the desired airflow established with the anchored flame condition (Sturgess et al., 1992), gaseous nitrogen was introduced into the air supply line to the research combustor. This was done far upstream so that the excess nitrogen was uniformly mixed with the air entering via the annular air jet surrounding the fuel jet. The nitrogen flow rate was set at a desired level, and a blowout

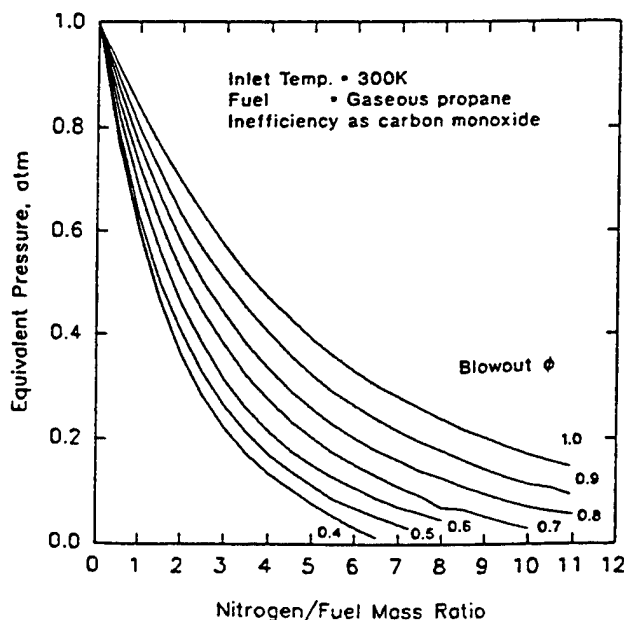


Fig. 10 Nitrogen-simulation calibration curve at 30 K

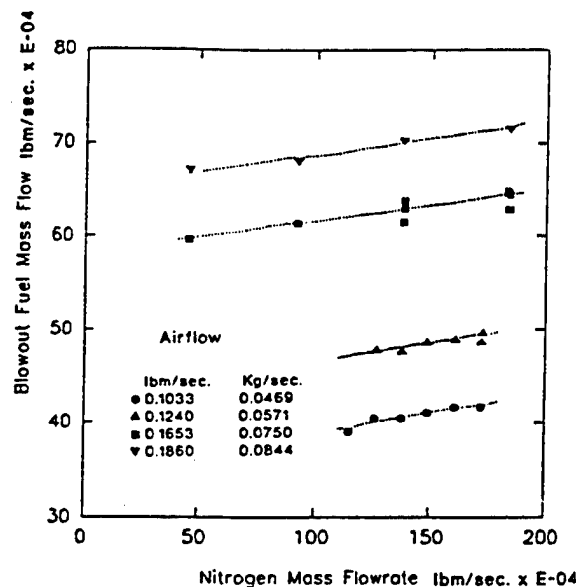


Fig. 11 Relationship between fuel flow at blowout and nitrogen flow at several airflows in the research combustor

sequence obtained by reducing the fuel flow rate until the flame was extinguished. Ignition was re-established, the airflow reset at the previous value in conjunction with the fuel flow, a new nitrogen flow rate was selected, and blowout was again obtained.

This procedure was repeated until a maximum nitrogen flow condition was reached. The combustor has been operated with nitrogen mass flow rates up to 55 percent of the air mass flow rate. No difficulties were encountered at this extreme condition. Repeatability and hysteresis were checked through obtaining blowouts by turning down the nitrogen flow rate range, and also by holding nitrogen and fuel flow rates constant while the airflow rate was increased. In addition, test points were repeated on different days with a different observer.

Examples of the basic results are displayed in Fig. 11, and show at a given airflow that increasing the nitrogen flow rate linearly increases the fuel flow rate at which a blowout takes place. In the figure, the multiple test points shown at a given nitrogen flow rate for the 0.653 lbm/sec (0.075 kg/s) airflow represent the day-to-day repeatability of the blowout. Increasing the combustor airflow increases the fuel flow at which blowout occurs, but does not change its dependency on the nitrogen flow rate.

Figure 12 gives an indication of the range of equivalent pressures represented by the nitrogen simulation, for various airflows. It ranges from just less than one atmosphere down to one-tenth of an atmosphere for these tests. The equivalent pressures were obtained from Fig. 10 for the blowout conditions given in Fig. 11. When the equivalent pressures are displayed against the mass ratio of nitrogen to fuel at blowout in this form, the data for the different airflows collapse onto a single curve representing the blowout characteristic for the research combustor. Note that for nitrogen to fuel mass ratios greater than about 5, there is a loss of effectiveness of the technique.

When excess nitrogen is introduced into the air supply, the visual appearance of the flame and its behavior does not change from that observed for zero excess nitrogen (Sturgess et al., 1992; Heneghan et al., 1990). Figure 13 gives a description of the flame behavior at constant airflow as the nitrogen flow rate is increased. Visually, there is no change in the equivalence ratio at which flame lift takes place. The equivalence ratio for lean blowout does increase, in accord with the behavior of Fig. 11. Blowout with excess nitrogen follows the same sequence

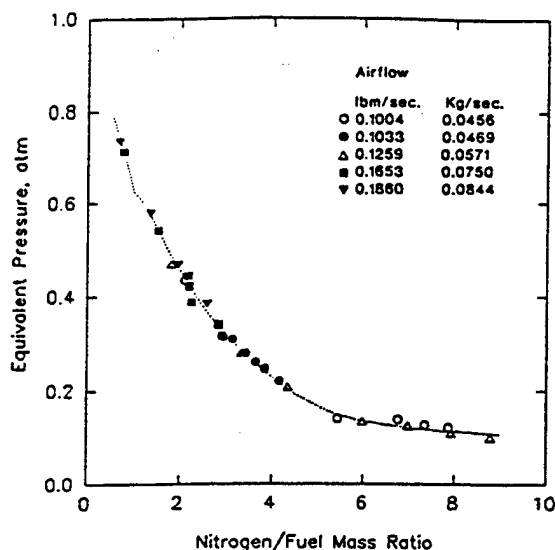


Fig. 12 Relationship between equivalent pressure and nitrogen to fuel mass ratio at blowout in the research combustor

of events as was observed for zero excess nitrogen (Sturgess et al., 1992; Heneghan et al., 1990).

### Correlation of Experimental Data

As described above, the equivalence ratio at blowout,  $\phi_{LBO}$ , of a well-stirred reactor can be related to the gas loading parameter,  $\dot{m}/VP^*F$ , for the combustor. Here, the mass flow rate is interpreted as  $\dot{m}_{Tot}$ , which is the sum of the air, excess nitrogen, and fuel mass flow rates. The fuel is included in this sum since its volume is not insignificant; the nitrogen flow rate is generally several times that of the fuel. Thus, the residence time in the reactor is materially affected by these flows.

For the present experiments the temperatures of the reactants were not varied, and the values for air, excess nitrogen and

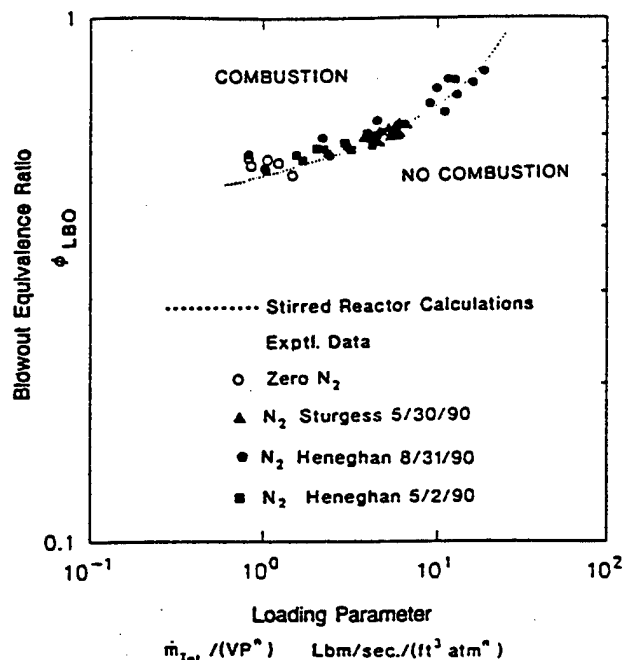


Fig. 14 Correlated blowout data for the research combustor, and comparison with the calculated well-stirred reactor blowout characteristic for the research combustor

propane were sensibly equal. Therefore, the temperature correction factor  $F$ , is taken as unity as a matter of convenience.

The pressure is interpreted as the effective pressure, and depends on the quantity of excess nitrogen flowing, as given by Fig. 12.

The (constant) volume is taken as the total combustor volume minus the volume of the combustor associated with flame lift.

The apparent order of the reaction,  $n$ , is taken as equal to  $\phi$  for lean mixtures. However, this is for propane/air systems. When a diluent is present, the order is reduced. The expression,

$$n = \frac{2\phi_{LBO}}{(1 + \dot{m}_{N2}/\dot{m}_{air})} \quad (16)$$

is used to account for this. When no excess nitrogen is present, Eq. (16) reverts to the pure air form.

In Fig. 14 the data in terms of  $\phi_{LBO}$  and  $\dot{m}_{Tot}/VP^*$  are plotted in logarithmic form. The measured data define most of the lean portion of the stability loop for the research combustor. The data cover points at atmospheric pressure with zero excess nitrogen, as well as those at atmospheric pressure with excess nitrogen; a variety of airflows were used.

The figure shows that the loading parameter correlates the blowout equivalence ratios very well. This can be appreciated when considering the repeatability shown in Fig. 11. The blowout data extend over three orders of magnitude of loading parameter, and range from a blowout equivalence ratio of around 0.5 to around 0.8.

### Verification of Calibration

Use of the simulation calibration curves for effective pressure (Fig. 12) resulted in a very satisfactory correlation of experimental lean blowout data obtained at constant true pressure for wide ranges of air and excess nitrogen flows. Fortunately, since the research combustor with zero excess nitrogen appeared to behave like a well-stirred reactor (Sturgess et al., 1992; Heneghan et al., 1990), an independent check of the calibration can be made through the use of well-stirred reactor theory.

Switnenbank (1974) presented a dissipation gradient approach for defining perfectly stirred regions of combustors. This

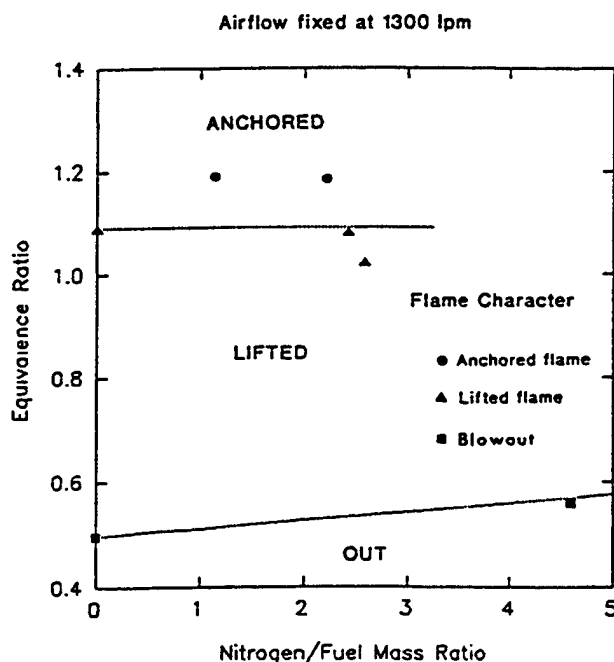


Fig. 13 Flame behavior in the research combustor at fixed airflow as nitrogen to fuel mass ratio is varied

approach was applied to the research combustor, using a computational fluid dynamics (CFD) calculation to provide the turbulence characteristics.

Based on the dissipation gradient analysis, the rapid-stirring region of the research combustor was identified as the volume enclosing the highly turbulent portion of the flow. It was found that the surface contour enclosing 96 percent of the turbulence kinetic energy and 99 percent of its rate of dissipation corresponded to a surface over which the total dissipation gradient had a value of 10.0, which is 100 times the value recommended by Swithenbank. This well-stirred region extended over most of the length of the combustor, with exceptions of portions of the step recirculation zone and the stagnation region on the upstream face of the orifice plate placed at the combustor exit.

While the turbulence characteristics of a flow can be used to define a region of rapid mixing, this alone is not a sufficient condition for a well-stirred reactor. For stable reaction to take place within the rapid mixing region, the fuel and air mixture must locally fall inside the flammability limits, a source of continuous ignition (mixture at exit temperature) must be present, and local flow velocities must not exceed the local turbulent burning velocity.

CFD analysis was again used to provide necessary information to determine places within the defined rapid mixing region where stable combustion could take place for conditions close to blowout. On the basis of these calculations and the observations of the lifted flame position, which was found to remain roughly constant as equivalence ratio was reduced, a suitable well-stirred reactor volume was defined. This was 44 percent of the total combustor volume, and corresponded to a lifted flame mean position of about 40 cm (16 in.) from the central portion of the step, assuming that the flame completely filled the cross section. Visual observations of the flame indicated that on the centerline of the combustor the closest position to the step-plane of the lifted flame was about 16 cm (6 in.) downstream. Of course, the real flame never completely filled the cross section.

With a well-stirred reactor defined, the stirred reactor network code MARK2I by David Pratt and Brian Pratt was used to make calculations for the research combustor. The MARK2I code uses the CREK chemical kinetics code (Pratt and Wornack, 1976) and a hydrocarbon reaction mechanism by Roberts et al. (1972). The research combustor near blowout was modeled in MARK2I as a single, perfectly stirred reactor with separate air and fuel inlets, and a single discharge of products; there was no recirculation of products. It was operated with gaseous propane as fuel and air as oxidant, with equal inlet temperature of 293 K. The volume was that defined above, although two other volumes were used for spot checks to see the sensitivity to volume. This was done because of the uncertainty associated with the flame position. (The results for the range of volumes were subsequently correlated successfully by the loading parameter, via the volume term incorporated in it.) The model was operated at a number of air mass flow rates, with several pressure levels of atmospheric and less, for each airflow. No cases with excess nitrogen were run.

Shown on the stability plot of Fig. 14 is a line representing the blowout characteristic calculated by the well-stirred reactor code. The line runs through the correlated experimental blowout data very nicely, thereby confirming that the research combustor is behaving as a well-stirred reactor. Furthermore, since the loading variation in the well-stirred reactor calculations was achieved through variations in mass flow rate and true operating pressure while the experimental data were correlated on the basis of mass flow rate and equivalent pressure, the agreement verifies the calibration (Fig. 12) of the nitrogen dilution technique.

## Discussion

A technique has been presented whereby the lean reaction of gaseous propane in air at subatmospheric pressures can be

simulated by approximating the subatmospheric pressure reaction rate with a reaction rate at atmospheric pressure in the presence of excess gaseous nitrogen as a diluent.

The technique has been calibrated through the assumption of a one-step global reaction mechanism for propane/air/excess nitrogen systems in which nitrogen remains inert, and where combustion inefficiency is accounted for solely through the CO/CO<sub>2</sub> balance in the products. A global reaction rate expression in Arrhenius form for a bimolecular, single-step reaction was calibrated using experimental data from the literature. Finally, the relationship between excess nitrogen and the equivalent pressure was established by comparing appropriate reaction rate expressions with separate variation in pressure and diluent mass flow rate. This relationship forms a calibration for the simulation technique at blowout conditions. The calibration is valid for well-stirred and partially stirred reactors using propane as a fuel in a lean mixture with air. The specific calibration curve presented is for 300 K inlet temperature of reactants, although similar curves for other temperatures are readily constructed.

Lean blowout data in a research combustor, obtained using the simulation technique, were successfully correlated using the conventional loading parameter in which the pressure term was taken as the equivalent pressure obtained from the calibration. The range of equivalence ratios covered by the variation in loading parameter was from near the flammability limit to near the maximum heat release rate; the range of loading parameter obtained extended over three orders of magnitude. These were achieved at atmospheric pressure and with a limited range of mass flow rates. The lean stability of the research combustor was completely defined by these data.

The combustor was operated without difficulty with an excess nitrogen mass flow rate up to 60 percent of the air mass flow rate. At this condition the equivalent pressure corresponded to 0.1 atmosphere. However, it is not recommended that the maximum excess nitrogen flow rate be greater than about 45 percent of the air mass flow rate. This is because of inaccuracies in the calibration curve (lower right-hand corner of Fig. 10), at operating conditions with very high levels of excess nitrogen.

The effective order of the reaction when excess nitrogen is used becomes a function of the mass ratio of excess nitrogen to air, as well as equivalence ratio at blowout. There was no visual evidence that the excess nitrogen changed the flame characteristics in any way from that observed without excess nitrogen.

A final check on the accuracy of the calibration was made by comparing the correlated experimental results using the simulation against well-stirred reactor calculations based on propane/air systems for true subatmospheric pressures. This comparison was justified since it was known from the initial test results (Sturgess et al., 1992; Heneghan et al., 1990) that the research combustor had well-stirred reactor lean blowout performance when operated at atmospheric pressure without any excess nitrogen. The subsequent agreement in the stirred reactor calculation comparison confirmed the accuracy of the calibration.

The demonstration of the successful calibration for the nitrogen dilution simulation of low operating pressures opens an important possibility for small-scale facility combustion experiments. Their operating range may be extended for certain low pressure effects in an easy, inexpensive, and safe fashion while the convenience of operating at atmospheric pressure is maintained.

Experimental lean blowout data have been obtained in the research combustor over a wide range of equivalence ratios. These data will provide a good data base for lean blowout modeling. The fact that the research combustor has been definitively shown to behave as a well-stirred reactor when operated in the lifted flame condition is an important help in understanding, and hence modeling, the lean blowout process.

## Conclusions

- 1 The nitrogen dilution technique for simulating the effects on chemical reaction rates of low pressures has been successfully calibrated. The calibration removes the simulation from being a qualitative technique, to being a quantitative one. It permits certain low-pressure combustion effects to be examined while maintaining the convenience of operating at atmospheric pressure.
- 2 The lean blowout data obtained in a research combustor via the low-pressure simulation technique were correlated by the familiar loading parameter when the effective pressure was used for actual pressure and the reaction order was made a function of the excess nitrogen.
- 3 Nitrogen dilution enables the loading parameter for the research combustor to be extended over three orders of magnitude, and the blowout equivalence ratio to be increased from near the flammability limit to close to the maximum heat release condition. This enables the lean stability of the combustor to be adequately defined.
- 4 The research combustor at blowout conditions behaves like a classical well-stirred reactor.

## Acknowledgments

This work was supported by the U.S. Air Force Wright Research and Development Center, Aero Propulsion and Power Laboratory, under Contract No. F33615-87-C-2822 to Pratt & Whitney, East Hartford, CT (Contract Monitor: Lt. A. L. Lesmerises) and Contract No. F33615-87-C-2767 to University of Dayton, Dayton, OH (Contract Monitor: Dr. W. M. Roquemore).

## References

Bragg, S. L., 1953, Aeronautical Research Council, Paper No. 16170, CF 272, U.K., Sept.

- Clarke, A. E., Odgers, J., and Ryan, P., 1960, "Further Studies of Combustion Phenomena in a Spherical Reactor," *Proc. 8th Symposium (International) on Combustion*, The Combustion Institute, pp. 983-994.
- Greenhough, V. W., and Lefebvre, A. H., 1956, "Some Applications of Combustion Theory to Gas Turbine Development," *Proc. Sixth Symposium (International) on Combustion*, Reinhold Publishing Co., pp. 858-869.
- Heneghan, S. P., Vangsness, M. D., Ballal, D. R., Lesmerises, A. L., and Sturgess, G. J., 1990, "Acoustic Characteristics of a Research Step Combustor," AIAA Paper No. AIAA-90-1851.
- Herbert, M. V., 1960, "A Theoretical Analysis of Reaction Rate Controlled Systems; Part II," *Proc. 8th Symposium (International) on Combustion*, The Combustion Institute, pp. 970-982.
- Kretschmer, D., and Odgers, J., 1972, "Modeling of Gas Turbine Combustors—A Convenient Reaction Rate Equation," *ASME JOURNAL OF ENGINEERING FOR POWER*, pp. 173-180.
- Lefebvre, A. H., and Halls, G. A., 1959, "Simulation of Low Combustion Pressures by Water Injection," *Proc. Seventh Symposium (International) on Combustion*, Butterworths Scientific Publications, London, pp. 654-658.
- Lefebvre, A. H., 1961, "Some Simple Techniques for the Performance Evaluation of Gas Turbine Combustion Systems," *Experimental Methods in Combustion Research*, J. Surugue, ed., AGARD, Pergamon Press.
- Lewis, B., and von Elbe, G., 1987, *Combustion, Flames and Explosion of Gases*, 3rd ed., Academic Press.
- Longwell, J. P., Frost, E. E., and Weiss, M. A., 1953, "Flame Stability in Bluff-Body Recirculation Zones," *Ind. Eng. Chem.*, Vol. 45, No. 8, pp. 1629-1633.
- Norster, E. R., 1968, "Subsonic Flow Flameholder Studies Using a Low Pressure Simulation Technique," *Proc. Intl. Prop. Symp. Combustion in Advanced Gas Turbine Systems*, I. E. Smith, ed., Cranfield Intl. Symp. Series, Vol. 10, Pergamon Press, pp. 79-94.
- Pratt, D. T., and Wormeck, J. J., 1976, "CREK—A Computer Program for Calculation of Combustion Reaction Equilibrium and Kinetics in Laminar or Turbulent Flow," Rpt. No. WSU-ME-TEL-76, Dept. Mech. Engrg., Washington State University.
- Roberts, R., Aceto, L. D., Kollrack, R., Teixeira, D. P., and Bonnell, J. M., 1972, "An Analytical Model for Nitric Oxide Formation in a Gas Turbine Combustor," *AIAA J.*, Vol. 10, No. 6, pp. 820-826.
- Sturgess, G. J., Sloan, D. G., Lesmerises, A. L., Heneghan, S. P., and Ballal, D. R., 1992, "Design and Development of a Research Combustor for Lean Blow-Out Studies," *ASME JOURNAL OF ENGINEERING FOR GAS TURBINES AND POWER*, Vol. 114, pp. 13-19.
- Swithenbank, J., 1974, "Flame Stabilization in High Velocity Flow," *Combustion Technology—Some Modern Developments*, H. B. Palmer and J. M. Beer, eds., Academic Press, pp. 91-125.

## **APPENDIX K**

### **Effects of Back-Pressure in a Lean Blowout Research Combustor**

**G. J. Sturgess, S. P. Heneghan, M. D. Vangsness,  
D. R. Ballal, A. L. Lesmerises, L. Shouse**

**G. J. Sturgess**

Pratt & Whitney,  
East Hartford, CT 06108

**S. P. Heneghan**

**M. D. Vangsness**

**D. R. Ballal**

University of Dayton,  
Dayton, OH 45469

**A. L. Lesmerises**

**D. Shouse**

Wright Laboratories,  
Wright-Patterson Air Force Base,  
Dayton, OH 45433

## Effects of Back-Pressure in a Lean Blowout Research Combustor

*Experimental information is presented on the effects of back-pressure on flame-holding in a gaseous fuel research combustor. Data for wall temperatures and static pressures are used to infer behavior of the major recirculation zones, as a supplement to some velocity and temperature profile measurements using LDV and CARS systems. Observations of flame behavior are also included. Lean blowout is improved by exit blockage, with strongest sensitivity at high combustor loadings. It is concluded that exit blockage exerts its influence through effects on the jet and recirculation zone shear layers.*

### Introduction

Combustion stability is extremely important in gas turbine engines for aircraft use. It is becoming more difficult to ensure that adequate stability margins can be maintained because of current design trends toward airblast atomization of liquid fuel, high temperature rise, and low emissions combustors.

As part of a comprehensive research program to investigate, understand, and model lean blowouts in the combustors of aircraft gas turbine engines (Sturgess et al., 1991a), three combustors are utilized. These vehicles consist of a research combustor, a technology combustor, and a generic gas turbine combustor, which reflect the three-phase approach to the problem. The purpose of the research combustor is to yield fundamental information on the lean blowout process to assist in understanding the events taking place during blowout, and so guide in modeling them.

In gas turbine combustor design, it is generally recognized that the end of the flame-holding primary zone is determined by the transverse combustion air jets entering through the combustor liners (Lefebvre, 1983). For combustors using either pure airblast or hybrid pressure-atomizing primary/airblast secondary fuel injectors, it has been observed that dynamic interactions can occur between the axially directed jets of atomized fuel/air mixture from the injectors, and these transverse combustion air jets. Recirculation zones of the "external"

(Gupta et al., 1984) or "inside-out" type (Sturgess et al., 1990) seem to be especially prone to this behavior. The interaction can be exacerbated if the airflow through the combustor dome (including the injectors) is a significant proportion of the combustor total flow, and if the transverse air jets are close to the dome.

It was therefore felt that the important back-pressure effect exerted on the flame through the presence of the combustion air jets should be included in any simulation of a gas turbine combustor primary zone.

In the research combustor, which was intended for the study of the breakdown of flame stabilization in the primary zone, the essential features of a typical primary zone of modern combustors were reproduced in simplified form (Sturgess et al., 1992a). Combustion air jets were not included directly due to the complication involved; however, the back-pressure of these jets was represented by means of exit blockage from the combustor.

### Research Combustor

The research combustor consists of a central fuel jet of gaseous propane surrounded by an unheated co-axial air jet, with the confluence of the jets centrally located in a nominally circular cross-sectional duct (Sturgess et al., 1992b). The duct is closed at its forward end to give a backward-facing step. The combustor exit is open to the atmosphere; low pressure effects on lean blowout are simulated by means of dilution through injection of excess nitrogen into the air supply (Sturgess et al., 1991b). The combustor is mounted vertically on an

Contributed by the International Gas Turbine Institute and presented at the 37th International Gas Turbine and Aeroengine Congress and Exposition, Cologne, Germany, June 1-4, 1992. Manuscript received by the International Gas Turbine Institute February 6, 1992. Paper No. 92-GT-81. Associate Technical Editor: L. S. Langston.

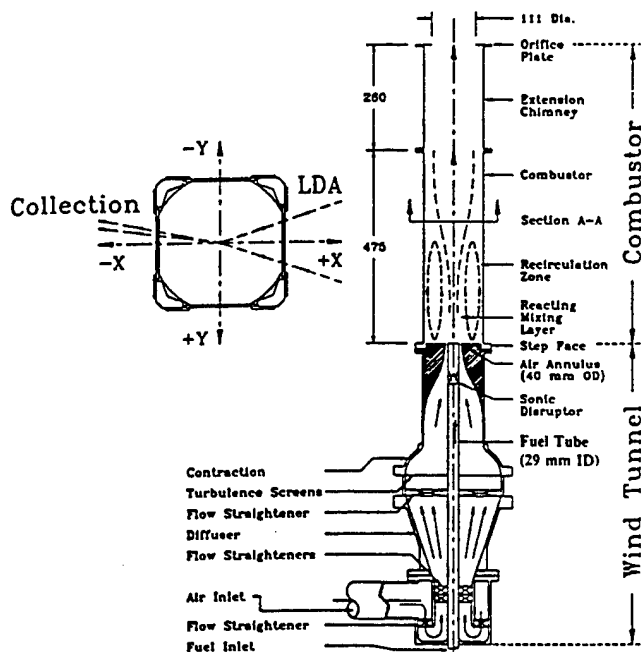


Fig. 1 Research combustor, showing axes convention

airflow-conditioning unit, which traverses through a cutout in a fixed optical bench, Fig. 1.

The combustion tunnel was designed and constructed in two sections: a fixed upstream window section providing optical access as needed, and a replaceable downstream chimney. The chimney is available in two lengths, and the combustor can be run with either of these, or with no chimney at all. The combustor has a hydraulic diameter of 150 mm, giving length to diameter ( $L/D$ ) ratios of 3.167, 4.9, and 6.513, respectively, depending on the chimney arrangement. The inner diameter of the fuel tube is 29.97 mm with a 2-deg half-angle taper over 120 mm of its length, and the outer diameter of the air passage at discharge is 40 mm.

Provision is made for combustor exit blockage. The geometric values of exit blockage are 21.0, 45.1, and 62.0 percent of the combustion cross section. These blockages are achieved by means of thin orifice plates. For the 45.1 percent geometric blockage, "top-hat" exits with tailpipe length to diameter ( $L/D$ ) values of 1.0 and 2.1, respectively, are also available.

The optical windows can be replaced by metal plates containing arrays of thermocouples for wall temperature measurements, and tapings for static pressure measurements. The combustor may be run with any combination of windows and plates.

### LDA Arrangement

Mean and fluctuating velocity component measurements are obtained by means of a laser-Doppler anemometer (LDA) system (Sturgess et al., 1992b), using 10-deg off-axis forward scattering. The effective probe volume is  $50 \times 300 \times 750 \mu\text{m}$ .

The combustor is mounted vertically in the facility (Sturgess et al., 1992a), and its centerline constitutes the  $z$  axis, with zero taken as the plane of the step. The  $x$  and  $y$  axes are diametral to the combustor cross section, with the  $x$  axis aligned with the LDA axis. Velocities parallel to and increasing in the direction of the  $z$  axis, and velocities normal to and directed away from the axis, are considered positive.

The effective optical window within which data may be taken is defined by:  $-68.7 < x < +68.7 \text{ mm}$ , and  $-22 < y < 33 \text{ mm}$ ; in the downstream direction it is  $+2 < z < 358 \text{ mm}$ .

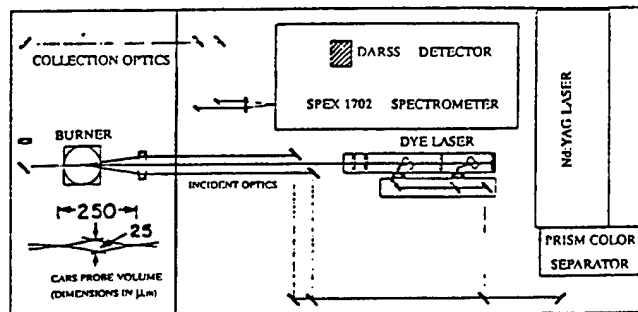


Fig. 2 Arrangement of the CARS system optics

This window permits reasonable access to the major flow field features (Sturgess et al., 1992b).

For error assessments, see Sturgess et al. (1992b).

### CARS Arrangement

The laser source for the coherent anti-Stokes Raman Spectroscopy (CARS) optics is a Nd:YAG pulse laser with 10 ns time resolution. The frequency-doubled source green beam (532 nm) is equally divided into four parts: two of these serve as pump beams, while the remaining two pump a dye laser oscillator and amplifier. The dye laser is tuned to provide a red broad-band Stokes beam (110 FWHM) centered at 607 nm. The red Stokes beam and the two green pump beams are then focused together by a 25 cm focal length lens in a BOXCAR configuration. A  $25 \times 250 \mu\text{m}$  measuring spot size is achieved. The CARS signal is collected by a Spex 1702 spectrometer, 1024-element DARSS camera, and Tracor-Northern multi-channel analyzer (Fig. 2). The raw data are processed by a MODCOMP minicomputer.

From the raw data the temperatures are determined by comparing the actual nitrogen spectra to the calculated spectra, using a least-squares fit. The calculation of a nitrogen CARS spectrum requires knowledge of the instrument slit function. Error problems associated with the assumption of a constant slit function when the optical path contains density and/or temperature gradients are avoided by use of a simple method of determining slit functions from the collected data at actual temperature and turbulence levels, by applying local thermodynamic equilibrium principles (Heneghan et al., 1991). This method has been shown to yield improvements in the precision of the CARS measurement (Heneghan and Vangsness, 1991).

Both fuel and air flows were monitored by separate electronic flow control units to within  $\pm 0.5$  percent and  $\pm 1.5$  percent, respectively. The combined error produced an uncertainty of  $\pm 1.5$  percent in equivalence ratio, or  $\pm 30 \text{ K}$  in temperature. Usually, 500 samples were taken for each CARS measurement to ensure that the error in rms temperature was less than 10 K. The rms temperature is susceptible to CARS instrument noise (Heneghan and Vangsness, 1990). However, in combusting flow the temperature fluctuations are much greater than the instrument noise, and thus the measurement precision (reproducibility) is good. It is estimated overall that the CARS mean temperature measurement accuracy is within 50 K, while the precision is well within 20 K. Unlike the LDA, CARS temperature measurements are time-averaged without density-biasing effects.

### Isothermal Flow Field

Development of the isothermal flow field in the research combustor with a free outlet is fully discussed by Sturgess et al. (1992b). Briefly, at a simulated blowout condition, the



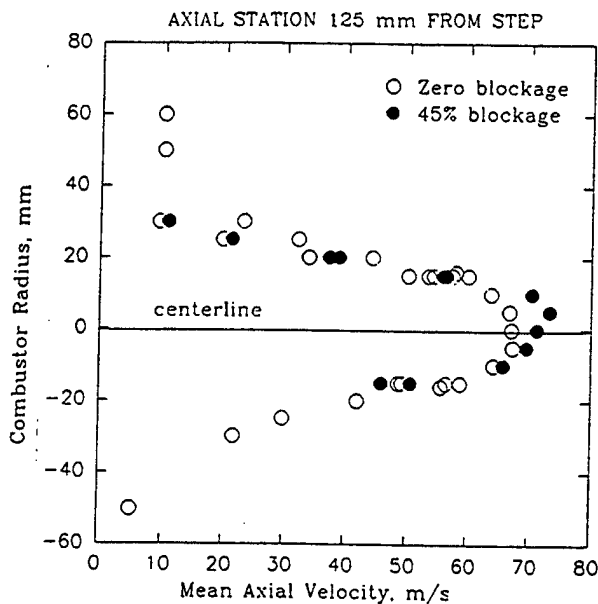


Fig. 3 Radial profiles of mean axial velocity in isothermal flow 125 mm downstream from the step-plane, showing central flow net acceleration with exit blockage

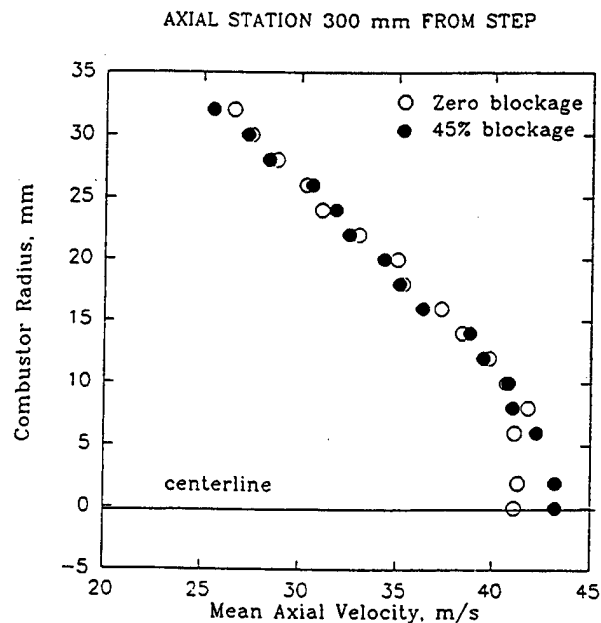


Fig. 4 Radial profiles of mean axial velocity in isothermal flow 300 mm downstream from the step-plane, showing central flow net acceleration with exit blockage

annular air jet immediately entrains the central fuel jet, generating a small central recirculation bubble of length 17 mm with a beginning about 15 mm downstream of the jet confluence. The individual jets thus quickly merge as they expand into the combustor, and soon lose their identities. This merging is complete by 138 mm from the step. The step generates a large recirculation zone of axial length 7.7 step heights, and with vortex centers about 3.1 step heights downstream.

The addition of exit blockage by orifice plate exerts an obvious effect on the radial profiles of mean axial velocity as the flow accelerates along the combustor centerline to form a vena contracta in the exit plane, with a toroidal recirculation zone forming on the forward face of the orifice plate. For the 4.9  $L/D$  combustor the near-field is unaffected, but the centerline flow acceleration is evident as close as 125 mm downstream from the step-plane. Figures 3 and 4 demonstrate this at the 125 and 300 mm stations, respectively, for 45.1 percent blockage. Note that the acceleration effect is ameliorated to some extent by the expansion of the combined jets into the combustor.

There were no changes apparent in the fluctuating velocities with the addition of exit blockage.

The flow field with reaction present is the process of being measured. The features described under isothermal conditions are unchanged in character by the heat release.

### Effects of Blockage on Flame Behavior

The research combustor operates with three basic flame conditions, depending on the equivalence ratio. For  $\phi > 1.05$  approximately, a thin, sheathlike pilot flame is anchored close to the step near the outer diameter of the air passage (Sturgess et al., 1991b). The fuel source for this pilot flame is the step recirculation zone. The major heat release is then precipitated downstream in more or less distributed fashion, by the action of this pilot. Downstream flame-holding takes place in the shear layers associated with the central and step recirculation zones (Sturgess et al., 1992b). For  $\phi < 1.05$  approximately, the pilot flame is highly intermittent (Roquemore et al., 1991), and the main flame is lifted (Sturgess et al., 1991b), allowing considerable premixing of reactants to take place prior to combustion. The lifted flame is positioned between 160 to 300 mm

from the step-plane. When  $\phi$  reaches 1.5 to 2.0 and before a rich blowout, a separated flame condition is again established where the pilot flame is no longer apparent to the eye, but the main flame does not lift in this case. It is located about 30 to 40 mm downstream from the step.

Lean blowout data were correlated on the basis of a combustor loading parameter (Sturgess et al., 1991b), derived from reaction rate theory as

$$LP = \dot{m}_{\text{Tot}} / (VP^n F)$$

where for gaseous fuels and with simulation of low pressures by excess nitrogen injection,

$$\dot{m}_{\text{Tot}} = \dot{m}_{\text{fuel}} + \dot{m}_{\text{air}} + \dot{m}_{\text{nitrogen}}$$

$V$  = reactor volume

$P$  = effective pressure

$n$  = apparent global reaction order

$$= 2\phi / (1 + \dot{m}_{\text{nitrogen}} / \dot{m}_{\text{air}})$$

$\phi$  = equivalence ratio

$F$  = temperature correction factor (to 400 K)

$$= 10^{0.00143T_{\text{in}}/3.72}$$

$T$  = inlet temperature of reactants in K.

Use of  $LP$  for blowout correlations follows from the adoption of a stirred reactor modeling approach (Sturgess et al., 1992a). It also forms a useful way of characterizing the degree of "flame straining" present in the combustor.

Figure 5 provides a map of flame behavior as a lean blowout is approached, obtained by visual observation. The combustor  $L/D$  was 4.9, and the exit was a 45.1 percent blockage orifice plate. Inlet temperatures for the reactants were constant at 293 K, and no excess nitrogen was injected. The Reynolds number of the annular air jet was in the range of 24,800 to 46,000. The attached and lifted flame conditions are illustrated in Fig. 2 of Sturgess et al. (1991b).

The range of the loading parameter in Fig. 5 is such that lean blowouts were obtained close to the flammability limits for propane/air mixtures at ambient conditions (Lewis and

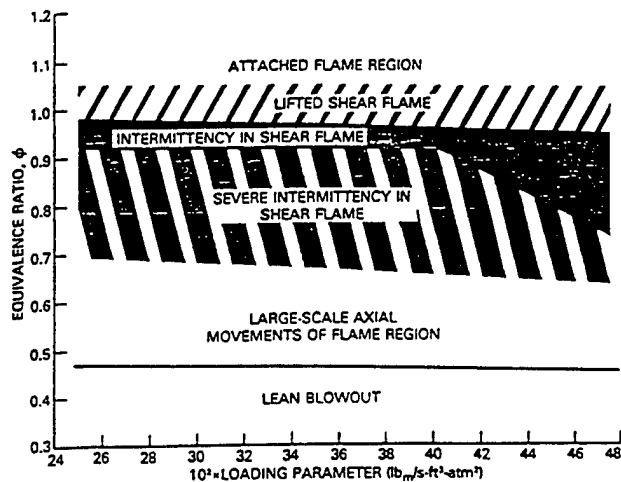


Fig. 5 Flame behavior as lean blowout is approached at low combustor loadings with 45 percent exit blockage

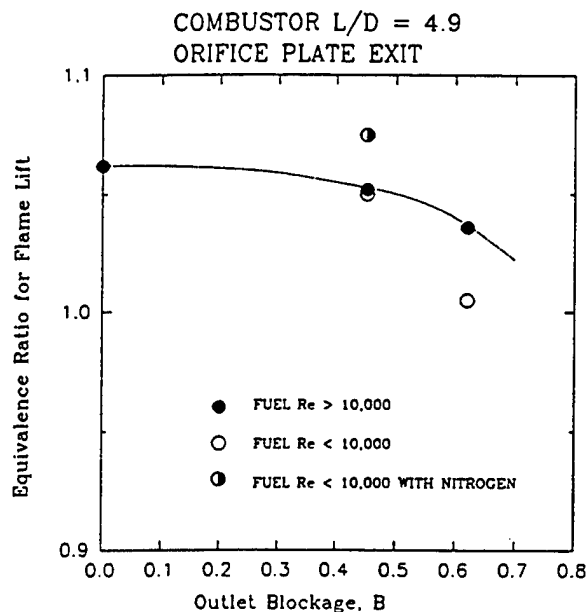


Fig. 6 Dependence of equivalence ratio for flame lift on exit blockage for low and intermediate combustor loadings

von Elbe, 1961). The flame behavior seen is both reversible and repeatable. Flame lift can be seen at about 1.05 equivalence ratio, and is insensitive to loading parameter over the limited range covered. Subsequent tests (Sturgess et al., 1991b) with injection of excess gaseous nitrogen into the air stream showed no effects on equivalence ratio for flame-lift. When the fuel flow was progressively reduced at constant airflow, or the airflow was progressively increased at constant fuel flow, the same sequence of flame events leading to a blowout took place. These events are shown in Fig. 5. Eventually, an oscillatory flow situation develops, with large-scale axial movements of the entire lifted flame about a mean position. This motion leads, in due course, to lean blowout.

The existence of the sequence of flame behaviors did not change qualitatively with differences in exit blockage. However, the equivalence ratio for flame lift was observed to decrease slightly with increase in blockage due to orifice plates (Fig. 6). Similar behavior was observed with increase in tailpipe  $L/D$  for the 45.1 percent blockage top-hat section (Fig. 7).

The significance of the 10,000 Reynolds number for the fuel jet in Figs. 6 and 7 is that this value represents a critical threshold for transition to turbulent flow for propane (Lewis and von Elbe, 1961).

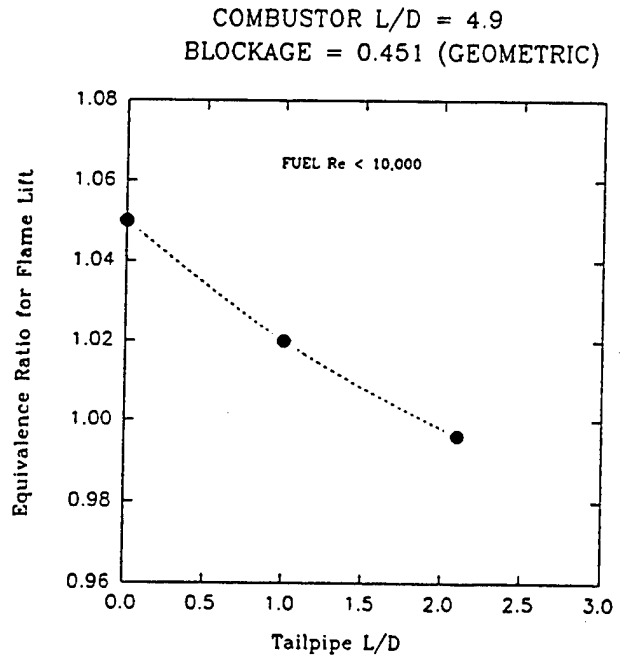


Fig. 7 Dependence of equivalence ratio for flame lift on tailpipe length for 45 percent geometric exit blockage

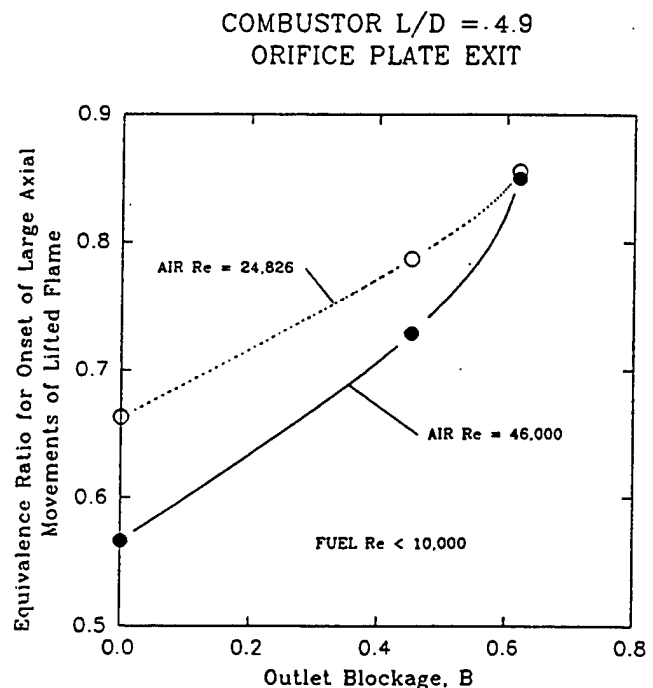


Fig. 8 Influence of exit blockage and combustor loading on equivalence ratio for onset of axial movements of the lifted flame

A fairly strong influence on the equivalence ratio for the onset of the large-scale axial oscillation of the lifted flame was observed, as shown in Fig. 8. Increased blockage raises this equivalence ratio and is therefore destabilizing, opposite to the effect on flame lift. Note the significance of air jet Reynolds numbers.

It is apparent that the loss of the important pilot flame marks the beginning of a lean blowout sequence. A similar importance of the pilot flame is observed as a rich blowout is approached. Figure 9 shows the dependence of rich equivalence ratio for loss of the pilot flame (to result in a separated main flame), on exit blockage in the 4.9  $L/D$  combustor. Note that on the rich side, decreasing equivalence ratio denotes a maximum loss

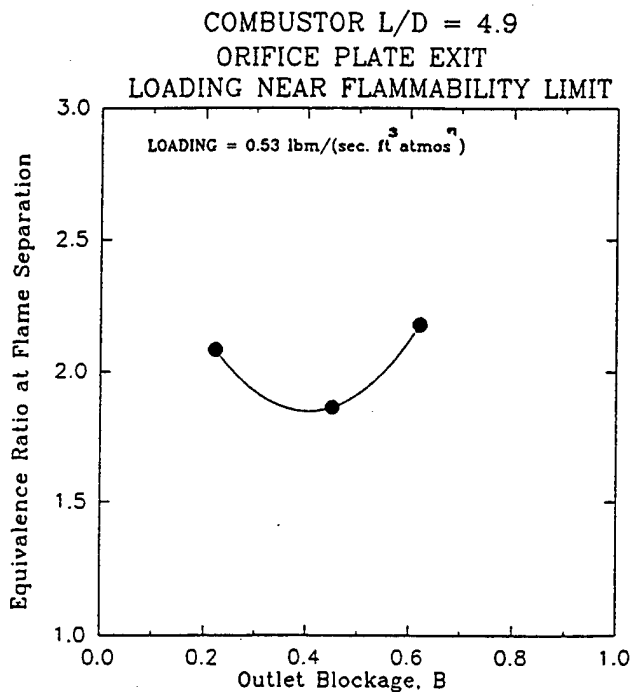


Fig. 9 Dependence of equivalence ratio for flame separation on exit blockage for low combustor loading

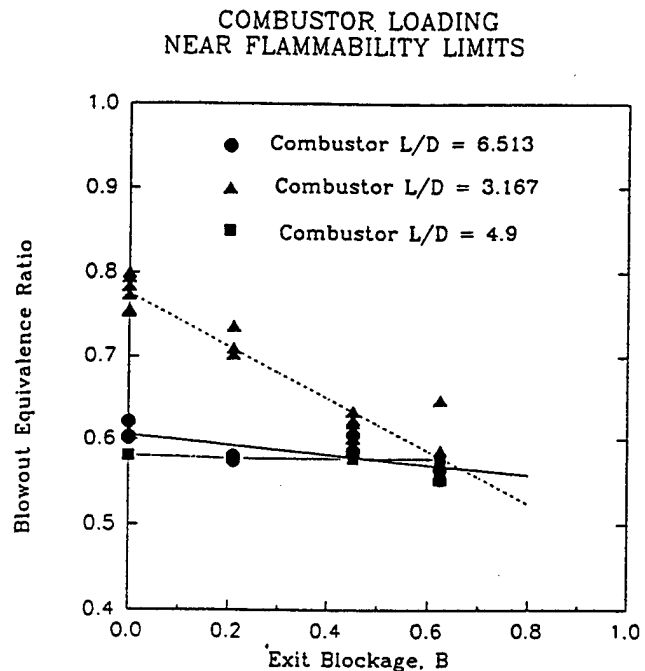


Fig. 11 Influence of exit blockage on lean blowout at low combustor loading in three combustor lengths

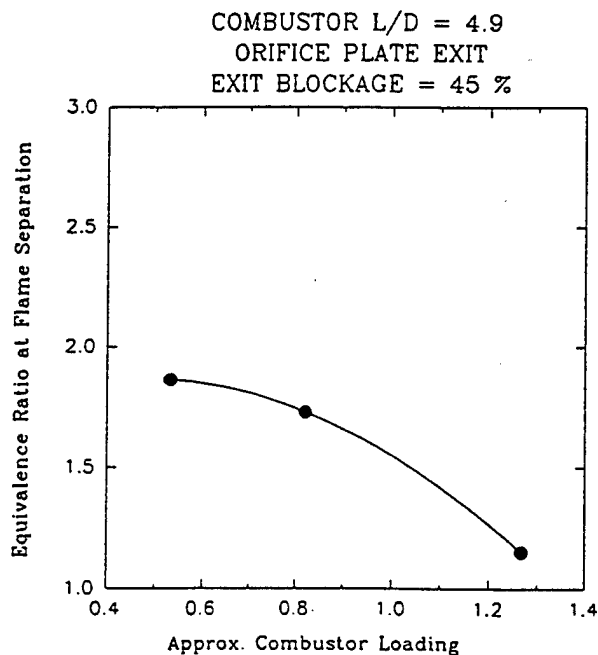


Fig. 10 Influence of combustor loading on equivalence ratio for flame separation at 45 percent exit blockage

of stability at 45.1 percent blockage. At given blockage this rich equivalence ratio for pilot flame loss decreases as the combustor loading is increased; Fig. 10 demonstrates this for the 4.9  $L/D$  combustor at 45.1 percent exit blockage by orifice plate.

#### Direct Effects on Lean Blowout

It was observed for low values (about  $0.18 \text{ lb}_m/(\text{sec. ft.}^3 \text{atmos.})$ ) close to the flammability limits for propane/air mixtures at these conditions) of the loading parameter that the blowout equivalence ratio decreased linearly as the exit

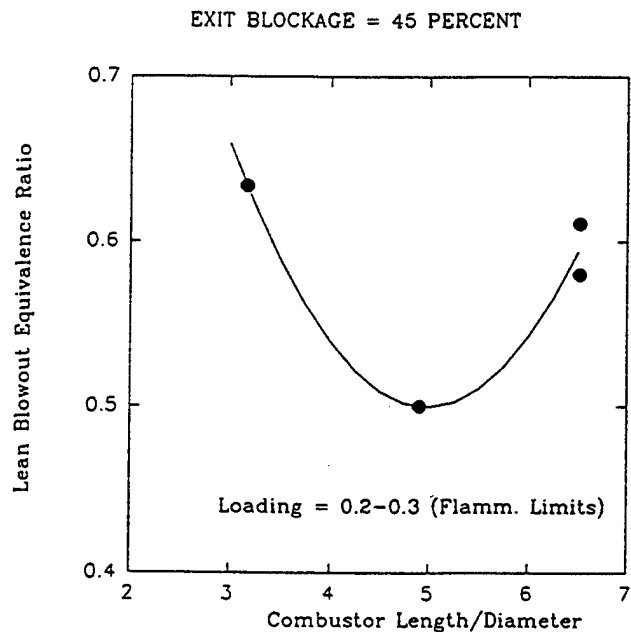


Fig. 12 Dependence of lean blowout at low loadings on combustor length with 45 percent exit blockage

blockage by orifice plate was increased. This is shown in Fig. 11, and is somewhat surprising since the lifted flame is positioned (Roquemore et al., 1991) in the regions where the mean flow is beginning to be accelerated due to the blockage (Figs. 3 and 4), at least in isothermal flow. Heat release should increase the flow acceleration. The improvement in stability depended on the combustor  $L/D$  ratio; for a given blockage, the shorter the combustor the less stable it was and the greater its sensitivity to the exit blockage. For the 4.9  $L/D$  combustor at this loading, the lean blowouts were virtually independent of exit blockage.

For a fixed exit orifice plate blockage of 45.1 percent at slightly higher loading parameter, the dependency on  $L/D$  is given in Fig. 12, where it can be seen that an optimum  $L/D$

# COMBUSTOR LOADING NEAR PEAK HEAT RELEASE RATE

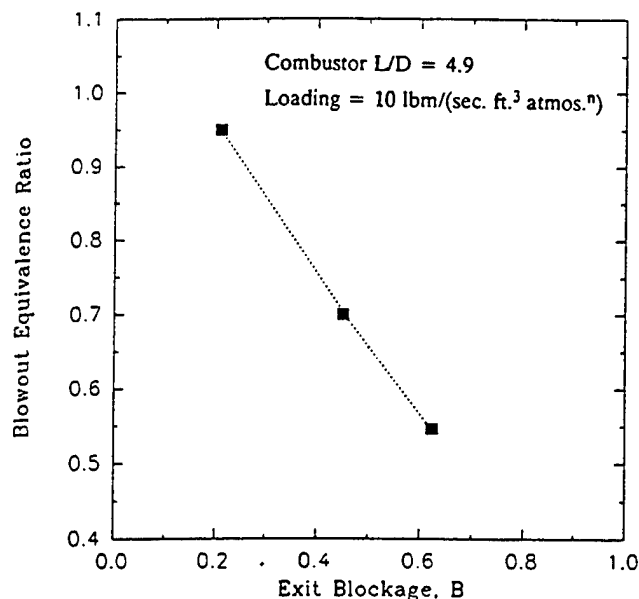


Fig. 13 Influence on lean blowout of exit blockage at high combustor loading

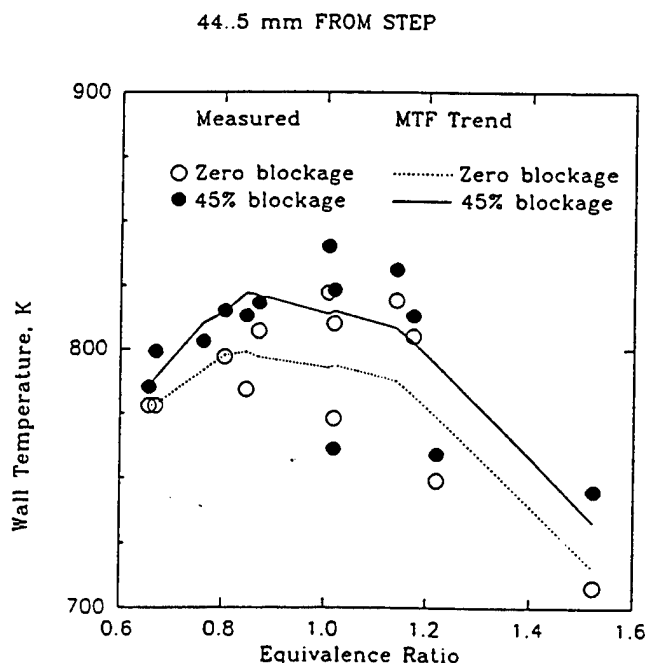


Fig. 14 Comparison of actual wall temperatures with smoothed values over a range of equivalence ratios, showing influence of exit blockage

exists. Close to the flammability limits there is also a fairly strong sensitivity of blowout equivalence ratio to combustor loading parameter. The existence of the optimum combustor length for maximum stability close to the flammability limits (Lewis and von Elbe, 1961) can be attributed to the occurrence of acoustic coupling (organ-pipe resonance driving eddy shedding off the step at 55 Hz) at large  $L/D$  (Heneghan et al., 1990), and outlet interference with flame holding at small  $L/D$ .

At 45.1 percent exit blockage the peak amplitude of the 55 Hz frequency signal measured inside the combustor by Kistler pressure transducers was increased by a factor of 5.5 when the

combustor  $L/D$  was increased from 3.167 to 6.513. For the 4.9  $L/D$  combustor with 45.1 percent exit blockage (and the acoustic treatment described by Heneghan et al., 1990), the peak-to-peak amplitudes for low-frequency oscillations (1–600 Hz) were less than  $0.69 \text{ N/m}^2$ , for high-frequency oscillations (1–5 kHz) the amplitudes were less than  $6.9 \text{ N/m}^2$ .

Figure 13 displays the sensitivity to exit blockage in the 4.9  $L/D$  combustor operating at loadings ( $10 \text{ lb}_m/(\text{sec. ft.}^3 \text{atmos.}^n)$ ) near the peak heat release rate condition (obtained with a combination of high airflow rates and injection of excess nitrogen as a diluent). Again, the blowout equivalence ratio decreases linearly with increasing blockage. However, when contrasted with the sensitivity to blockage for this combustor near the flammability limits (Fig. 11), it is seen that blockage exerts a much more powerful influence on stability at this higher loading.

The general conclusion can be drawn that exit blockage improves the lean stability of the research combustor. The effectiveness of blockage in improving the stability in a combustor of given length depends on the loading at which the combustor is operated. Of the three combustor lengths evaluated (and for operation at low loadings at least), the 4.9  $L/D$  combustor has the best stability at any blockage level between 0 and 62 percent. Exit blockage reduces the rich stability of the research combustor, and the extent of this also depends on the combustor loading.

## Wall Temperature Behavior

The wall temperatures for the combustor are needed to provide boundary condition information for subsequent computational fluid dynamic calculations to be made in attempts to model the lean blowout process. They can also provide, by inference, additional information concerning development of major flow features in the combustor.

Wall temperatures are most conveniently expressed in non-dimensional form, sometimes known as Metal Temperature Factor (MTF), and defined by

$$\text{MTF} = \frac{T_s - T_{in}}{T_{ad,fl} - T_{in}}$$

where

$T_s$  = wall temperature

$T_{ad,fl}$  = adiabatic flame temperature.

For premixed flames, MTF represents a normalized wall temperature, and is particularly useful in the present case therefore, because of the partial premixing that takes place when the flame is lifted.

Figure 14 compares, at 44.5 mm downstream from the step and inside the step recirculation zone, actual thermocouple temperatures over a range of equivalence ratios against temperatures derived from the MTF trend with downstream distance. Data are provided for zero and 45.1 percent exit blockage in the 4.9  $L/D$  combustor. The tests were made for a variety of jet velocity ratios and combustor flow functions. No effect of velocity ratio was apparent, and substantial increase in flow function resulted in only a negligible increase in MTF.

The figure shows that wall temperatures in the recirculation zone increase with combustor exit blockage by about 20 to 25 K for 45.1 blockage. Peak temperatures occur at equivalence ratios in the range of 0.9 to 1.1. For the attached flame condition ( $\phi \geq 1.05$ ), temperature levels are about 820 K, and fall to about 780 K as lean blowout is approached.

The form of MTF variation with equivalence ratio is shown in Fig. 15 for a station 146 mm downstream from the step (still inside the recirculation zone). The behavior in the figure is typical of all axial stations along the combustor. MTF decreases with increasing equivalence ratio up to an equivalence ratio of about 0.95, and then becomes independent out to a

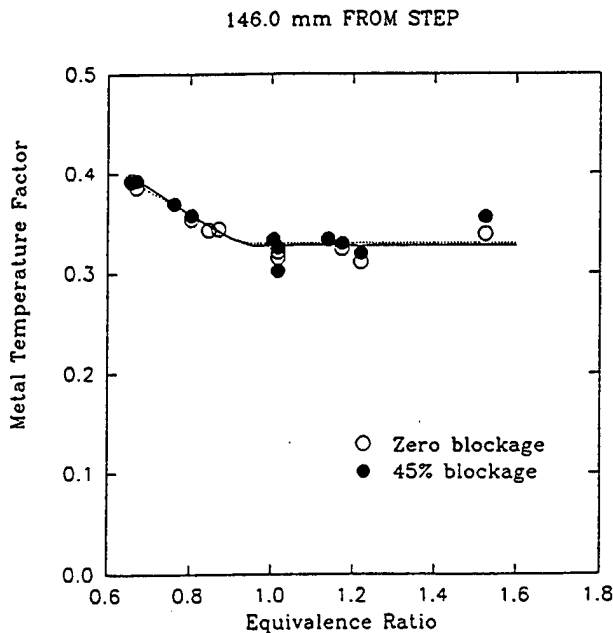


Fig. 15 Normalized wall temperatures at 126 mm from step-plane for zero and 45 percent exit blockage, showing influence of equivalence ratio

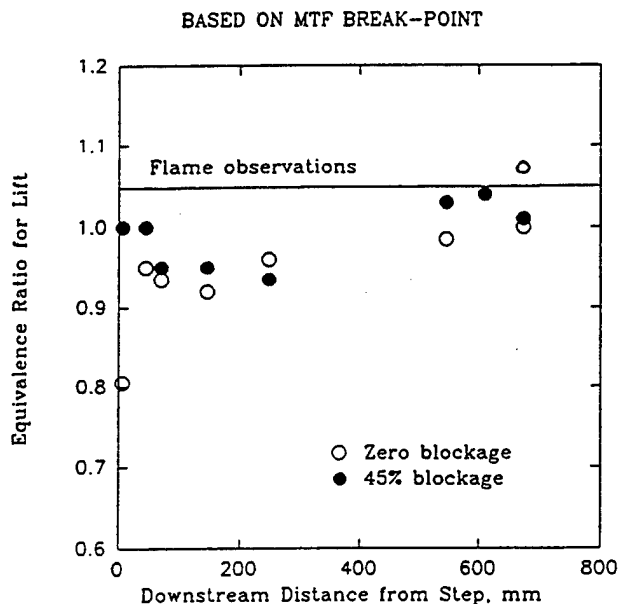


Fig. 16 Indicated equivalence ratios for flame-lift from wall temperatures, compared with direct observations

value of 1.6. There is negligible effect of blockage on MTF at this station.

The "break" in the curve of Fig. 15 may be interpreted as representing the flame-lift condition. The inferred equivalence ratios for flame-lift based on this break for different axial locations are shown in Fig. 16 compared with the equivalence ratios for flame-lift based on direct observation (Fig. 6). As might be anticipated, inferences based on data from downstream are in better agreement with direct observations. No effect of blockage is apparent on the inferred flame-lift, which does not conflict with direct observation in Fig. 6.

The variations of the maximum value of MTF with equivalence ratio for 0, 45.1, and 62 percent geometric blockages are given in Fig. 17; the flame condition—lifted or attached—is delineated based on Fig. 6. The values of maximum MTF, and the positions at which they occur, were derived at each

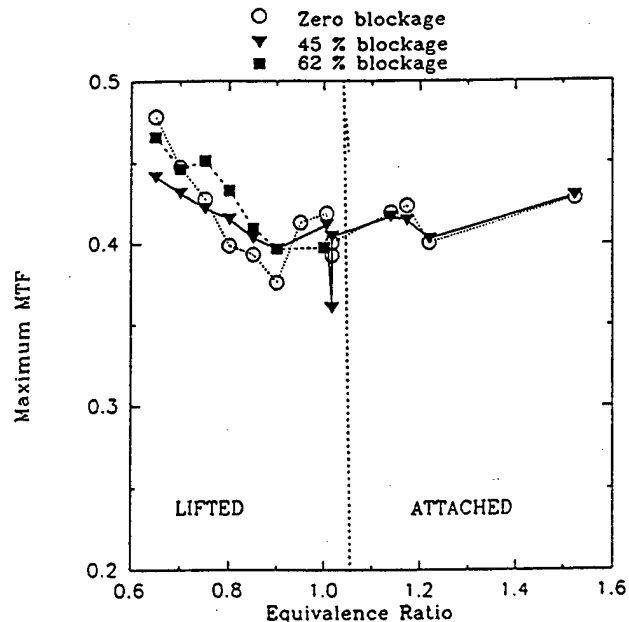


Fig. 17 Variations of maximum normalized wall temperatures for lifted and attached flames at several values of exit blockage

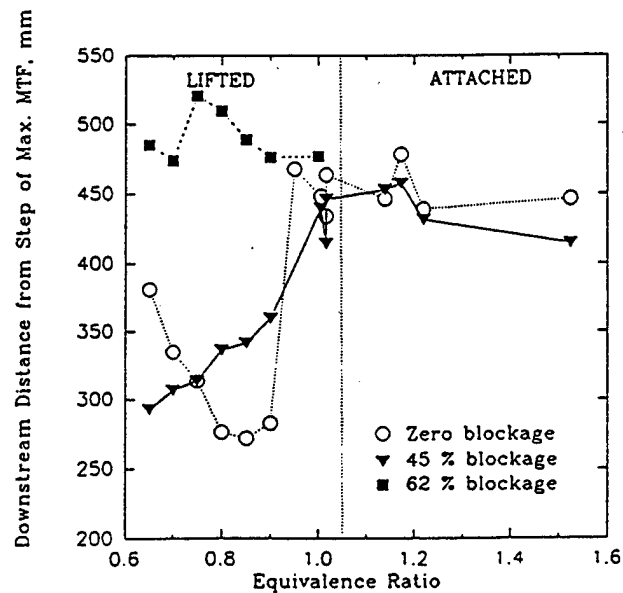


Fig. 18 Dependency of position of maximum normalized wall temperature on exit blockage for lifted and attached flames

equivalence ratio from differentiation of curve fits to MTF versus axial distance information obtained from the curves in plots such as given in Fig. 15.

Figure 17 indicates that maximum MTF reaches its minimum value at about the equivalence ratio for flame-lift. Exit blockage does not affect the value of maximum MTF, but maximum MTF does increase as lean blowout is approached.

When the position at which maximum MTF is reached is plotted in similar fashion in Fig. 18, a strong effect of blockage is apparent for lifted flames; equivalence ratios for attached flames do not influence this position significantly. For the three blockages shown, the position of maximum MTF is roughly constant around 450 mm from the step for attached flames.

When equivalence ratio is reduced so that a lifted flame is established, an unrestricted combustor exit results in the position of maximum MTF initially moving back toward the step. However, for an equivalence ratio of 0.9, the closest position

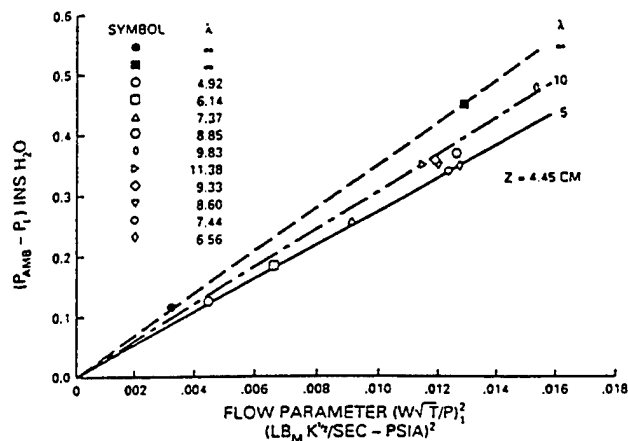


Fig. 19 Dependency of wall static pressures in the step recirculation zone on inlet flow parameter and jet velocity ratio in isothermal flow with a free exit

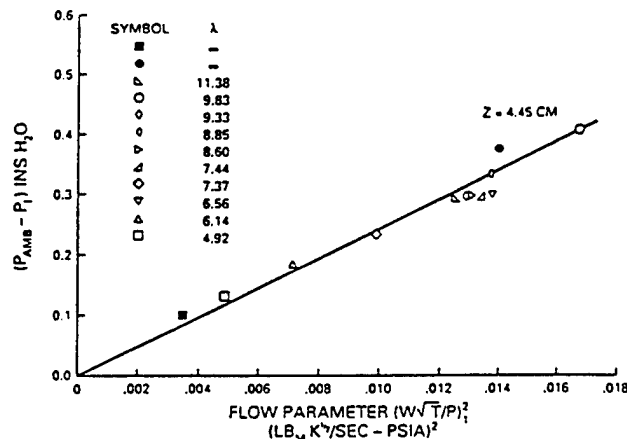


Fig. 20 Suppression of dependency of wall static pressure on jet velocity ratio by exit blockage (45 percent) in isothermal flow

to the step is reached at about 270 mm; thereafter, as equivalence ratio is further lowered toward a lean blowout, the position again moves downstream as the flame-lift increases.

The addition of exit blockage introduces an additional recirculation zone (on the orifice plate upstream face) into the combustor, and the existence of this recirculation is how blockage exerts an influence on the position of maximum MTF. The position of maximum MTF is associated with the reattachment plane of the step recirculation zone since this is where the jet shear layers reach the combustor wall (Sturgess et al., 1992b). These jet shear layers are where the majority of the heat release takes place during combustion, whether or not the pilot flame is attached (Sturgess et al., 1991a). Movements of the position of maximum MTF therefore reflect, albeit in crude fashion, movements of the reattachment plane for the step recirculation zone. The lack of blockage-effect on the value of maximum MTF (Fig. 17) indicates that heat release in the jet shear layers is not substantially changed by combustor exit blockage; however, the trajectory of these shear layers is (Fig. 18), possibly due to flow acceleration as a result of the heat release. The behavior evident in Fig. 18 for 45.1 and 62 percent blockage is the result of interactions between the step and orifice plate recirculation zones, due to heat release rate as equivalence ratio is varied, and modified by the two flame conditions.

With this flow model, the lifted-flame (partially premixed) behavior for maximum MTF in Fig. 18 at zero exit blockage is consistent with the findings of Morrison et al. (1987), Pitz and Daily (1983), and Stevenson et al. (1982) for premixed flames that a step recirculation zone at fixed (turbulent) Reynolds number decreases in size with increasing equivalence ratio. The minimum distance occurring at an equivalence ratio of 0.9 suggests that pilot flame attachment becomes evident before the directly observed equivalence ratio of 1.05 (Fig. 6). Examination of the intermittency of the pilot flame (Roquemore et al., 1991; Chen, 1991) tends to confirm this suggestion.

### Wall Static Pressures

For an atmospheric pressure discharge combustor with exit blockage, wall static pressures provide means for a convenient assessment of the extent of the additional recirculation zone set up on the orifice plate upstream face. With a free exit, the difference between ambient pressure and wall static pressure in the combustor reaches zero in the exit plane. However, when the exit is restricted, this difference reaches zero at some position inside the combustor (Heneghan et al., 1990). The position where this occurs marks the stagnation plane for the aft recirculation zone on the orifice plate.

In isothermal flow the wall static pressure at a given station

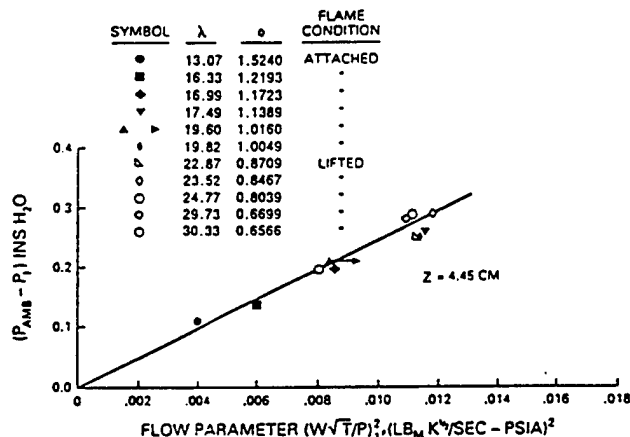


Fig. 21 Suppression of dependency of wall static pressure on jet velocity ratio by combustion with a free exit

is a function of the jet velocity ratio  $\lambda$ , and the inlet flow parameter, as can be seen for a station 44.5 mm downstream, in Fig. 19. As Fig. 20 demonstrates, when exit blockage is introduced, the dependency of wall static pressure on velocity ratio is suppressed. Combustion also suppresses the dependency on jet velocity ratio, even for a free exit. This is illustrated in Fig. 21, where it is also shown that the flame condition does not exert an influence.

Again using curve fits and differentiation, the axial positions along the combustor at which atmospheric pressure was attained were found. Typical wall static pressure axial distributions are given in Fig. 3 of Heneghan et al. (1990). Figure 22 shows that in isothermal flow this condition was reached at a constant 580 mm approximately, with 45.1 percent exit blockage, and was so regardless of inlet flow parameter or jet velocity ratio. With combustion and the same blockage, the position for atmospheric pressure was a strong function of equivalence ratio, as Fig. 23 shows, where the leading-edge of the aft recirculation zone moves progressively forward in the combustor as equivalence ratio is reduced, independent of flame condition.

At 62 percent blockage the position at which atmospheric pressure was attained was always greater than 600 mm from the step, and thus could not be accurately determined from the static tap positions available.

### Relationship Between Recirculation Zones

The information on the end of the step recirculation zone inferred from MTF data (Fig. 18) can be combined with the

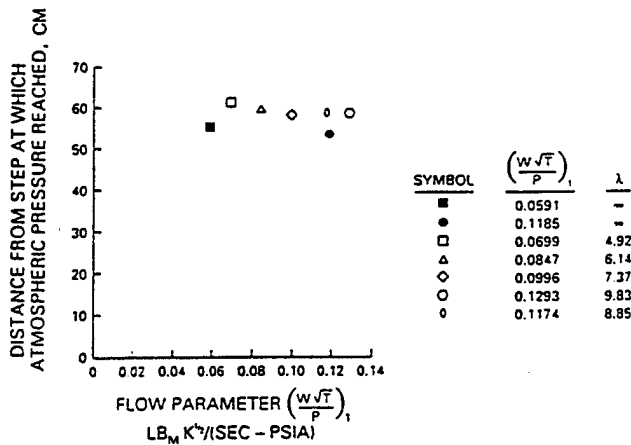


Fig. 22 Independence from inlet flow parameter and jet velocity ratio of position where atmospheric pressure is reached on the combustor wall, in isothermal flow with 45 percent exit blockage

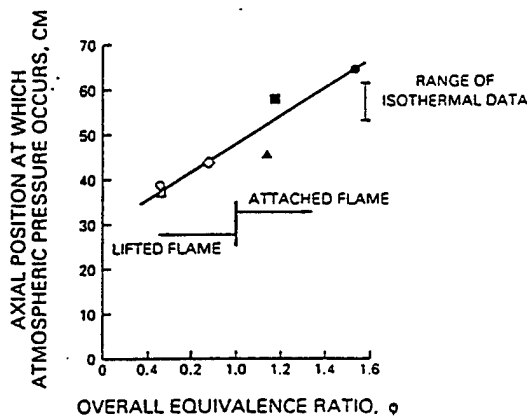


Fig. 23 Variation of downstream position where wall static pressure reaches atmospheric with equivalence ratio at 45 percent exit blockage

information on the beginning of the orifice plate recirculation zone from the static pressure data (Fig. 23) in order to examine the relationship between these two important flow features in the restricted-exit combustor.

Figure 24 shows a combination of Figs. 18 and 23 for 45.1 percent exit blockage with combustor flow. It can be deduced that there is always positive separation between the end of the step recirculation zone and the beginning of the orifice plate recirculation zone for this blockage. Furthermore, for lifted flames, this separation is maintained at a constant distance of about 80 mm, so that direct interference never happens. For attached flames, the separation distance increases, as Fig. 25 shows.

For 62 percent blockage, it appears as though direct interference between zones does not occur either, despite the fact that the inferred position of the end of the step recirculation zone is farther downstream at around 500 mm for all equivalence ratios (Fig. 18).

### Gas Temperature Profiles

Limited gas temperature measurements were made using the CARS system. Profiles along the combustor centerline and, radially, close to the step, were taken at 0, 45.1, and 62 percent exit blockage by orifice plates in order to assess what blockage did to the all-important step recirculation zone. This was a quick preliminary look made prior to more extensive field-mapping of temperature to be reported separately.

The axial profiles of mean temperature along the combustor centerline at 45.1 percent exit blockage for lifted and attached

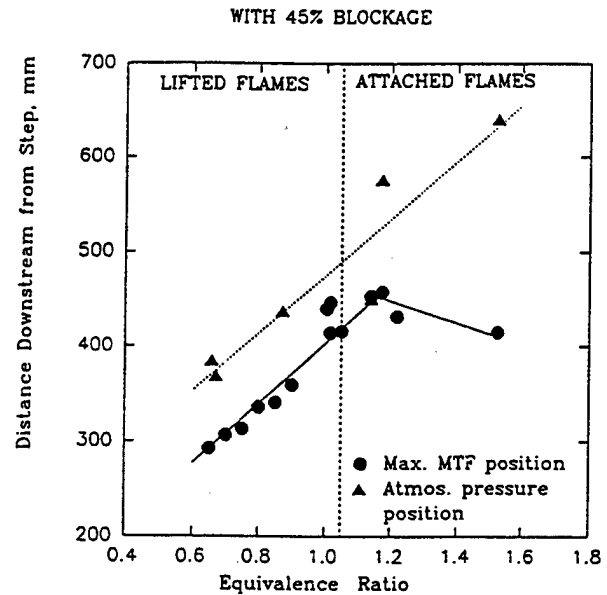


Fig. 24 Downstream positions where atmospheric pressure and maximum normalized wall temperature are attained as equivalence ratio is varied for fixed exit blockage

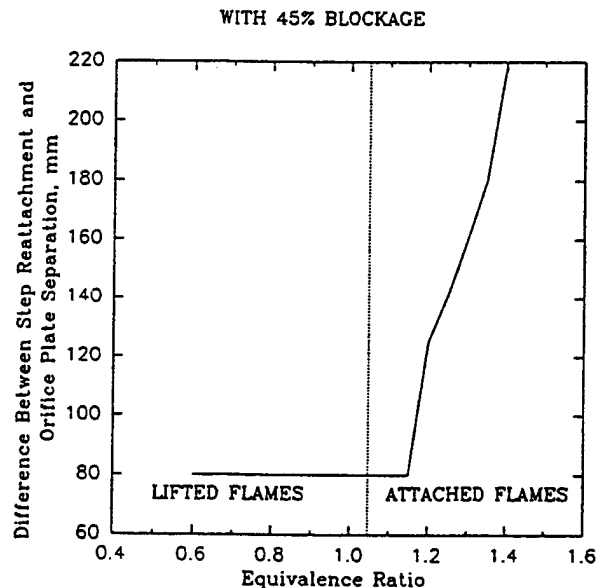


Fig. 25 Distance between recirculation zones for lifted and attached flames at fixed exit blockage

flames are given in Fig. 26, where the temperatures are presented as the ratio of actual temperature to the adiabatic flame temperature. The combustor loadings in both cases are in the range of 0.7 to 0.76 lb<sub>m</sub>/(sec.ft.<sup>3</sup>atmos.<sup>3</sup>), i.e., fairly near the lean flammability limit. For both flames the temperature initially falls, and then increases again for distances greater than 100 mm from the step-plane. By consideration of Sturgess et al. (1992b), the increases in centerline mean temperature can be associated with the inner edge of the reacting jets shear layer reaching the centerline and thereby introducing sufficient oxidant for extensive chemical reaction to take place on the centerline. The initial distance in this profile can therefore be viewed as a conditional thermochemical potential core region. Note that the position of mean temperature increase is in the region where in isothermal flow the centerline mean axial velocity begins to accelerate with the 45.1 percent exit blockage (Fig. 3). Also, for the attached flame, the dimensionless mean temperature level is generally increased over that for the lifted flame.

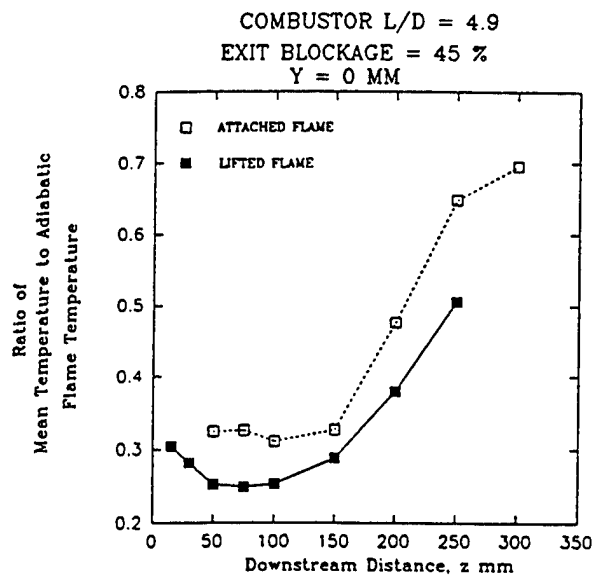


Fig. 26 Centerline profiles of dimensionless mean gas temperature for attached and lifted flames at fixed exit blockage

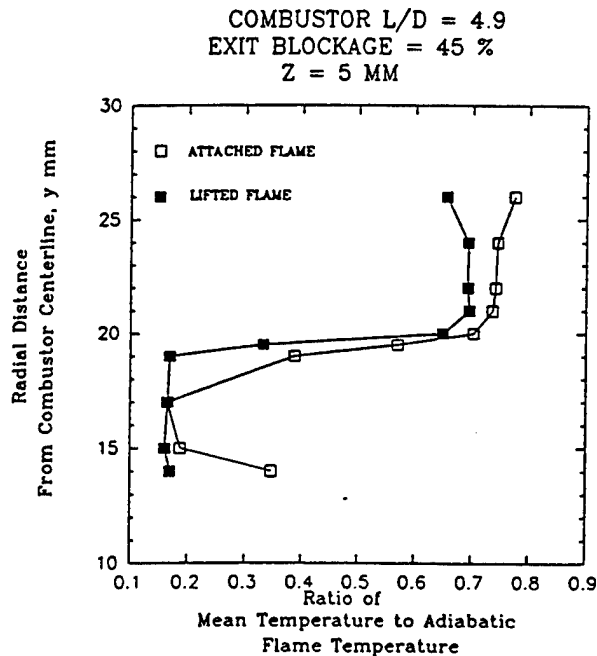


Fig. 27 Radial profiles of dimensionless mean gas temperature in the step region for attached and lifted flames at fixed exit blockage

Radial profiles of dimensionless mean temperature for the condition above are given in Fig. 27 for a downstream station 5 mm from the step. Comparison of these profiles reveals the effect of the attached flame on mean temperature, and shows the pilot flame to be located at a radius of 17 to 20 mm. The probability distribution functions (p.d.f.) confirm this definition. This is somewhat consistent with the mean position of 24 mm radius for the attached flame determined at 10 mm downstream with thin filament pyrometry (TFP) (Roquemore et al., 1991). Again, the levels of dimensionless temperature are higher at all radial positions for the attached flame condition. The p.d.f.'s for the lifted flame condition agree with the measurements of the spontaneous OH emission given by Roquemore et al. (1991), that there is a finite probability of the pilot flame being present part of the time, even though the main flame is fully lifted and an anchored pilot flame is not directly observed. For both lifted and attached flames, the step

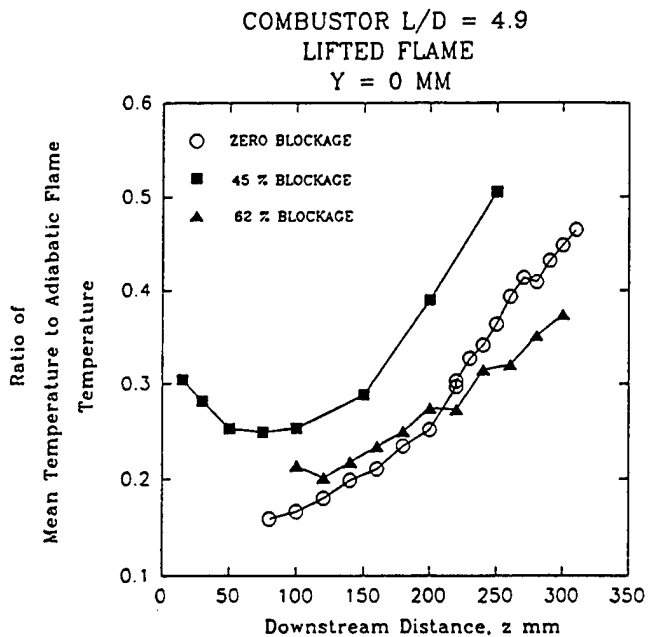


Fig. 28 Comparison of centerline profiles of dimensionless mean gas temperatures for lifted flames at various exit blockages

recirculation zone provides a significant high-temperature reservoir for the combustion processes developing in the shear layers.

Note that both Figs. 26 and 27 indicate an elevation of gas temperatures over the inlet conditions close to the confluence of the jets and around the region encompassing the small, central recirculation bubble (Sturgess et al., 1992b). Although not yet supported by strong direct evidence, it has been hypothesized (Sturgess et al., 1992a) that nonstationary flow interactions of the fuel and air jets with the central recirculation bubble result in additional radial mass transport of reactants. Such mass transport could account for early chemical reaction and hence, the observed elevated temperatures close to the orifice. The p.d.f. at a radius of 14 mm for an equivalence ratio of 1.36 at a combustor loading of 0.428 lb<sub>m</sub>/(sec.ft.<sup>3</sup>atmos.<sup>-1</sup>) shows that there is an equal probability of the flame being present and of fluid at inlet temperatures. This radius marks the position of the outer edge of the fuel tube. For this temperature condition to be so, either direct flame or a hot gas ignition source from the step recirculation zone must be transported completely across the annular air-jet path (see Fig. 1).

The addition of blockage increases the centerline mean temperatures for lifted flames at loadings fairly near the lean flammability limit. The effect is particularly strong for distances closer to the confluence of the jets than 100 mm as Fig. 28 shows. The radial profiles of dimensionless mean temperature indicate that blockage slightly increases the temperature in the step recirculation zone.

The centerline profiles of the ratio of the rms value of fluctuating temperature to mean temperature for 0, 45.1, and 62 percent exit blockage in the 4.9 L/D combustor are given in Fig. 29. The equivalence ratios are such that the flames were all lifted, and the combustor loadings were 0.7 to 0.76 lb<sub>m</sub>/(sec.ft.<sup>3</sup>atmos.<sup>-1</sup>). The fluctuating temperatures superimposed on the mean temperatures are not significantly affected by exit blockage. What is noteworthy, however, is the dramatic increase in the fluctuating component for distances closer than 50 mm to the jet origins. This is associated in particular with the forward stagnation point of the small, central recirculation zone, which for isothermal flow is situated at about 14 mm from the origin.

Figure 30 presents radial profiles of the ratio of rms tem-



COMBUSTOR  $L/D = 4.9$   
LIFTED FLAME  
 $Y = 0$  MM

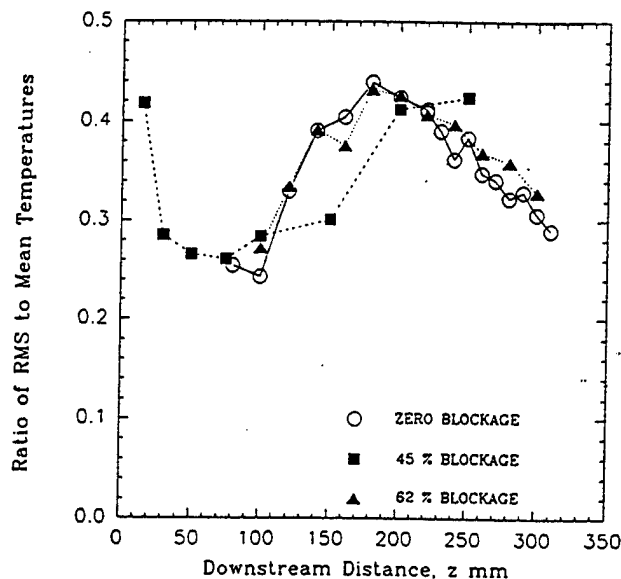


Fig. 29 Comparison of centerline profiles of dimensionless fluctuating gas temperatures for lifted flames at various exit blockages

COMBUSTOR  $L/D = 4.9$   
LIFTED FLAME  
 $Z = 5$  MM

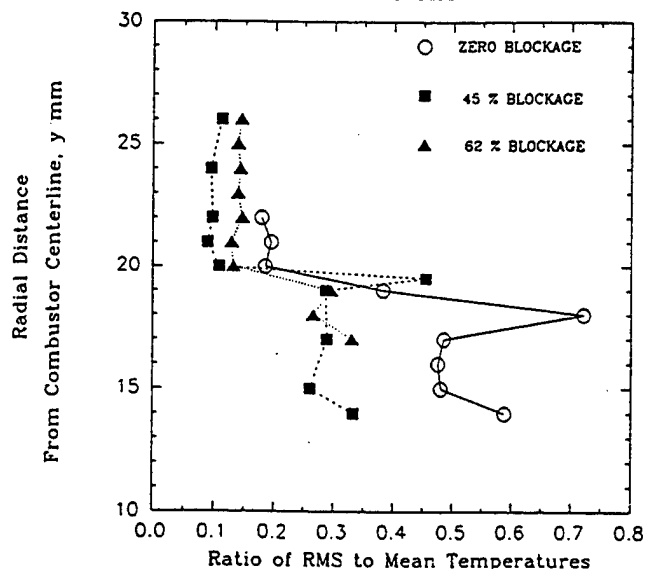


Fig. 30 Radial profiles of dimensionless fluctuating gas temperatures in the step region for lifted flames at various exit blockages

perature to mean temperature at 5 mm downstream from the step-plane for a range of exit blockage at the same operating conditions as for the previous figure, i.e., lifted flame at light loadings. Temperature fluctuations in the step recirculation zone are not much affected by the exit blockage. In sharp contrast, the existence of any blockage at all exerts a powerful suppressing effect on fluctuations in the jet shear layers.

Whether the flame is lifted or attached, there are no changes in temperature fluctuations in the step recirculation zone at 5 mm downstream with 45.1 percent exit blockage. There appear to be some differences for the two flame conditions in the shear layers (possibly the pilot flame), but the present data are not sufficient to be sure.

## Discussion

The long-term intent for the research program, of which this effort is but a part, is to derive calculation procedures for lean blowout in gas turbine engine combustors. One of the calculation procedures being developed for this purpose is computational fluid dynamics (CFD). For viability, CFD should be able to provide a reasonable simulation of the real physical behavior involved in the lean blowout process. It is therefore required that significant flame events in the blowout process be experimentally identified and characterized. The attached, separated, and lifted flames, and the influence of combustor geometry on the operational conditions under which these are encountered, hence form a significant part of the data base. The ability to calculate these characteristics will form a critical test of the efficacy of any CFD modeling of lean blowout.

The research combustor exhibits a distinct and repeatable flame pattern change as it blows out on the lean side (Fig. 5). There are similarities in the flame changes for both rich and lean blowouts. A key element in these sequences of flame change is the loss of the thin, sheathlike pilot flame anchored at the outer diameter of the air jet. This pilot flame serves as a continuous ignition source for the main flame that then originates in the shear layers associated with the fuel and air jets, and the recirculation zones. For rich blowouts, loss of the pilot flame does not result in obvious changes in the main flame, either in position or character. It tends to remain con-

centrated in the shear layers. However, for lean blowouts, loss of the pilot flame causes the main flame to lift to a downstream position. This clearly allows significant premixing of reactants to occur, with the result that the main flame in its lifted position is more distributed across the width of the combustor. Blowout in the separated rich flame takes place suddenly; in the lifted lean flame, blowout is preceded by the onset of large-scale axial oscillations of the main flame about its mean position (Fig. 5).

The flame events described are controlled by the operating equivalence ratio of the combustor (Figs. 5 and 10). The equivalence ratios at which flame events occur are modified by the existence of back-pressure applied at the exit from the combustor (Figs. 6–9). The sensitivity of the event-equivalence ratios to the exit back-pressure depends on the combustor loading, and this sensitivity generally increases with the loading (Figs. 8 and 10).

The application of exit back-pressure to the research combustor exerts a favorable influence on the lean blowout (Fig. 11). At fixed combustor loading, the effect depends on the combustor length-to-diameter ratio. When acoustic effects and direct loss of the step recirculation zone (Fig. 12) are eliminated through use of an appropriate combustor length, the changes in blowout due to exit blockage are sensitive to combustor loading (Figs. 11 and 13). Predictably, they are strongest at high loadings approaching the peak heat release rate condition. At low combustor loadings, the improvement in stability due to blockage is consistent with a more persistent anchored flame (Figs. 6 and 7), but conflicts with an earlier onset of large-scale axial movements of the lifted flame (Fig. 8).

The presence of the outlet blockage changes the isothermal flow field in the combustor by causing acceleration of the mean axial velocities about the centerline (Figs. 3 and 4), and by introducing an additional recirculation zone on the upstream face of the orifice plate placed at the combustor exit. Acceleration of the central flow is evident as close as 125 mm downstream from the step plane (Fig. 3), or, at an  $L/D$  of 0.83 in the 4.9  $L/D$  combustor at 45.1 percent blockage. This is upstream of the reattachment plane for the step recirculation, which is at about 2.82  $L/D$  (Sturgess et al., 1992a). With a

free exit in isothermal flow, the central flow decelerates as the fuel and air jets merge and expand into the combustor around the step recirculation zone. The net acceleration that results with exit blockage represents a modification of the shear layers, and thus, flame holding in these shear layers can be expected to be changed.

The wall static pressure measurements in the step recirculation zone show that combustion suppresses a sensitivity to jet velocity ratio that is apparent in isothermal flow (Figs. 19 and 21); the addition of exit blockage in isothermal flow exercises a similar effect (Fig. 20).

With combustion, it can be inferred from wall thermocouple measurements that the position of the step recirculation zone reattachment shifts according to the equivalence ratio (Fig. 18). For lifted flames, the dependency on equivalence ratio is modified by the degree of outlet blockage (Fig. 18). From wall static pressure tap measurements, it is inferred that the size of the orifice plate recirculation is also influenced by combustion (Fig. 23). For a lifted flame at a given blockage, the movement of these two stagnation planes with equivalence ratio is such that a constant separation between them exists (Figs. 24 and 25), i.e., there is no direct interference. When the attached pilot flame condition is established, movement of the step recirculation zone attachment essentially ceases (Fig. 24). However, the orifice recirculation zone continues to decrease in size (Fig. 24), with the result that the separation between stagnation planes is increased (Fig. 25). Therefore, it is unlikely that the lean blowout improvement with exit blockage is associated with direct modification of the step recirculation zone.

The "quick-look" at mean gas temperature profiles shows the existence of the pilot flame for equivalence ratios when it is present (attached flame), and indicates slightly increased temperatures in the step recirculation zone and on the combustor centerline in the near-field. For lifted flames, exit blockage exerts its greatest effect in the near-field on the combustor centerline, particularly associated with the small, central recirculation bubble; there is little effect in the step recirculation zone. The CARS p.d.f.'s confirm earlier findings by OH emission and TFP measurements that the pilot flame is intermittently present even when direct observations indicate that it is lost and the main flame is lifted.

Fluctuating gas temperatures along the combustor centerline are insensitive to exit blockage (Fig. 29); however, they once again confirm the strong dynamic nature of the flow associated with the central recirculation bubble that is generated by entrainment of the central fuel jet by the much stronger surrounding annular air jet (Sturgess et al., 1992b). In the near-field (at 5 mm) the radial profiles of fluctuating temperature suggest that exit blockage is a dampening effect, only slightly in the step recirculation, but much more strongly in the jet shear layers (Fig. 30).

Back-pressuring the flame (by exit blockage in this case) exerts a powerful stabilizing effect on lean blowout, especially at the high combustor loadings that can represent critical operating conditions for military aircraft. Direct action of back-pressure on the step recirculation zone does not seem to take place. The back-pressure acts most strongly on the initial processes occurring in the jet shear layers by modifying their trajectories and turbulence characteristics. These initial processes emerge as being critical to the overall flame stabilization, whether the main flame is attached or lifted. Evidence is building (here and in earlier work) that dynamic behavior of the flow in the near-field can control the combustion process, perhaps through radical changes in radial mass transport.

The present results confirm that future attention should be directed at the pilot flame, the circumstances of its existence, and its contribution to the main flame. The dynamic interactions of the central recirculation bubble with the jet shear layers and of the jet shear layers with the step recirculation zone must be explored in detail, and characterized if possible.

It would be desirable if such future studies could include a mass transport experiment, and time-resolved flow visualization of the combustion in the shear layers.

## Conclusions

1 Back-pressure by means of exit blockage does exert an effect on the lean blowout characteristics of a combustor. The effect is weakest at low combustor loadings near the flammability limits, and strongest at high combustor loadings near the peak heat release rate. Modification of the effect occurs with changes in combustor length-to-diameter ratio.

2 Direct interference effects of exit blockage on the step recirculation zone do not occur.

3 The major effects of exit blockage on lean blowout are due to changes in the fuel and air jet shear layers, and in the interaction of this shear layer with the step recirculation zone and with the central recirculation bubble. Dynamic processes appear to play a significant part in these interactions.

4 Future experimental work should concentrate on the near-field region, the dynamic interactions taking place there, and the circumstances governing the existence and role of the anchored flame.

5 The combustor exhibits consistent and well-characterized flame behavior that depends on equivalence ratio and exit blockage. The ability to represent this behavior will provide a stringent test of the realism of any numerical modeling (CFD) of this combustor.

## Acknowledgments

The authors wish to acknowledge the contributions to this work from their colleagues at Wright-Patterson Air Force Base and Pratt & Whitney, and also from Dr. P. Hedman, Brigham Young University, Provo, Utah. The University of Dayton work was supported by the U.S. Air Force Wright Laboratories, under Contract No. F33615-87-C-2767 (Contract Monitor Dr. W. M. Roquemore), and Pratt & Whitney was supported under Contract No. F33615-87-C-2822 (Contract Monitors 1st Lt. A. L. Lesmerises and Mr. D. Shouse). The authors thank the Air Force and Pratt & Whitney for permission to publish the results of this research.

## References

- Chen, T. H., 1991, private communication.
- Gupta, A. K., Lilley, D. G., and Syred, N., 1984, *Swirl Flows*, Abacus Press.
- Heneghan, S. P., and Vangsness, M. D., 1990, "Instrument Noise and Weighting Factors in Data Analysis," *Experiments in Fluids*, Vol. 9, pp. 290-294.
- Heneghan, S. P., Vangsness, M. D., Ballal, D. R., Lesmerises, A. L., and Sturgess, G. J., 1990, "Acoustic Characteristics of a Research Step Combustor," AIAA Paper No. AIAA-90-1851 (to appear in *Journal of Propulsion and Power*).
- Heneghan, S. P., and Vangsness, M. D., 1991, "Analysis of Slit Function Errors in Single-Shot Coherent Anti-Stokes Raman Spectroscopy (CARS) in Practical Combustors," *Reviews of Scientific Instruments*, Vol. 62, pp. 2093-2099.
- Heneghan, S. P., Vangsness, M. D., and Pan, J. C., 1991, "Simple Determination of the Slit Function in Single Shot CARS Thermometry," *Journal of Applied Physics*, Vol. 69, pp. 2692-2695.
- Lefebvre, A. H., 1983, *Gas Turbine Combustion*, Hemisphere Publishing Corp., McGraw-Hill, New York.
- Lewis, B., and von Elbe, G., 1961, *Combustion, Flames and Explosion of Gases*, 2nd ed., Academic Press, New York.
- Morrison, G. L., Tatterson, G. B., and Long, M. W., 1987, "A 3-D Laser Velocimeter Investigation of Turbulent, Incompressible Flow in an Axisymmetric Sudden Expansion," AIAA Paper No. AIAA-87-0119.
- Pitz, R. W., and Daily, J. W., 1983, "Combustion in a Turbulent Mixing Layer Formed at a Rearward Facing Step," *AIAA Journal*, Vol. 21, No. 11, pp. 1565-1569.
- Roquemore, W. M., Reddy, V. K., Hedman, P. O., Post, M. E., Chen, T. H., Goss, L. P., Trump, D., Vilimpoc, V., and Sturgess, G. J., 1991, "Experimental and Theoretical Studies in a Gas-Fueled Research Combustor," AIAA Paper No. AIAA-91-0639.
- Stevenson, W. H., Thompson, H. D., Gold, R. D., and Craig, R. R., 1982, "Laser Velocimeter Measurements in Separated Flow With Combustion," presented at the International Symposium of Laser-Doppler Anemometry in Fluid Mechanics, Lisbon, Portugal, Paper No. 11.5.

Sturgess, G. J., Sloan, D. G., Roquemore, W. M., Reddy, V. K., Shouse, D., Lesmerises, A. L., Ballal, D. R., Heneghan, S. P., Vangsness, M. D., and Hedman, P. O., 1991a, "Flame Stability and Lean Blowout—A Research Program Progress Report," *Proc. 10th ISABE*, Nottingham, United Kingdom, pp. 372-384.

Sturgess, G. J., Heneghan, S. P., Vangsness, M. D., Ballal, D. R., and Lesmerises, A. L., 1991b, "Lean Blowout in a Research Combustor at Simulated Low Pressures," ASME Paper No. 91-GT-359.

Sturgess, G. J., Sloan, D. G., Lesmerises, A. L., Heneghan, S. P., and Ballal, D. R., 1992a, "Design and Development of a Research Combustor for Lean Blowout Studies," ASME JOURNAL OF ENGINEERING FOR GAS TURBINES AND POWER, Vol. 114, pp. 13-19.

Sturgess, G. J., Heneghan, S. P., Vangsness, M. D., Ballal, D. R., and Lesmerises, A. L., 1992b, "Isothermal Flow Fields in a Research Combustor for Lean Blowout Studies," ASME JOURNAL OF ENGINEERING FOR GAS TURBINES AND POWER, Vol. 114, pp. 435-444.

## **APPENDIX L**

### **Fuels and Combustion Technology for Advanced Aircraft Engines**

**G. J. Sturgess, S. P. Heneghan,  
M. D. Vangsness, D. R. Ballal**

---

# AGARD

ADVISORY GROUP FOR AEROSPACE RESEARCH & DEVELOPMENT

7 RUE ANCELLE 92200 NEUILLY SUR SEINE FRANCE

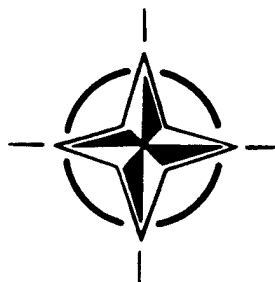
---

**Paper Reprinted from  
AGARD Conference Proceedings 536**

## **Fuels and Combustion Technology for Advanced Aircraft Engines**

(Les Propergols et les Systèmes de Combustion  
pour les Moteurs d'Aéronefs)

*Presented at the Propulsion and Energetics Panel 81st Symposium held  
in Fiuggi, Italy, 10th—14th May 1993.*



**NORTH ATLANTIC TREATY ORGANIZATION**

---

# STUDIES OF LEAN BLOWOUT IN A RESEARCH COMBUSTOR

by

D.R. Ballal, M.D. Vangsness and S.P. Heneghan

University of Dayton  
300 College Park  
Dayton, Ohio 45469  
United States

G.J. Sturgess

Pratt and Whitney Engineering  
East Hartford, CT 06108  
United States

## 1. SUMMARY

A prime requirement in the design of a modern gas turbine combustor is good lean blowout (LBO) stability to ensure an adequate stability margin. Therefore, a geometrically simple, optically accessible, and acoustically decoupled research combustor was designed to reproduce the gross features of the flow field in a modern annular gas turbine combustor. Its LBO was measured using methane and propane fuels. We successfully observed and documented a systematic and detailed sequence of events comprising an attached flame, a lifted shear flame, an intermittent shear flame, the large-scale instability of the flame front, and LBO. Also, for the sake of comparison, a generic gas turbine combustor was tested and its LBO limits were measured.

We found that LBO in the research combustor behaved like a perfectly stirred reactor (PSR) for values of combustor-loading spanning three orders of magnitude. Also, LBO was successfully correlated using a simple PSR theory. Finally, Swithenbank's dissipation gradient approach and an eddy dissipation model with a built-in characteristic extinction time criterion, when coupled with CFD, offer the possibility of an *a priori* calculation of LBO. The lean stability of a generic gas turbine combustor at peak heat release rates was less than that in a research combustor. Also, in the generic combustor, the flame changes from a lifted to an attached position depending upon how combustor loading is achieved. Due to such complications, modeling of the LBO process that works reasonably well with the research combustor will be seriously challenged by the blowout behavior evidenced in the generic gas turbine combustor.

## LIST OF SYMBOLS

$C_\mu$	constant
$D$	laminar diffusion coefficient
$E$	activation energy
$K$	turbulent kinetic energy
LBO	lean blowout
LP	loading parameter
$L/D$	length/diameter ratio
$m$	mass flow rate
$n$	reaction order
$P$	pressure
PSR	perfectly stirred reactor
$R$	gas constant
Re	Reynolds number
$S$	species source term

$T$	temperature
$V$	combustion volume
$x, y, z$	radial, transverse, and axial distance resp.
$\epsilon$	turbulent dissipation rate
$\phi$	equivalence ratio
$\nu$	kinematic viscosity
$\rho$	density
$\sigma$	Schmidt number
$\tau$	residence time

## Subscripts

a	air
ext	extinction
f	fuel
o	oxygen
nit, $N_2$	nitrogen
tot	total

## 2. INTRODUCTION

A prime requirement in the design of a modern gas turbine combustor is good combustion stability, especially near lean blowout (LBO), to ensure an adequate stability margin. For the aircraft engine, combustor blow-off limits are encountered during low engine speeds at high altitudes over a range of combustor air loading parameters. This is illustrated in Fig. 1 as a loss in the operating envelope. It is the task of the combustion engineer to design a combustor such that all its steady-state operating points lie inside the envelope. This envelope should be extensive enough to encompass the under- and over-shoots associated with the different response rates to the throttle movements of the fuel system and the rotating machinery. Further, the current and likely future design trends towards airblast atomization, high temperature rise, and low emissions are eroding the safety margins. For these reasons, the U.S. Air Force Wright Laboratory, Aero Propulsion and Power Directorate (WL/PO), Wright-Patterson Air Force Base, Ohio initiated a joint Government, Industry, and University research program to understand and model LBO in aircraft combustors. This paper describes the major results and discusses various factors that influence LBO in research and practical combustors.

In a modern annular gas turbine combustor (Fig. 2), flame is stabilized by producing a recirculation zone in the flow field. This zone is generated by a combination of three mechanisms: an axial swirling air jet associated with each

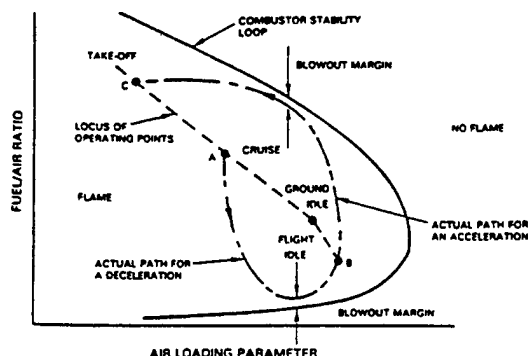


Fig. 1: Engine operating envelope superimposed on the combustor stability loop, illustrating the stability margins at blowout.

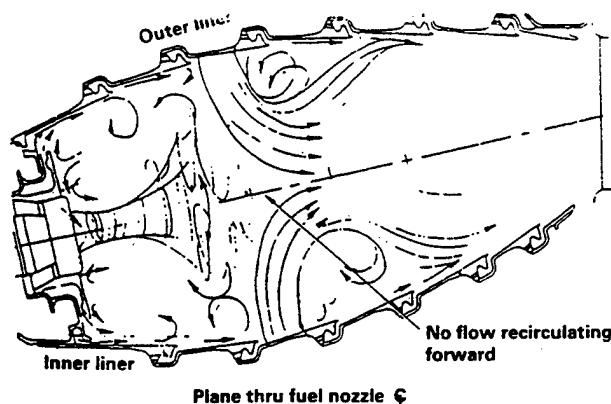


Fig. 2: Flow pattern in a modern annular combustor.

fuel introduction, sudden expansion of the axial swirling jets as they enter the primary zone, and back pressure provided by an array of radial air jets at the end of the primary zone. To obtain low exhaust emissions, Pratt & Whitney currently tailors the combustor flow control mechanisms to produce an "inside-out" recirculation pattern (Fig. 2). Therefore, the research combustor was required to reproduce this type of recirculation pattern. At the same time, it had to provide stable combustion over a reasonably wide variation in its loading, be geometrically simple for ease of experimentation and computation, and provide adequate optical access for measurements.

This paper discusses fundamental processes in the near-field region of the combustor that elucidate how LBO occurs in practical combustors, factors relating to combustor geometry

(e.g., back pressure) and operating conditions (e.g., equivalence ratio, fuel and air velocity) that influence LBO, a map of flame behavior vs. combustor loading, and the application of reaction rate theory to the correlation of LBO results.

### 3. EXPERIMENTAL WORK

**Research Combustor:** We designed a research combustor to simulate three main features of the flow field in a modern annular gas turbine combustor; (i) a reactive shear layer formed between fuel and air jets, (ii) the inside-out type of recirculation zone, and (iii) the interaction between and back-pressure exerted by transverse combustion air jets and axially directed jets of fuel-air mixture. A complete description of the combustor design and development is provided by Sturgess et al. [1].

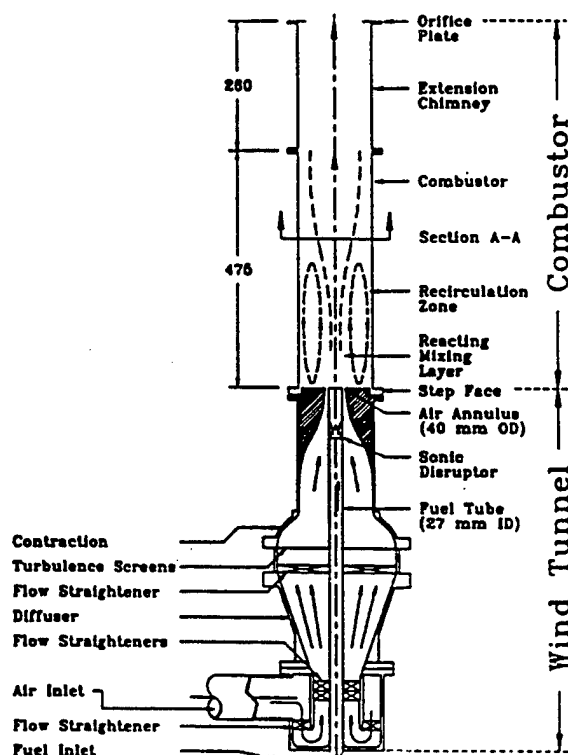


Fig. 3: Schematic diagram of a research combustor for LBO studies.

Fig. 3 shows a schematic diagram of the research combustor. It consists of a 27-mm (i.d.) central fuel tube of low-speed gaseous propane or methane surrounded by a 40-mm (i.d.) high-speed coaxial air jet exhausting into a dump combustor. This arrangement produces an intense reactive shear layer between fuel and airstreams. The duct is closed at its forward end to yield a 55-mm-high, backward-facing step. This step provides an inside-out recirculation zone which feeds high-temperature combustion products into the shear layer and thus provides a source of continuous ignition to

stabilize the flame. A perforated conical baffle inserted five diameters upstream of the fuel tube serves to acoustically isolate the fuel supply from the combustion process. As shown in Fig. 3, the step combustor is mounted vertically on a small wind tunnel. The combustor duct is comprised of two separate sections. The first section holds optical quartz windows (or metal panels with thermocouples and static pressure tapings for wall temperature and pressure measurements, respectively) on all four sides; the second one is a 250-mm extension inconel chimney. The chimney exit is blocked with an orifice plate which simulates the back-pressure effect of a practical combustor. The combustor has a hydraulic mean diameter of 150 mm, is 475 mm long, and has an exit orifice blockage of 21%, 45%, or 62%. The combination of combustor and its extension chimney yields (L/D) ratios of 3.17, 4.9, and 6.5, respectively.

**Test Conditions:** The combustion laboratory provides gaseous propane and methane fuels up to 20 Kg/hr. Both fuelstream ( $Re = 1,733$  to  $17,333$ ) and airstream ( $Re = 7,233$  to  $72,322$ ) were monitored to within 1.5%. Ignition of the combustor was satisfactorily accomplished using a retractable torch igniter. As the LBO condition was approached, the attached diffusion flame lifted from the fuel tube and was stabilized slightly downstream. This was the region of most interest and relevance to the present study.

**Instrumentation:** A three-component LDA system for velocity measurements and a CARS system for flame-temperature measurements were used. The optical window size permitted data acquisition in the range  $x = -70$  to  $+70$  mm,  $y = -33$  to  $+33$  mm, and  $z = 2$  to  $360$  mm.

The LDA uses the green (514.5 nm) and blue (488 nm) lines of a 15 W Argon-ion laser as a source; two measurement channels were separated by polarization while a third uses the blue beam. The scattered signals were collected in a forward direction at 10 degrees off axis. The effective probe volume was  $50 \times 300 \times 750 \mu\text{m}$ , the Bragg cell frequency shift was 5 MHz, and  $\text{Al}_2\text{O}_3$  seed particles were used. After allowing for seed biasing, the measurement uncertainty in mean velocity was 1%, in rms velocity it was 5%, and in skewness and kurtosis it was 7%.

The CARS system employed a BOXCARS configuration. Here, the frequency-doubled source green beam (532 nm) was split into four beams. A  $25 \times 250 \mu\text{m}$  measuring spot size was achieved. The CARS temperatures were determined, see Heneghan et al., [2], by applying the principle of local thermodynamic equilibrium. Usually, 500 samples were taken for each CARS measurement. It was estimated that the overall CARS mean temperature measurement accuracy is within 50K, while the precision is well within 20K. Unlike the LDA, the CARS measurements are time-averaged without density-biasing effects.

#### 4. RESULTS

**Acoustic Decoupling:** Combustion-induced acoustic oscillations can severely limit the operating range of some practical combustors—especially parallel-wall duct

combustors. The acoustic characteristics of this research combustor were investigated because it was feared that eddy-shedding off the step might satisfy the Rayleigh criterion, which, in turn, could set up resonance in the combustor and fuel supply tube. Heneghan et al. [3] have described the results of this investigation in detail. It was found that an acoustic isolator in the fuel tube and an air inlet convergence that eliminated vortex generation at the inlet significantly decrease acoustic coupling. Finally, a research step combustor with an  $L/D = 4.9$  and fitted with an orifice plate with a blockage ratio = 0.45 provided the best combination of LBO and freedom from acoustic coupling.

**Isothermal Flow Field:** Next, we measured the isothermal flow field in the combustor corresponding to the fuel and air-jet velocity ratios at the combustor blowout conditions. This investigation is described by Sturgess et al. [4]. Fig. 4 shows a typical result. The LDA measurements revealed the presence of the primary zone flow features (i.e., a near-field region comprising the jet shear layer and a small, central recirculation zone generated by the large momentum ratio between the fuel and the air jets; an outer recirculation zone stabilized on the step; and the far-field region, in which the individual jets lose their identity and exhibit self-similarity).

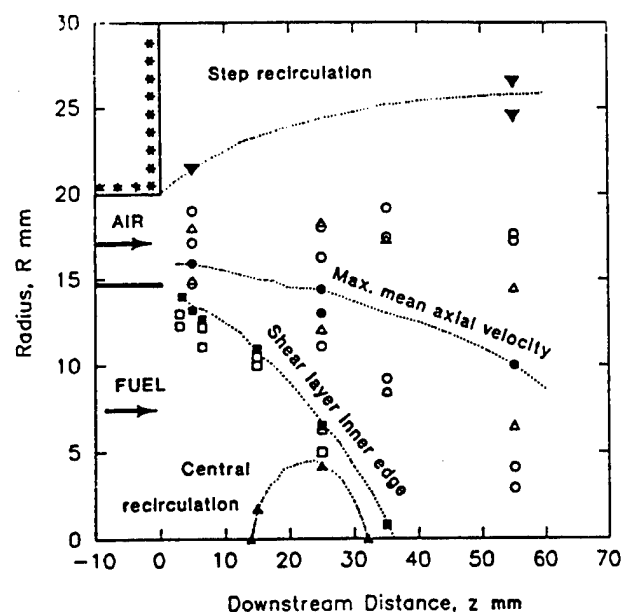


**Fig. 4: Isothermal flow field results illustrating the near-field region, recirculation zones, and the far-field region; (■, ▲, ▼—mean axial velocity, □, ○—turbulence intensities, and △—max. velocity gradient).**

**Flame Visualization:** Fig. 5 illustrates the sequence of events leading to LBO. As the overall equivalence ratio was reduced below unity, the attached flame moved further downstream into the combustor in a characteristic lifted-flame position and form. Continuing reduction in the



equivalence ratio produces an onset of flow instability in the lifted flame, an increase in the amplitude of the instability, the onset of intermittency, severe intermittency, and, finally, the onset of strong axial flame instability. This sequence clearly highlights the complexity of the LBO mechanism in a modern annular gas turbine combustor.

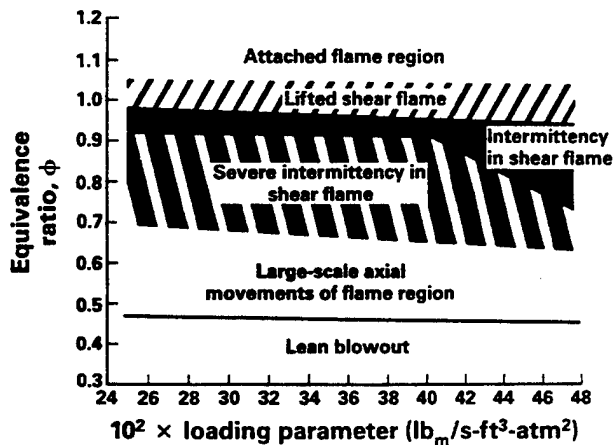


Fig. 5: Sequence of events leading to LBO as observed by flame visualization.

In our research combustor, the piloting action of the flame in the jet shear layers by the attached flame at the step appears to be crucial to combustor stability. Thus, successful modeling of the combustor stability requires the prediction of the attached flame and its lift. The OH images of the attached flame, see Sturgess et al., [5], show that its structure at any given time is associated with local vortices shed from the inner edge of the combustor step. Also, the instantaneous OH images reveal that combustion takes place in a more distributed form via relatively large "packets" of reaction.

**Lean Blowout:** We measured LBO as a function of air loading parameter (LP) over a range of propane fuel flows. However, this did not yield a complete combustor stability loop. To achieve a wide variation in LP with the simple atmospheric pressure research combustor, a subatmospheric pressure simulation was used. As explained in Ref. [6], excess gaseous nitrogen was introduced into the air supply upstream of the combustor as a diluent to lower the concentration of reactants and/or reaction temperature by virtue of its heat capacity. Fig. 6 illustrates a calibrated relationship between equivalent pressure and (nitrogen/fuel) mass ratio at blowout in the research combustor. This technique permitted (i) the simulation of subatmospheric pressure as low as 0.1 atm, (ii) the completion of the combustor stability loop (ranging from  $\phi = 0.5$  to 0.9), and (iii) increased LP by two orders of magnitude.

Fig. 7 shows the LBO performance of our research combustor and stability loops for several well-stirred reactors from the

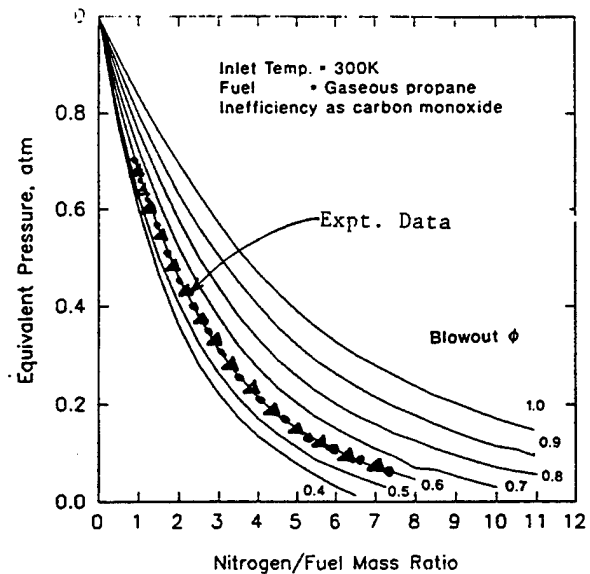


Fig. 6: Calibration curves for simulating subatmospheric pressure by using nitrogen dilution.

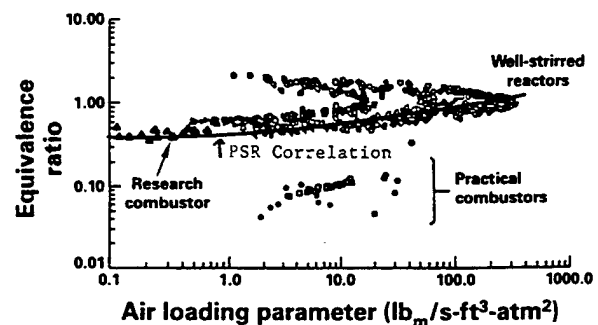


Fig. 7: LBO vs. LP data for the research combustor showing a comparison between the measured and the predicted results.

literature, as well as two partial loops for practical gas turbine combustors. For these results, the standard LP was derived from the global reaction rate theory, but modified to include the effects of inert excess nitrogen;

$$LP = m_{tot}/(VP^n), \quad (1)$$

$$m_{tot} = m_f + m_a + m_{nit}, \quad (2)$$

$$\text{and } n = 2 \phi_{LBO} / (1 + m_{nit}/m_a). \quad (3)$$

The trend of LBO vs. air loading shown in Fig. 7 is very similar to that found for a perfectly stirred reactor (PSR); the latter approaching the characteristics of a future generation of

ideal premixed, prevaporized, near-stoichiometric combustors. Thus, it is reasonable to conclude that our research combustor correctly reproduced the LBO processes of a real gas turbine combustor. Also plotted in this figure are results for a gas turbine combustor fitted with a vaporizer tube and another one fitted with a strongly swirling prefilming airblast atomizer. In addition to their different fuel injection patterns, these two combustors had completely different flow fields (as compared to the combustor of Fig. 1) due to their different shapes, method of fuel introduction, and liner hole patterns. These results clearly suggest that a simple and general correlation for LBO is not possible. However, as will be shown later, direct calculation for each combustor offers the only possibility of making reliable *a priori* estimates of stability in gas turbine combustors.

To simulate the presence of dilution air jets, we investigated the effects of back pressure on the LBO in our research combustor. These results are discussed in detail in Ref. [7]; a typical result is presented in Fig. 8. As seen in the figure, LBO was improved by increasing the exit blockage. However, we found that (see Ref. 7) above a blockage of 45%, (i) significant interference occurs between the outlet and the combustor flame holding, and (ii) LBO does not improve much. Thus, we concluded that an exit blockage of 45 percent provides the best combustion stability and optimal configuration (i.e., for a combustor of exit blockage = 45 percent and  $L/D = 4.9$ , the LBOs were virtually independent of blockage and acoustic coupling). For a lightly loaded combustor (near the flammability limits), exit blockage exerts a weak influence on LBO, primarily through its effect on the jet and the recirculation zone shear layers. For high combustor loadings (near the peak heat release rate), exit blockage had a strong effect on the LBO via the dynamic behavior of the flow in the near-field (especially the interaction of the central recirculation bubble with the jet shear layers) and of the jet shear layers with the step recirculation zone.

## 5. ANALYSIS

Complete calculation of stability by using the CFD techniques to define the combustor flow field locally is not a viable approach. LBO is dominated by the kinetics of chemical reaction; therefore, CFD calculations of a large number of chemical reactions would be required to yield the correct heat release. For example, for hydrocarbon fuels, a general transport equation of the form,

$$\frac{\partial}{\partial x_j} \langle \rho u_j m_i - \Gamma_{eff} (\partial m_i / \partial x_j) \rangle = S_m \quad (4)$$

where  $i$  denotes chemical species,  $m_i$  is the mass fraction of  $i$ , and  $S_m$  is a species source term, would have to be solved for each species. The computational burden of doing so is presently unacceptable in the context of the complicated flow field and confining boundaries of the real gas turbine combustor. Therefore, the chemistry was uncoupled from the fluid dynamics and analysis of LBO was addressed at three levels of increasing difficulty:

1. characteristic time modeling based on a phenomenological approach, with CFD providing local flow properties,
2. stirred reactor network modeling established on the basis of CFD analysis of the flow field, and
3. subgrid-level stirred reactor modeling using reactor extinction criteria based on the characteristic time model (1) above.

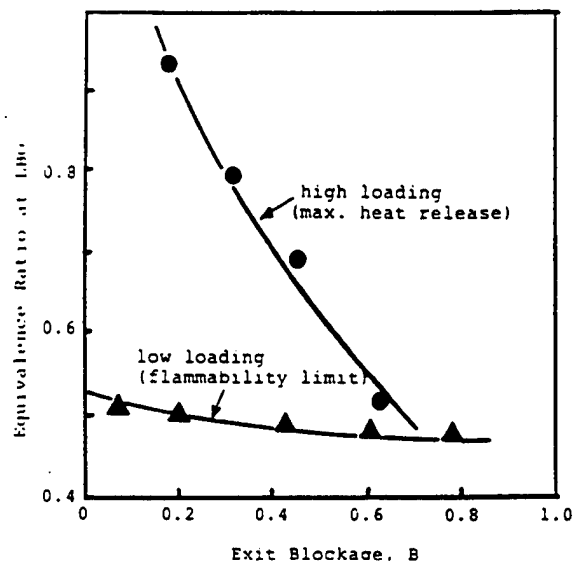


Fig. 8: Influence of exit blockage on LBO at low and high combustor-loadings.

**Characteristic Time Approach:** This approach is based on the reaction-quench model which assumes that, at LBO, flame propagation will cease when the rate of mixing between small turbulent eddies of cold reactants and hot products is greater than the local chemical reaction rate. This quenching criteria finds its origin in the work of Lockwood and Megahed [8] and yields:

$$1.5 \{ D + C_{\mu} K^2 / \sigma_t \epsilon \} / \nu \{ 1 + S_L / (\epsilon \nu)^{0.25} \} > 1.0 \quad (5)$$

where  $D$  is the laminar diffusion coefficient,  $K$  is the kinetic energy of turbulence,  $\epsilon$  is the dissipation rate,  $C_{\mu}$  is a constant,  $\sigma_t$  is the turbulent Schmidt number, and  $S_L$  is the laminar flame speed.

Since the quenching criterion requires turbulence parameters for evaluation, isothermal flow CFD calculations were performed to provide this information at each grid node. Quenching was examined on a point-by-point basis to ascertain if any part of the flow field could support combustion. Further, two additional conditions were imposed; (i) local fuel/air ratio must be within the flammability limits, and (ii) local mean velocities should be

less than or equal to turbulent burning velocity. In a somewhat limited evaluation, Eq. (5) showed promise in the step combustor in delineating between operating conditions where combustion was possible and where it was not. Eventually, this approach provided the reactor extinction criteria for the subgrid-level stirred reactor modeling.

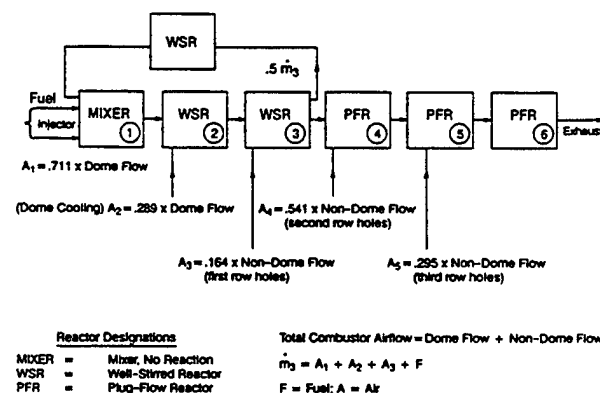


Fig. 9: A typical simulation of a combustor primary zone using the PSR network.

**Local Stirred Reactor Modeling:** In this approach, the combustor volume is represented by an equivalent global stirred reactor network. This enables the calculation of stability from thermo-chemistry considerations. We applied Swithenbank's [9] dissipation gradient approach for defining PSR regions in the combustor. Fig. 9 shows a typical reactor network that simulates the generic combustor primary zone. To establish such a global reactor network, considerable and careful post-processing of a CFD solution for the generic combustor was performed. Flow structures were identified by visualization, connectivity and local mass flow rates were assigned, and flow topology mapping techniques, e.g., Ref. [10], were used. Based on the Swithenbank approach [9], a rapid mixing region of the combustor was established from CFD calculations. This region was defined as the volume contained within a surface contour containing 96% of the turbulence kinetic energy and 99% of its dissipation rate, and over which the total dissipation gradient was not less than ten times the minimum value recommended by Swithenbank. From within this rapid-mixing region, a PSR volume was defined by super-imposing an additional space encompassing fuel/air mixtures falling inside the flammability limits for propane and air. For the research combustor, the resulting reactor was 44% of the combustor volume and corresponded reasonably well to the lifted flame observed in the real combustor. As shown in Ref. [6], good agreement was found between predictions and experiments for the research combustor.

Thus, networks of stirred reactors, particularly when established from CFD calculations, appear to offer possibilities for calculating limiting LBO performance. However, care may be needed in interpreting the results of

such calculations since only the thermochemical limits to combustion can be determined.

**Subgrid Scale Reactor Modeling:** The eddy dissipation concept (EDC) of Byggstoyl and Magnussen [11] represents a general model for chemical reaction in turbulent flow. In the EDC model, the reactants are homogeneously mixed within the fine structure (Kolmogoroff eddies) of turbulence; therefore, these fine structures can be treated as PSRs. If the volume and the mass exchange rate between the reactors and the surrounding fluid are known, chemical reactions occurring within the PSRs can be calculated using a system of equations. Since the Kolmogoroff scale is always less than the CFD grid size, the modeling represents a subgrid scale approach. In contrast to the characteristic time analysis and local stirred reactor modeling, this approach tests the individual reactor stability within the CFD calculations.

Use of full or even reduced chemical kinetics imposes a high cost on the calculations. Therefore, an alternative approach was to assume a one-step, irreversible reaction step and/or fast chemistry, then use a local quenching criterion. The validity of the calibrated, global, single-step reaction mechanism approach was tested by comparing it to the data of Kretschmer and Odgers [12] and Clarke et al. [13]. Also, an extinction residence time was defined as  $\tau_{ext} = (\rho / \dot{m})_{ext}$ , where  $\dot{m}$  is the total inlet mass flow rate per unit volume of the reactor. Thus, when  $\tau_{hydro} \leq \tau_{ext}$  reactions occur, the hydrodynamic residence time in the fine scales can be related to the bulk fluid through the mass fraction of fine structures present in the flow. This characteristic time approach to LBO within the EDC model was implemented with fast chemistry for propane-air combustion and tested for an attached flame at fuel-rich conditions.

The axisymmetric CFD calculations were made using the Pratt and Whitney two-dimensional PREACH code. Three constraints were applied on the chemical reaction; (i) the EDC model with characteristic time-based extinction criterion was implemented, (ii) the local mixture should be within flammability limits (lean  $\phi = 0.2$  or  $0.5$  depending upon reactant temperature and upper  $\phi$  to  $2.0$ ), and (iii) turbulence effects on the flame burning velocity. Fig. 10 shows typical calculated isotherms for what should be the attached-flame condition. These results show that the stoichiometric contour crosses the step recirculation zone from the confluence of the jets and reaches the combustor wall about halfway between the step and the recirculation reattachment plane. We can infer from these temperature contours that the main flame exists in the jet shear layers and originates about 10 cm from the step-plane (i.e., it is lifted and not attached). It is thick and follows the stoichiometric contour across the recirculation zone. There is some agreement between the characteristics of the inferred flame and the actual flame observed in the time-mean photographs and in the near-instantaneous pictures of laser-induced OH fluorescence where concentrated islands of reaction in the jet shear layer thicken the flame region. However, it was found that this model calculated the lifted-flame condition but was

Curve  
Label Value

10 1200.0  
11 1300.0  
12 1400.0  
13 1500.0  
14 1600.0  
15 1700.0  
16 1800.0  
17 1900.0  
18 2000.0  
19 2100.0

## Isotherms

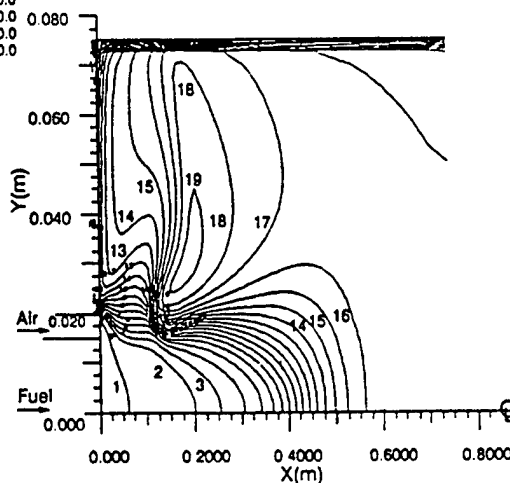


Fig. 10: Isotherms (curve values in degrees K) calculated using the EDC model for the attached-flame conditions in a research combustor

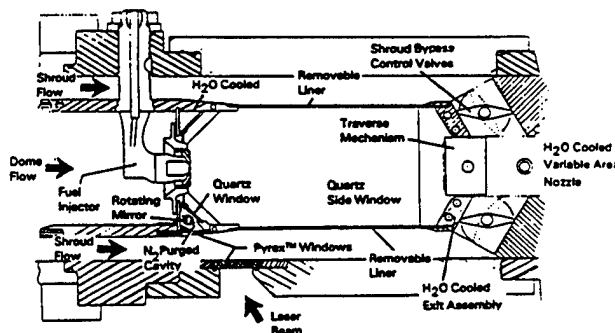


Fig. 11: Schematic diagram illustrating the design features of the generic gas turbine combustor.

unsuccessful in predicting the all-important attached-flame condition. Summarizing:

(a) A research step combustor was successfully developed. It produced three important features of the flow field that affect LBO in a practical combustor; (i) a reactive shear layer at the exit to the fuel nozzle, (ii) inside-out recirculation zones, and (iii) back pressure provided by dilution air jets.

(b) The step combustor acoustic characteristics were optimized; this permitted its operation in a stable and

predictable manner. A detailed sequence of events leading to LBO and comprising the attached-flame region, lifted shear flame, intermittent shear flame, and the large-scale instability of the flame front was observed.

(c) The combustor flow-field measurements revealed three regions: near-field, step-recirculation, and far-field regions. In these regions, the turbulent fuel-air mixing and entrainment were governed by a potential core, a central recirculation bubble, and a self-similar jet development, respectively.

(d) The LBO process ( $\phi = 0.4$  to 1.2) in the step combustor behaved like a PSR for LP values in the range of 0.1 to 100 lb/s-ft<sup>3</sup>-atm<sup>2</sup>. Also, the LBO was successfully correlated with a standard LP derived from the PSR theory. Finally, Swithenbank's [9] dissipation gradient approach and an EDC model (Ref. 11) with a built-in characteristic extinction time criterion offer the possibility of an *a priori* calculation of LBO.

## 6. GENERIC GAS TURBINE COMBUSTOR

A final test of this research and modeling effort is to be able to predict LBO in an actual gas turbine combustor. To perform such a test, a generic gas turbine combustor was designed with three special requirements; (i) its LBO performance should be consistent with that of an actual gas turbine combustor, (ii) its geometric configuration and flow distribution should be variable so that the effects of residence time and mixture ratio on the LBO can be studied, and (iii) good optical access should be available for discerning the flow field and combustion zone.

Fig. 11 shows a schematic of a Pratt and Whitney designed generic combustor which is a four-injector, planar-section, simplified geometry version of a modern Pratt and Whitney annular combustor sector. This sector employs airblast-atomizing fuel injectors, an engine-type injector/dome interface, and the "inside-out" recirculation zones. The liners, upper and lower, are removable and may contain any desired pattern of air ports. The metal liners do not have any specific internal film cooling but are provided with a thermal-barrier coating and are convectively cooled by the shroud flows. Ignition is accomplished by means of a hydrogen torch ignitor. Individually metered air is supplied to the dome and upper and lower shrouds, provisions are made to supply gaseous nitrogen for subatmospheric pressure simulation, and, finally, fuel can be either propane or methane. This combustor is designed to operate at 65 psia with a variation in dome air from 10% to 40% of the total combustor air flow. The facility in which the combustor is installed is capable of supplying air up to 30 lbs/sec at ambient temperature and fuels up to 30 lbs/hr. Finally, side walls made of fused quartz and contained in water-cooled housings are provided for flow visualization. Sturgess and Shouse [14] have provided a detailed description of the construction, operation, and LBO tests on this combustor.

Fig. 12 illustrates the primary zone stability (LBO) of the generic combustor with lifted and attached flames against the LBO data obtained from the research combustor as well as

the predictions for the research combustor. The generic combustor data were obtained for the 10%, 15%, and 20% dome flow. Since the flames near blowout in the research combustor were all lifted, the partial premixing characteristic of the lifted flames in both combustors should be similar. The LBO stability of the generic combustor at peak heat release rates appears to be less than that of the research combustor. One likely reason may be the different fuel-air mixing rates in the generic combustor.

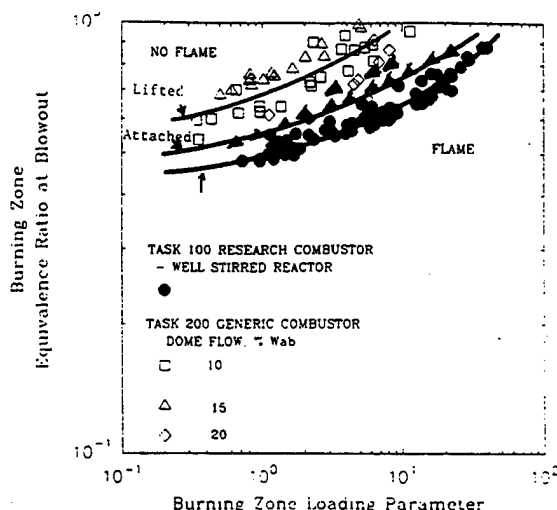


Fig. 12: LBO vs. LP data for the generic gas turbine combustor operating in the lifted- and attached-flame modes compared with data for the research combustor.

It appears that the gross features of the LBO can be successfully correlated by the combustor-loading parameter based on the PSR approach for a specific combustor. However, a simple phenomenological correlation is unlikely to explain the details of the LBO process. For example, the LBO process at simulated low pressures is rather complicated in a generic combustor. It contains quasi-staging of fuel as the loading increases with subsequent flame stabilization by the combustion air jets as well as the primary zone. When jet stabilization exists, LBO is insensitive to dome airflow and vice versa. Finally, the flame changes from a lifted to an attached position and, at a given loading, either flame can exist depending on how combustor-loading is achieved. Due to such complications, correlations of experimental data cannot be general enough to form a unique design curve which can determine the LBO stability margin of a practical gas turbine combustor. Thus, modeling of the LBO process, which works reasonably well with the research combustor, will be seriously challenged by the blowout behavior evidenced in the generic gas turbine combustor.

## 7. CONCLUSIONS

Following is the summary and conclusions of our research.

1. A geometrically simple, optically accessible, and acoustically decoupled research combustor to reproduce the gross features of the flow field in a modern annular gas turbine combustor was designed and its LBO was measured.
2. We successfully observed and documented a systematic and detailed sequence of events comprising an attached-flame, lifted shear flame, intermittent shear flame, large-scale instability of the flame front, and the LBO. These individual events clearly highlight the complexity of the LBO mechanism.
3. Simple phenomenological correlation based on PSR theory was successful. The LBO process ( $\phi = 0.4$  to  $1.2$ ) in the research combustor behaved like a PSR for LP values in the range of  $0.1$  to  $100 \text{ lb/s-ft}^3\text{-atm}^2$ . Also, the LBO was successfully correlated with a standard LP dissipation gradient approach and an EDC model (Ref. 11) with a built-in characteristic extinction time criterion offer the possibility of an *a priori* LBO calculation.
4. LBO stability at peak heat release rates in a generic gas turbine combustor was less than in the research combustor. Also, the flame changes from a lifted to an attached position and, at a given loading either flame can exist depending on how combustor-loading is achieved. Due to such complications, it was not possible to uniquely determine the LBO stability margin of a practical gas turbine combustor. Thus, modeling of the LBO process, which works reasonably well with the research combustor, will be seriously challenged by the blowout behavior evidenced in the generic gas turbine combustor.

## 8. ACKNOWLEDGEMENTS

This research was supported by the U.S. Air Force Wright Laboratory, Aero Propulsion and Power Directorate, Wright-Patterson Air Force Base, OH, under Contract No. F33615-92-C-2207. Mr. C. M. Frayne served as the Technical Monitor.

## 9. REFERENCES

1. Sturgess, G. J., Sloan, D. G., Lesmerises, A. L., Heneghan, S. P., and Ballal, D. R., "Design and Development of a Research Combustor for Lean Blowout Studies," ASME Journal of Engineering for Gas Turbines and Power, 114, 1990, pp 13-19.
2. Heneghan, S. P., Vangsness, M. D., and Pan, J. C., "A Simple Determination of the Slit Function in Single Shot CARS Thermometry," Journal of Applied Physics, 69, 1991, pp 2692-2695.

3. Heneghan, S. P., Vangsness, M. D., Ballal, D. R., Lesmerises, A. L., and Sturgess, G. J., "Acoustic Characteristics of a Research Step Combustor," AIAA Paper No. AIAA-90-1851, to appear in AIAA Journal of Propulsion.
4. Sturgess, G. J., Heneghan, S. P., Vangsness, M. D., Ballal, D. R., and Lesmerises, A. L., "Isothermal Flow Fields in a Research Combustor for Lean Blowout Studies," ASME Journal of Engineering for Gas Turbines and Power, 114, 1992, pp 435-444.
5. Sturgess, G. J., Sloan, D. G., Roquemore, W. M., Shouse, D., Lesmerises, A. L., Ballal, D. R., Heneghan, S. P., Vangsness, M. D., and Hedman, P. O., "Flame Stability and Lean Blowout-A Research Program Progress Report," in Proceedings of Tenth ISABE, Nottingham, England, 1991, pp 372-384, Paper No. 91-7037.
6. Sturgess, G. J., Heneghan, S. P., Vangsness, M. D., Ballal, D. R., and Lesmerises, A. L., "Lean Blowout in a Research Combustor at Simulated Low Pressures," ASME Paper No. 91-GT-359, to appear in ASME Journal of Engineering for Gas Turbines and Power, 1992.
7. Sturgess, G. J., Heneghan, S. P., Vangsness, M. D., Ballal, D. R., Lesmerises, A. L., and Shouse, D., "Effects of Back Pressure in a Lean Blowout Research Combustor," ASME Paper No. 92-GT-81, to appear in ASME Journal of Engineering for Gas Turbines and Power, 1992.
8. Lockwood, F., and Megahead, I. E. A., "Extinction of Turbulent Reacting Flows," Combustion Science and Technology, 19, 1978, pp 77-80.
9. Swithenbank, J., "Flame Stabilization in High Velocity Flows," Combustion Technology-Some Modern Developments, ed. H. B. Palmer and J. M. Beer, Academic Press, New York, NY, 1974, pp 91-125.
10. Perry, A. E., and Chong, M. S., "A Description of Eddy Motions and Flow Patterns Using Critical-Point Concepts," Annual Reviews of Fluid Mechanics, 19, 1987, pp 125-155.
11. Byggstoyl, S. and Magnussen, B. F., "A Model for Flame Extinction in Turbulent Flow," Turbulent Shear Flows-4, eds. L. J. S. Bradbury, F. Durst, B. E. Launder, F. W. Schmidt, and J. H. Whitelaw, Springer-Verlag, Berlin, 1985.
12. Kretschmer, D., and Odgers, J., "Modeling of Gas Turbine Combustors-A Convenient Reaction Rate Expression," ASME Journal of Engineering for Power, 94, 1972, pp 173-180.
13. Clarke, A. E., Harrison, A. J., and Odgers, J., "Combustion Stability in a Spherical Combustor," Seventh Symposium (Int.) on Combustion, The Combustion Institute, Pittsburgh, PA, 1958, pp 664-673.
14. Sturgess, G. J., and Shouse, D., "Lean Blowout Research in a Generic Gas Turbine Combustor with High Optical Access," A Paper Submitted to the 38th ASME Gas Turbine and Aeroengine Congress and Exposition, Cincinnati, OH, May 24-27, 1993.

## Discussion

### Question 1. D.K. Hennecke

In the experiments, you did not simulate the cooling films. Don't you think that they would influence the size and shape of the "inside out" vortex as the films flow against the vortex flow?

### Author's Reply

The influence of the cooling film on the size and shape of the "inside out" recirculation zone is negligibly small. This is because in modern annular combustors the cooling air film is pretty much confined to the wall boundary layer. Also, the mass and momentum of the "inside out" recirculation zone is perhaps two orders of magnitude (or more) greater than that of the cooling film. Therefore, the cooling film, at best, causes only a minor perturbation of the "inside out" vortex flow. For this reason, it was not considered worthwhile to add complexity of simulating the cooling film in the research combustor hardware.

## **APPENDIX M**

### **Sooting Correlations for Premixed Combustion**

**Fumiaki Takahashi**

# 7

## Sooting Correlations for Premixed Combustion

*Fumiaki Takahashi*

University of Dayton Research Institute, 300 College Park,  
Dayton, OH 45469.

Soot threshold data in the literature for hydrocarbon-air premixed combustion systems (including Bunsen-type burners, Meker-type multitubular burners, and well-stirred reactors) under atmospheric pressure have been analyzed statistically. The conventional equivalence ratio at sooting ( $\phi_c$ ) for both Meker-type burner flames and well-stirred reactors is approximately 15 percent larger (on average) than that for laminar Bunsen flames because of backmixing. Although the effective equivalence ratio at sooting ( $\psi_c$ ) (for which carbon monoxide and water vapor are considered to be the combustion products) correlates well with the number of C-C bonds of the fuel molecule (compared to other single-parameter correlations), discrimination between aliphatics and aromatics is relatively weak. The carbon-to-oxygen ratio at sooting ( $C/O_c$ ) is nearly constant for alkanes, but for alkenes and alkynes it strongly correlates to the adiabatic flame temperature ( $T_f$  at  $\phi = 1.5$ ). The number density of carbon atoms (in the hot products) at sooting is practically constant for each combustion system within experimental uncertainties and almost independent of homologous series; thus, the fuel structure and the reaction-zone mode are insignificant in soot threshold. A multiple linear-regression analysis shows that the oxygen-to-fuel molar ratio of the mixture at sooting correlates remarkably well (the coefficient of determination:  $r^2 = 0.988$ ) with the fuel's predeterminable parameters, including the carbon number, C/H ratio, heat of formation,  $T_f$  at  $\phi = 1.5$ , and averaged-distance-sum connectivity index.



## SOOTING CORRELATIONS FOR PREMIXED COMBUSTION

### 1. INTRODUCTION

The emission of carbonaceous particulates from practical combustion systems (such as industrial furnaces, diesel, and gas-turbine engine combustors) and fires (including oil-well and forest fires) may exert a significant impact on the environment and human health. In such combustors, the soot deposition has negative consequences in the maintenance and efficiency of the device. The emission of smoke from military aircraft engines is undesirable because it leaves an infrared and visible signature. In advanced aircraft engine combustors (which approach stoichiometry), soot formation in the fuel-rich primary zone imposes the upper limit of fuel flow in the operating cycle. The threshold for incipient soot formation of various hydrocarbon fuels has been measured in both diffusion and premixed combustion systems in the laboratory. Although the laboratory experiments are suitable to determine the effects of various factors (such as fuel structure, flame temperature, and pressure) on the soot formation process, the characteristics of soot emissions from practical combustors are far more complicated because of the effects of turbulence, recirculation, inhomogeneous fuel-air mixing, local temperature distribution, soot oxidation, and so forth. Nevertheless, if the general trend of the tendency to form soot for various hydrocarbon fuels is determined in laboratory experiments, it will be possible to better interpret the results obtained in complex practical systems and to predict the sooting tendencies of new advanced fuels.

For premixed combustion, the tendency for incipient soot formation has been determined [1-10] for a number of hydrocarbons in various combustion systems (including Bunsen-type burners, Meker-type multitubular burners, and well-stirred reactors) by metering the critical fuel concentration in the mixture at sooting. Each combustion system generates markedly different reaction zone structures; Bunsen-type burners form well-defined laminar flames, Meker-type burners generate brushy "flat" flames, and well-stirred reactors create highly turbulent reacting flows. Therefore, the soot threshold data obtained in both Meker-type burners and well-stirred reactors include the effect of backmixing caused by turbulence at a different degree. Based on the concept of competition between the fuel pyrolysis and soot-precursor oxidation rates in the soot formation processes (initially introduced by Millikan [11]), Takahashi and Glassman [8] have analyzed systematically their soot threshold data for temperature-controlled Bunsen-type flames to determine the effects of the flame temperature and the

## SOOTING CORRELATIONS FOR PREMIXED COMBUSTION

structure of the fuel molecule. Although the effective equivalence ratio at sooting ( $\psi_c$ ) and the number of C-C bonds in the fuel molecule ( $n_{C-C}$ ) served as better correlating variables [8,9], their discriminating power between aliphatics and aromatics is relatively weak, as noted later by Ramer *et al.* [12]. Harris *et al.* [10] have more recently measured soot threshold and flame temperature using a honeycomb flat-flame burner.

To prepare this paper, the soot threshold data in the literature are thoroughly analyzed for various fuel-air premixed combustion systems. The data span 74 hydrocarbon fuels including both aliphatics and aromatics with the carbon numbers one to sixteen. The approach of this study is essentially parametric: the output of a system (i.e., soot threshold expressed in different forms) is correlated to various input parameters, determined from the properties of the mixture. Thus, this approach will not provide information of the path (chemical kinetics) leading to incipient soot formation. Instead, an attempt is made to determine controlling factors that are common to the data base for various fuels, research groups, and combustion methods. If the controlling factors are revealed, one can examine their effects on the physicochemical model of soot threshold (i.e., the competition between the fuel pyrolysis and soot-precursor oxidation rates) and gain a better understanding of the process necessary to develop a global kinetic model. Furthermore, differences in the soot threshold data among the research groups and combustion methods are revealed in this paper by examining the soot threshold data systematically.

## 2. PROCEDURES

The soot threshold in premixed combustion is expressed, in general, by the fuel-to-oxygen molar ratio, which is then normalized by molar oxygen requirement per unit mole of the fuel for a "stoichiometric" condition for the specific combustion products considered. Table I shows the definitions of the three normalized fuel-to-oxygen molar ratios at sooting ( $\phi_c$ ,  $\psi_c$ , and  $[C/O]_c$ ), the number of moles of oxygen required per unit mole of the fuel ( $Z_\phi$ ,  $Z_\psi$ , and  $Z_{C/O}$ ), and the combustion products considered. The three normalized fuel-to-oxygen molar ratios at sooting can be converted from one to another by multiplying the ratio of the oxygen requirements. Here,  $X_F$  and  $X_O$  are the mole fractions of the fuel and oxygen in the mixture, respectively;  $n_C$  and  $n_H$  are, respectively, the number of carbon and hydrogen atoms

# SOOTING CORRELATIONS FOR PREMIXED COMBUSTION

**TABLE 1**  
Normalized critical fuel/oxygen ratios at sooting

Name	Definition	Oxygen requirement	Combustion products
Conventional equivalence ratio	$\phi_c = (X_F/X_{O_2})_c$	$Z_\phi = n_C + n_H/4$	$CO_2, H_2O$
Effective equivalence ratio	$\psi_c = (X_F/X_{O_2})_c$	$Z_\psi = n_C/2 + n_H/4$	$CO, H_2O$
Carbon-to-oxygen ratio	$(C/O)_c = (X_F/X_{O_2})_c Z_{C/O}$	$Z_{C/O} = n_C/2$	$CO, H_2$

in the fuel molecule, and the subscript c denotes the critical condition at which incipient soot emission (yellow luminosity) is observed by the naked eye. The carbon-to-oxygen ratio at sooting has been widely used in early years from a thermodynamic viewpoint [11,13]. The effective equivalence ratio at sooting has been introduced [8] by considering more realistic combustion products of fuel-rich oxidation. Calcote and Manos [14] proposed the threshold soot index as  $TSI = a - b\phi_c$  (for premixed flames), which scales 0 to 100 with a progressively increasing order of the sooting tendency. Constants  $a$  and  $b$  are determined for a given set of data obtained by each group using a particular combustion method. To examine differences in the original soot threshold data between research groups and combustion methods, the data in this study are standardized at the group level and the method level separately, using relative magnitudes of  $\phi_c$ .

A multiple linear regression method was used to analyze the soot threshold data with the fuel properties (such as the heat of formation [ $\Delta H_{f,298}^\circ$ ]), topological indices [15], and their derivatives of the fuel molecule such as the carbon number ( $n_C$ ), carbon-to-hydrogen ratio ( $n_C/n_H$ ), number of C-C bonds ( $n_{C-C}$ ), hydrogen-deficiency number (HD), and averaged-distance-sum connectivity index ( $J$ ). The carbon number is an appropriate index for analyzing straight-chain molecules, but it is not well suited to branched or cyclic molecules. The hydrogen-deficiency number is defined by formulating any hydrocarbon as  $C_{n_C}H_{2n_C} + 2 - 2HD$ , and it reflects the number of independent cycles, rings, and double bonds in a molecule. The averaged-distance-sum connectivity index [16,17] measures the relative prevalence of open chains and closed rings within the molecule. Hanson and Rouvray [18] have concluded that the combined index of  $J$  times HD is the most significant index, among other topological indices, in correlating the

## SOOTING CORRELATIONS FOR PREMIXED COMBUSTION

soot threshold data for diffusion flames. The number of C-C bonds, in which a double bond is counted as two and a triple bond is counted as three, can be expressed as

$$n_{C-C} = 2n_C - n_H/2 = n_C + HD - 1. \quad (1)$$

Thus, both  $n_{C-C}$  and HD are functions of the carbon number and hydrogen number (or  $n_C/n_H$ ). The C/H ratio and the heat of formation essentially determine the adiabatic flame temperature ( $T_f$ ).

The soot threshold data under premixed conditions investigated in this paper have been measured in three types of combustion systems: Bunsen-type burners [1,2,8], Meker-type burners [3,5,7], and well-stirred reactors [4,6]. Because the Bunsen-type burners are simple single-tube burners and form a conical laminar flame, the effect of differences in burner configuration and dimensions must be minimal compared to the other methods. The term "Meker-type burners" in this paper designates various designs of multitubular (or honeycomb) burners, which generate a brushy "flat" flame composed of multiple conical flamelettes. The well-stirred reactors include two different designs: hemispherical [4] and spherical [6].

### 3. RESULTS AND DISCUSSION

Table 2 shows the fuel properties and the critical equivalence ratio at sooting for 74 hydrocarbon fuels obtained by eight research groups. Because these experiments used air as the oxidizer and, thus, flame temperature was not controlled, the temperature effect must be included in the data analysis. The heats of formation are taken from the literature [19,20] unless otherwise noted in the table. The averaged-distance-sum connectivity index was calculated by a computer program described by Balaban and Filip [17]. To directly compare the soot threshold data before normalization to yield the equivalence ratios, the oxygen-to-fuel molar ratios at sooting ( $[X_{O_2}/X_F]_c$ ) are calculated from the  $\phi_c$  data and plotted in Figure 1. The data points with a large scatter ( $>9\%$  from the average) within the same method will be excluded from the analysis; those data points are ethane, propane, and benzene by Grumer *et al.* [2], and cyclohexane and benzene by Flossdorf and Wagner [3].

Because the soot threshold data differ between the combustion methods and even among the research groups using the same method, standardizing factors are calculated for direct comparisons. Each group

## SOOTING CORRELATIONS FOR PREMIXED COMBUSTION

 TABLE 2  
 Fuel properties and the critical equivalence ratio at sooting

Fuel	Formula	$\Delta H_{f,0}^{\circ}$ (kcal/mol)	$J$	$T_f$ ( $\phi = 1.5$ ) (K)	Critical equivalence ratio at sooting ( $\phi_c$ )						
					Bunsen-type burner	Meker-type burner	Well-stirred reactor				
					ST <sup>a</sup>	GHR <sup>b</sup>	TG <sup>c</sup>	FW <sup>d</sup>	CM <sup>e</sup>	OP <sup>f</sup>	W <sup>g</sup>
<i>Alkanes</i>											
Methane	CH <sub>4</sub>	-17.89	0.000	1900	1.80						
Ethane	C <sub>2</sub> H <sub>6</sub>	-20.24	1.000	1957	1.67	1.88	1.71	1.65			
Propane	C <sub>3</sub> H <sub>8</sub>	-24.82	1.633	1969	1.56	1.62	1.63	1.77	1.74	1.91	
Butane	C <sub>4</sub> H <sub>10</sub>	-30.15	1.975	1973	1.49	1.57	1.56	1.76			
2-Methylpropane	C <sub>4</sub> H <sub>10</sub>	-32.15	2.324	1964			1.55				
Cyclopentane	C <sub>5</sub> H <sub>10</sub>	-18.46	2.402	2013						1.81	
Pentane	C <sub>5</sub> H <sub>12</sub>	-35.00	2.191	1976	1.47						
Isopentane	C <sub>5</sub> H <sub>12</sub>	-36.92	2.540	1970	1.49						
Cyclohexane	C <sub>6</sub> H <sub>12</sub>	-29.43	2.339	1992	1.52		1.43	2.40	1.70	1.81	
Hexane	C <sub>6</sub> H <sub>14</sub>	-39.96	2.339	1978	1.45		1.46	1.63			
Isohexane	C <sub>6</sub> H <sub>14</sub>	-41.66	2.627	1974	1.45						
Methylcyclohexane	C <sub>7</sub> H <sub>14</sub>	-36.99	2.123	1985						1.73	
Heptane	C <sub>7</sub> H <sub>16</sub>	-41.89	2.447	2053			1.69		1.69	1.70	
Ethylcyclohexane	C <sub>8</sub> H <sub>16</sub>	-41.05	2.125	1988						1.69	
Cyclooctane	C <sub>8</sub> H <sub>16</sub>	-30.10	2.000	2012						1.84	
Octane	C <sub>8</sub> H <sub>18</sub>	-49.82	2.530	1981	1.39	1.34	1.71				

# SOOTING CORRELATIONS FOR PREMIXED COMBUSTION

Isocane (2,2,4-Trimethylpentane)	$C_8H_{18}$	-53.57	2.716	1973	1.45				1.80
Nonane	$C_9H_{20}$	-54.74	2.592	1983					1.77
Decalin									
(Decahydronaphthalene)	$C_{10}H_{18}$	-41.98	1.925	1994	1.27				1.63
Decane	$C_{10}H_{22}$	-59.67	2.648	1983					1.77
Undecane	$C_{11}H_{24}$	-64.60	2.691	1984					1.64
Bicyclohexyl	$C_{12}H_{22}$	-63	1.800	1976					1.69
Dodecane	$C_{12}H_{26}$	-69.52	2.727	1985					1.68
Isododecane	$C_{12}H_{26}$	-71.15	2.817	1982	1.41				
Tridecane	$C_{13}H_{28}$	-74.45	2.758	1985					1.71
Tetradecane	$C_{14}H_{30}$	-79.38	2.785	1986					1.74
Hexadecane	$C_{16}H_{34}$	-89.23	2.828	1986	1.35				
Alkenes									
Ethylene	$C_2H_4$	12.50	2.000	2188	1.82	1.86	1.84	1.99	2.10
Propene	$C_3H_6$	4.88	2.187	2108	1.67	1.65			2.14
1,3-Butadiene	$C_4H_6$	26.33	2.732	2188		1.62		1.69	2.04
1-Butene	$C_4H_8$	-0.03	2.297	2079	1.56	1.57			2.03
2-Methylpropene	$C_4H_8$	-4.04	2.803	2061		1.40			1.83
Cyclopentene	$C_5H_8$	7.87	2.324	2095				1.80	
Pentene	$C_5H_{10}$	-5.00	2.402	2062	1.54				
Cyclohexene	$C_6H_{10}$	-1.28	2.255	2063		1.39		1.69	
1-Hexene	$C_6H_{12}$	-9.96	2.488	2050		1.45		1.84	
4-Methylcyclohexene	$C_7H_{12}$	-10.38	2.319	2041				1.71	
Heptene	$C_7H_{14}$	-14.89	2.559	2041	1.45				
1,5-Cyclooctadiene	$C_8H_{12}$	17	2.286	2102				1.89	

## SOOTING CORRELATIONS FOR PREMIXED COMBUSTION

TABLE 2 (Continued)

Fuel	Formula	$\Delta H_{f,m}^\circ$ (kcal/mol)	$J$	$T_f$ ( $\phi = 1.5$ ) (K)	Critical equivalence ratio at sooting ( $\phi$ )					
					Bunsen-type burner	Meker-type burner	Well-stirred reactor			
					ST <sup>a</sup>	GHR <sup>b</sup>	TG <sup>c</sup>	FW <sup>d</sup>	CM <sup>e</sup>	OP <sup>f</sup>
1-Octene	C <sub>8</sub> H <sub>16</sub>	-19.82	2.616	2035		1.36				1.77
1-Nonene	C <sub>9</sub> H <sub>18</sub>	-24.74	2.664	2030						1.77
1-Decene	C <sub>10</sub> H <sub>20</sub>	-29.67	2.704	2026						1.67
1-Dodecene	C <sub>12</sub> H <sub>24</sub>	-39.52	2.767	2021						1.72
1-Tridecene	C <sub>13</sub> H <sub>26</sub>	-44.45	2.792	2018						1.71
1-Tetradecene	C <sub>14</sub> H <sub>28</sub>	-49.36	2.814	2016						1.75
1-Hexadecene	C <sub>16</sub> H <sub>32</sub>	-59.23	2.851	2014						1.69
<i>Alkynes</i>										
Acetylene	C <sub>2</sub> H <sub>2</sub>	54.19	3.000	2574	2.08	2.01		2.05		1.89
1-Pentyne	C <sub>5</sub> H <sub>8</sub>	34.50	2.484	2195						1.96
1-Hexyne	C <sub>6</sub> H <sub>10</sub>	29.55	2.544	2160						1.96
1-Heptyne	C <sub>7</sub> H <sub>12</sub>	24.62	2.599	2135						1.84
2-Heptyne	C <sub>7</sub> H <sub>12</sub>	24.62	2.782	2135						1.78
1-Octyne	C <sub>8</sub> H <sub>14</sub>	19.70	2.647	2116						1.88
1-Decyne	C <sub>10</sub> H <sub>18</sub>	9.85	2.723	2090						
<i>Aromatics</i>										
Benzene	C <sub>6</sub> H <sub>6</sub>	19.85	3.000	2235	1.43	1.18	1.44	2.43	1.55	1.43
Toluene	C <sub>7</sub> H <sub>8</sub>	11.95	3.021	2081	1.33	1.34	1.33	1.43	1.52	1.50
										1.39

# SOOTING CORRELATIONS FOR PREMIXED COMBUSTION

Styrene	$C_8H_8$	35.22	2.991	2134			1.68
Ethylbenzene	$C_8H_{10}$	7.12	2.832	2068			1.55
O-Xylene	$C_8H_{10}$	4.54	3.135	2061			1.47 1.46 1.31
M-Xylene	$C_8H_{10}$	4.12	3.078	2060			1.51 1.47 1.30
P-Xylene	$C_8H_{10}$	4.29	3.032	2060	1.27 <sup>k</sup>		1.43 <sup>k</sup> 1.50 1.46 1.30
1-Phenyl-1-Propyne	$C_9H_8$	66.5 <sup>j</sup>	2.937	2199			1.53
Indene	$C_9H_8$	36 <sup>i</sup>	2.625	2122			1.48
Propylbenzene	$C_9H_{12}$	1.87	2.615	2057			1.58
1,2,4-Trimethylbenzene	$C_9H_{12}$	-3.33	3.172	2045			1.44
1,3,5-Trimethylbenzene	$C_9H_{12}$	-3.84	3.166	2044			1.44
Cumene	$C_9H_{12}$	0.94	2.848	2055	1.28	1.30	1.56 1.56 1.61 1.40
(Isopropylbenzene)	$C_9H_{12}$	75 <sup>j</sup>	2.480	2202			1.52 1.39
Dicyclopentadiene	$C_{10}H_{10}$						
Tetralin (1,2,3,4-							
Tetrahydronaphthalene)	$C_{10}H_{12}$	6.60	2.414	2061	1.05	1.22	1.48 1.44 1.31
Butylbenzene	$C_{10}H_{14}$	-3.30	2.427	2049			1.54
Diethylbenzene	$C_{10}H_{14}$	-5.02	2.871	2046			1.51
P-Cymene	$C_{10}H_{14}$	-6.90	2.894	2042			1.61
1-Methylnaphthalene	$C_{11}H_{10}$	27.93	2.767	2090	1.03	1.16	1.42 1.52
Pentylbenzene	$C_{11}H_{16}$	-8.23	2.276	2043			1.56
Cyclohexylbenzene	$C_{12}H_{16}$	3 <sup>j</sup>	2.083	2058			1.54

<sup>a</sup> (ST) Street and Thomas [1]; <sup>b</sup> (GHR) Grumer, Harris, and Rowe [2]; <sup>c</sup> (TG) Takahashi and Glassman [8]; <sup>d</sup> (FW) Flossdorf and Wagner [3]; <sup>e</sup> (CM) Calcote and Miller [5]; <sup>f</sup> (OP) Olson and Pickens [7]; <sup>g</sup> (W) Wright [4]; <sup>h</sup> (B) Blazowski [6]; <sup>i</sup> Estimated from  $\Delta H_{f,liq}^\circ$  for liquid state and the estimated heat of vaporization; <sup>j</sup> Estimated from  $\Delta H_{f,liq}^\circ$  of two species by the principle of additivity; <sup>k</sup> Xylenes.



# SOOTING CORRELATIONS FOR PREMIXED COMBUSTION

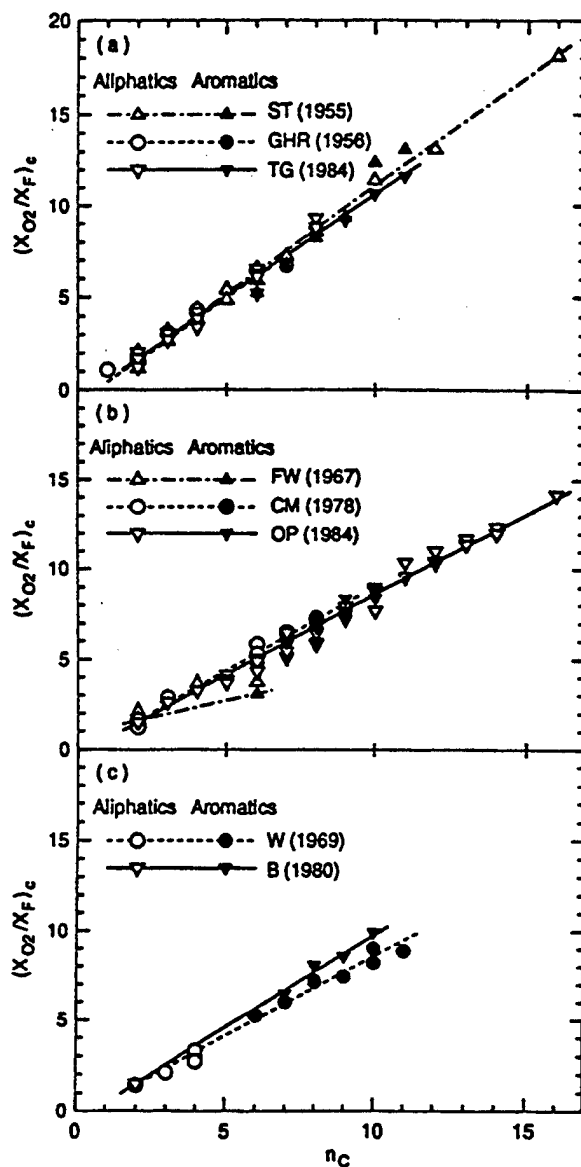


FIGURE 1. Soot threshold data expressed as the critical oxygen/fuel molar ratio at sooting: (a) Bunsen-type burners, (b) Meker-type burners, (c) well-stirred reactors.

# SOOTING CORRELATIONS FOR PREMIXED COMBUSTION

factor ( $f_G$ ) within the same method is determined as follows. (1) For fuels for which the data are commonly available from at least two different groups, relative magnitudes of  $\phi_c$  are calculated by dividing  $\phi_c$  by their average. (2) Next, an average is taken of the relative magnitudes of  $\phi_c$  over different fuels in each group. Similarly, each method factor ( $f_M$ ) is obtained as follows. (1) For fuels for which the group averages are commonly available from at least two different methods, relative magnitudes of the averaged  $\phi_c$  are calculated by dividing the averaged  $\phi_c$  by their average. (2) Next, an average is taken of the relative magnitudes of the averaged  $\phi_c$  over different fuels for each method. Table 3 shows the group and method factors which can be used for all  $(X_F/X_{O_2})_c$ ,  $\phi_c$ ,  $\psi_c$ , and  $(C/O)_c$ . Thus, these correlating variables, standardized for the same method ( $[X_F/X_{O_2}]'_c$ ,  $\phi'_c$ ,  $\psi'_c$ , and  $[C/O]'_c$ ) or for all data ( $[X_F/X_{O_2}]''_c$ ,  $\phi''_c$ ,  $\psi''_c$ , and  $[C/O]''_c$ ), are expressed as

$$\begin{aligned} (X_F/X_{O_2})'_c &= (X_F/X_{O_2})_c/f_G, & \phi'_c &= \phi_c/f_G, \\ \psi'_c &= \psi_c/f_G, & (C/O)'_c &= (C/O)_c/f_G, \end{aligned} \quad (2)$$

$$\begin{aligned} (X_F/X_{O_2})''_c &= (X_F/X_{O_2})'_c/f_M, & \phi''_c &= \phi'_c/f_M, \\ \psi''_c &= \psi'_c/f_M, & (C/O)''_c &= (C/O)'_c/f_M. \end{aligned} \quad (3)$$

The group factors in Table 3 show that Bunsen-type flames have the least minimum-to-maximum scatter ( $\sim 3\%$  on average) between the groups, Meker-type burners are the next ( $\sim 6\%$ ), and well-stirred reactors deviate the most ( $\sim 10\%$ ). The method factors indicate that the soot thresholds for both the Meker-type burners and well-stirred reactors are approximately 15% larger (on average) than those for Bunsen-type flames. There are several possible causes of the scatter of the data. First, the soot threshold is determined by the experimenter as the onset of (yellow) luminosity emission; thus, it is not based on quantitative measurements (such as the soot volume fraction) and therefore includes human bias error. Second, the results depend on system configuration. The conical Bunsen-type flames are affected less by heat losses to the burner wall than are "flat" Meker-type burner flames. In brushy Meker-type burner flames and well-stirred reactors, backmixing caused by turbulence must broaden the reaction zone and disperse soot particles, thus delaying detection of luminosity. Furthermore, Bunsen (and Meker) flames of heavy hydrocarbons may suffer nonuniform transport effects; the preferential diffusion of lighter components (oxygen) makes the mixture near the flame (let) tip locally fuel richer.

# SOOTING CORRELATIONS FOR PREMIXED COMBUSTION

TABLE 3  
Standardizing factors for the soot threshold data

Method and investigators	Number of data	Group factor $f_G$	Method factor $f_M$
<i>Bunsen-type Burner</i>			0.915
Street and Thomas (1955)	25	0.987	
Grumer <i>et al.</i> (1956)	7 <sup>a</sup>	1.015	
Takahashi and Glassman (1984)	21	1.006	
<i>Meker-type Burner</i>			1.058
Flossdorf and Wagner (1967)	4 <sup>b</sup>	0.980	
Calcote and Miller (1978)	11	0.974	
Olson and Pickens (1984)	55	1.034	
<i>Well-Stirred Reactor</i>			1.054
Wright (1969)	14	1.050	
Blazowski (1980)	8	0.950	

<sup>a</sup> Excluding ethane, propane, and benzene.

<sup>b</sup> Excluding cyclohexane and benzene.

Figure 2 shows the soot threshold data for the three methods expressed by a conventional plot of  $\phi'_c$  as a function of  $n_c$ . The coefficient of determination ( $r^2$ ) (i.e., the square of the correlation between the observed  $y$ -value and the predicted  $y$ -values) for Bunsen-type burners, Meker-type burners, and well-stirred reactors are, respectively, 0.642, 0.261, and 0.746. The data set for Meker-type burners has a least correlation. The scatter of the data points between  $C_2$  aliphatics and aliphatics versus aromatics ( $n_c > 6$ ) is noticeable in the plots for both Bunsen-type (Fig. 2(a)) and Meker-type (Fig. 2(b)) burner flames. For the well-stirred reactor data (Fig. 2(c)),  $r^2$ -value is high because of the scarce data points which are well-separated for aliphatics ( $n_c < 4$ ) and aromatics ( $6 > n_c$ ). Figure 3 shows a replot of the data points in Figure 2 by  $\psi_c$  as a function of  $n_{c-c}$ . The scatter becomes smaller in the new plot ( $r^2 = 0.829, 0.571$ , and  $0.787$  for each method) as the effective equivalence ratio, which is more realistic in fuel-rich conditions, is used. The effect of the carbon number and C/H ratio are taken into account in  $n_{c-c}$  (Eq. (1)). However, separation between the aliphatics and aromatics still exists for large  $n_{c-c}$ , as was noted by Ramer *et al.* [12].

# SOOTING CORRELATIONS FOR PREMIXED COMBUSTION

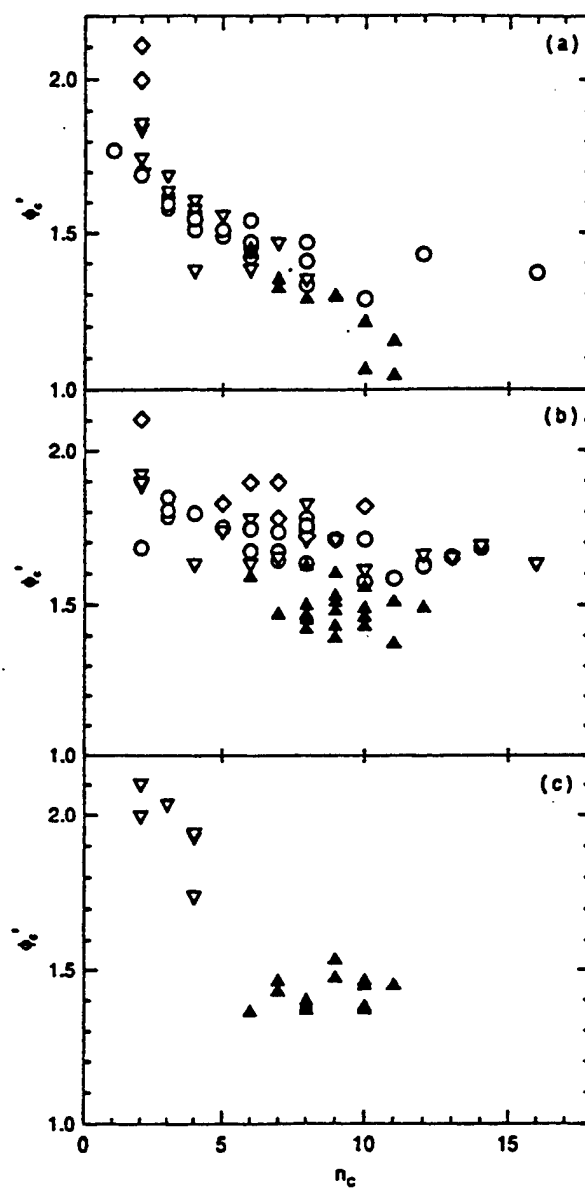


**FIGURE 2.** Soot threshold data expressed as the critical conventional equivalence ratio at sooting versus the carbon number: (a) Bunsen-type burners, (b) Meker-type burners, (c) well-stirred reactors.  $\circ$ , Alkanes;  $\nabla$ , alkenes;  $\diamond$ , alkynes;  $\blacktriangle$ , aromatics.

# SOOTING CORRELATIONS FOR PREMIXED COMBUSTION

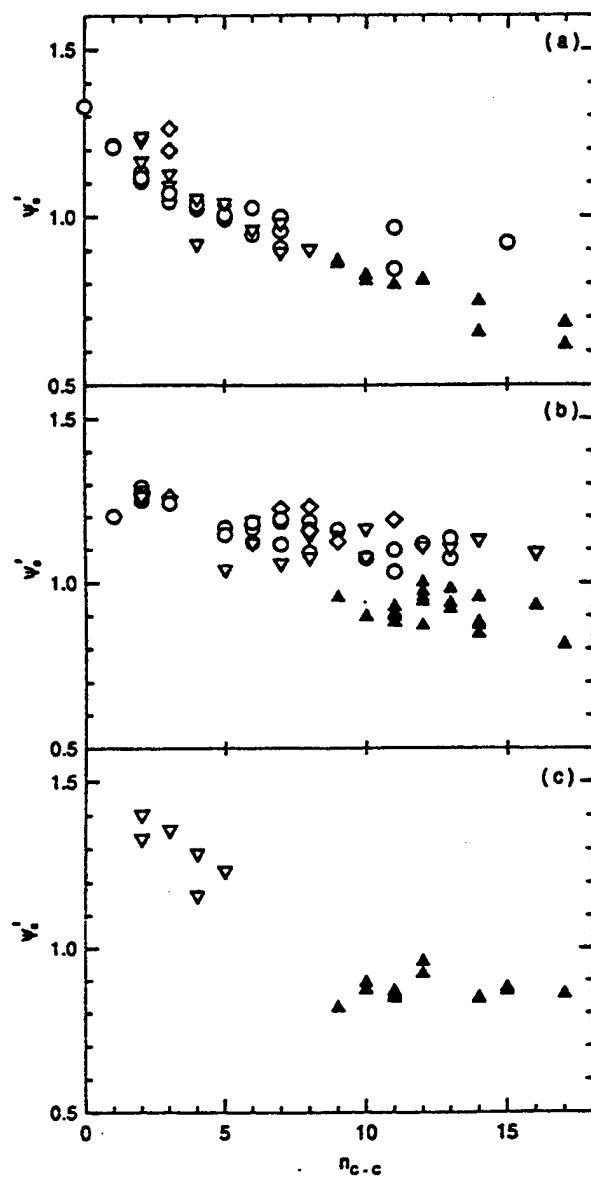


FIGURE 3. Soot threshold data expressed as the critical effective equivalence ratio at sooting versus the number of C-C bonds: (a) Bunsen-type burners, (b) Meker-type burners, (c) well-stirred reactors. O, Alkanes; V, alkenes;  $\diamond$ , alkynes;  $\blacktriangle$ , aromatics.

## SOOTING CORRELATIONS FOR PREMIXED COMBUSTION

Figure 4 shows a replot of the data points by  $(C/O)_c$  as a function of  $n_c$ . The coefficients of determination are  $r^2 = 0.846, 0.743$ , and  $0.298$  for each method. For Bunsen-type burner flames (Fig. 4(a)),  $(C/O)_c$  is nearly constant ( $0.47 \pm 0.05$ ) for  $C_1$  to  $C_{16}$  alkanes and increases for smaller alkenes ( $\sim 0.61$  for ethylene) and acetylene ( $\sim 0.83$ ). Although the constancy  $(C/O)_c \approx 0.5$  for alkanes has long been known [13], the deviation of the data points for ethylene and acetylene has not yet been fully explained. Aromatic fuels are among the scatter of the data points for aliphatics, and no apparent separation between aliphatics and aromatics is observed. A similar trend is observed for Meker-type burner flames with slightly higher values of  $(C/O)_c$  and a larger scatter. Although the data points for well-stirred reactors do not show a clear trend because of the insufficient number of data, they quantitatively follow the data points for Meker-type burner flames. Unlike conventional and effective equivalence ratios, the oxygen requirement for the carbon-to-oxygen ratio is independent of the hydrogen number (see Table 1). Thus, the apparent decreasing trend of both  $\phi'_c$  and  $\psi'_c$  with increasing  $n_c$  and the separation between aliphatics and aromatics for large  $n_c$  are primarily due to counting  $n_H$  as well as  $n_C$ .

Because the variations in  $(C/O)_c$  apparently depend on the homologous series, they must be related to the properties of the fuel and the flame temperature. Figure 5 shows the mole fractions of the fuel and oxygen in the mixture at the sooting limit. In general,  $X_{F_c}$  decreases and  $X_{O_{2,c}}$  increases (thus,  $[X_F/X_{O_2}]_c$  decreases), while the stoichiometric oxygen requirements ( $Z_{\phi}$ ,  $Z_{\psi}$ , and  $Z_{C/O}$ ) increase with increasing  $n_c$ , thereby determining the dependencies of  $\phi_c$ ,  $\psi_c$ , and  $(C/O)_c$  on  $n_c$  (see Table 1). Figure 6 shows the adiabatic flame temperatures at the sooting limits ( $T_{fc}$ ) calculated by the NASA CEC89 program [21]. Although the actual flame temperature must be lower than the calculated adiabatic temperature,  $T_{fc}$  should sufficiently discriminate the actual differences due to the type of fuel and the equivalence ratio. For alkanes, the adiabatic flame temperature increases over 500 K from methane ( $\sim 1540$  K) to hexadecane ( $\sim 2090$  K) as  $\phi_c$  decreases from 1.8 to 1.35. For alkenes, variations in  $T_{fc}$  are relatively small (1950 K to 2150 K). Acetylene has the highest flame temperature ( $\sim 2400$  K), as expected; for aromatics, the variations in  $T_{fc}$  are generally higher (2050 K to 2350 K) than aliphatics.

Multiplying  $(C/O)_c$  by  $2X_{O_{2,c}}$  yields  $n_c X'_{F_c}$  (see Table 1), which will become the number of carbon atoms per mole of the mixture by multiplying further by Avagadro's number. Since the variation in  $X_{O_{2,c}}$  is relatively small (0.18 to 0.21) over all  $C_1$  to  $C_{16}$  hydrocarbon fuels,  $n_c X'_{F_c}$

# SOOTING CORRELATIONS FOR PREMIXED COMBUSTION

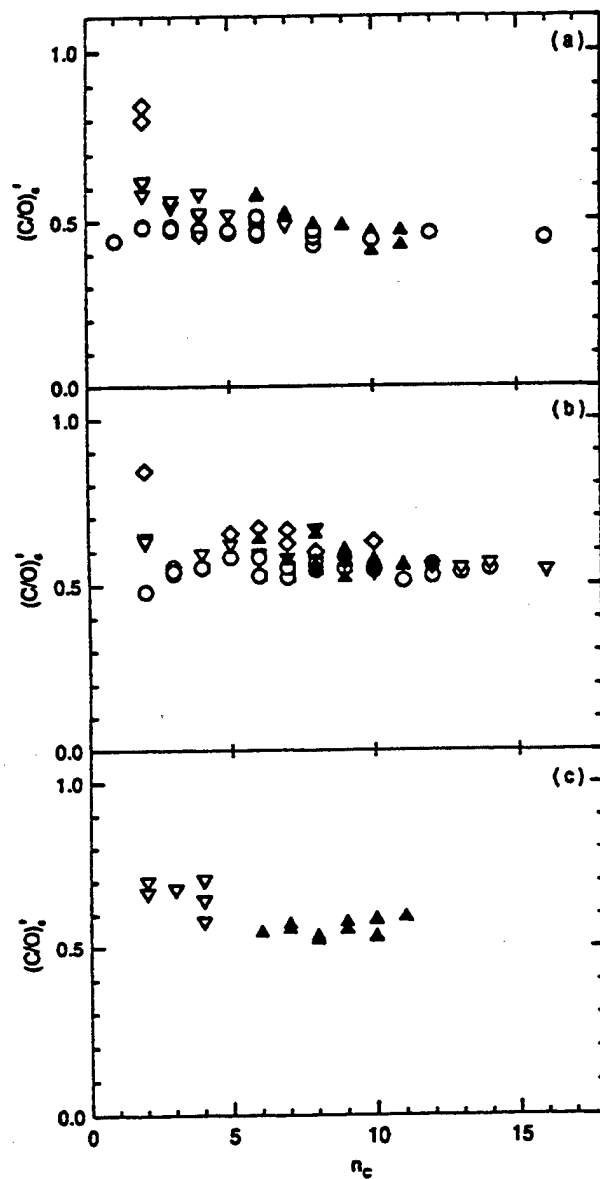
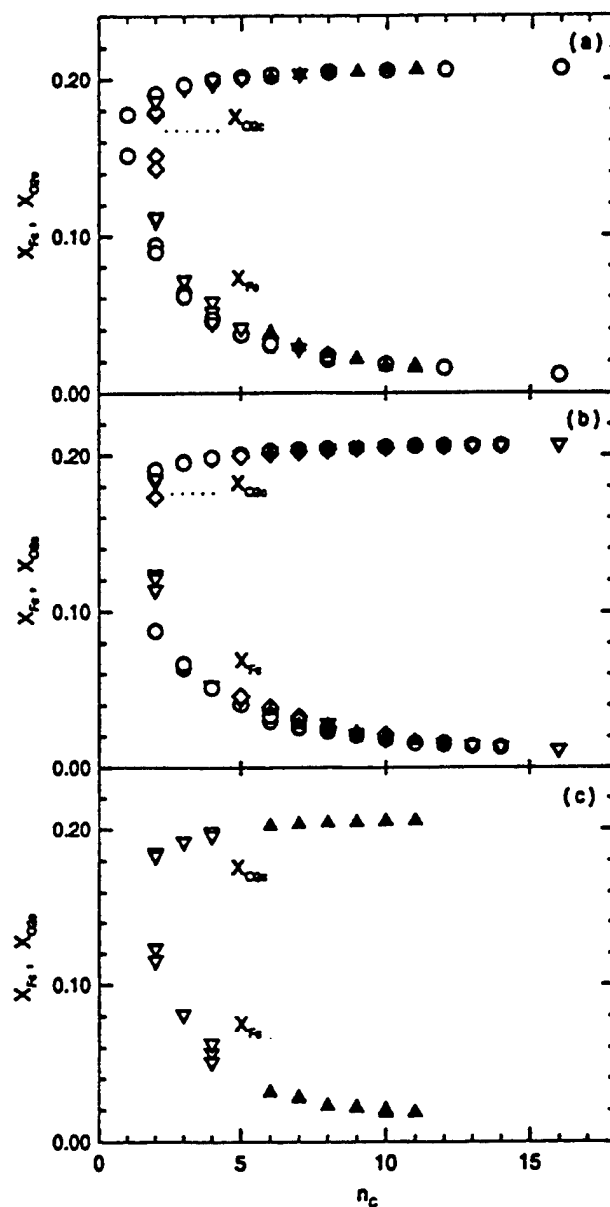


Figure 4. Soot threshold data expressed as the critical C/O ratio at sooting, standardized for each method: (a) Bunsen-type burners, (b) Meker-type burners, (c) well-stirred reactors. O, Alkanes; V, alkenes; ◇, alkynes; ▲, aromatics.

# SOOTING CORRELATIONS FOR PREMIXED COMBUSTION



**FIGURE 5.** Mole fractions of fuel and oxygen in the fuel-air mixture at sooting: (a) Bunsen-type burners, (b) Meker-type burners, (c) well-stirred reactors. O, Alkanes; V, alkenes;  $\diamond$ , alkynes;  $\blacktriangle$ , aromatics.



# SOOTING CORRELATIONS FOR PREMIXED COMBUSTION

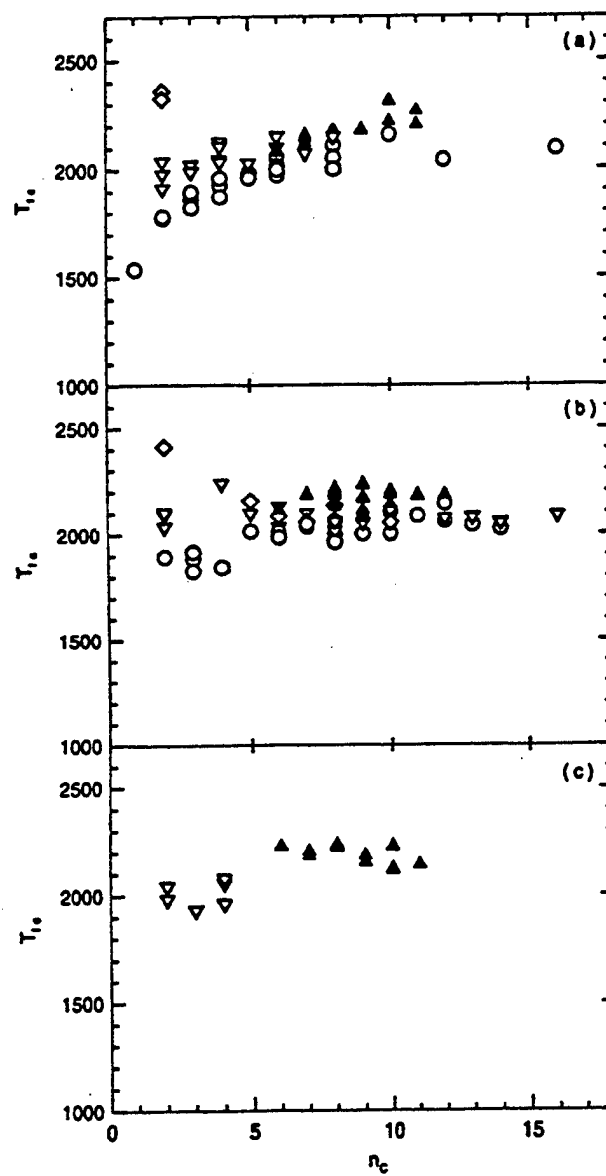


FIGURE 6. Adiabatic flame temperature of the fuel-air mixture at sooting: (a) Bunsen-type burners, (b) Meker-type burners, (c) well-stirred reactors. O, Alkanes; V, alkenes;  $\diamond$ , alkynes;  $\blacktriangle$ , aromatics.

## SOOTING CORRELATIONS FOR PREMIXED COMBUSTION

exhibits a dependency on  $n_C$  (not shown) similar to  $(C/O)_c$ . The number density of carbon atoms at atmospheric pressure may be expressed as  $N'_C = K n_C X'_{F_c} T_{F_c}$ , where  $K$  is a constant (Avagadro's number times pressure divided by the universal gas constant;  $0.734 \times 10^{28} \text{ K/m}^3$ ). Figure 7 shows variations in  $N'_C/K$  with  $n_C$ . For Bunsen-type and Meker-type burner flames (Figs. 7(a) and 7(b)),  $N'_C/K$  is fairly constant for alkanes ( $\pm 12\%$  and  $\pm 10\%$ , respectively) over a wide range (a factor of 16) of  $n_C$ . The difference in  $N'_C/K$  between  $C_2$  aliphatics is significantly smaller ( $\pm 12\%$ ) than that of  $(C/O)_c$  ( $\pm 27\%$ ) shown in Figure 4. Data points for aromatics are among the scatter of aliphatics. The scatter in  $N'_C/K$  appears to be larger for the well-stirred reactors (Fig. 7(c)), but its variation over  $C_2$ - $C_{11}$  hydrocarbons is still moderate ( $\pm 17\%$ ). Note that  $T_{F_c}$  is the calculated adiabatic flame temperature, and the deviation from the actual gas temperature must be least for Bunsen-type flames and becomes larger for Meker-type flames and well-stirred reactors. More data points (and perhaps the actual flame temperature measurement) are required to determine the concrete trend for well-stirred reactors. Nevertheless, considering the wide range of  $n_C$  (and large experimental uncertainties [ $\pm 9\%$ ]),  $N'_C/K$  may be regarded as practically constant for all fuels for each combustion method.

This striking result implies that the soot threshold of hydrocarbon-air mixtures is determined by the number density of carbon atoms introduced into the system, independent of the types of the fuel and combustor. Therefore, information on the original fuel molecule, including the number of carbon (and hydrogen) atoms and the chemical structure (depending on its homologous series and branched chain), and the structure of the reaction zone (either a narrow flame zone or broad turbulent reacting flow) are unimportant in determining the sooting limit. This result is consistent with the earlier conclusion [8,9] that, in premixed flames, the fuel structure has no significant effect on soot threshold. Soot (surface and mass) growth occurs and reaches a visually recognizable level in the post-reaction zone. The onset of soot formation occurs earlier at a position in the flame where some oxygen molecules still remain and, thus, the concentrations of oxidizing species and soot precursors may vary depending on the fuel type. By contrast, in the post-reaction zone, the parent fuel molecules no longer exist; only their rich oxidation products exist, which are not different in character from those of various homologous series. This concept is supported by the results of Harris and Weiner [22], who found that toluene addition to an aliphatic fuel has no effect on soot formation other than that which results from the increased number of carbon atoms in the fuel.

# SOOTING CORRELATIONS FOR PREMIXED COMBUSTION

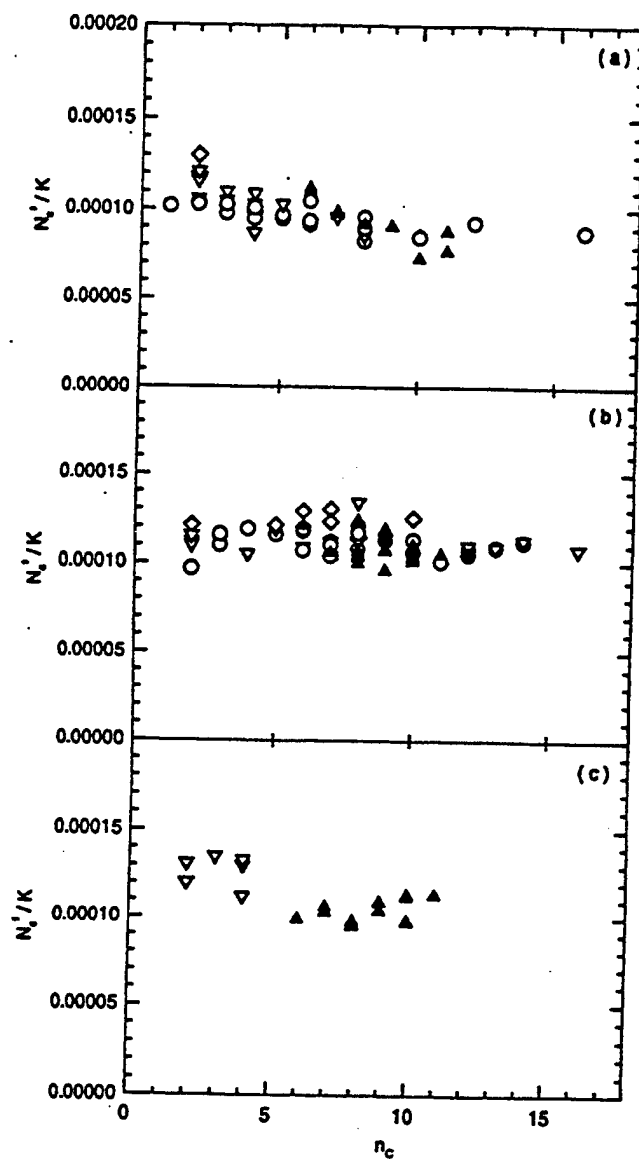


FIGURE 7. Soot threshold data expressed as the critical carbon number density at sooting, standardized for each method: (a) Bunsen-type burners, (b) Meker-type burners, (c) well-stirred reactors. O, Alkanes; V, alkenes;  $\diamond$ , alkynes;  $\blacktriangle$ , aromatics.

## SOOTING CORRELATIONS FOR PREMIXED COMBUSTION

Moreover, a similar trend in the results obtained by well-stirred reactors suggests that the mode of the process, whether sequential in the narrow laminar flame zone or simultaneous in the turbulent reacting flow, does not have a significant effect on soot threshold.

Although the argument based on the constant number density of carbon atoms described above must reflect the critical condition for incipient soot formation, the effects of various parameters on the sooting limits are not readily known. It is of great practical use if the soot threshold data are expressed as functions of parameters predeterminable from the properties of the fuel-air mixture. Figure 8 shows the adiabatic flame temperature at  $\phi = 1.5$ , C/H ratio, heat of formation, and averaged-distance-sum connectivity index of the fuel. These variables are independent of the soot threshold. The trend in  $T_f$  at  $\phi = 1.5$  (Fig. 8(a)) qualitatively resembles the variations in  $(C/O)_c$  for Bunsen-type flames (Fig. 4(a)). Figure 9 shows the variation in  $(C/O)_c$  as a function of  $T_f$  at  $\phi = 1.5$ .  $r^2$ -values are 0.846, 0.743, and 0.298, respectively, for Bunsen burners, Meker burners, and well-stirred reactors. For both Bunsen-type and Meker-type burner flames, there is a strong correlation between these variables with slightly different slopes. The trend in  $n_C/n_H$  also resembles that in  $(C/O)_c$  for aliphatics, but the data points for aromatics are markedly higher than aliphatics. The flame temperature is dependent on the C/H ratio and the heat of formation of the fuel because  $n_C/n_H$  essentially determines the ratio between lower-enthalpy carbon-containing combustion products ( $CO_2$ ,  $CO$ ) and higher-enthalpy water vapor, and  $\Delta H_{f,\infty}^\circ$  determines the enthalpy of the initial combustible mixture, thereby defining the heat release. Alkynes (particularly acetylene) and aromatic fuels, which have higher  $n_C/n_H$  and  $\Delta H_{f,\infty}^\circ$ , result in higher  $T_f$  at  $\phi = 1.5$  than those of alkenes and alkanes. Although the averaged-distance-sum connectivity index discriminates multiple bonds in alkenes and alkynes, it also discriminates branched-chain aliphatics, thus creating more scatter in alkane homologous series. Since the soot threshold data exhibit no significant difference between straight-chain and branched-chain aliphatics, the contribution of  $J$  to the sooting correlations may be weak, except for a smaller  $n_C$  ( $< 5$ ).

Although the correlation between the soot threshold and a single parameter (such as  $\psi'_c$  vs.  $n_{C-C}$ , or  $(C/O)_c$  vs.  $T_f$  at  $\phi = 1.5$ ) reveals the effect of some controlling parameters, there are apparent limitations (e.g., the weak discrimination between homologous series [aliphatics vs. aromatics, in particular] and the weak predictive power for a pure fuel and mixtures whose tendency to form soot is unknown). To determine

# SOOTING CORRELATIONS FOR PREMIXED COMBUSTION

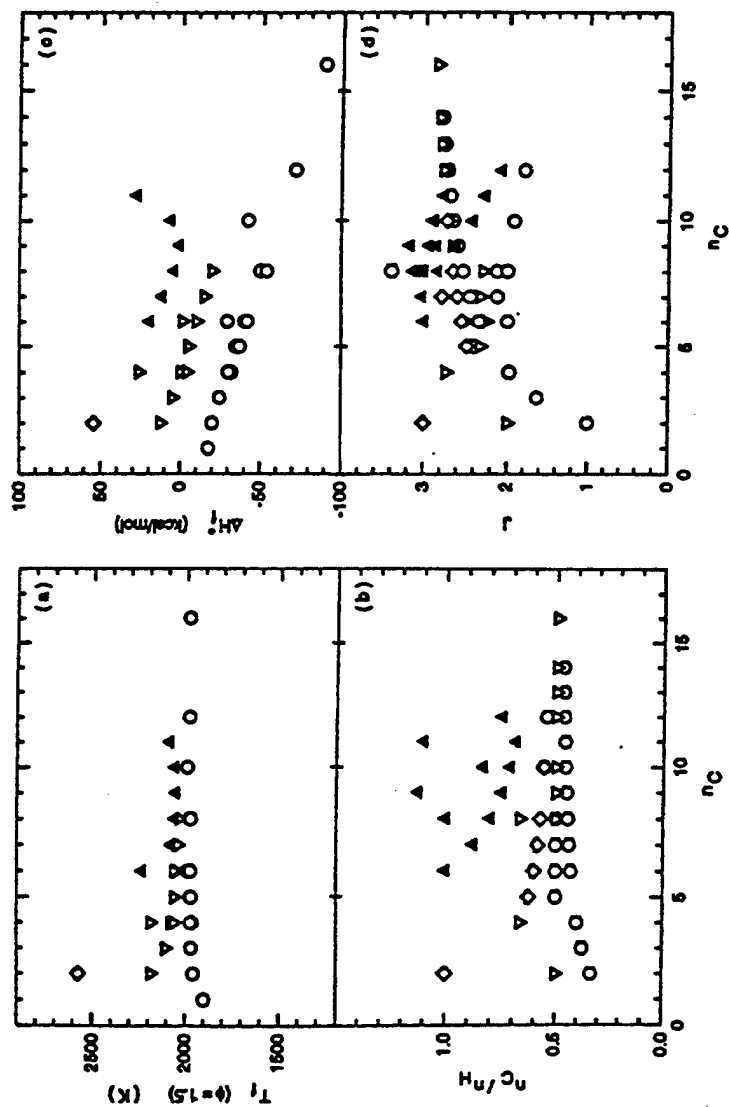


FIGURE 8. (a) Adiabatic flame temperature at  $\phi_c = 1.5$ , (b) C/H ratio, (c) heat of formation, (d) averaged distance-sum connectivity (Balaban) index. O, Alkanes; V, alkenes; ◇, alkynes; ▲, aromatics.

# SOOTING CORRELATIONS FOR PREMIXED COMBUSTION

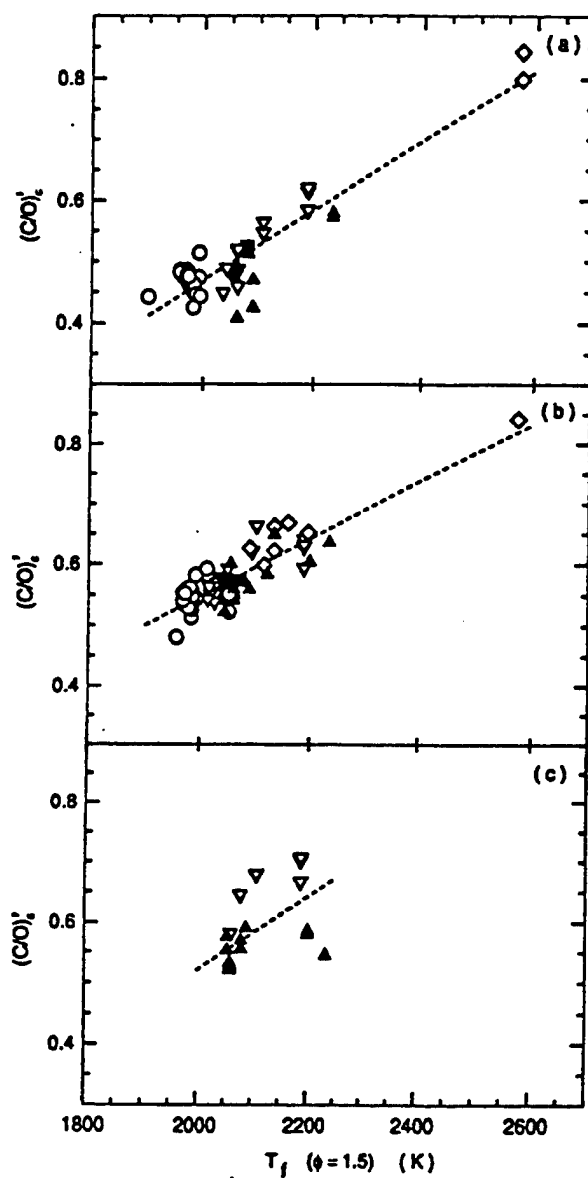


FIGURE 9. Correlations between the critical C/O ratio at sooting, standardized for each method, and the adiabatic flame temperature at  $\phi = 1.5$ . (a) Bunsen-type burners, (b) Meker-type burners, (c) well-stirred reactors. O, Alkanes; V, alkenes;  $\diamond$ , alkynes;  $\blacktriangle$ , aromatics.

# SOOTING CORRELATIONS FOR PREMIXED COMBUSTION

TABLE 4  
Multiple regression analysis of the soot threshold data ( $y = a_0 + a_1 n_C + a_2 n_C/n_H + a_3 \Delta H_{in}^\circ + a_4 J + a_5 T_f[\phi = 1.5]$ )

$y$	$r^2$	$a_i$	Constant	$n_C$	$n_C/n_H$	$\Delta H_{in}^\circ$	$J$	$T_f(\phi = 1.5)$
$\phi_c''$	0.844	$a_i$	-1.081	-0.0107	-0.699	-0.00076	-0.0706	0.001616
		$t_i$	-5.11	-3.04	-9.22	-1.49	-3.64	15.32
$\psi_c''$	0.885	$a_i$	-0.360	-0.0088	-0.618	-0.00062	-0.0670	0.000968
		$t_i$	-2.46	-3.61	-11.8	-1.77	-4.99	13.26
$(C/O)_c''$	0.821	$a_i$	-0.720	-0.0019	-0.0813	-0.00014	-0.0036	0.000649
		$t_i$	-9.71	-1.57	-3.05	-0.76	-0.52	17.52
$(X_{O_2}/X_F)_c''$	0.988	$a_i$	1.750	0.9500	1.163	-0.01062	-0.1030	-0.00115
		$t_i$	1.82	59.6	3.38	-4.61	-1.17	-2.39

# SOOTING CORRELATIONS FOR PREMIXED COMBUSTION

more systematically the contributions of various parameters to the sooting threshold data expressed in various forms, multiple linear regression analyses were made for the whole data set. Table 4 summarizes the selective results of multiple linear regression analysis for each of four dependent variables ( $\phi_c''$ ,  $\psi_c''$ ,  $[C/O]_c''$ , and  $[X_{O_2}/X_F]_c''$ ) with five independent variables ( $n_C$ ,  $n_C/n_H$ ,  $\Delta H_{F,300}^\circ$ ,  $J$ , and  $T_i$  at  $\phi = 1.5$ ) listed in Table 2. The table includes the coefficient of determination, the coefficients of the regression equation ( $a_i$ ), and the  $t$ -ratios ( $t_i$ ) (i.e.,  $a_i$  divided by the standard deviation of  $a_i$ ). Although various numbers (one to four) of the independent variables have been tested, only the results for four variables are shown in Table 4 because they provide the best regression for each dependent variable. The coefficient of determination is highest (0.988) for,  $(X_{O_2}/X_F)_c''$ , indicating that nearly 99% of the variation in  $y$ -value can be explained by means of the straight-line prediction equation. Figure 10 shows the experimental values of

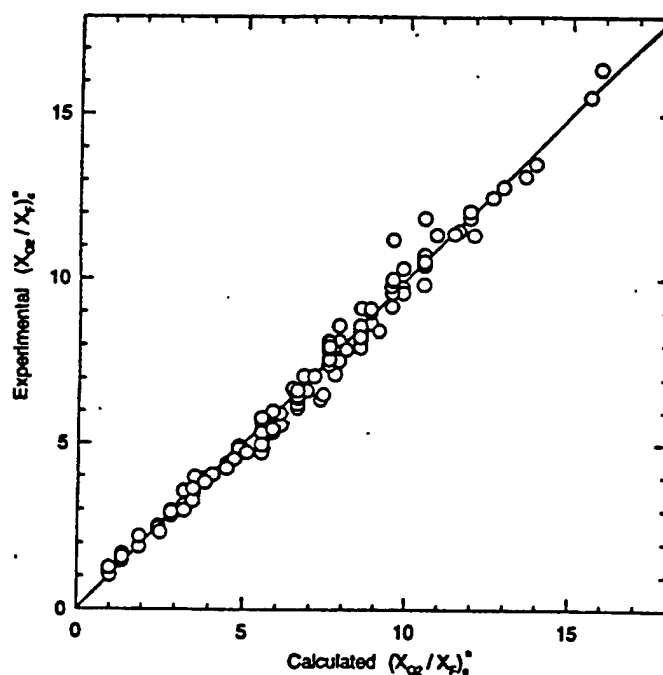


FIGURE 10. Correlations between the experimental and calculated oxygen-to-fuel ratio at sooting for all data.



## SOOTING CORRELATIONS FOR PREMIXED COMBUSTION

$(X_{O_2}/X_F)_c^*$ , versus calculated values for all the data points. The t-ratio indicates the relative contribution of each term to each y-value. For  $\phi_c^*$ ,  $\psi_c^*$ , and  $(C/O)_c^*$ , the temperature effect is significant; for  $(X_{O_2}/X_F)_c^*$ ,  $n_C$  has a predominant contribution because it is not been normalized by the oxygen requirement including  $n_C$ . For  $\phi_c^*$  and  $\psi_c^*$ ,  $n_C/n_H$  makes an appreciable contribution because  $n_H$  is counted in the normalization (see Table 1), whereas for  $(C/O)_c^*$ , it is less significant than the constant term, as expected from its near-constant trend (Fig. 4).

## 4. CONCLUSIONS

Thorough analyses of the experimental data available in the literature for 74 hydrocarbon fuels ( $C_1$  to  $C_{16}$  aliphatics and  $C_6$  to  $C_{12}$  aromatics) burning with air revealed the effects of various factors in determining the soot threshold in premixed combustion. The critical carbon-to-oxygen ratio is nearly constant for alkanes but strongly correlates to the adiabatic flame temperature at a fuel-rich condition ( $\phi = 1.5$ ) for alkenes and alkynes. The oxygen-to-fuel molar ratio of the mixture at sooting correlates remarkably well (the coefficient of determination:  $r^2 = 0.988$ ) with the carbon number, C/H ratio, heat of formation,  $T_f$  at  $\phi = 1.5$ , and averaged-distance-sum connectivity index. For hydrocarbon-air combustion, soot threshold is determined by a critical number density of carbon atoms introduced into the system independent of the types of fuel and combustor. Therefore, information on the original fuel molecule, including the number of carbon (and hydrogen) atoms and the chemical structure (depending on its homologous series and branched chain), and the mode of the reaction zone (either a narrow flame zone or broad turbulent reacting flow) are unimportant in determining the sooting limit. The scatter of the experimental data tends to cover physically meaningful trends, and a more quantitative detection of the soot threshold is desirable.

## ACKNOWLEDGEMENTS

This work was supported by the U.S. Air Force, Wright Laboratory, Aero Propulsion and Power Directorate, Fuels and Lubrication Division, Wright-Patterson Air Force Base, Ohio, under Contract No. F33615-92-C-2207 (Technical Monitor: C. W. Frayne).

# SOOTING CORRELATIONS FOR PREMIXED COMBUSTION

## REFERENCES

1. J. C. Street and A. Thomas, *Fuel* **34** (1955): 4-36.
2. J. Grumer, M. E. Harris, and V. R. Rowe, Report of Investigations 5225 (Bureau of Mines, Pittsburgh, Pennsylvania, 1956).
3. J. Flossdorf and H. Gg. Wagner, *Z. Phys. Chem. Neue Folge* **54** (1967): 113-128.
4. F. J. Wright, *Twelfth Symposium (International) on Combustion* (The Combustion Institute, Pittsburgh, Pennsylvania, 1969), p. 867.
5. H. F. Calcote and W. J. Miller, *Ionic Mechanisms of Carbon Formation in Flames*, TP-371 (AeroChem Research Laboratories, Inc., Princeton, New Jersey, 1978).
6. W. S. Blazowski, *Combust. Sci. Tech.* **21** (1980): 87-96.
7. D. B. Olson and J. C. Pickens, *Combust. Flame* **57** (1984): 199-208.
8. F. Takahashi and I. Glassman, *Combust. Sci. Tech.* **37** (1984): 1-19.
9. F. Takahashi, J. Bonini, and I. Glassman, Eastern States Section/The Combustion Institute Meeting, Paper No. 98 (Clearwater Beach, Florida, December 1984).
10. M. M. Harris, G. B. King, and N. M. Laurendeau, *Combust. Flame* **64** (1986): 99-112.
11. R. C. Millikan, *J. Phys. Chem.* **66** (1962): 794-799.
12. E. R. Ramer, J. F. Merklin, and C. M. Sorensen, *Combust. Sci. Technol.* **54** (1987): 407-412.
13. B. S. Haynes and Gg. Wagner, *Prog. Energy Combust. Sci.* **7** (1981): 229-273.
14. H. F. Calcote and D. M. Manos, *Combust. Flame* **49** (1983): 289-304.
15. D. H. Rouvray, *Scientific American* **254** (1986): 40-47.
16. A. T. Balaban, *Pure & Appl. Chem.* **55** (1983): 199-206.
17. A. T. Balaban and P. Filip, *Math. Chem.* **16** (1984): 163-190.
18. M. P. Hanson and D. H. Rouvray, *J. Phys. Chem.* **91** (1987): 2981-2985.
19. D. R. Stull and E. F. Westrum, Jr., *The Chemical Thermodynamics of Organic Compounds*. (John Wiley & Sons, New York, 1969).
20. R. C. Weast (Ed.), *Handbook of Chemistry and Physics* (CRC Press, Cleveland, Ohio, 1973), 54th ed.
21. S. Gordon and B. J. McBride, *Computer Program for Calculation of Complex Chemical Equilibrium Compositions, Rocket Performance, Incident and Reflected Shocks, and Chapman-Jouguet Detonations* (National Aeronautics and Space Agency, Washington, D. C., 1976), SP-273 Interim Revision.
22. S. J. Harris and A. M. Weiner, *Combust. Sci. Technol.* **38** (1984): 75-87.

## **APPENDIX N**

### **PIV Measurements of Flat Plate Film Cooling Flows With High Free Stream Turbulence**

**Sivaram P. Gogineni, Richard B. Rivir,  
David J. Pestian, Larry P. Goss**

**AIAA 96-0617**

**PIV MEASUREMENTS OF FLAT PLATE FILM  
COOLING FLOWS WITH HIGH FREE STREAM  
TURBULENCE**

Sivaram P. Gogineni  
Systems Research Labs  
Dayton, OH

Richard B. Rivir  
Aero Propulsion and Power Directorate  
Wright Patterson AFB, OH

David J. Pestian  
Univ. of Dayton Research Institute  
Dayton, OH

Larry P. Goss  
Innovative Scientific Solutions Inc.  
Dayton, OH



**34th Aerospace Sciences  
Meeting & Exhibit  
January 15-18, 1996 / Reno, NV**

# PIV MEASUREMENTS OF FLAT PLATE FILM COOLING FLOWS WITH HIGH FREE STREAM TURBULENCE

Sivaram P. Gogineni  
Systems Research Labs  
Dayton, OH

David J. Pestian  
University of Dayton Research Institute  
Dayton, OH

Richard B. Rivir \*  
Aero Propulsion and Power Directorate  
Wright Patterson AFB, OH

Larry P. Goss  
Innovative Scientific Solutions Inc.  
Dayton, OH

## Abstract

Two color double pulsed Particle Image Velocimetry measurements of simulated turbine film cooling flows have been made for blowing ratios of 0.5, 0.7, 1.0, and 1.5 in the near field of the film cooling hole,  $x/d \leq 2.5$  for free stream turbulence levels of 1%, 6%, 12%, and 17%. Increases in the jet spread with free stream turbulence are up to 2 times the 1% free stream turbulence case for blowing ratios up to 1.0.

## Nomenclature

- d film cooling hole diameter (1.905 cm)
- M coolant blowing (mass flux) ratio ( $\rho_c U_c / \rho_{fs} U_{fs}$ )
- Re Reynolds Number based on film cooling hole diameter ( $\rho_c U_c d / \mu$ )
- Tu x turbulence intensity ( $u' / U$ )
- U time mean local streamwise velocity (m/s)
- x streamwise distance measured from the downstream lip of the injection hole (cm)
- y vertical distance from the injection surface (cm)
- $\Lambda$  integral turbulence scale (cm)

## Introduction

The character of the flow into the axial turbine rotor blade row of a gas turbine engine is largely determined by the upstream nozzle guide vanes. The close spacing of vanes and blades subject the blades to unsteady flows with scales which may range from half of the passage width, due to the passage vortex, to the order of the blade boundary layer thickness.

Many modern turbine stages employ film cooling to permit near stoichiometric combustor operating temperatures. Film cooling air is injected through rows of small (0.8mm diameter typical) holes in the blade surface. The coolant air is supplied from the compressor exit flow and is maintained at essentially constant pressure.

The objective of the present study is to provide a more detailed characterization of the coolant injection phenomenon and its interaction with the free stream disturbances. The Reynolds number based on the coolant hole diameter of 1.9 cm is approximately 20,000, which is typical for a turbine. The facility can be supplied with freestream turbulence levels ranging from less than 1% to over 17%. Freestream turbulence is an important feature of gas turbines which must be present to properly simulate the turbine aerodynamics and heat transfer. The velocity ratio (coolant velocity / freestream velocity) varies depending on where the film cooling is located on the blade, so this parameter will also be investigated. Because the effectiveness of film cooling is governed by the rate at which the coolant jets mix with the hotter surrounding flow, both freestream turbulence and the velocity ratio influence the rate of mixing and therefore the performance of any specific film cooling design. PIV measurements provide a simultaneous realization of a plane of the flow with a spatial resolution of 1.4mm for 3 diameters downstream of the film injection hole. These measurements allow computation of vorticity and dissipation.

## Experimental Facility

The measurements of this study were made in an open loop film cooling wind tunnel described in detail

---

\* AIAA Associate Fellow  
Copyright © 1996 by the American Institute of Aeronautics and Astronautics, Inc. All rights reserved.

by Bons, et al. 1994, and 1995. Figure 1 shows an overall view of the facility and a top view of the cooling hole arrangement and the heat transfer surface. The main flow passes through a conditioning plenum containing perforated plates, honeycomb, screens, and a circular-to-rectangular transition nozzle. Downstream of the transition nozzle, at the film cooling station location, free stream turbulence levels of 0.7 to 17% can be achieved with velocity and temperature profiles uniform to within 1% at the film cooling station.

A single row of 1.905 cm film cooling holes at an injection angle of 35 degrees to the primary flow is investigated. The length to diameter ratio of the film cooling holes evaluated is 2.4. The integral turbulence scale to film hole diameter is 2.88 to 4.23, depending on the turbulence level and turbulence generation mechanism (Bons et al., 1994). The momentum thickness to hole diameter ratio typically is 0.05, and a typical film cooling hole Reynolds number is 20,000.

#### Two-Color Particle Image Velocimetry

PIV techniques have been used for a number of years to measure velocity distributions in planar cross sections of a given flow field as described in detail in earlier work (Lourenco et al., 1989 and Adrian, 1991). One of the difficulties involved in implementing this otherwise attractive velocimetry technique however, is the directional ambiguity, namely, the inability to determine the temporal sequence of particle pairs and thus the direction of the measured velocity. Several techniques that have been developed to resolve this ambiguity use a single color lasers and image shifting by means of either scanning, or rotating mirrors, pulse tagging, calcite crystals, and polarizing beam splitters. The mechanical motion associated with the mirrors imposes some limitations on velocity measurements. Pulse tagging uses pulses of different duration (Grant et al., 1990), but limits the technique to low velocity flows, since the time resolution is not adequate to prevent image blurring in high speed flows. Calcite crystals exploit the polarization of the light scattered from the seed particles but the magnitude and orientation of the shift can change in the film plane because the light is collected from a finite solid angle (Landreth et al., 1988). In addition, for a given camera magnification, the velocity bias can not be altered unless the crystal thickness is changed or several crystals are used in series. A polarizing beam splitter and two quarter wave plates also utilize polarization principle and provide constant velocity bias throughout the flow field so that synchronization with other hardware is not necessary (Lourenco, 1993).

A two-color PIV system that was developed by Goss et al., 1991, (Figure 1) has the following advantages: (i) the directional ambiguity is resolved using the color coding of the particle images, (ii) higher data yields are attainable, and (iii) the system is particularly suitable for combustion diagnostics. The system uses color to temporally mark the location of the seed particles in the flow field. The green (532 nm) laser output from a frequency-doubled Nd:YAG laser and the red (610 nm) laser output from a Nd:YAG pumped dye laser are combined by a dichroic beam splitter and directed through sheet forming optics. The laser sheet energy is typically 20 mJ/pulse and the sheet thickness is less than 1 mm in the test section. The Laser sheet orientation is illustrated in Figure 1. The temporal delay between the two lasers is controlled by a pulse generator and is set as a function of the gas velocity, optical magnification and interrogation spot size. In the present experiments, the time delay is 12  $\mu$ sec and is monitored by a photodiode.

The jet fluid is seeded with sub-micron (nominally 0.5  $\mu$ m) smoke particles. Mie scattering from the seed particles is recorded on commercial 35 mm color film that is digitized into individual red, green, and blue components at a resolution of 2700 pixels per inch. Several techniques such as Young's fringe analysis, auto-correlation, etc. are available for image analysis for monochromatic double pulse images. However, these methods do not take into account the color information in the present PIV images. The cross correlation technique implemented in the present work exploits the spectral separation of the red and green images and eliminates approximately one half of the possible particle images from each interrogation region.

The present cross-correlation technique is based on intensity maps of the red and green images of scattered light. Consider the intensity distributions of the red and green images  $r(x,y)$  and  $g(x,y)$  and their corresponding Fourier transforms  $R(a,b)$  and  $G(a,b)$ . The two-dimensional cross-correlation function

$$\begin{aligned} h(x,y) &= \iint_R r(\alpha,\beta) g(x+\alpha,y+\beta) d\alpha d\beta \\ &= F^{-1}[F(r(x,y)) F(g^*(x,y))] \\ &= F^{-1}[R(\alpha,\beta) G^*(\alpha,\beta)] \end{aligned} \quad (1)$$

is employed to determine the magnitude and direction of the average velocity over the interrogation area. (Note that unlike processing methodologies that are based on autocorrelation, the direction of the velocity vectors is uniquely determined.)

The correlation function (1) is calculated over small segments (interrogation domains) of the PIV image. In order to process the digitized PIV image, it is dissected into small sub regions. The dimensions of each interrogation domain depend on the particle density, estimated local velocity gradients, particle image size, and the desired spatial resolution. The maximum displacement of each particle must be less than half of the interrogation spot. In the present experiments, the interrogation domain measuring  $64 \times 64$  pixels corresponding to  $1.4 \times 1.4$  mm in the measured flow. In order to enhance the overall resolution, the interrogation domains are overlapped by one-half the domain size. The peak of the correlation map calculated by Eq. (1) corresponds to the average velocity displacement within the interrogation spot. An intensity weighted peak searching routine is used to determine the exact location of the peak to a sub-pixel accuracy. The number of particle pairs that are normally necessary to ensure a desirable signal to noise ratio is reduced to four or five pairs when the cross-correlation analysis is employed.

#### Uncertainty Analysis

The experimental uncertainties are calculated based on knowledge of the instrumentation used and a simple root-mean-squared error analysis (Kline and McClintock 1953). This method assumes contributions to uncertainties arise mainly from unbiased and random sources. The large out of plane velocities and large fluctuating components required dense seeding and very short interpulse times which began to challenge the capability of the film for temporal resolution. Uncertainty in the velocity measurement arises from the time required to keep the large out of plane velocities and fluctuating components within the laser sheet during both pulses. The resulting number of pixels, typically 12, of displacement and the sub pixel resolution of 0.25 pixels then dictate the uncertainty of  $\pm 2\%$ . The spatial resolution used in the data presented is 2.8mm. The data was acquired at a resolution of 1.4mm using 45 pixels per mm for a spatial resolution accuracy of 1.5%.

#### Results and Discussion

The film flow has been seeded with a 50% mixture of water and Propylene Glycol with a nominal diameter of 1 micron or less. This technique allows measurements of the film flow only. Blowing ratios of 0.5, 0.7, 1.0, and 1.5 were investigated for 1%, 6%, 12%, and 17% turbulence intensities. 10 to 30 images were taken for each flow case. The double pulsed PIV images and the reduced velocity plots will be presented. There is a very large mean velocity distribution in the vicinity of the film hole as shown in previous publications, Schauer and Bons, 1994, resulting in a vulcano like structure for this flow condition with a velocity ratio of up to +120% to 80% of free stream over the film hole. This range of velocities is also observed in the PIV measurements.

Shown in Figures 2 and 3 are typical double pulsed two color measurements for blowing ratios of 0.7, and 1.0 at the four turbulence levels. At the same blowing ratio the free stream turbulence levels of 1 % and 17% in the Figure 2 comparison clearly shows near doubling of the jet spread for the 17% turbulence case. This is consistent with previous averaged hot wire and thermocouple measurements. The film jet spread angle has two slopes, one nominally over the film hole, and a second slope after the film hole opening. Also illustrated in Figures 2 and 3 is the roll up of the film cooling jet boundary layer in the opposite direction of what would be the anticipated free stream shear layer roll up. The free stream has not been seeded in this case which is why the free shear layer does not appear in these realizations of the flow. The corresponding instantaneous velocity vector fields are shown in Figures 4 and 5. The range of film jet velocities at the exit are comparable to those observed in Schauer and Bons, 1994. Extensive regions of low velocity flow are indicated following the exit with very high activity in the shear layer. Again the jet spread with turbulence intensity is quite clear.

The indicated jet spread, growth of the shear layer, and growth of the scales was obtained from these realizations of the flow by digitizing their envelopes. The angle of the flow over the film cooling hole and the angle after the film cooling hole for 2.5 diameters is illustrated in Figure 6 for all blowing ratios and turbulence levels investigated. A least squares fit has been plotted for both angles in Figure 6. In Figure 7 we have digitized the thickness of the shear layer as a function of turbulence and blowing ratio. Figure 7 shows a regular growth in shear layer thickness with turbulence intensity and blowing ratio until we reach a blowing ratio of 1.5. At 1.5 the jet

momentum dominates the turbulence and the two curves remain coincident for 1.5 diameters. Although we have attempted to choose representative realizations, these are individual realizations of the flow. In reality there should be an envelope around each of these sets of data. The film injection angle is 35° as previously indicated. The initial blowing angle is less than the injection angle for blowing ratios less than 1, and approximately equal to the injection angle at a blowing ratio of 1.0 and 1% turbulence intensity. Both angles are observed to decrease with turbulence intensity for the 1.5 blowing ratio case. Both angles increase up to a blowing ratio of 1.0 with increasing turbulence intensity. At a blowing ratio of 1.5 the film momentum dominates that of the free stream with both angles decreasing with increasing turbulence. The shear layer over the film hole, is clearly driven primarily by the blowing ratio and the free stream then dominating the eddy size after the film hole. The shedding frequency of the shear layer increases, the scale size decreases, over the film hole with blowing ratio. The roll up frequency for the shear layer after the film hole decreases, the scale size increases, with both blowing ratio and turbulence level.

In Figure 8 the vorticity distribution has been calculated from  $\omega = 1/2(\partial U / \partial y - \partial V / \partial x)$  and the contours plotted for the blowing ratio of 1.0 case. The vorticity plots for all cases investigated show an increase in vorticity activity with both blowing ratio and turbulence intensity. The peaks in vorticity are well correlated with the shear layer velocities as is indicated in Figures 3, 5, and 8. These representations need to have the seeding optimized by further reducing the amount of seed introduced.

#### Concluding Remarks

PIV measurements of film cooling flows have indicated augmentation of jet spread for increased turbulence for  $M \leq 1$ . A systematic increase in jet and shear layer spread with turbulence intensity and blowing ratio has been documented near the film cooling hole for a Reynolds number of 20K. The blowing ratios of 0.5, 0.7, and 1.0 showed a doubling for the spread angles in going from turbulence levels of 1% to 17% with nearly a linear relationship with blowing ratio and turbulence level, while the 1.5 blowing ratio showed a decrease in spread angles. Increased jet spread implies a lower effectiveness and a proportionately higher mixed out temperature or lower cooling effectiveness.

#### Acknowledgments

This work was performed under partial sponsorship of the Air Force Office of Scientific Research project 2307S. Dr. James McMichael was the program manager.

#### References

- Adrian, R. J., 1991, "Particle Imaging Techniques for experimental fluid mechanics," *Ann Rev Fluid Mech*, 23, pp. 261-304.
- Bons, MacArthur, and Rivir, 1994, "The Effect of High Freestream Turbulence on Film Cooling Effectiveness," ASME 94-GT-51, International Gas Turbine and Aeroengine Congress and Exposition, The Hague, Netherlands.
- Bons, Rivir, MacArthur and Pestian, 1995, "The Effect of Unsteadiness on Film Cooling Effectiveness," AIAA 95-0306, 33rd Aerospace Sciences Meeting and Exhibit, Reno NV.
- Grant, I. And Liu, A., 1991, "Directional Ambiguity Resolution in Particle Image Velocimetry by Pulse Tagging," *Experiments in Fluids*, 10, 71-76, 1990, 3, pp. 36-42.
- Goss, L. P., Post, M. E., Trump, D. D., and Sarka, B., 1991, "Two Color Particle Imaging Velocimetry," *J. Laser Applications*, 3, pp. 36-42.
- Kline, S. J. and McClintock, F. S., Jan 1953, "Describing Uncertainties in Single-Sample Experiments," *Mechanical Engineering*, pp. 3-8.
- Landreth, C. C. and Adrian, R. J., 1988, "Electro-Optical Image Shifting for Particle Image Velocimetry," *Appl. Optics*, 27 pp. 4216-4220.
- Lourenco, L. M., 1993, "Velocity Bias Technique for Particle Image Velocimetry Measurements of High Speed Flows," *Appl. Optics*, 32, pp. 2159-2162.
- Lourenco, L. M., Krothapalli, A., and Smith, C. A., 1989, "Particle Image Velocimetry," *Advances in Fluid Mechanics Measurements* (M. Gad-el-Hak, ed.), Springer-Verlag, Berlin, pp. 127-199.
- Schauer, J. J., and Bons, J. P., 1994, "Film Cooling Jet Mixing with Free Stream Turbulence," 1994 ICHMT International Symposium on Turbulence, Heat and Mass Transfer, Lisbon, Portugal.



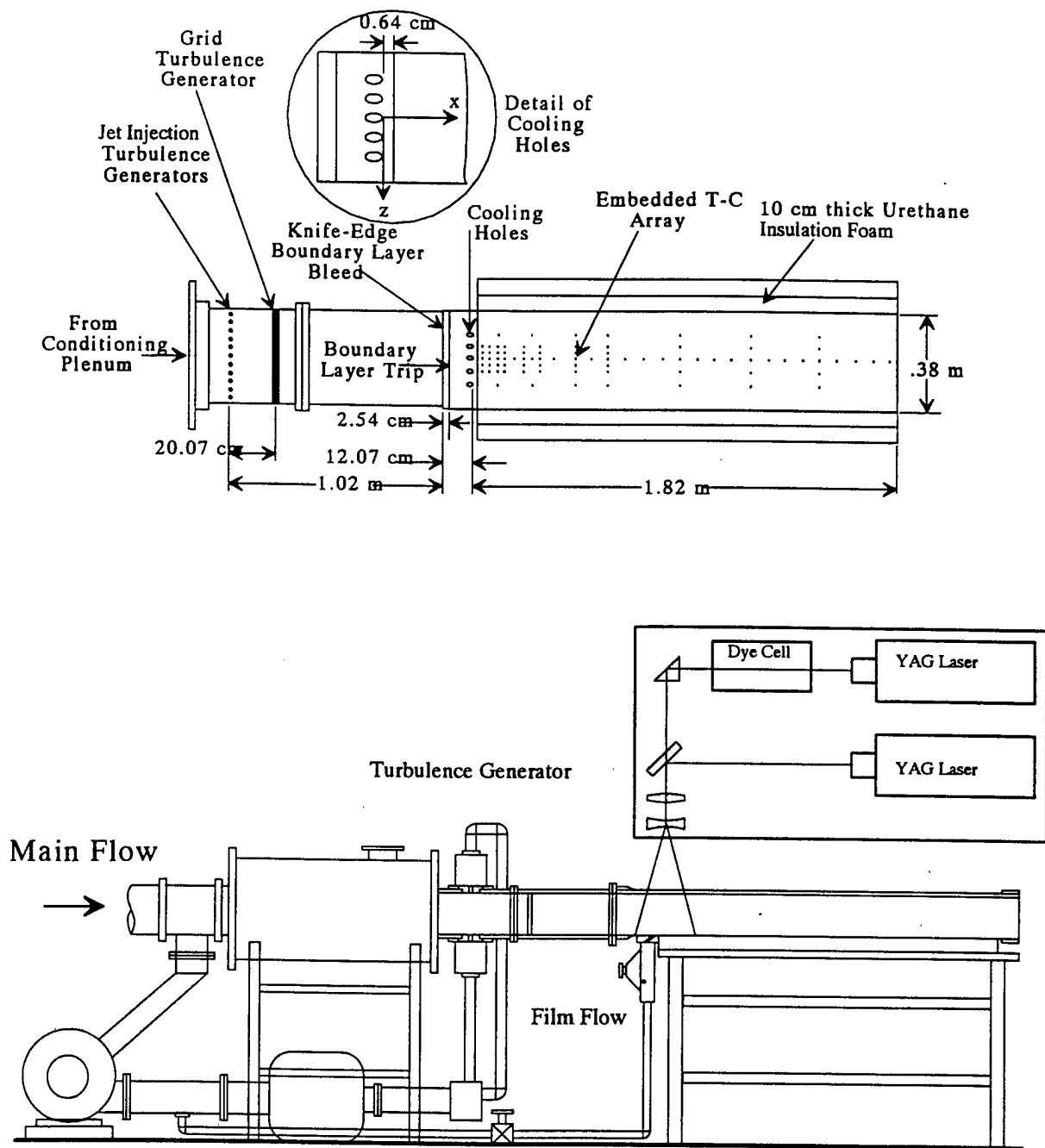


Figure 1. Top View of Facility and PIV Installation Schematic

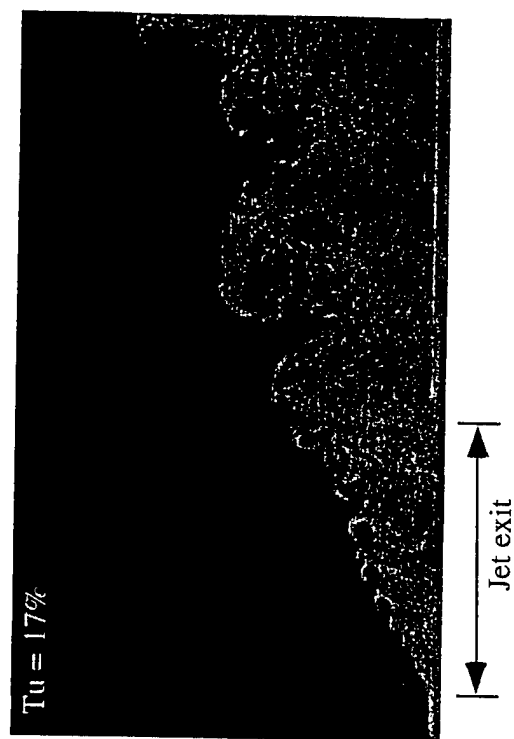
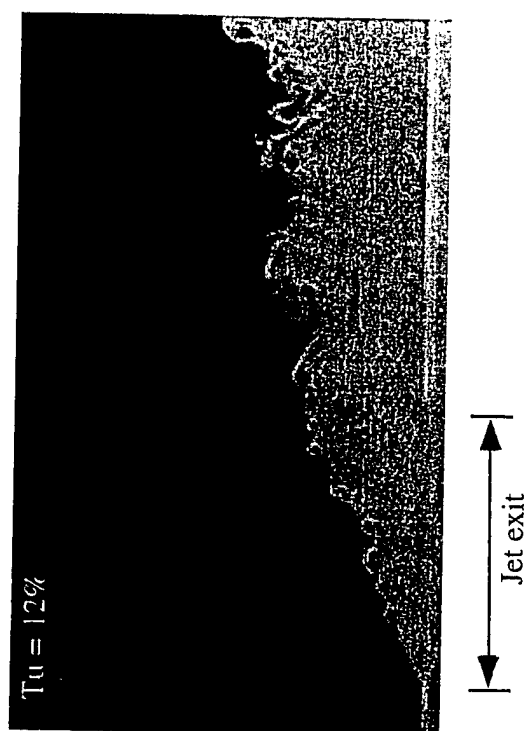
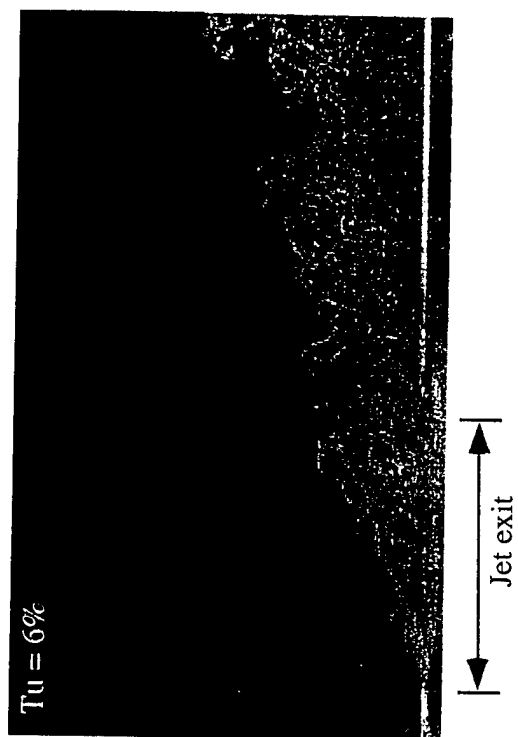
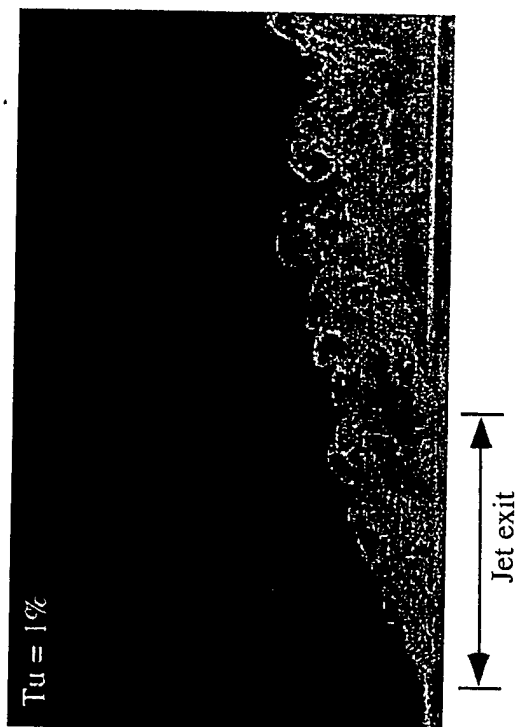


Figure 2. Double Pulsed PIV Images ( $M = 0.7$ ,  $Re = 20K$ )

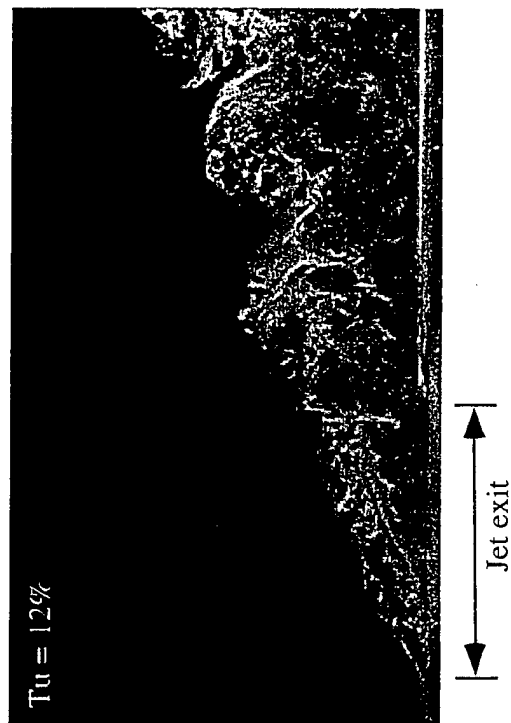
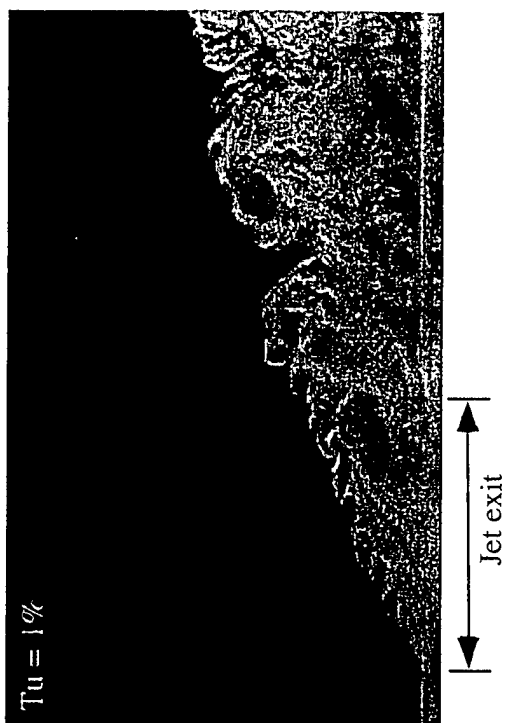
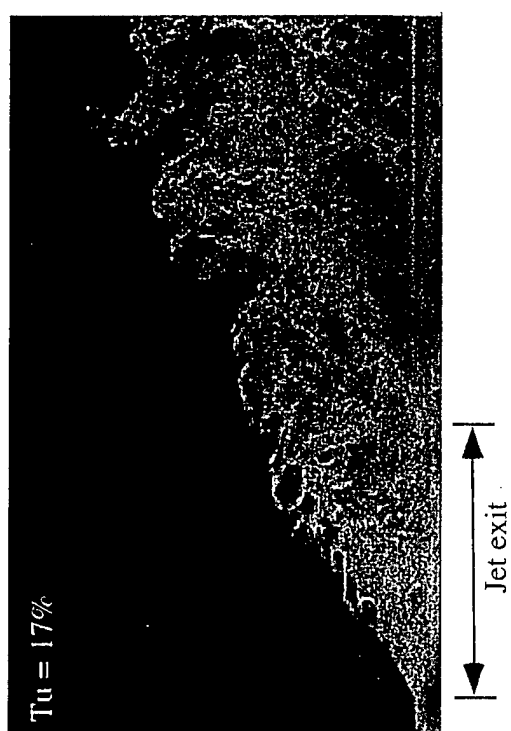
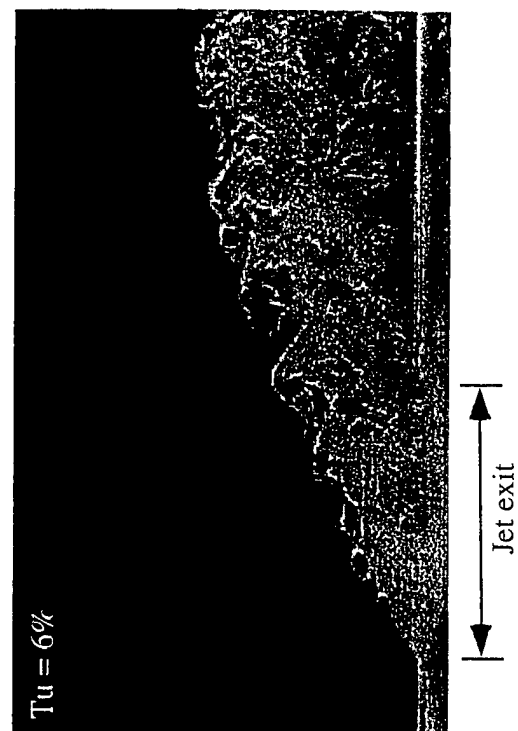


Figure 3. Double Pulsed PIV Images ( $M = 1.0$ ,  $Re = 20K$ )

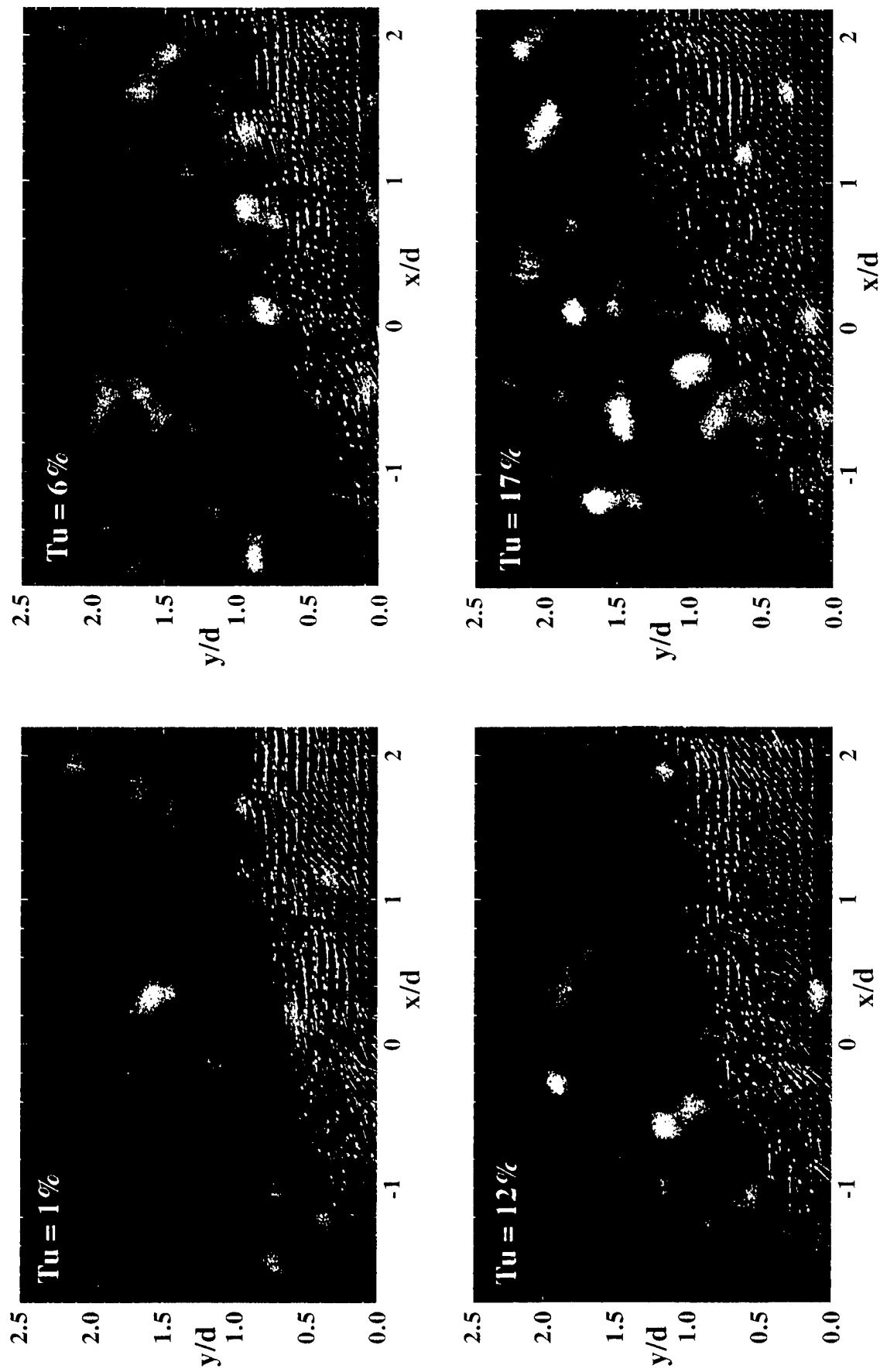


Figure 4. Instantaneous Velocity Distributions ( $M=0.7$ ,  $Re=20,000$ )

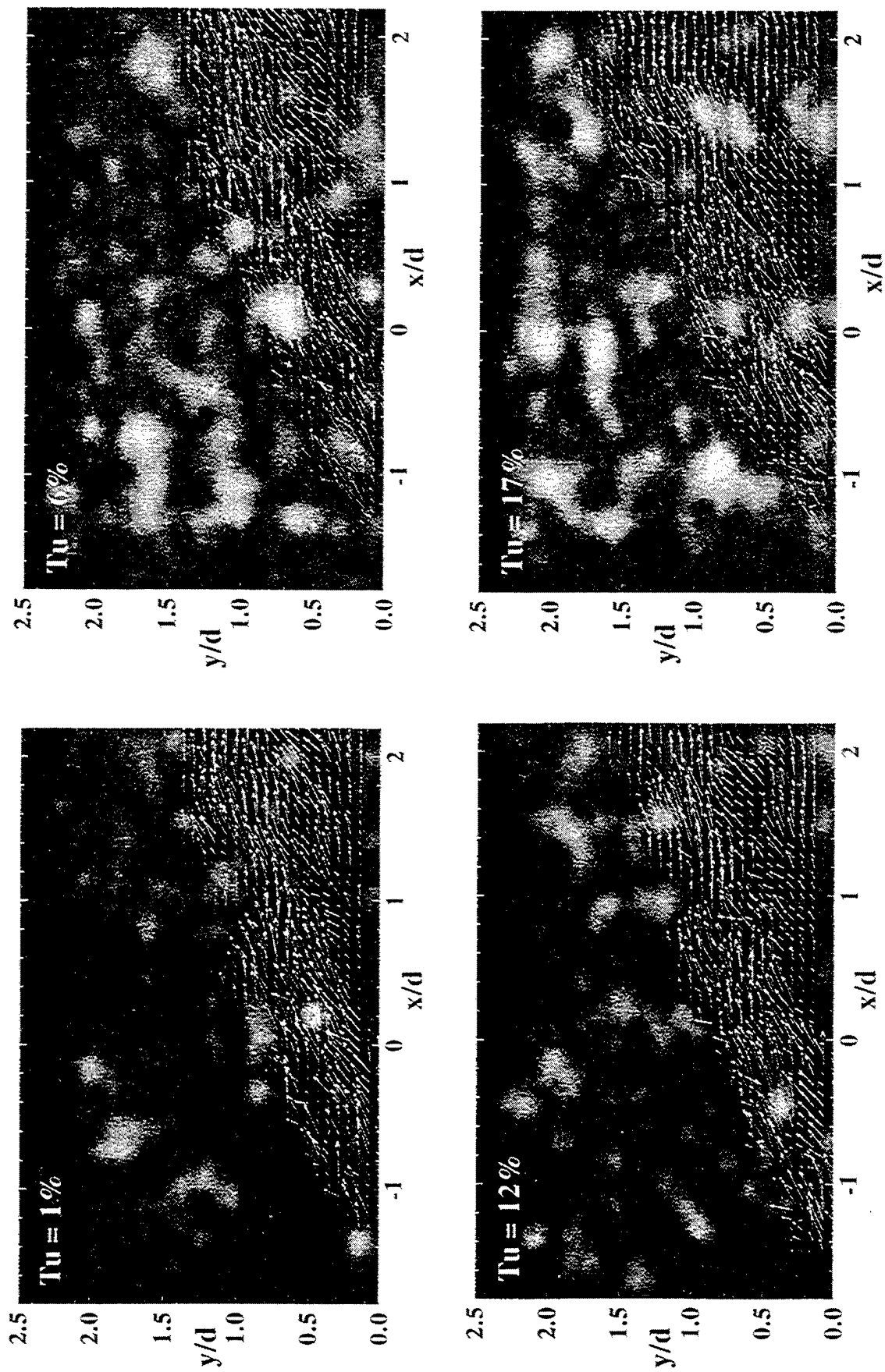


Figure 5. Instantaneous Velocity Distributions ( $M=1.0$ ,  $Re=20,000$ )

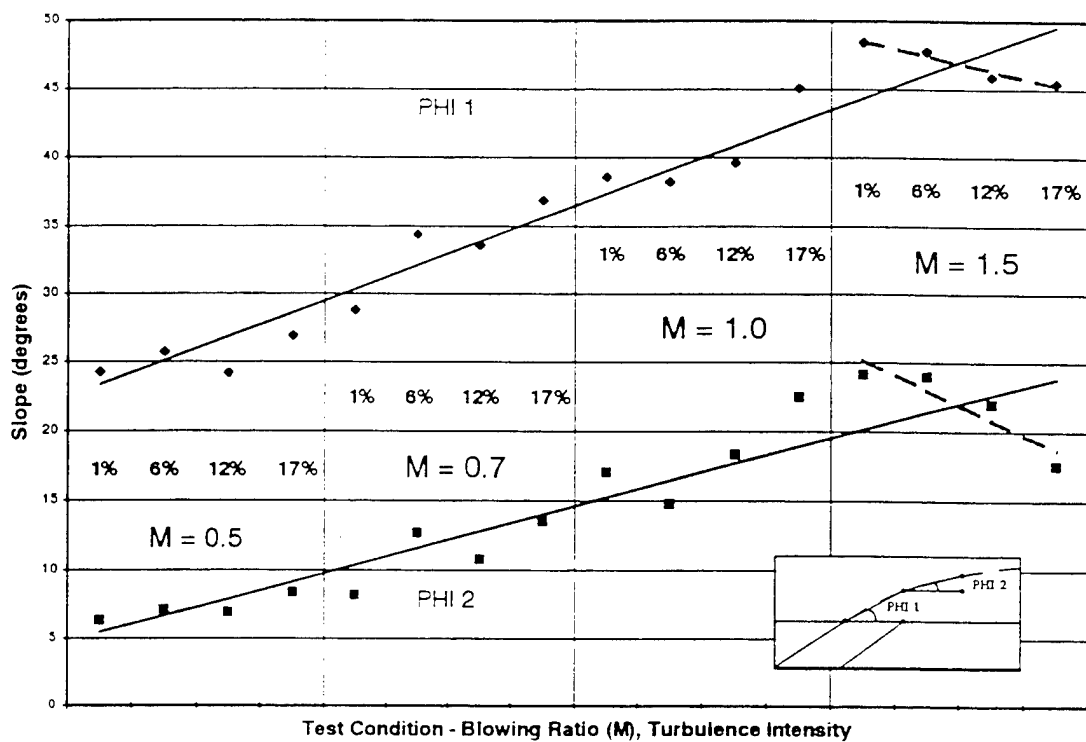


Figure 6. Angles of the Exiting Film Cooling Flow for the First 2.5 Diameters

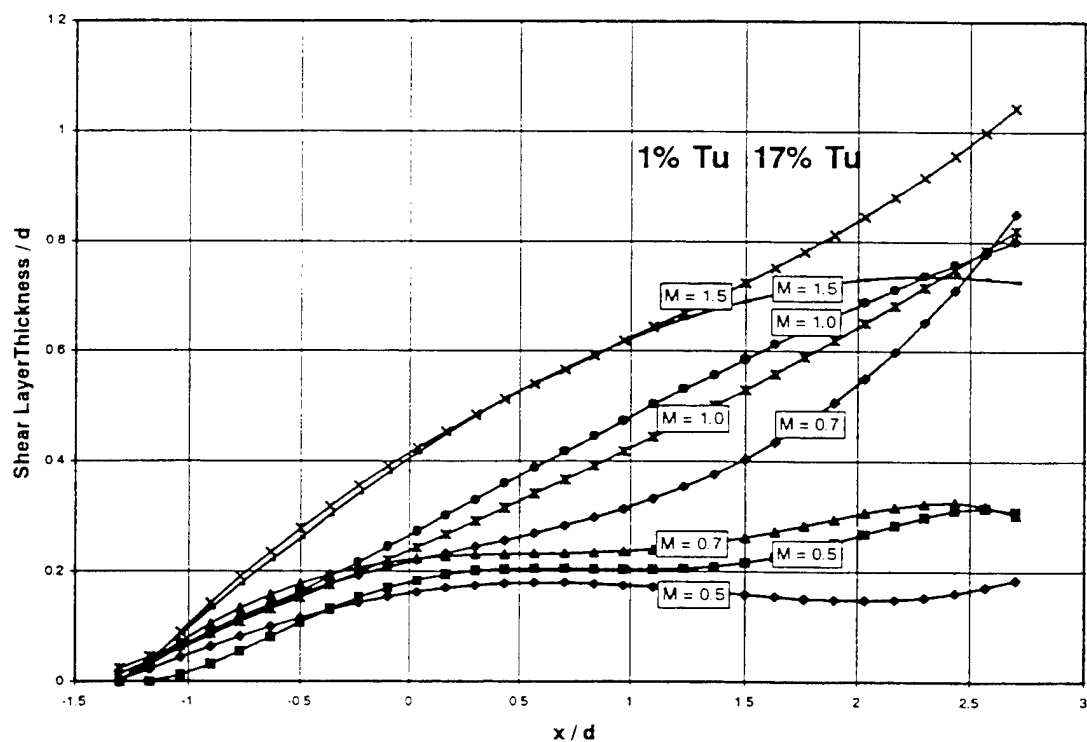


Figure 7. Growth of the Shear Layer Thickness Near the Film Cooling Jet Exit

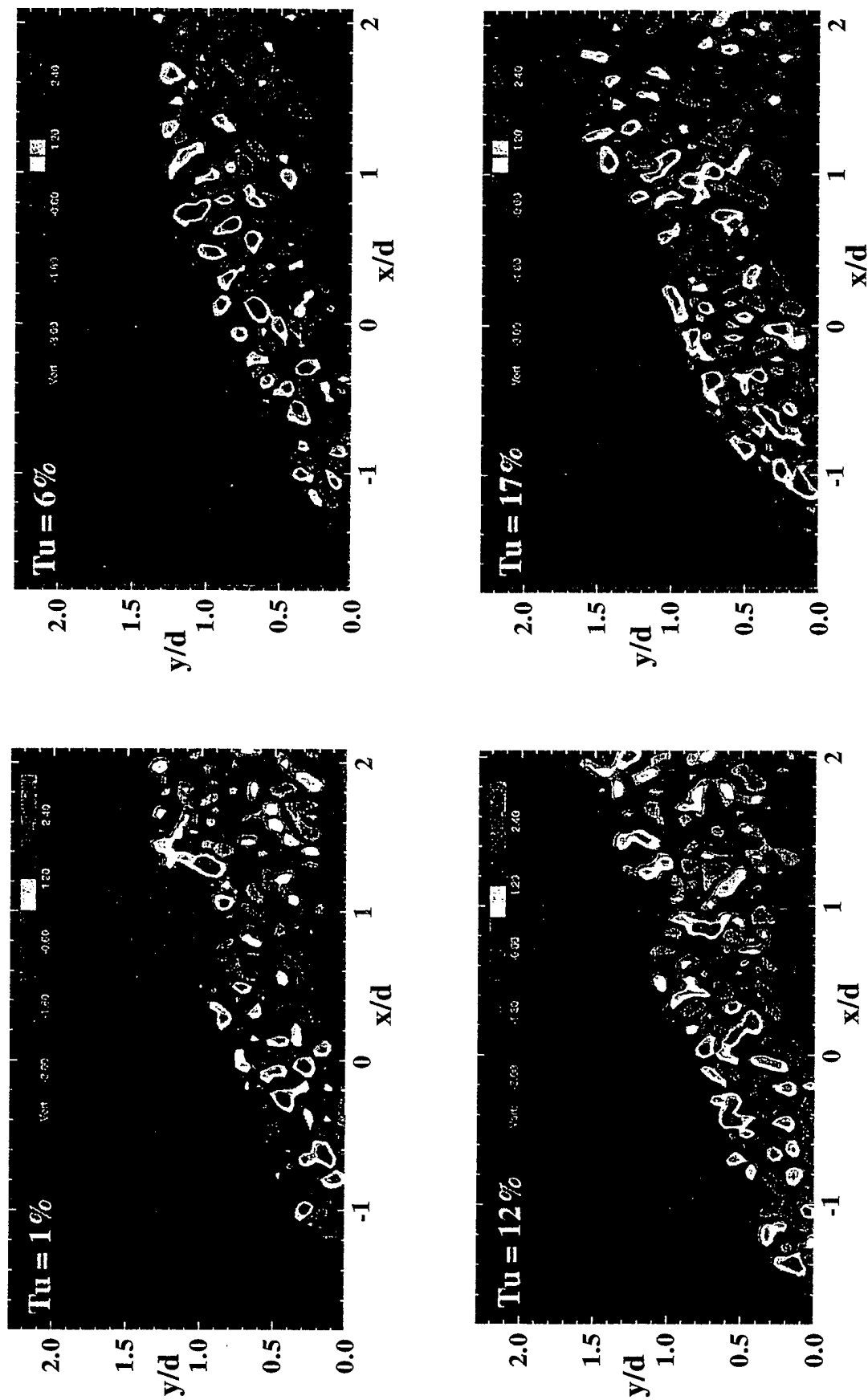


Figure 8. Instantaneous Vorticity Distributions ( $M=1.0$ ,  $Re=20,000$ )

## **APPENDIX O**

### **The Effect of Unsteadiness on Film Cooling Effectiveness**

**Jeffrey P. Bons, Richard B. Rivir, David J. Pestian,  
Charles D. MacArthur**





**AIAA 95-0306**

# **The Effect of Unsteadiness on Film Cooling Effectiveness**

Jeffrey P. Bons, Richard B. Rivir, and Charles D. MacArthur  
Aero Propulsion and Power Directorate  
US Air Force Wright Laboratory  
Wright Patterson AFB, Ohio

David J. Pestian  
Aerospace Mechanics Division  
University of Dayton Research Institute  
Dayton, Ohio

**33rd Aerospace Sciences  
Meeting and Exhibit  
January 9-12, 1995 / Reno, NV**

# THE EFFECT OF UNSTEADINESS ON FILM COOLING EFFECTIVENESS

Jeffrey P. Bons, Richard B. Rivir\*, and Charles D. MacArthur  
Aero Propulsion and Power Directorate  
US Air Force Wright Laboratory  
Wright-Patterson AFB, Ohio

David J. Pestian  
Aerospace Mechanics Division  
University of Dayton Research Institute  
Dayton, Ohio

## Abstract

A unique feature of turbine rotor blade film cooling is the main flow unsteadiness caused by the upstream stator vanes. The combined effect of the vane inviscid flow field and the trailing edge wake results in a rapidly changing external pressure at the film cooled blade surface. Because the film flow through the cooling holes is usually unchoked, the varying external pressure results in a modulation of the mass flow through the holes. This study examined the effect of coolant flow modulation on the film effectiveness and the heat transfer downstream of a row of film cooling holes. Coolant oscillation frequencies and amplitudes were selected to match typical modern gas turbine engine conditions when represented in the appropriate non-dimensional forms. Time average blowing rate (the ratio of coolant mass flux to free stream mass flux) was varied from 0.6 to 1.5. Measurements were made of the flow velocity and temperature fields, the adiabatic film effectiveness, and the film cooling heat transfer using a constant flux heat transfer surface. Both the axial (streamwise) and lateral (cross stream) distributions of these quantities were measured from a single row of five circular holes angled at 60 degrees with respect to the surface normal. Frequency spectra taken from measurements of the fluctuating velocity were used to find the extent of the influence of the driving frequency downstream. The observed effect of the coolant flow oscillation was to decrease effectiveness

in the streamwise direction, while having little or no influence on effectiveness in the cross stream direction. The rate of decrease of streamwise effectiveness is, however, a strong function of blowing rate, frequency, and amplitude of the fluctuations.

## Nomenclature

- d film cooling hole diameter (1.905 cm)
- f frequency (Hz)
- h convective heat transfer coefficient ( $W/m^2K$ )
- H shape factor ( $\delta^*/\theta$ )
- $L_{gx}$  x turbulence length scale (cm)
- M coolant blowing (mass flux) ratio:  $(\rho_c U_c / \rho_{fs} U_{fs})$
- Re Reynolds Number based on film cooling hole diameter
- T static temperature (K)
- $Tu_x$  x turbulence intensity ( $u'/U$ )
- U time mean local streamwise velocity (m/s)
- $u'$  fluctuating streamwise velocity component (m/s)
- x streamwise distance measured from the downstream lip of the injection hole (m)
- y vertical distance from the injection surface (m)
- z spanwise distance measured from the center of the injection hole (m)
- $\delta^*$  displacement thickness (cm)
- $\theta$  Boundary layer momentum thickness (cm)
- $\Omega$  reduced frequency (freestream velocity / coolant hole diameter/oscillation frequency)
- $\eta$  film cooling effectiveness:  $(T_w - T_{aw})/(T_c - T_{aw})$

---

\*Associate Fellow

## Subscripts

aw	adiabatic wall
c	coolant fluid
w	at the wall
nofc	no film cooling
fc	film cooling
fs	free stream
wfc	wall with film cooling

## Introduction

The character of the flow into the axial turbine rotor blade row of a gas turbine engine is largely determined by the upstream nozzle guide vanes. The close spacing of vanes and blades subject the blades to a periodic potential flow field as well as a significant wake velocity defect from the often blunt vane trailing edges. Therefore, as the rotor blades pass behind successive vanes, an oscillatory surface pressure field is produced. In addition, if the turbine is transonic, shock waves from the vane row will cause added pressure fluctuations at the blade surface.

Many modern turbine stages employ film cooling to permit near stoichiometric combustor operating temperatures. Film cooling air is injected through rows of small (0.5 mm diameter typical) holes in the blade surface. The coolant air is supplied from the compressor exit flow and is maintained at essentially constant pressure. As such, when the pressure on the "wetted" side of the blade oscillates (and if the flow in the film cooling hole is not choked) the coolant exit velocity fluctuates as well. These fluctuations are of significant magnitude and have been measured by Abhari (1991) in a blowdown turbine facility and by Rigby et al. (1990) in a turbine cascade with simulated guide vane wakes.

The objective of the present study is to provide a more detailed characterization of the unsteady coolant injection phenomenon. A film cooling research facility was modified to permit oscillation of the injected film cooling over a constant heat flux flat plate. The Reynolds number based on the coolant hole diameter of 1.9 cm is approximately 20,000, typical for a turbine. The facility has the added feature that it can be supplied with freestream turbulence levels ranging from less than 1% to over 17%. Freestream turbulence is another important feature of gas turbines which must be present to properly simulate the turbine aerodynamics and heat transfer. The film cooling jet is modulated with a speaker located in the side wall of the coolant supply plenum. The experimental facility has an oscillating

film cooling inlet pressure rather than the oscillating freestream pressure found in the actual turbine, but the result is identical. The velocity ratio (coolant velocity / freestream velocity) varies sinusoidal at a constant frequency and amplitude. To properly model the engine environment, the jet was modulated at reduced frequencies ( $\Omega$  = freestream velocity / coolant hole diameter / modulation frequency and amplitudes typical of modern turbine rotors. Typical reduced frequencies which are of interest are in the range of 20 to 200. This translates to 5 to 50 Hertz for this large scale experiment. Results for 5, 10 and 20 hertz will be reported.

The combined effect of these flow disturbances on the film cooling of the rotor blades is to force the mass flow rate through the blade surface cooling holes to be modulated at the vane passing frequency. Because the effectiveness of film cooling is governed by the rate at which the coolant jets mix with the hotter surrounding flow, the modulation of the jet exit flow is expected to influence the rate of mixing and therefore the performance of any specific film cooling design.

## Experimental Facility

The measurements of this study were made in an open loop film cooling wind tunnel described in detail by Bons, et al. 1994. Figure 1 shows an overall view of the facility and a top view of the cooling hole arrangement and the heat transfer surface. The tunnel is supplied with a nominal 1.5 kg/s air flow from a blower located exterior to the laboratory. This air supply includes provisions for both heating and cooling the flow between 288 and 325 K, depending on the required experimental set points and local atmospheric temperature. The film cooling flow can also be heated 10-20 °C above the free stream. The main flow passes through a conditioning plenum containing perforated plates, honeycomb, screens, and a circular-to-rectangular transition nozzle. Downstream of the transition nozzle, at the film cooling station location, free stream turbulence levels of 0.7 % (+/- 0.05) can be achieved with velocity and temperature profiles uniform to within 1% at the film cooling station. Table 1 lists the characteristics of the flow at the film cooling station.

Unsteady film cooling flow was provided by sinusoidal pulsing of the injected coolant. The driver for the coolant pulsation was a 25.4 cm diameter 150 W audio speaker contained in the wall of the coolant supply plenum. A Hewlett Packard 3312A Function

Generator produces the sinusoidal wave and is then amplified using an MP Electronics Model 2250MB Power Amplifier. A schematic cross section of the plenum illustrating the speaker orientation is shown in the insert in Figure 1.

Table 1. Flow Characteristics at  $x/d=0, z/d=1.5$

	No Turbulence Generation	Jet Generated Turbulence (Velocity Ratio = 14)
<u>Data at <math>y/d = 2.6</math></u>		
Tu (%)	0.7 to 0.96	17.3
Lgx (cm)		7.73
<u>Data at <math>y = \delta</math></u>		
U(m/s)	16.03	16.82
Re <sub>d</sub>	19085	20026
u' (m/s)	0.59	3.16
Tu (%)	3.68	18.79
Lgx (cm)		8.05
Lgx/d		4.23
$\delta$ (cm)	1.22	1.26
$\delta^*$ (cm)	0.123	0.123
$\theta$ (cm)	0.0927	0.0965
H	1.33	1.27
$\theta/d$	0.0487	0.051
Re <sub><math>\theta</math></sub>	929	1015

#### Instrumentation and Data Reduction

The data presented in this report were taken using a single 4 $\mu$ m diameter tungsten hot wire and an array of thermocouples. The hot wire and a flow temperature thermocouple (0.33 mm bead diameter) located 0.5 cm downstream (and at the same y and z) from the hot wire probe are both mounted on a vertical traverse. A magnetically encoded linear position indicator (Sony model #SR50-030A) affixed to the traverse was used to determine the probe position to within 2.5 $\mu$ m. National Instruments data acquisition and Labview software were used to acquire and process the hot wire and thermocouple voltages.

Hot wire voltages were obtained using a TSI Model #IFA-100 anemometer and a National Instruments NB-MIO-16XL-18 A-to-D board. Each mean velocity measurement is obtained from the average of 1000 points taken at 200 samples per second, from which the fluctuating component of velocity,  $u'$ , was also calculated. The velocity

computation algorithm corrects for local variations in pressure, temperature, and humidity.

Length scales were calculated by integrating to the first zero crossing of the autocorrelation coefficient function for the velocity obtained from the hot wire signal. Each length scale represents the average of 20 autocorrelations (each with 2048 velocity data points taken at 2000 samples per second).

The temperature measurements were made using a KAYE ice point reference junction which was multiplexed using an Hewlett Packard 3852 and measured with a Hewlett Packard 44701A integrating voltmeter with an integration period of 0.017 seconds for each sample. The referenced signal from the thermocouple used for flow temperature measurements was read using the NB-MIO-16XL-18 A-to-D board.

#### Film Cooling Effectiveness and Reduction in h Measurements

The heat transfer measurements are run in reverse from typical engine conditions with the wall heated. The wall is operated as a constant heat flux surface for heat transfer measurements and as an adiabatic wall for film cooling effectiveness measurements. The wall is the highest temperature in the system. The film cooling temperature is the next highest temperature and the free stream the lowest temperature. Nominally greater than a 10°C differential is established between each of these temperatures.

To calculate the film effectiveness, the facility was run without film cooling to determine the adiabatic wall temperature,  $T_{aw}$ , for each setting of freestream turbulence. These results were reported by Bons et al., 1994 for turbulence levels of 0.9, 5, 12 and 17%. The film cooling fluid temperature is determined by a thermocouple centered in the middle ( $z=0$ ) film cooling hole. A 1.27 cm diameter ASME orifice is used to determine the mean velocity of the film cooling flow,  $U_{fc}$ . This average velocity,  $U_{fc}$ , and the local freestream velocity,  $U_{fs}$ , were used in to determine the film cooling blowing ratio  $M$  as:

$$M = (\rho_c U_c / \rho_{fs} U_{fs}) \quad (1)$$

When measurements of heat transfer are made the thin stainless foil surface is resistively heated by passing a current through it. The power dissipated per unit area, the temperature distribution on the heated plate, and the free stream temperature are measured to allow calculation of the heat transfer

coefficient. When film cooling is added, this also adds a third temperature to the problem which must be accounted for. The percent reduction of the heat transfer coefficient with film cooling is calculated as:

$$\% \Delta h = (h_{nafc} - h_{fc}) * 100 / (h_{nafc} * (T_{fc} - T_{fs})) \quad (2)$$

#### Measurement of the Forcing Amplitude for the Film Cooling Flow

To measure the power of the pulsed signal introduced to the film cooling flow a Brüel & Kjær microphone was inserted into the side of the film cooling plenum perpendicular to the axis of the speaker. The output from the microphone's power supply is measured using the NB-MIO-16XL-18 board. The three signals connected to the A-to-D board are read sequentially (velocity, microphone, and the flow thermocouple). The signal from the microphone was monitored and maintained at 2 VAC throughout all tests involving pulsed film cooling. Using the microphone to measure the power of the modulated signal eliminates inconsistencies caused by inefficiencies of the speaker at different frequencies. The power spectrum results in this paper are the result from averaging 50 power spectra of 4096 samples evenly incremented over the 4760 data points taken at each measurement point.

#### Uncertainty Analysis

The experimental uncertainties are calculated based on knowledge of the instrumentation used and a simple root-mean-squared error analysis (Kline and McClintock, 1953). This method assumes contributions to uncertainties arise mainly from unbiased and random sources. For the film effectiveness calculation, the uncertainties in thermocouple measurements come from two sources: the error of the thermocouple device and random fluctuations in the actual local temperature being sensed while at a constant operating point. The latter of these two is greater ( $\pm 0.11$  °C) and yields an uncertainty in  $h$  of  $\pm 0.008$  at  $M=1$ , and  $\pm 0.016$  at  $M=0.5$ , (using a histogram of experimental results). The insulated test surface downstream of the film cooling injection point is considered to be essentially adiabatic. The ratio of the convective heat flux at the test surface to conduction along any path below the surface for typical flow conditions is of order 100. This indicates that the local temperature on the surface is dominated by the convection process and is an accurate indicator of film effectiveness and the heat transfer coefficient for the surface. Uncertainty in the velocity measurement stems primarily from the

calibration fit accuracy. The error is within  $\pm 1.0\%$  at flow rates of interest when compared to a co-located Kiel probe velocity measurement. Due to the 0.5 cm streamwise displacement of the hot wire and the flow thermocouple, in regions of steep temperature gradients (near  $x/d=0$ ), the temperature from the thermocouple which is used in the velocity computation algorithm is as much as 1.2 °C lower than the actual temperature at the hot wire probe. This results in a maximum additional error in  $U$  of 2% very near the injection hole (decreasing rapidly with  $x/d$ ), and was not corrected for.

### Results and Discussion

#### Heat Transfer Characteristics for Low (0.7%) and High Turbulence (17%), No Film Cooling

The Stanton number shows a 20 % increase in the heat transfer due to the increase to 17 % in turbulence intensity in Figure 2. This amplitude is representative of the level encountered due to the wake crossing by the rotor. The low turbulence, 0.7% case shows agreement with the widely accepted correlation of Kays and Crawford (1980) for zero pressure gradient, turbulent flat plate boundary layers to within 5% after a short starting length effect. This represents the baseline case to which the film cooling and forced film cooling measurements will be compared.

#### Centerline Adiabatic Film Cooling Effectiveness at Low Turbulence

At low turbulence conditions ( $Tu=0.7\%$ ) when the film flow is forced there is an orderly attenuation of the film cooling effectiveness as the frequency is increased from 5 to 20 Hertz as is shown in Figure 3a. The decrease represents a reduction of effectiveness of nominally 30% over the zero forcing case at a blowing ratio of 1.0. The centerline film cooling reduction in the cases for a blowing ratio less than 1.0 show a particularly large (4:1) reduction in the centerline effectiveness between the unforced and forced cases, Figure 3b. The blowing ratio of 1.0 showed a higher maximum (Figure 3c) and also a higher effectiveness far down stream than the forced cases for the blowing ratios less than 1.0 and 1.5. Although the  $M=1.5$  case is not shown, both velocity and temperature profiles indicate that there should not be much difference between the forced and unforced effectiveness curves for the 1.5 case as the forcing drops to about a 5% amplitude perturbation.

#### Velocity and Temperature Profiles for the Low Turbulence Cases

The axial velocity and the rms turbulence profiles are shown in Figure 4 at an  $x/d$  of 0. The forcing increases the velocity and the velocity gradient near the wall significantly for the blowing ratio of 0.6. The  $M=1.0$  case shows an increase in the apparently separated film jet away from the wall. The  $M=1.5$  case shows very little effect on the mean velocity profile with a very small attenuation near the maximum with forcing. The rms profiles all show an increase with an increase in frequency. The near wall rms velocity fluctuation for the 0.6 and 1.0 cases nearly doubles.

The temperature ratio profiles are shown in Figure 5. The  $M=0.6$  temperature profiles show a spread and a significant attenuation of 70% with forcing. As the blowing ratio is increased to 0.7 the attenuation is reduced to 65% (Figure 5a). At  $M=0.8$  the attenuation is further reduced to 60% (Figure 5b). All the resulting curves for the different forcing frequencies then collapse to a single profile as the blowing ratio is further increased. The  $M=1.0$  temperature ratio profiles (Figure 5c) maximum and their gradients at the wall show ordered decreases as the driving frequency changes from 0 to 20 to 10 Hertz. The  $M=1.0$  effectiveness profiles are ordered with the temperature and velocity gradients at the wall. Although not shown here, the  $M=1.5$  temperature profiles all collapsed to a single profile with and without forcing, within the accuracy of our measurements. No significant impact on the cooling effectiveness for the  $M=1.5$  is expected since the modulation of the film flow is reduced to 5%..

As seen from Figures 5, the modulation results in enhanced mixing with the freestream thus reducing the maximum coolant temperature even at the first measurement station ( $x/d = 0$ ). At the same time, the time averaged penetration of the coolant fluid into the freestream, Figure 4, increases with modulation. This effect has also been reported by Vermeulen et al. (1990) for a normal jet in cross flow. The magnitude of these two effects varies with blowing ratio and jet modulation frequency and amplitude. The net result is a lower film effectiveness, as determined from the array of wall thermocouples downstream of the coolant hole. Wall thermocouples located laterally across the coolant path show no increase in spanwise diffusion attributed to the jet modulation.

#### Heat Transfer Reduction with Film Cooling and Forcing, Low Turbulence ( $Tu=0.7\%$ )

The percent reduction in the heat transfer (Equation 2,  $\% \Delta h$ ) normalized by  $(T_{fe}-T_{fb})$  is shown in Figure 6 for three blowing ratios,  $M=0.7$ , 1.0, and

1.5. The  $M=0.7$  case shows a large reduction in heat transfer on the centerline of the film cooling hole and is the only case that also shows a reduction in  $\% \Delta h$  on the midline between the film cooling holes. As the blowing ratio is increased the reduction of the  $\% \Delta h$  on the centerline is likewise reduced for increased blowing ratios. Lift off of the coolant flow is indicated in the  $M=1.5$  curve by the initial negative values for the  $\% \Delta h$ . The mid line shows an augmentation of the heat transfer (- reduction of  $\% \Delta h$ ) for the  $M=1.0$  and 1.5 cases as the free stream is pumped down to the plate surface by the pair of counter rotating vortices of the film.

Figure 7 shows forcing for the blowing ratio of 0.7 and low turbulence. The reduction with forcing is quite large with over a 5:1 reduction for all blowing ratios. Just as with no forcing all midline  $\% \Delta h$ 's are positive with forcing. Figure 8 shows the reduction in  $\% \Delta h$  for forced flows with low turbulence at a blowing ratio of 1.0. There is little difference between forced and unforced flows for  $M=1.0$  or greater. The reduction in  $\% \Delta h$  effectively collapses to a single curve on the centerline with slightly less heating or augmentation after an  $x/d$  of 15.

#### Heat Transfer Reduction with Film Cooling, High Turbulence ( $Tu=17\%$ )

Figure 9 shows the heat transfer reduction with  $M=0.7$ , 1.0, and 1.5 for a free stream turbulence level of 17%. The  $M=0.7$  centerline shows a  $>50\%$  reduction at an  $x/d$  of 10 and a augmentation ( $-\% \Delta h$ ) of 100% of the unforced flow between the film cooling holes. The augmentation with the high turbulence level between the film holes, the midline, is reduced and lost at an increasing rate with  $x/d$  as the blowing ratio is increased above 1.0 when compared against the forced low turbulence case.

Temperature and velocity profiles are virtually unchanged with the exception of the rms profile which is displaced by the change in free stream turbulence and the increased scale of turbulence which is as indicated in Table 1 4.23\*d.

#### Power Spectra of Velocity Fluctuations

Profiles of the forced flow were taken on the centerline of the center film cooling hole at  $x/d = 1, 9$ , and 18 for forcing frequencies of 5, 10 and 20 Hertz. Figure 10 shows the results of profiles of the measured power at the driving frequency for a blowing ratio of  $M=0.75$ . At  $x/d = 1$ , there are two power peaks which appear to represent the shear layers or edges of the film cooling jet. The amplitude ordering of the 5 Hertz driver is reversed in these two

peaks, with the 5 Hertz signal the largest at the second peak. At an  $x/d = 9$  and 18 there are single peaks ordered in increasing amplitudes of 5, 20 and 10 Hertz. There appears to be a possible phase shift at  $x/d=9$  with the maximum of the 5 Hertz driver leading the 10 and 20 Hertz drivers, (occurring closer to the wall). The maximum of the 5 Hertz driver at the  $x/d=18$  location clearly lags the maximum of the 10 and 20 Hertz drivers, occurring at nearly twice the  $y$  location of the 10 and 20 Hertz drivers.

### Concluding Remarks

The forcing of the film cooling flow by a periodic driver resulted in reductions in the film cooling effectiveness (70% at  $M=0.6$ ) which were observed to be nearly equivalent to those observed with continuous random free stream fluctuations of similar amplitude. These reductions in film effectiveness became progressively smaller as the blowing ratio increased, 65% at  $M=0.7$ , 60% at  $M=0.8$ . Since the drivers for the forcing film flows were maintained at a constant amplitude, the relative amplitude of the forcing flow decreased proportionately as the blowing ratio increased until at  $M=1.5$  the forcing amplitude was nominally down to 5% of the film flow velocity.

The temperature profiles for forced film cooling flows and their near wall gradients mimic the reduction in film cooling effectiveness for blowing ratios less than 1.0. At  $M=1.5$  the nondimensional temperature profiles have collapsed to a single profile with and without forcing.

The  $\% \Delta h$  heat transfer reduction with film cooling and forcing for low turbulence was observed to be similar to the film cooling effectiveness results. Only the blowing ratio of 0.7 showed a reduction both on the centerline as well as between the film cooling holes.

The forcing power profiles through the boundary and film cooling layers indicated a pair of strong peaks near the film hole. The 5 Hertz drivers amplitude relative to the amplitude of the 10 and 20 Hertz drivers was reversed for the twin peaks. The 5 Hertz driver also showed a greater attenuation with downstream distance from the film hole and an earlier maximum closer to the film hole than did the 10 and 20 Hertz forcing flows.

The forced flows show a detrimental effect on film cooling flows comparable to that observed in non periodic high turbulence experiments at comparable amplitudes. Though the unsteadiness has an undesirable effect on film cooling, the results of

increased mixing and penetration could make modulation a beneficial technology for dilution jets in combustors and combustor liners.

### Acknowledgments

This work was performed under partial sponsorship of the Air Force Office of Scientific Research project 2307/BW. Dr. James McMichael was the program manager.

### References

- Abhari, R.S., 1991, "An Experimental Study for the Unsteady Heat Transfer Process in a Film Cooled Fully Scaled Transonic Turbine Stage," Ph.D. Thesis, Department of Aeronautics and Astronautics, Massachusetts Institute of Technology, Cambridge, MA.
- Abhari, R.S. and Epstein, A.H., 1992, "An Experimental Study of Film Cooling In A Rotating Transonic Turbine," ASME Paper 92-GT-201, The 37th ASME International Gas Turbine & Aeroengine Congress, Cologne, Germany.
- Bons, J.P., MacArthur, C.D., and Rivir, R.B., 1994, "The Effect of High Freestream Turbulence on Film Cooling Effectiveness," ASME Paper 94-GT-51, to be published in the ASME *Journal of Turbomachinery*.
- Kays, W.M. and Crawford, M.E., 1980, *Convective Heat and Mass Transfer*, 2nd Ed., McGraw-Hill, p. 193.
- Kline, S.J. and McClintock, F. S., 1953, "Describing Uncertainties in Single-Sample Experiments," *Mechanical Engineering*, pp. 3-8.
- Rigby, M.J., Johnson, A.B., and Oldfield, M.L.B., 1990, "Gas Turbine Rotor Blade Film Cooling with and without Simulated NGV Shock Waves and Wakes", ASME Paper 90-GT-78.
- Vermeulen, P.J., Chin, C.F., and Yu, K.W., 1990, "Mixing of an Acoustically Pulsed Air Jet with a Confined Crossflow," *AIAA Journal of Propulsion and Power*, Vol. 6, No. 6, pp. 777-783.

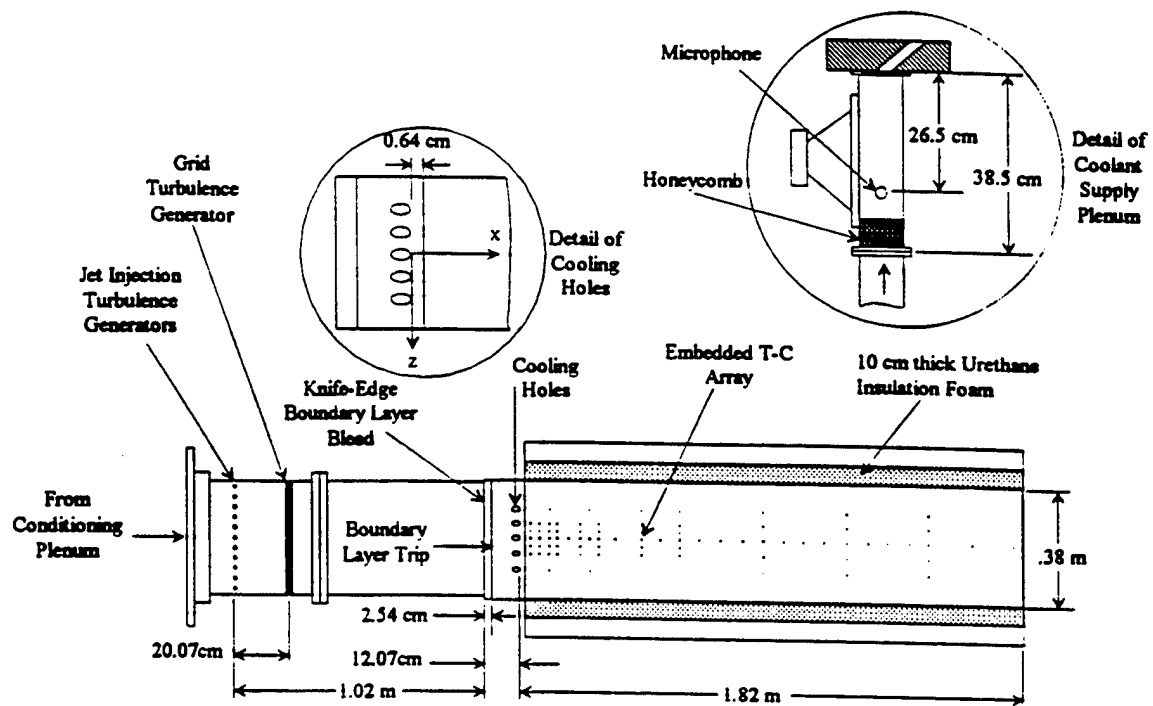


Figure 1. Top View of Experimental Film Cooling Facility

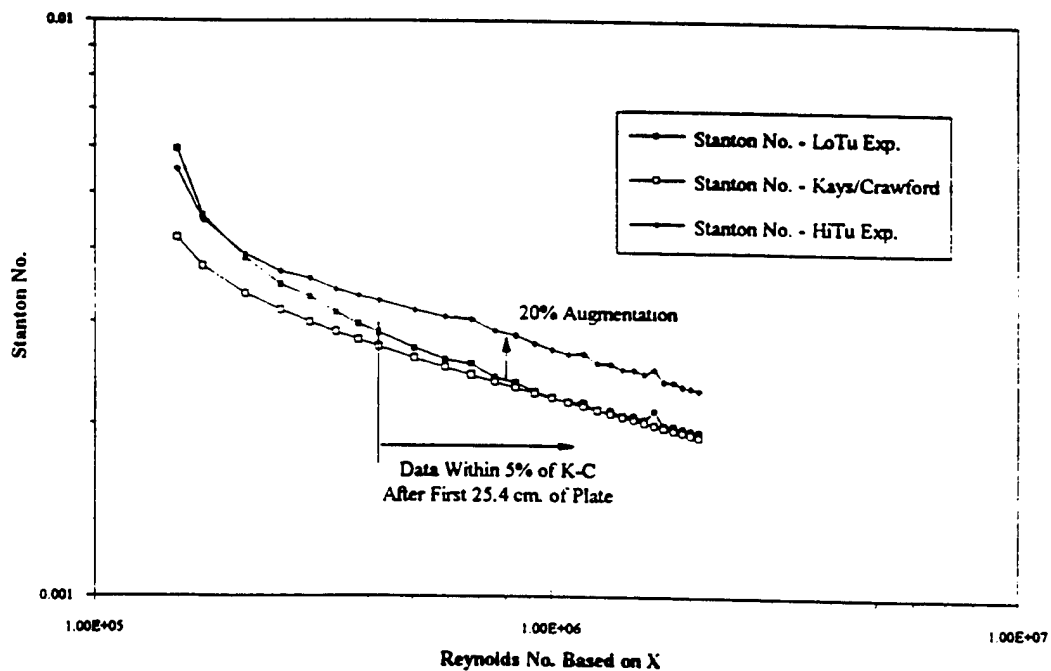


Figure 2. Stanton vs. Reynolds for: 0.7% Tu and 17% Tu at 17 m/s  $U_{fs}$



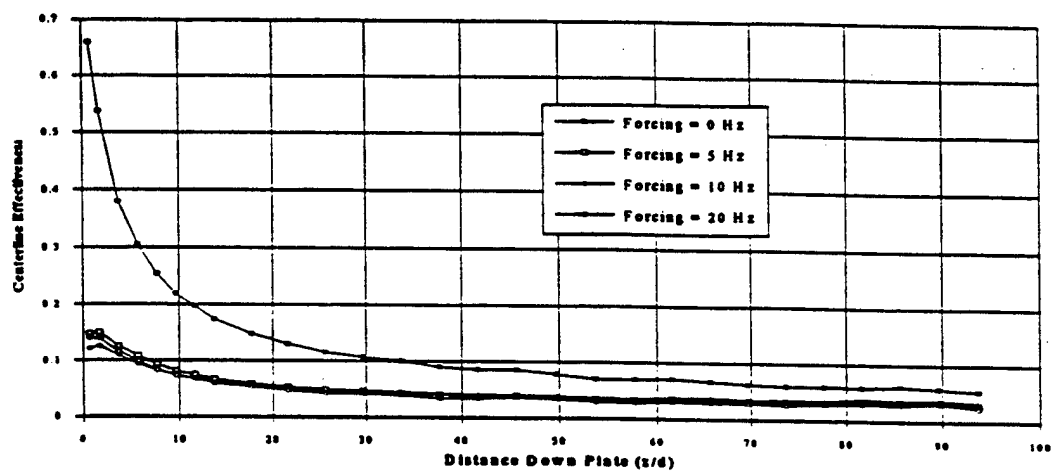


Figure 3a. Centerline Effectiveness at  $M = 0.6$

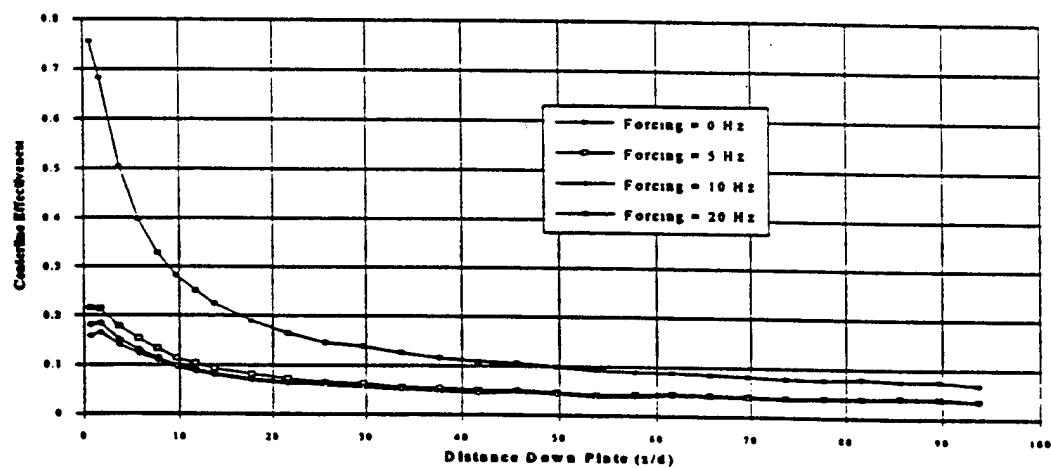


Figure 3b. Centerline Effectiveness at  $M = 0.8$

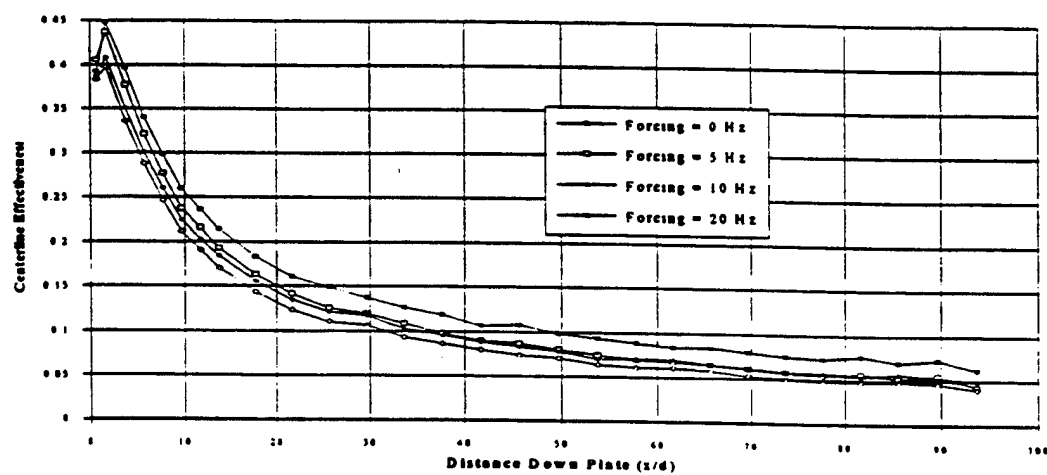


Figure 3c. Centerline Effectiveness at  $M = 1.0$

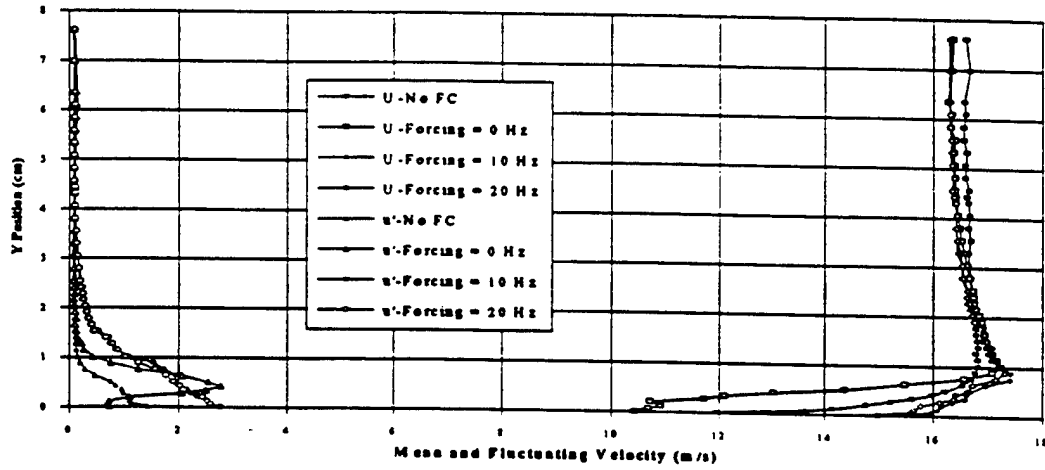


Figure 4a. Mean and Fluctuating Velocity Profiles at  $x/d = 0$ ,  $Tu = 0.7\%$ , and  $M = 0.7$

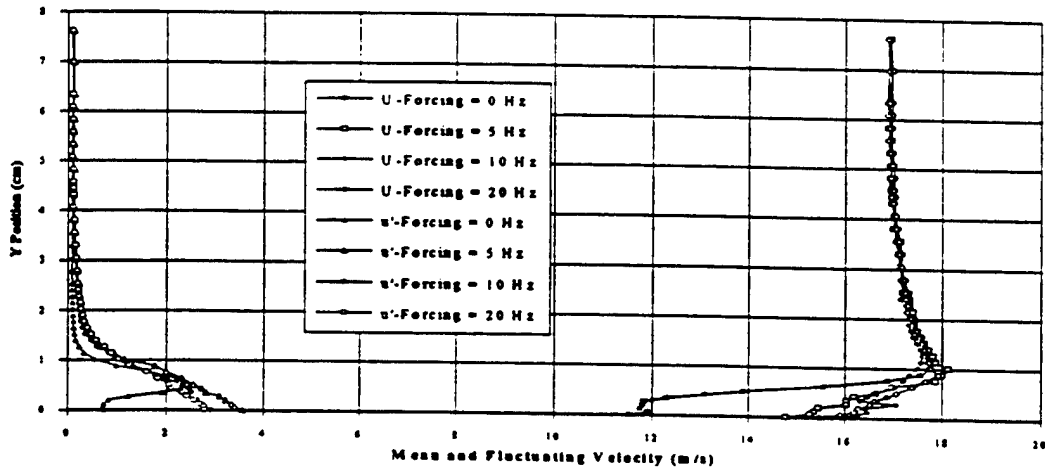


Figure 4b. Mean and Fluctuating Velocity Profiles at  $x/d = 0$ ,  $Tu = 0.7\%$ , and  $M = 0.8$

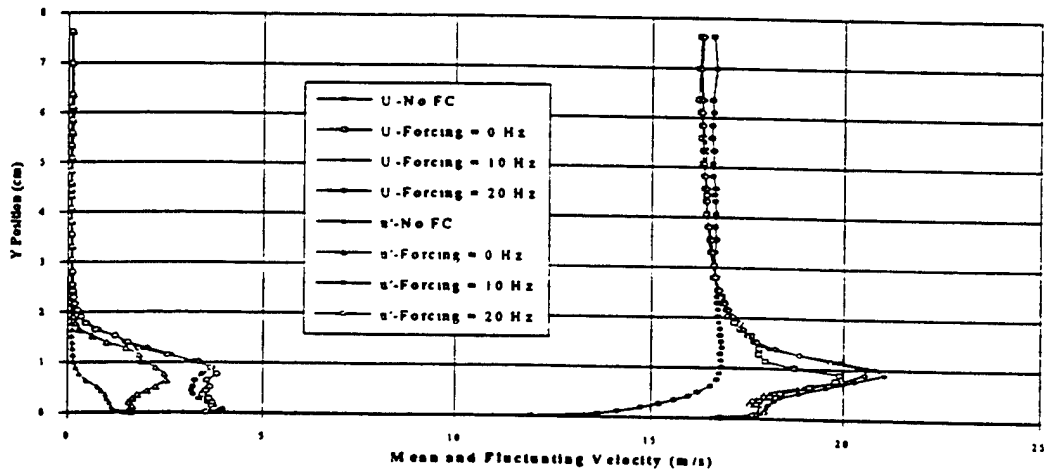


Figure 4c. Mean and Fluctuating Velocity Profiles at  $x/d = 0$ ,  $Tu = 0.7\%$ , and  $M = 1.0$

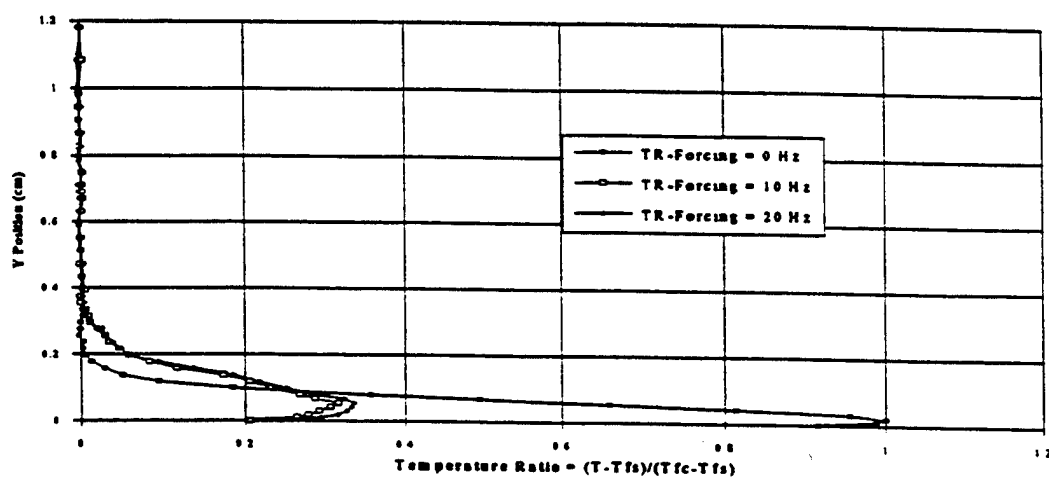


Figure 5a. Temperature Ratio Profiles at  $x/d = 0$ ,  $Tu = 0.7\%$ , and  $M = 0.7$

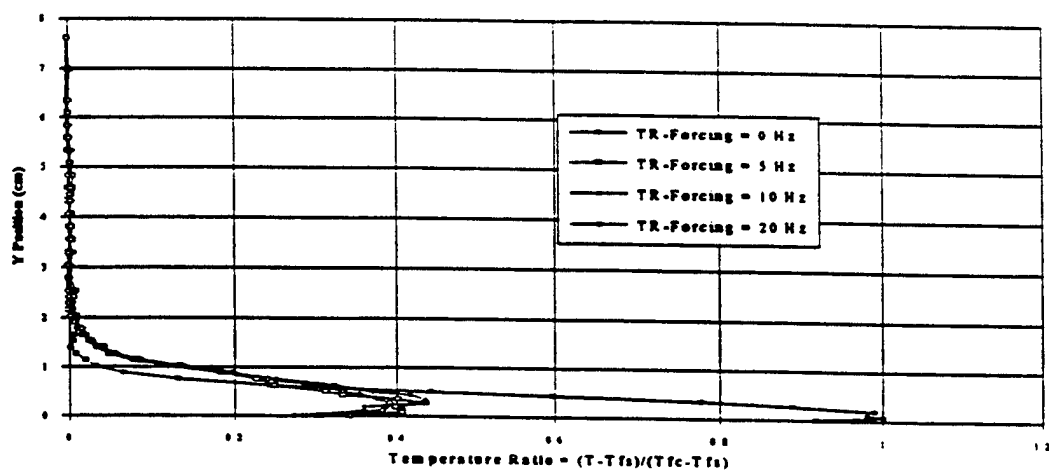


Figure 5b. Temperature Ratio Profiles at  $x/d = 0$ ,  $Tu = 0.7\%$ , and  $M = 0.8$

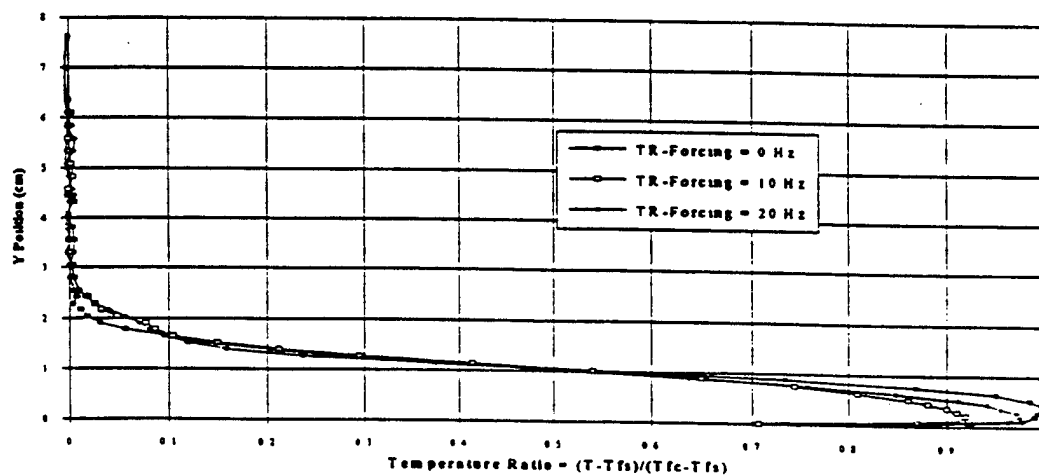


Figure 5c. Temperature Ratio Profiles at  $x/d = 0$ ,  $Tu = 0.7\%$ , and  $M = 1.0$

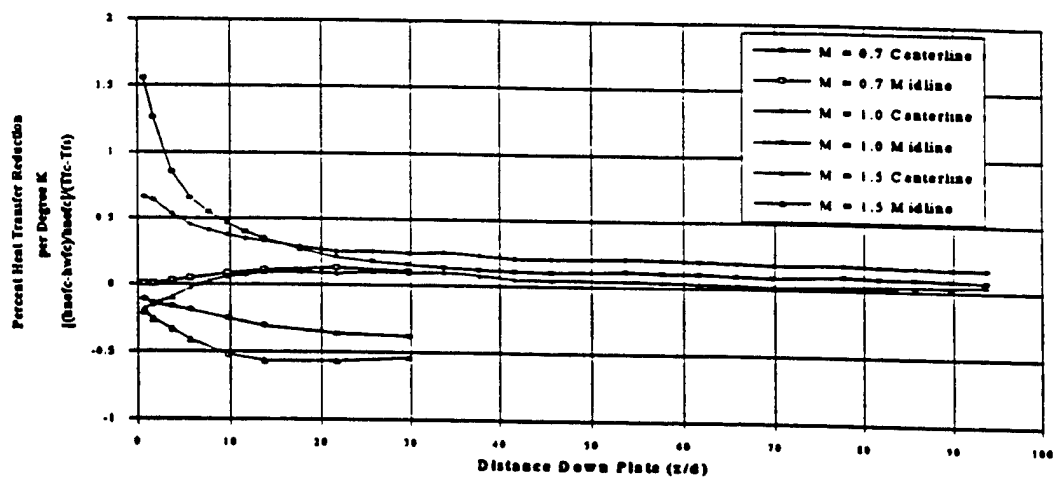


Figure 6. Percent Heat Transfer Reduction with FST = 0.7%, Q = 2250 Watts and 3 Cooling Holes

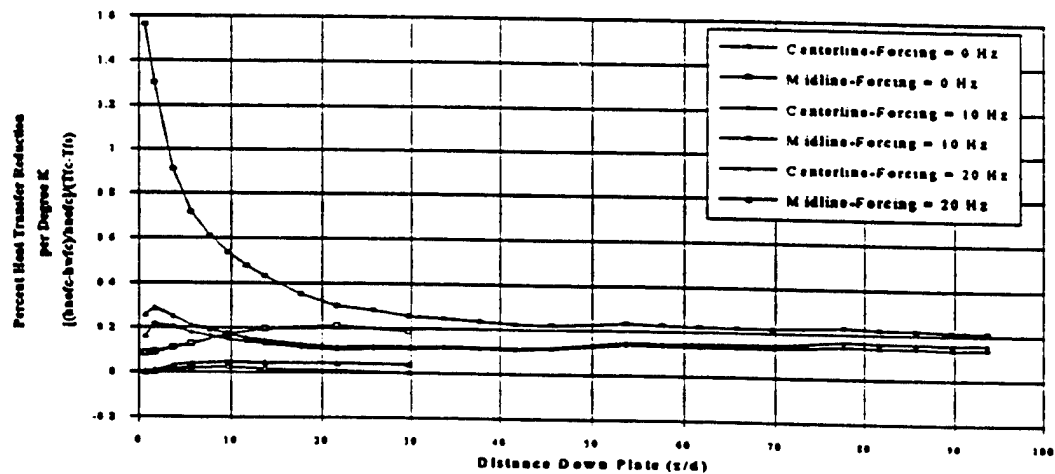


Figure 7. Percent Heat Transfer Reduction with M = 0.7, FST = 0.7%, Q = 2330 Watts and 3 Cooling Holes

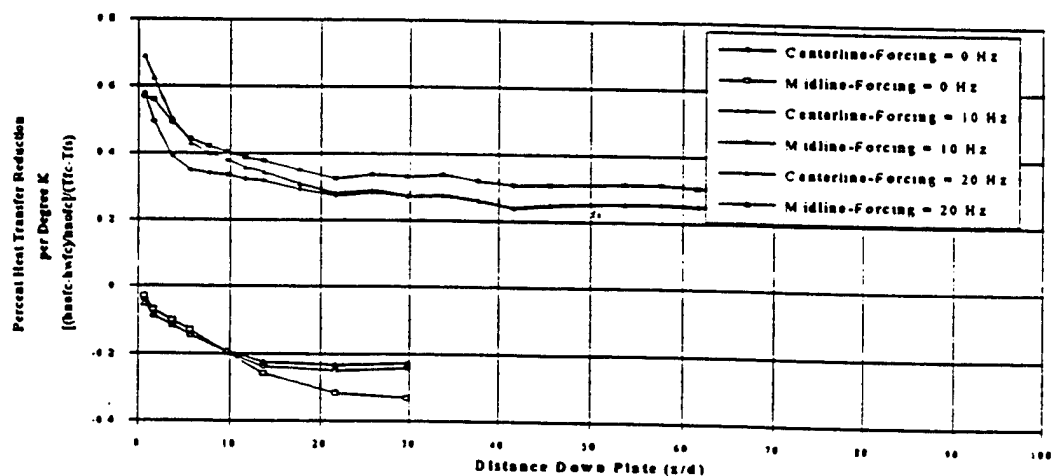


Figure 8. Percent Heat Transfer Reduction with M = 1.0, FST = 0.7%, Q = 2330 Watts and 3 Cooling Holes

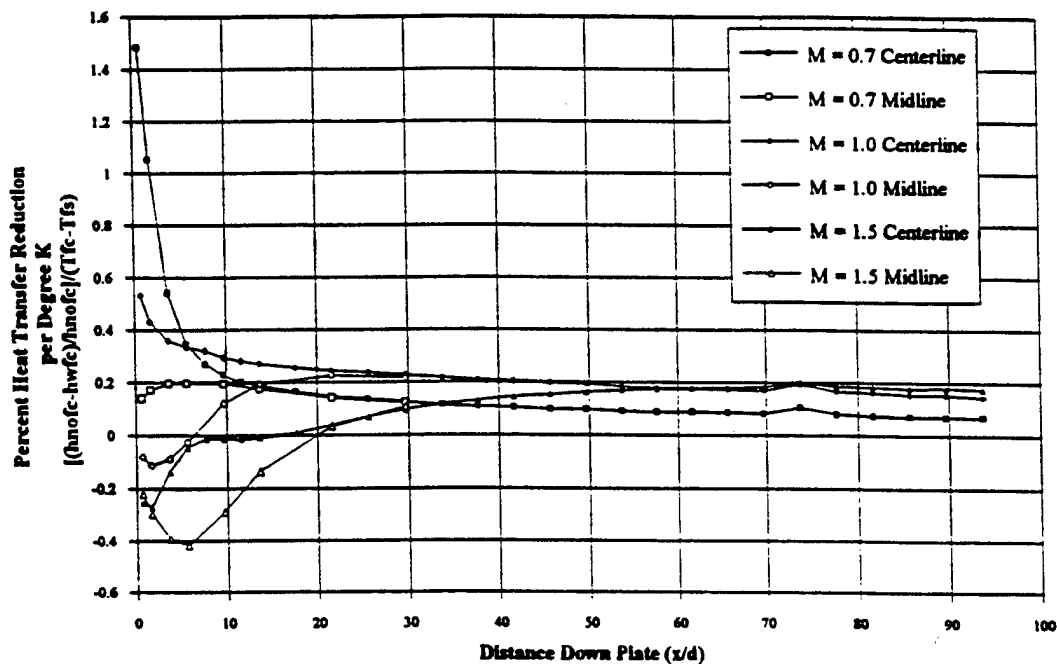


Figure 9. Percent Heat Transfer Reduction with FST = 17%, Q = 2327 Watts and 3 Cooling Holes

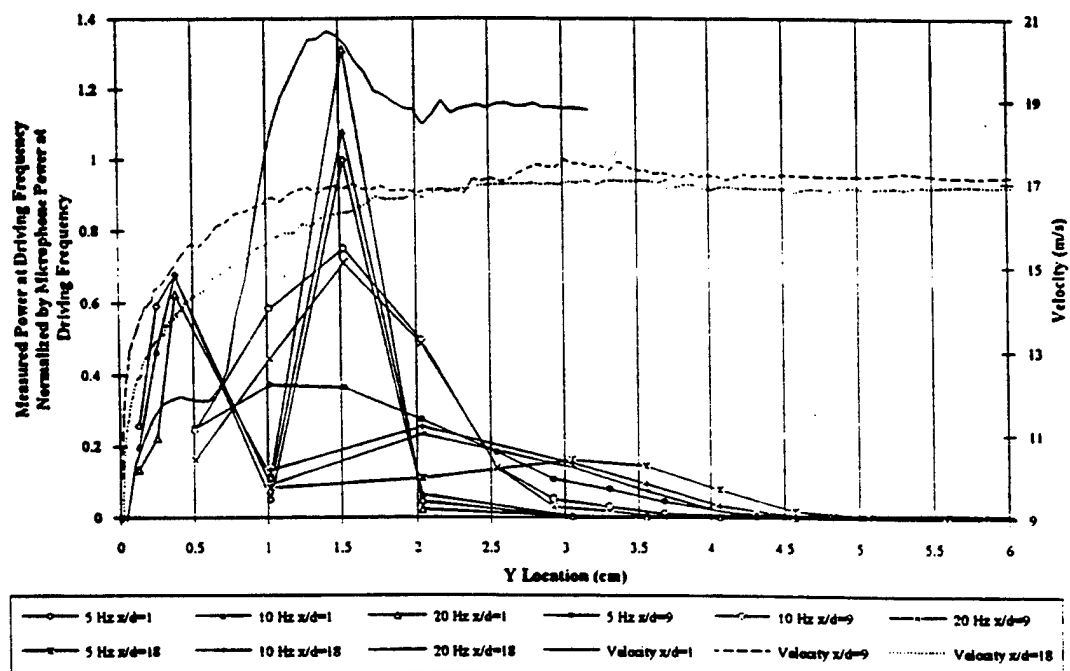


Figure 10. Microphone Power at Driving Frequency and Velocity vs. Y Location, M = 0.8

## **APPENDIX P**

### **Awards, Publications, and Presentations**

**AWARDS, PUBLICATIONS, AND PRESENTATIONS**  
**CONTRACT NO. F33615-92-C-2207**  
**(June 1992 to December 1997)**

**Honors and Awards**

1. R. E. Kauffman and J. D. Wolf (1992): R & D Top 100 Award for the Development of RULER Family of Instruments, Museum of Science & Industry, Chicago, IL.
2. F. Takahashi (1992): AIAA Best Paper Award (Combustion Section) AIAA Mini-Symposium, Dayton OH.
3. F. Takahashi (1992): Session Chairman, Central States Section, The Combustion Institute, Columbus, OH.
4. D. R. Ballal, S. P. Heneghan, J. C. Pan, and M. D. Vangsness (1992): ASME International Gas Turbine Institute (IGTI) Best Combustion and Fuels Research Paper Award.
5. D. R. Ballal (1992): Fellowship of ASME
6. R. E. Kauffman (1993): Wohlleben-Hochwalt Outstanding Professional Research Award, University of Dayton, Dayton, OH.
7. D. R. Ballal (1993): Fellowship of AIAA.
8. D. R. Ballal (1993): AIAA National Energy Systems Award.
9. J. Zelina (1993): AIAA Gordon C. Oates Graduate Fellowship Award.
10. M. D. Durbin (1993): AIAA Best Paper Award (Combustion Section) AIAA Mini-Symposium, Dayton OH.
11. F. Takahashi (1993): Session Chairman, Eastern States Section, The Combustion Institute, Princeton, NJ.
12. J. Zelina (1994): AIAA Best Paper Award (Combustion Section) AIAA Mini-Symposium, Dayton OH.
13. M. D. Durbin (1994): ASME Travel Fellowship Award.
14. W. A. Rubey (1994): Plenary Lecture Award, 16th International Symposium on Capillary Chromatography, Riva del Garda, Italy.
15. J. Zelina and D. R. Ballal (1994): AIAA Best Paper Award, AIAA Intersociety Energy Conversion Engineering Conference, Monterey, CA.

16. F. Takahashi (1994): "Laser Sheet Visualization of a Flame," Front Cover, Aerospace America, August.
17. R. E. Kauffman (1994): PERFECT-Added to Military Fuel Specification MIL-T-5624R.
18. USAF Improved Jet Fuel (1994): Aviation Week & Space Technology, December 12-19.
19. UDRI Fuels Team (1994): USAF Letter of Commendation, December. 20.
20. F. Takahashi and S. P. Heneghan (1995): Wohlleben-Hochwalt Outstanding Professional Research Award, April.
21. J. Zelina (1995): AIAA Best Paper Award (Combustion Section) AIAA Mini-Symposium, Dayton OH., June.
22. S. P. Heneghan (1995): Session Chairman, ASME Turbo Expo. '95, Houston, TX, June.
23. D. R. Ballal (1995): Chairman, Combustion and Fuels National Committee, ASME-International Gas Turbine Institute, July.
24. F. Takahashi (1995): Invited Foreign Researcher, National Institute for Resources and Environment, MITI, Japan, August.
25. D. Pestian (1995): Best Poster Paper, Gallery of Fluid Motion, American Physical Society Meeting, Irvine, CA, October.
26. F. Takahashi (1996): Session Chairman, Central States Section, The Combustion Institute, St. Louis, MO, May.
27. D. R. Ballal (1996): Program Chairman, ASME Turbo Asia '96 Congress, Jakarta, Indonesia, November.
28. J. Blust (1996): AIAA Best Paper Award (Combustion Section) AIAA Mini-Symposium, Dayton OH., October.
29. D. R. Ballal (1996): Faculty Award for Scholarship, School of Engineering, University of Dayton, Dayton, OH, August.
30. D. R. Ballal (1996): ASME Leadership Award, Presented by ASME President, Jakarta, Indonesia, November.
31. D. R. Ballal (1996): Invited Participant, Workshop on "Aviation Fuels & Fire Safety," National Research Council, Washington, D.C., November.
32. F. Takahashi (1997): Session Chairman, Central States Section, The Combustion Institute, Point Clear, AL, April.



33. D. R. Ballal (1997): Alumni Award In Scholarship, University of Dayton, Dayton, OH, April.
34. F. Takahashi (1997): Session Chairman, Second International Symposium on Scale Modeling, Lexington, KY, June.
35. F. Takahashi (1997): Session Chairman, 33<sup>rd</sup> AIAA/ASME/SAE/ASEE Joint Propulsion Conference, Seattle, WA, July.
36. S. P. Heneghan (1997): Invited Speaker, Ohio Valley Chromatography Symposium, Hueston Woods, June.
37. R. C. Striebich (1997): Invited Speaker, Ohio Valley Chromatography Symposium, Hueston Woods, June.

### **Patents**

1. R. E. Kauffman, "Voltammetric Method for Measuring Peroxide Concentration," U. S. Patent No. 5,480,808, January 1996.
2. R. E. Kauffman, "Freshness and Stability Test for Predicting Oxidation Degradation," U.S. Patent No. 5,239,258, August 1993.
3. W. A. Rubey and R. C. Striebich, "Method for Admitting and Receiving Samples in a Gas Chromatographic Column," U. S. Patent Applied For No. 08/851,888, May 1997.

## Journal Publications

1. F. Takahashi and M. D. Vangsness, "Near-Field CARS Measurements and the Local Extinction of Turbulent Jet Diffusion Flames," *Dynamics of Heterogeneous Combustion and Reacting Systems*, AIAA Progress in Astronautics and Aeronautics Series, Vol. 152, pp. 37-55, 1993.
2. S. P. Heneghan, D. L. Geiger, S. D. Anderson, and W. D. Schultz, "Static Tests of Jet Fuel Thermal and Oxidative Stability," *AIAA Journal of Propulsion and Power*, **9**, 5 (1993).
3. S. Zabarnick, "Chemical Kinetic Modeling of Jet Fuel Autoxidation and Antioxidant Chemistry," *Industrial and Engineering Chemistry Research*, Vol. 32, pp. 1012-1017, 1993.
4. S. P. Heneghan, T. F. Williams, C. R. Martel and D. R. Ballal, "Studies of Jet Fuel Thermal Stability in Flowing Systems," *Transactions of ASME, Journal of Engineering for Gas Turbines and Power*, Vol. 115, pp. 480-486, (1993).
5. T. Edwards and S. Zabarnick, "Supercritical Fuel Deposition Mechanisms," *Industrial & Engineering Chemistry Research* **32**, 3117 (1993).
6. S. P. Heneghan, C. R. Martel, T. F. Williams, and D. R. Ballal, "Effects of Oxygen and Fuel Additives on The Thermal Stability of Jet Fuels," *Transactions of ASME, Journal of Gas Turbine and Power*, Vol. 117, pp. 120-124, 1995.
7. D. R. Ballal, M. D. Vangsness, S. P. Heneghan, and G. J. Sturgess, "Studies of Lean Blowout in a Research Combustor," NATO Advisory Group on Aerodynamics Research and Development, AGARD-CP-536, Paper Number 18, 1993.
8. S. P. Heneghan and S. Zabarnick, "Oxidation of Jet Fuels and the Formation of Deposits," *Fuel* **73**, 35 (1994).
9. M. D. Durbin and D. R. Ballal, "Studies of Lean Blowout in a Step Swirl Combustor," *Transactions of ASME, Journal of Gas Turbine and Power*, Vol. 118, pp. 72-78, Jan. 1996.
10. J. Blust, T. F. Williams, C. R. Martel, and V. R. Katta, "The Role of Buoyancy in Fuel Thermal Stability Studies," *AIAA Journal of Thermophysics and Heat Transfer*, Vol. 9, pp. 159-168, 1994.
11. S. Zabarnick, "Studies of Jet Fuel Thermal Stability and Oxidation Using a Quartz Crystal Microbalance and Pressure Measurements," *Industrial and Engineering Chemistry Research*, Vol. 33, pp.1348-1354, 1994.
12. J. Zelina and D. R. Ballal, "Combustion Studies in a Well Stirred Reactor," *AIAA Journal of Propulsion and Power*, Vol. 11, pp. 132-139, 1995.

13. F. Takahashi, W. J. Schmoll, and J. L. Dressler, "Characteristics of a Velocity-Modulated Pressure-Swirl Atomizing Spray Measured by the Phase-Doppler Method," *AIAA Journal of Propulsion and Power*, Vol. 11, pp. 955-963, 1995.
14. F. Takahashi, W. J. Schmoll, G. L. Switzer, and D. T. Shouse, "Structure of a Spray Flame Stabilized on a Production Engine Combustor Swirl Cup," *Proceedings of 25th Symposium (Int.) on Combustion*, The Combustion Institute, pp. 183-191, 1994.
15. F. Takahashi, W. J. Schmoll, and J. L. Dressler, "Characterization of a Velocity-Modulation Atomizer," *Reviews of Scientific Instruments*, Vol. 65, pp. 3563-68, 1994.
16. F. Takahashi, "Sooting Correlations for Premixed Combustion," *Physical & Chemical Aspects of Combustion: A Tribute to Irvin Glassman* (Eds. R. F. Sawyer and F. L. Dryer) Gordon & Breach, New York, NY, 1996.
17. F. Takahashi and V. R. Katta, "Numerical Experiments on the Vortex-Flame Interactions in a Jet Diffusion Flame," *AIAA Journal of Propulsion and Power*, Vol. 11, pp. 170-176, 1995.
18. S. Zabarnick and R. R. Grinstead, "Studies of Jet Fuel Additives Using a Quartz Crystal Microbalance and Pressure Monitoring at 140C," *Industrial and Engineering Chemistry Research*, Vol. 33, pp. 2771-77, 1994.
19. S. Zabarnick and R. R. Grinstead, "Studies of Jet Fuel Thermal Stability Using a Quartz Crystal Microbalance," PREPRINTS, *Division of Petroleum Chemistry*, American Chemical Society, pp. 51-57, 1994.
20. R. E. Kauffman, "Standard Test Method for Hydroperoxide Number of Aviation Turbine Fuels--An ASTM Standard," To appear in *Annual Book of the American Society of Testing and Materials (ASTM) Standards*, 1998.
21. S. Zabarnick and J. Zelina, "Chemical Kinetics of NO<sub>x</sub> Production in a Well Stirred Reactor," AIAA Paper No. 94-3828, *Proceedings of 29th Intersociety Energy Conversion Engineering Conference*, pp. 649-653, AIAA, Washington D.C., 1994.
22. M. D. Durbin and D. R. Ballal, "Optimizing the Combustion Performance of a Step Swirl Combustor," AIAA Paper No. 94-3825, *Proceedings of 29th Intersociety Energy Conversion Engineering Conference*, pp. 631-635, AIAA, Washington D.C., 1994.
23. J. Zelina, R. C. Striebich, and D. R. Ballal, "Pollutant Emissions Research Using a Well Stirred Reactor," AIAA Paper No. 94-3827, in *Proceedings of 29th Intersociety Energy Conversion Engineering Conference*, pp. 644-648, AIAA, Washington D.C., 1994.
24. M. D. Durbin and D. R. Ballal, "Studies of Combustion and Emissions in a Model Step Swirl Combustor," *Proceedings of the FACT Vol. 18*, pp. 17-21, *ASME (Int.) Joint Power Generation Conference*, New York, NY, 1994.

25. J. Zelina and D. R. Ballal, "Studies of Pollutant Emissions in a Well Stirred Reactor," *Proceedings of the FACT Vol. 18, pp. 12-16, ASME (Int.) Joint Power Generation Conference*, New York, NY, 1994.
26. S. P. Heneghan and R. E. Kauffman, "Analytic Tests and Their Relation to Jet Fuel Stability," *Proceedings of the 5th (Int.) Conference on the Stability and Handling of Liquid Fuels*, Vol. 1, pp. 29, Rotterdam, Netherlands, 1995.
27. S. P. Heneghan and L. P. Chin, "Autoxidation of Jet Fuels: Implications for Modeling and Thermal Stability," *Proceedings of the 5th (Int.) Conference on the Stability and Handling of Liquid Fuels*, Vol. 1, pp. 91, Rotterdam, Netherlands, 1995.
28. S. Zabarnick and R. Grinstead, "Studies of Jet Fuel Additives Using the Quartz Crystal Microbalance and Pressure Monitoring at 140C," *Proceedings of the 5th (Int.) Conference on the Stability and Handling of Liquid Fuels*, Vol. 1, pp. 275, Rotterdam, Netherlands, 1995.
29. K. E. Binns, G. L. Dieterle, and T. F. Williams, "System Evaluation of Improved Thermal Stability Jet Fuels," *Proceedings of the 5th (Int.) Conference on the Stability and Handling of Liquid Fuels*, Vol.1, pp. 401, Rotterdam, Netherlands, 1995.
30. W. A. Rubey, R. C. Striebich, M. D. Tissandier, and D. A. Tirey, "Gas Chromatographic Measurements of Trace Oxygen and Other Dissolved Gases in Thermally Stressed Jet Fuel," *Journal of Chromatographic Science*, Vol. 33, pp. 433-437, August, 1995.
31. F. Takahashi, M. D. Vangsness, and M. D. Durbin, "Stabilization of Hydrogen-Jet Diffusion Flames With and Without Swirl," *Transport Phenomenon In Combustion*, (S. H. Chan, Ed.) Vol. 1, pp. 593-604, Taylor & Francis, Washington D.C., 1996.
32. F. Takahashi, W. J. Schmoll, D. D. Trump, and L. P. Goss, "Vortex-Flame Interactions and Extinction of Turbulent Jet Diffusion Flames," *Proceedings of the 26th Symposium (Int.) on Combustion, The Combustion Institute*, pp. 145-152, 1996.
33. F. Takahashi and V. R. Katta, "Unsteady Extinction Mechanisms of Jet Diffusion Flames," *Proceedings of the 26th Symposium (Int.) on Combustion, The Combustion Institute*, pp. 1151-1160, 1996.
34. F. Takahashi, M. S. Anand, M. D. Vangsness, M. D. Durbin, and W. J. Schmoll, "An Experimental and Computational Study of Swirling Hydrogen Jet Diffusion Flames," *Transactions of ASME, Journal of Engineering for Gas Turbines and Power*, Vol. 119, pp. 305-314, 1997.
35. M. D. Durbin, M. D. Vangsness, D. R. Ballal, and V. R. Katta, "Study of Flame Stability in a Model Step Combustor," *Transactions of ASME, Journal of Engineering for Gas Turbines and Power*, Vol. 118, pp. 308-315, 1996.

36. S. Zabarnick, P. Zelesnik, and R. B. Grinstead, "Jet Fuel Deposition and Oxidation: Dilution, Materials, and Oxygen Effects," *Transactions of ASME, Journal of Engineering for Gas Turbines and Power*, Vol. 118, pp. 271-277, 1996.
37. J. S. Ervin, S. P. Heneghan, C. R. Martel, and T. F. Williams, "Surface Effects on Deposits from Jet Fuels," *Transactions of ASME, Journal of Engineering for Gas Turbines and Power*, Vol. 118, pp. 278-285, 1996.
38. J. Zelina and D. R. Ballal, "Combustor Stability and Emissions Research Using a Well Stirred Reactor," ASME Paper No. 95-GT-109, and *Transactions of ASME, Journal of Engineering for Gas Turbines and Power*, Vol. 119, pp. 70-75, 1997.
39. F. Takahashi, M. D. Vangsness, M. D. Durbin, and W. J. Schmoll, "Structure of Turbulent Hydrogen Jet Diffusion Flames with and without Swirl," *Transactions of ASME, Journal of Heat Transfer*, Vol. 118, pp. 877-884, 1996.
40. J. S. Ervin, S. P. Heneghan, T. F. Williams, and M. A. Hanchak, "Reduced Dissolved Oxygen and Jet Fuel Deposition," *Proceedings of the 30th Intersociety Energy Conversion Engineering Conference*, pp. 210-216, July 1995.
41. J. S. Ervin and T. F. Williams, "Dissolved Oxygen Concentration and Jet Fuel Deposition," *Industrial and Engineering Chemistry Research*, Vol. 35, pp. 899-904, 1996.
42. J. Zelina, J. Blust, and D. R. Ballal, "Combustion of Liquid Fuels in a Well Stirred Reactor," ASME Paper No. 96-GT-047, Presented at ASME Turbo Expo. '96, Birmingham, U.K., June 1996.
43. S. Zabarnick, P. Zelesnik, and S. Whitacre, "Silver Corrosion and Sulfur Detection using a Quartz Crystal Microbalance with Silver Electrode Surfaces," *Industrial and Engineering Chemistry Research*, Vol. 35, pp. 2576-2580, 1996.
44. S. P. Heneghan, S. Zabarnick, D. R. Ballal, and W. E. Harrison, III "JP-8+100: Development of a Thermally Stable Jet Fuel," *Transactions of ASME, Journal of Energy Resource Technology*, Vol. 118, pp. 170-179, October 1996.
45. S. Zabarnick, S. D. Whitacre, and P. Zelesnik, "Further Studies of JP-8+100 Additive Candidates in the QCM," PREPRINTS, Division of Petroleum Chemistry, Vol. 41, No. 2, pp. 438-441, March 1996.
46. J. S. Ervin, T. F. Williams, and V. R. Katta, "Global Kinetic Modeling of Aviation Fuel Fouling in Cooled Regions in a Flowing System," *Industrial and Engineering Chemistry Research*, Vol. 35, pp. 4028-4032, 1996.

47. S. P. Heneghan, S. Zabarnick, and D. R. Ballal, "Designing High Thermal Stability Jet Fuels for the 21st Century," *Proceedings of 31st Intersociety Energy Conversion Engineering Conference*, pp. 486-493, August 1996.
48. J. Zelina and D. R. Ballal, "Emissions Studies in a Well Stirred Reactor and Applications to Combustion Modeling," *Proceedings of FACT, Vol. 21, ASME (Int.) Joint Power Generation Conference*, pp. 255-263, October 1996.
49. G. J. Sturgess, A. L. Lesmerises, S. P. Heneghan, M. D. Vangsness, and D. R. Ballal, "Lean Blowout in a Research Combustor at Simulated Low Pressures," *Transactions of ASME, J. of Engineering for Gas Turbines and Power*, Vol. 118, pp. 773-781, 1996.
50. B. Beaver, R. DeMunshi, S. P. Heneghan, S. D. Whitacre, and P. Neta, "Model Studies Directed at the Development of New Thermal Oxidative Stability Enhancing Additives for Jet Fuels," *Energy and Fuels*, Vol. 11, pp. 396-408, 1997.
51. F. Takahashi and V. R. Katta, "A Numerical Study of a Methane Diffusion Flame over a Flat Surface," To appear in *Proceedings of the Second International Symposium on Scale Modeling*, 1998.
52. S. Zabarnick, "Pseudo-Detailed Chemical Kinetic Modeling of Antioxidant Chemistry for Jet Fuel Applications," *Energy and Fuels*, Vol. 12, pp. 547-553, 1998.
53. S. Zabarnick and S. D. Whitacre, "Aspects of Jet Fuel Oxidation," ASME paper NO. 97-GT-219, and *Transactions of ASME, Journal of Engineering for Gas Turbine and Power*, Vol. 120, pp. 519-525, 1998.
54. J. S. Ervin and S. P. Heneghan, "The Meaning of Activation Energy and Reaction Order in Autoaccelerating Systems," *Transactions of ASME, Journal of Engineering for Gas Turbine and Power*, Vol. 120, pp. 468-473.
55. R. E. Kauffman, "The Effects of Different Sulfur Compounds on Jet Fuel Oxidation and Deposition," *Transactions of ASME, J. of Engineering for Gas Turbines and Power*, Vol. 119, pp. 322-328, 1997.
56. S. P. Heneghan and W. E. Harrison, III, "JP-8 + 100: The Development of High Thermal Stability Jet Fuel," *Proceedings of the Sixth International Conference on Stability and Handling of Liquid Fuels*, Vancouver BC, Canada, Vol. 1, pp. 271-283, 1997.
57. S. P. Heneghan and M. D. Vangsness, "Additive Stability in JP-8—Metal Alloy Systems at Elevated Temperatures," *Proceedings of the Sixth International Conference on Stability and Handling of Liquid Fuels*, Vancouver BC, Canada, Vol. 1, pp. 285-293.
58. D. H. Kalt, "Evaluation of JP-8+100 Fuel Compatibility with Aircraft Fuel System Materials: The Effect of Detergent/Dispersant on Aircraft Materials," *Proceedings of the Sixth*

International Conference on Stability and Handling of Liquid Fuels, Vancouver BC, Canada,  
Vol. 1, pp. 251-269, 1997.

## Presentations

1. S. P. Heneghan, D. L. Geiger and E. M. Steward, "Analysis of Sulfur Containing Compounds by Gas Chromatography (GC) Atomic Emission Detection," PittCon 93, Atlanta, GA, March 1993.
2. R. C. Striebich, S. Zabarnick, and W. A. Rubey, "Determination of Jet Fuel Compositional Changes in Flowing Heated Tube Experiments," PittCon 93, Atlanta, GA, March 1993.
3. W. A. Rubey, S. L. Mazer, P. C. Hayes, and E. M. Steward, "Analysis of Turbine Engine Fuels and Complex Industrial Organic Mixtures Using a Multidimensional GC and GC-MS System," 24th Ohio Valley Chromatographic Symposium, Hueston Woods, OH, June 1993.
4. S. D. Anderson and W. A. Rubey, "The Identification of Sulfur-Containing Compounds in Jet Fuel Using Multidimensional Gas Chromatography with Mass Selective Detection," 24th Ohio Valley Chromatographic Symposium, Hueston Woods, OH, June 1993.
5. S. Zabarnick, "Studies of Jet Fuel Thermal Stability using a Quartz Crystal Microbalance and GC Analysis," A paper presented at the CRC Fuels Meeting, Alexandria, VA, April, 1993.
6. S. P. Heneghan and B. Grinstead, "Analysis of Hetero-Atom compounds in Jet Fuels," Ohio Valley Chromatography Symposium, Heuston Woods, OH, June 1993.
7. K. E. Binns, W. E. Harrison III, S. D. Anderson, and R. W. Morris, "High Heat Sink Fuels for Improved Aircraft Thermal Management," A paper presented at the International Conference on Environmental Systems, Colorado Springs, CO, Reprint in *Transactions of the Society of Automotive Engineers, Journal of Aerospace*, 1994.
8. F. Takahashi, W. J. Schmoll, and M. D. Vangsness, "Structure of a Spray Flame Stabilized on a Production Engine Combustor Swirl Cup by Phase-Doppler Anemometer," Presented at the Eastern States Section/The Combustion Institute Meeting, October 1993.
9. M. D. Durbin, M. D. Vangsness, and F. Takahashi, "Stability of Hydrogen/Air Double-Concentric Jet Diffusion Flames with and without Swirl," Presented at the Eastern States Section/The Combustion Institute Meeting, October 1993.
10. S. P. Heneghan, S. Zabarnick, B. R. Grinstead, and D. L. Geiger, "Analysis of Fuel Deposit Precursors using Gas Chromatography/ Atomic Emission Detection," Federation of Analytic Chemistry and Spectroscopy Societies, Detroit, MI, October 1993.
11. S. Zabarnick, "Thermal Stability Measurements of Jet Fuel Using a Quartz Crystal Microbalance," ASTM D02 Meeting on Petroleum Products and Lubricants, Dallas, TX, December 1993.



12. R. E. Kauffman, "Development of a Rapid, Portable Hydroperoxide Test for Jet Fuels," ASTM D02 Meeting on Petroleum Products and Lubricants, Dallas, TX, December 1993.
13. R. C. Striebich and W. A. Rubey, "A Convenient Method for Analyzing Dissolved Oxygen in Hydrocarbon Matrices Using Gas Chromatography-Mass Spectrometry," Presented at the American Chemical Society Conference on Fuel Thermal Stability, San Diego, CA, March, 1994.
14. R. E. Kauffman, "Development of a Rapid, Portable Hydroperoxide Test for Jet Fuels," Presented at the American Chemical Society Conference on Fuel Thermal Stability, San Diego, CA, March, 1994.
15. S. Zabarnick and B. Grinstead, "Studies of Jet Fuel Thermal Stability using a Quartz Crystal Microbalance," Presented at the American Chemical Society Conference on Fuel Thermal Stability, San Diego, CA, March, 1994.
16. S. P. Heneghan, "Global Oxidation of Jet Fuels: Determining and Understanding the Parameters," Presented at The American Chemical Society Symposium on Autooxidation of Distillate Fuels, San Diego, CA, March, 1994.
17. P. H. Taylor, R. C. Striebich, L. Ostruska, and B. Dellinger, "Auto-Oxidation of N-Decane/Aniline/Thiophenol Mixtures," Presented at The American Chemical Society Symposium on Autooxidation of Distillate Fuels, San Diego, CA, March, 1994.
18. R. E. Kauffman, "Effect of Different Sulfur Compounds on the Deposition and Oxidation Mechanism of Hydrotreated Jet Fuels," Coordinating Research Council, Fuel Chemistry Group, Washington, D.C., April 1994.
19. R. E. Kauffman, "New, Rapid Techniques for Determining Hydroperoxide Contents, Oxidation Stability, and Thermal Stability of Jet Fuels," Presented at the 39th ASME (Int.) Gas Turbine Conference, Hague, Netherlands, June 1994.
20. R. C. Striebich and W. A. Rubey, "Surface Adsorption Studies Using Inverse Gas Chromatography and Inverse Liquid Chromatography," Presented at The American Chemical Society Symposium on Autooxidation of Distillate Fuels, San Diego, CA, March, 1994.
21. L. P. Chin, V. R. Katta, and S. P. Heneghan, "Computer Modeling of Deposits Formed in Jet Fuels," Presented at The American Chemical Society Symposium on Autooxidation of Distillate Fuels, San Diego, CA, March, 1994.
22. D. L. Geiger, R. Grinstead, and S. Zabarnick, "The Analysis of Thermally Stressed and Unstressed Jet Fuels for Sulfur, Nitrogen, and Oxygen by Solid Phase Extraction and Gas Chromatography-Atomic Emission Detection," Presented at the Society for Applied Spectroscopy, Ohio State University, Columbus, OH, February 1994.

23. R. E. Kauffman, "Oxidation Stability of California Diesel Engine Fuels," California State Legislature, Sacramento, CA, May 1994.
24. F. Takahashi, W. J. Schmoll, and J. L. Dressler, "Characterization of a Velocity-Modulation Atomizer," A paper for presentation at The Central States Section Meeting, The Combustion Institute, Madison, WI, June 1994.
25. M. Vangsness and W. J. Schmoll, "Applications of a Neural Net Simulator to CARS Temperature Measurements," A paper presented at The Central States Section Meeting, The Combustion Institute, Madison, WI, June 1994.
26. S. P. Heneghan, D. L. Geiger, and S. L. Locklear, "Quantifying Mass Transfer of Jet Fuels by Supercritical Fluid ( $\text{CO}_2$ ) Extraction using Gas Chromatography and Atomic Emissions Detection," Ohio Valley Chromatographic Symposium, Heuston Woods, OH, June 1994.
27. F. Takahashi, M. D. Durbin, M. D. Vangsness, and W. J. Schmoll, "Structure of the Stabilizing Region of Hydrogen Jet Diffusion Flames," Poster presentation at The 25th Symposium (Int.) on Combustion, The Combustion Institute, July, 1994.
28. J. Zelina, R. C. Striebich, J. W. Blust, and L. F. Truett, III, "Studies of Halon Decomposition in the Well Stirred Reactor," A paper for presentation at The Central States Section Meeting, The Combustion Institute, Madison, WI, June 1994.
29. G. L. Dieterle and K. E. Binns, "Evaluation of High Thermal Stability Fuels for Future Aircraft," AIAA Paper No. 94-3171, presented at 30th AIAA/ASME/SAE/ASEE Joint Propulsion Conference, June 1994.
30. J. Zelina and D. R. Ballal, "Combustion and Emissions Studies Using a Well Stirred Reactor," AIAA Paper No. 94-2903, presented at 30th AIAA/ASME/SAE/ASEE Joint Propulsion Conference, June 1994.
31. M. D. Durbin and D. R. Ballal, "Characteristics of Swirl Flames in a Step Combustor," AIAA Paper No. 94-3272, presented at 30th AIAA/ASME/SAE/ASEE Joint Propulsion Conference, June 1994.
32. R. Grinstead, "Analysis of Jet Fuel Extracts and Deposits," Presented at the Coordinating Research Council Meeting, Washington, D.C., April 1994.
33. R. C. Striebich and W. A. Rubey, "A Convenient Method for Analyzing Dissolved Oxygen in Hydrocarbon Matrices Using Gas Chromatography-Mass Spectrometry," Submitted to *Journal of Energy and Fuels*, American Chemical Society, Washington, D.C. August 1994.
34. F. Takahashi, "Regression Analyses of the Soot Threshold Data for Premixed Combustion," Paper for presentation at the Eastern States Meeting, The Combustion Institute, Clearwater Beach, FL, December, 1994.

35. G. L. Dieterle and K. E. Binns, "Extended Duration Thermal Stability Test of Improved Thermal Stability Jet Fuel," ASME Paper No. 95-GT-69 presented at the ASME Turbo Expo '95, Houston, TX, June 1995.
36. R. E. Kauffman, "The Effect of Different Sulfur Compounds on the Oxidation and Deposition Mechanisms of Jet Fuel," ASME Paper No. 95-GT-222 for presentation at the ASME Turbo Expo '95, Houston, TX, June 1995.
37. S. P. Heneghan, D. R. Ballal, W. E. Harrison III, and H. C. Mongia, "Advanced Jet Fuels--JP-4 to JP-8 and Beyond," ASME Paper No. 95-GT-223, for presentation at the ASME Turbo Expo '95, Houston, TX, June 1995.
38. F. Takahashi, W. J. Schmoll, D. D. Trump, and L. P. Goss, "Vortex-Flame Interactions and the Local Extinction of Turbulent Jet Diffusion Flames," AIAA Paper No. 95-0139, Presented at 33rd Aerospace Sciences Meeting, Reno, NV, January 1995.
39. J. S. Ervin, R. E. Kauffman, and D. H. Kalt, "Effects of Thermal Stressed Jet Fuels on O-Rings," AIAA Paper No. 95-0287, Presented at 33rd Aerospace Sciences Meeting, Reno, NV, January 1995.
40. D. J. Pestian, J. P. Bons, R. B. Rivir, and C. D. MacArthur, "Effect of Unsteadiness on Film Cooling Effectiveness," AIAA Paper No. 95-0306, Presented at 33rd Aerospace Sciences Meeting, Reno, NV, January 1995.
41. F. Takahashi, M. D. Vangsness, and W. J. Schmoll, "Structure of the Stabilizing Region of the Methane Jet Diffusion Flames," Central States Section Meeting, The Combustion Institute, San Antonio, TX, April 1995.
42. J. Zelina and D. R. Ballal, "Model Predictions of Pollutant Emissions in a Well Stirred Reactor," ASME Paper No. 95-GT-48, to be presented at ASME COGEN Turbo Power 95 Conference, Vienna, Austria, Aug. 23-26, 1995.
43. J. S. Ervin, S. P. Heneghan, T. F. Williams, and M. A. Hanchak, "Effects of Reduced Dissolved Oxygen Concentration on Jet Fuel Deposit Formation," Presented at the American Chemical Society Symposium on Coke Formation and Mitigation, Chicago, IL, Aug. 1995.
44. F. Takahashi and V. R. Katta, "Numerical Experiments on the Local Extinction of Jet Diffusion Flames," Presented at the 15th International Colloquium on the Dynamics of Explosions and Reactive Systems, Boulder, CO, August 1995.
45. F. Takahashi, M. D. Durbin, and M. D. Vangsness, "Stabilization of Hydrogen Jet Diffusion Flames With and Without Swirl," Presented at the Eighth International Symposium on Transport Phenomenon in Combustion, San Francisco, CA, July 1995.

46. F. Takahashi, "Structure and Stability of Turbulent Diffusion Flames," Invited Lecture, Thermal energy and Combustion Department, National Institute for Resources and Environment, Ministry of International Trade and Industry, Tsukuba, Japan, August 1995.
47. F. Takahashi, "Vortex-Flame Interaction and Stability of Jet Diffusion Flames," Invited Lecture, Department of Chemical System Engineering, The University of Tokyo, Tokyo, Japan, August 1995.
48. F. Takahashi, "Vortex-Flame Interaction and the Local Extinction of Jet Diffusion Flames," Invited Lecture, Department of Mechanical Engineering, Keio University, Yokohama, Japan, August 1995.
49. R. Striebich, W. Rubey, and R. Grinstead, "Analysis of Halon-1301 Combustion Products Using GC-MS in a Wide- Bore Porous Layer Open Tubular (PLOT) Column," presented at the 17th International Symposium on Capillary Chromatography and Electrophoresis, Wintergreen, VA, May 1995.
50. R. Striebich, R. Grinstead, J. Zelina, and J. Blust, "Studies of Halon-1301 Decomposition in a Well Stirred Reactor," presented at the 4th International Congress on Toxic Combustion Byproducts, Berkeley, CA, June 1995.
51. S. Zabarnick and P. Zelesnik, "Studies of Jet Fuel Thermal Stability and Oxidation Applications of QCM," presented at the CRC-Aviation Group Meeting, Alexandria, VA, April 1995.
52. S. Zabarnick, P. Zelesnik, and R. Grinstead, "Jet Fuel Deposition and Oxidation: Dilution, Materials, Oxygen, and Temperature Effects," presented at the 21st Annual Mini-Symposium on Aerospace Science and Technology, Dayton, OH, March 1995.
53. R. Grinstead, R. Striebich, J. Blust, and J. Zelina, "Analytical Evaluation of Halon Combustion by FTIR and GC-MS," presented at the 21st Annual Mini-Symposium on Aerospace Science and Technology, Dayton, OH, March 1995.
54. F. Takahashi, J. W. Blust, J. Zelina, R. C. Striebich, and C. W. Frayne, "Soot Threshold Measurements Using a Well Stirred Reactor," Presented at the Eastern States Section Meeting, The Combustion Institute, Worcester, MA, October, 1995.
55. J. S. Ervin, T. F. Williams, S. P. Heneghan, and S. Zabarnick, "The Effects of Dissolved Oxygen Concentration, Fractional Oxygen Consumption, and Additives on JP-8 Thermal Stability," ASME Paper No. 96-GT-132, Presented at the ASME Turbo Expo., Birmingham, U.K., June 1996.
56. D. G. Holmberg and D. Pestian, "Wall Jet Turbulent Boundary Layer Heat Flux, Velocity, Temperature Spectra, and Time Scales," ASME Paper No. 96-GT-529, Presented at the ASME Turbo Expo., Birmingham, U.K., June 1996.

57. D. Pestian, R. B. Rivir, S. Gogineni, and D. Trump, "PIV Measurements of Periodically Forced Flat Plate Film Cooling Flows With High Freestream Turbulence," ASME Paper No. 96-GT-236, Presented at the ASME Turbo Expo., Birmingham, U.K., June 1996.
58. F. Takahashi, M. D. Vangsness, M. D. Durbin, and W. J. Schmoll, "Structure of Turbulent Hydrogen Jet Diffusion Flames With and Without Swirl," presented at ASME (Int.) Mechanical Engineering Congress and Exposition, Paper No. HTD-317-2, pp. 183-193, San - Francisco, CA, November 1995.
59. F. Takahashi and V. R. Katta, "Numerical Experiments on the Local Extinction of Jet Diffusion Flames," AIAA Paper No. 96-0521, presented at the 34th Aerospace Sciences Meeting, Reno, NV., January 1996.
60. D. Pestian, R. B. Rivir, S. Gogineni, and L. P. Goss, "PIV Measurements of Flat Plate Film Cooling Flows With High freestream Turbulence," AIAA Paper No. 96-0617, presented at the 34th Aerospace Sciences Meeting, Reno, NV., January 1996.
61. S. P. Heneghan, S. Zabarnick, D. R. Ballal, and W. E. Harrison III, "JP-8+100: The Development of High Thermal Stability Jet Fuel," AIAA Paper No.96-0403, presented at the 34th Aerospace Sciences Meeting, Reno, NV., January 1996.
62. J. S. Ervin, T. F. Williams, and V. R. Katta, "The Effects of JP-8 Thermal Stability Additives on Deposition in Heated and Cooled Regions in a Flowing System," Presented at the ACS Symposium on Structure of Jet Fuels, New Orleans, LA, March 1996.
63. S. Zabarnick, S. D. Whitacre, and P. Zelesnik, "Further Studies of JP-8 + 100 Additive Candidates in the QCM," Presented at the ACS Symposium on Structure of Jet Fuels, New Orleans, LA, March 1996.
64. S. P. Heneghan, T. F. Williams, S. D. Whitacre, and J. S. Ervin, "The Effects of Oxygen Scavenging on Jet Fuel Thermal stability," Presented at the ACS Symposium on Structure of Jet Fuels, New Orleans, LA, March 1996.
65. Binns and G. L. Dieterle, "Evaluation of the JP-8+100 Additive Candidates in the Extended Duration Thermal stability Test System," Presented at the American Chemical Society Symposium on Structure of Jet Fuels, New Orleans, LA, March 1996.
66. F. Takahashi and V. R. Katta, "A Numerical Study of the Stability of Methane Jet Diffusion Flames," Presented at the Central States Section, The Combustion Institute, St. Louis, MO, May 1996.
67. F. Takahashi, W. J. Schmoll, M. D. Vangsness, and V. R. Katta, "The Stabilizing Region of Methane-Jet Diffusion Flames," Poster presentation at the 26th International Symposium on Combustion, Naples, Italy, July 1996.

68. J. J. Schauer and D. J. Pestian, "Film Cooling Heat Transfer With High Free Stream Turbulence," Presented at the ASME (Int.) Mechanical Engineering Congress and Exhibition, Atlanta, GA, November 17-22, 1996.
69. F. Takahashi, M. D. Vangsness, M. D. Durbin, and W. J. Schmoll, "LDV and CARS Measurements in Swirling and Nonswirling Turbulent Jet Diffusion Flames," Proceedings of the International Workshop on Measurement and Computation of Turbulent Nonpremixed Flames, Naples, Italy, July 1996 (available on the internet: <http://www.ca.sandia.gov/tdf/Proceedings.html>; <http://www.ca.sandia.gov/tdf/DataSums/TakahashiH2.html>).
70. F. Takahashi and V. R. Katta, "Further Analysis of the Stabilizing Region of Methane Jet Diffusion Flames," Eastern States Section Meeting, The Combustion Institute, Hilton Head, S.C., December 1996.
71. J. S. Ervin, S. P. Heneghan, S. Zabarnick, and W. E. Harrison III, "Development of Advanced Jet Fuels: Modeling Aspects," ASME (Int.) Mechanical Engineering Congress and Exhibition, Atlanta, GA, November, 1996.
72. J. S. Ervin and S. P. Heneghan, "The Meaning of Activation Energy and Reaction Order in Autoaccelerating Systems," ASME Paper No. 97-GT-224, presented at the ASME Turbo Expo., Orlando, FL, June 1997.
73. J. S. Ervin, T. F. Williams, and S. Zabarnick, "Modeling of Jet Fuel Oxidation at Low Temperature," AIAA Paper No. 97-0272, 35th AIAA Aerospace Sciences Meeting, Reno, NV, January 1997.
74. J. W. Blust, M. G. Getz, and S. Zabarnick, "Probe Design Optimization for the Well Stirred Reactor," AIAA Paper No. 97-0907, 35th AIAA Aerospace Sciences Meeting, Reno, NV, January 1997.
75. G. L. Dieterle and K. E. Binns, "System Evaluation of JP-8+100 Additives at High Bulk Temperature," ASME Paper No. 97-GT-071, presented at the ASME Turbo Expo., Orlando, FL, June 1997.
76. D. H. Kalt, "Evaluation of JP-8+100 Fuel Compatibility with Aircraft Fuel Systems Materials," Presented at the ASME Turbo Expo., Orlando, FL, June 1997.
77. F. Takahashi and V. R. Katta, "A Numerical Investigation of the Stabilizing Mechanism of Methane Jet Diffusion Flame," AIAA Paper No. 97-0251, 35th AIAA Aerospace Sciences Meeting, Reno, NV, January 1997.
78. F. Takahashi and V. R. Katta, "A Numerical Analysis of a Methane Diffusion Flame over a Flat Plate," To be presented at the Central States Section Meeting, The Combustion Institute, Point Clear, AL, April 1997.

79. S. Zabarnick, "UDRI Contributions to the JP-8+100 Program," JP-8+100 Program Review, WPAFB, OH, March 1997.
80. S. P. Heneghan, S. Zabarnick, and D. R. Ballal, "Designing High Thermal Stability Jet Fuels for the 21<sup>st</sup> Century," presented at the 31<sup>st</sup> Intersociety Energy Conversion Engineering Conference, Washington DC, August 1996.
81. R. C. Striebich and B. Ohler, "Surface Adsorption of Jet Fuel Metal Deactivator using Inverse Liquid Chromatography," presented at the Ohio Valley Chromatography Symposium, Hueston Woods, OH, June 1997.
82. M. Getz, J. Blust, J. M. Calo, T. Miller, J. O. Ballenthin, and R. Striebich, "Modeling of the Response of a Well Stirred Combustor to the Injection of Fire Suppressants," Presented at *The 5<sup>th</sup> International Congress on Toxic Combustion Byproducts*, Dayton, OH, June 1997.
83. J. O. Ballenthin, T. Miller, J. M. Calo, Striebich, J. Blust, and M Getz, "Free-Jet, Molecular Beam Mass Spectrometer System for Monitoring the Gas Phase Composition in a Well Stirred Reactor," presented at *The 5<sup>th</sup> International Congress on Toxic Combustion Byproducts*, Dayton, OH, June 1997.
84. J. M. Calo, J. O. Ballenthin, T. Miller, Striebich, J. Blust, and M Getz, "Transient Studies of the Effects of Fast Pulse Injections of Fire Suppressants into the Well Stirred Reactor," presented at *The 5<sup>th</sup> International Congress on Toxic Combustion Byproducts*, Dayton, OH, June 1997.
85. F. Takahashi and V. R. Katta, "A Numerical Study of a Methane Diffusion Flame Over a Flat Plate," Presented at the Second International Symposium on Scale Modeling, Lexington, KY, June 1997.
86. S. Zabarnick and S. D. Whitacre, "Aspects of Jet Fuel Oxidation," ASME Paper No. 97-GT-219, Presented at the ASME Turbo Expo, '97, Orlando, FL, June 1997.
87. R. E. Kauffman, "Simple Analytical Techniques to Determine the Dispersal Capacity and Metal Deactivator Additive Concentration of JP-8 + 100 and ther jet Fuels," ASME Paper No. 97-GT-77, Presented at the ASME Turbo Expo, '97, Orlando, FL, June 1997.
88. W. A. Rubey, R. C. Striebich, and S. D. Anderson, "Water Measurement Techniques: Analysis for Dissolved and Total Water in Turbine Engine Fuels," Presented at the JP-8 + 100 Program Review Conference, WPAFB, OH, March 1997.

## UDRI Reports

1. F. Takahashi, M. D. Vangsness, and M. D. Durbin, "LDV Measurements in Swirling and Non-Swirling Coaxial Turbulent Air Jets--No. 5: 45 degree swirler, 100 m/s," University of Dayton Technical Report, UDR TR 93-22, May 1993.
2. F. Takahashi, M. D. Vangsness, and M. D. Durbin, "LDV Measurements in Swirling and Non-Swirling Coaxial Turbulent Air Jets--No. 6: 45 degree swirler, 25 m/s," University of Dayton Technical Report, UDR TR 93-23, June 1993.
3. F. Takahashi, M. D. Vangsness, and M. D. Durbin, "LDV Measurements in Swirling and Non-Swirling Coaxial Turbulent Air Jets--No. 7: 60 degree swirler, 25 m/s," University of Dayton Technical Report, UDR TR 93-24, July 1993.
4. F. Takahashi, M. D. Durbin, and M. D. Vangsness, "LDV Measurements in Swirling and Non-Swirling Coaxial Turbulent Hydrogen Jet Diffusion Flames--No. 1: No Swirl, 25 m/s," University of Dayton Technical Report, UDR TR 93-88, September 1993.
5. T. F. Williams, C. R. Martel, and J. W. Blust, "Studies of Thermal Stability of Jet Fuels--Volume I: Experimental Work," University of Dayton Technical Report, UDR TR 94-10, January 1994.
6. T. F. Williams, C. R. Martel, and J. W. Blust, "Studies of Thermal Stability of Jet Fuels--Volume II: Data Sets," University of Dayton Technical Report, UDR TR 94-11, January 1994.
7. S. P. Heneghan, R. R. Grinstead, R. C. Striebich, and S. Zabarnick, "Jet Fuel Thermal Stability and Analytic Test Data," University of Dayton Technical Report, UDR TR 94-20, February 1994.
8. S. Zabarnick, "Evaluation of Jet Fuels and Jet Fuel Additives Using the Quartz Crystal Microbalance and Pressure Measurements," University of Dayton Technical Report, UDR TR 94-63, March 1994.
9. R. Grinstead, "Evaluation of JP-8+100 Additives by the Isothermal Corrosion Oxidation Test and the Microcarbon Residue Test," University of Dayton Technical Report, UDR TR 94-85, May 1994.
10. F. Takahashi, M. D. Vangsness, M. D. Durbin, and W. J. Schmoll, "CARS Temperature Measurements in Swirling and Non-Swirling Coaxial Turbulent Hydrogen Jet Diffusion Flames," University of Dayton Technical Report, UDR TR 94-89, June 1994.
11. F. Takahashi, M. D. Durbin, W. J. Schmoll, and M. D. Vangsness, "LDV Measurements in Swirling and non-Swirling Coaxial Turbulent Hydrogen Jet Diffusion Flames--No. 2: No Swirl, 100 m/s," University of Dayton Technical Report, UDR TR 94-115, July 1994.



12. F. Takahashi, M. D. Durbin, W. J. Schmoll, and M. D. Vangsness, "LDV Measurements in Swirling and non-Swirling Coaxial Turbulent Hydrogen Jet Diffusion Flames--No. 3: 30-degree Swirl, 100 m/s," University of Dayton Technical Report, UDR TR 94-116, August 1994.
13. F. Takahashi, M. D. Durbin, W. J. Schmoll, and M. D. Vangsness, "LDV Measurements in Swirling and non-Swirling Coaxial Turbulent Hydrogen Jet Diffusion Flames--No. 4: 45-degree Swirl, 100 m/s," University of Dayton Technical Report, UDR TR 94-117, September 1994.
14. S. Zabarnick, P. Zelesnik, and S. D. Whitacre, "Evaluation of Jet Fuels and Jet Fuel Additives Using the Quartz Crystal Microbalance and Pressure Measurements-Part II," University of Dayton Technical Report, UDR TR 95-98, November 1995.
15. D. Kalt, "Fuel and Fuel System Materials Compatibility Test program for a JP-8+100 Fuel Additive: Vol 1: Betz/Dearborn-8Q462 Thermal Stability Additive Package," University of Dayton Technical Report No. UDR TR 97-01, January 1997.
16. S. Zabarnick, S. D. Whitacre, and M. S. Mick, "Evaluation of Jet Fuels and Jet Fuel Additives Using the Quartz Crystal Microbalance and Pressure Measurements: Part III" University of Dayton Technical Report No. UDR TR 97-108, June 1997.